

SERIES

Forum Umwelttechnik und Wasserbau: vol. 27

Series Editors: Markus Aufleger, Anke Bockreis, Wolfgang Rauch

innsbruck university press



Johannes Kammerlander

**Long-Term Evolution of Bed Load Transport in
Steep Mountain Streams and its Link with the
Supply of Mobile Sediment**

Field data evidence, experimental insights and
computational improvements

Johannes Kammerlander

Institut für Infrastruktur, Arbeitsbereich Wasserbau

Dissertation, Fakultät für Technische Wissenschaften, Universität Innsbruck

Betreuer / Erstbegutachter:

Univ.-Prof. Dr.-Ing. habil. Markus Aufleger

Arbeitsbereich Wasserbau, Leopold-Franzens-Universität Innsbruck

Zweitbegutachter:

Dr. habil. Alain Recking

UR Érosion torrentielle, neige et avalanches, Irstea

Die Dissertation wurde im Februar 2017 an der Fakultät für Technische Wissenschaften der Leopold-Franzens-Universität Innsbruck eingereicht. Die vorliegende Buchversion unterscheidet sich von der Originalarbeit im Format und geringfügig auch im Text. Alle inhaltlichen Änderungen sind entsprechend ausgewiesen.

Die wissenschaftliche Ausarbeitung dieser Dissertation erfolgte zu einem großen Teil im Rahmen von zwei drittmittelfinanzierten Forschungsprojekten. Die Daten und Auswertungen des ersten Themenblocks (Kapitel B) sind Teil des Forschungsprojekts *DevoBeTA-CC* (B286218), welches durch das Förderprogramm *Austrian Climate Research Programme* (ACRP) vom Klima- und Energiefonds finanziert ist. Im zweiten Themenblock (Study E in Kapitel C) stammen die Daten aus dem Forschungsprojekt *Bedload mobility at steep slopes*, gefördert von der Alpinen Forschungsstelle Obergurgl der Universität Innsbruck.

Diese Publikation wurde mit finanzieller Unterstützung des Vizerektorats für Forschung der Leopold-Franzens-Universität Innsbruck gedruckt.

© innsbruck university press, 2018

Universität Innsbruck

1. Auflage

Alle Rechte vorbehalten.

www.uibk.ac.at/iup

ISBN 978-3-903187-08-5

Danksagung

Diese Arbeit ist das nachträgliche Resultat einer sehr schönen Zeit am Arbeitsbereich Wasserbau der Universität Innsbruck. Ein herzliches Danke an alle die mich in dieser intensiven Zeit begleiteten und mir freundschaftlich, kollegial oder fachlich zur Seite standen!

Ein ganz großer Dank gebührt meinem Doktorvater Prof. Markus Aufleger. Es war für mich ein Glücksfall, dass ich nach Abschluss meiner Diplomarbeit an der Universität für Bodenkultur in Wien mit dem Arbeitsbereich Wasserbau in Kontakt gekommen bin. Prof. Markus Aufleger hat mich in sein Team aufgenommen und er bot mir die Möglichkeit das Vorhaben „Dissertation“ überhaupt erst anzugehen.

Ein großer Dank geht auch an die beiden Ass.-Profs. Stefan Achleitner und Bernhard Gems. Zu Beginn meiner Anstellung hatte Stefan Achleitner die vage Idee von einem Forschungsprojekt „Geschiebetransport in Hochgebirgsbächen“. Mit großem Interesse nahm ich diese Idee auf und wir konnten gemeinsam einen Projektantrag erarbeiten der schlussendlich auch genehmigt wurde. Ich danke deshalb dem Klima- und Energiefonds für die Finanzierung unseres Vorhabens. Mit Bernhard Gems verbindet mich eine mehrjährige Bürogemeinschaft, die sowohl fachlich als auch freundschaftlich geprägt war. Bei reichlich Kaffee und dem allmorgendlichen Kipferl haben wir viel diskutiert und sind dabei auf zahlreiche Forschungsfragen gestoßen. Einigen davon konnten wir in kleinen Forschungsprojekten auch näher nachgehen. Ich danke der Universität Innsbruck, im Speziellen der AFO, für die Bereitstellung der dafür notwendigen Geldmittel.

Für die Ausarbeitung einer Dissertation benötigt man neben reichlich Motivation zu meist auch Messdaten. Der vorliegenden Arbeit liegen sehr, sehr viele Messdaten zu grunde, wobei nur ein Teil davon auch von mir erhoben wurde. Ich bedanke mich bei den einstigen Diplomanden Daniel Kößler, Bernhard Eichner und Bernd Steidl für die gewissenhafte Bearbeitung von Labor- und Feldversuchen. Die daraus gewonnenen Messdaten sind ein wesentlicher Teil meiner Doktorarbeit. Des Weiteren bedanke ich mich bei dem Tiroler Wasserkraftbetreiber TIWAG für die Bereitstellung von operativen Aufzeichnungen und das Ermöglichen von zusätzlichen Messungen an deren Wasserfassungen. Ich hoffe mit dieser Arbeit und den darin enthaltenen Auswertungen etwas an die Verantwortlichen bei der TIWAG zurückgeben zu können.

I'd also like to thank Mr. Alain Recking for taking the time to carefully read, comment and evaluate this thesis. Mr. Recking is an expert in the scientific field of bed load transport and he gave me many valuable hints how to improve the dissertation.

Schlussendlich ist eine Dissertation auch zeitintensiv und das bekommen häufig die zu spüren, die einem am Nächsten sind. Dies gilt umso mehr, wenn die Dissertation neben der regulären Arbeit verfasst wird. Ich bedanke mich bei meiner Freundin Heidi für die Geduld und das Verständnis, die oftmals mehr als notwendige Ablenkung und die entgegengesetzte Liebe. Ich bedanke mich auch bei meinen Eltern Hubert und Brigitte, dass sie mir diese Ausbildung ermöglichten und mir stets mit vielen kleinen Ratschlägen zur Seite standen.

Vielen Dank!

Innsbruck, Dezember 2017

KURZFASSUNG

Kleine Hochgebirgsbäche sind bedeutende Sedimentlieferanten für die alpinen Talflüsse und beeinflussen deren Geschiebehaushalt und dadurch auch deren morphologischen und ökologischen Zustand. Allerdings ist wenig zu den Geschiebemengen von Hochgebirgsbächen bekannt. Die gegenständliche Dissertation befasst sich mit dem Geschiebehaushalt von kleinen und zumeist steilen Hochgebirgsbächen. Es geht dabei um den Geschiebetransport in hydrologischen Normaljahren; der Geschiebetransport während extremer Hochwassereignisse oder Murgängen wird nicht behandelt.

Die Arbeit ist in zwei übergeordnete Abschnitte (*Kapitel B* und *C*) gegliedert und jeder Abschnitt besteht aus in sich geschlossenen, aber einander abgestimmten Untersuchungen (*Studies*).

Der erste Abschnitt (*Kapitel B*) nähert sich dem Thema mit einer großen Palette an Messdaten. Es handelt sich dabei um (i) lange Zeitreihen von Jahresgeschiebefrachten von 20 Hochgebirgsbächen der Nordtiroler Zentralalpen (*Study A*), (ii) Zeitreihen von Geschiebetransportraten (zeitliche Auflösung von 15 min) aus zwei (*Study B* und *Study D*) und (iii) Feldmessdaten zu den Transportraten und deren Korngrößenverteilung aus drei dieser 20 Bäche (*Study C*).

Die *Study A* geht der Frage nach, ob es einen statistischen Zusammenhang zwischen dem Geschiebehaushalt und topografischen Parametern der Einzugsgebiete gibt. Die Ergebnisse zeigen einen linearen Zusammenhang zwischen der mittleren Jahresgeschiebefracht und der Einzugsgebietsgröße und eine exponentielle Abhängigkeit zur Vergletscherung. Es wird eine empirische Formel vorgestellt, die eine Abschätzung der mittleren Jahresgeschiebefracht für unbeobachtete Einzugsgebiete mit vergleichbarer Gebietscharakteristik erlaubt. Ein praktisches Anwendungsbeispiel findet sich in *Kapitel D Conclusion*. Neben der räumlichen Variabilität weisen die Jahresgeschiebefrachten auch eine starke zeitliche Variabilität auf. Die Verteilungen sind durchwegs rechtsschief, was einem häufigen Vorkommen von Jahren mit relativ geringen Frachten und einem seltenen Vorkommen von ganz großen Frachten entspricht. Hierbei ist die Variabilität der Jahresgeschiebefrachten nicht allein auf die jahresweise unterschiedlichen Abflussverhältnisse zurückzuführen. So wird in trockenen Jahren verhältnismäßig mehr Geschiebe transportiert (höhere Transporteffizienz) als in feuchten. Die Größenordnung der Jahresgeschiebefracht scheint demnach vor allem durch die jährlich begrenzte Verfügbarkeit von feinem Geschiebe reguliert zu sein und weniger durch den Jahreswasserabfluss. Ein alleiniger Zusammenhang zwischen Abfluss und Geschiebetransport ist in den untersuchten Hochgebirgsbächen demnach nicht gegeben.

Auf der Grundlage von mehrjährigen Geschiebetransport- und Abflussganglinien von zwei Hochgebirgsbächen konnte die zeitliche Variabilität des Geschiebetransports näher untersucht werden (*Study B*). Der Zusammenhang zwischen Geschiebetransport und Abfluss ist zwar deutlich erkennbar, die Schwankungsbreite ist allerdings enorm und umfasst rund vier Größenordnungen. Die stärksten Schwankungen treten bei geringen bis mittleren Abflussverhältnissen auf, also in jenem Abflussspektrum in dem sich das transportierte Geschiebe beinahe ausschließlich aus feinem Sediment zu-

sammensetzt. Zudem zeigen sich auch zeitliche Unterschiede in der Geschiebetransport-Abfluss Beziehung. Die Ursache dieser großen Schwankungen liegt in der zeitlich veränderlichen Geschiebeverfügbarkeit. Es handelt sich dabei um die Menge an feinem Geschiebe, welches aus etwaigen Geschiebeherden mobilisiert und entlang dem Bachlauf transportiert wird. Je nach Abflussursprung (Schneeschmelze, Gletscherschmelze, Niederschlag) werden Geschiebeherde einmal mehr und einmal weniger aktiviert. An einem der beiden Bäche ist die primäre Sedimentquelle das Gletschervorfeld, was eine starke Mobilisierung während der Gletscherschmelze, also im Spätsommer, vermuten lässt. Dies bestätigt sich auch in den Messwerten: es zeigt sich darin eine alljährliche Zunahme der relativen Geschiebeführung (Geschiebetransport dividiert durch Abfluss) über das Sommerhalbjahr. Bei ein und demselben Abfluss wird demnach im Frühjahr mehrheitlich viel weniger Geschiebe transportiert als im Spätsommer.

Im Rahmen einer zweijährigen Feldmesskampagne wurde die Fraktionierung des transportierten Geschiebes bei unterschiedlichen Abflussverhältnissen erhoben. Die Kornverteilungen des transportierten Geschiebes erwiesen sich als durchwegs fein und deuten auf einen selektiven Bewegungsbeginn für unterschiedliche Korngrößen hin. In *Study C* werden dazu die kritische Sohlschubspannung bzw. der kritische Abfluss der einzelnen Korngrößen bestimmt und Ausgleichsfunktionen (hiding functions) angepasst. Die Messdaten zeigen, dass kleine Sedimentkörner bereits bei mittleren Abflüssen und das Mittelkorn bei mäßiger Hochwasserführung transportiert werden.

Die *Study D* beschäftigt sich mit der Berechnung von Geschiebetransport mittels empirischer Transportformeln. Die Berechnungen erfolgen nach der ingenieurmäßig profilweisen Methode und die Berechnungsergebnisse werden einer Vielzahl an simultanen Messwerten von Abfluss und Geschiebetransportrate gegenübergestellt. Keine der angewendeten Transportformeln vermag den mittleren beobachteten Zusammenhang wiederzugeben. Für eine bestimmte Art von Transportformel wird eine Kalibriermethode vorgestellt, die zu einer deutlichen Verbesserung in der Übereinstimmung von berechneten und mittleren beobachteten Werten führt. Diese Methode eignet sich im Besonderen für praktische Anwendungen und ein Fallbeispiel findet sich in *Kapitel D Conclusion*.

Der zweite Abschnitt (*Kapitel C*) dieser Dissertation widmet sich diesem beobachteten Zusammenhang zwischen Geschiebeverfügbarkeit und Transport im Detail. In *Study E* werden die Ergebnisse von Laborversuchen präsentiert, in welchen der Transport von feinem Geschiebe „über“ eine ansonsten stabile Sohle näher untersucht wurde. Diese und weitere Versuchsergebnisse bilden schließlich die Grundlage für die Evaluierung/Weiterentwicklung von numerischen Berechnungsansätzen (*Study F*).

Im Wasserbaulabor der Universität Innsbruck wurde dazu eine 0.03 m/m steile Gerinnestrecke der Gurgler Ache (Ötztal, Austria) im Maßstab 1:20 nachgebaut. Ein besonderes Augenmerk lag in der naturgetreuen Nachbildung der Deckschicht mit ihren morphologischen Strukturen (vereinzelte Störsteine, kleine Stufen-Beckensequenzen). Ausgehend von diesem Anfangszustand erfolgten mehrere Versuchsreihen, in denen relativ feines, eingefärbtes Sediment zugegeben und der Weitertransport im Gerinne untersucht wurde. Die einzelnen Versuche unterschieden sich im Abfluss und/oder der

Korngröße des zugegebenen Sediments. Die Modellversuche zeigten, dass bei geringen Abflüssen vorwiegend das zugegebene Sediment transportiert wurde, während sich die eigentliche Bachsohle kaum änderte. Dies war insofern verwunderlich, da das zugegebene Sediment teilweise deutlich größer war als der Feinanteil an der Deckschicht; dennoch wurde das zugegebene Material bevorzugt transportiert. Die Begründung dieser höheren Mobilität von zugegebenem Sediment wird in dessen höheren Exponiertheit gegenüber der Strömung vermutet. Denn, das zugegebene Sediment füllte die Unregelmäßigkeiten der Deckschicht teilweise auf und bedeckte somit einen Teil der ursprünglichen Sohle. Dadurch dürfte es der Strömung stärker ausgesetzt und deshalb auch leichter transportiert worden sein. Hierbei ist festzuhalten, dass das Ausmaß dieser „Überdeckung“ gering und die Strömung nach wie vor durch die Sohlstrukturen der groben Sedimentkörner beeinflusst war. Die Experimente bestätigten somit, dass die Verfügbarkeit von mobilem Sediment (Zugabe) einen starken Einfluss auf die Intensität des Geschiebetransports bei mittleren Abflüssen hat. Und das, obwohl sich nur geringe Veränderungen in der Sohlmorphologie und den Fließverhältnissen zeigten.

Das Ziel der *Study F* ist es schließlich, diese Wechselwirkung von Geschiebeverfügbarkeit und -transport in einem numerischen Modell nachzubilden. Es werden dazu die oben beschriebenen, sowie zusätzliche Laborversuche mit einem geschiebehydraulischen 1d-Modell nachgerechnet. Das Hauptaugenmerk der Simulation liegt in der Wahl der Ausgleichsfunktion (hiding function) und dem Berechnungsansatz zur Durchmischung von fraktioniertem Eintrag und dem Sohlmaterial (Durchmischungsmodell). Für beide Modellkomponenten wird, neben bestehenden Berechnungsmethoden, auch je eine neue Methode präsentiert. Die besten Ergebnisse werden mit dem neu formulierten Durchmischungsmodell erzielt, welches die Abhängigkeit zwischen Durchmischungstiefe und Strömungsbelastung explizit berücksichtigt. Mit diesem neuen Durchmischungsmodell lässt sich der zeitliche Verlauf des Geschiebetransports sowie dessen Kornzusammensetzung sehr gut reproduzieren.

ABSTRACT

In an alpine environment, the small mountain streams represent the upper part of the fluvial network. Bed load fluxes originating from these headwater or tributary streams are an important sediment source for their receiving gravel bed streams and hence, they influence the sediment budget of the entire alpine river network. However, there exist only a few studies that deal with the bed load budget of these small mountain streams and long-term records of field data are generally sparse.

This Ph.D. thesis is dedicated to the bed load transport in steep mountain streams during hydrological normal years; the bed load transport that occurs during extreme flood events or debris flows is not part of it. The thesis is divided into two superordinate chapters (*Chapter A* and *B*), and each chapter consists of self-contained studies.

The first chapter (*Chapter A*) covers the analysis of a large field data set. The data contain (i) long time series of annual bed load volumes of 20 steep mountain streams of the Central Alps in Northern Tyrol (*Study A*), (ii) long time series of bed load transport rates (temporal resolution of 15 min) from two of these 20 streams (*Study B* and *Study D*), and (iii) field data of bed load transport rates and their grain size distribution from three of these 20 streams (*Study C*).

Study A deals with the research question of whether there is a statistical relationship between the bed load budget and topographical parameters of the catchment. The results show a linear relationship between the average annual bed load volume and the catchment size, and an exponential correlation with the relative glacier area. Since the bed load budget of steep mountain streams is mainly controlled by the water runoff, stream morphology, and sediment availability, an approach is presented which enables to separate these driven factors in the second part of *Study A*. Based on that, the between-site and within-site variability of transport efficiency are determined. Results suggest that the sediment availability regulates the within-site variability of annual bed load volumes, at least during hydrological ordinary years. The transport efficiency is on average higher in dry years than in wet ones. At one study site, the impact of an exceptional flood event on bed load transport is quantified. The event caused an increase in bed load transport efficiency of about one order of magnitude which successively decreased to its former level within three years.

At two streams, long time series of bed load transport rates are available. These data provide a detailed insight into the temporal variability of bed load transport (*Study B*). Despite the significant correlation of bed load transport rate and water discharge, the scatter range is enormous and extends over four orders of magnitude. The scatter is largest at low to moderate flows, i.e. in the discharge range in which the transported bed load is almost exclusively composed of sand and gravel. In addition, the scatter is not independently distributed but it shows a temporal link. Finally, the large scatter of instantaneous bed load transport rates is attributed to variable bed load supply conditions. It means that the availability of fine gravel changes with time. At one of the two streams, the primary gravel source is the glacier forefield, which suggests a strong mobilization during the glacier melt, i.e. late summer. This is also confirmed by the measured data: the efficiency of transporting bed load (e.g. the ratio of bed load rate and discharge) increases in course of the summer.

In course of a two-year field measurement campaign, the rate and the grain size distribution of bed load transport was surveyed at three steep mountain streams. In contrast to the coarse stream bed with a large portion of cobbles and boulders, the transported bed load was comparatively fine and consisted almost entirely of gravel. In *Study C*, the critical shear stress and the critical discharge of the individual grain size fractions are determined. These data are then used to fit hiding functions. The data show that gravel grains are already mobilized at moderate flows, while cobble grains are entrained at moderate flood events.

In *Study D*, the applicability of six bed load transport equations to compute bed load transport rate by means of hydraulic parameters is tested. Therefore, the stream reaches just upstream of the two water intake structures with long-time series of discharge and bed load transport rate are simplified to a representative cross section. The hydraulic computations are based on a 1d approach, assuming uniform flow. The computation results reveal that neither of the six different bed load transport equations reproduces the observed relation between water discharge and bed load transport rate well. To enhance the performance of one bed load transport equation, a procedure is presented that uses the dimensionless reference shear stress as a calibration parameter.

The second part of this Ph.D. thesis (*Chapter B*) is devoted to this observed relationship between sediment supply and bed load transport. In *Study E*, the results of flume experiments are presented. In the experiments, the transport of fine sediment over an armored bed surface are investigated. These data are then used for the evaluation and development of numerical approaches (*Study F*).

The experimental tests were performed in the hydraulic laboratory of the University of Innsbruck. Therefore, a stream reach of an example mountain stream (Gurgler Ache, Austria) was rebuilt on a scale of 1:20. The initial condition was a self-stabilized bed surface that featured similar morphologic patterns as its prototype reference. During an experimental test, fine bed load was supplied at flow conditions ranging from one-third to twice the critical discharge for the bed surface. At flows not exceeding the critical discharge, the time series of the bed load transport rate at the downstream model boundary featured consistent patterns which are attributed to distinct phases: (i) a temporal lag, (ii) an equilibrium state, and (iii) a post-supply phase. Bed load transport occurred even at flows distinctly below that for incipient motion of the bed surface. But, with the mass of total bed load outflow approaching the supply amount, the mass did not exclusively consist of supplied grains. The coarser the supplied bed load, the more sediment was mobilized from the bed surface. At higher flows, the processes differed. Total bed load outflow exceeded the supply amount and the break-up of the armor layer caused a refining of the bed surface. The experimental tests confirm that the availability of mobile bed load strongly controls the occurrence and the magnitude of bed load transport in armored mountain streams. Concurrently, the alteration of the bed surface (due to sediment feeding) was small and the increase in bed load transport rate is not solely attributed to a decrease of flow resistance. It also results from an increase of the mobile sediment's exposure towards the flow.

In *Study F*, this feedback system between the availability of mobile sediment and the magnitude of transport is simulated numerically. A hydraulic 1d model was developed

that enables the simulation of the main processes involved. The focus is put on two distinct model elements, the hiding function and the approach of balancing the fractional bed material and bed load (mixing concept). For both of these numerical model elements, several existing approaches are used and two new ones are formulated. The computational results show that the choice of the mixing concept is crucial for reproducing the experimental observations (e.g. temporal progression of bed load transport rate; grain size distribution of bed load and bed material). The new mixing concept that incorporates the relationship between penetration depth and flow strength is most suitable for this purpose.

INHALTSVERZEICHNIS

| | |
|---|-----------|
| A INTRODUCTION | 1 |
| A.1 Background..... | 1 |
| A.2 Bed load transport in steep mountain streams..... | 3 |
| A.3 Bed load transport predictions..... | 5 |
| A.4 Remaining uncertainties in bed load transport predictions | 7 |
| A.5 Objectives and structure of the thesis..... | 9 |
| Part 1 – Long-term dynamics of bed load transport in steep mountain streams (chapter B)..... | 9 |
| Part 2 – The feedback between supply and transport rate of mobile bed load in steep streams (chapter C)..... | 10 |
| A.6 References of chapter A <i>Introduction</i>..... | 11 |
| B LONG-TERM DYNAMICS OF BED LOAD TRANSPORT IN STEEP MOUNTAIN STREAMS..... | 15 |
| B.1 Field data and data accuracy..... | 15 |
| B.1.1 Annual bed load volumes | 15 |
| 1.1.1 Data basis..... | 15 |
| 1.1.2 Study sites | 16 |
| 1.1.3 Measuring system..... | 20 |
| 1.1.4 Determination of annual bed load volumes..... | 26 |
| 1.1.5 Accuracy of annual bed load volumes | 29 |
| 1.1.6 Remaining uncertainties of annual bed load volumes | 34 |
| B.1.2 Time series of water discharge | 35 |
| B.1.3 Time series of bed load accumulation..... | 36 |
| 1.3.1 Data basis..... | 36 |
| 1.3.2 From the vertical stress to the deposit height | 37 |
| 1.3.3 From deposit height to deposit volume..... | 42 |
| 1.3.4 Partitioning of suspended load and bed load..... | 45 |
| 1.3.5 Workflow to determine accumulated bed load volume..... | 48 |
| 1.3.6 Accuracy of accumulated bed load volume | 49 |
| B.1.4 Time series of bed load transport rate..... | 53 |
| 1.4.1 Bed load transport rate based on the time series of bed load accumulation | 53 |
| 1.4.2 Trap efficiency of the settling basin | 56 |
| 1.4.3 Workflow to determine bed load transport rate | 59 |
| 1.4.4 Verification of the approach..... | 59 |
| B.1.5 Additional field data..... | 61 |
| B.1.6 References of chapter B.1 <i>Field data and data accuracy</i> | 65 |
| B.2 Supporting information of ‘<i>Field data and data accuracy</i>’ | 67 |
| B.2.1 Experimental modelling of bed load overpassing a bottom rack intake | 67 |
| 2.1.1 Scope of the experimental modelling..... | 67 |
| 2.1.2 Methods..... | 67 |
| 2.1.3 Results..... | 69 |
| 2.1.4 Discussion | 70 |

| | |
|--|------------|
| 2.1.5 References of chapter B.2.1 <i>Experimental modelling of bed load overpassing a bottom rack intake</i> | 71 |
| B.2.2 Verification of the transect-by-number method for assessing the bed surface grain size distribution | 72 |
| 2.2.1 Background and scope | 72 |
| 2.2.2 Methods | 72 |
| 2.2.3 Results | 76 |
| 2.2.4 Conclusion | 79 |
| 2.2.5 References of chapter B.2.2 <i>Verification of the transect-by-number method for assessing the bed surface grain size distribution</i> | 79 |
| B.3 Study A: Variability of annual bed load volumes in small, high-altitude mountain streams | 81 |
| B.3.1 Introduction | 81 |
| B.3.2 Methods | 83 |
| 3.2.1 Statistics of annual bed load volumes | 83 |
| 3.2.2 Transport efficiency | 84 |
| B.3.3 Results | 88 |
| 3.3.1 Mean annual bed load volumes | 88 |
| 3.3.2 Frequency distribution of annual bed load volumes | 90 |
| 3.3.3 Transport efficiency | 94 |
| B.3.4 Discussion | 103 |
| 3.4.1 Annual bed load volumes | 103 |
| 3.4.2 Transport efficiency | 104 |
| B.3.5 Conclusion | 106 |
| B.3.6 References of Study A | 106 |
| B.3.7 Appendix | 108 |
| B.4 Study B: Temporal variability of bed load transport rate in two glacier-fed mountain streams | 111 |
| B.4.1 Introduction | 111 |
| B.4.2 Field sites and bed load transport data | 112 |
| 4.2.1 Oberbergbach | 112 |
| 4.2.2 Pitzbach | 114 |
| 4.2.3 Bed load transport data | 115 |
| B.4.3 Methods | 117 |
| 4.3.1 Statistics of the $Q-Q_b$ relation | 117 |
| 4.3.2 Year-wise and month-wise power functions | 118 |
| B.4.4 Results | 120 |
| 4.4.1 Statistics of the $Q-Q_b$ relation | 120 |
| 4.4.2 Fitted power functions | 124 |
| B.4.5 Discussion | 130 |
| 4.5.1 Breakpoints of the $Q-Q_b$ relation | 130 |
| 4.5.2 Variability of the $Q-Q_b$ relation | 130 |
| B.4.6 References of Study B | 133 |
| B.5 Study C: Fractional bed load transport in steep mountain streams | 135 |
| B.5.1 Introduction | 135 |
| 5.1.1 Bed load transport relations | 135 |
| 5.1.2 Incipient motion | 138 |
| B.5.2 Field sites | 138 |
| 5.2.1 General remarks | 138 |
| 5.2.2 Oberbergbach | 139 |

| | | |
|------------|--|------------|
| 5.2.3 | Pitzbach | 141 |
| 5.2.4 | Laengentalerbach | 142 |
| B.5.3 | Methods of the field survey | 143 |
| 5.3.1 | Fractional bed load transport rate | 143 |
| 5.3.2 | Water discharge and flow velocity | 144 |
| 5.3.3 | Channel geometry | 145 |
| B.5.4 | Methods of calculations | 145 |
| 5.4.1 | Flow hydraulics | 145 |
| 5.4.2 | Derivation of fractional reference shear stress by means of the reference transport method | 146 |
| 5.4.3 | Derivation of fractional incipient motion by means of the flow competence method | 147 |
| B.5.5 | Results | 148 |
| 5.5.1 | Hydraulic geometry | 148 |
| 5.5.2 | Critical conditions obtained with the reference transport method | 149 |
| 5.5.3 | Fractional bed load transport | 151 |
| 5.5.4 | Critical conditions obtained with the competence method | 152 |
| 5.5.5 | Incipient motion of the D_{50} and the exceeding duration | 156 |
| B.5.6 | Discussion | 157 |
| 5.6.1 | Dimensionless references shear stress | 157 |
| 5.6.2 | Conformity between dimensionless reference and critical shear stress | 158 |
| 5.6.3 | Interpretation of the hiding exponent b | 158 |
| 5.6.4 | Conclusion | 160 |
| B.5.7 | References of Study C | 160 |
| B.6 | Study D: Applicability of bed load transport equations in two glacier fed mountain streams..... | 163 |
| B.6.1 | Introduction | 163 |
| B.6.2 | Field data | 164 |
| 6.2.1 | Discharge and bed load transport rates | 164 |
| 6.2.2 | Reach characteristics of the Oberbergbach | 164 |
| 6.2.3 | Reach characteristics of the Pitzbach | 165 |
| B.6.3 | Methods | 165 |
| 6.3.1 | Application of bed load transport equations | 165 |
| 6.3.2 | Hydraulic computations | 166 |
| 6.3.3 | Bed load transport equations | 167 |
| B.6.4 | Results | 170 |
| 6.4.1 | Comparison of bed load transport predictions and observations | 170 |
| 6.4.2 | Adjusting the Schneider et al. (2015) approach | 172 |
| 6.4.3 | Sensitivity of the parameters | 173 |
| B.6.5 | Discussion | 174 |
| B.6.6 | References of Study D | 175 |
| C | THE FEEDBACK BETWEEN SUPPLY AND TRANSPORT RATE OF MOBILE BED LOAD IN STEEP STREAMS..... | 177 |
| C.1 | Study E: The effect of sediment supply on bed load transport | 177 |
| C.1.1 | Introduction | 177 |
| 1.1.1 | Propagation of supplied sediment | 178 |
| 1.1.2 | Impact on bed stability | 179 |
| C.1.2 | Flume experiments | 180 |
| 1.2.1 | Experimental setup | 180 |
| 1.2.2 | Experimental procedure | 181 |

| | | |
|------------|--|------------|
| 1.2.3 | Measurement devices | 184 |
| 1.2.4 | Flow hydraulics..... | 185 |
| C.1.3 | Results | 187 |
| 1.3.1 | Incipient motion of supplied bed load..... | 187 |
| 1.3.2 | Bed load transport rate and its temporal progression..... | 188 |
| 1.3.3 | Partitioning of total bed load | 191 |
| 1.3.4 | Grain size distribution of total bed load | 192 |
| 1.3.5 | Grain size distribution of the bed surface..... | 194 |
| 1.3.6 | Bed stability..... | 195 |
| C.1.4 | Discussion | 197 |
| 1.4.1 | Propagation of supplied bed load over an armored bed surface | 197 |
| 1.4.2 | Effect of sediment supply on bed load transport | 198 |
| 1.4.3 | Effects of bed load supply on bed stability | 199 |
| C.1.5 | Conclusion..... | 200 |
| C.1.6 | References of Study E..... | 200 |
| C.2 | Study F: Numerical approach for simulation of phase 1 bed load transport in steep streams | 203 |
| C.2.1 | Introduction..... | 203 |
| C.2.2 | Theory development..... | 204 |
| 2.2.1 | Bed state dependence of the hiding function | 204 |
| 2.2.2 | Active layer thickness – flow strength dependence..... | 205 |
| C.2.3 | Experimental data..... | 206 |
| 2.3.1 | General remarks..... | 206 |
| 2.3.2 | Feeding experiments | 206 |
| 2.3.3 | Armoring experiments | 209 |
| C.2.4 | Modeling framework | 213 |
| 2.4.1 | Model discretization and flow hydraulics | 213 |
| 2.4.2 | Flow resistance partitioning | 214 |
| 2.4.3 | Bed load transport rate | 214 |
| 2.4.4 | Mixing – mass balancing | 217 |
| 2.4.5 | Progress of simulation | 221 |
| C.2.5 | Theory Application..... | 221 |
| 2.5.1 | Bed state dependence of the hiding function (b_5 and β_5)..... | 221 |
| 2.5.2 | Active layer thickness – flow strength dependence (mixing concept 3) | 223 |
| C.2.6 | Results | 225 |
| 2.6.1 | Feeding experiments | 225 |
| 2.6.2 | Armoring experiments | 244 |
| 2.6.3 | Summary of model results | 263 |
| C.2.7 | Discussion and conclusion | 267 |
| 2.7.1 | Bed load transport equation..... | 267 |
| 2.7.2 | Modeling the effect of bed load supply on transport rate | 269 |
| 2.7.3 | Modeling the bed surface coarsening in response to sediment starving | 271 |
| C.2.8 | References of Study F..... | 272 |
| D | CONCLUSION | 275 |
| D.1 | Overview of the thesis' research issues | 275 |
| D.2 | Part 1 - Long-term dynamics of bed load transport in steep mountain streams | 277 |
| D.2.1 | Study A: Variability of annual bed load volumes in small, high-altitude mountain streams | 277 |

| | | |
|------------|--|------------|
| 2.1.1 | Contribution to research..... | 277 |
| 2.1.2 | Practical application: Estimation of annual bed load volumes..... | 278 |
| D.2.2 | Study B: Temporal variability of bed load transport rate in two glacier-fed mountain streams..... | 280 |
| D.2.3 | Study C: Fractional bed load transport in steep mountain streams | 281 |
| D.2.4 | Study D: Applicability of bed load transport equations in two glacier-fed mountain streams..... | 282 |
| 2.4.1 | Contribution to research..... | 282 |
| 2.4.2 | Practical application | 282 |
| D.3 | Part 2 - The feedback between supply and transport rate of mobile bed load in steep streams | 285 |
| D.3.1 | Study E: Effect of sediment supply on bed load transport..... | 285 |
| D.3.2 | Study F: Numerical approach for the simulation of phase 1 bed load transport in steep stream..... | 286 |
| 3.2.1 | Contribution to research..... | 286 |
| 3.2.2 | Outlook for practical application | 286 |
| D.4 | References of chapter D Conclusion | 289 |
| E | LIST OF FIGURES AND TABLES..... | 291 |
| E.1 | List of Figures | 291 |
| E.2 | List of Tables..... | 300 |

A INTRODUCTION

A.1 Background

In recent years, the necessity of predicting the long-term behavior of sediment transport has increased. On the one hand, the effects of technical measures (e.g. retaining measures, hydropower, etc.) in the river system are to be evaluated (European Commission, 2000). On the other hand, long-term ecological studies that are strongly linked to the sediment budgets or the river morphology are more and more evolving (Junker et al., 2014; Duan et al. 2009). Thinking on future trends, this is accompanied with an alteration of the boundary conditions due to climate change.

The sediment load of the rivers is usually partitioned into the suspended load and the bed load. In this respect, bed load transport is associated with solid particles that move by rolling, sliding or jumping along the riverbed and the rate of bed load transport is defined by the bed load's volume passing a certain location per unit time. The suspended load is associated with fine sediment particles that are floating throughout the entire water column.

In an alpine environment, the bed load dominates in the riverbed and thus, it has a major influence on the river morphology. In addition, steep mountain streams or mountain creeks feature relevant topographical and morphological differences to their lowland counterparts (Montgomery and Buffington, 1997), such as (i) overall steep and locally variable channel gradients, (ii) large, immobile boulders or channel spanning bed forms which feature high stability and (iii) low relative flow depths. Summarizing, the riverbed of steep mountain streams is often poorly sorted and segregated into a variety of structures (Church and Halwas, 2002; Lenzi, 2001). This small-scale variability of the morphologic patterns results in very complex flow hydraulics in steep mountain streams (Nitsche et al., 2012; Church and Zimmermann, 2007; Wilcox, 2005). In comparison with low-gradient gravel-bed rivers, the flow resistance is higher (Zimmermann, 2010), amongst others due the permanent changes between sub- and supercritical flow conditions (Wilcox et al., 2006) and the spill drag around macro-roughness elements like immobile boulders (Yager et al., 2007; Pagliara and Chiavaccini, 2006).

A.2 Bed load transport in steep mountain streams

The magnitude of the bed load transport rate depends on the hydraulic forces acting on the riverbed and the retaining strength of the solid particles. Typically, the hydraulic force increases with discharge, and thus, higher bed load transport rates are observed during flood events than periods of low flow. The retaining strength of the bed material is significantly related to the grain size (in particular grain mass), with small particles being easier eroded than coarse ones.

A fully verified theoretical basis on bed load transport in mountain streams is still a topic in need of further research but recently published field data suggest that there exist different phases of transport at different discharge levels (Recking, 2012; Jackson and Beschta, 1982). At low and moderate water flows (phase 1), bed load transport occurs, if at all, at a very minute rate and it solely consists of small grain sizes (e.g. Palt, 2001). Consequently, the coarse particles at the bed surface remain immobile, while bed load is either mobilized from local patches of fines (gravel and cobble) or supplied from upstream reaches and passes over the riverbed. If the water discharge increases, coarse grains will be partially mobilized but the proportion in total bed load is still much smaller than their abundance at the bed surface (phase 2). Finally, the bed material is fully mobile at very high flow, which is associated with phase 3. In steep mountain streams with step-pool morphology, phase 3 transport conditions are restricted to exceptional flood events with occurrence intervals of about 50 years (Turowski et al., 2009; Lenzi et al., 2004). Thus, phase 3 transport does not directly affect the magnitude of bed load transport during hydrological ordinary years (without exceptional floods). Phase 2 transport is usually associated with ordinary flood events, which are likely to occur several times a year (e.g. Ryan et al., 2002) and phase 1 transport prevails for the rest of the time. Although bed load transport associated with phase 1 reveals very minute rates, it may significantly contribute to total bed load transport of a certain year; simply because of its long lasting occurrence.

A.3 Bed load transport predictions

Predicting bed load transport rate by means of hydraulic parameters, which are used to quantify the flow's competence to mobilize bed load, goes far back in history and is associated with the significant works of e.g. Shields (1936), Meyer-Peter and Müller (1949; MPM), Einstein (1950) or Bagnold (1980). Their approaches are mainly based on empiric data from flume experiments featuring simplified boundary conditions (e.g. nearly uniform sediment, rectangular flumes) and low channel gradients, and thus an application to steep streams poses severe uncertainties. Bed load transport in steep streams was specifically addressed by Smart and Jäggi (1983) and Rickenmann (1990), who extended the MPM data set by additional flume experiments facing high channel gradients and variable fluid densities. However, applying these equations to flood hydrographs often yields implausible large bed load volumes (Chiari and Rickenmann, 2011; Nitsche et al., 2011). Extensive research was conducted to either explain or account for this inconsistency between flume experiments and the field observations (Rickenmann, 2001; Yager et al., 2007; Yager et al., 2012a; Nitsche et al., 2011; Recking, 2010). For example, accounting for the momentum loss due to macro-roughness elements enhances the predictive capability of these flume based approaches (e.g. Chiari and Rickenmann, 2011; Nitsche et al., 2011). But applying these approaches to annual hydrographs, calculated transport rates often have to be reduced by several orders of magnitude to attain a plausible magnitude of the annual bed load volume (Klar, 2016).

Recently, essential research is conducted by means of measuring bed load transport in the field (e.g. Schneider et al., 2015; Rickenmann et al., 2014; Bunte et al., 2004; King et al., 2004). Thereby, knowledge on bed load transport dynamics is increased (e.g. Schneider et al., 2014; Turowski, 2010; Garcia et al., 2007) and empirical approaches are derived for the estimation of incipient motion (e.g. Bunte et al., 2013; Bathurst, 2013; Turowski et al., 2011) and bed load transport rate (e.g. Yager et al., 2012a; Recking, 2012; Recking, 2010). But in comparison with flume experiments, the field data reveal a large scatter, even within a single site. In a consequence, the application of recent bed load transport equations (e.g. Schneider et al., 2015; Recking, 2013) to unmonitored sites still show severe uncertainties, but they are expected to be closer than previous, flume-based approaches. This is particularly true for phase 1 transport conditions, which are associated with low transport rates over long periods of moderate discharges, respectively.

A.4 Remaining uncertainties in bed load transport predictions

One reason for the scattered relation between hydraulic parameters and in-situ measured bed load transport rates might be the limited accuracy of the field data. For example, the bed load transport rate is usually measured with bed load traps (Bunte et al., 2004), Helley-Smith samplers (King et al., 2004) or impact sensors (Rickenmann et al., 2014), with all techniques featuring uncertainties. Furthermore, the grain size distribution is highly variable in steep mountain streams (even within single, homogeneous reaches), but it is a sensitive parameter for hydraulic parameters. In addition, the flow hydraulics are very complex in step-pool channels with tumbling flows that alternate between subcritical in the pools and supercritical over the steps (Church and Zimmermann, 2007). All these patterns are difficult to quantify in detail in the field. This is a possible reason why most of the studies that are available in literature focus on the reach-scale by using to reach averaged parameters.

However, the scatter of the field data and the limited predictive capability of derived bed load transport equations are not solely attributed to the measuring uncertainty. There are additional mechanisms in nature that cause the relation between flow competence and bed load transport rate to differ, either between different sites or over time.

For example the consolidation of the bed material or the interlocking of keystones cause an increase of the bed stability (Reid et al., 1985, Church and Zimmermann, 2007; Prancevic and Lamb, 2015); both of these phenomena are likely to depend on the discharge history: i.e. the less often the armored bed surface breaks up, the higher its consolidation (Reid et al., 1985). Furthermore, the supply of mobile bed load is limited in steep mountain streams, since the proportion of relatively stable patches (e.g. steps, large boulders) is increased. In this respect, mobile bed load means the sediment that can be entrained and transported at a certain water discharge, respectively. The incipient motion of fine bed load is affected by the hiding of small grains behind larger calibers (Parker and Klingeman, 1982). However, the intensity of hiding (or the magnitude of the critical discharge for fine bed load) varies between different streams (Bathurst, 2013), but differs also over time within a single stream (Turowski et al., 2011).

In general, the relation between hydraulic parameters and observed bed load transport rate is significant, but the predictive capability is limited. This is attributed to the multiple mechanisms involved, such as the high momentum losses due to macro-roughness (Yager et al., 2012a), the hiding of small grains and the protrusion of large calibers (Bathurst, 2013; Bunte et al., 2013) and the interlocking of keystones that increase bed stability (Church and Zimmermann, 2007; Lamarre and Roy, 2008; Prancevic and Lamb, 2015). In addition, bed load transport rate is very sensitive to several morphologic patterns, such as the grain size distribution or the spatial arrangement of the grains (Turowski et al., 2011), the embedding of the bed surface (Bathurst, 2013) and the supply of mobile bed load (Mao et al., 2014, Recking, 2012; Yager et al., 2012b).

An impressive example of the adaptability of steep mountain streams are the experiences from the operation of water diversion structures by TIWAG, a hydropower company in Austria (Tschada and Hofer, 1990). At these structures, the water discharge is diverted, while the bed load deposits in a settling basin. Once the bed load accumulation within the settling basin exceeds a certain limit, the gate, located at the downstream end of the settling basin, is opened and the captured bed load is flushed into the downstream enclosing reach. Thus, the total bed load entering from upstream is periodically released to the downstream reach, while the residual water discharge is

limited to the structure's design capacity, which is exceeded only during flood events. Assuming a rigid relation between bed load transport rate and discharge, the downstream reach would face severe channel bed aggradation, since a decrease of discharge is associated with a decrease of bed load transport. However, these water diversion structures are operating since several decades (since 1965), with a sufficient onward movement of the bed load even by the very limited residual flow (Tschada and Hofer, 1990). This is in good agreement with observations at similar sites in the United States (Ryan, 1997), where the morphologic parameters derived from diverted channels did not reveal substantial differences with similar, but free-flowing channels.

A.5 Objectives and structure of the thesis

The research presented in this thesis focuses on the magnitude and variability of bed load transport in steep mountain streams. It is hypothesized that the bed load transport in steep mountain streams depends on both, the flow competence to transport bed load and the supply conditions of mobile sediment. The impact of both issues on the bed load transport is assessed by means of (i) a large field data set, (ii) experimental investigation in a flume and (iii) numerical computations. The (i) large data set provides evidence and insights of the long-term dynamics of bed load transport, and it enables a quantification of its magnitude and variability in nature. The physical processes of the feedback between supply and bed load transport rate are investigated in more detail by means of the (ii) laboratory tests. These results are then used to develop a (iii) computational approach that accounts for this feedback system of bed load supply and transport in steep streams.

The thesis is divided into two main parts that comprise in total five major studies and additional remarks about the derivation of the data. The studies are organized like research articles and they are more or less self-contained but refer to each other.

Part 1 – Long-term dynamics of bed load transport in steep mountain streams (*chapter B*)

In the first part of the thesis, a large data set of annual bed load volumes (*Study A*) and high-resolution bed load transport rates (*Study B*) is compiled and analyzed. The data used in both of these studies are based on the operational records at water intake structures which are operated by TIWAG. The derivation of annual bed load volumes and bed load transport rates, as well as the accuracy of the data, is presented in detail at the beginning of the first part (section B.1 and B.2). In addition, fractional bed load transport rates were measured in three steep mountain streams. The data are used for the verification of the bed load transport rates derived from the records at the water intake structures, and additionally, the field data are used in *Study C* to investigate the fractional mobility of bed load. Furthermore, the observed relation between discharge and bed load transport rate is compared with the computational results obtained with empiric bed load transport equations in *Study D*.

The studies of this first part are dedicated to the following research questions:

Study A: Variability of annual bed load volumes in small, high-altitude mountain streams

- What is the magnitude of annual bed load volumes in steep mountain streams and what are the main driving factors?
- Is the temporal variability of annual bed load volumes solely associated with the year-wise differences of the annual discharge hydrograph or additionally affected by changing sediment supply conditions?

Study B: Temporal variability of bed load transport rate in two glacier-fed mountain streams

- To which extent does the relation between discharge and bed load transport rate vary with time at a single site?
- Is the scatter of this relation independently distributed or are there seasonal differences?

Study C: Fractional bed load transport in two glacier fed mountain streams

- Are the incipient motion and the bed load mobility of different grain sizes size-selective or equal?
- How often is the critical discharge of the bed surface D_{50} exceeded during a year?

Study D: Applicability of bed load transport equations in two steep mountain streams

- Is the observed relationship between discharge and bed load transport rate sufficiently reproduced by empiric bed load transport equations?
- In the case that the bed load transport equation is suitable, is a straightforward adjustment of the main empiric model parameters possible?

Part 2 – The feedback between supply and transport rate of mobile bed load in steep streams (chapter C)

The second part of the thesis addresses the feedback between alterations of sediment supply and bed load transport rate. Therefore, flume experiments were accomplished at the hydraulic laboratory of the University of Innsbruck (*Study E*). These, as well as additional experimental results, are then used to test existing and further developed modeling approaches which enable the computation of the feedback between bed load supply and bed load transport rate (*Study F*).

Study E: Effect of sediment supply on bed load transport

- What happens if mobile bed load is supplied to an armored stream at discharges lower than the critical discharge of the bed surface?
- Does the introduced bed load pass over the bed surface or does it interact with the bed material?
- Is the bed stability affected by the sediment supply conditions?

Study F: Numerical approach for simulation of phase 1 bed load transport in steep streams

- Are the feedback mechanisms between bed load transport and sediment supply reproducible with fractional bed load transport calculations that consider bed material sorting?
- How can common model approaches be improved?

A.6 References of chapter A *Introduction*

- Bagnold, R. A. (1980), An empirical correlation of bedload transport rates in flumes and natural rivers, *Proc. R. Soc. London, Ser. A*, 372, 453-473.
- Bathurst, J. C. (2013), Critical conditions for particle motion in coarse bed materials of nonuniform size distribution, *Geomorphology*, 197, 170-184.
- Bunte, K., Abt, S., Potyondy, J. P. and Ryan, S. E. (2004), Measurement of coarse gravel and cobble transport using portable bedload traps, *J. Hydraul. Eng.*, 130(9), 879-893, doi: 10.1061/~ASCE!0733-9429~2004!130:9~879
- Bunte, K., S. R. Abt, K. W., Swingle, D. A. Cenderelli, and J. M. Schneider (2013), Critical Shields values in coarse-bedded steep streams, *Water Resour. Res.*, 49, 7427-7447, doi: 10.1002/2012WR012672
- Chiari, M. and D. Rickenmann (2010), Back-calculation of bedload transport in steep channels with a numerical model, *Earth Surf. Proc. Land.*, 36, 805-815, doi 10.1002/esp.2108.
- Church, M., and K. L. Halwas (2002), Channel units in small, high gradient streams on Vancouver Island, British Columbia, *Geomorphology*, 43, 243-256.
- Church, M., and A. Zimmerman (2007), Form and stability of step-pool channels: Research progress, *Water Ressour. Res.*, 43, W03415, doi: 10.1029/2006WR005037
- Duan, X, Wang, Z., Xu, M & Zhang, K. 2009. Effect of streambed sediment on benthic ecology. *Int. J. Sediment Res.*, 24, 325-338.
- Einstein, H. A. (1950), The bed load function for sediment transportation in open channel flows, *Technical Bulletin No. 1026*, USDA, Washington, D.C.
- European Commission (2000), Directive 2000/60/EC of the European Parliament and of the Council of 23 October 2000 establishing a framework for Community action in the field of water policy - Water Framework Directive. Official Journal L 327, 22/12/2000: 1-73.
- Garcia, C., H. Cohen, I. Reid, A. Rovira, X. Ubeda, and J. B. Laronne (2007), Process of initiation of motion leading to bed load transport in gravel-bed rivers, *Geophys. Res. Lett.*, 24, L06403, doi: 10.1029/2006GL028865
- Jackson, W. L., and R. L. Beschta (1982), A model of two-phase bed load transport in an Oregon coast range stream, *Earth Surf. Proc. Land.*, 7, 517-527.
- Junker, J., F.U.M. Heimann, C. Hauer, J.M. Turowski, D. Rickenmann, M. Zappa and A. Peter (2015), Assessing the impact of climate change on brown trout (*Salmo trutta fario*) recruitment, *Hydrobiologia*, 751(1), 1-21, doi: 10.1007/s10750-014-2073-4
- King, J.G., W. W. Emmett, P. J. Whiting, R. P. Kenworthy, and J. J. Barry (2004), Sediment transport data and related information for selected coarse-bed streams and rivers in Idaho, *Gen. Tech. Rep. RMRS-GTR-131*, U.S. Dep. of Agric., For. Serv., Rocky Mt. Res. Stn, Fort Collins, Colo.
- Klar, R. (2016), Langzeitsimulation des Geschiebetransports in alpinen Tälern - Weiterentwicklung von Methoden zur Modellierung der langfristigen Sohlagenentwicklung und zur Ermittlung von Hochwassergefahren in inneralpinen Tälern, Ph.D. thesis, Univ. of Innsbruck, Innsbruck, Austria, 331 p (in German).
- Lamarre, H. and A. G. Roy (2008), A field study on the development of sedimentary structures in a gravel-bed river, *Earth Surf. Proc. Land.*, 33, 1064-1081, doi: 10.1002/esp.1602
- Lenzi, M. A. (2001), Step-pool evolution in the Rio Cordon, Northeastern Italy. *Earth Surf. Proc. Land.*, 26, 991-1008, doi: 10.1002/esp.239
- Lenzi, M. A., L. Mao, and F. Comiti (2004), Magnitude-frequency analysis of bed load data in an Alpine boulder bed stream, *Water Resour. Res.*, 40, W07201, doi: 10.1029/2003WR002961
- Meyer-Peter, E., and R. Müller (1948), Formulas for bed-load transport, in Proceedings of the 2nd Meeting of the International Association for Hydraulic Structures Research, pp. 39–64, Int. Assoc. Hydraul. Res., Delft, Netherlands
- Montgomery, D. R., and J. M. Buffington (1997), Channel-reach morphology in mountain drainage basins, *Geol. Soc. Am. Bull.*, 109(5), 596-611.
- Nitsche, M., D. Rickenmann, J. W. Kirchner, J. M. Turowski, and A. Badoux (2012), Macroroughness and variations in reach-averaged flow resistance in steep mountain streams, *Water Resour. Res.*, 48, W12518, doi: 10.1029/2012wr012091
- Nitsche, M., D. Rickenmann, D., J. M. Turowski, A. Badoux, and J. W. Kirchner (2011), Evaluation of bed load transport predictions using flow resistance equations to account for macro roughness in steep streams, *Water Resour. Res.*, 47, W08513, doi: 10.1029/2011WR010645
- Pagliara, S. and P. Chiavaccini (2006), Flow resistance of rock chutes with protruding boulders, *J. Hydraul. Eng.*, 132(6), 545-552, doi: 10.1061/(ASCE)0733-9429(2006)132:6(545)

- Palt, S. M. (2001), Sedimenttransportprozesse im Himalaya-Karakorum und ihre Bedeutung für Wasserkraftanlagen (Sediment transport processes in the Himalaya-Karakorum and its relevance regarding hydro power utilization), Ph.D. thesis, Univ. Fridericiana zu Karlsruhe, Karlsruhe, Germany (in German).
- Parker, G., and P. C. Klingeman (1982), On why gravel bed streams are paved, *Water Resour. Res.*, 18(5), 1409-1423.
- Prancevic, J.P. and M.P. Lamb (2015), Particle friction angles in steep mountain channels, *J. Geophys. Res.-Earth*, 120, 242-259, doi: 10.1002/2014JF003286
- Recking, A. (2010), A comparison between flume and field bed load transport data and consequences for surface-based bed load transport prediction, *Water Resour. Res.*, 46, W03518, doi: 10.1029/2009WR008007
- Recking, A. (2012), Bedload transport in rivers: from the flume to the field, Habilitation dissertation, Univ. of Grenoble, Grenoble, France, 88 p. Available from Internet: <http://www.irstea.fr/recking>
- Recking, A. (2013), Simple Method for Calculating Reach-Averaged Bed-Load Transport, *J. Hydraul. Eng.*, 139(1), 70-75, doi: 10.1061/(ASCE)HY.1943-7900.0000653
- Reid, I., L. E. Frostick, and J. T. Layman (1985), The incidence and nature of bedload transport during flood flows in coarse-grained alluvial channels. *Earth Surf. Proc. Land.*, 10, 33-44.
- Rickenmann, D. (1990), Bedload transport capacity of slurry flows at steep slopes, Ph.D. thesis, ETHZ, Zurich, Switzerland, 249 p.
- Rickenmann, D. (2001), Comparison of bed load transport in torrents and gravel bed streams, *Water Resour. Res.*, 37(12), 3295-3305
- Rickenmann, D., J. M. Turowski, B. Fritschi, C. Wyss, J. Laronne, R. Barzilai, I. Reid, A. Kreisler, J. Aigner, H. Seitz, and H. Habersack (2014), Bed load transport measurements with impact plate geophones: comparison of sensor calibration in different gravel-bed streams, *Earth Surf. Proc. Land.*, 39(7), 928-942, doi: 10.1002/esp.3499
- Ryan, S. E., L. S. Porth, and C. A. Troendle (2002), Defining phases of bedload transport using piecewise regression, *Earth Surf. Proc. Land.*, 27, 971-990, doi: 10.1002/esp.387
- Ryan, S. (1997), Morphologic response of subalpine streams to transbasin flow diversion, *J. Am. Water Resour. As.*, 33(4), 839-854.
- Schneider, J. M., D. Rickenmann, J. M. Turowski, K. Bunte, and J. W. Kirchner (2015a), Applicability of bed load transport models for mixedsize sediments in steep streams considering macro-roughness, *Water Resour. Res.*, 51, 5260-5283, doi: 10.1002/2014WR016417
- Schneider, J. M., J. M. Turowski, D. Rickenmann, R. Hegglin, S. Arrigo, L. Mao and J. W. Kirchner (2014), Scaling relationships between bed load volumes, transport distances, and stream power in steep mountain channels, *J. Geophys. Res.-Earth*, 119, doi: 10.1002/2013JF002874
- Shields, A. (1936), Anwendung der Ähnlichkeitsmechanik und der Turbulenzforschung auf die Geschiebebewegung, *Mitteilungen der Preussischen Versuchsanstalt für Wasserbau und Schiffbau, Heft 26*, Berlin, Germany.
- Smart, G.M. and M.N.R. Jäggi (1983), Sediment transport on steep slopes, *Mitteilungen der Versuchsanstalt für Wasserbau, Hydrologie und Glaziologie an der ETH Zürich*, No. 64, ETH Zurich, Switzerland.
- Tschada, H and B. Hofer (1990), Total solid load from the catchment area of the Kaunertal hydroelectric power station: the results of 25 years of operation, *Hydrology in Mountain Regions II – Artificial Reservoirs, Water and Slopes, Proceedings of two Lausanne Symposia, IAHS Publ. no. 194*.
- Turowski, J. M., E. M. Yager, A. Badoux, D. Rickenmann, and P. Molnar (2009), The impact of exceptional events on erosion, bed load transport and channel stability in a step-pool channel, *Earth Surf. Proc. Land.*, 34, 1661-1673, doi: 10.1002/esp.1855
- Turowski, J. M. (2010), Probability distributions of bed load transport rates: A new derivation and comparison with field data, *Water Resour. Res.*, 46, W08501, doi: 10.1029/2009WR008488
- Turowski, J. M., A. Badoux, and D. Rickenmann (2011), Start and end of bed load transport in gravel-bed streams, *Geophys. Res. Lett.*, 38, L04401, doi: 10.1029/2010GL046558
- Wilcox, A. C. (2005), Interactions between flow hydraulics and channel morphology in step-pool streams, Ph.D. thesis, Colorado State University, Fort Collins, Colorado, 227 p.
- Wilcox, A. C., J. M. Nelson, and E. E. Wohl (2006), Flow resistance dynamics in step-pool channels: 2. Partitioning between grain, spill, and woody debris resistance, *Water Resour. Res.*, 42, W05419, doi: 10.1029/2005WR004278
- Yager, E. M., J. W. Kirchner, and W. E. Dietrich (2007), Calculating bed load transport in steep boulder bed channels, *Water Resour. Res.*, 43, W07418, doi: 10.1029/2006WR005432
- Yager, E. M., W. E. Dietrich, J. W. Kirchner, and B. W. McArdell (2012a), Prediction of sediment transport in step-pool channels, *Water Resour. Res.*, 48, W01541, doi: 10.1029/2011WR010829.

- Yager, E. M., J. M. Turowski, D. Rickenmann, and B. W. McArdell, (2012b), Sediment supply, grain protrusion, and bed load transport in mountain streams, *Geophys. Res. Lett.*, 39, L10402, doi: 10.1029/2012GL051654
- Zimmermann, A. (2010), Flow resistance in steep streams: An experimental study, *Water Resour. Res.*, 46, W09536, doi: 10.1029/2009WR00791

B LONG-TERM DYNAMICS OF BED LOAD TRANSPORT IN STEEP MOUNTAIN STREAMS

B.1 Field data and data accuracy

B.1.1 Annual bed load volumes

1.1.1 Data basis

The assessment of the long-term dynamics of the annual bed load volume in steep mountain streams requires data which go far back in history. In this respect, the records of operational flushings at bottom rack intake structures operated by TIWAG (Tiroler Wasserkraft AG; Figure B-1), a hydropower company in Austria, represent a unique data set (e.g. Sommer and Laufer, 1982). It is used to quantify annual bed load volumes of 20 mountain streams over a time span of up to 49 years.

An overview of the study sites is given in the following section 1.1.2 and the procedure of data generation is described in the sections 1.1.3 to 0.

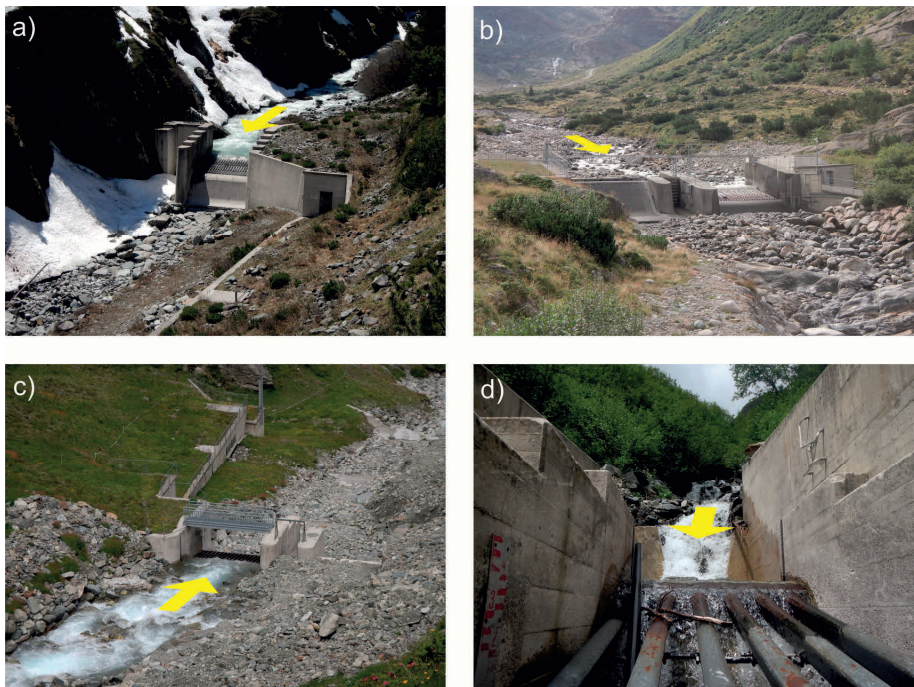


Figure B-1: Examples of the water intake structures analyzed in this thesis with a) the Oberbergbach, b) the Pitzbach, c) the Laengentalerbach, and d) the Schoentalbach water intake structure of TIWAG

1.1.2 Study sites

The study sites comprise twenty small catchments which are situated in the Central Eastern Alps in Austria, each within a linear distance of less than 50 km. An overview is given in Figure B-2 and Figure B-3.

All sites belong to the Oetztal-Stubai basement, which is built up by crystalline rock consisting mainly of gneiss. Depending on site characteristics and history, the bedrock is large-scale superimposed by unconsolidated sediment, such as colluvial deposits and moraines.

The mean elevation of the catchments ranges between 2358 m and 2855 m a.s.l and thus, all catchments predominantly belong to the alpine or nival level, while areas covered with forests are negligibly small. Mean annual precipitation is between 1093 mm for the catchment located in the very south-west (Tscheybach) and almost 1300 mm for the catchments located in the very north-eastern part (Liesenerbach). However, catchment characteristics differ obviously regarding their size (3 km^2 to 27 km^2), relative glacier area (0 % to 53 %), mean catchment slope (53 % to 92 %) and mean channel gradient (4 % to 49 %; Table B-1).

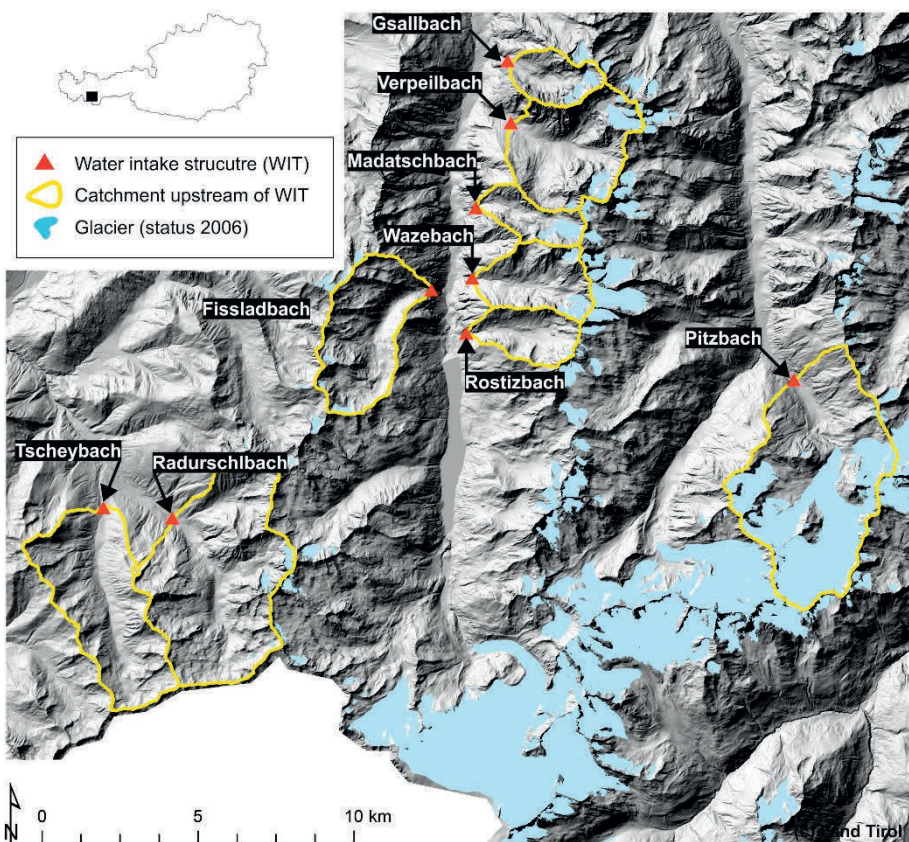


Figure B-2: Location of the field sites - western part. The water intake structures belong to the Kaunertal hydropower station of TIWAG.

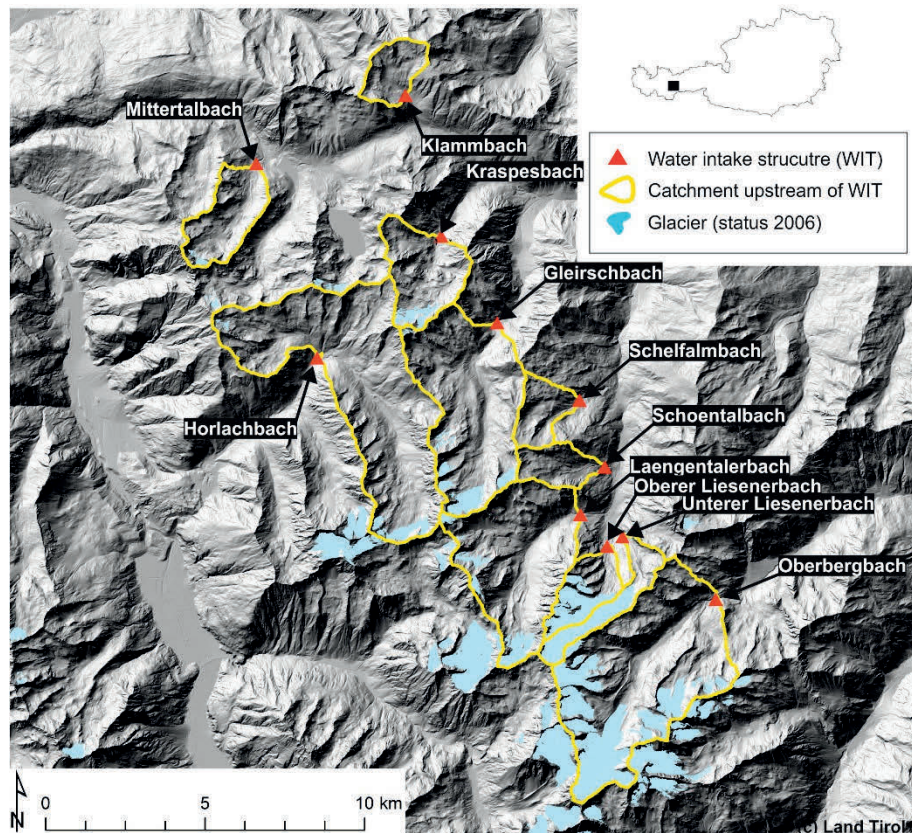


Figure B-3: Location of the field sites - eastern part. The water intake structures belong to the hydropower station Sellrain-Silz of TIWAG

Table B-1: List of main characteristics of the study sites – part 1

| Site | Longitude | Latitude | Catchment Size | Relative glacier area (km ² /km ²) ^a | | | MAP ^b | MAR ^b | HQ1.5 ^b |
|----------------------|---------------|---------------|--------------------|--|------|-------------|------------------|------------------|---------------------|
| | (deg min sec) | (deg min sec) | (km ²) | 1969 | 1998 | 2006 | (mm/a) | (mm/a) | (m ³ /s) |
| Schoentalbach | 11° 7' 53" E | 47° 7' 36" N | 2.77 | 0.00 | 0.00 | 0.00 | 1237 | 472 | 0.41 |
| Schelfalmbach | 11° 7' 17" E | 47° 8' 44" N | 2.91 | 0.00 | 0.00 | 0.00 | 1277 | 753 | 0.68 |
| Klammbach | 11° 3' 2" E | 47° 13' 55" N | 2.95 | 0.00 | 0.00 | 0.00 | 1282 | 1331 | 0.87 |
| Unterer Liesenerbach | 11° 8' 19" E | 47° 6' 24" N | 3.34 | 0.57 | 0.55 | 0.53 | 1260 | 1359 | 1.01 |
| Oberer Liesenerbach | 11° 7' 56" E | 47° 6' 15" N | 3.66 | 0.51 | 0.48 | 0.45 | 1288 | 1329 | 1.25 |
| Madatschbach | 10° 45' 3" E | 47° 0' 9" N | 3.82 | 0.16 | 0.14 | 0.12 | 1129 | | |
| Gsallbach | 10° 45' 52" E | 47° 2' 41" N | 3.89 | 0.13 | 0.09 | 0.08 | 1118 | | |
| Rostizbach | 10° 44' 47" E | 46° 57' 59" N | 4.81 | 0.01 | 0.01 | 0.01 | 1117 | | |
| Mittertalbach | 10° 59' 18" E | 47° 12' 47" N | 5.14 | 0.03 | 0.02 | 0.02 | 1278 | 1425 | 1.79 |
| Kraspesbach | 11° 3' 53" E | 47° 11' 32" N | 6.31 | 0.11 | 0.08 | 0.07 | 1288 | 1272 | 1.72 |
| Wazebach | 10° 43' 55" E | 46° 58' 44" N | 6.71 | 0.13 | 0.10 | 0.09 | 1102 | | |
| Fissladbach | 10° 45' 57" E | 47° 1' 37" N | 11.40 | 0.04 | 0.02 | 0.02 | 1099 | 1144 | 2.72 |
| Verpeilbach | 10° 44' 57" E | 46° 58' 56" N | 12.12 | 0.11 | 0.09 | 0.08 | 1099 | | |
| Laengentalerbach | 11° 7' 16" E | 47° 6' 47" N | 15.17 | 0.09 | 0.08 | 0.07 | 1269 | 1378 | 4.21 |
| Tscheybach | 10° 35' 36" E | 46° 54' 59" N | 16.39 | 0.00 | 0.00 | 0.00 | 1093 | 895 | 2.59 |
| Gleirschbach | 11° 5' 15" E | 47° 10' 3" N | 16.69 | 0.10 | 0.08 | 0.07 | 1282 | 1205 | 4.53 |
| Oberbergbach | 11° 7' 16" E | 47° 6' 47" N | 23.67 | 0.34 | 0.30 | 0.28 | 1273 | 1576 | 8.70 |
| Radurschlbach | 10° 37' 20" E | 46° 54' 48" N | 24.03 | 0.03 | 0.02 | 0.01 | 1238 | 1058 | 5.01 |
| Horlachbach | 11° 0' 47" E | 47° 9' 29" N | 25.63 | 0.04 | 0.03 | 0.02 | 1259 | 1237 | 5.81 |
| Pitzbach | 10° 53' 4" E | 46° 57' 8" N | 27.15 | 0.54 | 0.48 | 0.46 | 1130 | 1682 | 12.93 |

^a The relative glacier areas are based on the glacier surveys of the years 1969, 1998 and 2006 according to Fischer et al. (2015). If not explicitly noted, the relative glacier areas are of the year 2006 (bold) are used in this study.

^b Definitions are as follows: MAP, mean annual precipitation (based on INCA RR data (2003 to 2013) of ZAMG); MAR, mean annual runoff volume per unit area (based on the discharge data of TIWAG); HQ1.5, peak discharge with a return period of 1.5 years

Table B-2: List of main characteristics of the study sites – part 2

| Site | min SL | max SL | mean CS ^b | sd CS ^b | mean RG ^b | sd RG ^b | mean SG ^b | sd SG ^b | 10 th perc SG ^b | mean DS | mean DL |
|----------------------|--------|--------|----------------------|--------------------|----------------------|--------------------|----------------------|--------------------|---------------------------------------|---------|----------------------|
| | (m) | (m) | (°) | (°) | (m/m) | (m/m) | (m/m) | (m/m) | (m/m) | (m/m) | (m/km ²) |
| Schoentalbach | 1781 | 3000 | 33.0 | 0.34 | 0.44 | 0.17 | 0.43 | 0.04 | 0.38 | 0.20 | 1659 |
| Schelfalmbach | 1960 | 3002 | 30.1 | 0.30 | 0.23 | 0.13 | 0.23 | 0.05 | 0.18 | 0.12 | 1758 |
| Klammbach | 2052 | 2876 | 31.5 | 0.37 | 0.14 | 0.09 | 0.10 | 0.04 | 0.04 | 0.13 | 1151 |
| Unterer Liesenerbach | 1978 | 3322 | 28.1 | 0.52 | 0.37 | 0.14 | 0.41 | 0.17 | 0.22 | 0.17 | 1903 |
| Oberer Liesenerbach | 1983 | 3296 | 32.8 | 0.50 | 0.41 | 0.15 | 0.49 | 0.15 | 0.36 | 0.18 | 1472 |
| Madatschbach | 1808 | 3438 | 40.8 | 0.51 | 0.37 | 0.20 | 0.32 | 0.06 | 0.24 | 0.19 | 1291 |
| Gsallbach | 1828 | 3273 | 42.6 | 0.56 | 0.21 | 0.14 | 0.25 | 0.15 | 0.18 | 0.22 | 1118 |
| Rostizbach | 1794 | 3392 | 36.6 | 0.37 | 0.46 | 0.14 | 0.32 | 0.17 | 0.11 | 0.14 | 1252 |
| Mittertalbach | 1941 | 2996 | 34.1 | 0.47 | 0.11 | 0.09 | 0.08 | 0.03 | 0.05 | 0.09 | 1343 |
| Kraspesbach | 1925 | 3055 | 35.0 | 0.40 | 0.14 | 0.08 | 0.25 | 0.12 | 0.12 | 0.09 | 1403 |
| Wazebach | 1797 | 3528 | 38.0 | 0.38 | 0.34 | 0.12 | 0.29 | 0.12 | 0.18 | 0.13 | 1271 |
| Fissladbach | 1798 | 3141 | 32.3 | 0.33 | 0.20 | 0.13 | 0.16 | 0.13 | 0.07 | 0.05 | 1613 |
| Verpeilbach | 1805 | 3410 | 39.6 | 0.53 | 0.16 | 0.08 | 0.17 | 0.02 | 0.15 | 0.06 | 1373 |
| Laengentalerbach | 1954 | 3319 | 36.9 | 0.49 | 0.15 | 0.09 | 0.08 | 0.04 | 0.04 | 0.04 | 1363 |
| Tscheybach | 1797 | 3056 | 30.7 | 0.26 | 0.09 | 0.08 | 0.06 | 0.03 | 0.02 | 0.04 | 1368 |
| Gleirschbach | 1985 | 3188 | 32.0 | 0.38 | 0.20 | 0.16 | 0.10 | 0.07 | 0.03 | 0.03 | 1435 |
| Oberbergbach | 1985 | 3457 | 32.0 | 0.43 | 0.08 | 0.08 | 0.10 | 0.09 | 0.02 | 0.03 | 1737 |
| Radurschlbach | 1788 | 3352 | 33.3 | 0.38 | 0.04 | 0.06 | 0.07 | 0.03 | 0.03 | 0.03 | 1464 |
| Horlachbach | 1914 | 3181 | 32.5 | 0.36 | 0.09 | 0.09 | 0.10 | 0.04 | 0.06 | 0.02 | 1373 |
| Pitzbach | 1808 | 3549 | 28.1 | 0.40 | 0.08 | 0.07 | 0.17 | 0.14 | 0.07 | 0.03 | 1725 |

^a Definitions are as follows: min SL, sea level at the water intake structure; max SL, maximum sea level of the catchment; mean CS, mean slope of the catchment in degree; sd CS, standard deviation of catchment slope in degree; mean RG, mean channel gradient of the reach upstream of the water intake structure (reach gradient); sd RG, standard deviation of the reach gradient; mean SG, mean channel gradient of multiple reaches comprising the entire main channel which drains more than two third of the catchment (stream gradient); sd SG, standard deviation of the stream gradient; 10thperc SG, 10th percentile of the stream gradient; mean DS, mean slope of the drainage network which is defined by all raster cells (10x10m²) which drain an area larger than 200 ha; mean DL, length of the drainage network divided by the catchment area

^b Channel gradients of both scales, reach and stream, were determined by a digital elevation model with a resolution of 1x1 m²

1.1.3 Measuring system

The water intake structures are constructed according to a standardized scheme (Tyrolean Weir system according to *Drobir* (1981); Figure B-4) and fulfil the requirements of a bed load measuring station (e.g. *Turowski*, 2010; *Rickenmann and Fritsch*, 2010; *Rickenmann*, 2001; *Hofer*, 1985; *Sommer and Lauffer*, 1982; *Tschada*, 1975). Water and transported sediment are abstracted via an intake channel which is covered by a bottom rack (sloped in flow direction with beam spacing of 15 cm; Figure B-4a). The magnitude of water intake is limited by the structures' dimensions only, with no residual water at flows beyond the structure's capacity, which is barely exceeded at most sites. However, water and sediment with diameters smaller than about 15 cm divert to a settling basin (Figure B-4b). Typically, these settling basins are dimensioned in a way that sediment larger than about 0.5 mm deposits totally (*Hofer*, 1985; *Neuner* (operating manager of the hydropower station Kraftwerksguppe Sellrain-Silz of the TIWAG), personal communication, October 2014) while finer grains, as well as water discharge, pass a lateral overflow and flow into a diversion tunnel.

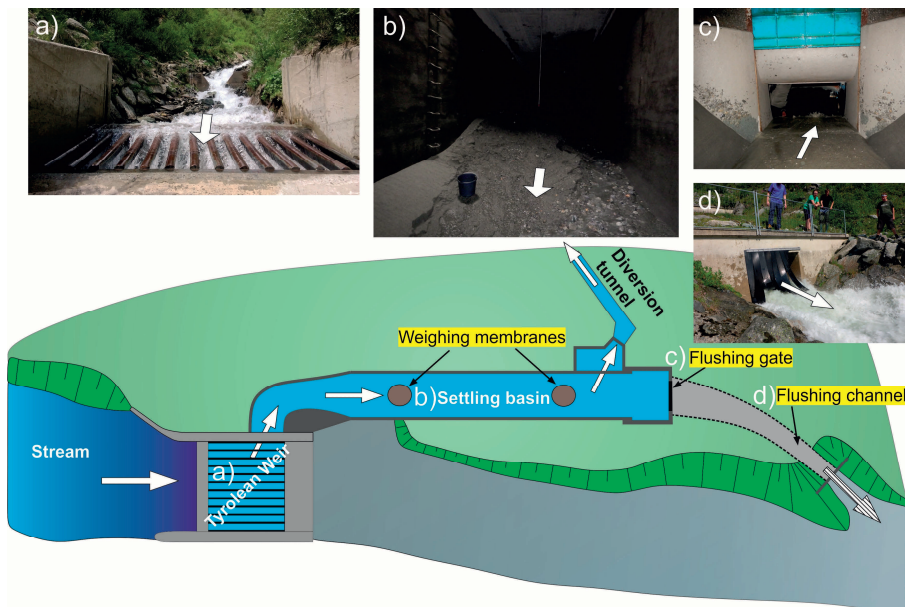


Figure B-4: Schematic ground plan of a water intake structure operated by TIWAG

In order to avoid too large sediment accumulations within the settling basin, at least two pressure gauges (weighing cells or load membranes) with a diameter of about 1 m are located lengthways at the bottom (Figure B-4b and Figure B-5). These weighing cells register the vertical stress originated by the deposited sediment and initiate a hydraulic flushing (Figure B-4c) once the vertical stress exceeds a certain threshold (*Tschada*, 1975). During this hydraulic flushing the deposited sediment is sluiced out of the settling basin and it is returned into the stream reach downstream of it (Figure B-4d). The upper membrane is located at the upper quarter point of the settling basin,

while the lower one is close to the lowermost quarter point. However, the bed load deposits predominantly in the region of the upper membrane and the hydraulic flushings are almost exclusively triggered by that one. The lower membrane acts for safety reasons in order to avoid any congestion in case the upper membrane fails.

Schematic view of the settling basins

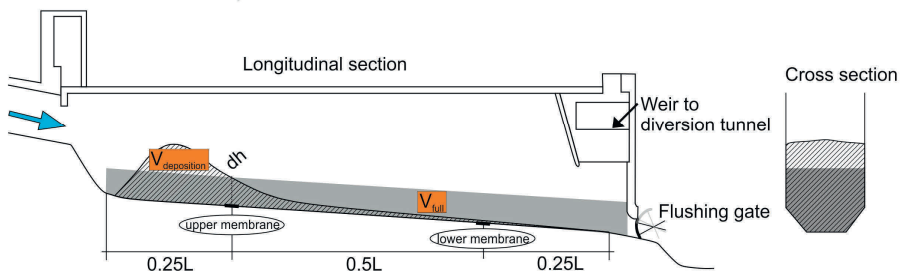


Figure B-5: Schematic longitudinal view of the settling basin of a water intake structure operated by TIWAG

The hydraulic weighing device even compensates the fluctuations of the water level and enables to gauge submerged sediment load only (*Schober*, 1961; *R. Neuner*, personal communication, October 2014). The reliability of this flushing system was successfully tested in the early sixties (*Schober*, 1961) and it is in common use at several water intakes operated by the hydropower company TIWAG since then (e.g. *Tschada and Hofer*, 1990; *Sommer and Lauffer*, 1982; *Tschada*, 1975).

At selected water intake structures, this measuring system was further upgraded from a mechanical (first described in *Schober*, 1961) to a digital device, enabling data transmission. However, the functionality of triggering hydraulic flushings did not change and it is the same since their construction (*R. Neuner*, personal communication, October 2014).

1.1.3.1 Count of hydraulic flushings

The number of hydraulic flushings is progressively recorded by a mechanical numerator, which is implemented at each water intake structure. Since the year 1965, the staff of TIWAG reads the counts of hydraulic flushings on a monthly or yearly interval and they record it in the corresponding logbook (nowadays an Excel file).

But not all hydraulic flushings are triggered automatically by exceeding a certain threshold of deposit weight. For instance, hydraulic flushings are as well triggered manually in the course of maintenance works and inspections at the water intake structures (most likely at the beginning and at the end of the summer season). A differentiation is possible since hydraulic flushings which were triggered manually are marked in the logbook.

At 15 out of 20 water intake structures, discharge is continuously registered and records are available since 1985 (in 15 minutes interval, see Table B-8 in section 0). Theoretically, the moment of each hydraulic flushing can be determined more precisely based on these continuous discharge records. During each hydraulic flushing, the water diversion is interrupted and total discharge flows through the sediment trap and

back into the stream. Since the diverted discharge is gauged separately, there are sudden breakpoints in the hydrographs due to the hydraulic flushings (Figure B-6).

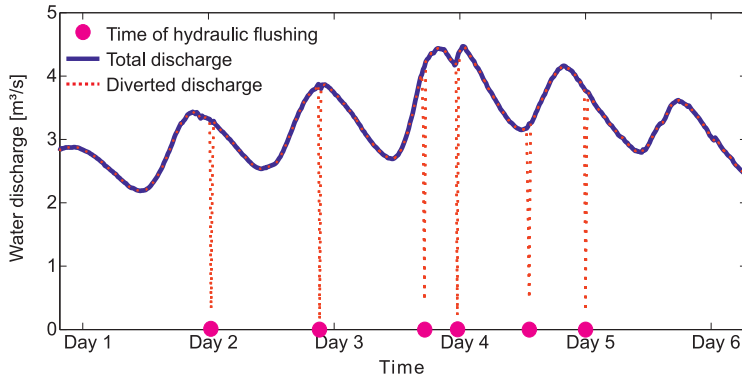


Figure B-6: Example of the continuous discharge data with a temporal resolution of 15min

In order to detect these discontinuities of the discharge hydrograph automatically, an algorithm was first applied to the total time series of discharge data. Although the discontinuities of the discharge hydrograph were detected sufficiently by the algorithm, each discontinuity was further checked manually for plausibility. The comparison of the annual counts of hydraulic flushings, which were derived either from the logbook or the continuous discharge hydrographs, reveal some differences (Figure B-7). These differences are comparatively small in catchments with frequent hydraulic flushings (usually large catchments), while differences are huge for catchments with a low number of hydraulic flushings per year.

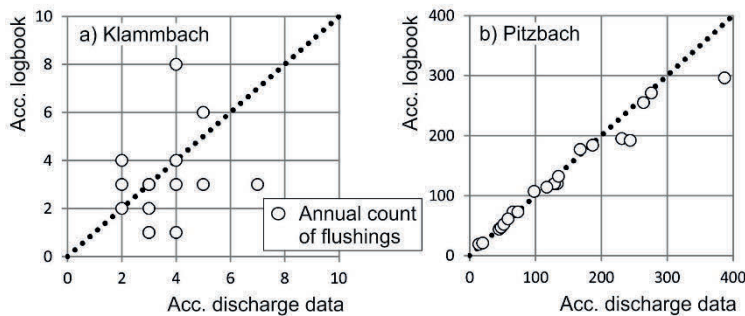


Figure B-7: Differences of annual counts of hydraulic flushings either determined from the logbook or the discharge hydrograph

The hydraulic flushings registered in the logbook of each water intake structure are assumed to be more reliable, than back-tracing them from the discharge hydrographs. First, discharge data do not enable a separation of manually or automatically triggered hydraulic flushings. In addition, hydraulic flushings are sometimes triggered two times

in a row (for example at the beginning and at the end of maintenance works), which is not traceable by discharge hydrographs as well. Furthermore, any error in data transmission or any post-processing of discharge data could cause additional or level out existing discharge discontinuities. Hence, the count of hydraulic flushings is predominantly based on the logbook of the corresponding water intake structure.

For nine sites, logbook based counts are available since 1965, while the observation period goes back to 1997 for the remaining eleven sites. However, for ten of these eleven sites, discharge data are available every 15 min since 1985, which enabled a rough determination of the number of hydraulic flushings for the period 1985 to 1996 based on hydrograph discontinuities. Although the latter approach features larger uncertainties, data are assumed to be sufficiently accurate for an order of magnitude analysis of annual bed load volumes.

Table B-3: Annual counts of hydraulic flushings at the water intake structures of the hydropower station Sellrain-Silz. The left (first) number refers to the annual count of hydraulic flushings which were triggered automatically by exceeding a predefined deposit height and the right (second) number represents the manually triggered flushings. In case the second number is replaced by ‘-’, the count data were derived from the discharge hydrograph rather than the logbook. In years with no data, the annual counts of hydraulic flushings were either not available or they were rejected due to bad quality.

| Site --- Year | Oberberg- bach | Unterer Liesener- bach | Oberer Liesener- bach | Laengen- talbach | Schoen- talbach | Schelf- almbach | Gleirsch- bach | Kraspes- bach | Klamm- bach | Horlach- bach | Mitteral- bach |
|---------------------|-------------------|------------------------------|-----------------------------|---------------------|--------------------|--------------------|-------------------|------------------|----------------|------------------|-------------------|
| 1985 | 4 / - | 8 / - | 1 / - | | 1 / - | 24 / - | 0 / - | 1 / - | | 2 / - | |
| 1986 | 15 / - | 10 / - | 8 / - | | 3 / - | 9 / - | 4 / - | 7 / - | | 5 / - | |
| 1987 | 58 / - | 16 / - | | 4 / - | 5 / - | 10 / - | 10 / - | 11 / - | | 6 / - | |
| 1988 | 64 / - | 18 / - | 14 / - | 3 / - | 6 / - | 5 / - | 7 / - | 2 / - | | 3 / - | |
| 1989 | 45 / - | 10 / - | 3 / - | 2 / - | 8 / - | 14 / - | 4 / - | 2 / - | | 1 / - | |
| 1990 | 61 / - | 6 / - | 3 / - | 3 / - | 3 / - | 21 / - | 8 / - | 0 / - | | 2 / - | |
| 1991 | 80 / - | 48 / - | 2 / - | 0 / - | 4 / - | | 5 / - | 1 / - | | 2 / - | |
| 1992 | 62 / - | 73 / - | 27 / - | 10 / - | 6 / - | 12 / - | 14 / - | 3 / - | 1 / - | 4 / - | |
| 1993 | 19 / - | 183 / - | 5 / - | 5 / - | 4 / - | 3 / - | 13 / - | 6 / - | 4 / - | 3 / - | |
| 1994 | 23 / - | 236 / - | 7 / - | 6 / - | 4 / - | 4 / - | 7 / - | 4 / - | 3 / - | 2 / - | |
| 1995 | 4 / - | 354 / - | 2 / - | 2 / - | 8 / - | 4 / - | 13 / - | 15 / - | 3 / - | 14 / - | |
| 1996 | 5 / - | 128 / - | 1 / - | 1 / - | 2 / - | 1 / - | 3 / - | 1 / - | 0 / - | 1 / - | |
| 1997 | 18 / 11 | 418 / 3 | 2 / 3 | 4 / 2 | 3 / 3 | 1 / 2 | 6 / 4 | 6 / 2 | 0 / 4 | 1 / 3 | 0 / 2 |
| 1998 | 50 / 4 | 529 / 8 | 4 / 1 | 5 / 5 | 9 / 3 | 1 / 2 | 9 / 2 | 3 / 16 | 0 / 3 | 1 / 3 | 0 / 2 |
| 1999 | 29 / 8 | 99 / 8 | 9 / 1 | 5 / 7 | 12 / 4 | 0 / 2 | 6 / 9 | 5 / 8 | 1 / 2 | 2 / 2 | 2 / 2 |
| 2000 | 60 / 5 | 102 / 5 | 3 / 2 | 3 / 2 | 3 / 2 | 1 / 2 | 8 / 2 | 3 / 10 | 0 / 3 | 1 / 2 | 0 / 2 |
| 2001 | 29 / 2 | 91 / 6 | 1 / 2 | 3 / 3 | 1 / 2 | 1 / 2 | 6 / 2 | 2 / 2 | 0 / 3 | 1 / 2 | 0 / 2 |
| 2002 | 21 / 3 | 265 / 2 | 2 / 1 | 6 / 3 | 2 / 3 | 3 / 2 | 18 / 5 | 116 / 6 | 2 / 3 | 1 / 2 | 0 / 2 |
| 2003 | 83 / 3 | 256 / 4 | 20 / 4 | 40 / 5 | 6 / 2 | 7 / 2 | 15 / 2 | 12 / 5 | 9 / 2 | 31 / 2 | 11 / 2 |
| 2004 | 24 / 2 | 149 / 2 | 3 / 2 | 38 / 3 | 6 / 2 | 1 / 2 | 36 / 2 | 29 / 2 | 5 / 2 | 3 / 2 | 5 / 2 |
| 2005 | 20 / 2 | 42 / 2 | 2 / 2 | 34 / 2 | 3 / 2 | 2 / 2 | 41 / 6 | 22 / 9 | 2 / 2 | 4 / 6 | 1 / 2 |
| 2006 | 38 / 3 | 193 / 2 | 1 / 1 | 16 / 4 | 0 / 3 | 0 / 3 | 18 / 1 | 8 / 6 | 0 / 2 | 3 / 1 | 1 / 4 |
| 2007 | 31 / 3 | 37 / 7 | 0 / 5 | 29 / 7 | 0 / 4 | 0 / 2 | 0 / 3 | 1 / 3 | 0 / 3 | 0 / 1 | 0 / 3 |
| 2008 | 35 / 2 | 43 / 8 | 4 / 1 | 21 / 3 | 1 / 2 | 0 / 2 | 12 / 3 | 7 / 4 | 1 / 1 | 2 / 3 | 0 / 2 |
| 2009 | 39 / 2 | 23 / 0 | 5 / - | 7 / 2 | 6 / 2 | 0 / 2 | 2 / 2 | 5 / 3 | 2 / 2 | 2 / 1 | 0 / 3 |
| 2010 | 74 / 2 | 19 / 1 | 4 / 0 | 15 / 2 | 11 / 6 | 0 / 3 | 12 / 3 | 0 / 6 | 2 / 3 | 0 / 1 | 0 / 4 |
| 2011 | 36 / 4 | 21 / - | 4 / - | 1 / 1 | 0 / 2 | 0 / 2 | 0 / 2 | 0 / 2 | 1 / 1 | 0 / 0 | 1 / 1 |
| 2012 | 49 / 2 | 17 / 1 | 4 / 0 | 33 / 1 | 3 / 2 | 0 / 2 | 4 / 2 | 3 / 2 | 2 / 2 | 2 / 1 | 0 / 1 |
| 2013 | 27 / 2 | 25 / 3 | 4 / 1 | 19 / 2 | 6 / 2 | 3 / 2 | 6 / 4 | 4 / 2 | 3 / 2 | 2 / 3 | 3 / 3 |

Table B-4¹: Annual counts of hydraulic flushings at the water intake structures of the Kaunertal hydropower station. The left (first) number refers to the annual count of hydraulic flushings which were triggered automatically by exceeding a predefined deposit height and the right (second) number represents the manually triggered flushings.

| Site --- Year | Gsallbach | Verpeil- bach ^a | Madatsch- bach | Wazebach | Rostiz- bach | Fisslad- bach | Pitzbach | Radurschl- bach | Tschey- bach |
|---------------------|-----------|-------------------------------|-------------------|----------|-----------------|------------------|----------|--------------------|-----------------|
| 1965 | 95 / 0 | 51 / 0 | 79 / 0 | 79 / 0 | 183 / 0 | 64 / 0 | 424 / 0 | 228 / 0 | 137 / 0 |
| 1966 | 46 / 0 | 8 / 0 | 25 / 0 | 19 / 0 | 10 / 0 | 13 / 0 | 54 / 0 | 11 / 0 | 4 / 0 |
| 1967 | 76 / 0 | 9 / 0 | 67 / 0 | 9 / 0 | 120 / 0 | 21 / 0 | 149 / 0 | 23 / 0 | 43 / 0 |
| 1968 | 8 / 0 | 2 / 0 | 19 / 0 | 5 / 0 | 4 / 0 | 10 / 0 | 105 / 0 | 8 / 0 | 11 / 0 |
| 1969 | 53 / 0 | 14 / 0 | 24 / 0 | 10 / 0 | 6 / 0 | 15 / 0 | 163 / 0 | 32 / 0 | 40 / 0 |
| 1970 | 28 / 0 | 25 / 0 | 15 / 0 | 28 / 0 | 34 / 0 | 23 / 0 | 237 / 0 | 65 / 0 | 106 / 0 |
| 1971 | 4 / 0 | 3 / 0 | 23 / 0 | 6 / 0 | 1 / 0 | 2 / 0 | 315 / 0 | 3 / 0 | 13 / 0 |
| 1972 | 14 / 0 | 27 / 0 | 14 / 0 | 2 / 0 | 1 / 0 | 0 / 0 | 75 / 0 | 47 / 0 | 29 / 0 |
| 1973 | 7 / 0 | 6 / 0 | 16 / 0 | 0 / 0 | 1 / 0 | 0 / 0 | 169 / 0 | 5 / 0 | 9 / 0 |
| 1974 | 5 / 0 | 4 / 0 | 16 / 0 | 20 / 0 | 4 / 0 | 4 / 0 | 80 / 0 | 17 / 0 | 21 / 0 |
| 1975 | 24 / 0 | 24 / 0 | 24 / 0 | 15 / 0 | 9 / 0 | 4 / 0 | 129 / 0 | 19 / 0 | 18 / 0 |
| 1976 | 0 / 0 | 0 / 0 | 0 / 0 | 19 / 0 | 0 / 0 | 1 / 0 | 72 / 0 | 1 / 0 | 14 / 0 |
| 1977 | 1 / 0 | 1 / 0 | 3 / 0 | 55 / 0 | 3 / 0 | 1 / 0 | 154 / 0 | 5 / 0 | 56 / 0 |
| 1978 | 5 / 0 | 4 / 0 | 2 / 0 | 10 / 0 | 2 / 0 | 4 / 0 | 88 / 0 | 13 / 0 | 58 / 0 |
| 1979 | 2 / 0 | 3 / 0 | 2 / 0 | 14 / 0 | 2 / 0 | 3 / 0 | 383 / 0 | 9 / 0 | 39 / 0 |
| 1980 | 3 / 0 | 4 / 0 | 3 / 0 | 11 / 0 | 2 / 0 | 4 / 0 | 74 / 0 | 22 / 0 | 69 / 0 |
| 1981 | 2 / 0 | 1 / 0 | 1 / 0 | 8 / 0 | 2 / 0 | 2 / 0 | 102 / 0 | 12 / 0 | 8 / 0 |
| 1982 | 1 / 0 | 2 / 0 | 1 / 0 | 3 / 0 | 1 / 0 | 1 / 0 | 106 / 0 | 12 / 0 | 8 / 0 |
| 1983 | 3 / 0 | 1 / 0 | 1 / 0 | 4 / 0 | 1 / 0 | 1 / 0 | 69 / 0 | 3 / 0 | 8 / 0 |
| 1984 | 2 / 0 | 2 / 0 | 5 / 0 | 1 / 0 | 1 / 0 | 1 / 0 | 60 / 0 | 2 / 0 | 14 / 0 |
| 1985 | 12 / 0 | 1 / 0 | 3 / 0 | 6 / 0 | 3 / 0 | 2 / 0 | 141 / 0 | 11 / 0 | 6 / 0 |
| 1986 | 5 / 0 | 4 / 0 | 3 / 0 | 4 / 0 | 1 / 0 | 0 / 0 | 221 / 0 | 16 / 0 | 15 / 0 |
| 1987 | 11 / 0 | 2 / 0 | 2 / 0 | 5 / 0 | 11 / 0 | 0 / 0 | 210 / 0 | 26 / 0 | 76 / 0 |
| 1988 | 1 / 0 | 6 / 0 | 2 / 0 | 16 / 0 | 2 / 0 | 0 / 0 | 62 / 0 | 11 / 0 | 4 / 0 |
| 1989 | 3 / 0 | 9 / 1 | 1 / 22 | 0 / 4 | 24 / 10 | 1 / 0 | 45 / 0 | 20 / 2 | 24 / 0 |
| 1990 | 1 / 0 | 0 / 2 | 25 / 2 | 2 / 0 | 6 / 1 | 0 / 0 | 14 / 0 | 1 / 1 | 48 / 1 |
| 1991 | 4 / 0 | 2 / 18 | 27 / 0 | 1 / 2 | 0 / 0 | 0 / 0 | 557 / 0 | 12 / 2 | 28 / 1 |
| 1992 | 0 / 0 | 1 / 0 | 7 / 0 | 3 / 3 | 1 / 0 | 0 / 0 | 387 / 0 | 1 / 0 | 38 / 1 |
| 1993 | 2 / 0 | 2 / 0 | 14 / 1 | 1 / 0 | 0 / 0 | 1 / 0 | 231 / 0 | 2 / 0 | 20 / 0 |
| 1994 | 2 / 0 | | 27 / 0 | 6 / 0 | 1 / 0 | 0 / 0 | 264 / 0 | 2 / 0 | 21 / 0 |
| 1995 | 3 / 0 | | 16 / 0 | 8 / 0 | 20 / 0 | 6 / 0 | 48 / 0 | 21 / 1 | 89 / 1 |
| 1996 | 3 / 0 | | 20 / 1 | 4 / 1 | 0 / 0 | 1 / 0 | 20 / 0 | 0 / 0 | 20 / 1 |
| 1997 | 12 / 0 | | 17 / 1 | 2 / 2 | 0 / 1 | 0 / 0 | 66 / 0 | 1 / 1 | 30 / 1 |
| 1998 | 13 / 0 | | 65 / 0 | 1 / 2 | 2 / 1 | 0 / 0 | 133 / 0 | 1 / 0 | 20 / 0 |
| 1999 | 20 / 0 | | 33 / 2 | 6 / 1 | 18 / 1 | 0 / 0 | 244 / 0 | 6 / 1 | 109 / 4 |
| 2000 | 1 / 0 | | 15 / 0 | 1 / 2 | 1 / 0 | 0 / 0 | 187 / 0 | 0 / 2 | 46 / 2 |
| 2001 | 2 / 0 | | 17 / 0 | 11 / 0 | 2 / 0 | 0 / 0 | 129 / 0 | 2 / 0 | 38 / 1 |
| 2002 | 5 / 1 | | 10 / 1 | 14 / 2 | 3 / 0 | 0 / 0 | 52 / 0 | 2 / 1 | 38 / 0 |
| 2003 | 18 / 1 | | 22 / 0 | 37 / 1 | 1 / 1 | 2 / 0 | 135 / 0 | 0 / 0 | 21 / 1 |
| 2004 | 7 / 2 | | 2 / 3 | 7 / 2 | 1 / 0 | 3 / 0 | 73 / 1 | 1 / 1 | 27 / 1 |
| 2005 | 12 / 1 | | 16 / 1 | 10 / 2 | 0 / 1 | 1 / 0 | 58 / 1 | 3 / 0 | 17 / 0 |
| 2006 | 14 / 3 | | 8 / 4 | 19 / 9 | 6 / 3 | 1 / 0 | 117 / 1 | 2 / 1 | 24 / 0 |
| 2007 | 22 / 1 | | 4 / 1 | 10 / 3 | 1 / 0 | 0 / 0 | 276 / 0 | 0 / 0 | 14 / 1 |
| 2008 | 14 / 1 | | 3 / 3 | 15 / 1 | 10 / 1 | 1 / 0 | 166 / 4 | 3 / 0 | 102 / 2 |
| 2009 | 5 / 2 | | 5 / 1 | 20 / 0 | 3 / 1 | 0 / 0 | 98 / 0 | 0 / 0 | 27 / 1 |
| 2010 | 30 / 1 | | 6 / 1 | 6 / 2 | 5 / 0 | 1 / 0 | 178 / 0 | 1 / 0 | 42 / 0 |
| 2011 | 1 / 1 | | 3 / 0 | 2 / 0 | 0 / 0 | 0 / 0 | 279 / 0 | 0 / 0 | 9 / 0 |
| 2012 | 7 / 0 | | 9 / 0 | 4 / 0 | 0 / 1 | 0 / 0 | 457 / 0 | 1 / 0 | 51 / 3 |
| 2013 | 8 / 0 | | 6 / 0 | 8 / 0 | 6 / 0 | 0 / 0 | 305 / 0 | 4 / 0 | 34 / 0 |

^a The count data of the years 1994 to 2013 were rejected due to a possible bias, which is attributed to a retention basin upstream of the water intake structure

¹ This Table B-4 was corrected afterwards and differs from that of the original version of the dissertation.

1.1.3.2 Deposit volumes

Based on the annual count of hydraulic flushings, the annual bed load volume is determined for each study site and for the entire time span of data availability. Therefore, the number of hydraulic flushings needs to be converted to the bed load volume, which requires knowledge regarding the volume of the sediment deposition within the settling basin just at the moment the flushing is initiated. *Tschada* (1975) analyzed the deposit volumes (dV) within the settling basins of nine water intake structures and found that the bed load predominantly accumulates in the upper part of the settling basin. He further computed the ratio of the observed deposit volume to a theoretical volume (tV); herein, tV is the volume in the case the deposit height at the upper weighing membrane is constant throughout the entire settling basin (Figure B-5). These site-specific ratios can be interpreted as a scaling factors (sf), which *Tschada* (1975) found to vary between 0.48 and 0.68, with a mean of 0.61 (Table B-5).

The theoretical volume can be determined by the dimensions of each settling basin and their triggering deposit height (dh) only, according:

$$tV = A(dh) \times L, \quad (B1)$$

where $A(dh)$ is the cross-sectional area at the upper weighing cell, occupied by sediment just before the hydraulic flushing is released. The multiplication with the scaling factor sf gives a sufficient estimate of the mean deposit volume in case the hydraulic flushings are triggered automatically, with:

$$dV = sf \times tV. \quad (B2)$$

For ten of the settling basins, no measurements regarding the deposit volumes (dV) are available, but a scaling factor of 0.61 is assumed to be a reasonable estimate.

At the water intake structures of the Pitzbach and the Oberbergbach, the vertical stress of the sediment deposition is measured by four rather than two weighing membranes since 1985. Furthermore, these data are recorded every 15 minutes which enables the back-calculation of the deposit volume just before a hydraulic flushing was initiated (*Hofer*, 1985). Based on these calculations, the mean scaling factor was derived for each of the two water intake structures separately (Table B-5).

The deposit volumes computed by means of equations B2 are only valid in case the hydraulic flushings are triggered automatically by exceeding a predefined threshold of vertical stress. Concerning the hydraulic flushings which were triggered manually in course of maintenance works, no information regarding the current deposit volume is available. However, it's obvious that the average deposit volume of manually triggered flushings is less than that of an automatically triggered one. Due to the lack of further information, the deposit volume of manually triggered flushing is assumed to be a certain fraction of the automatically triggered one. The fraction varies monthly with its minimum of 0.1 in the winter season (October to April) and its maximum of 0.5 in the summer. However, manually triggered hydraulic flushings are generally rare and the bias is assumed to be minor.

1.1.3.3 Proportion of bed load in bulked sediment deposition

In this study, bed load is defined by sediment larger than 1 mm. To account for the proportion of bed load in the bulked sediment deposition, the grain size distribution was measured within the settling basin of the Pitzbach and the Oberbergbach in sum-

mer 2015. Next to an obvious fining along the settling basin, with coarser grains depositing in the upper part, the proportion of grains coarser than 1 mm (pb) was about 60 % to 65 % of the total sediment deposition at both sites. *Strobl* (1980) and *Sommer and Lauffer* (1982) report $pb=0.65$, while *Sommer* (1980) used $pb=0.70$. To preserve the comparability with the latest study of *Sommer and Lauffer* (1982), the proportion of bed load in total load (pb) is defined by 0.65 in this study.

Furthermore, the porosity of the sediment deposition was assumed to be 30 %, which represents the mean porosity measured within the settling basin of the Pitzbach water intake during a survey in 2015 (*Eichner*, unpublished). Within the present study, the deposit volumes are reduced by these factors in order to account for solid bed load only.

1.1.4 Determination of annual bed load volumes

Table B-5 summarizes the main characteristics of the water intake structures necessary to determine the mean bed load volume in case a hydraulic flushing is triggered automatically, which is defined as:

$$bV = tV \times sf \times pb \times (1 - e). \quad (\text{B3})$$

Therein tV is the theoretical volume (equation B1), sf is the site-specific and temporally constant scaling factor and two empiric constants account for the proportion of bed load in total load (pb) and the porosity (e) of the sediment deposition, respectively.

The annual bed load volumes (ABV) are then determined for each study site by multiplying the annual count of hydraulic flushings ($N_{lb,i}$) and the bed load volume (bV):

$$ABV = N_{lb,i} \times bV. \quad (\text{B4})$$

Table B-5: Summary of the large data set of the annual count of hydraulic flushings and the parameters necessary to determine the mean bed load volume per flushing. Definitions are as follows: Q_A , design discharge of the water intake structure; dh , deposit height at which the hydraulic flushing is initiated; tV , volume in case the settling basin is evenly filled up to dh ; sf , scaling factor; dV , volume of the sediment deposition; bV , bed load volume without pores.

| Site | Q_A | dh | tV | sf | dV | Porosity (ϵ) | Proportion bed load (pb) | bV |
|----------------------|---------------------|---------|-------------------|-------------------|-----------------------------|----------------------------|------------------------------------|-------------------|
| | [m ³ /s] | [m] | [m ³] | | [m ³] | | | [m ³] |
| Schoentalbach | 0.5 | 0.88 | 17.2 | 0.61 ^a | 10.4 | 0.3 | 0.65 | 4.7 |
| Schelfalmbach | 0.5 | 0.90 | 20.1 | 0.61 ^a | 12.2 | 0.3 | 0.65 | 5.5 |
| Klammbach | 0.7 | 0.89 | 33.3 | 0.61 ^a | 20.1 | 0.3 | 0.65 | 9.2 |
| Unterer Liesenerbach | 0.8 | 0.85 | 26.8 | 0.61 ^a | 16.2 | 0.3 | 0.65 | 7.4 |
| Oberer Liesenerbach | 1.5 | 0.93 | 45.6 | 0.61 ^a | 27.6 | 0.3 | 0.65 | 12.6 |
| Madatschbach | 0.8 | 0.50 | 11.4 | 0.6 | 6.8 | 0.3 | 0.65 | 3.1 |
| Gsallbach | 0.8 | 0.50 | 15.3 | 0.58 | 8.9 | 0.3 | 0.65 | 4.0 |
| Rostizbach | 1.0 | 0.50 | 9.7 | 0.59 | 5.7 | 0.3 | 0.65 | 2.6 |
| Mittertalbach | 0.9 | 0.90 | 31.0 | 0.61 ^a | 18.7 | 0.3 | 0.65 | 8.5 |
| Kraspesbach | 1.2 | 0.91 | 36.7 | 0.61 ^a | 22.2 | 0.3 | 0.65 | 10.1 |
| Wazebach | 1.4 | 0.50 | 17.9 | 0.62 | 11.1 | 0.3 | 0.65 | 5.0 |
| Fissladbach | 2.3 | 0.50 | 28.1 | 0.66 | 18.5 | 0.3 | 0.65 | 8.4 |
| Verueilbach | 2.5 | 0.50 | 22.7 | 0.61 | 13.8 | 0.3 | 0.65 | 6.3 |
| Laengentalerbach | 2.9 | 1.05 | 67.7 | 0.61 ^a | 41.0 | 0.3 | 0.65 | 18.6 |
| Tscheybach | 3.0 | 0.50 | 24.8 | 0.61 | 15.1 | 0.3 | 0.65 | 6.9 |
| Gleirschbach | 3.6 | 1.05 | 88.8 | 0.61 ^a | 53.7 | 0.3 | 0.65 | 24.5 |
| Oberbergbach | 5.5 | 1.25 | - | - | 40.0 ^b | 0.3 | 0.65 | 18.2 |
| Radurschlbach | 4.4 | 0.50 | 34.6 | 0.68 | 23.5 | 0.3 | 0.65 | 10.7 |
| Hoflachbach | 4.9 | 0.90 | 97.0 | 0.61 ^a | 58.7 | 0.3 | 0.65 | 26.7 |
| Pitzbach | 5.4 | 0.5 / 2 | 39.1 / - | 0.48 / - | 18.8 / 44.2 ^b | 0.3 | 0.65 | 8.5 / 20.1 |

^a Scaling factors are estimated according the mean of those given in Tschada (1975)

^b Volume is based on field data based back-calculations of the sediment deposition (section B.1.3) and represents the mean value

Table B-6: Annual bed load volumes at the water intake structures of the Kaunertal hydro-power station. In years with no data, the annual counts of hydraulic flushings were either not available or they were rejected due to bad quality. The data refer to the solid volume without pores. To obtain the deposit volume, the solid volume has to be divided by 0.7 (see Table B5).

| Site --- | Gsallbach | Verpeil- bach | Madatsch- bach | Wazebach | Rostizbac h | Fisslad- bach | Pitzbach | Radurschl- bach | Tschey- bach |
|-------------|-----------|------------------|-------------------|----------|----------------|------------------|----------|--------------------|-----------------|
| Year | [m³] | [m³] | [m³] | [m³] | [m³] | [m³] | [m³] | [m³] | [m³] |
| 1965 | 384 | 321 | 246 | 399 | 477 | 540 | 3621 | 2441 | 943 |
| 1966 | 186 | 50 | 78 | 96 | 26 | 110 | 461 | 118 | 28 |
| 1967 | 307 | 57 | 209 | 45 | 312 | 177 | 1272 | 246 | 296 |
| 1968 | 32 | 13 | 59 | 25 | 10 | 84 | 897 | 86 | 76 |
| 1969 | 214 | 88 | 75 | 50 | 16 | 127 | 1392 | 343 | 275 |
| 1970 | 113 | 158 | 47 | 141 | 89 | 194 | 2024 | 696 | 730 |
| 1971 | 16 | 19 | 72 | 30 | 3 | 17 | 2690 | 32 | 89 |
| 1972 | 57 | 170 | 44 | 10 | 3 | 2 | 640 | 503 | 200 |
| 1973 | 28 | 38 | 50 | 1 | 3 | 2 | 1443 | 54 | 62 |
| 1974 | 20 | 25 | 50 | 101 | 10 | 34 | 683 | 182 | 145 |
| 1975 | 97 | 151 | 75 | 76 | 23 | 34 | 1102 | 203 | 124 |
| 1976 | 1 | 2 | 1 | 96 | 1 | 8 | 615 | 11 | 96 |
| 1977 | 4 | 6 | 9 | 278 | 8 | 8 | 1315 | 54 | 385 |
| 1978 | 20 | 25 | 6 | 50 | 5 | 34 | 751 | 139 | 399 |
| 1979 | 8 | 19 | 6 | 71 | 5 | 25 | 3271 | 96 | 268 |
| 1980 | 12 | 25 | 9 | 56 | 5 | 34 | 632 | 236 | 475 |
| 1981 | 8 | 6 | 3 | 40 | 5 | 17 | 2418 | 128 | 55 |
| 1982 | 4 | 13 | 3 | 15 | 3 | 8 | 2513 | 128 | 55 |
| 1983 | 12 | 6 | 3 | 20 | 3 | 8 | 1636 | 32 | 55 |
| 1984 | 8 | 13 | 16 | 5 | 3 | 8 | 1422 | 21 | 96 |
| 1985 | 48 | 6 | 9 | 30 | 8 | 17 | 3342 | 118 | 41 |
| 1986 | 20 | 25 | 9 | 20 | 3 | 2 | 5239 | 171 | 103 |
| 1987 | 44 | 13 | 6 | 25 | 29 | 2 | 4978 | 278 | 523 |
| 1988 | 4 | 38 | 6 | 81 | 5 | 2 | 1470 | 118 | 28 |
| 1989 | 12 | 60 | 37 | 10 | 76 | 8 | 905 | 225 | 165 |
| 1990 | 4 | 6 | 81 | 10 | 16 | 2 | 282 | 16 | 334 |
| 1991 | 16 | 69 | 84 | 10 | 1 | 2 | 11202 | 139 | 196 |
| 1992 | 1 | 6 | 22 | 23 | 3 | 2 | 7783 | 11 | 265 |
| 1993 | 8 | 13 | 44 | 5 | 1 | 8 | 4646 | 21 | 138 |
| 1994 | 8 | | 84 | 30 | 3 | 2 | 5309 | 21 | 145 |
| 1995 | 12 | | 50 | 40 | 52 | 51 | 965 | 230 | 615 |
| 1996 | 12 | | 64 | 23 | 1 | 8 | 402 | 3 | 140 |
| 1997 | 48 | | 54 | 15 | 1 | 2 | 1327 | 16 | 210 |
| 1998 | 52 | | 202 | 10 | 6 | 2 | 2675 | 11 | 138 |
| 1999 | 81 | | 106 | 33 | 48 | 2 | 4907 | 70 | 764 |
| 2000 | 4 | | 47 | 10 | 3 | 2 | 3761 | 11 | 322 |
| 2001 | 8 | | 53 | 56 | 5 | 2 | 2594 | 21 | 265 |
| 2002 | 22 | | 33 | 76 | 8 | 2 | 1046 | 27 | 262 |
| 2003 | 75 | | 68 | 189 | 4 | 17 | 2715 | 3 | 148 |
| 2004 | 31 | | 10 | 39 | 3 | 25 | 1474 | 16 | 189 |
| 2005 | 50 | | 51 | 56 | 1 | 8 | 1172 | 32 | 117 |
| 2006 | 63 | | 30 | 117 | 20 | 8 | 2359 | 27 | 165 |
| 2007 | 91 | | 14 | 56 | 3 | 2 | 5551 | 3 | 100 |
| 2008 | 59 | | 13 | 78 | 27 | 8 | 3375 | 32 | 708 |
| 2009 | 23 | | 17 | 101 | 9 | 2 | 1971 | 3 | 189 |
| 2010 | 123 | | 20 | 34 | 13 | 8 | 3580 | 11 | 289 |
| 2011 | 4 | | 9 | 10 | 1 | 2 | 5611 | 3 | 62 |
| 2012 | 28 | | 28 | 20 | 1 | 2 | 9191 | 11 | 360 |
| 2013 | 32 | | 19 | 40 | 16 | 2 | 6134 | 43 | 234 |

Table B-7: Annual bed load volumes at the water intake structures of the hydropower station Sellrain-Silz. In years with no data, the annual counts of hydraulic flushings were either not available or they were rejected due to bad quality. The values refer to the solid volume without pores. To obtain the deposit volume, the solid volume has to be divided by 0.7 (see Table B5).

| Site --- | Oberberg- bach [m³] | Unterer Liesener- bach [m³] | Oberer Liesener- bach [m³] | Laengen- talerbach [m³] | Schoen- talbach [m³] | Schelf- almbach [m³] | Gleirsch- bach [m³] | Kraspes- bach [m³] | Klamm- bach [m³] | Horlach- bach [m³] | Mitteral- bach [m³] |
|-------------|---------------------------|--------------------------------------|-------------------------------------|-------------------------------|----------------------------|----------------------------|---------------------------|--------------------------|------------------------|--------------------------|---------------------------|
| Year | | | | | | | | | | | |
| 1985 | 29 | 100 | 19 | | 6 | 587 | 3 | 9 | | 17 | |
| 1986 | 111 | 126 | 149 | | 17 | 220 | 40 | 64 | | 43 | |
| 1987 | 428 | 201 | | 19 | 28 | 245 | 101 | 101 | | 51 | |
| 1988 | 472 | 226 | 261 | 14 | 33 | 122 | 71 | 18 | | 26 | |
| 1989 | 332 | 126 | 56 | 9 | 44 | 342 | 40 | 18 | | 9 | |
| 1990 | 450 | 75 | 56 | 14 | 17 | 514 | 81 | 2 | | 17 | |
| 1991 | 590 | 603 | 37 | 1 | 22 | | 51 | 9 | | 17 | |
| 1992 | 1128 | 538 | 339 | 186 | 28 | 66 | 342 | 30 | 9 | 34 | |
| 1993 | 346 | 1349 | 63 | 93 | 19 | 17 | 318 | 61 | 37 | 26 | |
| 1994 | 419 | 1740 | 88 | 112 | 19 | 22 | 171 | 40 | 27 | 17 | |
| 1995 | 73 | 2610 | 25 | 37 | 38 | 22 | 318 | 152 | 27 | | 119 |
| 1996 | 91 | 944 | 13 | 19 | 9 | 6 | 73 | 10 | 2 | | 9 |
| 1997 | 406 | 3088 | 44 | 89 | 20 | 10 | 191 | 69 | 16 | 61 | 7 |
| 1998 | 943 | 3925 | 54 | 132 | 49 | 10 | 240 | 105 | 12 | 56 | 7 |
| 1999 | 597 | 758 | 119 | 158 | 65 | 4 | 257 | 89 | 18 | 80 | 24 |
| 2000 | 1134 | 769 | 48 | 71 | 18 | 10 | 215 | 81 | 12 | 48 | 7 |
| 2001 | 542 | 691 | 25 | 80 | 9 | 10 | 166 | 28 | 12 | 48 | 7 |
| 2002 | 406 | 1959 | 31 | 136 | 16 | 22 | 492 | 1201 | 28 | 48 | 7 |
| 2003 | 1534 | 1902 | 274 | 789 | 32 | 43 | 386 | 145 | 90 | 849 | 101 |
| 2004 | 451 | 1104 | 48 | 729 | 32 | 10 | 900 | 301 | 53 | 101 | 49 |
| 2005 | 379 | 316 | 35 | 649 | 18 | 15 | 1071 | 266 | 26 | 176 | 15 |
| 2006 | 712 | 1430 | 19 | 332 | 6 | 7 | 452 | 109 | 7 | 93 | 24 |
| 2007 | 577 | 296 | 29 | 602 | 9 | 4 | 32 | 23 | 12 | 13 | 11 |
| 2008 | 644 | 345 | 51 | 419 | 8 | 3 | 330 | 91 | 14 | 93 | 9 |
| 2009 | 717 | 170 | 63 | 145 | 32 | 4 | 68 | 64 | 26 | 61 | 11 |
| 2010 | 1365 | 142 | 50 | 295 | 64 | 7 | 325 | 28 | 30 | 13 | 17 |
| 2011 | 688 | 155 | 50 | 24 | 3 | 3 | 15 | 8 | 12 | 7 | 11 |
| 2012 | 910 | 129 | 50 | 625 | 18 | 4 | 117 | 38 | 26 | 67 | 4 |
| 2013 | 502 | 187 | 56 | 365 | 33 | 19 | 181 | 51 | 33 | 88 | 33 |

1.1.5 Accuracy of annual bed load volumes

1.1.5.1 Procedure of determining the accuracy

In order to determine the accuracy of the annual bed load volumes, the uncertainty of each parameter is assessed separately and added up according to the error propagation of independent variables.

1.1.5.2 Accuracy of the annual count of hydraulic flushings

Regarding (i) the annual count of hydraulic flushing, the comparison of the two different data sets (either derived from the logbook or from the discharge hydrograph) enables a rough estimate of the measuring error. Although the discharge based approach faces uncertainties, the margins of mean differences are used to quantify the measuring accuracy of the annual counts. This procedure of estimating the error of annual counts is rather conservative. However, the comparisons comprise all study sites and years where both data sets were available (15 sites with a maximum time span of 28 years). The yearly counts of the discharge based data deviate from the logbook data on average in a range of -68 % and 62 %, except one outlier (the Fissladbach) where differences are on average 280 % (Figure B-8).

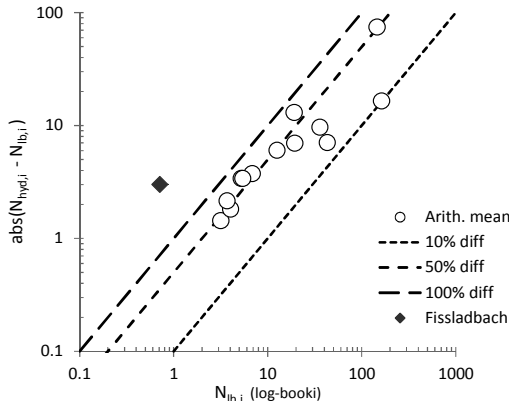


Figure B-8: Absolute difference of mean annual count of hydraulic flushings, determined either manually from the discharge hydrographs (N_{hyd}) or from the logbook (N_{lb}), plotted against the mean of the logbook data

The error range of the count data of hydraulic flushings is determined for each site separately by means of the relative mean difference times the yearly count:

$$s_N = \frac{\text{mean}(|N_{\text{ib},i} - N_{\text{hyd},i}|)}{\text{mean}(N_{\text{ib},i})} \times N_{\text{ib},i} \quad (\text{B5})$$

with $N_{\text{ib},i}$ and $N_{\text{hyd},i}$ the number of hydraulic flushings determined according to the logbook (lb) and the discharge hydrograph (hyd) in the i th year, respectively. For those sites at which only logbook data are available, the error range is assessed by the overall mean relative difference, respectively.

1.1.5.3 Accuracy of the scaling factor

Next to the number of hydraulic flushings, (ii) the scaling factor is a key parameter in determining the volume of the bed load deposition within the settling basin. The scaling factors reported in *Tschada* (1975) refer to the site-specific mean, but they might differ over time.

In course of a Ph.D. thesis, *Strobl* (1980) analyzed the deposit volumes within the settling basin of the Pitzbach in the year 1975 in more detail. Just before the threshold for triggering a hydraulic flushing would have been exceeded, the water intake was deactivated, the water which was stored in the settling basin was carefully released and the sediment deposition was surveyed (*Strobl*, 1980). The overall shape of the sediment deposition, as well as the deposit height at the upper membrane, was similar during all three surveys. In contrast, the position and magnitude of the maximum deposit height (or the crest of the sediment cone) varied considerably. Hence, the deposit volume differed as well (spanning from 17.3 m^3 to 33.7 m^3), reaching its minimum as the crest was located directly above the weighing membrane. *Strobl* (1980) suggested that the location of the deposit crest and consequently, the deposit volume, depend on the

history or magnitude of water discharge: with increasing discharge, the vertex of the sediment deposition migrates downstream.

In the year 1979, *Hofer* (1985) examined the longitudinal profile of the deposit cone within the sediment trap of the Pitzbach 33 times, always shortly before the flushing was initiated. Therefore, *Hofer* measured the deposit height at twelve points, which were centred across and distributed along the settling basin. He did that by sinking a pole from the top outside of the sediment trap through boreholes down to the sediment deposition. Assuming a crosswise horizontal surface, the deposit volume was determined by calculating the cross-sectional deposit area and integrating it over the basin's length. *Hofer* (1985) confirms that the position of the maximum deposit height (or the crest of the sediment deposition) varies in longitudinal direction, somehow depending on the history of water discharge (Figure B-9). The latter was defined by the mean discharge of the timespan between two flushings, by considering discharges exceeding incipient motion conditions only.

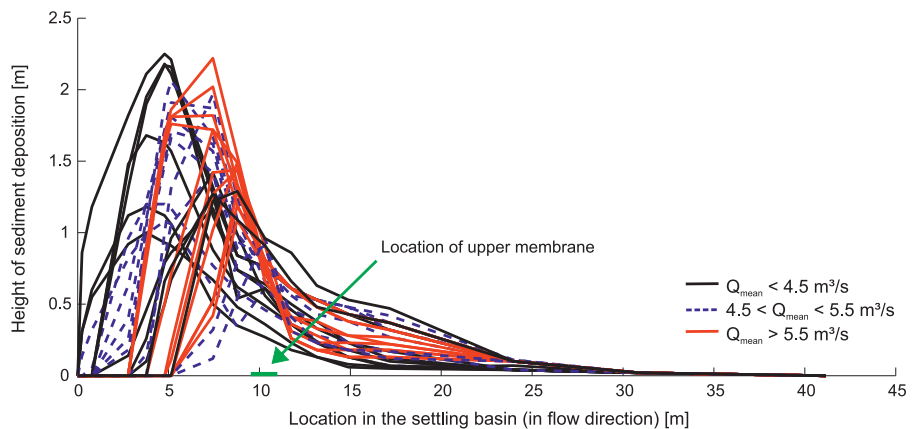


Figure B-9: Longitudinal profiles of the sediment deposition in the settling basin of the Pitzbach according to *Hofer* (1985). The data are separated into three groups, depending on the mean discharge since the previous hydraulic flushing.

Hofer (1985) could not quantify the relationship between the water discharge and the deposit volume (Figure B-10a) because the threshold at which the hydraulic flushing is initiated changed three times in course of his measuring period (summer of 1979). The data of *Hofer* (1985) were reanalyzed by taking the scaling factor (*Tschada*, 1975) which represents a non-dimensional (standardized) measure, instead of the deposit volume. The scaling factor is determined by rearranging equation B2 to

$$sf = \frac{dV}{tV}, \quad (B6)$$

with the theoretical volume (tV) computed according to equation B1 and the deposit volume (dV) as given in *Hofer* (1985).

The mean scaling factor is 0.45, but the data scatter and they reveal a weak dependency with the mean water discharge (Figure B-10b). At low discharges, the scaling

factor is higher, possibly because the crest of the sediment depositions is located upstream of the weighing membrane. As discharge increases, the scaling factor decreases, because the deposit cone might be located in the proximity of the load cell. Thus, it is constrained to the threshold stress. At very high discharges the scaling factor increases again, suggesting that the deposit cone migrates further downstream.

The back-calculated scaling factors follow a normal distribution with a standard deviation (s_{sf}) of 0.20 and thus a coefficient of variation of 45 %. Thereby, the mean value of 0.45 corresponds well with that reported by *Tschada* (1975) ($sf = 0.48$) nine years before *Hofer* conducted his measurements. Consequently, the scaling factors determined by *Tschada* (1975) for quantifying the mean deposit volume within the settling basins are reliable. The remaining error range is determined by the standard error $s_{e,sf} = s_{sf} / \sqrt{N_i}$, with N_i the number of hydraulic flushings within a year, respectively.

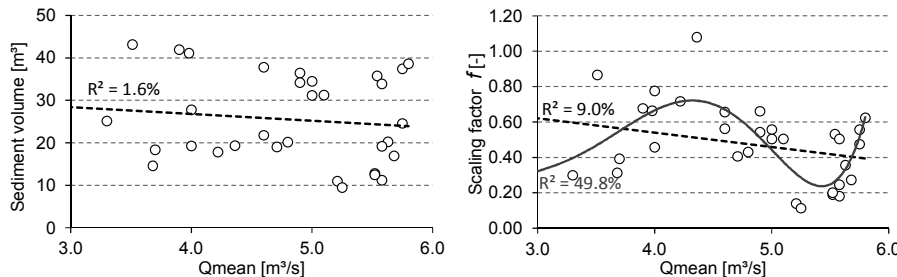


Figure B-10: The deposit volume in the settling basin (a) and the scaling factors (b) plotted against the mean water discharge (Qmean) since the last hydraulic flushing (reanalyzed from Hofer, 1985).

1.1.5.4 Accuracy of the proportion of bed load in total load and porosity

The (iii) proportion of bed load (grains larger than 1 mm) in the total load (pb) is defined by 65 %, which corresponds with earlier reported values (e.g. *Sommer and Lauffer*, 1982). In addition, it is close to the values obtained by recent surveys, where pb was between 60 % and 65 %. However, additional analyses which are not presented in detail suggest a standard deviation (s_{pb}) of 13 %. Despite a lack of evidence, the variability of pb may depend on discharge history, with larger proportions of bed load at higher discharges. In contrast, the scaling factor (sf) is known to negatively depend on discharge history, with an underestimation for periods of low discharge and vice versa. Consequently, the bias originated by the uncertainty of pb counteracts the bias originated by the scaling factor. In terms of a conservative view and because of the lack of evidence, the error range of pb is defined by the standard error $s_{e,pb} = s_{pb} / \sqrt{N_i}$.

Finally, the porosity is assumed to be constant for all study sites and it is set to $\epsilon=0.3$, which represents the mean value measured at the Pitzbach water intake structure (*Eichner*, unpublished). The accuracy of this parameter is estimated by the standard

deviation $p_{\text{overpassing}} = 0.24 \left(\frac{Q}{Q_A} \right)^2 - 0.48 \left(\frac{Q}{Q_A} \right) + 0.24$, which gives a reasonable range

for the porosity of deposited bed load consisting predominately of sand and gravel (e.g. *Tognacca*, 1999).

1.1.5.5 Overall accuracy

Summarizing, the error of the annual bed load volumes is determined by means of the error propagation of independent variables:

$$s_{ABV} = \sqrt{\left(\frac{\partial ABV}{\partial N_i} \times s_N \right)^2 + \left(\frac{\partial ABV}{\partial sf} \times \frac{s_{sf}}{\sqrt{N_i}} \right)^2 + \left(\frac{\partial ABV}{\partial pb} \times \frac{s_{pb}}{\sqrt{N_i}} \right)^2 + \left(\frac{\partial ABV}{\partial (1-e)} \times s_{(1-e)} \right)^2} = \\ \sqrt{\left(\frac{s_N}{N_i} \right)^2 + \left(\frac{s_{sf}}{sf \times \sqrt{N_i}} \right)^2 + \left(\frac{s_{pb}}{pb \times \sqrt{N_i}} \right)^2 + \left(\frac{s_{(1-e)}}{(1-e)} \right)^2} \times ABV. \quad (B7)$$

The accuracy of annual bed load volumes varies between the different sites but varies also in time (Figure B-11). Except for one outlier (Fissladbach), the site-specific mean relative uncertainty of annual bed load volumes (s_{ABV} / ABV) ranges between 0.87 (Verpelbach) and 0.16 (Pitzbach).

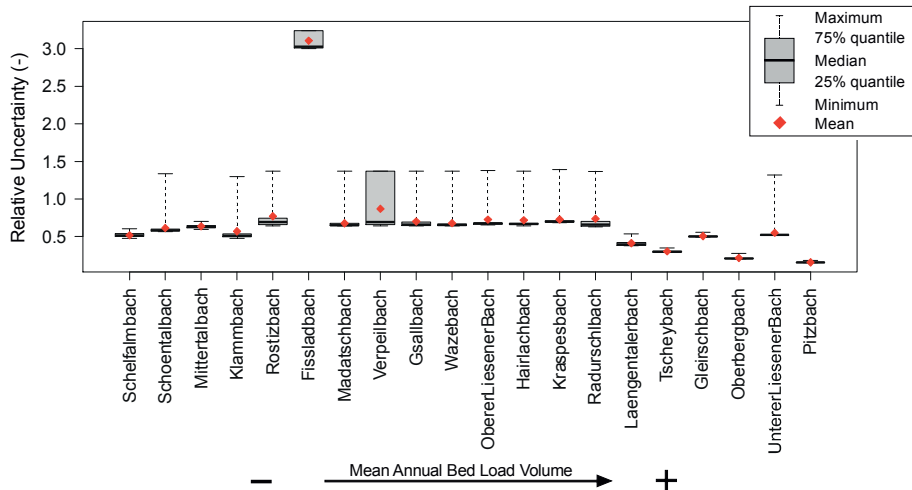


Figure B-11: Uncertainty of annual bed load volumes of all study sites

1.1.6 Remaining uncertainties of annual bed load volumes

Although the data accuracy is determined by means of conservative assumptions, there remain some uncertainties which could not be addressed.

- First, the bed load coarser than the beam spacing (0.15 m) is not captured within the settling basin but overpasses the water intake structure. Sediment particles of that size roughly correspond with the D_{84} in low sloped reaches and the D_{50} of steep reaches. According to several tracer experiments at the Pitzbach, the proportion of bed load coarser than 0.15 m in total annual bed load is within a range of 0.2 % and 2 % (Strobl, 1980). In addition, visual observations during the years 2014 and 2015 at the Oberbergbach revealed that particles coarser than 0.15 m are solely transported during high-flow events. However, this error source is comparatively small and thus, it is neglected.
- Second, bed load finer than 0.15 m might overpass the water intake at flows beyond the structures capacity. In this regard, experimental investigations in the hydraulic laboratory confirmed a high trapping efficiency of the water intake structures even at high flow (see '*Experimental modelling of bed load overpassing a bottom rack intake*' in section B.2.1).
- Third², the water intake structures might have been overloaded during exceptional flood events or debris flow events. By that, the bottom rack is completely clogged with sediment and the water intake is out of order. Consequently, these data of annual bed load volumes do not sufficiently include (underestimate) the bed load volumes during such extreme events. But according to the records of TIWAG, such events are very rare: the average occurrence interval is site-specific and ranges between approx. five years to > 30 years. This somewhat corresponds with observations made in other steep mountain creeks, where exceptional, channel-forming events are associated with an occurrence interval larger than 10 to 50 years (Turrowski et al., 2009; Church and Zimmermann, 2007; Lenzi et al., 2004). In this respect, a clear separation of annual bed load volumes during hydrologically ordinary years and bed load volumes of exceptional, channel-forming extreme events seems justified. The data set of ABV as it is presented and analysed in this thesis refers to hydrologically ordinary years only, with no exceptional flood events or debris flow events.

² This passage was slightly extended and it differs from the original version of the dissertation.

B.1.2 Time series of water discharge

At 15 out of 20 water intake structures, the water discharge is continuously gauged by TIWAG and records are available since 1985 and in with a temporal resolution of 15 minutes.

The time series of water discharge was carefully checked for plausibility and completeness. In the case of either implausible discharge records or temporal gaps, the complete year of discharge data was rejected. Additionally, the reliability of the discharge records was successfully verified by comparing in-situ measurements of water discharge (see section B.1.5) with the records provided by TIWAG (at the water intake structures). The deviation is less than 10 %, which is sufficient for the subsequent analysis. However, the period in which reliable discharge data are available is given in Table B-8.

Table B-8: Period in which reliable discharge data are available for subsequent analysis. The temporal resolution of discharge records is 15 minutes.

| Site | Period of discharge data [years] |
|----------------------|-------------------------------------|
| Schoentalbach | 1985 - 2012 |
| Schelfalmbach | 1985 - 2012 |
| Klammbach | 1985 - 2012 |
| Unterer Liesenerbach | 1985 - 1999 |
| Oberer Liesenerbach | 1985 - 2012 |
| Madatschbach | ----- |
| Gsallbach | ----- |
| Rostizbach | ----- |
| Mittertalbach | 1985 - 2012 |
| Kraspesbach | 1985 - 2012 |
| Wazebach | ----- |
| Fissladbach | 1985 - 2012 |
| Verpeilbach | ----- |
| Laengentalerbach | 1985 - 2012, 2014, 2015 |
| Tscheybach | 1985 - 2012 |
| Gleirschbach | 1985 - 2012 |
| Oberbergbach | 1992 - 2012, 2014, 2015 |
| Radurschlbach | 1985 - 2012 |
| Hoflachbach | 1985 - 2012 |
| Pitzbach | 1989 - 2011, 2014, 2015 |

B.1.3 Time series of bed load accumulation

1.3.1 Data basis

At the water intakes located at the Pitzbach and Oberbergbach (Table B-1) the automatic flushing device was supplemented by two additional load membranes, positioned in the between the existing ones. Since the mid-90s the measuring system transmits the vertical stress measured by these load membranes continuously to a root server, where they are stored since then. The quality of the data was assessed visually, by plotting them against time. If only one out of the four load membranes was not operating (missing values) or if the temporal progression of vertical stress was implausible, the complete year was rejected. However, some load membranes at the Oberbergbach water intake structure revealed an offset, which differed from one to the next year. This offset was corrected by simply adding a yearly constant value.

In Table B-9 the individual years used are highlighted. After the quality check of the data, there remain thirteen years during which data requirements are fulfilled for the 'Oberbergbach', while there remain ten years for the 'Pitzbach'. Hence, a considerable amount of continuously registered deposit loads (15 min interval) is available for further analyses at both sites.

Table B-9: Data of sediment weight (vertical stress) used for subsequent analysis

| Year | Assignment | Water intake structure Oberbergbach | Water intake structure.Pitzbach |
|------|-------------------------------|-------------------------------------|---------------------------------|
| | | Offset correction (mbar) | Assignment |
| 1994 | no data | | accepted |
| 1995 | no data | | accepted |
| 1996 | no data | | accepted |
| 1997 | rejected - missing values | | accepted |
| 1998 | accepted | #1: -10 / #3: -50 | accepted |
| 1999 | accepted | #1: -20 / #3: -50 | rejected - missing values |
| 2000 | accepted | #1: -10 / #3: -15 | accepted |
| 2001 | accepted | #3: -45 | accepted |
| 2002 | rejected - implausible values | | accepted |
| 2003 | rejected - implausible values | | accepted |
| 2004 | accepted | | accepted |
| 2005 | accepted | #2: -15 / #4: -15 | rejected - implausible values |
| 2006 | accepted | #2: -10 / #4: -10 | rejected - implausible values |
| 2007 | accepted | #2: -15 / #4: -15 | rejected - implausible values |
| 2008 | accepted | #1: -10 / #2: -10 | rejected - implausible values |
| 2009 | accepted | #2: -10 / #4: -10 | rejected - implausible values |
| 2010 | accepted | #1: -5 | rejected - implausible values |
| 2011 | rejected - implausible values | | rejected - implausible values |
| 2012 | rejected - implausible values | | rejected - implausible values |
| 2013 | no data | | no data |
| 2014 | accepted | | no data |
| 2015 | accepted | #2: +5 / #3: +5 | rejected - implausible values |

1.3.2 From the vertical stress to the deposit height

1.3.2.1 Procedure

Since the water pressure is compensated by the load membranes, the height of the sediment deposition is determined by dividing the measured stress with the submerged bulk density of the bed load (including the pore volume).

Theoretically, this procedure is not valid since the vertical stress acting on the bottom of the sediment trap does not necessarily correspond to the total weight of the bulk sediment. The shear stress acting on the side walls of the settling basin (due to wall friction) reduce the vertical stress of the sediment deposition acting on and registered by the load membranes. Hence, the registered vertical stress does not necessarily correspond with the total weight of the sediment deposition. Further, there might be a mechanical interaction of the surrounding, loosely bedded sediment and the load membrane (*Aufleger*, 1999), which is neglected by this procedure.

Aufleger (1996) tested a variety of hydraulic pressure gauges experimentally and determined their reliability. Thereby the size of the experimental embankment was similar to the sediment deposition within a settling basin, but pressure gauge devices differed. In general, larger pressure gauges proved to give more reliable pressure estimates. For instance, the mean proportion of measured vertical stress to total load was 0.99 for the largest pressure gauges ($0.4 \times 0.4 \text{ m}^2$) in an experimental test with gravel-sized sediment. In comparison, pressure gauges within the sediment traps are circular with a diameter of 1 m and are flush-mounted into the floor of the sediment trap. Both positively affects the accuracy of the pressure gauging system (*Aufleger*, 1999). However, the hydraulic pressure gauges discussed by *Aufleger* (1999) (stiff hydraulic pressure gauges) are different to those in the settling basins (rubber membranes with a Niro Rochester frame). Due to the lower E-modulus of the membranes, higher indentations are expected as sediment accumulates (as with hydraulic pressure gauges), favouring an arching effect. Thus, the total load might be underestimated in the case of higher sediment deposits.

The ratio of vertical stress ($p_{z, \text{sed}}$) and deposit height (dh) is considered as a calibration parameter which approaches the bulked specific submerged weight in case that the total load is transmitted to the load membranes. The latter induces no shear stress at the side walls, a linear increase of vertical stress with deposit height and no disturbing interactions between sediment and load membrane. Bulk specific weight of sediment under water is defined by:

$$\gamma_b = g (\rho_s - \rho_w) (1 - p), \quad (\text{B8})$$

where g is the gravitational acceleration, ρ_s and ρ_w the sediment and water density, and p the porosity, respectively. Assuming $\rho_s=2650 \text{ kg/m}^3$, $\rho_w=1000 \text{ kg/m}^3$ and $p=0.3$, the submerged specific weight of the sediment deposition is 11 kN/m^3 or 1.1 mbar/cm , respectively.

To account for pressure relocations and additional uncertainties, the vertical stress is converted to the corresponding deposit height by a calibration factor ($\gamma'_{z, \text{sed}}$ [mbar/cm]) rather than by the bulked specific weight. This calibration factor is defined by the ratio of the vertical stress of submerged sediment ($p_{z, \text{sed}}$ [mbar]) and deposit height (dh [cm])

$$\gamma_{z,sed} = \frac{p_{z,sed}}{dh} \quad (B9)$$

and determined based on historic and recent measurements. It is worth to note, that the long-term records of the weighing membranes ($p_{z,sed}$) are in the unit of *mbar* and the sporadic measurements of the deposit height are given in the unit *cm*. In order to make an application of this procedure easier, these units are used to determine $\gamma_{z,sed}$.

1.3.2.2 Application to Pitzbach

Hofer (1985) measured the deposit height above the load membranes and read out the corresponding vertical stress measured by the load membranes. Different from now, the vertical stress were defined in percent of the triggering stress and it already accounted for the buoyancy of the sediment deposition. In order to use these historic measures for determining the calibration factor $\gamma_{z,sed}$, *Hofer's* (1985) data were corrected for the buoyancy according

$$\gamma_{z,sed} = \gamma_{z,sed} \frac{\rho_s}{(\rho_s - 1)}, \quad (B10)$$

The modified data are plotted in Figure B-12 and their median values are close but lower than the expected one (1.1 mbar/cm). Except for some outliers, the scatter of measured values is low, considering the overall measuring accuracy and variability of the boundary conditions. The latter comprise the variable geometric patterns of the deposit cone and the variable grain size distribution of deposited sediment in both, space and time. Figure B-12a further suggests a weak dependency on deposit height, but the trend is not consistent, since it is negative for membrane 3 and membrane 4, while positive for membrane 2 and non-existent for membrane 1.

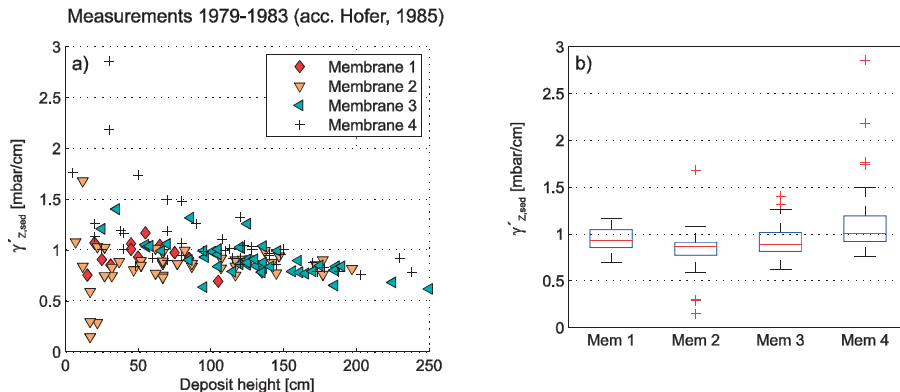


Figure B-12: a) Submerged specific weight plotted against deposit height and b) boxplot of $\gamma_{z,sed}$, separated according to the four load membranes (mem 1 to mem 4); the data are based on the measurements conducted in the years 1979 to 1983 by *Hofer* (1985).

The flushing system at the water intake structure of the Pitzbach was changed from a mechanical to a digital device in 1985, which enabled data transmission. Thus, the relation of deposit height and vertical stress of Hofer (1985) refers to a slightly different measuring device than it is actually used. In this respect, the operator of the water intake structures (TIWAG) performed additional measurements of the deposit height in the years 1994 to 1997. Furthermore, vertical stress is recorded continuously in an interval of 15 min, enabling the determination of the corresponding values at the time manual measurements of the deposit height were conducted. The ratio of vertical stress and deposit height, both measured independently, is plotted in Figure B-13b. Although the median values are still close to the expected one (1.1 mbar /cm) for three of the membranes, the scatter of specific submerged weight (Figure B-13b) as well as its dependence on deposit height (Figure B-13a) are more pronounced than in Figure B-12.

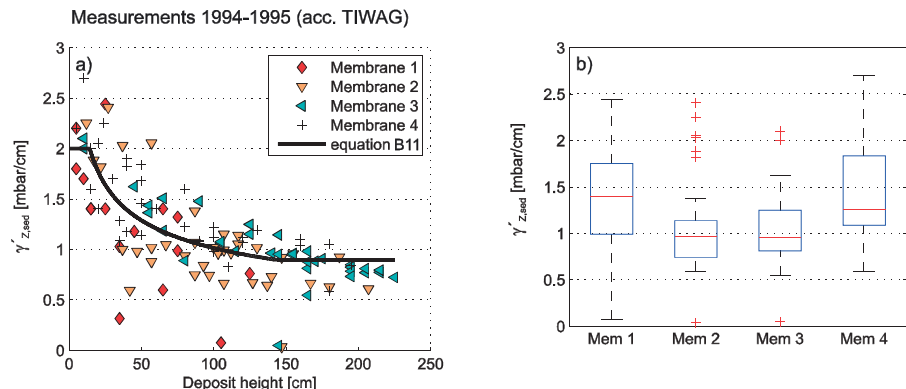


Figure B-13: a) Submerged specific weight plotted against deposit height and b) boxplot of $\gamma'_{z,sed}$, separated according to the four load membranes (mem 1 to mem 4); data are based on the measurements conducted in the years 1994 and 1995 (TIWAG, unpublished)

The large scatter is attributed to the data inaccuracy rather than temporal differences of $\gamma'_{z,sed}$. First of all, measurements of deposit height face an uncertainty range of about 10 cm at the Pitzbach water intake. In a consequence, low deposit heights have to be interpreted with caution. Additionally, the vertical stress is back-traced from the recorded time series rather than measured simultaneously as by Hofer (1985), which requires an exact date and time of each survey. Hence, $\gamma'_{z,sed}$ is assumed to depend on the deposit height solely and the remaining scatter is attributed to data inaccuracy. The vertical stress is converted to the deposit height according to the same procedure for all membranes by assuming a nonlinear relation (Figure B-13a). Regressing Box-Tidwell transformed specific submerged weight and log-transformed deposit height yields

$$\gamma'_{z,sed} = \exp(-23.13 + 24.78 \times dh^{-0.0148}), \quad (\text{B11})$$

with the deposit height (dh) in centimetres. In order to avoid unrealistic values for the specific weight in case of very low or very high deposit heights, it is limited to the range $0.9 < \gamma_{z, \text{sed}} < 2$ (Figure B-13b). Finally, vertical stress is converted to deposit height according

$$dh = \frac{p_{z, \text{sed}}}{\gamma_{z, \text{sed}}} = \frac{p_{z, \text{sed}}}{\min(2, \max(0.9, \exp(-23.13 + 24.78 \times dh^{-0.0148})))} \quad (\text{B12})$$

Since equation B12 needs to be solved iteratively, the starting value was determined by assuming $\gamma_{z, \text{sed}} = 1 \text{ mbar/cm}$.

The performance of this approach (equation B12) is tested by calculating the deposit height which triggers a hydraulic flushing. At the water intake of the Pitzbach, hydraulic flushings are on average triggered automatically at a deposit height of about 1.8 m, which is regularly controlled by the hydropower operator TIWAG. Applying equation B12 to the time series of the four weighing membranes yields a deposit height for each weighing membrane. The maximum of these four values just before a hydraulic flushing was initiated, corresponds with the deposit height that triggered the hydraulic flushing. The time series of the maximum deposit heights (just before a hydraulic flushing) is plotted in Figure B-14 and the back-calculation confirms well with reported triggering height (1.8 m).

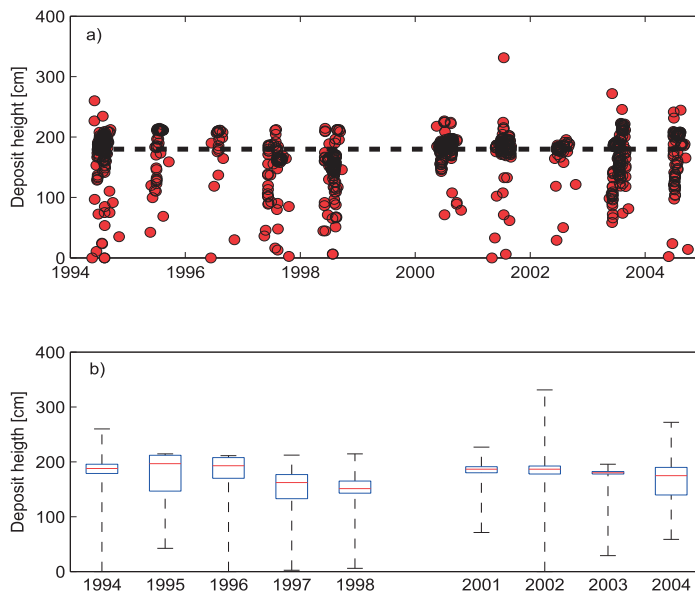


Figure B-14: a) Time series of the maximum deposit height at the time a hydraulic flushing was initiated (red dots) and the theoretical triggering height (180 cm) at the Pitzbach settling basin. The maximum deposit heights were back-calculated from the vertical stress measured by the four membranes and by solving equation B12 iteratively; b) year wise boxplots of maximum deposit heights.

1.3.2.3 Application to Oberbergbach

The deposit height in the settling basin of the water intake at the Oberbergbach was measured six times in the year 2015. In contrast to the Pitzbach water intake structure, no historic surveys are available. Additionally, only six bore holes are present at the Oberbergbach, while there are twelve at the Pitzbach. Four of them are located just above the four load membranes and thus $\gamma_{Z, \text{sed}}$ is determined as in section 1.3.2.2.

Furthermore, the comparison of recorded vertical stress and surveyed deposit height enabled a first quality check of the data. In course of that, the membranes #2 and #3 were found to be interchanged, suggesting an error in data transmission or data storing. The ratio of vertical stress and deposit height is much more consistent when membrane #2 and #3 are switched. Additionally, the longitudinal profile of back-calculated deposit heights seems much more plausible (Figure B-15).

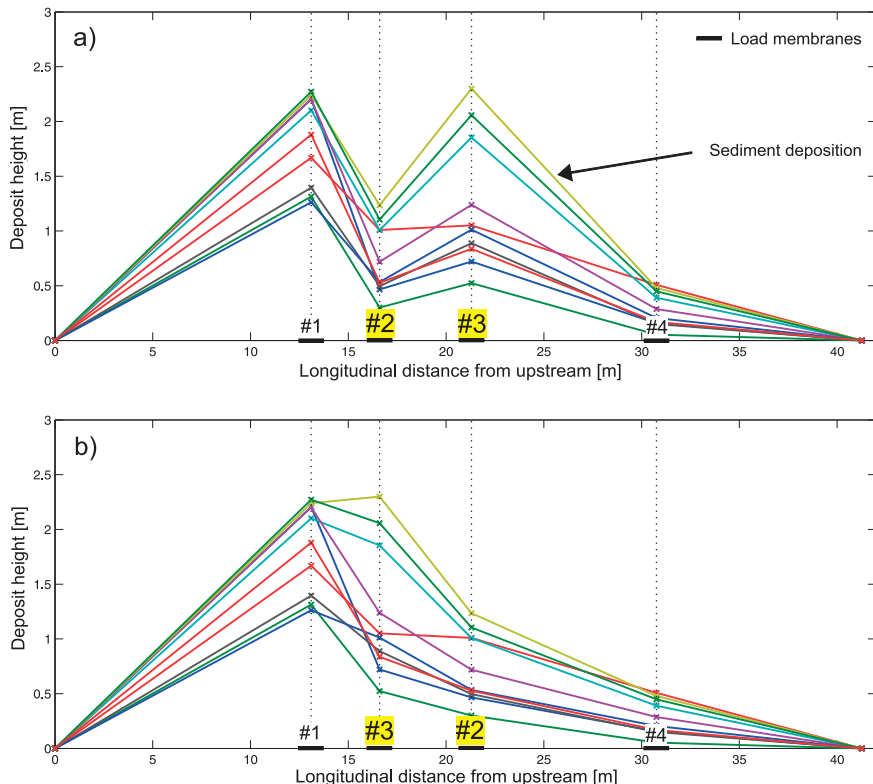


Figure B-15: Longitudinal profile of back-calculated deposit heights along the settling basin of the Oberbergbach: a) using the original attribution of load membranes and b) changing membrane #2 and #3. The latter is much more plausible since a bimodal deposition was never observed in course of the field surveys.

Hence, the load membranes #2 and #3 were changed and the constant offset of +5 mbar was corrected (Table B-9) before $\gamma_{z, \text{sed}}$ was determined according equation B9. Plotting $\gamma_{z, \text{sed}}$ against the deposit height (Figure B-16) yields a similar but slightly shifted relation as observed in the settling basin at the Pitzbach, which is approximated by

$$\gamma_{z, \text{sed}} = -0.159 \times \log(dh) + 1.48. \quad (\text{B13})$$

Equation B13 is limited to the range $0.6 < \gamma_{z, \text{sed}} < 1.6$ (Figure B-16a), in order to avoid unrealistic values for the specific weight in the case of very low or very high deposit heights. Finally, vertical stress is converted to deposit height according:

$$dh = \frac{p_{z, \text{sed}}}{\gamma_{z, \text{sed}}} = \frac{p_{z, \text{sed}}}{\min(1.6, \max(0.5, -0.159 \times \log(dh) + 1.48))} \quad (\text{B14})$$

In analogy to section 1.3.2.2, equation B14 is solved iteratively by using $\gamma_{z, \text{sed}} = 1 \text{ mbar/cm}$ as starting value.

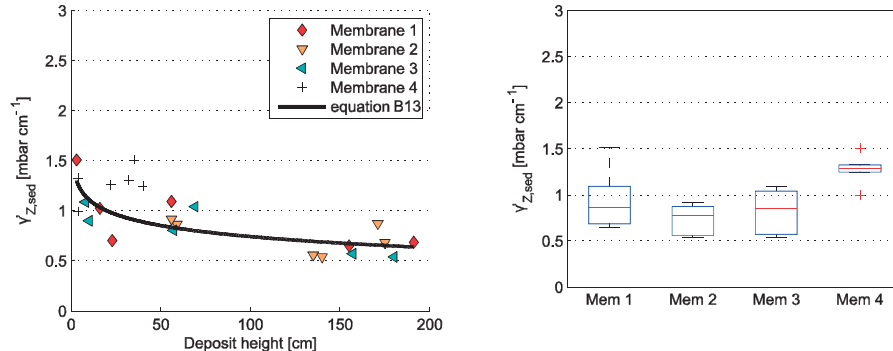


Figure B-16: a) The calibration factor $\gamma_{z, \text{sed}}$ (which is determined by the ratio of vertical stress and deposit height) is plotted against deposit height and **b)** boxplot of derived values separated according to the four load membranes (mem 1 to mem 4); data of deposit heights are based on the field measurements conducted in summer 2015, while vertical stress was recorded automatically by TIWAG

1.3.3 From deposit height to deposit volume

In analogy with Hofer (1985), the deposit volume is determined by calculating the cross-sectional deposit area (assuming a crosswise horizontal surface) in a first step and integrating it along the chamber length in a second step.

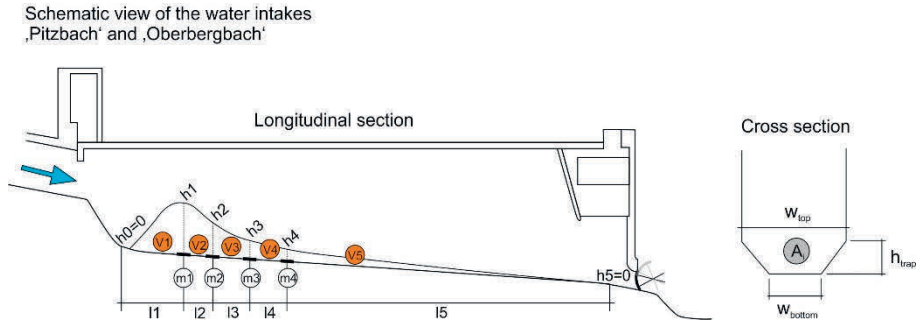


Figure B-17: Geometry of the water intake structures

According to the metrics of the settling basins at both sites, the Pitzbach and the Oberbergbach, the cross-sectional area at the time i (A_i ; Figure B-17) is defined by

$$A_i = \min(h_i, h_{trap}) \cdot \left(\frac{W_{top} - W_{bottom}}{2 \cdot h_{trap}} \cdot \min(h_i, h_{trap}) + W_{bottom} \right) + \max(h_i - h_{trap}, 0) \cdot w_{top}, \quad (\text{B15})$$

with the abbreviations given in Figure B-17. The assumption of a crosswise horizontal surface of the sediment deposition could be verified in course of field surveys within the settling basin of both sites.

In contrast, the sediment deposition was obviously unevenly distributed in the longitudinal direction. The volume of deposited sediment is calculated by integrating the cross-sectional area occupied by the sediment over the entire length of the settling basin. The integration is based on the six integration points, which are the upper and lower end of the settling basin and the locations of the load membranes, respectively. While the cross-sectional area occupied by the sediment is assumed to be zero at the boundaries, it is determined by equation B15 for the remaining points. But, using only six integration points results in some inaccuracy, which is visually illustrated in Figure B-18.

Therefore, the integration is performed section-wise according to the trapezoidal rule (see Figure B-17) in combination with weighing factors (f_i)

$$V = \sum_{i=1}^5 V_i = \sum_{i=1}^5 \frac{A_i + A_{i+1}}{f_i} \cdot l_i, \quad (\text{B16})$$

These weighing factors were calibrated by means of minimizing the differences of calculated volume, based either on only six (approximated volume; blue dots in Figure B-18) or twelve (accurate volume; black diamonds in Figure B-18) integration points. The results obtained by both methods are visually compared in Figure B-19, exhibiting a sufficient conformity.

The detailed data of deposit heights are only available at the settling basin of the Pitzbach water intake structure. At that site, the deposit heights can be measured at twelve bore holes, which are distributed over a distance of approx. 42 m. In contrast, only six bore holes are present at the water intake structure of the Oberbergbach. Hence, the weighting factors (f_i) are calibrated according to the data at the Pitzbach only but used at both sites.

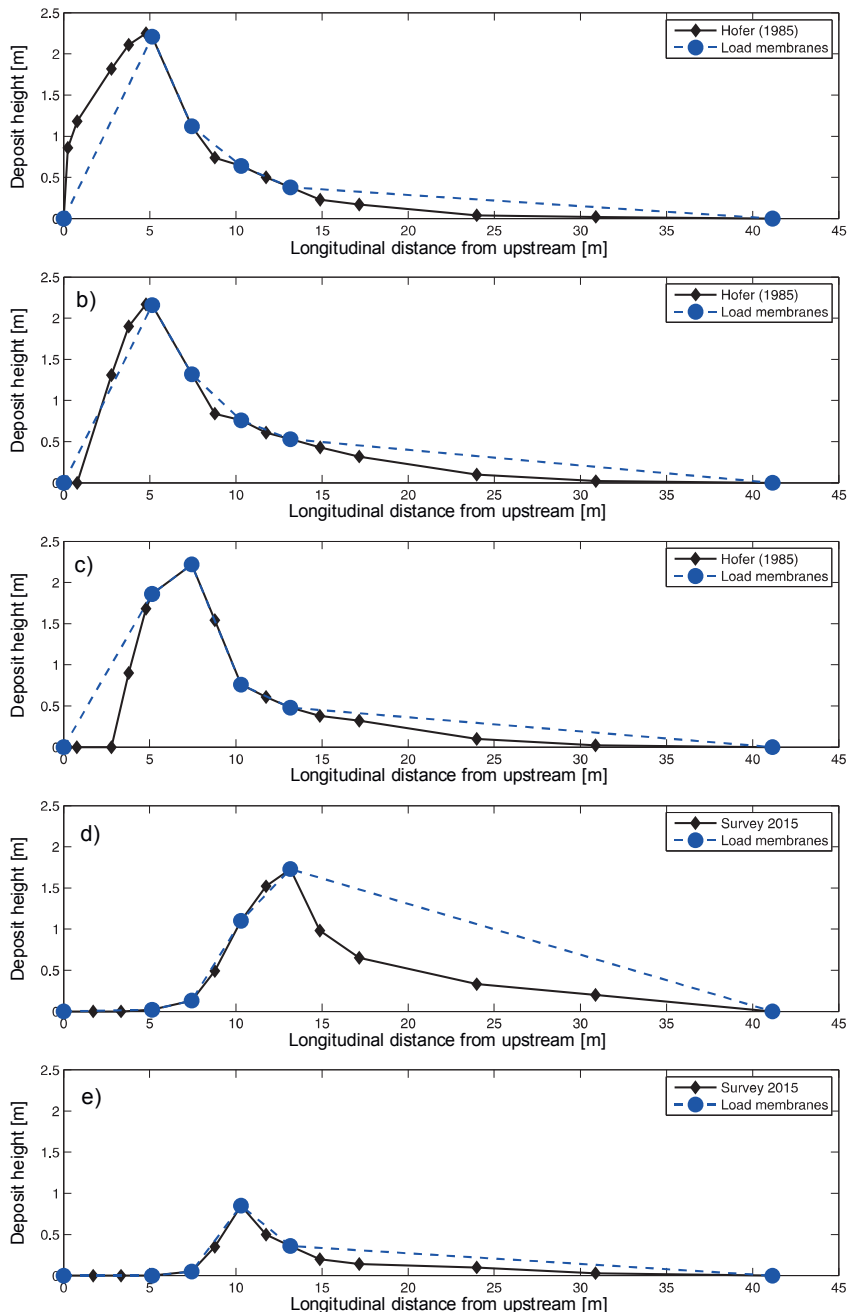


Figure B-18: Longitudinal profile of the accumulated sediment in the settling basin of the Pitzbach water intake structure

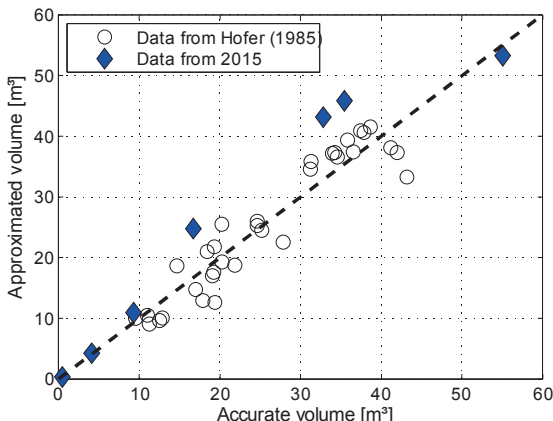


Figure B-19: Comparison of calculated volumes obtained by using all data of deposit heights (x-axis) or only those which are located at the load membranes (y-axis)

1.3.4 Partitioning of suspended load and bed load

1.3.4.1 General remarks

The sediment deposition in the settling basins of both water intake structures (Pitzbach and Oberbergbach) typically feature a lengthwise fining. Hence, only a certain fraction of the total sediment is attributed to bed load, while sediment which accumulates near the lower end of the settling basin is attributed to suspended load. In this study, bed load is defined by sediment particles coarser than 1 mm. This threshold diameter is assumed constant and thus, a possible increase with increasing discharge is not accounted for. The reasons for this choice are:

- (i) The size fraction 1.0 – 2.0 mm often dominates the bulked bed load transport during moderate flows (see Table B-14 in section B.1.5).
- (ii) At the Pitzbach and comparable mountain streams, 90 to 100 % of the suspended load is finer than 0.25 mm (e.g. Hofer, 1985; Sommer, 1980).
- (iii) The same threshold diameter was used in earlier studies dealing with the same field sites (e.g. Sommer and Laufer, 1982).

1.3.4.2 Pitzbach

Extensive measurements were accomplished at the water intake structure of the Pitzbach in the year 1979. Thereby, several sediment samples were taken along the settling basin (Strobl, 1980; Figure B-20). In comparison to the bed surface of the Pitzbach, which shows a median diameter of about 0.16 m, the grain size distributions of the accumulated bed load were very fine. Additionally, the results exhibit an obvious fining from the upper to the lower end of the settling basin, indicating a clear segregation between bed load and suspended load. Assuming the threshold diameter of 1.0 mm, the median diameter (D_{50}) of the accumulated sediment falls below this

threshold between S3 ($D_{50}=1.5$ mm) and S4 ($D_{50}=0.3$ mm), which is the centre of the settling basin (see Figure B-20).

Schematic view of the sample locations of Strobl (1980)
at the water intake 'Pitzbach'

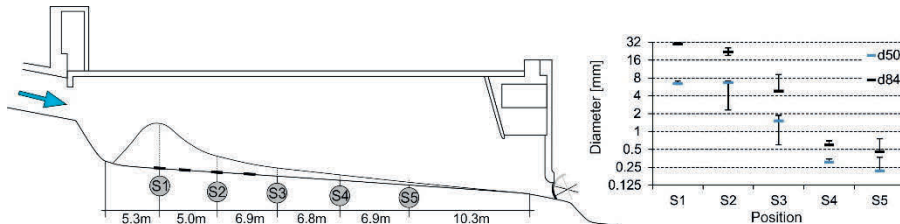


Figure B-20: Location (left) and characteristic grain sizes (right) of the sediment samples of Strobl (1980)

In the summer of 2015, similar surveys than those reported by Strobl (1980) were performed at both sites, the Pitzbach, and the Oberbergbach. Therefore, the water in the settling basins was carefully released and the sediment deposition was surveyed regarding both, geometric patterns and grain size distributions.

At the settling basin of the Pitzbach, the boundary where sediment was predominately coarser or finer than 1.0 mm was again located in the centre (Figure B-21).

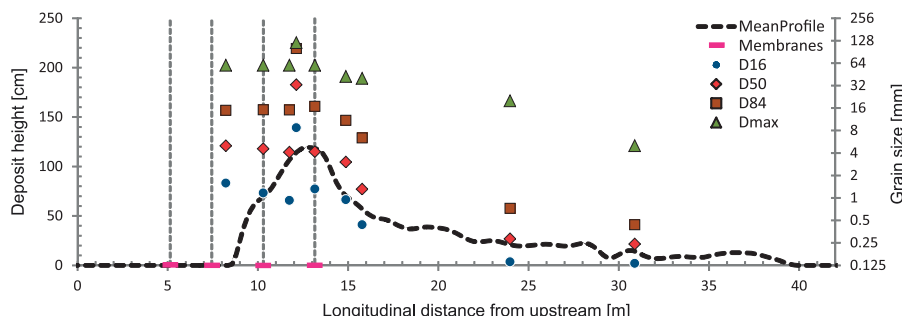


Figure B-21: Mean longitudinal profile of deposit height and characteristic grain sizes in the settling basin of the Pitzbach on 5th August 2015

Hence, only the upper half of this settling basin is considered to trap bed load. In a consequence, equation B16 is only applied from the upper end of the settling basin to approx. 7.40 m below the lowest weighing membrane (representing the midpoint of the settling basin). Due to that, the weighing factors (f_i) were calibrated once more (see section 1.3.3) by means of considering the upper half of the settling basin only. The results obtained are visually compared in Figure BB-22.

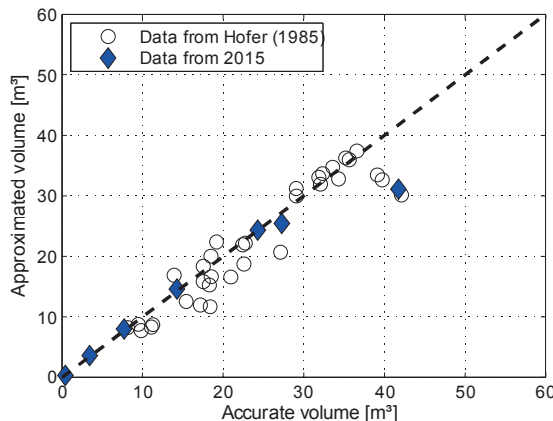


Figure BB-22: Comparison of calculated bed load volumes obtained by using all data of deposit height (x-axis) or only those four which are located at the weighing membranes (y-axis); in contrast to Figure B-19 volumes refer to bed load only, neglecting any sediment accumulation in the lower half of the settling basin.

1.3.4.3 Oberbergbach

Similar patterns were observed in the settling basin of the Oberbergbach water intake. Although there was an obvious segregation of coarse and fine sediment in the proximity of the longitudinal centre, a fraction of the accumulated fines was still attributable to bed load (Figure B-23).

At the upper two weighing membranes, the accumulated sediment is totally considered as bed load. However, at the third weighing membrane, only 50 % are contributed to bed load, while all sediment below $x=26$ m is interpreted as suspended load only. In this respect, the grain size distribution of the lowermost sample (at the load membrane 4) is probably biased by coarse grains that were relocated from the upper part in course of the water release.

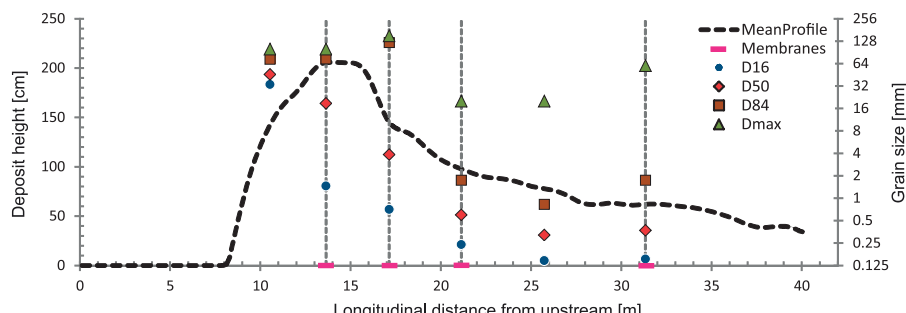


Figure B-23: Mean longitudinal profile of deposit height and characteristic grain sizes in the settling basin of the Oberbergbach on 24th July 2015

1.3.5 Workflow to determine accumulated bed load volume

The vertical stress of the deposited sediment is registered continuously by four load membranes at the two water intake structures Oberbergbach and Pitzbach. The vertical stress is given in [mbar] and converted to the bulked deposit height [cm] either by equation B12 (Pitzbach) or equation B14 (Oberbergbach). These equations account for the nonlinear relation of vertical stress and deposit height and need to be solved iteratively with the starting value defined by:

$$dh_i[\text{cm}] = \frac{\rho_{Z,\text{sed}} [\text{mbar}]}{1 [\text{mbar/cm}]} \quad (\text{B17})$$

The calculated deposit heights refer to the location of each of the four load membranes and thus, they represent measures which are distributed along the settling basin. Based on the deposit heights, the cross-sectional area (A_i) occupied by the sediment is determined according to equation B15 by means of the geometrics of the settling basins; thereby the assumption of a crosswise horizontal surface was verified in course of the surveys.

Finally, the total sediment volume is calculated by piecewise integration of A_i lengthways of the settling basin. Therefore, an invariable upper and lower end of the sediment deposition (first and last integration point) have to be defined. At the settling basin of the Pitzbach, these points refer to the upper and lower end of the settling basin (Figure B-17). In contrast, the uppermost integration point is set to 5 m downstream of the upper end of the settling basin at the Oberbergbach. This location was determined by the field surveys.

In order to account for the shape of the sediment accumulation, the trapezoidal rule is applied but calibrated by means of weighing factors (Table B-10):

$$V = \sum_{i=1}^5 \frac{A_i + A_{i+1}}{f_{i,\text{total}}} \cdot I_{i,\text{total}} \quad (\text{B18})$$

However, only a fraction of the total sediment deposition refers to bed load, while suspended load accumulates in the lower part of the settling basin. The differentiation between either of these two transport processes is defined by a threshold grain size of 1 mm. Since historic and recent field data reveal a downstream fining, only the upper part of the settling basin is considered to trap bed load. In a consequence, the cross-sectional area occupied by the sediment is not integrated along the entire length of the settling basin but limited to approx. half of it. Additionally, the cross-sectional area at each interpolation point is scaled by the proportion of bed load (pb in Table B-10). Typically, $pb=1$ in case that the weighing cell is located in the upper part and $pb=0$ in the lower part. However, at the weighing cell in the center of settling basin at the Oberbergbach, the cross-sectional area is reduced by a factor of 0.5 in order to account for bed load only.

Since the longitudinal extent of integration is different to equation B18, the weighing factors (f_i) were re-calibrated in order to reproduce the shape of the deposit cone properly (Table B-10). Finally, the deposit volume of bulked bed load is computed according

$$V_{\text{bedload}} = \sum_{i=1}^5 \frac{A_i \times pb_i + A_{i+1} \times pb_{i+1}}{f_{i,\text{bedload}}} \cdot I_{i,\text{bedload}} \quad (\text{B19})$$

Table B-10: Summary of all parameters used to determine the deposit volume of either the total sediment or only the bed load, based on the deposit height at six integration points and the corresponding five sub-sections (Figure B-17)

| | | h_{trap} [m] | w_{bottom} [m] | w_{top} [m] | $l_{i,total}$ [m] | $f_{i,total}$ [-] | $l_{i,bedload}$ [m] | $f_{i,bedload}$ [-] | pb_i [-] |
|--------------|-------------|-------------------|---------------------|------------------|----------------------|----------------------|------------------------|------------------------|---------------|
| Oberbergbach | Upper end | 1.25 | 2 | 4 | 8.1 | 3 | 8.1 | 3 | - |
| | Membrane #1 | 1.25 | 2 | 4 | 3.5 | 2 | 3.5 | 2 | 1 |
| | Membrane #2 | 1.25 | 2 | 4 | 4.7 | 2 | 4.7 | 2 | 1 |
| | Membrane #3 | 1.25 | 2 | 4 | 9.46 | 2 | 4.73 | 2 | 0.5 |
| | Membrane #4 | 1.25 | 2 | 4 | 10.5 | 4 | 0 | - | 0 |
| Pitzbach | Upper end | 0.94 | 1.5 | 3 | 5.14 | 3 | 5.14 | 3 | - |
| | Membrane #1 | 0.94 | 1.5 | 3 | 2.3 | 2 | 2.3 | 2 | 1 |
| | Membrane #2 | 0.94 | 1.5 | 3 | 2.86 | 2 | 2.86 | 2 | 1 |
| | Membrane #3 | 0.94 | 1.5 | 3 | 2.86 | 2 | 2.86 | 2 | 1 |
| | Membrane #4 | 0.94 | 1.5 | 3 | 27.99 | 4 | 7.41 | 3 | 1 |

Definitions are as follows: h_{trap} , the height of the trapezoidal cross section; w_{bottom} , the bottom width of the settling basin; w_{top} , the corresponding top width at $h=h_{trap}$; $l_{i,total}$, the downstream length to the next integration point; $f_{i,total}$, weighting factor to account for the longitudinal shape of the entire sediment deposition; $l_{i,bedload}$, the downstream length to the next integration point which refers to bed load; $f_{i,bedload}$, weighting factor to account for the longitudinal shape of the bed load deposition only; pb_i , the proportion of bed load in total load at a certain integration point

1.3.6 Accuracy of accumulated bed load volume

1.3.6.1 Procedure of accuracy assessment

The bed load volume is calculated according to the procedure presented in section 1.3.5, which is basically based on (i) the conversion of the vertical stress to the deposit height, (ii) the integration of the cross-sectional area along the settling basin, and (iii) the separation of bed load and suspended load.

The error margins arising from each of these calculation steps is assessed by (i) the uncertainty of the calibration factor, (ii) the error introduced due to the numerical integration with a limited size of fix points, and (iii) the uncertainty of the proportion of bed load in the total sediment deposition.

1.3.6.2 From vertical stress to deposit height

The vertical stress which is registered by four weighing membranes is converted to the deposit height according:

$$dh = \frac{\rho_{z,sed}}{\gamma_{z,sed}} \quad (B20)$$

Therein, the calibration factor $\gamma_{z,sed}$ represents an empiric surrogate of the specific submerged weight. It is calculated by a site-specific, nonlinear equation, which represents the best-fit estimate of a data set that comprises simultaneously measured deposit height and vertical stress. The accuracy of $\gamma_{z,sed}$ is determined by the standard deviation of the residuals at the settling basin of the Pitzbach (Figure B-24). In this

respect, the data which are out of the plausible range $[0.5 < \gamma_{Z, \text{sed}} < 2.5]$ were removed beforehand. The histogram of residuals is illustrated in Figure B-24b and it confirms normality with a standard deviation of $s_{\gamma_{Z, \text{sed}}} = 0.29$.

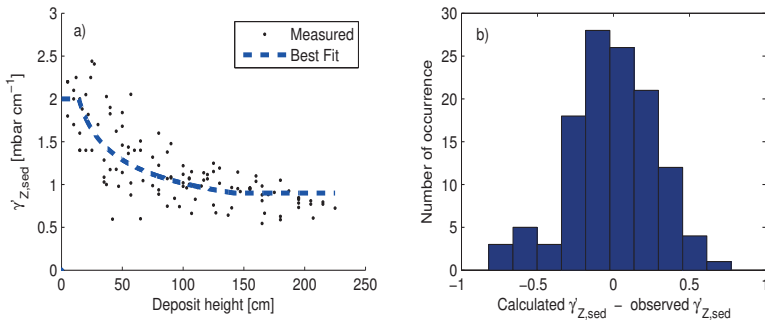


Figure B-24: a) The calibration factor $\gamma_{Z, \text{sed}}$ plotted against deposit height and b) the histogram of the residuals; all data refer to the Pitzbach only.

1.3.6.3 From deposit height to deposit volume

The volume is computed by the numerical integration of the cross-sectional area along the settling basin. Therefore, the trapezoidal rule is applied with six integration points (at both ends and at the four weighing cells). In order to cope with this limited amount of integration points, weighing factors (f_i) were calibrated by means of minimizing the differences between approximated and exact volumes (Figure BB-22). The error that results from numerical integration is simply defined by the coefficient of variation (cv_{Int}) of by assuming the expected value to be unity:

$$cv_{\text{Int}} = \sqrt{\frac{\sum \left(\frac{V_{\text{approx.}}}{V_{\text{exact}}} - 1 \right)^2}{n-1}} \quad (\text{B21})$$

The uncertainty range is about +/-25 % when the entire sediment volume is determined by equation B18, while it is only +/-15 % when the volume refers to bed load only (equation B19).

1.3.6.4 Partitioning of suspended load and bed load

Only a fraction of the total sediment deposition is attributed to bed load. According to multiple field surveys, sediment that accumulated in the upper part of the settling basin was predominately larger than the threshold grain size of 1.0 mm, while it was finer in the lower part. The uncertainty was assessed by comparing the back-calculated bed volume (according section 1.3.5) with three in-situ measurements and it is about 10 %.

1.3.6.5 Total uncertainty

1.3.6.5.1 Method

Due to the complexity of the approach for determining the volume of accumulated bed load based on the vertical stress at four weighing membranes (section 1.3.5), the overall uncertainty is assessed by a Monte Carlo simulation.

The calculation scheme (highlighted in section 1.3.5) is applied by using the vertical stress registered by the four weighing membranes at a given time. In addition, the uncertainty is determined by 10,000 realisations which account for (i) the uncertainty range of the calibration factor $\gamma_{z, \text{sed}}$ (section 1.3.6.2) which is normally distributed with a standard deviation of 0.29, (ii) the uncertainty range arising from the numerical integration which is assessed by a factor that is normally distributed with a mean and standard deviation of 1 and 0.15 (section 1.3.6.3) and (iii) the uncertainty range attributed to the partitioning of bed load and suspended load which is also assessed by a factor that is normally distributed with a mean of 1, but a standard deviation of 0.1; in addition, pb_i must not exceed 1, respectively.

1.3.6.5.2 Reference Scenario

The volume is calculated by means of the vertical stress that was registered by the weighing membranes in the settling basin of the Oberbergbach on 24th July 2015 at 8.00 am. This scenario refers to the sediment deposition which was surveyed with a total station and automatic object identifier at 9.00 am. Thereby, the surface of the deposit cone was measured by 150 points, while the geometrics of the settling basin were determined by the plan documents provided by the TIWAG. The survey points were then mapped to a grid of 0.16x0.16 m² by means of spline interpolation as implemented in the ArcGIS software.

The cross-sectional area occupied by the bulked sediment is determined according to equation B15 every 0.16 m. Its integration along the settling basin yields a total, bulked sediment volume of 94 m³. The longitudinal profile of the proportion that is attributed to bed load was assessed by six sediment samples, which were spatially distributed along the settling basin (Figure B-23). Accounting for that gives a bulked bed load volume of 62 m³. Hence, the bed load contributes to 65 % on the total sediment volume, which corresponds well with earlier investigations at the Pitzbach water intake by Strobl (1980).

1.3.6.5.3 Results

The variation of the calibration factor $\gamma_{z, \text{sed}}$ causes a variation of deposit height which is illustrated in Figure B-25. However, since the calibration factor $\gamma_{z, \text{sed}}$ was varied for all four weighing membranes independently, the effect on bed load volume remains comparatively small: the strong increase of deposit height at a single membrane is likely compensated by a decrease at another one. Hence, the uncertainty of the calibration factor effects the bed load volume by +/- 19 %.

In combination with the two remaining uncertainties, the coefficient of variation of the determined bed load volume is

$$cv_{bv} = \sqrt{0.19^2 + 0.15^2 + 0.1^2} = 0.26 \quad (\text{B22})$$

In contrast to the scatter that is attributed to the uncertainty range of certain parameters, the bed load volume determined by the approach is very close to that measured in course of the survey (Figure B-26).

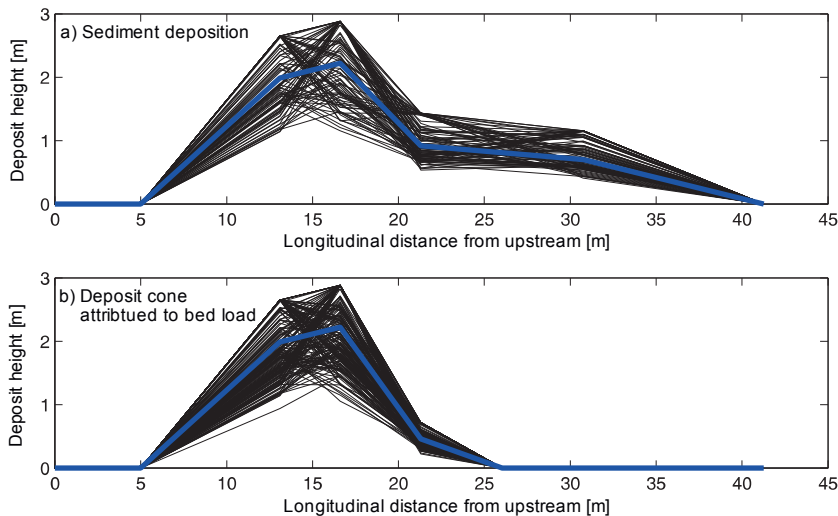


Figure B-25: Longitudinal profiles of deposit height based on 10,000 realisations in which the calibration factor $\gamma_{Z,\text{sed}}$ varies according to a normal distribution with a standard deviation of 0.29; a) total sediment deposition and b) sediment accumulation that is attributed to bed load only.

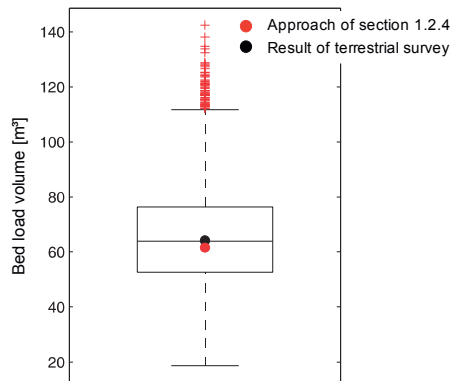


Figure B-26: Uncertainty range of the bed load volume determined by four weighing membranes; the scenario comprises the sediment deposition on 25th July 2015 in the settling basin of the Oberbergbach water intake structure.

B.1.4 Time series of bed load transport rate

1.4.1 Bed load transport rate based on the time series of bed load accumulation

As stated above, at the two water intake structures located at the Oberbergbach and the Pitzbach, the vertical stress of submerged sediment is measured by four weighing membranes since several years. The data are recorded in a temporal interval of 15 minutes.

The application of the procedure described in section 1.3.5 enables an approximation of the bed load volume [m^3] within the settling basins. Here, the time series of vertical stresses is used to generate a time series of the bed load volume accumulated within the settling basin (Figure B-27).

The bed load volume represents a cumulative quantity of bed load transport. Hence, the difference in the bed load volume at two times divided by its time span corresponds with the mean bed load transport rate. Since the time series of bed load volume features the same interval than the time series of vertical stress (15 minutes), bed load transport rate is determined in units of $\text{m}^3/15 \text{ min}$.

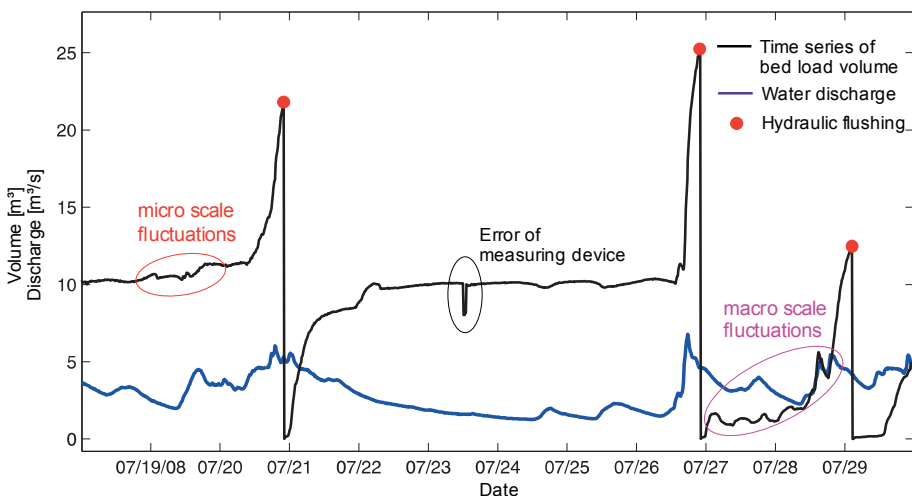


Figure B-27: Time series of bed load accumulation within the settling basin and total water discharge at the water intake structure of the Oberbergbach

During the period of two successively triggered hydraulic flushings, the time series of the deposit volume has to increase monotonically (Figure B-27), because sediment cannot escape from the settling basin. This confines the bed load transport rate to values larger or equal zero.

However, in the case of a very low increase of the deposit volume (low transport rates) the time series is superimposed by randomly distributed fluctuations (Figure B-27). Possible reasons for these fluctuations are attributed either to the uncertainty of the calculation scheme (section 1.3.6), but more important to random fluctuations of the

vertical stress acting on the weighing membranes. The latter originates from relocations of the sediment within the settling basin, either at the micro-scale (low amplitude and low period fluctuations) or at the macro-scale (high amplitude fluctuations at random times, but typically during the rising limb of the hydrograph). Additionally, errors of the measuring device or data transmission cause individual peaks or sinks.

To cope with these fluctuations, the time series of bed load accumulation is split into parts of monotonic and non-monotonic increase (Figure B-28). This is performed for all periods of two successive hydraulic flushings separately. The hydraulic flushings themselves are semi-automatically assessed by tracing back the moments at which accumulated bed load abruptly decreased to zero (Figure B-27).

In order to fulfil the requirements of a monotonic increasing function (blue rectangles in Figure B-28), the bed load volume at a given time ($V_{b,i}$) must be larger or equal than for the previous ones ($V_{b,i-j}$), while it must be smaller or equal than the next ones ($V_{b,i+j}$). The algorithm applied does not only compare the current value with the immediately previous or following one, but the lag is set to a one-day interval for the Oberbergbach ($N=96$ time steps; Figure B-29) and an interval of $N=20$ time steps (300 min) at the Pitzbach:

$$\max_{j=1}^N(V_{i-j}) \leq V_{b,i} \leq \min_{j=1}^N(V_{i+j}) \quad (\text{B23})$$

This lag distance was defined by trial and error in order to exclude local sinks or peaks, respectively. In the case that this constraint is fulfilled at two subsequent times, the bed load transport rate [$\text{m}^3/15 \text{ min}$] is determined by:

$$Q_{b,i}[\text{m}^3/\text{s}] = \frac{(V_{b,i} - V_{b,i-1})[\text{m}^3] \times (1 - e)}{900[\text{s}]} \quad (\text{B24})$$

Herein, e refers to the porosity of the deposited bed load which is assumed with 30 %. For all remaining times (red dots in Figure B-28), bed load transport rate is determined based on a smoothed and filtered time series of bed load accumulation. Therefore, the central moving average with a lag distance of 10 time steps is calculated and the time series is thinned out to every 10th value.

Starting at the end of the period (V_n) (of two subsequent hydraulic flushings), the algorithm searches then for the nearest previous time ($n-i$) where both constraints

$$V_{n-i} < V_n \cap V_{n-i} > V_{n-i-1} \quad (\text{B25})$$

$$V_{n-i} > \frac{1}{N} \sum_{j=2}^5 V_{n-i-j} \quad (\text{B26})$$

are fulfilled (Figure B-30).

This aggregated time series increases monotonically but features irregular time steps. Therefore, the patchy time series of bed load volume is mapped onto the initial time series with a temporal interval of 15 min by linear interpolation. The bed load transport rate [m^3/s] for all remaining times is then determined by equation B24, where V_b refers to the smoothed, monotonic increasing time series (red dots in Figure B-28), respectively.

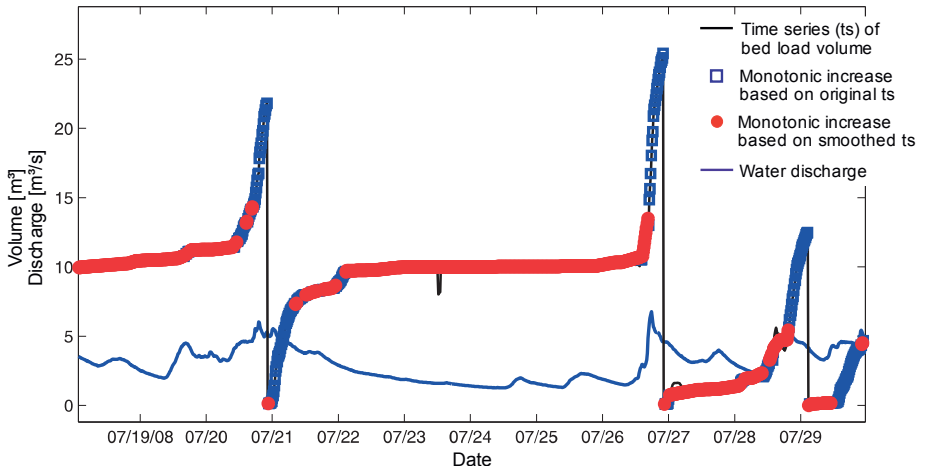


Figure B-28: The time series of bed load volumes at the Oberbergbach is split into the group (i) which already features a monotonic increase (blue rectangles) and (ii) which needs to be smoothed acc. equation B25 and B26 (red dots) to get non-negative transport rates

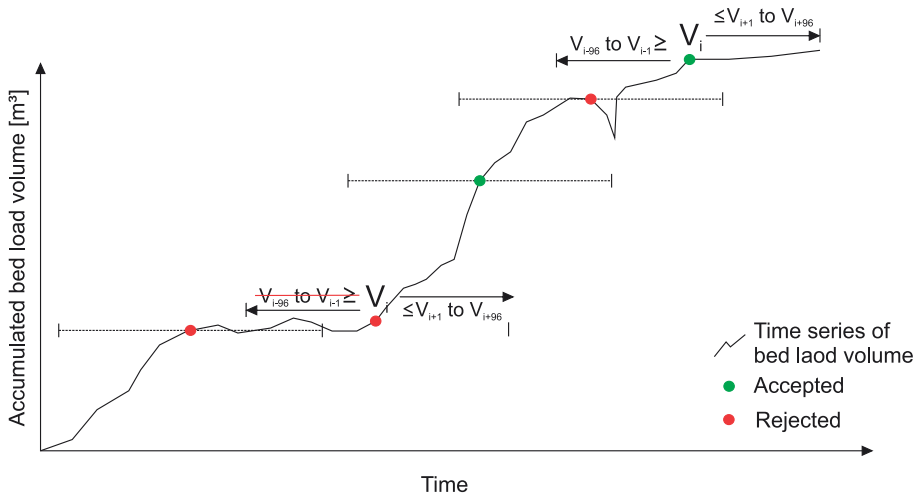


Figure B-29: Scheme of the algorithm that determines if the time series of bed load accumulation is monotonically increasing at a certain time (equation B23)

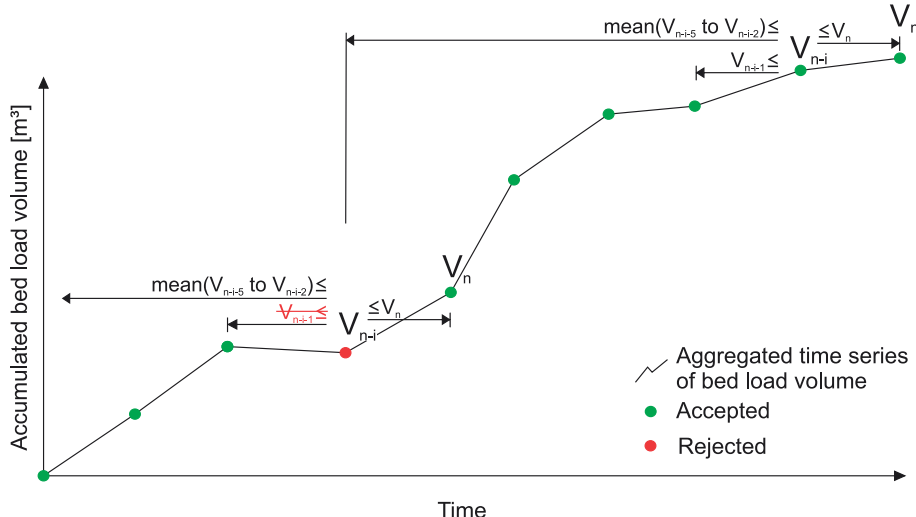


Figure B-30: Scheme of the algorithm that smooths the time series to get a monotonic increasing graph (equation B25 and B26)

1.4.2 Trap efficiency of the settling basin

1.4.2.1 General remarks

The efficiency of the two water intake structures in trapping bed load is influenced by two boundary conditions: (i) the design discharge which is given by the structure's capacity and (ii) the beam spacing of the bar rack above intake channel where water and sediment are diverted into the settling basin. Furthermore, there is no sediment deposition in course of a hydraulic flushing.

1.4.2.2 Overpassing sediment – part 1

The design discharge of the water intake structures Pitzbach and Oberbergbach is 5.4 m³/s and 5.5 m³/s (Table B-5), respectively. Total runoff regularly exceeds the structure's capacity in the summer months due to either rainfall-induced floods or glacier melt during hot periods. In the case of discharges lower than the design discharge, the entire run off is abstracted and hence, all sediment with diameters smaller than 15 cm are diverted to the settling basin. In contrast, when discharge exceeds the structure's capacity, the residual water falls over the downstream weir and remains in the natural channel (Figure B-31). By that, a fraction of the bed load which is transported to the water intake structure might overpass as well. Although the sediment density is much larger than water density (expecting it to settle down), fine sediment is lifted up by the vortices and the high turbulence in the intake channel, while coarse grains (even with diameters smaller than the bar spacing of 15 cm) bounce over the bottom rack.



Figure B-31: Water intake structure at the Oberbergbach with the water discharge slightly exceeding the design discharge of $5.5 \text{ m}^3/\text{s}$

In course of an experimental investigation (see '*Experimental modelling of bed load overpassing a bottom rack intake*' in section B.2.1), the proportion of bed load overpassing the bottom rack was found to be about 6 % of the total bed load transport. Although the likelihood that a certain grain size overpasses the rack depends on the water discharge, the relation is not consistent. Finer grains are more likely lifted out of the intake channel at discharges barely exceeding the structure's capacity, while the proportion of coarse grains increases with flow.

In order to cope this decrease of trapping efficiency at discharges exceeding the design discharge, the bed load transport rate determined by the approach in section 1.4.1 is raised by 6 % if the $Q > 1.5 \times Q_A$. In the run off range $Q_A < Q < 1.5 \times Q_A$ the decrease in trapping efficiency is assumed to follow the quadratic polynomial function

$$p_{\text{overpassing}} = 0.24 \left(\frac{Q}{Q_A} \right)^2 - 0.48 \left(\frac{Q}{Q_A} \right) + 0.24 \quad (\text{B27})$$

Equation B27 was derived by means of the two constraints (i) $p_{\text{overpassing}} = 0$ at $Q = Q_A$ (no residual flow) and (ii) $p_{\text{overpassing}} = 0.06$ at $Q = 1.5Q_A$, respectively.

In a consequence, total bed load transport ($Q_{b,\text{total}}$) rate is defined by

$$Q_{b,\text{total}} = Q_{b,\text{sb}} \times (1 + p_{\text{overpassing}}) \quad (\text{B28})$$

Herein, $Q_{b,\text{sb}}$ refers to the bed load transport rate determined by the step-wise increase of bed load volume in the settling basin (section 1.4.1).

1.4.2.3 Overpassing sediment – part 2

Since the bottom rack intake at both sites features a bar spacing of 0.15 m, all transported stones exceeding this size cannot be trapped in the settling basin. The threshold grain size refers to the smallest axis of the sediment (c-axis), because the bar rack is constructed lengthways in flow direction.

Several field surveys were conducted in the 1970s in order to quantify the order of magnitude that these coarse stones contribute to total bed load transport at the Pitzbach (*Strobl*, 1980; *Sommer*, 1980). During the summer of 1975, *Strobl* (1980) counted all stones which clogged the bottom rack intake at the Pitzbach. In total, 120 stones with a mean diameter in the range of 0.15 m to 0.6 m deposited on the rack, which corresponds to a volume of approx. 2 m^3 . In contrast, the mean annual bed load volume at the Pitzbach is about 2392 m^3 (solid volume without pores), while it was about 944 m^3 in the year 1975. However, the coarse grains which overpassed the bottom rack intake were not assessed in the course of this survey but it was estimated to the same order of magnitude (*Strobl*, 1980).

Additionally, tracer stones were put on the stream bed of the Pitzbach in the spring of 1976. While only one out of a few hundred stones was mobilized in the subsequent summer, about ten to twenty stones were mobilized one year later and more than the half of all traced stones were relocated after the third summer season (*Sommer*, 1980).

In course of the field surveys accomplished in summer 2014 (May to August), the stones clogging the bottom rack intake at the Oberbergbach were counted almost every second week. In total about 130 stones were counted on the bottom rack, which corresponds with a volume of less than 1 m^3 . Thereby, an increase of clogging stones was observed only during periods where water discharge exceeded $8 \text{ m}^3/\text{s}$. In addition, the number of coarse stones that did not clog but overpassed the bottom rack is estimated to less than 5 m^3 for the summer 2014; in contrast the annual bed load volume in the year 2014 was about 350 m^3 , whereas the mean annual bed load volume is 662 m^3 (see *Study A* in section B.3).

Summarizing, historic and recent field surveys reveal that the proportion of bed load that is not trapped by the bottom rack due to its size, is negligibly small. This conclusion is solely valid for years without an exceptional extreme event.

Regarding the time series of bed load transport rate at the two sites (Pitzbach and Oberbergbach), the uncertainty due to overpassing stones larger than the bar spacing is neglected. The bias is assumed to be compensated by the consideration of the reduced trapping efficiency at high flows (section 1.4.2.2).

1.4.2.4 Bed load transport rate during a hydraulic flushing

At the water intake structures of the Pitzbach and the Oberbergbach, the hydraulic flushing of the settling basin lasts about 12 min. During this time the weighing system does not register the vertical stress and thus, the entering sediment is not measured. In a consequence, the bed load transport rate is not assessed by the approach given in the previous sections for, on average, two time steps per hydraulic flushing. To account for this bias, the bed load transport rate at the time of a hydraulic flushing is estimated by the bed load transport rate that was back-calculated just before and immediately afterwards.

1.4.3 Workflow to determine bed load transport rate

The time series of bed load accumulation in the settling basin is split into a monotonic increasing part and the remaining time series according to equation B23. The time series of bed load accumulation is then aggregated by means of a moving average approach and smoothed against certain, random fluctuations according to equation B25 and B26. Afterwards, the aggregated series is mapped onto the previous time series by linear interpolation.

The difference of bed load accumulation between two subsequent times is then used to determine the bed load transport rate. It is first computed by the monotonic increasing part of the original time series (equation B24). For all remaining times, it is calculated by the smoothed time series.

In order to account for the reduced trapping efficiency in case of high discharges, the bed load transport rate is increased according to equation B27 and B28. Finally, the bed load transport rate during a hydraulic flushing is estimated by the previous and next one.

1.4.4 Verification of the approach

1.4.4.1 Direct versus indirect measurements of bed load transport rates

The approach presented in the previous section enables to determine the bed load transport rates by means of the time series of the vertical stress acting on the bottom of the settling basin. The parameters required for this approach are calibrated by means of field surveys. However, due to the scatter of measured quantities, the data pose an uncertainty range.

To evaluate the goodness of the data, the bed load transport rates derived from the vertical stress within the settling basin (derived transport rates) are compared against an independent data set. The latter relies on field measurements with bed load traps (observed transport rates), which were accomplished at two study reaches at the Oberbergbach (see section B.1.5). The first field site is located just upstream of the water intake structure and the second field site is about 800 m further upstream. However, only very few bed load transport rate data are available for field site 1 and thus, the measured transport rates of both sites are used for the comparison.

The bed load transport rates of both data sets are plotted against discharge in Figure B-33. Due to illustrative reasons, the discharge measured at the field site is used for both data sets in Figure B-32, and the lateral inflow between the field site and the water intake structure is neglected. The filled circles refer to the 'observed transport rates' (bed load trap data) and the diamonds are associated with the 'derived transport rates'. The two symbols with the same color apply to the same point of time, respectively.

Most of the simultaneously assessed bed load transport rate are close to each other. Surprisingly, the match is the worst for the four highest transport rates, plotting to the right in Figure B-32; the derived transport rates are much lower than the observed transport rates. It is worth to note that each of these four observed transport rates data were measured in the field site 2, which is about 800 m upstream. The 'derived transport rates' approach 10^{-1} kg/s about nine hours later, suggesting for a time delay between both sites, rather than a bias.

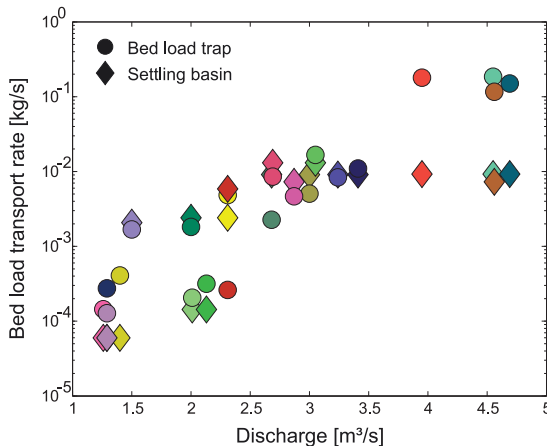


Figure B-32: Bed load transport rates at given times at the Oberbergbach determined by either the field measurements (with bed load traps acc. Bunte et al., 2004) or the bed load accumulation in the settling basin. The transport rates are plotted against the discharge measured at the study site, respectively.

Finally, the conformity of both data sets is illustrated by plotting them against each other (Figure B-33). The data match well at transport rates ranging between 10^{-3} kg/s and 10^{-2} kg/s, while the ‘derived transport rates’ are on average lower for the low and high transport rates. The deviation of the low transport rates is attributed to the uncertainty introduced by the linear interpolation during times with insignificant increase (see section 1.4.1), while the deviation of the high transport rates is attributed to the time delay rather than an inconsistency.

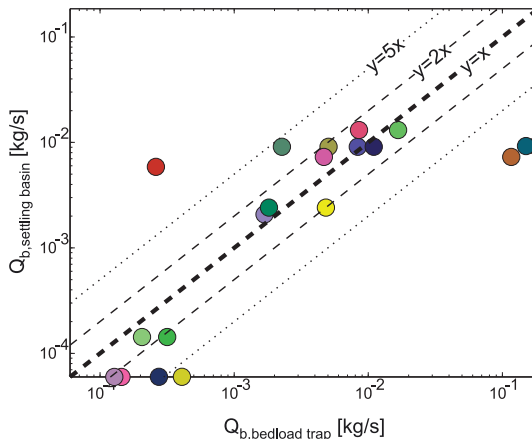


Figure B-33: Conformity of bed load transport rates at the Oberbergbach either determined by field measurements (with bed load traps acc. Bunte et al. (2004)) or by bed load accumulation in the settling basin

B.1.5 Additional field data

At three mountain streams, the bed load transport rate, the water discharge, the flow velocity and the bed surface grain size distribution was measured sporadically in course of field surveys. Site locations were in the proximity of the water intake structures, with a maximum distance of 800 m (Oberbergbach, site 2).

Bed load transport rate was measured with bed load traps according to *Bunte et al.* (2004). In contrast to *Bunte's* traps, a mesh opening of 1.4 mm rather than 4.0 mm was used (for further details see *Eichner*, 2015). However, the sampling efficiency was unaffected by the tighter net, since the bed load traps hardly altered flow velocity in front of it.

The discharge was measured according to the salt dilution method (e.g. *Foster*, 2000; *Morgenschweis*, 2010), either to validate the discharge records at the water intake structure or to account for lateral inflows in between. Based on the harmonic mean tracer travel time and the distance between injection and conductivity measurement (e.g. *Nitsche et al.*, 2012), mean flow velocity was determined sporadically. Additionally, the bed surface grain size distributions were assessed by transect-by-number analysis and converted to volume-by-weight samples according to a modified approach of *Fehr* (1987). This approach is consistent with grid-by-number samples (for further details see '*Verification of the transect-by-number method for assessing the bed surface grain size distribution*' in section A.1.1).

In total, 54 measurements of bed load transport rate were accomplished during the summer seasons 2014 and 2015. At one study site (Pitzbach), the field data are supplemented by 23 measurements, which were derived by *Hofer* (1985), according to a similar procedure (Table B-11). Simultaneously, mean flow velocity was measured 21 times at specific discharges in the range of 0.16 and 0.51 m²/s. A rough overview of site characteristics is given in Table B-11, the entire data set of total bed load transport rates and additional parameters in Table B-13, the fractional proportions of bed load transport in Table B-14 and the fractional proportions of the bed surface sediment in Table B-12. For a detailed description of the field sites the reader is referred to *Study C* (section B.5).

Table B-11: Overview of reach characteristics of the study sites at the Ob: Oberbergbach, Lb: Laengentalerbach and Pb: Pitzbach, with the bed surface grains sizes of which 50 % ($D_{50,S}$) and 84 % ($D_{84,S}$) are finer by weight

| Field site | Reach slope [m/m] | Reach length [m] | $D_{50,S}^b$ [m] | $D_{84,S}^b$ [m] | Number of bed load data [-] | Discharge range [m³/s] |
|--------------------|----------------------|---------------------|---------------------|---------------------|--------------------------------|---------------------------|
| Ob #1 | 0.076 | 60 | 0.21 | 0.49 | 5 | 1.29 - 2.13 |
| Ob #2 | 0.020 | 177 | 0.04 | 0.11 | 16 | 1.26 - 4.69 |
| Lb #1 | 0.040 | 34 | 0.07 | 0.12 | 12 | 0.76 - 1.13 |
| Lb #2 | 0.069 | 86 | 0.07 | 0.27 | 12 | 1.48 - 2.75 |
| Pb #1 | 0.080 | 86 | 0.17 | 0.51 | 5 | 3.11 - 4.83 |
| Pb #1 ^a | | | | | 10/23 | 1.90 - 5.05 |

^a data of Hofer (1985) with 10 measurements of fractional and 23 measurements of total bed load transport rates

^b Grain size data are based on the volume-by-weight grain size distribution of the bed surface which was measured according the transect-by-number method (see section A.1.1)

Table B-12: Bed surface grain size distribution of the five field sites, with the upper bound D_{ub} and the representative diameter D_i of the grain size class

| Grain size | | Volume by weight proportion | | | | |
|------------------|---------------|-----------------------------|-------------|--------------|--------------|--------------|
| D_{ub} (mm) | D_i (mm) | Ob#1 (-) | Ob#2 (-) | Lb #1 (-) | Lb #2 (-) | Pb #1 (-) |
| 10 | 3 | 0.08 | 0.14 | 0.11 | 0.06 | 0.12 |
| 20 | 14 | 0.07 | 0.16 | 0.09 | 0.12 | 0.05 |
| 30 | 24 | 0.06 | 0.10 | 0.08 | 0.10 | 0.04 |
| 40 | 35 | 0.05 | 0.10 | 0.08 | 0.08 | 0.03 |
| 60 | 49 | 0.05 | 0.18 | 0.10 | 0.09 | 0.04 |
| 80 | 69 | 0.05 | 0.07 | 0.12 | 0.08 | 0.05 |
| 100 | 89 | 0.03 | 0.05 | 0.15 | 0.07 | 0.03 |
| 120 | 110 | 0.03 | 0.07 | 0.11 | 0.03 | 0.05 |
| 150 | 134 | 0.03 | 0.06 | 0.11 | 0.06 | 0.05 |
| 200 | 173 | 0.04 | 0.07 | 0.04 | 0.08 | 0.09 |
| 250 | 224 | 0.04 | 0.02 | - | 0.05 | 0.06 |
| 300 | 274 | 0.10 | - | - | 0.04 | 0.06 |
| 350 | 324 | 0.04 | - | 0.02 | 0.03 | 0.03 |
| 400 | 374 | 0.07 | - | - | 0.03 | 0.07 |
| 500 | 447 | 0.10 | - | - | 0.02 | 0.07 |
| 600 | 548 | 0.07 | - | - | 0.03 | 0.06 |
| 800 | 693 | 0.05 | - | - | 0.04 | 0.05 |
| 1000 | 894 | 0.03 | - | - | - | 0.04 |
| 1200 | 1095 | - | - | - | - | - |
| 1500 | 1342 | - | - | - | - | 0.02 |
| 2000 | 1732 | - | - | - | - | - |
| > 2000 | - | - | - | - | - | - |

Table B-13: Measurements of bed load transport rate, with the total flow width w_t at the measuring cross section, the active width associated with bed load transport w_a , the mean discharge during the measurement Q , the duration of the measurement md and the bed load transport rate extrapolated to the cross-section Q_b

| Stream | Reach | Id | Date | Start | End | w_t | w_a | Q | md | Q_b |
|----------------|-------|------------|--------------|---------|---------|-------|-------|--------|-------|----------|
| | | | [dd.mm.yyyy] | [HH:MM] | [HH:MM] | [m] | [m] | [m³/s] | [min] | [kg/h] |
| Oberbergbach | Ob #1 | 1_20140605 | 05.06.2014 | 13:30 | 16:30 | 7.1 | 6.1 | 1.50 | 180 | 6.059 |
| | Ob #1 | 1_20140712 | 12.07.2014 | 12:46 | 14:46 | 7.0 | 4.9 | 2.01 | 120 | 0.735 |
| | Ob #1 | 2_20140712 | 12.07.2014 | 15:10 | 17:10 | 7.0 | 4.9 | 2.13 | 120 | 1.143 |
| | Ob #1 | 1_20140818 | 18.08.2014 | 12:34 | 14:30 | 11.2 | 6.4 | 1.29 | 116 | 0.989 |
| | Ob #1 | 1_20140818 | 18.08.2014 | 14:47 | 15:47 | 11.2 | 6.4 | 1.40 | 60 | 1.475 |
| | Ob #2 | 1_20140806 | 06.08.2014 | 11:32 | 12:32 | 6.5 | 6.0 | 2.68 | 60 | 8.167 |
| | Ob #2 | 2_20140806 | 06.08.2014 | 12:45 | 13:45 | 6.5 | 6.0 | 3.00 | 60 | 18.200 |
| | Ob #2 | 3_20140806 | 06.08.2014 | 14:00 | 14:30 | 6.5 | 6.0 | 3.24 | 30 | 30.067 |
| | Ob #2 | 4_20140806 | 06.08.2014 | 14:43 | 15:13 | 6.5 | 6.0 | 3.41 | 30 | 39.533 |
| | Ob #2 | 1_20140807 | 07.08.2014 | 10:20 | 12:20 | 6.4 | 5.9 | 2.00 | 120 | 6.539 |
| | Ob #2 | 2_20140807 | 07.08.2014 | 12:38 | 13:38 | 6.4 | 5.9 | 2.31 | 60 | 17.405 |
| | Ob #2 | 3_20140807 | 07.08.2014 | 13:50 | 14:35 | 6.4 | 5.9 | 2.69 | 45 | 30.724 |
| | Ob #2 | 4_20140807 | 07.08.2014 | 14:52 | 15:22 | 6.4 | 5.9 | 3.05 | 30 | 60.049 |
| | Ob #2 | 1_20140819 | 19.08.2014 | 11:12 | 13:12 | 5.8 | 5.2 | 1.26 | 120 | 0.523 |
| | Ob #2 | 2_20140807 | 19.08.2014 | 13:24 | 15:24 | 5.8 | 5.2 | 1.29 | 120 | 0.456 |
| | Ob #2 | 1_20140517 | 17.06.2015 | 13:18 | 14:30 | 7.4 | 7.0 | 2.31 | 72 | 0.940 |
| | Ob #2 | 1_20150715 | 15.07.2015 | 13:40 | 14:45 | 9.2 | 8.9 | 3.95 | 65 | 645.599 |
| | Ob #2 | 2_20150715 | 15.07.2015 | 16:42 | 16:57 | 9.2 | 8.9 | 4.55 | 15 | 666.511 |
| | Ob #2 | 3_20150715 | 15.07.2015 | 17:22 | 17:29 | 9.2 | 8.9 | 4.69 | 7 | 539.933 |
| | Ob #2 | 1_20150716 | 16.07.2015 | 09:31 | 10:32 | 9.1 | 8.8 | 2.87 | 61 | 16.783 |
| | Ob #2 | 2_20150716 | 16.07.2015 | 13:41 | 13:52 | 9.1 | 8.8 | 4.56 | 11 | 419.200 |
| Laengtalerbach | Lb #1 | 1_20140606 | 06.06.2014 | 13:30 | 16:30 | 7.1 | 7.0 | 1.13 | 180 | 1.556 |
| | Lb #1 | 1_20140903 | 03.09.2014 | 11:45 | 13:45 | 4.1 | 3.0 | 0.76 | 120 | 0.557 |
| | Lb #1 | 2_20140801 | 03.09.2014 | 14:03 | 15:20 | 4.1 | 3.0 | 0.77 | 77 | 0.442 |
| | Lb #1 | 3_20140801 | 03.09.2014 | 15:35 | 17:35 | 4.1 | 3.0 | 0.79 | 120 | 0.598 |
| | Lb #1 | 1_20140904 | 04.09.2014 | 10:59 | 12:29 | 4.4 | 3.1 | 0.94 | 90 | 2.547 |
| | Lb #1 | 2_20140801 | 04.09.2014 | 12:50 | 13:50 | 4.4 | 3.1 | 0.95 | 60 | 1.712 |
| | Lb #1 | 3_20140801 | 04.09.2014 | 14:10 | 15:10 | 4.4 | 3.1 | 0.95 | 60 | 4.006 |
| | Lb #1 | 1_20140905 | 05.09.2014 | 11:00 | 12:15 | 4.4 | 3.1 | 0.89 | 75 | 0.670 |
| | Lb #1 | 2_20140801 | 05.09.2014 | 12:27 | 13:31 | 4.4 | 3.1 | 0.89 | 64 | 3.449 |
| | Lb #1 | 1_20140906 | 06.09.2014 | 12:45 | 13:28 | 4.3 | 3.4 | 1.02 | 43 | 3.416 |
| | Lb #1 | 2_20140906 | 06.09.2014 | 13:57 | 14:45 | 4.3 | 3.4 | 1.01 | 48 | 4.165 |
| | Lb #1 | 3_20140906 | 06.09.2014 | 15:13 | 15:27 | 4.3 | 3.4 | 0.97 | 14 | 2.380 |
| | Lb #2 | 1_20140729 | 29.07.2014 | 11:35 | 13:35 | 6.8 | 6.1 | 1.49 | 120 | 2.559 |
| | Lb #2 | 2_20140729 | 29.07.2014 | 13:53 | 15:53 | 6.8 | 6.1 | 1.48 | 120 | 2.881 |
| | Lb #2 | 1_20140728 | 28.07.2014 | 11:55 | 13:55 | 6.9 | 6.2 | 1.64 | 120 | 2.049 |
| | Lb #2 | 2_20140728 | 28.07.2014 | 14:21 | 15:53 | 6.9 | 6.2 | 1.68 | 92 | 10.131 |
| | Lb #2 | 1_20140713 | 13.07.2014 | 13:15 | 15:15 | 6.8 | 6.3 | 1.48 | 120 | 1.641 |
| | Lb #2 | 1_20140711 | 11.07.2014 | 13:30 | 16:30 | 6.8 | 6.3 | 1.54 | 180 | 11.076 |
| | Lb #2 | 1_20140801 | 01.08.2014 | 09:42 | 10:42 | 7.1 | 6.3 | 2.56 | 60 | 132.604 |
| | Lb #2 | 2_20140801 | 01.08.2014 | 10:57 | 11:27 | 7.1 | 6.3 | 2.51 | 30 | 127.431 |
| | Lb #2 | 3_20140801 | 01.08.2014 | 12:10 | 12:40 | 7.1 | 6.3 | 2.46 | 30 | 111.806 |
| | Lb #2 | 1_20140730 | 30.07.2014 | 12:05 | 13:05 | 6.8 | 6.1 | 2.72 | 60 | 93.838 |
| | Lb #2 | 2_20140730 | 30.07.2014 | 13:27 | 13:57 | 6.8 | 6.1 | 2.50 | 30 | 175.273 |
| | Lb #2 | 3_20140730 | 30.07.2014 | 14:12 | 14:42 | 6.8 | 6.1 | 2.75 | 30 | 134.946 |
| Pitzbach | Pb #1 | 1_20150616 | 16.06.2015 | 13:00 | 13:30 | 8.4 | 7.2 | 4.82 | 30 | 1101.120 |
| | Pb #2 | 2_20150616 | 16.06.2015 | 13:37 | 13:57 | 8.4 | 7.2 | 4.83 | 20 | 999.000 |
| | Pb #3 | 1_20150618 | 18.06.2015 | 11:33 | 11:56 | 7.4 | 6.4 | 3.14 | 23 | 10.574 |
| | Pb #4 | 2_20150618 | 18.06.2015 | 12:03 | 13:03 | 7.4 | 6.4 | 3.12 | 60 | 16.178 |
| | Pb #5 | 3_20150618 | 18.06.2015 | 13:18 | 14:08 | 7.4 | 6.4 | 3.11 | 50 | 16.640 |

Table B-14: Volume-by-weight proportion of fractional bed load transport, with the sieving range given in the headline. The *Id* enables for an attribution to the data presented in Table B-13

| Stream Reach | Id | Grain size fraction [mm] | | | | | | | | | | | | |
|------------------|------------------|--------------------------|-------|-------|--------|---------|---------|---------|---------|---------|----------|-----------|-------|--|
| | | 0 - 1 | 1 - 2 | 2 - 5 | 5 - 10 | 10 - 20 | 20 - 30 | 30 - 40 | 40 - 60 | 60 - 80 | 80 - 100 | 100 - 120 | > 120 | |
| | | [·] | [·] | [·] | [·] | [·] | [·] | [·] | [·] | [·] | [·] | [·] | [·] | |
| Oberbergbach | Ob #1 1_20140605 | 0.202 | 0.346 | 0.340 | 0.093 | 0.019 | - | - | - | - | - | - | - | |
| | Ob #1 1_20140712 | - | 0.429 | 0.400 | 0.086 | 0.086 | - | - | - | - | - | - | - | |
| | Ob #1 2_20140712 | 0.018 | 0.351 | 0.439 | 0.140 | 0.053 | - | - | - | - | - | - | - | |
| | Ob #1 1_20140818 | 0.006 | 0.206 | 0.274 | 0.145 | 0.188 | 0.181 | - | - | - | - | - | - | |
| | Ob #1 1_20140818 | 0.005 | 0.05 | 0.189 | 0.211 | 0.094 | 0.248 | 0.252 | - | - | - | - | - | |
| | Ob #2 1_20140806 | 0.016 | 0.392 | 0.429 | 0.098 | 0.053 | 0.012 | - | - | - | - | - | - | |
| | Ob #2 2_20140806 | 0.013 | 0.351 | 0.460 | 0.143 | 0.033 | - | - | - | - | - | - | - | |
| | Ob #2 3_20140806 | 0.018 | 0.365 | 0.415 | 0.155 | 0.036 | 0.011 | - | - | - | - | - | - | |
| | Ob #2 4_20140806 | 0.022 | 0.427 | 0.414 | 0.097 | 0.024 | 0.017 | - | - | - | - | - | - | |
| | Ob #2 1_20140807 | 0.025 | 0.480 | 0.442 | 0.050 | 0.002 | - | - | - | - | - | - | - | |
| | Ob #2 2_20140807 | 0.025 | 0.376 | 0.476 | 0.116 | 0.008 | - | - | - | - | - | - | - | |
| | Ob #2 3_20140807 | 0.050 | 0.471 | 0.409 | 0.064 | 0.006 | - | - | - | - | - | - | - | |
| | Ob #2 4_20140807 | 0.049 | 0.506 | 0.369 | 0.060 | 0.010 | 0.006 | - | - | - | - | - | - | |
| | Ob #2 1_20140819 | 0.013 | 0.429 | 0.518 | 0.040 | - | - | - | - | - | - | - | - | |
| | Ob #2 2_20140807 | 0.013 | 0.429 | 0.518 | 0.040 | - | - | - | - | - | - | - | - | |
| | Ob #2 1_20140517 | 0.031 | 0.590 | 0.311 | 0.037 | 0.031 | - | - | - | - | - | - | - | |
| | Ob #2 1_20150715 | 0.051 | 0.263 | 0.373 | 0.173 | 0.088 | 0.029 | 0.008 | 0.016 | - | - | - | - | |
| | Ob #2 2_20150715 | 0.036 | 0.234 | 0.285 | 0.158 | 0.184 | 0.071 | 0.020 | 0.013 | - | - | - | - | |
| | Ob #2 3_20150715 | 0.038 | 0.253 | 0.327 | 0.165 | 0.118 | 0.063 | 0.015 | 0.021 | - | - | - | - | |
| | Ob #2 1_20150716 | 0.020 | 0.353 | 0.408 | 0.142 | 0.078 | - | - | - | - | - | - | - | |
| | Ob #2 2_20150716 | 0.036 | 0.308 | 0.324 | 0.158 | 0.096 | 0.043 | 0.035 | - | - | - | - | - | |
| Laengentalerbach | Lb #1 1_20140606 | 0.053 | 0.553 | 0.368 | 0.026 | - | - | - | - | - | - | - | - | |
| | Lb #1 1_20140903 | 0.015 | 0.390 | 0.510 | 0.075 | 0.010 | - | - | - | - | - | - | - | |
| | Lb #1 2_20140801 | 0.029 | 0.322 | 0.526 | 0.117 | 0.006 | - | - | - | - | - | - | - | |
| | Lb #1 3_20140801 | 0.014 | 0.292 | 0.417 | 0.139 | 0.083 | 0.056 | - | - | - | - | - | - | |
| | Lb #1 1_20140904 | 0.005 | 0.208 | 0.335 | 0.254 | 0.122 | 0.015 | 0.061 | - | - | - | - | - | |
| | Lb #1 2_20140801 | 0.010 | 0.278 | 0.338 | 0.109 | 0.119 | 0.039 | 0.107 | - | - | - | - | - | |
| | Lb #1 3_20140801 | 0.004 | 0.177 | 0.476 | 0.273 | 0.069 | - | - | - | - | - | - | - | |
| | Lb #1 1_20140905 | 0.020 | 0.306 | 0.449 | 0.122 | 0.102 | - | - | - | - | - | - | - | |
| | Lb #1 2_20140801 | 0.005 | 0.075 | 0.151 | 0.071 | 0.089 | 0.070 | - | 0.539 | - | - | - | - | |
| | Lb #1 1_20140906 | 0.008 | 0.110 | 0.141 | 0.079 | 0.149 | 0.158 | 0.356 | - | - | - | - | - | |
| | Lb #1 2_20140906 | 0.009 | 0.156 | 0.235 | 0.087 | 0.003 | - | - | 0.510 | - | - | - | - | |
| | Lb #1 3_20140906 | - | 0.263 | 0.316 | 0.105 | 0.033 | 0.283 | - | - | - | - | - | - | |
| | Lb #2 1_20140729 | 0.027 | 0.267 | 0.367 | 0.200 | 0.113 | 0.027 | - | - | - | - | - | - | |
| | Lb #2 2_20140729 | 0.018 | 0.219 | 0.314 | 0.178 | 0.124 | 0.148 | - | - | - | - | - | - | |
| | Lb #2 1_20140728 | 0.037 | 0.472 | 0.389 | 0.083 | 0.019 | - | - | - | - | - | - | - | |
| | Lb #2 2_20140728 | 0.011 | 0.139 | 0.226 | 0.069 | 0.046 | 0.013 | - | - | - | - | 0.496 | - | |
| | Lb #2 1_20140713 | 0.015 | 0.262 | 0.385 | 0.138 | 0.046 | 0.154 | - | - | - | - | - | - | |
| | Lb #2 1_20140711 | 0.005 | 0.088 | 0.194 | 0.233 | 0.263 | 0.218 | - | - | - | - | - | - | |
| | Lb #2 1_20140801 | 0.020 | 0.157 | 0.293 | 0.201 | 0.154 | 0.059 | 0.066 | 0.038 | 0.012 | - | - | - | |
| | Lb #2 2_20140801 | 0.157 | 0.147 | 0.208 | 0.183 | 0.234 | 0.023 | 0.027 | 0.009 | 0.011 | - | - | - | |
| | Lb #2 3_20140801 | 0.019 | 0.163 | 0.311 | 0.210 | 0.171 | 0.060 | 0.066 | - | - | - | - | - | |
| | Lb #2 1_20140730 | 0.029 | 0.091 | 0.269 | 0.155 | 0.118 | 0.043 | 0.096 | 0.068 | 0.039 | 0.092 | - | - | |
| | Lb #2 2_20140730 | 0.020 | 0.144 | 0.259 | 0.185 | 0.131 | 0.035 | 0.043 | 0.129 | 0.019 | 0.034 | - | - | |
| | Lb #2 3_20140730 | 0.027 | 0.174 | 0.289 | 0.143 | 0.096 | 0.050 | 0.049 | 0.086 | 0.086 | - | - | - | |
| Pitzbach | Pb #1 1_20150616 | 0.144 | 0.176 | 0.249 | 0.218 | 0.212 | - | - | - | - | - | - | - | |
| | Pb #2 2_20150616 | 0.015 | 0.176 | 0.181 | 0.336 | 0.194 | 0.065 | 0.005 | 0.028 | - | - | - | - | |
| | Pb #3 1_20150618 | 0.013 | 0.410 | 0.436 | 0.077 | 0.013 | 0.051 | - | - | - | - | - | - | |
| | Pb #4 2_20150618 | 0.017 | 0.410 | 0.449 | 0.087 | 0.037 | - | - | - | - | - | - | - | |
| | Pb #5 3_20150618 | 0.018 | 0.387 | 0.426 | 0.121 | 0.049 | - | - | - | - | - | - | - | |

B.1.6 References of chapter B.1 *Field data and data accuracy*

- Aufleger, M. (1996), Ein Beitrag zur Auswertung von Erddruckmessungen in Staudämmen, *Wasserbau und Wasserwirtschaft*, 78, Lehrstuhl für Wasserbau und Wasserwirtschaft, Techn. Univ. Munich, Munich, Germany, 178 p. (in German).
- Bunte, K., Abt, S., Potyondy, J. P. and Ryan, S. E. (2004), Measurement of coarse gravel and cobble transport using portable bedload traps, *J. Hydraul. Eng.*, 130(9), 879-893, doi: 10.1061/~ASCE/0733-9429~2004!130:9~879
- Church, M., and A. Zimmerman (2007), Form and stability of step-pool channels: Research progress, *Water Resour. Res.*, 43, W03415, doi: 10.1029/2006WR005037
- Drobir, H. (1981), Entwurf von Wasserfassumgen im Hochgebirge (Design of Water Intake at High Altitudes), *Oesterreichische Wasserwirtschaft*, 33, 243-253
- Eichner, B. (2015), Untersuchungen zum Geschiebetransport in Hochgebirgsbächen, Master thesis, University of Innsbruck, Innsbruck, Austria (in German).
- Eichner, B. (unpublished), Entsandervermessung WF Pitzbach, Internal Report of Field Survey, Unit of Hydraulic Engineering, Univ. of Innsbruck, Austria.
- Fehr, R. (1987), Geschiebeanalysen in Gebirgsflüssen - Umrechnung und Vergleich von verschiedenen Analyseverfahren [Bed material analyses in mountain streams - Transformation and comparison of various analyses procedures], *Mitteilungen der Versuchsanstalt für Wasserbau, Hydrologie und Glaziologie an der ETH Zürich*, No. 92, 139 pp., ETH Zurich, Switzerland.
- Fischer, A., Seiser, B., Stocker-Waldhuber, M., Mitterer, C. ad Abermann, J. (2015), The Austrian Glacier Inventories GI 1 (1969), GI 2 (1998), GI 3 (2006), and GI LIA in ArcGIS (shapefile) format. doi: 10.1594/PANGAEA.844988.
- Foster, I. D. L., Ed. (2000), Tracers in Geomorphology, Wiley, Chichester.
- Hofer, B., 1985, Der Feststofftransport von Hochgebirgsbächen am Beispiel des Pitzbachs (Sediment transport of mountain streams: example of Pitzbach stream), Ph.D. thesis, Univ. Innsbruck, Innsbruck, 131 p (in German).
- Lenzi, M. A., L. Mao, and F. Comiti (2004), Magnitude-frequency analysis of bed load data in an Alpine boulder bed stream, *Water Resour. Res.*, 40, W07201, doi: 10.1029/2003WR002961
- Morgenschweis, G. (2010), Hydrometrie. Springer Verlag, Berlin Heidelberg.
- Nitsche, M., D. Rickenmann, J. W. Kirchner, J. M. Turowski, and A. Badoux (2012), Macroroughness and variations in reach-averaged flow resistance in steep mountain streams, *Water Resour. Res.*, 48, W12518, doi: 10.1029/2012wr012091.
- Rickenmann, D. (2001), Comparison of bed load transport in torrents and gravel bed streams, *Water Resour. Res.*, 37(12), 3295-3305.
- Rickenmann, D. and B. Fritschl (2010), Bedload transport measurements using piezoelectric impact sensors and geophones, *U.S. Geological Survey Scientific Investigations Report 2010-5091*, (published online 2010). Available in the Internet: <http://pubs.usgs.gov/sir/2010/5091/papers/listofpapers.html>
- Schober, W. (1961), Selbsttätige Entkiesungs- und Entsandungsanlagen (Automatic flushing of desilting chambers), *Oesterreichische Wasserwirtschaft*, Springer-Verlag, Wien, 99-108.
- Sommer, N., and H. Lauffer (1982), Untersuchungen über den Feststofftransport in Gebirgsbächen der Ostalpen (Sediment transport in mountain streams of the Eastern Alps), in *Proceedings of the 14th International Dam Conference*, Rio de Janeiro, Brazil.
- Sommer, N. (1980), Investigations on the Bed Load and Suspended Load and the Transport of Dissolved Matter in Mountain Streams, *Interpraevent* 1980 (2), 69-94 (in German).
- Strobl, M. (1980), Schwebstoff- und Geschiebeführung in Gletscherbächen der zentralen Ötztaler Alpen (Tirol) und Untersuchung über den Gebirgsabtrag im Gebiet des Mittelbergferners (Suspended load and bed load transport in glacial streams in the Ötztal Alps and investigations of mountain denudation erosion at the Mittelbergferner). PhD thesis, Univ. Innsbruck, Innsbruck (in German).
- Tognacca, C. (1999), Beitrag zur Untersuchung der Entstehungsmechanismen von Murgängen, Ph.D. thesis, ETH Zurich, Zurich, Switzerland (in German).
- Tschada, H. (1975), Beobachtungen über die Geschiebefracht von Hochgebirgsbächen (Observations on bed load volumes in mountain streams), *Interpraevent*, 1975 (1), 109-126.
- Tschada, H and B. Hofer (1990), Total solid load from the catchment area of the Kaunertal hydroelectric power station: the results of 25 years of operation, *Hydrology in Mountain Regions II – Artificial Reservoirs, Water and Slopes, Proceedings of two Lausanne Symposia, IAHS Publ. no. 194*.

- Turowski, J. M., E. M. Yager, A. Badoux, D. Rickenmann, and P. Molnar (2009), The impact of exceptional events on erosion, bed load transport and channel stability in a step-pool channel, *Earth Surf. Proc. Land.*, **34**, 1661-1673, doi: 10.1002/esp.1855.
- Turowski, J. M. (2010), Probability distributions of bed load transport rates: A new derivation and comparison with field data, *Water Resour. Res.*, **46**, W08501, doi: 10.1029/2009WR008488.

B.2 Supporting information of 'Field data and data accuracy'

B.2.1 Experimental modelling of bed load overpassing a bottom rack intake

2.1.1 Scope of the experimental modelling

The bottom rack intake at the Schwarzach ($46^{\circ}55'18''$ N, $12^{\circ}31'32''$ E) was rebuilt in the hydraulic laboratory of the University of Innsbruck at a scale of 1:10. The actual scope of the physical scale model was the optimization of the flow and certain hydraulic structures. However, the physical scale model of the bottom rack intake was then used to perform simple experiments on the trapping efficiency at flows exceeding the structure's capacity. The geometry of the bottom rack was very similar to that at the Oberbergbach and the Pitzbach (Table B-15).

Table B-15: Characteristic measures of the bottom rack intakes considered in this study

| Site | Length [m] | Width [m] | Beam spacing [m] | α_{screen} [deg] | β_{channel} [deg] | Length | Width |
|--------------|---------------|--------------|------------------------|-----------------------------------|-----------------------------------|--------|-------|
| Schwarzach | 4.2 | 4.5 | 0.15 | 12 | 119 | | |
| Oberbergbach | 3.8 | 6 | 0.15 | 11 | 131 | | |
| Pitzbach | 4 | 6 | 0.15 | 11 | 122 | | |

2.1.2 Methods

2.1.2.1 Experimental setup

A 4 m long channel was built upstream of the bottom rack intake with a gradient of 0.04 m/m. The channel was rectangular with smooth side walls and a constant width of 0.5 m. The flume bed was fixed by a mixture of concrete and coarse stones in order to avoid bed erosion but to preserve a channel roughness which is typical for steep mountain streams. The bottom rack intake itself featured a width of 0.45 m and the lateral contraction at the weir was hydraulically optimized by means of rounded side walls (Figure B-34). Like the intake structure, the rack was constructed in the scale of 1:10 of the prototype reference. The bars were circular shaped and featured a clear width of 15 mm and a rack width of 8 mm.

Several experimental runs were performed in order to investigate the trapping efficiency of the bottom rack intake at high discharges. During each experimental run, water discharge was constant and sediment was fed at the upstream end of the flume. The water discharge was set to a predefined multiple of the design discharge ($Q_A=14.8 \text{ l/s}$); the latter is the maximum runoff that completely diverts into the intake channel. The sediment was collected either at the downstream end of the intake channel (diversion flow) or downstream of the inclined rack where the residual water overflows the second weir (residual flow; Figure B-35).

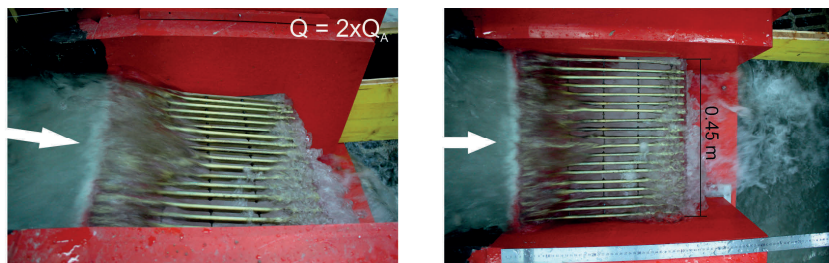


Figure B-34: Physical scale model of a bottom rack intake at which the efficiency in trapping bed load is investigated

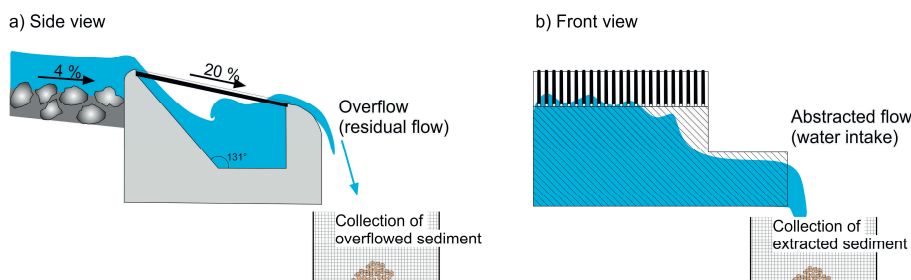


Figure B-35: Scheme of the experimental setup

In total, 35 experimental runs were performed which differed in the water discharge (5 variants) and the grain size of supplied sediment (7 variants). The range of discharge varied within 1.5 to 3.5 times Q_A and grain sizes ranging from 1 mm to 16 mm were considered (Table B-16). In prototype dimensions, the range of grain sizes corresponds with 10 mm and 160 mm, which sufficiently covers the grain sizes of bed load transport at high flows (Table B-14 in section B.1.5) for all except the finest particles.

In five out of seven sediment variants, the grains featured a uniform size, while in two variants a mixture was used. The fine mixture revealed an arithmetic mean grain size (D_m) of 2.3 mm and a maximum grain size (D_{max}) of 12 mm, while the D_m and the D_{max} of the coarse mixture were 4.3 mm and 16 mm, respectively. The sediment was composed of rounded quartz grains with a mean density of 2.68 g/cm³ and it was transported as bed load in all runs.

2.1.2.2 Experimental procedure

At constant discharge, 100 kg of sediment was manually supplied at a constant rate to the flume. The feeding rate oriented on the transport capacity. The bed load transport rate is herein defined by the total weight of collected sediment divided by the duration of the experiment. Hence, the travelling time of the bed load is neglected (Table B-16).

Once all sediment was supplied, the water discharge remained until no more grains were transported. However, in all except one experimental run, the entire amount of supplied sediment was transported out of the flume.

Table B-16: Overview of the boundary conditions (grain size and discharge) and the bed load transport rate [kg/min; in model scale] of each experimental run

| Supplied grain size [mm] | Multiple of Q_A (14. l/s) [-] | | | | |
|--------------------------|---------------------------------|------|------|------|------|
| | 1.5 | 2.0 | 2.5 | 3.0 | 3.5 |
| $1.0 < D < 2.0$ | 6.7 | 10.0 | 12.5 | 14.3 | 20.0 |
| $2.0 < D < 5.6$ | 4.2 | 5.9 | 12.5 | 16.7 | 16.7 |
| $5.6 < D < 8.0$ | 2.3 | 5.3 | 7.7 | 16.7 | 14.3 |
| $8.0 < D < 12$ | 1.7 | 3.0 | 7.7 | 9.1 | 12.5 |
| $12 < D < 16$ | 0.2 | 1.4 | 3.7 | 3.8 | 6.3 |
| Fine mixture | 4.8 | 9.1 | 11.8 | 16.7 | 16.7 |
| Coarse mixture | 5.3 | 6.2 | 10.0 | 14.3 | 20.0 |

2.1.3 Results

The experiments revealed that a certain fraction of total bed load overpasses the bottom rack intake. Except for the coarsest grain size, the proportion ranges between 2 % and 12 % (Figure B-36).

The proportions of overpassing grains are consistent in terms of their abundance in the bed load. The results obtained by using a sediment mixture are in the same range as those obtained in course of the runs with uniform sized sediment. In Figure B-37 the proportions that were measured in course of the uniform sized experiments (y-axis) are plotted against the proportions of each grain size in the mixed sized experiments separately. Except for the coarsest fraction, they predominately plot within the range of a factor of two. It suggests, that coarse grains overpass the bottom rack relatively less frequently when they are limited in their frequency.

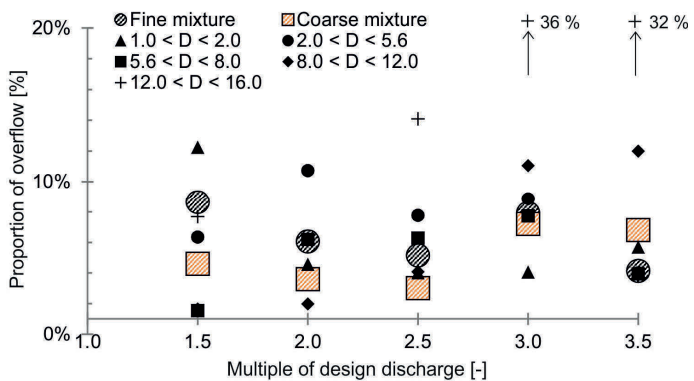


Figure B-36: Proportion of total bed load that overpassed the bottom rack intake

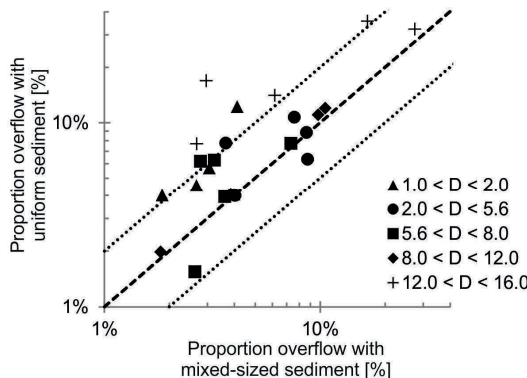


Figure B-37: Size-specific proportion of overpassing grains determined by using either sediment of uniform size or a sediment mixture

2.1.4 Discussion

In contrast to the initial expectation, the relationship between the proportion that overpasses the bottom rack intake and the water discharge is not consistent with different grain sizes. Fine grains overpass the water intake more likely as discharge barely exceeds Q_A , while it is the way around for coarse grains.

Based on visual observations, the fine sediment first tumbled into the weir channel and was then lifted up by the horizontal current that emerged at the downstream wall (Figure B-38a). But at higher discharges, the flow hydraulics in the intake channel changed. In this regard, Brunella et al. (2003) found a rapid shift towards a surface jet flow with one horizontal vortex that spins onto the intake channel bottom at the downstream wall (Figure B-38b). The impinging jet plunged onto the downstream wall (rather than the channel bottom), suggesting the formation of a vortex against the flow direction. Hence, fine sediment might be pushed to the intake bottom at high flows, resulting in lower proportions that overpass the bottom rack.

In contrast, coarse sediment more likely bounces over the screen. On the one hand, coarse grain features a higher momentum than small ones and additionally, coarse grains more likely hit the bottom rack. In this respect, the momentum of transported sediment increases with flow velocity and thus, with discharge, resulting in an increase of overpassing grains.

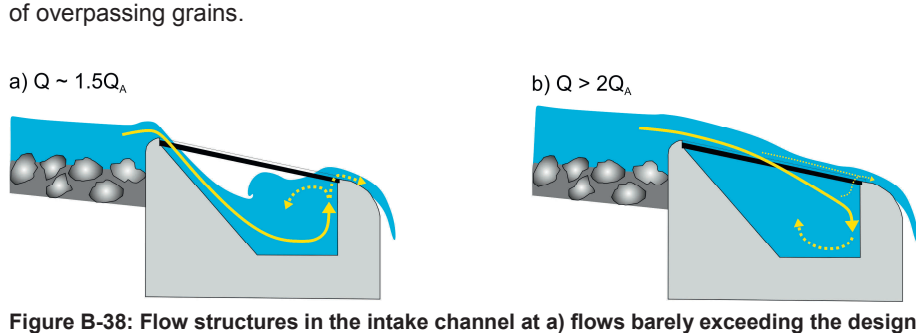


Figure B-38: Flow structures in the intake channel at a) flows barely exceeding the design discharge and b) sufficiently larger than the design discharge

2.1.5 References of chapter B.2.1 *Experimental modelling of bed load over-passing a bottom rack intake*

Brunella, S., W. H. Hager and H.-E. Minor (2003), Hydraulics of Bottom Rack Intake, *Journal of Hydraulic Engineering*, 129, 1, doi: 10.1061/(ASCE)0733-9429(2003)129:1(2)

B.2.2 Verification of the transect-by-number method for assessing the bed surface grain size distribution

2.2.1 Background and scope

Knowledge of the grain size distribution of the bed material present in a river reach is crucial for determining bed stability, flow resistance and bed load transport capacity. In this respect, characteristic grain diameters of the bed material represent a sensitive parameter of widely used empiric formulae. The application of fractional bed load transport formulae even requires knowledge about the proportion of each grain size fraction considered.

In this study, the applicability of the transect-by-number analysis for measuring the bed surface grain size distribution of steep mountain streams is verified. The transect-by-number analysis is easy to perform in the field and it is widely used in Austria and Switzerland (e.g. Schneider *et al.*, 2015; Chiari and Rickenmann, 2010). However, the frequency distribution obtained has to be converted into a volume-by-weight distribution, which is usually done according to Fehr (1987). But this approach was originally designed to convert the transect-by-number sample of the bed surface into the volume-by-weight distribution of the subsurface. Two modifications of Fehr's (1987) approach could be found in the literature that enable a conversion into the volume-by-weight distribution of the bed surface. To the author's knowledge, neither of them was ever verified. In a consequence, there remains a lack of knowledge for using the transect-by-number analysis to determine the bed surface's grain size distribution.

2.2.2 Methods

2.2.2.1 General remarks

At four field sites as well as in an experimental flume, the grain size distribution of the bed surface was measured by two different surface sampling methods. The first method is the transect-by-number analysis, while the second method is the Wolman count. Both of them are described in more detail in the following subsections 0 and 2.2.2.3.

The Wolman count refers to the grid-by-number technique and it is in common use in the U.S. (e.g. Bunte *et al.*, 2013; King *et al.*, 2004). The frequency distribution obtained by the grid-by-number method directly corresponds with the volume-by-weight distribution (Bunte and Abt, 2001) and no additional conversions are necessary. Thus, it represents a suitable reference that the volume-by-weight frequency distribution obtained by the converted transect-by-number analysis should match. In this respect, three different conversion techniques are applied and results are compared to the reference method (grid-by-number).

There exist additional uncertainties in measuring the bed surface grain size distribution, which are not addressed in this study, such as the operator's experiences in selecting a representative sampling location (Wohl, 1996), the sample size (Bunte *et al.*, 2009; Steidl, 2016) as well as the method for particle selection and size estimation (Bunte *et al.*, 2009).

2.2.2.2 Wolman count

2.2.2.2.1 Field application

The Wolman pebble count is an easy technique to measure the bed surface grain size distribution in gravel or cobble bed streams. Therefore, an operator traverses the channel bed and randomly collects a particle present on the bed surface. In order to ensure the randomness, *Wolman* (1954) proposed to pick up the particle from beneath the tip of the boot while looking away (heel-to-toe). In contrast, *Bunte and Abt* (2001) suggest the use of a regular grid for selecting the bed surface particles rather than the heel-to-toe method. Regardless of the sampling procedure, the sample must comprise at least 100 particles and each picked up particle is classified into the corresponding diameter class. In order to avoid double counts, the minimum step spacing equals the maximum grain size.

2.2.2.2.2 Conversion to volume-by-weight distribution of the bed surface

Assuming a constant density, the conversion of a frequency distribution of counts to a frequency distribution of weight is theoretically proportionate to D_i^3 . Furthermore, *Church et al.* (1987) suggest that the conversion of a grid sample to a volumetric sample is related by D_i^{-3} . Thus, the frequency distribution obtained by the grid-by-number technique corresponds with the volume-by-weight distribution (*Bunte and Abt*, 2001). No conversion is needed and the measured grain size distribution can be directly used for subsequent analysis.

2.2.2.3 Transect-by-number method

2.2.2.3.1 Field application

At a representative location immediately next to the water, a lace is fixed in the flow direction. The intermediate axis of each particle coarser than about 1 cm that is below the lace is measured and attributed to the corresponding diameter class. According to *Fehr* (1987), the sample should consist of at least 150 stones, with a minimum of 30 particles within the most frequent diameter class. The measurement yields a frequency distribution of the counted particles lying below the lace. This transect-by-number sample needs to be converted to a volume-by-weight sample.

2.2.2.3.2 Conversion to volume-by-weight distribution of the subsurface

Fehr (1987) suggests that the conversion of a line sample to a volumetric sample is related by D_i^{-2} , which yields

$$\Delta p_i \propto \Delta q_i \times D_i^{-1}. \quad (\text{B29})$$

Herein, Δp_i and Δq_i are the proportions of the i th grain size fraction by weight and number and D_i is the mean grain size of the i th grain size fraction (diameter class). *Fehr* (1987) calibrated this approach by means of experimental tests in a hydraulic laboratory. However, *Fehr* (1987) focused on the subsurface grain size distribution of gravel and cobble-bed streams and he proposed a method to convert a transect-by-number sample of the bed surface to the corresponding volume-by-weight subsurface distribution. According to his approach, the transect-by-number frequency of the bed

surface grains coarser than 1 cm is first converted to the volume-by-weight frequency of the subsurface according

$$\Delta p_i = \frac{\Delta q_i \times D_i^\alpha}{\sum_{i=1}^n (\Delta q_i \times D_i^\alpha)}, \quad (B30)$$

with $\alpha=0.8$ and n the number of grain size fractions. The transect-by-number method does not include the very fine tail of the grain size distribution ($D < 1$ cm). In case that there are no separate measurements of the fine tail of the grain size distribution, *Fehr* (1987) suggests raising the fine tail by 25 % according

$$\Delta p_{i,c} = 0.25 + 0.75 \times \Delta p_i. \quad (B31)$$

In order to get a smooth transition of the fine tail towards the coarse tail of the grain size distribution, *Fehr* (1987) developed several methods for fitting additional samples or empiric distribution of the fine tail. These methods are not addressed in this study.

2.2.2.3.3 Conversion to volume-by-weight distribution of the bed surface

Rickenmann (2014) suggests a modification of the *Fehr's* (1987) approach by replacing equation B31 by

$$\Delta p_{i,c} = 0.11 + 0.89 \times \Delta p_i \quad (B32)$$

to obtain the grain size distribution of the bed surface. But this method does not account for the fact, that equation B30 already comprises the conversion from bed surface to subsurface conditions. In addition, a constant amount of sediment smaller than 1 cm, regardless of site characteristics, affects the accuracy negatively.

In this respect, *Rosport* (1997) extended the transect-by-number method by integrating fine sediment that is not measurable by means of picking and counting. Different from counting individual particles below the lace, *Rosport* (1997) measured the length that the lace traversed certain patches of fines. This procedure is easily applicable in the field since fine sediment is typically segregated into patches, rather than isolated particles. Thus, surveying fine sediment ($D < 1$ cm) at the patch-scale seems adequate to represent fine particle's abundance on the bed surface. The total count of fine sediment particles below the lace is simply defined by

$$N_1 = \frac{L_1}{D_1}. \quad (B33)$$

Herein N_1 and D_1 are the count and the mean diameter of the particles that are within the residual grain size fraction which is too small to measure individually ($0 \text{ cm} < D < 1 \text{ cm}$ in the field surveys) and L_1 is the total length that the lace traversed patches of fines. In addition, *Rosport* (1997) replaced the exponent in equation B30 ($\alpha=0.8$) with $\alpha=1.8$, which *Fehr* (1987) found to reproduce the volume-by-weight distribution in case that the bed surface was not armored (and thus, equals the subsurface).

To the author's knowledge, the applicability of both methods for assessing the volume-by-weight distribution of the bed surface grain size distribution has not been addressed so far. Because of that, three different modifications of *Fehr's* (1987) approach

(Table B-17) are tested against the reference method, the grid-by-number method or Wolman count, respectively.

Table B-17: Methods used to convert the transect-by-number sample into a volume-by-weight distribution of the bed surface

| Reference | Equations |
|-----------------------|------------------------------|
| <i>Fehr</i> (1987) | B30 ($\alpha=0.8$) and B31 |
| <i>Rosport</i> (1997) | B30 ($\alpha=1.8$) and B33 |
| NEW | B30 ($\alpha=0.8$) and B33 |

2.2.2.4 Field surveys

The field sites are located in two small mountain streams, the Oberbergbach and the Krapsesbach (see Table B-1 in section 1.1.2).

At the Oberbergbach, both methods were applied at two sample sites, each within an accumulation reach featuring a plane bed and a bed gradient of about 0.02 m/m. The stream bed predominantly consists of gravels, and cobbles and the main channel course is occasionally reshaped during moderate flood events.

The sample sites at the Krapsesbach are within a transport reach. The bed surface is stabilized and features a step-pool morphology. The channel course is assumed to be static since it did not change during the summer season of 2014.

At each sample site, Wolman counts were performed at the wetted bed surface by measuring at least 100 stones that were beneath the tip of the boot while walking through the water. Each stone was picked up and its intermediate axis was measured and classified into the corresponding diameter class.

The transect-by-number analysis was performed next to the water course at a location that revealed similar patterns as the wetted bed surface. The intermediate axis of each sediment particle that was below the lace and coarser than 1 cm was measured individually. In addition, the length of patches consisting of finer sediment was measured and summed up at the end of the survey. The volume-by-weight distributions of the transect-by-number samples were determined by either of the approaches given in Table B-17 and compared against the grain size distribution obtained by the Wolman count.

2.2.2.5 Laboratory tests

Flume experiments were conducted to investigate the bed surface coarsening due to sediment starving in a steep channel. Therefore, a 0.5 m wide and 7 m long, rectangular flume was built at the hydraulic laboratory of the University of Innsbruck (*Steidl*, 2015). The bed gradient was either 0.05 m/m or 0.1 m/m and the bed featured a step-pool morphology. At the end of several experimental runs, the bed surface grain size distribution was measured according to both methods, the transect-by-number, and the grid-by-number method.

The experimental setup and the measuring facilities of the laboratory contributed to a high measuring accuracy. For the grid-by-number sampling, the laser pointer was traversed along a regular grid and the bed surface particle that intersected with the grid point was categorized into the corresponding diameter class, respectively.

Regarding the transect-by-number method, a laser was used instead of a lace, enabling a more precise identification whether or not a particle is within the sampling transect (usually intersecting the lace). In contrast to the field application, even the particles smaller than 1 cm were assessed individually. In a consequence, equation B33 is zero and thus, the corresponding volume-by-weight distribution is defined by B30 solely for *Rosport's* (1997) and the new approach. It is worth to note, that the sediment grain size distribution was truncated at 0.5 mm and certain grain size fractions were colored differently. Both contributes to a high accuracy in determining the diameter class of the sampled particles.

2.2.3 Results

2.2.3.1 Field surveys

The grain size distribution obtained with the Wolman count (*Wolman*, 1957) was best reproduced by new approach (NEW in Table B-17) for converting a transect-by-number sample into a volume-by-weight distribution. In Figure B-39 the volume-by-weight grain size distributions are illustrated that were obtained by either of the approaches for the sample site 1 at the Oberbergbach. The approach of *Rosport* (1997) yields a grain size distribution that is obviously coarser than the reference method suggests. In contrast, both, the original approach of *Fehr* (1987) and the new approach (Table B-17), reveal minor differences against the grain size distribution obtained with the Wolman count (reference method). But the fine tail is overestimated by *Fehr's* (1987) approach.

However, the maximum grain size differs with respect to the sampling method used: it is 250 mm for the transect-by-number analysis, but 350 mm for the Wolman count. The difference is attributed to the spatial variability of the bed surface grain size distribution since the transect-by-number sample and the Wolman count were not performed at the same location.

In order to evaluate the performance of the conversion approaches, the characteristic grain sizes D_{30} , D_{50} , D_{84} , and D_{90} are computed from each converted transect-by-number grain size distribution and scaled by the characteristic grain sizes obtained with the Wolman count. According to Figure B-40, the new approach slightly overestimates the grain size of certain percentiles. In a consequence, the grain size distribution is coarser than the reference distribution. The opposite is true for the approach of *Fehr* (1987) which tends to overestimate the finer fractions and thus, yields smaller characteristic grain sizes as the Wolman count. The approach of *Rosport* (1997) yields the worst results since the ratios' means are far from unity.

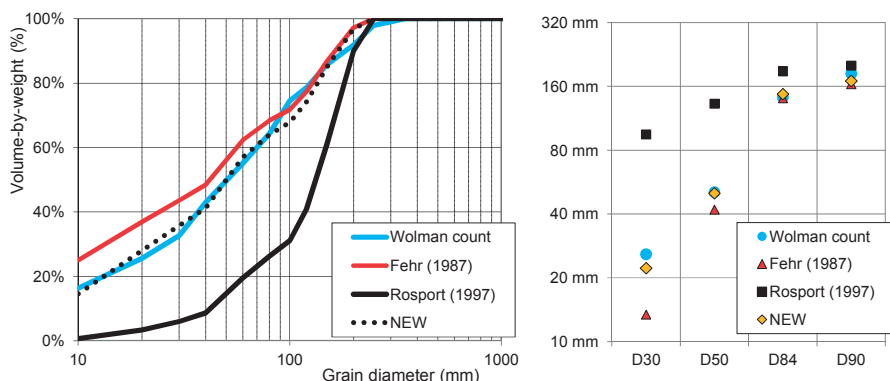


Figure B-39: Grain size distribution (left) and characteristic grain sizes (right) at the sample site 1 of the Oberbergbach

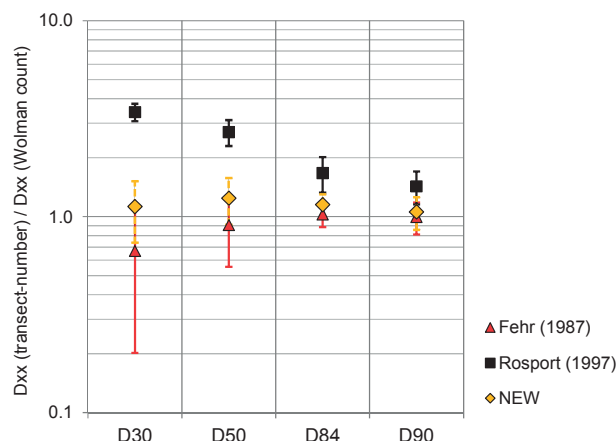


Figure B-40: Characteristic grain sizes of the converted transect-by-number grain size distributions divided by the reference size from the Wolman count: dots represent the mean of all four (2x2) field sites and the error bars represent the standard deviations.

2.2.3.2 Laboratory tests

In analogy with the field surveys, the new approach for converting a transect-by-number analysis into a volume-by-weight grain size distribution match the grain size distributions obtained with the grid-by-number technique best (Figure B-41).

Fehr's (1987) approach reveals a severe overestimation of the fine tail, which is solely attributed to the artificial increase of the fine tail by equation B31. Thus, the results suggest that there is no need of equation B31 when the sample includes the entire range of grain sizes.

The approach of *Rosport (1997)* yields a volume-by-weight grain size distribution that is far too coarse, which corresponds well with the results obtained by the field surveys.

In Figure B-42, the volume-by-weight grain size distributions obtained with any of the three conversion approaches are compared against the reference method (grid-by-number) by means of several characteristic grain sizes. Each dot in Figure B-42 refers to the mean of all five experimental tests and the error bar represents the standard deviation. Figure B-42 is in good agreement with the example given in Figure B-41: the fine tail is obviously overestimated when Fehr's (1987) approach is used, while it is by far underestimated with Rosport's (1997) approach. Since the maximum grain size is by definition identical for all volume-by-weight distributions obtained by the transect-by-number method, differences decrease with increasing grain size.

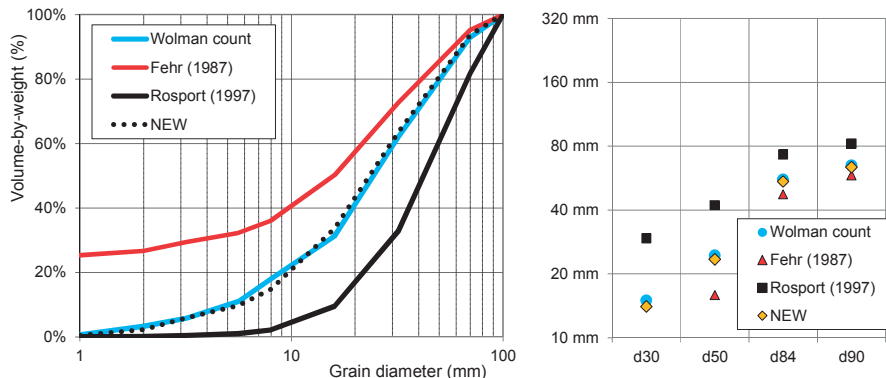


Figure B-41: Grain size distribution (left) and characteristic grain sizes (right) in the flume ($S=0.1 \text{ m/m}$) that was exposed to 15 l/s while sediment starving

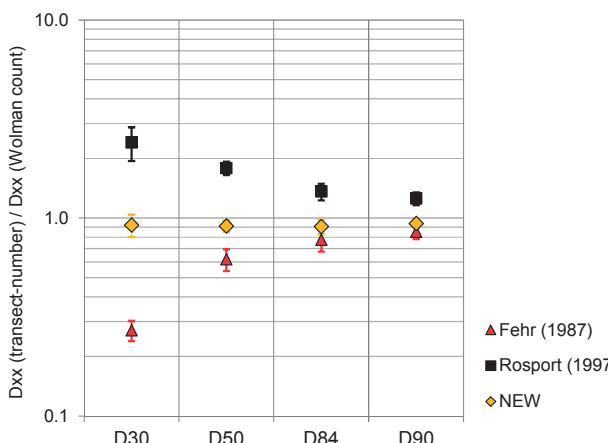


Figure B-42: Characteristic grain sizes of the converted transect-by-number grain size distributions divided by the reference size of the Wolman count: dots represent the mean of all flume samples and the error bars represent the standard deviations.

In contrast to the field experiments, the scatter is much smaller and thus, the results are more robust. This is attributed to the higher measuring accuracy in the laboratory and the fact, that both techniques were applied on the (formerly) wetted bed surface.

2.2.4 Conclusion

The transect-by-number technique sufficiently corresponds with the grid-by-number method, when it is converted into a volume-by-weight distribution according to equation B30 (with $\alpha=0.8$) and B33. This finding is supported by both, the field surveys and the laboratory tests. Consequently, the transect-by-number technique is applicable for assessing the bed surface grain size distribution in steep mountain streams.

2.2.5 References of chapter B.2.2 *Verification of the transect-by-number method for assessing the bed surface grain size distribution*

- Bunte, K., and S. R. Abt (2001a), Sampling surface and subsurface particle-size distributions in wadable gravel- and cobble-bed streams for analyses in sediment transport, hydraulics, and streambed monitoring. *Gen. Techn. Rep. RMRS-GTR-74*, 428 pp, U.S. Department of Agriculture, Forest Service, Fort Collins, CO.
- Bunte, K., S. R. Abt, J. P. Potyondy and K. W. Swingle (2009), Comparison of three pebble count protocols (EMAP, PIBO, and SFT) in two mountain streams, *J. Am. Water Resour. Assoc.*, 45, 5, 1210-1227.
- Bunte, K., S. R. Abt, K. W., Swingle, D. A. Cenderelli, and J. M. Schneider (2013), Critical Shields values in coarse-bedded steep streams, *Water Resour. Res.*, 49, 7427-7447, doi: 10.1002/2012WR012672.
- Chiari, M., and D. Rickenmann (2010), Back-calculation of bedload transport in steep channels with a numerical model, *Earth Surf. Proc. Land.*, 36, 805-815, doi: 10.1002/esp.2108.
- Church, M., D.G. McLean and J.F. Walcott (1987), River bed gravels: sampling and analysis, In: *Sediment Transport in Gravel-Bed Rivers*, C.R. Thorne, J.C. Bathurst and R.D. Hey (eds.), John Wiley and Sons, Chichester, UK, p. 43 – 88.
- Fehr, R. (1987), Geschiebeanalysen in Gebirgsflüssen - Umrechnung und Vergleich von verschiedenen Analyseverfahren [Bed material analyses in mountain streams - Transformation and comparison of various analyses procedures], *Mitteilungen der Versuchsanstalt für Wasserbau, Hydrologie und Glaziologie an der ETH Zürich*, No. 92, 139 pp., ETH Zurich, Switzerland.
- King, J.G., W. W. Emmett, P. J. Whiting, R. P. Kenworthy, and J. J. Barry (2004), Sediment Transport Data and related Information for selected coarse-bed streams and rivers in Idaho, *Gen. Tech. Rep. RMRS-GTR-131*, U.S. Dep. of Agric., For. Serv., Rocky Mt. Res. Stn, Fort Collins, Colo.
- Rickenmann, D. (2014), Methoden zur quantitativen Beurteilung von Gerinnoprozessen in Wildbächen, *WSL Berichte*, Heft 9, ISSN 2296-3456
- Rosport M. (1997), Fließwiderstand und Sohlstabilität steiler Fließgewässer unter Berücksichtigung gebirgsbachtypischer Sohlstrukturen, *Mitteilungen des Instituts für Wasserwirtschaft und Kulturtechnik, Heft 196*, Univ. Karlsruhe, Germany.
- Schneider, J. M., D. Rickenmann, J. M. Turowski, and J. W. Kirchner (2015), Self-adjustment of stream bed roughness and flow velocity in a steep mountain channel, *Wat. Resour. Res.*, 51, 7838-7859, doi: 10.1002/2015WR016934.
- Steidl, B. (2015), Deckschichtentwicklung und Auswirkung externer Geschiebezugabe auf die Sohlmorphologie und die Fließgeschwindigkeit bei Wildbächen, Master thesis at the University of Innsbruck. Innsbruck, Austria. (In German).
- Wohl, E. E., D. J. Anthony, S. W. Madson, and D. M. Thompson (1996), A comparison of surface sampling methods for coarse fluvial sediments, *Wat. Resour. Res.*, 32, 10, 3219-3226.
- Wolman, M.G. (1954), A method of sampling coarse bed material. *American Geophysical Union, Transactions*, 35, 951-956.

B.3 Study A³: Variability of annual bed load volumes in small, high-altitude mountain streams

B.3.1 Introduction

Small mountain streams represent the upper part of the fluvial network. Bed load fluxes originating from these headwater or tributary streams are an important sediment source for their receiving gravel bed streams and hence, they influence the sediment budget of the entire alpine river network (e.g. *Hinderer et al.*, 2013). There are several studies dealing with the annual bed load yield of mountain streams (a large compilation is given in *Hinderer et al.*, 2013) and most of them reveal a large variability over space (between different streams) and time (between different years). However, rather little is known about the reasons for this huge spatiotemporal variability of bed load yield (e.g. *Recking*, 2012; *Rickenmann*, 2001).

In general, bed load transport in a river reach results from the flow competence for mobilizing bed sediment. It depends on hydrologic (water discharge), topographic (channel gradient, flow width) and morphologic conditions (flow roughness, grain size distribution of the bed sediment). In steep streams, the morphologic structures (*Montgomery and Buffington*, 1997; *Schälchli*, 1995) are an additional key factor regarding the mobilization (*Bathurst*, 2013; *Lamb et al.*, 2008) and transportation of bed sediment (*Schneider et al.*, 2015a; *Ghilardi et al.*, 2014; *Nitsche et al.*, 2011). These bed structures act as macro-roughness elements on the flow patterns (*Rickenmann and Recking*, 2011; *Schneider et al.*, 2015b) and cause additional momentum losses due to spill and form drag (*Ghilardi et al.*, 2014; *Yager et al.*, 2007). Consequently, only a fraction of total flow energy remains available for bed load transport (*Schneider et al.*, 2015a; *Nitsche et al.*, 2011; *Rickenmann and Recking*, 2011).

Furthermore, bed load transport in steep, wide-graded mountain streams is partly size-selective, favouring small grains to be mobilised at moderate flows (*Bunte et al.*, 2013; *Bathurst*, 2013). While large boulders and their jammed state remain immobile even during ordinary flood events (*Church and Zimmermann*, 2007; *Turowski et al.*, 2009), fine material is mobilized from pools, temporary deposits or external sediment supply (*Palt*, 2001; *Jackson and Beschta*, 1982). As a consequence, the availability of mobile sediment is one major limiting factor for the actual bed load transport efficiency (*Recking*, 2012; *Rickenmann*, 2001; *Gintz et al.*, 1996). Hence, measured transport rates are often lower than the rates predicted by means of flow competence; even if momentum losses due to macro-roughness are accounted for (*Schneider*, 2015).

In this respect, *Rickenmann* (1997) analyzed a large field data set of bed load volumes of several bed load transport events in Swiss torrents. Therein, the scaling of bed load volume and cumulative excess discharge (water volume beyond incipient motion) evinced highly variable, suggesting that the transport efficiency is strongly influenced by additional factors not accounted for. Indeed, transport efficiency correlated with bed slope and relative flow depth at the order of magnitude scale; both of these parameters represent a substitute for macro-roughness. But the variability remained high and as

³ A condensed version of this Study A is published in German language in the *Österreichische Wasser- und Abfallwirtschaft* (doi: 10.1007/s00506-017-0378-z). The co-authors are Stefan Achleitner, Johannes Schöber, and Bernhard Hofer.

suggested by *Rickenmann* (2001), the transport efficiency was probably affected by sediment supply conditions as well.

In this study, the term ‘transport efficiency’ refers to the coefficient in bed load transport formulae. Assuming a threshold bed load transport formula (e.g. *Schoklitsch*, 1962; *Meyer-Peter and Müller*, 1948; *Bagnold*, 1980; *Rickenmann*, 1990), the transport efficiency is defined by the coefficient k :

$$Q_b = k \times (X - X_c)^\alpha, \quad (\text{B34})$$

with bed load transport rate Q_b , an arbitrary parameter of flow strength X and incipient motion X_c . The same is valid for reference-based bed load transport equations (e.g. *Wilcock and Crowe*, 2003; *Recking*, 2013):

$$Q_b^* = k \times \left(\frac{X}{X_c} \right)^\alpha, \quad (\text{B35})$$

where Q_b^* is the non-dimensional bed load transport rate (e.g. W or ϕ in *Parker and Klingeman*, 1982).

Independent of the equation’s type, the pre-factor k represents the position of the relation transport intensity (Q_b or Q_b^*) and flow competence ($(X-X_c)^\alpha$ or $(X/X_c)^\alpha$) at the log-scale. Thus, any changes of k cause a parallel shift of the bed load rating curve on the y-axis at the log-scale, which enables a calibration of the function by means of fitting k to measured data (Figure B-43). In contrast, *Recking* (2012) proposed a bed load transport equation which accounts for site-specific sediment supply conditions by adjusting the reference shear stress. The difference of both approaches is illustrated in Figure B-43.

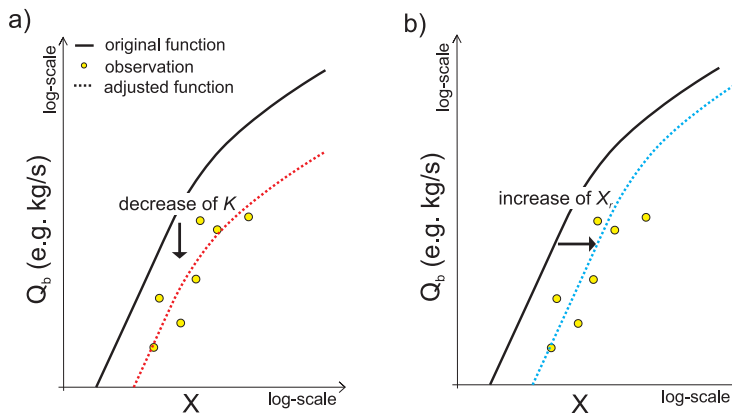


Figure B-43: Illustration of two possibilities to fit a bed load transport equation to measured data: adjusting the pre-factor k (left) or the reference parameter (right)

A between-site variation of this coefficient k is assumed to depend on both, topographic/morphologic boundary conditions (e.g. channel gradient, grain size distribution, etc.) and sediment supply. In contrast, a within-site variation of transport efficiency is attributed to supply conditions only. Since sediment availability increases after severe flood events (Yager *et al.*, 2012; Turowski *et al.*, 2009; Lenzi *et al.*, 2004; Hoffman and Gabet, 2007; Gintz *et al.*, 1996), the annual transport efficiency is expected to fluctuate in supply limited streams according to the flood history. It is further hypothesized that streams with high sediment supply reveal more consistent transport efficiencies than strongly supply limited sites.

In the present study, the large field data set of annual bed load volumes (ABV) of twenty mountain streams (section B.1.1) is analyzed regarding their between-site and temporal variability. The analysis is split into two main parts focussing on (i) the statistics of annual bed load volumes and its scaling with topographic and hydrologic parameters and (ii) the scaling of the transport efficiency between different sites and over time. In a consequence, the analysis follows a top-down order, starting with (i) a strictly empiric investigation on the catchment scale, which is followed by (ii) a more process-oriented approach that separates the influence of flow competence and sediment supply on bed load transport by means of transport efficiency.

B.3.2 Methods

3.2.1 Statistics of annual bed load volumes

The annual bed load volumes are summarized by several numerical descriptors including the arithmetic mean, the geometric mean, their standard deviations and certain percentiles of the empiric population for each study site separately. Ordinary and generalized linear models are applied to predict certain numerical descriptors by means of topographic parameters. Therefore, correlation analyses are performed to evaluate which potential explanatory variables (Table B-1 and Table B-2 in section 1.1.2) to use in a first step.

Since the data of annual bed load volumes span an observation period of up to 49 years (with a minimum of 17 years for the Horlachbach, see Table B-5 in section 1.1.4), the distribution of annual bed load volumes is analyzed for each study site separately. Parametric probability distributions suitable for positively skewed empiric populations are fitted and their performance is evaluated by multiple goodness-of-fit criteria. Therefore, the annual bed load volumes of each study site were standardized by the site-specific arithmetic mean beforehand:

$$X_{i,s} = \frac{ABV_{i,s}}{\frac{1}{n} \times \sum_{i=1}^n ABV_{i,s}}, \quad (B36)$$

where i refers to the year and s is the study site. Probability distributions considered in this study are the log-normal distribution, the gamma distribution, the Weibull distribution and the inverse gamma distribution. Parameter estimation was accomplished according to the maximum likelihood theory and the quantile matching estimation, using the package ‘fistdistrplus’ (Delignette-Muller *et al.*, 2014) in R (R Core Team, 2013). It is worth to explicitly note that empiric densities of annual bed load volumes refer to

hydrologically ordinary years only and do not accurately include bed load volumes of exceptional extreme events (see section B.1.1).

3.2.2 Transport efficiency

3.2.2.1 Objective

Since all study sites are situated quite close to each other, they feature similar boundary conditions regarding climate, land use and geology. Contrary, mean annual bed load volumes differ obviously, even when data are standardized by the catchment area. The remaining variance is hypothesized to be predominantly attributable to differences in annual stream flow, while a second-order dependency with bed load supply conditions, channel gradient or other site-related characteristics are possible.

In order to extract the influence of water discharge on bed load volumes, a bed load transport equation suitable for steep streams is used to calculate the cumulative annual flow competence and to determine an empiric coefficient which accounts for the bed load transport efficiency.

3.2.2.2 Bed load transport equation

Recently, Schneider et al. (2015a) fitted a Wilcock and Crowe's (2003) type bed load transport equation to a large field data set on bed load transport rates of gravel and boulder bed streams, comprising a wide range of stream gradients. In order to predict total bed load transport by means of total boundary shear stress (not explicitly accounting for momentum losses due to form drag), Schneider et al. (2015a) found a mean exponent of $\alpha=16.1$ to be most suitable for low to moderate flow intensities $\tau_{D50}^* / \tau_{rD50}^* < 1.2$:

$$W_{tot}^* = \begin{cases} 0.002 \times (\tau_{D50}^* / \tau_{rD50}^*)^{16.1} & \text{for } \tau_{D50}^* / \tau_{rD50}^* < 1.2 \\ 14 \times \left(1 - \frac{0.85}{(\tau_{D50}^* / \tau_{rD50}^*)^{0.7}}\right)^{4.5} & \text{for } \tau_{D50}^* / \tau_{rD50}^* > 1.2 \end{cases} \quad (B37)$$

Herein W_{tot}^* refers to the dimensionless bed load transport intensity (Parker and Klingeman, 1982), while τ_{D50}^* denotes the Shields stress and τ_{rD50}^* the reference Shields stress with respect to the D_{50} . The latter is defined as a function of channel gradient (Schneider et al., 2015a):

$$\tau_{r,D50}^* = 0.56 \times S^{0.5} \quad (B38)$$

This kind of Schneider et al.'s (2015a) equation properly fits the data obtained by the field measurements (Figure B-44a; section B.1.5), which are limited to low to moderate bed load transport intensities $\tau_{D50}^* / \tau_{rD50}^* < 1.2$.

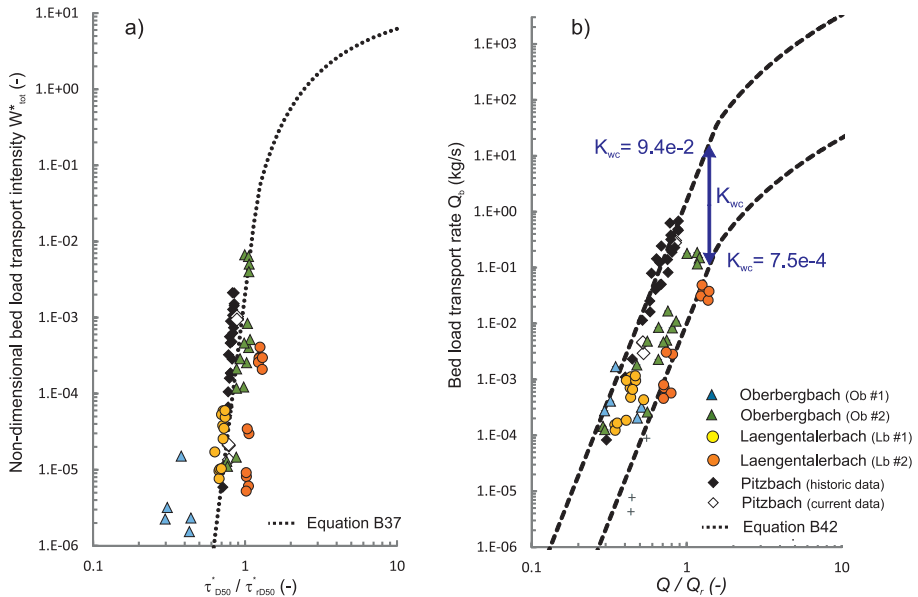


Figure B-44: a) Bed load transport rates plotted in terms of non-dimensional bed load transport intensity and relative shear stress (acc. Schneider et al., 2015a) with the rating curve according to equation B37 and b) bed load transport rate plotted against relative discharge with equation B42 fitted by eye to both, the Pitzbach (historic data) and the Laengentalerbach (Lb #2) data. The data are given in Table B-13 in section B.1.5.

At high flows ($\tau^*_{D50} / \tau^*_{rD50} > 1.2$), equation B37 approximates towards a constant value of 14 and specific bed load transport rate increases with shear stress to the power of 1.5. This agrees with common bed load transport formulas (Meyer-Peter and Müller, 1948; Rickenmann, 1990) which are derived via flume experiments facing no supply limitation.

The application of equation B37 to a certain field sites requires knowledge of the hydraulic geometry relation (to convert discharge to shear stress) and the grain size distribution of the bed sediment. Both are not available for many field sites of this study. To cope with that, the shear stress based equation B37 is converted to a discharge-based approach. Equation B37 is substituted by an adjusted power law equation of Ferguson (2007), which assumes a linear dependency of flow resistance and relative flow depth (d/D_{84}), and rearranged to the volumetric bed load transport rate (Figure B-44b). The derivation and all assumptions made are explicitly given in the Appendix of this study (section B.3.7). It yields to the final expression:

$$Q_b = \begin{cases} 0.002 \times \left(\frac{g^{0.2} S^{1.2} D_{84}^{0.6} w^{0.4}}{1.8^{0.6} (s-1)} \right) \times \left(\frac{Q}{Q_{r,D50}} \right)^{6.44} \times Q^{0.6} & \text{for } Q/Q_{r,D50} \leq 1.58 \\ 14 \times \left(\frac{g^{0.2} S^{1.2} D_{84}^{0.6} w^{0.4}}{1.8^{0.6} (s-1)} \right) \times \left(1 - \frac{0.831}{(Q/Q_{r,D50})^{0.28}} \right)^{4.5} \times Q^{0.6} & \text{for } Q/Q_{r,D50} > 1.58 \end{cases} \quad (\text{B39})$$

with the volumetric bed load transport rate Q_b ($m^3 s^{-1}$), the water discharge Q (m^3/s), the reference water discharge $Q_{r,D50}$ (m^3/s) of the D_{50} , the gravitational acceleration g (m/s^2), the channel gradient S (-), the diameter of which 84 % are finer by weight D_{84} (m), channel width w (m) and specific sediment weight s (-). Equation B39 marginally deviates from the original form according to Schneider *et al.* (2015a), as the originally reported factor 0.85 (equation B37) is corrected to 0.831 (equation B39).

In the following, the pre-factor of equation B39 is defined as the transport efficiency K , which summarizes geometric and morphologic parameters:

$$K(m^{1.2} s^{-0.4}) = \frac{g^{0.2} S^{1.2} D_{84}^{0.6} w^{0.4}}{1.8 \times (s-1)} \quad (\text{B40})$$

The parameters S , D_{84} , and w are highly variable in a single mountain stream, with S and D_{84} varying over almost one order of magnitude between reaches. In contrast, the bed load transport rate at low to moderate flows (phase 1 transport; see chapter A *Introduction*) is assumed to be relatively similar throughout the water course of the main channel that encloses upstream of the water intake structure. This is partly supported by the field data (section B.1.5), where bed load transport rates were measured in different reaches (Figure B-45). Although the scatter is large and the measurements were not done simultaneously, the overall trend of the data at the Oberbergbach seems unaffected by the channel gradient of the measuring location. In contrast, there remains a difference in the Laengentalbach data, although the Lb #1 is close to Lb #2 and the measuring locations are less than 50 m apart. These differences are attributed to a flood event in the late summer which was accompanied with a break-up of the bed surface. Thus, the differences are not associated with a different Q - Q_b relation of both sites, both with a change of the availability of mobile bed load.

Considering an equal Q - Q_b relation in two enclosing stream reaches (at low to moderate discharges), the differences of reach characteristics (mainly of bed slope and channel roughness) has to be compensated by the reference discharge in equation B39. Since $Q/Q_{r,D50}$ raises to a power of 6.44, the reference discharge faces a high sensitivity and any uncertainties cause big differences in bed load transport rate.

The reference discharge in equation B39 is therefore interpreted as a parameter representative at the multiple reach scale, rather than the reference criteria of the D_{50} within a certain reach. A representative parameter is the 1.5-years flow ($Q_{1.5a}$) (Mueller *et al.*, 2005), which is often used as a surrogate for bank full discharge (Bunte *et al.*, 2013; Emmett and Wolman, 2001). Ryan *et al.* (2002) found the break point between phase 1 (marginal bed load transport of fines) and phase 2 (transport of coarse bed material; partial to full mobility) at about 80 % of the 1.5-years flow.

Assuming the transition of $Q/Q_{r,D50} < 1.58$ (associated with marginal bed load transport; phase 1 transport conditions) to $Q/Q_{r,D50} > 1.58$ (associated with partial to

full mobility; phase 2 transport conditions) at 80 % of the 1.5-years flow, the reference discharge is defined by

$$Q_r = 0.5 \times Q_{1.5a} \quad (\text{B41})$$

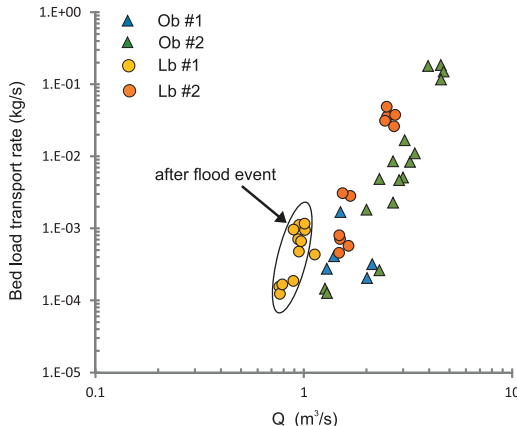


Figure B-45: Bed load transport rate plotted against water discharge. Dots refer to the Laengentalerbach, where Lb #1 (a short low-gradient reach with $S=0.04 \text{ m/m}$) was about 50 m downstream of Lb #2 ($S=0.069 \text{ m/m}$); triangles represent the data of the Oberbergbach, where Ob #1 ($S=0.076 \text{ m/m}$) is immediately upstream of the water intake structure and Ob #2 ($S=0.02 \text{ m/m}$) is a long, low-gradient reach approx. 800 m upstream of Ob #1. The data are given in Table B-13 in section B.1.5.

Consequently, equation B39 can be simplified to:

$$Q_b = \begin{cases} 0.002 \times K \times \left(\frac{Q}{0.5Q_{1.5a}} \right)^{6.44} \times Q^{0.6} & \text{for } \frac{Q}{0.5Q_{1.5a}} \leq 1.58 \quad (\text{a}) \\ 14 \times K \times \left(1 - \frac{0.831}{\left(\frac{Q}{0.5Q_{1.5a}} \right)^{0.28}} \right)^{4.5} \times Q^{0.6} & \text{for } \frac{Q}{0.5Q_{1.5a}} > 1.58 \quad (\text{b}) \end{cases} \quad (\text{B42})$$

3.2.2.3 Cumulative flow competence and annual transport efficiency

The bed load transport data presented in this study are cumulative on an annual basis and hence, they do not enable for a relation of transport rate against flow competence. Because of that, the presented approach (equation B42) is applied to cumulative rather than single bed load transport rates by integrating equation B42 over the duration of one year:

$$ABV = K \times \sum \begin{cases} 0.002 \times \left(\frac{Q}{0.5Q_{1.5a}} \right)^{6.44} \times Q^{0.6} \times dt & \text{for } \frac{Q}{0.5Q_{1.5a}} \leq 1.58 \\ 14 \times \left(1 - \frac{0.831}{\left(\frac{Q}{0.5Q_{1.5a}} \right)^{0.28}} \right)^{4.5} \times Q^{0.6} \times dt & \text{for } \frac{Q}{0.5Q_{1.5a}} > 1.58 \end{cases} \quad (B43)$$

where ABV (m^3) is the annual bed load volume and dt is the temporal resolution of the discharge hydrograph in seconds (900 sec), respectively. Rearranging equation B43 in terms of K finally enables the calculation of the annual transport efficiency:

$$K(m^{1.2}s^{-0.4}) = \frac{ABV}{\sum f(Q/Q_r)} \quad (B44)$$

As shown in equation B40, K , in its original form, is a function of geometric and morphologic parameters, which might be not constant over time. Since macro-scale changes in channel form and grain size distribution in steep mountain streams are typically limited to exceptional extreme events (Church and Zimmermann, 2007), these parameters are assumed temporally constant. Equation B44 is applied to all years and field sites where both, annual bed load volume and water discharge are available (Table B-1 in section 1.1.2). Results are then analyzed with respect to their temporal (within-site) and between-site variability by correlating numerical descriptors to topographic parameters of the study sites.

B.3.3 Results

3.3.1 Mean annual bed load volumes

The arithmetic mean of annual bed load volumes (solid volume; $mABV$) ranges between 17 m^3 (Schelfalmbach) and 2791 m^3 (Pitzbach; Table B-18). The normalization by catchment size ($\text{spec.}mABV$) yields a range of 3.0 m^3/km^2 (Fissladbach) to 278.5 m^3/km^2 (Unterer Liesenerbach), respectively.

The analysis of variance (stats package in the R software (R Core Team, 2013)) and partial correlation (ppcor package in the R software (Kim, 2011)) show a highly significant correlation of mean annual bed load volume with catchment size A and relative glacier area G (Figure B-46), with the null hypothesis of independence being rejected on a < 0.001 level. The relationship between $mABV$ and A is almost linear and thus, the specific mean annual bed load volume ($\text{spec.}mABV$) is independent of the catchment size (Figure B-46a). In contrast, the influence of G on $mABV$ is exponential (Figure B-46b).

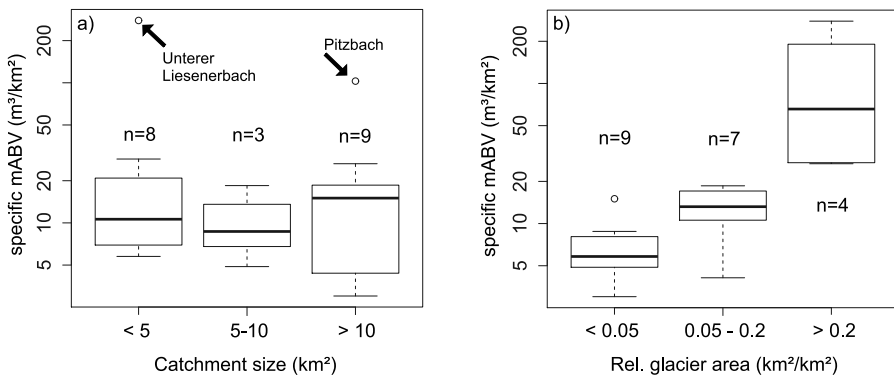


Figure B-46: Box and whiskers plot of the specific mean annual bed load volume ($\text{spec.mABV} = \text{mABV} / \text{CS}$). The data are separated according a) the catchment size and b) the relative glacier area, with n the number of data each class are. The unit of spec.mABV is m^3/km^2 with m^3 referring to solid density without pores.

The parameters describing the topography of the catchments, such as the mean catchment slope (mean CS in Table B-2 in section 1.1.2), the mean drainage slope (mean DS in Table B-2 in section 1.1.2), the drainage density (Strahler, 1957), the Melton ratio (Melton, 1957) and the relief ratio (Schumm, 1954) or characteristics of the main channel upstream of the water intake structures (mean RG, sd RG, mean SG, sd SG, 10thperc SG in Table B-2 in section 1.1.2) do not reveal significant correlations with the response variable at all. This is even the case if ABV is standardized by the catchment size beforehand.

Multiple regression analyses were performed by applying linear models and generalized linear models of the stats package as implemented in R (R Core Team, 2013). The best result was obtained with a simple linear regression model with log transformation of the response variable $mABV$ and the explanatory variable A :

$$\log(mABV) = a_1 + a_2 \log(A) + a_3 G \quad (\text{B45})$$

The best fit estimates and the standard error of the regression coefficients are $a_1 = 1.89 \pm 0.37$, $a_2 = 0.986 \pm 0.162$ and $a_3 = 5.65 \pm 0.79$. The final multiple regression equation is

$$mABV = 6.63 \times A^{0.986} \times \exp(5.65 \times G), \quad r^2 = 0.84 \quad (\text{B46})$$

with the $mABV$ in m^3 referring to the solid volume without pores, catchment size A in km^2 and relative glacier area G in km^2/km^2 . To obtain $mABV$ in terms of the deposit volume, the result of equation B46 needs to be divided by $(1-e)=0.7$ (Table B-5 in section 1.1.4). A conversion into the unit of mass (kg) requires a multiplication with the solid density of 2650 kg/m^3 .

The performance of the equation B46 is illustrated in Figure B-47, with most of the calculated annual bed load volumes plotting in the range $[0.5 < mABV_{\text{calculated}} / mABV_{\text{observed}} < 2]$.

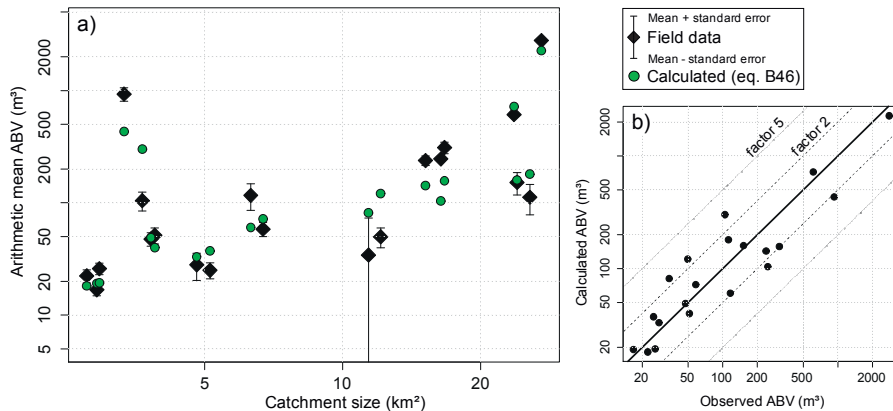


Figure B-47: Comparison between calculated and observed mean annual bed load volumes (ABV)

It is worth to note, that the relative glacier area G used in the regression analysis is based on the survey of 2006 (Fischer et al., 2015). Indeed, this parameter changed in course of the observation period which spans from 1965 to 2013 (Table B-1). According to the glacier surveys in the years 1969 and 1998, the relative glacier area was on average $0.03 \text{ km}^2/\text{km}^2$ or $0.01 \text{ km}^2/\text{km}^2$ larger than in 2006. However, using the relative glacier of the surveys 1969 or 1998 in the regression analysis (equation B45) has little impact on the fitted coefficients. They are still within the range given above.

3.3.2 Frequency distribution of annual bed load volumes

As known from the previous study of Schöberl (1983), the distribution of annual bed load volumes is positively $a \pm s_e$ skewed (Figure B-48), standard deviations are predominately large and approximately of the same order than the mean values (Table B-18).

Amongst other goodness of fit statistics, the Akaike and Bayesian information criterion reveal that the log-normal distribution is most suitable for describing the sampling distribution of 12 out of 20 sites. At the remaining study sites, the empiric distributions of annual bed load volumes are better reproduced by the inverse gamma distribution (at four sites), the gamma and the Weibull distribution (each at two sites).

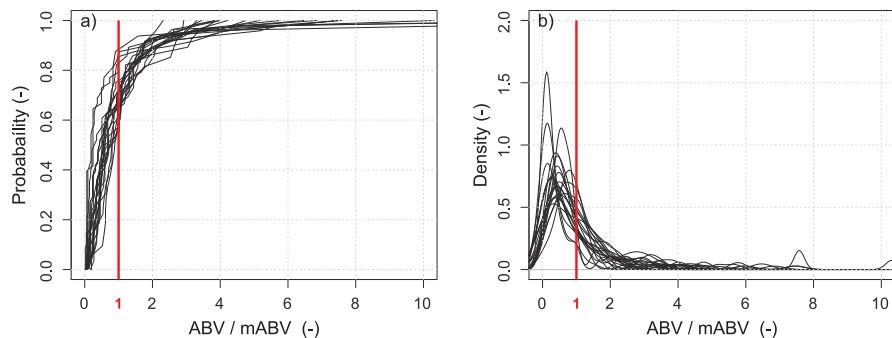


Figure B-48: a) Probability distribution and b) kernel density estimation (smoothed histogram) of ABV of all 20 sites

Table B-18: List of main characteristics of the empiric population of annual bed load volumes of each site; the variables refer to the solid volume. To obtain the deposit volume (m^3) requires, the values need to be divided by 0.7 and to obtain the mass requires a multiplication with 2650 kg/m^3 , respectively.

| Site | Years | Arithmetic Mean [m^3] | Standard Deviation [m^3] | Geometric Mean [m^3] | Median [m^3] | 25 th Percentile [m^3] | 75 th Percentile [m^3] | Skewness [-] |
|---------------------|-------|----------------------------------|-------------------------------------|---------------------------------|-------------------------|--|--|--------------|
| Schoentalbach | 27 | 22 | 16 | 16 | 18 | 9 | 32 | 1.3 |
| Schelfalmbach | 29 | 17 | 14 | 12 | 10 | 6 | 22 | 1.8 |
| Klammbach | 29 | 26 | 23 | 18 | 18 | 12 | 28 | 2.0 |
| UntererLiesenerBach | 29 | 930 | 958 | 537 | 538 | 296 | 1349 | 1.6 |
| ObererLiesenerBach | 29 | 104 | 122 | 68 | 54 | 44 | 119 | 2.8 |
| Madatschbach | 49 | 48 | 52 | 26 | 37 | 9 | 64 | 2.3 |
| Gsallbach | 49 | 51 | 76 | 23 | 22 | 8 | 57 | 2.9 |
| Rostizbach | 49 | 28 | 80 | 6 | 5 | 3 | 16 | 4.7 |
| Mittertalbach | 29 | 25 | 26 | 17 | 17 | 9 | 26 | 2.5 |
| Kraspesbach | 29 | 116 | 216 | 59 | 64 | 38 | 101 | 4.6 |
| Wazebach | 49 | 58 | 70 | 34 | 39 | 20 | 76 | 3.1 |
| Fissladbach | 49 | 34 | 84 | 9 | 8 | 2 | 25 | 4.8 |
| Verpelibach | 29 | 50 | 69 | 24 | 25 | 13 | 57 | 2.6 |
| Laengentalerbach | 28 | 238 | 232 | 140 | 141 | 67 | 340 | 1.2 |
| Tscheybach | 49 | 246 | 208 | 176 | 189 | 100 | 296 | 1.6 |
| Gleirschbach | 28 | 310 | 236 | 225 | 251 | 170 | 353 | 1.7 |
| Oberbergbach | 22 | 662 | 377 | 540 | 587 | 409 | 862 | 0.6 |
| Radurschlbach | 49 | 152 | 357 | 47 | 43 | 16 | 139 | 5.6 |
| Horlachbach | 17 | 112 | 188 | 60 | 61 | 48 | 93 | 3.8 |
| Pitzbach | 49 | 2791 | 2345 | 1986 | 2024 | 1102 | 3621 | 1.6 |

In order to assess the goodness of fit in a more practical way, certain percentiles of the fitted distributions were standardized by the corresponding percentiles of the empiric (measured) distribution. These ratios are illustrated as boxplots in Figure B-49. The fitted log-normal distributions reproduce the predefined percentiles of the empiric distributions within a factor of 1.5 for all except six cases. Though, the boxplot of the log-normal distributions reveal a systematic negative bias for the lowest percentile (5 %). In contrast, it tends to overestimate the occurrence of large annual bed load volumes.

However, the scatter and the bias are obviously larger for the gamma and the inverse gamma distribution (Figure B-49).

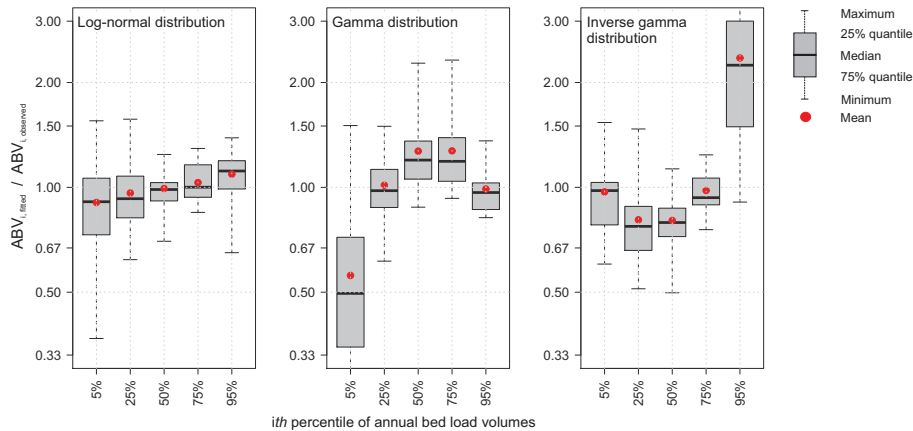


Figure B-49: Certain percentiles generated from the fitted probability distributions and divided by the same percentiles of the empiric distribution (measured data).

The log-normal distribution is a continuous probability distribution of a random variable x with the two parameters μ and σ . Assuming the annual bed load volume at a given site (ABV) to be a random variable which is log-normal distributed, the density function of ABV is defined by

$$f(x) = \frac{1}{x\sigma\sqrt{2\pi}} \exp\left[-\frac{(\ln(x)-\mu)^2}{2\sigma^2}\right] \quad \text{for } x > 0 \quad (\text{B47})$$

According to the maximum likelihood theory, the estimates of μ and σ match per definition with the logarithm of the geometric mean of the empiric population and its standard deviation. Hence, an estimation of these two parameters by means of suitable regression functions enables to calculate the probability distribution of annual bed load volumes.

In this respect, the geometric mean of annual bed load volumes proved to correlate with catchment size and relative glacier area (Figure B-50a) and the regression analysis yields

$$\hat{\mu} = 1.27 + 0.96 \ln(A) + 6.22G \quad r^2 = 0.76, \quad (\text{B48})$$

with the catchment size A in km^2 and the relative glacier area G in km^2/km^2 .

The standard deviation of log-transformed annual bed load volumes features a significant correlation with mean catchment slope (Figure B-50b), but the regression analysis reveals a poor performance. However, excluding three outliers improves the quality of the linear regression and yields

$$\hat{\sigma} = -0.046 + 0.031 \text{meanCS} \quad r^2 = 0.54, \quad (\text{B49})$$

with the mean catchment slope *meanCS* given in degree ($^{\circ}$).

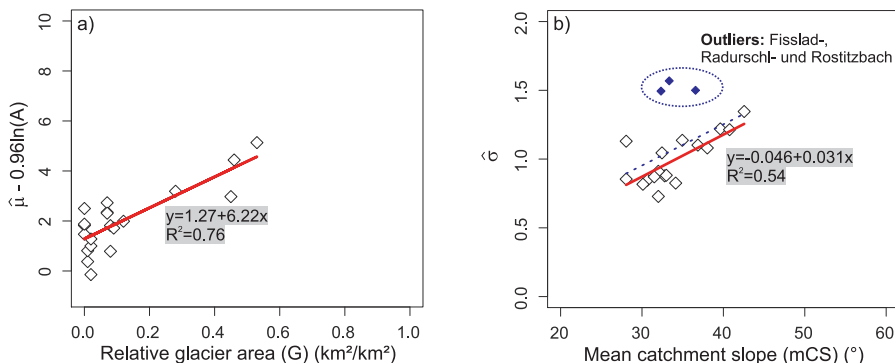


Figure B-50: Correlation and regression analysis of the parameter estimates μ (a) and σ (b) of the log-normal probability distribution with topographic parameters of the field sites.

The equations B47 and B48 enable for an estimate of the parameters of a log-normal distribution in order to estimate the frequency distribution of ABV by means of topographic quantities.

However, using this estimated probability function to determine certain percentiles of the distribution of annual bed load volumes results in severe differences with the observed percentiles. The discrepancy ratio of the estimated and observed percentiles is illustrated in Figure B-51b and it reveals a larger scatter compared with the fitted log-normal distribution. However, for more than 50 % of all field sites, the discrepancy ratio is less than a factor of two (Figure B-51b).

The equations B48 and B49 are particularly useful for similar field sites without long-term measurements of annual bed load volumes. In this respect it has to be mentioned that all study sites are small catchments within the Eastern Central Alps of Tyrol (Austria) and they feature similar boundary conditions regarding the geology (Gneiss, Phyllite and Schist). Consequently, the applicability of the proposed equations B48 and B49 are restricted to sites with similar boundary conditions.

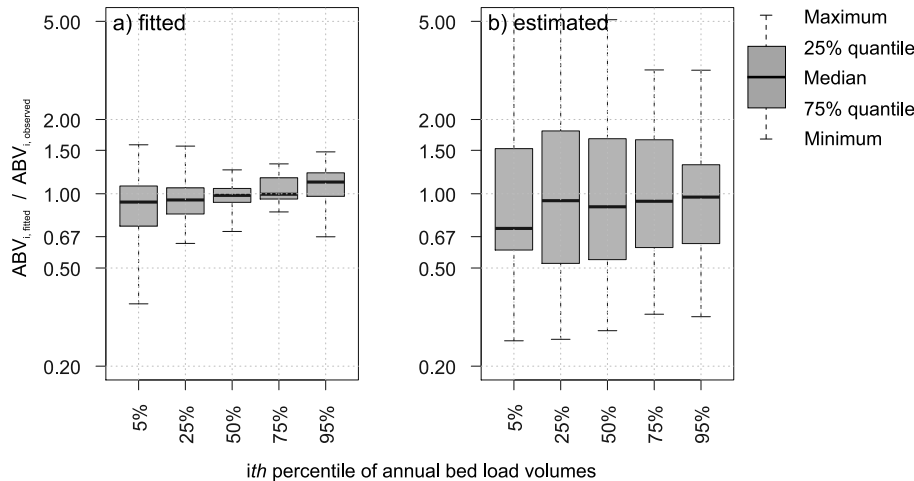


Figure B-51: Certain percentiles generated from the a) fitted log-normal probability distribution (identical to Figure B-49) and b) estimated log-normal probability distribution (equation B48 and B49) divided by the observed percentiles.

3.3.3 Transport efficiency

The range of obtained K (transport efficiency) is huge and spans over five orders of magnitude, with a global minimum of $1e-5$ and a maximum of $3e-1$. Considering the site-specific mean transport efficiency only (red dots in Figure B-52a), the range is still large, with a minimum of $7e-5$ and a maximum of $4e-2$, respectively. The within-site variability (total span in Figure B-52a) is significantly smaller for most sites. It ranges between one to three orders of magnitude, but it is of order two

$$\left(30 < \left[\max_{i=1}^n (\text{ABV}_i) / \min_{i=1}^n (\text{ABV}_i) \right] < 300 \right) \text{ at 12 of the 15 sites.}$$

is almost symmetric in the log-scale, indicating that K follows a log-normal probability distribution.

The magnitude of inner-quartile range (between the 25 th and 75 th percentile of K ; grey bars in Figure B-52a) differs with respect to the site. It is preferably small if the mean transport efficiency mK is large. Another measure for the within-site variability of K is the standard deviation of logarithmized K (sd of $\log(K)$). In Figure B-52b, sd of $\log(K)$ is plotted against mean K and the data confirm a weak relationship. If four outliers are neglected (blue triangles in Figure B-52b), sd of $\log(K)$ significantly correlates with mK . This means that the temporal variability of the transport efficiency is preferably small if the mean transport efficiency is large. In other words, the annual transport efficiency is predominately more balanced in streams with a high availability of mobile sediment (large mean transport efficiency). Thus, the influence of the water runoff on the annual bed load volume is stronger in these streams.

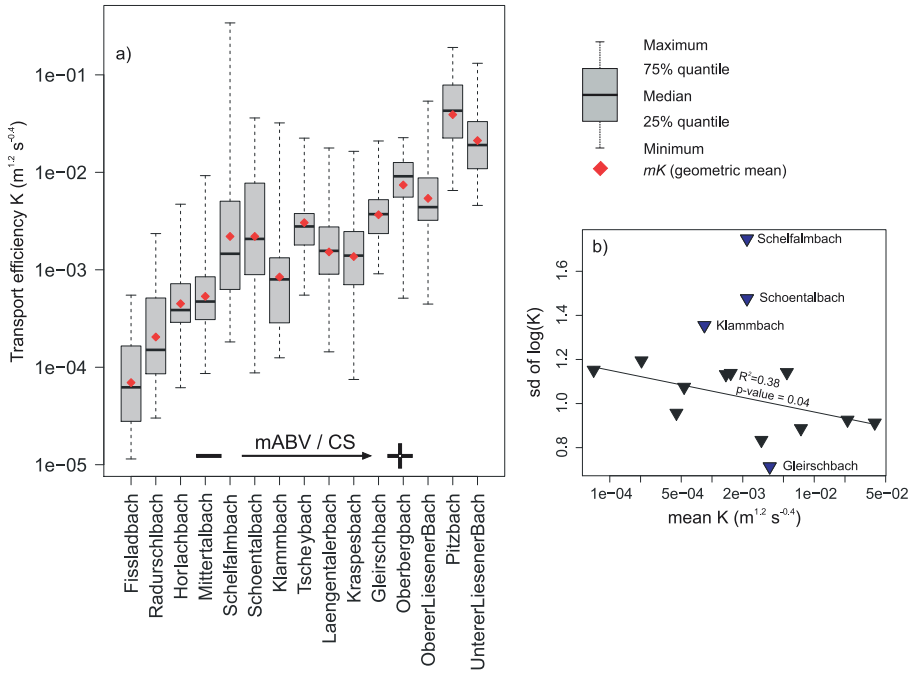


Figure B-52: a) Box plot of the annual transport efficiency for each site. The sites (x-axis) are ordered according to the mean specific annual bed load volume (m^3/km^2), and b) the standard deviation of log-transformed K ($sd \text{ of } \log(K)$) plotted against mean annual transport efficiency (mK); the black line represents a linear regression, with the four outliers (blue triangles) neglected.

3.3.3.1 Between-site variability

According to equation B46, the mean annual bed load volume ($mABV$) of the twenty study sites scales almost linearly with catchment size and exponentially with relative glacier area. In contrast, the geometric mean transport efficiency (mK) significantly correlates with relative glacier area only (Figure B-53).

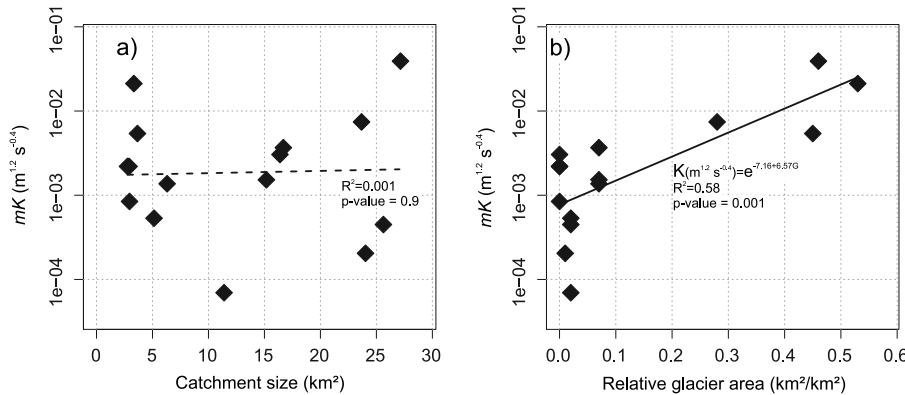


Figure B-53: Geometric mean transport efficiency K plotted against a) catchment size (data reveal no correlation) and b) relative glacier area with a significant exponential regression fitted to the data.

According to the derivation of the bed load transport equation used in this study (equation B43), the transport efficiency theoretically depends, amongst others, on the channel gradient (equation B40). However, at most study sites the bed slope is highly variable along its water course. There remain considerable uncertainties regarding the definition and quantification of the mean (representative) bed slope. Hence, the correlation of mean transport efficiency (mK) is evaluated against several gradients (Table B-2 in section 1.1.2) which differ either in the spatial scale (stream vs. reach scale) or the statistics used (mean, standard deviation or 10th percentile).

Correlating mK against any type of gradient reveals no significant relation of mean transport efficiency and bed slope (Figure B-54). However, a significant correlation is found between mK and the standard deviation of the stream slope (with the exception of Fisslabach; Figure B-54c). Furthermore, the mean reach gradient significantly correlates with mK when Fisslabach and all fields sites with large relative glacier area ($G > 0.2$, Figure B-54a) are removed. Power law fits give an exponent in the range of 1.1 (for $meanRG$) and 1.8 (for $sdSG$), which roughly corresponds with the theoretical definition of K (equation B40).

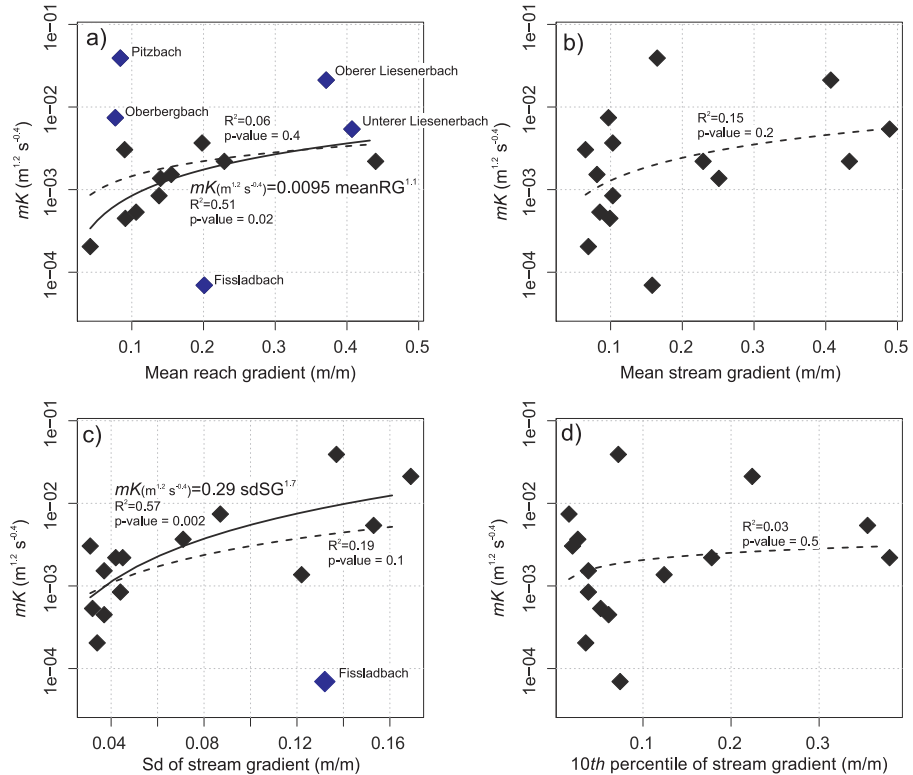


Figure B-54: Geometric mean transport efficiency K plotted against a) mean gradient of the reach immediately upstream of the water intake structure (meanRG), b) mean gradient of the stream draining two third of the total catchment (meanSG), c) standard deviation of stream gradient (sdSG) and d) the 10th percentile of stream gradient. Dashed lines represent non-significant trends including all data, while solid lines refer to significant trend lines excluding outliers (blue diamonds with site names) with the p -value of the coefficient of the explanatory variable smaller than 0.05, respectively. Regression equations are only given for significant trends.

3.3.3.2 Within-site variability

3.3.3.2.1 Temporal changes of transport efficiency and cumulative flow competence

In a first view, the transport efficiency and the flow competence are plotted against time in order to assess any temporal changes. Since the magnitude of both parameters differs between the sites, they were standardized by their site specific median beforehand. In addition, the field sites were separated according to their relative glacier area, because temporal changes may differ with respect to the hydrologic regime (e.g. glacier melt).

Indeed, the annual flow competence reveals a significant decrease during the years of observation at the field sites with glacier areas smaller than 0.2 (Figure B-55a-b), while there's no significant trend at the remaining sites. But, looking at the data in Figure B-55a-b in more detail shows that this significant trend is associated to the two years 2007 and 2011 with very low values of annual flow competence. If these years are excluded from the analysis, the significant trend diminishes. This is in good agreement with the time series of total water volume (not presented in this study), which does not reveal a significant trend as well.

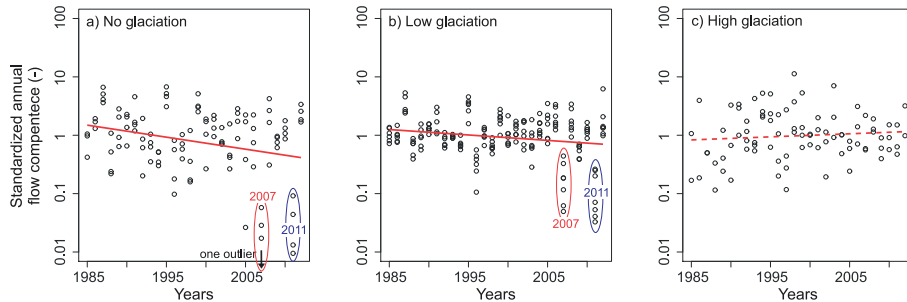


Figure B-55: Annual flow competence is standardized by the site-specific median and plotted against time. The data are separated according to the relative glacier area of the field sites (G) with a) no glacier in the catchment upstream of the water intake structure, b) $0 < G < 0.2$ and c) $G > 0.2$.

The annual transport efficiency shows a significant increase with time at the field sites with no glaciers. Comparing Figure B-55a Figure B-56b suggests that both trends are 'back-to-front'. At remaining field sites ($G > 0$) there is no significant trend at all.

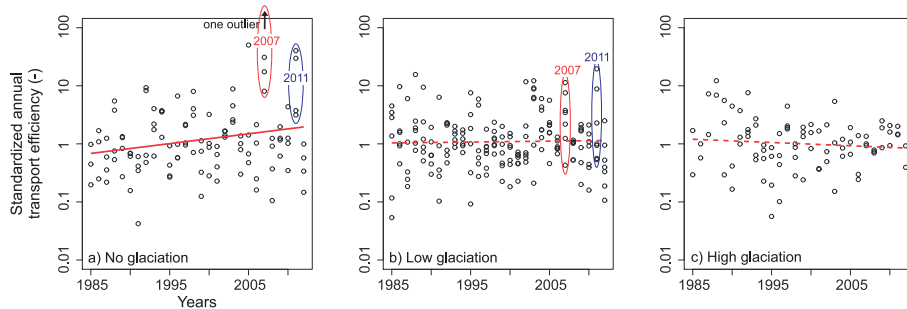


Figure B-56: Annual transport efficiency is standardized by the site-specific median and plotted against time. The data are separated according to the relative glacier area of the field sites (G) with a) no glacier in the catchment upstream of the water intake structure, b) $0 < G < 0.2$ and c) $G > 0.2$.

3.3.3.2.2 Correlation of transport efficiency and cumulative flow competence

Annual transport efficiency K (equation B44) features a negative correlation with its corresponding cumulative flow competence (left term in equation B43; Figure B-57), which means that K is on average lower in wet years (facing high cumulative flow competence) at given sites and vice versa. In contrast, the ratio of annual bed load volume and cumulative flow competence was initially expected to be independently distributed (zero slope in Figure B-57). However, this correlation can be attributed to both, the uncertainty of the approach used to calculate the flow competence or the effect of sediment supply on bed load transport. Therefore, the performance of the approach is verified by means of field data.

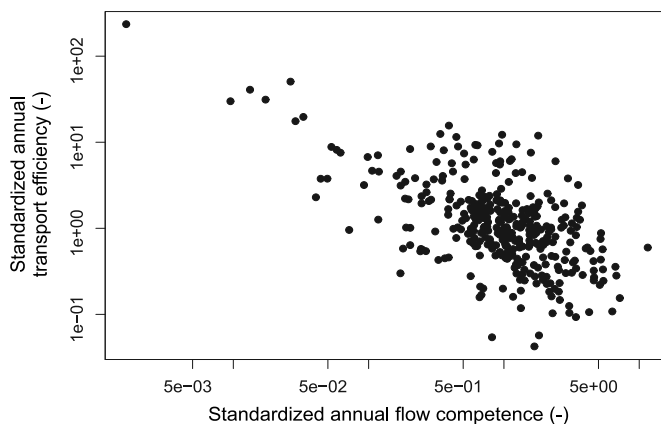


Figure B-57: Annual transport efficiency plotted against the corresponding annual flow competence, with both parameters standardized by their site-specific medians

Since the correlation between transport efficiency K and cumulative flow competence is negative (Figure B-57), the contribution of high flows on total flow competence might be overestimated. Hence, either (i) the relative increase with discharge at low to moderate flows (Q/Q_r)^{6.44} (expressed by the exponent 6.44) or (ii) the reference discharge might be too large.

The bed load transport measurements of this study (section B.1.5) confirm with an exponent of 6.44 in equation B43 since the relative increase of bed load transport rate with discharge is reproduced well (Figure B-58). Although the field sites are not located immediately upstream of the water intake structure for all except the Pitzbach site (Pb #1), the measured Q-Q_b relation is suitable for that purpose.

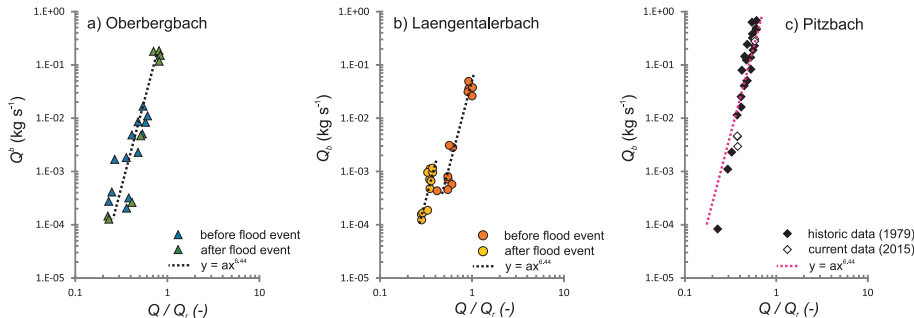


Figure B-58: Bed load transport rates of three different sites (a, b, c) plotted against relative discharge. The rate of change is similar as assumed by equation B43a with an exponent of 6.44 (dashed line is fitted by eye).

In addition, a bias of (ii) the reference discharge could also cause this observed correlation between annual flow competence and transport efficiency. In this study, the reference discharge is determined with $0.5Q_{1.5a}$ (equation B41) and thus, it is independent of the reach characteristics. In contrast, the analysis of the field data in *Study C* reveals that the reference discharge varies at the reach scale and thus, it is not solely dependent on the magnitude of the 1.5 years flow (equation B41). For example, the reference discharge $Q_{r,D50}$ of the stream reach enclosing upstream of the water intake structure of the Pitzbach is independently derived from the field data (*Study C*). The field data based $Q_{r,D50}$ is $5.1 \text{ m}^3/\text{s}$, while equation B41 yields $Q_r=6.5 \text{ m}^3/\text{s}$. The match between observed (*Study C*) and used $Q_{r,D50}$ (equation B41) is worse at the Laengentalerbach. At the field site LB#2 the observed $Q_{r,D50}$ (*Study C*) is $4.2 \text{ m}^3/\text{s}$, while equation B41 yields $2.1 \text{ m}^3/\text{s}$ and thus, underestimates the observed $Q_{r,D50}$ by a factor of 0.5. In order to evaluate if the uncertainty of Q_{ref} has an influence on the correlation between annual flow competence and transport efficiency, Monte Carlo simulations were performed. Therefore, the site specific Q_{ref} is not solely determined by equation B41 but additionally multiplied with a random variable that is uniformly distributed in the range of (0.5; 2). The cumulative annual flow competence is then recalculated according equation B43. In total, one hundred realizations (each with different values of Q_{ref}) were generated and all of them showed a significant correlation between annual flow competence and annual transport efficiency; even if outliers were rejected.

As a consequence, the correlation of annual transport efficiency and annual flow competence (Figure B-57) is not attributed to the uncertainty or a possible bias of the bed load transport formula (equation B43) used. The correlation suggests that the annual transport efficiency indeed depends on the discharge history of the corresponding year. Assuming the channel geometry and the bed surface grain size distribution to be constant over several years, the remaining reason for the variable transport efficiency are temporal differences in of sediment supply conditions. Surprisingly, this negative correlation between annual flow competence (right term in equation B43) and transport efficiency (middle term in equation B43) is significantly evident regardless if the stream's sediment supply conditions (a proxy for the mean transport efficiency) is low or high (Figure B-59).

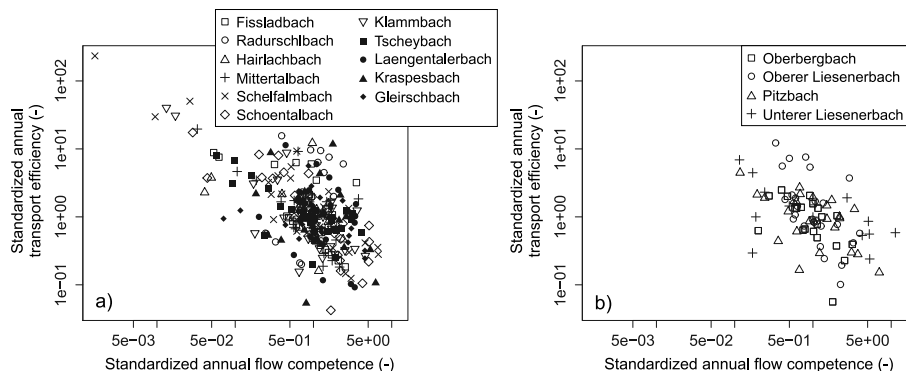


Figure B-59: Annual transport efficiency plotted against the corresponding annual flow competence, with both parameters standardized by their site-specific medians for a) the field sites with low and moderate mK and a relative glacier area $G < 0.2 \text{ km}^2/\text{km}^2$ and b) the field sites with large mK and a relative glacier area $G > 0.2 \text{ km}^2/\text{km}^2$

3.3.3.2.3 Impact of exceptional events

Annual differences in cumulative flow competence only explain a small fraction of the within-site scatter of transport efficiency since the correlation is generally weak. Therefore, the influence of certain flood events on the transport efficiency was assessed visually by plotting the yearly series of both, the transport efficiency and the standardized maximum discharge (Figure B-60). However, the time series of transport efficiency of the fifteen streams do not reveal a clear dependency towards previous flood events. Instead, the temporal variability appears either random or features cyclic patterns which could not be attributed to certain impact parameters yet.

Annual peak discharge might be an inaccurate parameter for assessing the changes in sediment supply conditions, because local sediment pulses originating from hillslopes of small tributary channels are not necessarily correlated to peak flow at the catchment scale. At one site (Kraspesbach), an exceptional event could be back-traced by aerial photographs and an event documentation of TIWAG. Although the event is not visible in the time series of annual peak discharge, it caused an obvious shift of sediment supply conditions (Figure B-61). Its effect on bed load transport is quantified by an increase of K of about one order of magnitude, which decreases to its former level within the following three years (Figure B-61).

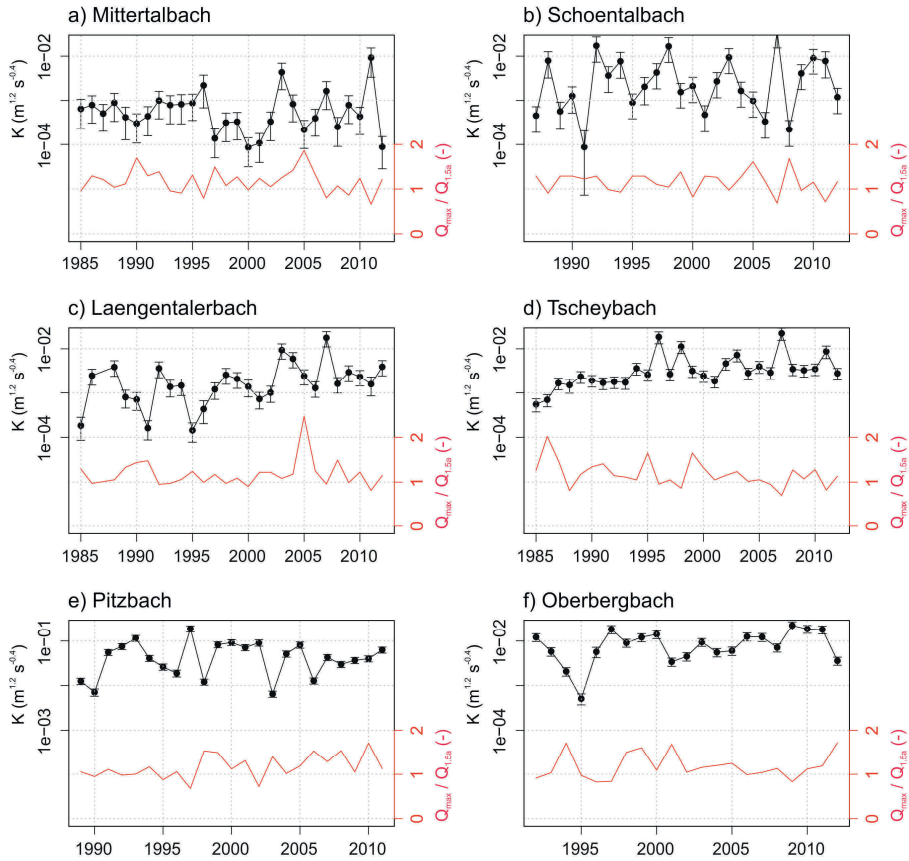


Figure B-60: Time series of annual transport efficiency (black) with the whiskers representing the error acc. equation B7 in section 1.1.5.5 and standardized annual peak discharge (red line) for three different sites with increasing mean transport efficiency from a) to f) (see Figure B-52): a-b) the Mittertalbach and the Schoentalbach represent supply limited mountain streams without obvious morphologic changes during the last decades; but nevertheless, the yearwise transport efficiency fluctuates strongly; c) the transport efficiency of the Langentalerbach reveals cyclic patterns which are attributed to sporadic sediment pulses from a small tributary channel immediately upstream of the water intake structure; d) the temporal evolution of the transport efficiency at the Tscheybach is very homogeneous which indicates a yearwise consistent relation between discharge and transport rate; e-f) the intensively glaciated Pitzbach and Oberbergbach feature overall large transport efficiencies with low scatter.

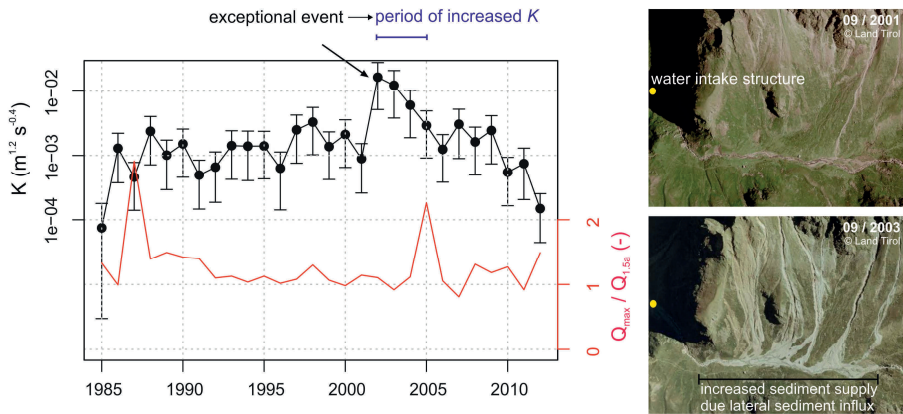


Figure B-61: Temporal evolution of the transport efficiency at the Kraspesbach. The strong increase of K in the year 2002 is attributed to an exceptional event which caused large relocations of sediment from the hillslopes in the river.

B.3.4 Discussion

3.4.1 Annual bed load volumes

The mean annual bed load volume of all study sites is significantly correlated with the catchment size and the relative glacier area, which confirms well with the comprehensive study of *Hinderer et al.* (2013). In contrast, the data do not reveal a significant dependency on topographic parameters, such as the mean catchment slope or channel gradient. This contradicts with empiric relations regarding bed load volumes during exceptional events in which the channel gradient is a key parameter (*Hampel*, 1980; *Kronfellner and Kraus*, 1984; *Gertsch*, 2009). Moreover, *Rickenmann* (2001) found the channel gradient to contribute on the bed load volumes even during ordinary events at the order of magnitude scale. All mountain streams analyzed in this study refer to step-pool streams with mean gradients larger than 0.07 m/m. Hence, possible contributions of channel gradient on annual bed load volumes in comparison to low-gradient streams are out of the study's scope.

The explanatory variables catchment size and relative glacier area are interpreted as surrogates for the hydrologic boundary conditions. Since all study sites are within a range of 50 km, climatic differences are small (Table B-1) and the annual runoff is predominately a function of the drainage area and the magnitude of glacier melt. This suggests that the hydrologic impact controls the magnitude of mean annual bed load volume much more than the steepness of the catchment; at least between these lithological similar sites. But the relation between the relative glacier area and the annual bed load volume is exponential, while the contribution of glacier melt on total runoff is expected to be almost linear. Thus, the relative glacier area is additionally interpreted as a parameter for the availability of mobile bed load.

3.4.2 Transport efficiency

3.4.2.1 Interpretation of varying transport efficiencies

In general, the yield of bed load in a given period is mainly influenced by the flow competence which is considered as a nonlinear function of the stream flow. Hence, some differences in annual bed load volumes, either within-site or between-site, arise from the differences in annual flow competence. The remaining variability is attributed to the overall transport efficiency (K) at a given site or its temporal variation. In this respect, recent studies reveal the strong influence of sediment supply on bed load transport efficiency at both scales, within single sites over time (Yager *et al.*, 2012; Turowski *et al.*, 2009; Lenzi, 2004; Gintz *et al.*, 1996) and between sites (Recking, 2012). However, a between-site variation of transport efficiency is influenced by both, the morphologic boundary conditions (e.g. channel gradient, grain size distribution, etc.) and sediment supply conditions. In contrast, the within-site variation of K is attributed to sediment availability only, since temporal changes of topographic (channel gradient, channel shape) or morphologic patterns (grain size distribution, bed structures) are assumed to be minor.

3.4.2.2 Between-site variability of transport efficiency

The ratio of annual bed load volume and cumulative flow competence is used as a proxy for the transport efficiency K . It represents the vertical location of the bed load transport rating curve in the log-log scale (Figure B-43). In this respect, the parameter K is dimensional, since the shear stress based approach of Schneider *et al.* (2015a) is converted to a discharge based one (section 3.2.2). Nevertheless, this approach enables a between-site comparison of mean transport efficiency, but the variability of K is not solely associated with differences in the sediment supply.

Based on equation B40, K theoretically increases, amongst others, with $S^{1.2}$ and $D_{84}^{0.6}$, and linearly effects bed load transport rate. According to the grain size distributions at the Oberbergbach and the Laengentalerbach the D_{84} increases with $aS^{1.0}$ and $aS^{1.1}$, while Schneider *et al.* (2015a) found the relation $D_{84}=aS^{0.7}$ at the Riedbach (Switzerland). Hence, K theoretically increases with bed slope to a power of approx. 1.6 to 1.9, when differences in flow width and submerged weight are neglected.

The dependence of K on bed slope is somehow supported by the data since the geometric mean transport efficiency increases linearly with (reach gradient) or $sdSG^{1.8}$ (standard deviation of the stream gradient); at least for not to moderate glaciated catchments (Figure B-54). In contrast, results reveal neither a significant correlation of mean transport efficiency with the mean gradient at the multiple reach scale (mSG) nor with its 10th percentile, a proxy for low gradient reaches present. This contradicts with the hypothesis that the low-gradient reaches regulate cumulative bed load transport (e.g. BAFU, 2013); at least at the year's scale and without exceptional extreme events.

However, mean transport efficiency is co-regulated by other than geometric properties of the stream. One explanatory parameter is the relative glacier area, since mean transport efficiency is highest in the four catchments with the highest relative glacier area (Figure B-53). Although the relative glacier area influences both, the hydrologic (Kormann *et al.*, 2015) and the sediment supply boundary conditions (Mao *et al.*, 2014), the overall higher transport efficiency in these streams is solely associated with an increased supply of mobile bed load.

3.4.2.3 Within-site variability of transport efficiency

3.4.2.3.1 *Interactions of sediment availability and flow competence*

Recently, Mao *et al.* (2014) reported seasonal differences in bed load transport rating curves at a glacier fed mountain stream in Italy. Bed load transport rates measured in the late summer were generally higher than those in the early summer, suggesting the runoff origin (glacier melt or snowmelt) and consequently, the sediment source, to contribute to transport efficiency (Mao *et al.*, 2014). Their results reveal that the transport efficiency does not solely vary because of severe changes in sediment availability due to exceptional flood events (Turowski *et al.*, 2009; Lenzi *et al.*, 2004), or large sediment influxes from tributaries (Hoffmann and Gabet, 2007). Even the activation of micro-scale sediment sources contribute to an increase in bed load transport rate; at least on a seasonal time scale. The results of this study further suggest that these micro-scale sources represent a kind of base level of sediment availability which does not linearly scale with annual flow competence. It seems that sediment availability regulates annual bed load as relatively more bed load is transported in dry years (featuring on average higher transport efficiencies) than in wet ones (Figure B-57). This means that the variability of annual bed load volumes is less pronounced than the variability of annual flow competence. In a consequence, measured annual bed load volumes reveal a smaller scatter than annual bed load volumes calculated by means of mean transport efficiency (mK) and cumulative flow competence (Figure B-62).

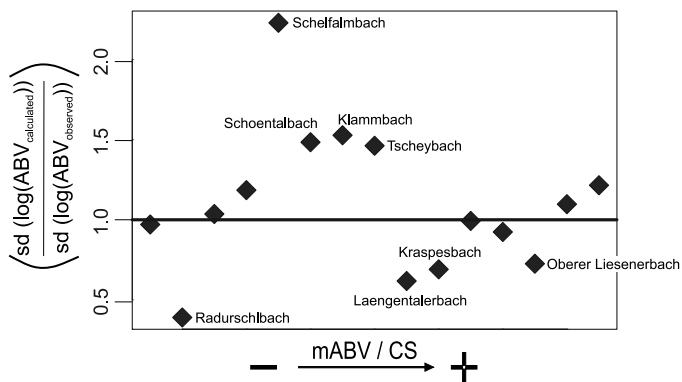


Figure B-62: Ratio of the log-transformed standard deviations of calculated annual bed load volumes (multiplying mean transport efficiency (mK) and annual cumulative flow competence) and the standard deviation of observed annual bed load volumes. A ratio larger than unity means that the calculated bed load volumes are more variable than the observed ones.

3.4.2.3.2 *Impact of exceptional events on transport efficiency*

Next to these micro-scale sediment sources, flood events impact the sediment availability due to the break-up of the bed surface and the release of fine subsurface sediment. However, the time series of annual transport efficiency does not reveal a consistent increase of transport efficiency after years with exceptional flood events. Only

at one site, the impact of an exceptional flood event could be back-traced to an increase of transport efficiency. The results shown in Figure B-61 correspond with the observation made in the Erlenbach (Yager *et al.*, 2012) in terms of both, the magnitude and duration of increased transport efficiency. Furthermore, Gintz *et al.* (1996) documented the morphologic impact of an exceptional event at the Lainbach River (Germany). Due to sediment overloading, step-pool structures were buried, but the channel recovered quickly within a period of two years. This time span also roughly corresponds to the recovery time of transport efficiency at the Kraspesbach (Figure B-61).

B.3.5 Conclusion

A large data set of annual bed load volumes of several small alpine catchments reveals a high variability regarding both, between different sites and over time.

Mean annual bed load volumes almost linearly scale with the catchment size. Since all study sites are close to each other, geologic and climate differences are small and their influence on the bed load budget is expected to be minor. Hence, the catchment size represents a proxy for the annual water flow. In addition, the mean annual bed load volumes correlate significantly with the relative glacier area. This is another contributor to the hydrologic boundary conditions, but also to the sediment supply conditions. In this respect, catchments with large relative glacier areas reveal higher transport efficiencies, which is attributed to an increased availability of mobile bed load. In addition, transport efficiency positively correlates with the channel gradient immediately upstream of the measuring station, as well as with the variability of bed slope at a multiple reach scale.

Within-site variability of the transport efficiency is much smaller and features a similar range for most of the study sites, regardless of overall supply conditions. In analogy to former studies, exceptional flood events cause an increase of the transport efficiency of about one order of magnitude which decreases to its former level within a few years. But the sediment availability regulates the annual amount of bed load transport even without any major shifts in sediment supply. Transport efficiencies are on average higher in dry years (featuring lower cumulative flow competence) than in wet ones. This reveals the regulating effect of sediment availability on annual bed load volumes in hydrologically ordinary years.

B.3.6 References of Study A

- Bagnold, R. A. (1980), An empirical correlation of bedload transport rates in flumes and natural rivers, *Proc. R. Soc. London, Ser. A*, 372, 453-473.
- Bathurst, J. C. (2013), Critical conditions for particle motion in coarse bed materials of nonuniform size distribution, *Geomorphology*, 197, 170-184.
- Bundesamt für Umwelt (BAFU) (2013), Abschätzung der mittleren jährlichen Geschiebefrachten in Vorfluter. (published online 2014) Available from Internet <http://www.bafu.admin.ch/wasser/13465/13486/14115/index.html?lang=de>
- Bunte, K., S. R. Abt, K. W., Swingle, D. A. Cenderelli, and J. M. Schneider (2013), Critical Shields values in coarse-bedded steep streams, *Water Resour. Res.*, 49, 7427-7447, doi: 10.1002/2012WR012672.
- Church, M., and A. Zimmerman (2007), Form and stability of step-pool channels: Research progress, *Water Resour. Res.*, 43, W03415, doi: 10.1029/2006WR005037
- Delignette-Muller, M. L., R. Pouillot, J.-B. Denis and C. Dutang (2014), fitdistrplus: help to fit of a parametric distribution to non-censored or censored data, R package version 1.0-2.

- Emmett, W. W., and M. G. Wolman (2001), Effective discharge and gravelbed rivers, *Earth Surf. Proc. Land.*, 26, 1369– 1380.
- Ferguson, R. (2007), Flow resistance equations for gravel- and boulder-bed streams, *Water Resour. Res.*, 43, W05427, doi: 10.1029/2006WR005422
- Gertsch, E., 2009. Geschiebebelieferung alpiner Wildbachsysteme bei Grossereignissen - Ereignisanalysen und Entwicklung eines Abschätzverfahrens (Bed load supply in alpine catchments facing exceptional extreme events – event analysis and development of a calculation approach), Ph.D. thesis, Univ. Bern, Bern, 230 p.
- Ghilardi, T., M. J. Franca, and A. J. Schleiss (2014), Bed load fluctuations in a steep channel, *Water Resour. Res.*, 50, 6557-6576, doi: 10.1002/2013WR01444
- Gintz, D., M. A. Hassan and K.-H. Schmidt (1996), Frequency and magnitude of bed load transport in a mountain river, *Earth Surf. Proc. Land.*, 21, 433-445.
- Hampel, R. (1980), Calculation of Gravel Load for Danger Zone Plans at Mountain Torrent Areas, *Interpraevent, 1980* (4), 83-91.
- Hinderer, M., M. Kastowski, A. Kamelger, C. Bartolini and F. Schlunegger (2013), River loads and modern denudation of the Alps – a review, *Earth-Sci. Rev.*, 118, 11-44, doi: 10.1016/j.earscirev.2013.01.001
- Hoffman, D. F., and E. J. Gabet (2007), Effects of sediment pulses on channel morphology in a gravel-bed river, *Geological Society of America Bulletin*, 119 (1-2), 116-125, doi: 10.1130/B25982.1
- Jackson, W. L., and R. L. Beschta (1982), A model of two-phase bed load transport in an Oregon coast range stream, *Earth Surf. Proc. Land.*, 7, 517-527.
- Kim, S (2012), ppcor: Partial and Semi-partial (Part) correlation. R package version 1.0. <http://CRAN.R-project.org/package=ppcor>
- Kormann, C., T. Francke, M. Renner, and A. Bronstert, (2015), Attribution of high resolution streamflow trends in Western Austria – an approach based on climate and discharge station data, *Hydrol. Earth Syst. Sci.*, 19, 1225–1245, doi: 10.5194/hess-19-1225-2015
- Kronfellner-Kraus, G., 1982: Über den Geschiebe- und Feststofftransport in Wildbächen (About bed load and sediment transport in torrents), *Oesterreichische Wasserwirtschaft*, 24, 1/2, 12-21.
- Lamb, M. P., W. E. Dietrich, and J. G. Venditti (2008), Is the critical Shields stress for incipient sediment motion dependent on channel-bed slope?, *J. Geophys. Res.-Earth*, 113(F2), doi: 10.1029/2007jf000831
- Lenzi, M. A. (2001), Step-pool evolution in the Rio Cordon, Northeastern Italy. *Earth Surf. Proc. Land.*, 26, 991–1008, doi: 10.1002/esp.239
- Lenzi, M. A., L. Mao, and F. Comiti (2004), Magnitude-frequency analysis of bed load data in an Alpine boulder bed stream, *Water Resour. Res.*, 40, W07201, doi: 10.1029/2003WR002961
- Mao, L., A. Dell'Agnese, C. Huincache, D. Penna, M. Engel, G. Niedrist and F. Comiti, (2014), Bedload hysteresis in a glacier-fed mountain river, *Earth Surf. Proc. Land.* 39, 964–976, doi: 10.1002/esp.3563
- Melton, M.A., (1957) An analysis of the relations among elements of climate, surface properties, and geomorphology. *Technical Report 11 389-042*. Office of Naval Research, Dep. Of Geology, Columbia University, New York.
- Meyer-Peter, E., and R. Müller (1948), Formulas for bed-load transport, in *Proceedings of the 2nd Meeting of the International Association for Hydraulic Structures Research*, pp. 39–64, Int. Assoc. Hydraul. Res., Delft, Netherlands
- Montgomery, D. R., and J. M. Buffington (1997), Channel-reach morphology in mountain drainage basins, *Geol. Soc. Am. Bull.*, 109(5), 596-611.
- Mueller, E. R., J. Pitlick, and J. N. Nelson, (2005), Variation in the reference Shields stress for bed load transport in gravelbed streams and rivers, *Water Resour. Res.*, 41, W04006, doi: 10.1029/2004WR003692
- Nitsche, M., D. Rickenmann, D., J. M. Turowski, A. Badoux, and J. W. Kirchner (2011), Evaluation of bed load transport predictions using flow resistance equations to account for macro roughness in steep streams, *Water Resour. Res.*, 47, W08513, doi: 10.1029/2011WR010645
- Palt, S. M. (2001), Sedimenttransportprozesse im Himalaya-Karakorum und ihre Bedeutung für Wasserkraftanlagen (Sediment transport processes in the Himalaya-Karakorum and its relevance regarding hydro power utilization), Ph.D. thesis, Univ. Fridericiana zu Karlsruhe, Karlsruhe, Germany (in German).
- Parker, G., and P. C. Klingeman (1982), On why gravel bed streams are paved, *Water Resour. Res.*, 18(5), 1409-1423.
- R Core Team (2013). R: A language and environment for statistical computing. R Foundation for Statistical Computing, Vienna, Austria. URL <http://www.R-project.org/>.
- Recking, A. (2012), Influence of sediment supply on mountain streams bedload transport, *Geomorphology*, 175-176, 139-150, doi: 10.1016/j.geomorph.2012.07.005

- Recking, A. (2013), Simple Method for Calculating Reach-Averaged Bed-Load Transport, *J. Hydraul. Eng.*, 139(1), 70-75, doi: 10.1061/(ASCE)HY.1943-7900.0000653
- Rickenmann, D. and A. Recking (2011), Evaluation of flow resistance in gravel-bed rivers through a large data set, *Water Resour. Res.*, 47, W07538, doi: 10.1029/2010WR009793
- Rickenmann, D. (1990), Bedload transport capacity of slurry flows at steep slopes, Ph.D. thesis, ETHZ, Zurich, Switzerland, 249 p.
- Rickenmann, D. (1997), Sediment transport in Swiss torrents, *Earth Surf. Proc. Land.*, 22, 937-951.
- Rickenmann, D. (2001), Comparison of bed load transport in torrents and gravel bed streams, *Water Resour. Res.*, 37(12), 3295-3305.
- Schächlili, U., (1991), Morphologie und Strömungsverhältnisse in Gebirgsbächen: ein Verfahren zur Festlegung von Restwasserabflüssen, *Mitteilungen der Versuchsanstalt für Wasserbau, Hydrologie und Glaziologie an der ETH Zürich*, No. 113, ETH Zurich, Switzerland.
- Schneider, J. M., D. Rickenmann, J. M. Turowski, K. Bunte, and J. W. Kirchner (2015a), Applicability of bed load transport models for mixedsize sediments in steep streams considering macro-roughness, *Water Resour. Res.*, 51, 5260-5283, doi: 10.1002/2014WR016417
- Schneider, J. M., D. Rickenmann, J. M. Turowski, and J. W. Kirchner (2015b), Self-adjustment of stream bed roughness and flow velocity in a steep mountain channel, *Wat. Resour. Res.*, 51, 7838-7859, doi: 10.1002/2015WR016934
- Schneider, J. M. (2015), Bedload transport, Flow Hydraulics, And Macro-Roughness in Steep Mountain Streams, Ph.D. thesis, ETH Zurich, Zurich, Switzerland.
- Schoklitsch, A. (1934), Der Geschiebetrieb und die Geschiebekraft, *Wasserwirtschaft*, 29 (4), 37-43.
- Schöberl, F. (1983), Statistische Untersuchungen über die Geschiebeverfrachtung in Hochgebirgsbächen (Statistical investigation of bed load volumes in mountain streams), *Interpraevent 1983* (1), 74-85.
- Schumm, S.A., (1954), The relation of drainage basin relief to sediment loss, *Int. Assoc. Hydrol. Sci.* 36, 216-219.
- Strahler, A. N. (1957), Quantitative analysis of watershed geomorphology, *Transactions, American Geophysical Union*, 38 (6), 913-920.
- Turowski, J. M., E. M. Yager, A. Badoux, D. Rickenmann, and P. Molnar (2009), The impact of exceptional events on erosion, bed load transport and channel stability in a step-pool channel, *Earth Surf. Proc. Land.*, 34, 1661-1673, doi: 10.1002/esp.1855.
- Wilcock, P. R., and J. C. Crowe (2003), Surface based transport model for mixed size sediment, *J. Hydraul. Eng.*, 129(2), doi: 10.1061/(ASCE)0733-9429(2003)129:2(120)
- Yager, E. M., J. W. Kirchner, and W. E. Dietrich (2007), Calculating bed load transport in steep boulder bed channels, *Water Resour. Res.*, 43, W07418, doi: 10.1029/2006WR005432
- Yager, E. M., J. M. Turowski, D. Rickenmann, and B. W. McArdell, (2012), Sediment supply, grain protrusion, and bed load transport in mountain streams, *Geophys. Res. Lett.*, 39, L10402, doi: 10.1029/2012GL051654

B.3.7 Appendix

Equation B37 is transformed to a discharge based approach by substituting flow depth by discharge. Therefore, the sporadically measured flow velocities (section B.1.5) were used to regress dimensionless velocity (U^{**}) with dimensionless discharge (q^{**}) according to *Rickenmann and Recking* (2011), giving:

$$U^{**} = 1.21 \times q^{**0.64} \quad (\text{B50})$$

Therein, the exponent of this dimensionless hydraulic geometry relation is similar to that obtained by *Schneider et al.* (2015a) for the Riedbach (Switzerland). Both almost correspond to a linear scaling of flow resistance with relative flow depth, as suggested by Ferguson (2007) for low d/D_{84} . Assuming this linear dependency to be valid, the following flow resistance equation is obtained:

$$\frac{u}{\sqrt{gdS}} = 1.8 \times \left(\frac{d}{D_{84}} \right)^1, \quad (\text{B51})$$

with the mean flow velocity u , flow depth d , channel slope S and the diameter of which 84 % are finer D_{84} .

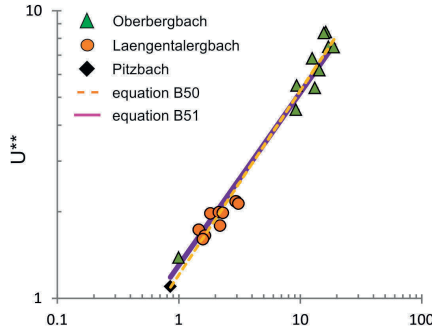


Figure B-63: Relationship between dimensionless discharge and dimensional velocity scaled by the D_{84} of the bed surface grain size distribution

Substituting the definition of the specific discharge ($q = u \times d$) into equation B51 gives:

$$q = 1.8 \times \left(\frac{d}{D_{84}} \right)^1 \sqrt{gdS} \times d = 1.8 \times \frac{\sqrt{gS}}{D_{84}} \times d^{2.5} \quad (\text{B52})$$

Consequently, flow depth d is defined by specific discharge according:

$$d = \left(\frac{q D_{84}}{1.8 \times \sqrt{gS}} \right)^{\frac{2}{5}} \quad (\text{B53})$$

The equation of Schneider *et al.* (2015a) as used in this study (equation B37) determines total bed load intensity (W^*) as function of Shield stress divided by the reference Shields stress which can be simplified to $f(d/d_r)$ according :

$$W_{tot}^* = f\left(\tau_{D50}^*/\tau_{r,D50}^*\right) = f\left(\frac{\frac{dS}{(s-1)D_{50}}}{\frac{d_{r,D50}S}{(s-1)D_{50}}}\right) = f\left(\frac{d}{d_{r,D50}}\right), \quad (\text{B54})$$

with the flow depth d and the reference flow depth $d_{r,D50}$. Substituting flow depth by equation B53 yields

$$W_{tot}^* = f\left(\frac{d}{d_c}\right) = f\left(\left(\frac{q}{q_{r,D50}}\right)^{\frac{2}{5}}\right) \quad (\text{B55})$$

In a consequence, equation B37 can be written in terms of specific discharge:

$$W^* = \begin{cases} 0.002 \times \left(\frac{q}{q_{r,D50}} \right)^{6.44} & \text{for } q/q_{r,D50} \leq 1.58 \\ 14 \times \left(1 - \frac{0.85}{\left(q/q_{r,D50} \right)^{0.28}} \right)^{4.5} & \text{for } q/q_{r,D50} > 1.58 \end{cases} \quad (\text{B56})$$

Further, bed load transport intensity W^* can be rearranged in terms of solid discharge $q_{b,vol}$

$$W_{tot}^* = \frac{(s-1)gq_{b,vol}}{u^{*3}} \rightarrow q_{b,vol} = \frac{W_{tot}^* \times (\sqrt{gdS})^3}{(s-1)g}, \quad (\text{B57})$$

Combining equation B56 and B57 and substituting flow depth by specific discharge gives:

$$q_{b,vol} = \begin{cases} 0.002 \times \left(\frac{q}{q_{r,D50}} \right)^{6.44} \times q^{0.6} \times \frac{g^{0.2} S^{1.2} D_{84}^{0.6}}{1.8^{0.6} (s-1)} & \text{for } q/q_{r,D50} \leq 1.58 \\ 14 \times \left(1 - \frac{0.85}{\left(q/q_{r,D50} \right)^{0.28}} \right)^{4.5} \times q^{0.6} \times \frac{g^{0.2} S^{1.2} D_{84}^{0.6}}{1.8^{0.6} (s-1)} & \text{for } q/q_{r,D50} > 1.58 \end{cases} \quad (\text{B58})$$

Finally, specific discharge can be substituted by total discharge according to the continuity equation $Q = q \times w$. Assuming the width w to be constant ($w = w_c$), equation B58 can be written in terms of total discharge (equation B43). Although flow width typically increases with discharge, its influence on the study outcomes is small.

B.4 Study B: Temporal variability of bed load transport rate in two glacier-fed mountain streams

B.4.1 Introduction

In *Study A*, the variation of annual transport efficiency is partly attributed to the differences in the supply conditions of mobile bed load. Thereby, the analysis presented in *Study A* is based on a continuous discharge hydrograph (with 15 min interval) and a large data set of annual bed load volumes, which is cumulative quantity of bed load transport. Thus, the *Study A* does not address the variation of bed load transport rate within a year but quantifies an overall mean transport efficiency for each year.

The question arises, if the variable nature of the transport efficiency remains even at a smaller time scale. In this respect, what is the scatter of bed load transport rate at a given site and over a long period of time? And is there an evidence that the scatter of bed load transport rate somehow depends on the supply conditions?

Indeed, the supply of mobile bed load is a major controlling factor regarding incipient motion (*Bathurst*, 2013; *Bunte et al.*, 2013; *Turowski et al.*, 2011) and the quantity of marginal and partial bed load transport (*Recking*, 2012; *Barry et al.* 2004; *Rickenmann*, 2001; *Habersack and Laronne*, 2001; *Garcia et al.*, 2000). In a consequence, if the supply in a certain stream reach changes, the relationship between bed load transport Q_b and discharge Q is expected to change as well.

A shift of the supply conditions of mobile bed load may occur due to either (i) the break-up of the armor layer and the subsequent release of subsurface sediment, (ii) the bed load entering from upstream but inner-channel sources or (iii) from hillslopes and tributary channels, respectively.

The (i) break-up of the bed surface is typically restricted to flood events, at least in steep boulder bed mountain streams (*Bunte et al.*, 2013; *Turowski et al.*, 2009; *Bathurst*, 2007). But, the morphologic patterns at the bed surface, like the spatial arrangement of the grains at the patch scale, may change even during moderate flows (*Turowski et al.*, 2011; *Garcia et al.*, 2007), causing the transport efficiency (the magnitude of bed load transport at a given discharge) to vary.

The bed load inflow from (ii) inner-channel or (iii) outer-channel sources are additional means for changes in supply conditions. The inner-channel sources of mobile bed load are often present in low-gradient accumulation reaches, typically featuring a plane bed and a braided water course. Usually, the transport efficiency in such accumulation reaches is comparatively high at moderate flows (due to the abundance of relatively fine bed load at the bed surface), while it is comparatively low at high flows (due to the low channel gradient).

In contrast, the mobilization of bed load from outer-channel sources does not solely depend on runoff in the main channel, but it depends on the runoff origin (*Mao et al.*, 2014; *Hofer*, 1985). In this respect, *Mao et al.* (2014) observed a seasonal shift of the hysteretic patterns of the Q - Q_b relation in a glaciated mountain basin, which they associated with the seasonal shift from a snowmelt to a glacier melt regime. In their example, the bed load transport efficiency was larger during the glacier melt period. In contrast, *Hofer* (1985) investigated the temporal pattern of the Q - Q_b relation at the Pitzbach and found that transport efficiency is highest when runoff due to either snow

or glacier melt is superimposed by rainfall-induced runoff, suggesting for an activation of outer-channel bed load sources.

However, there is a lack of knowledge regarding the magnitude the Q-Q_b relation varies over time, since long-term data of simultaneously measured discharge and bed load transport rate bed are spares. To contribute to this gap, a large data set of simultaneously measured bed load transport rates and water discharge is analyzed in this study. The data are derived from the operational records of two water intake structures, both operated by a hydropower company (TIWAG).

B.4.2 Field sites and bed load transport data

At the water intake structures situated in the Pitzbach and Oberbergbach, bed load transport rate was determined for a period of several years (see section B.1.4). Both are steep mountain streams, located in the Central Alps of Northern Tyrol and they drain a partially glaciated catchment of 27 km² (Pitzbach) and 24 km² (Oberbergbach). Both basins belong to the Oetztal-Stubai basement complex, which is built up by crystalline rock consisting mainly of gneiss. At the local scale, the bedrock is superimposed by unconsolidated sediment, such as colluvial deposits and moraines.

4.2.1 Oberbergbach

In the basin of the Oberbergbach, there are multiple small glaciers distributed in the sub-basins, with the main glacier in the very southwest (Figure B-64). The glacier mouth of the main glacier represents the origin of the Oberbergbach. In this uppermost part of the Oberbergbach, the stream course is braided and leads through the glacier forefield, which is almost one kilometer long. Downstream of a steep bedrock reach, the Oberbergbach reveals a semi-braided streambed, with a channel gradient of about 0.07 m/m in the upper and 0.02 m/m in the lower part of the long, U-shaped high mountain valley. As apparent in Figure B-65, the upper and lower part is separated by a short step in bedrock.

At an altitude of about 2140 m, the longitudinal profile reveals a severe change in slope, which is associated with the major valley step. Since the Pleistocene, the Oberbergbach incised in the bedrock and formed a gorge. Depending on the local channel slope, the Oberbergbach features either a cascade or step-pool morphology. Along with this gorge, there are three small tributaries entering the main channel. Although their drainage area is large, their contribution to the bed load budget is low.

The reach just upstream of the water intake structure is confined by bedrock and reveals a bed gradient of about 0.08 m/m; for additional reach characteristics see Study C (section B.5).

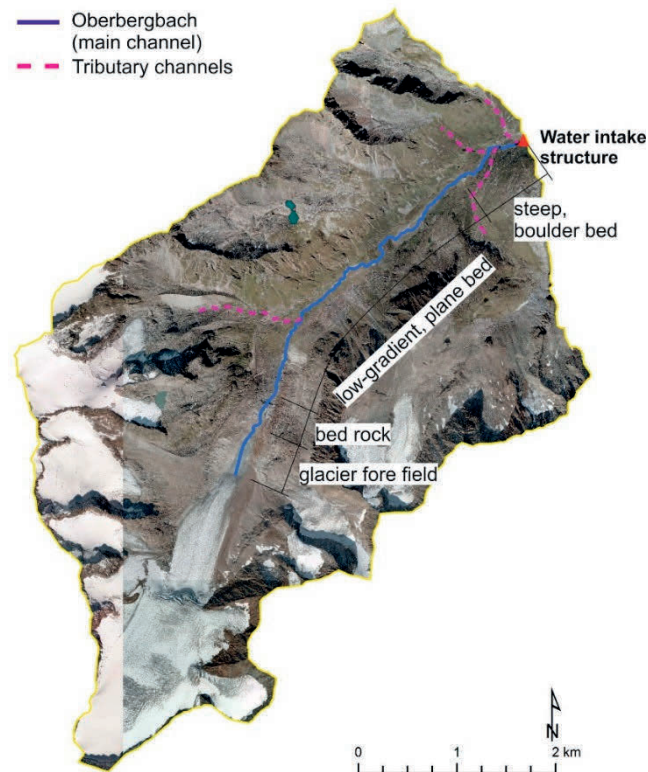


Figure B-64: Overview of the Oberbergbach and the basin that contributes to the runoff at the water intake structure

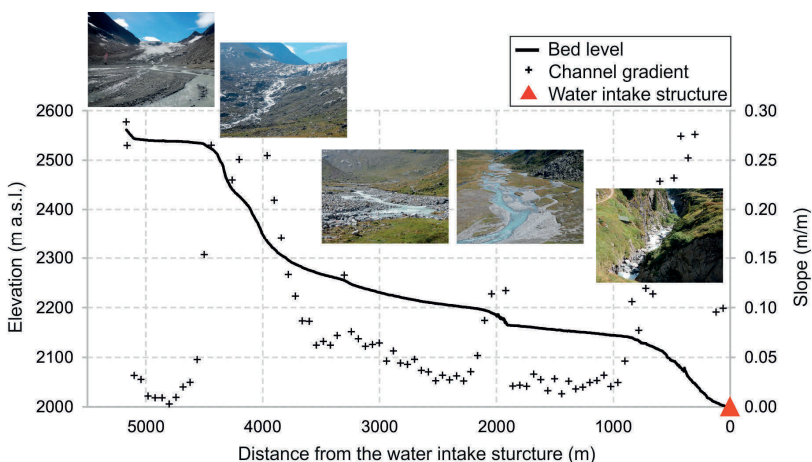


Figure B-65: Longitudinal profile of the bed level and the bed gradient of the Oberbergbach

4.2.2 Pitzbach

The head of the Pitzbach basin is covered by the Mittelberg glacier (Figure B-66). In contrast to the Oberbergbach basin, the recent glacier forefield is rather small, but it's growing in length due to the glacial retreat. It is worth to mention, that the glacier snout was below the location of the water intake structures in the 1850s (Figure B-67).

Downstream of two valley steps, the Pitzbach reveals a broad but coarse-bedded course, with a channel gradient ranging between 0.15 m/m in the upper part and 0.08 m/m at the water intake structure. Single-thread reaches with step-pool morphology dominate, in combination with numerous side bars consisting of loosely bedded boulders.

Since the entire stream was covered by the Mittelberg glacier until 'recently' (1850), the hillslopes of the upper part of the U-shaped valley are still covered by the side moraines. The runoff originating from the several sub-basins incised into the moraines and the file-shaped scars act as a permanent bed load source since then. However, these tributary channels are ephemeral and the water runoff is limited to rainfall events or snowmelt.

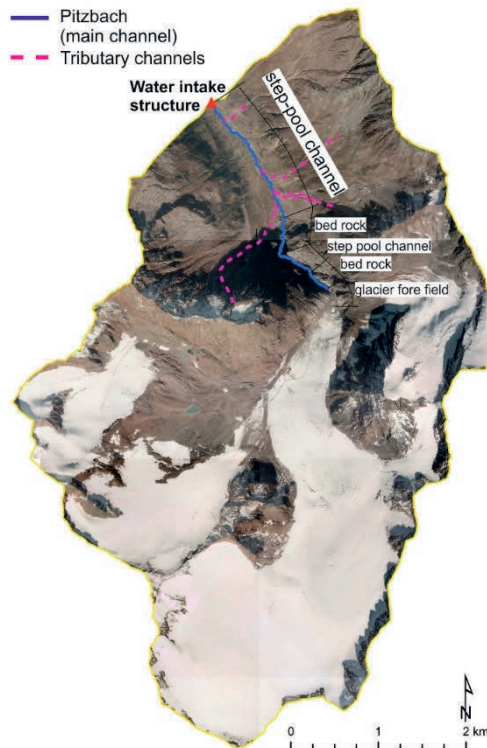


Figure B-66: Overview of Pitzbach and the basin that contributes to the runoff at the water intake structure

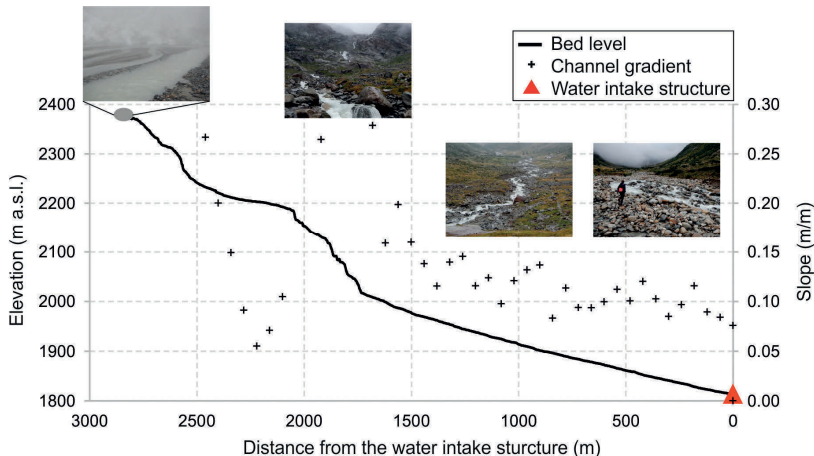


Figure B-67: Longitudinal profile of the bed level and the bed gradient of the Pitzbach

4.2.3 Bed load transport data

The period of data availability differs for both sites and only full year records are used. At the Pitzbach, the bed load transport rates could be determined for the periods 1994 to 1998 and 2000 to 2004, with each period starting on 01/01 and ending on 31/12, respectively. Thus, the Pitzbach data reveal a total time span of 10 years. At the Oberbergbach, the time span of bed load transport data comprises twelve years and includes the years 1998 to 2001, 2004 to 2010 and 2014.

In order to give an impression of the data, bed load transport rate Q_b is plotted against water discharge Q in Figure B-68. The visual interpretation of the Q - Q_b plot reveals a steep increase of $Q_b(Q)$ for discharges larger than approx. $0.5 \text{ m}^3/\text{s}$. In contrast, the correlation with discharge seems very weak and scattered for $Q < 0.5 \text{ m}^3/\text{s}$ at the Oberbergbach, while bed load transport rate is very low and constant for $Q < 0.5 \text{ m}^3/\text{s}$ at the Pitzbach (at least for the period 2002 to 2004; see Figure B-68).

At low bed load transport rates, the uncertainty of the data probably dominates over their magnitude. This is attributed to the inaccuracies of the approach used to derive bed load transport rates. The bed load transport rates analyzed in this study were determined by means of the sediment accumulation within the settling basin of water intake structures. A detailed description on that is given in the sections B.1.3 and B.1.4, but is shortly summarized in the following:

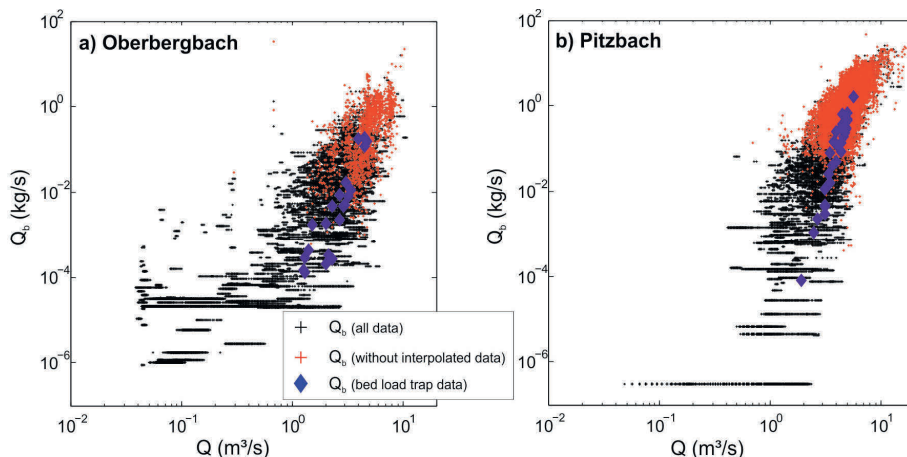


Figure B-68: Bed load transport rate determined by means of the time series of bed load accumulation within the settling basin of a) the Oberbergbach and b) the Pitzbach water intake structure (see section B.1.4). The data of these plots refer to the period a) 2008 to 2010 and b) 2002 to 2004. For comparison, bed load transport rate measured with the bed load traps in the summer seasons 2014 and 2015 (see section B.1.5) and those of Hofer (1985) are additionally included.

Within the settling basin of both water intake structures, the vertical stress that originates from the sediment deposition is measured at the basin's bottom and it is recorded in a 15 minutes interval. The difference between two time steps is associated with the increase of the sediment deposition and yields the average bed load transport rate during these 15 minutes. The vertical stress is transferred to the corresponding deposit height by means of a fitted function of simultaneously measured stress and height. However, the vertical stress is not measured entirely but at distinctive points only. Thus, the corresponding deposit height needs to be integrated over space to obtain the deposit volume. Although the integration procedure is calibrated, there remain uncertainties, which are the more pronounced the smaller the increase of sediment deposition. Possible relocations of the sediment within the settling basin cause small-scale fluctuations of the vertical stress. Due to that, the time series of bed load accumulation does not always increase monotonically (which should be the case in a closed system like the settling basin). Since bed load transport rate is restricted to values larger or equal zero, the time series of sediment accumulation needs to be interpolated over the duration of insignificant increase. By that, the gaps between directly derived bed load transport rates (determined by the volume increase within 15 min) are filled. The linear interpolation is used, resulting in a constant bed load transport rate for several time steps. Especially during long lasting low flows with insignificant sediment increase (typically from autumn to spring), this causes constant bed load transport rates over a wide range of discharges, which can be easily identified in the lower (lower left) part of the Q_b - Q plots in Figure B-68. In addition, the linear interpolation also causes bed load transport rates to be larger than zero at any time. However, any other interpolation method is expected to not enhance data accuracy, but to obscure the measuring uncertainty.

To get rid of the very uncertain data, the subsequent analysis is restricted to bed load transport rates at discharges larger than $0.5 \text{ m}^3/\text{s}$, which is a reasonable estimate of the incipient motion of the finest grain size fractions at both streams. In addition, outliers were identified by means of the very low and very high quantiles. Therefore, the water discharge was classified into groups (bins) with increments ranging from $0.03 \text{ m}^3/\text{s}$ (at low flows) and $0.16 \text{ m}^3/\text{s}$ (at high flows). For each discharge bin, the empiric distribution of observed bed load transport rates was determined in a first step. The 1 % and 99 % quantiles of these empiric distributions were then computed and bed load transport rates de- or exceeding these quantiles were removed. However, in order to account for the better accuracy at high transport rates, the upper threshold was increased up to 99.99 % for large water discharges, respectively. The remaining data are illustrated in Figure B-69.

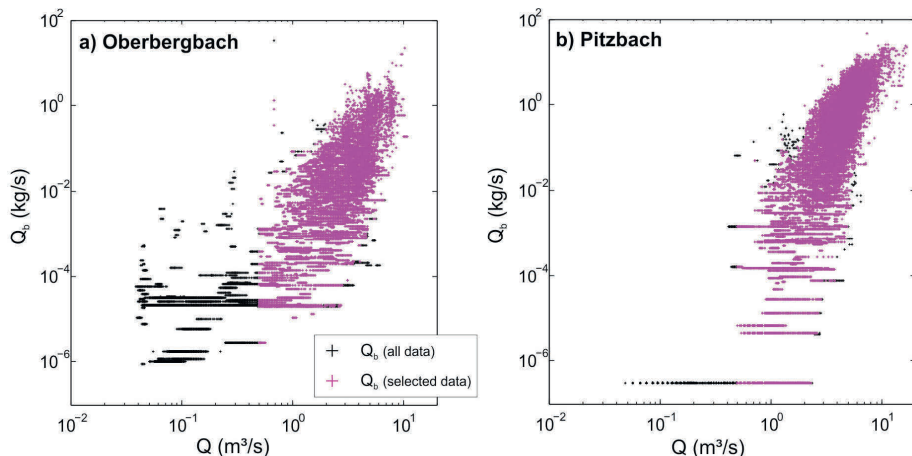


Figure B-69: Selected bed load transport rate data for subsequent analysis (magenta crosses) of a) the Oberbergbach (period 2008 to 2010) and b) the Pitzbach (period 2002 to 2004). For comparison, the total data set is plotted in the background and thus, the visible black crosses correspond with the rejected data.

B.4.3 Methods

4.3.1 Statistics of the $Q-Q_b$ relation

The $Q-Q_b$ relation is first analyzed visually by means of plotting Q against Q_b . The water discharge Q is used in the units of m^3/s within this study, while kg/s is used for Q_b . However, to convert Q_b into the unit m^3/s , a solid density of the bed load of 2650 kg/m^3 is recommended.

To improve the visual impression of the scatter of the $Q-Q_b$ relation, the discharge is classified into logarithmically distributed bins with the lower bound at $0.5 \text{ m}^3/\text{s}$ and an interval of 0.25 in the log-space. Consequently, the width of the discharge bins varies and it is $0.15 \text{ m}^3/\text{s}$ for the bin with the smallest discharges ($0.5 - 0.65 \text{ m}^3/\text{s}$) and attains $2.8 \text{ m}^3/\text{s}$ for the bin with the largest discharges at the Oberbergbach ($10.0 - 12.9 \text{ m}^3/\text{s}$) and $3.7 \text{ m}^3/\text{s}$ for Pitzbach ($12.9 - 16.6 \text{ m}^3/\text{s}$). For each discharge class, the geometric

mean bed load transport rate (binned mean) and the 5 % and 95 % quantiles are computed and illustrated.

Bed load transport rate is then fitted against discharge by means of power functions, either for the total range or piecewise. Therefore, the explanatory (discharge) and the response variable (bed load transport rate) are log-transformed and the ordinary linear regression model as implemented in R (*R Core Team*, 2013) is applied. In the case of piecewise regression, the explanatory variable is split into three groups and a separate trend is fitted to each group with the constraint that they match at the breakpoint. Thus, the piecewise regression enables for both, the assessment of the trends and the identification of breakpoints, respectively.

Since Q_b differs over several orders of magnitude for a constant Q , the scatter of the Q - Q_b relation is investigated in a second step, by using the entire data set. The discharge range is therefore again classified into logarithmically distributed bins. For each discharge class, the empiric density distribution of bed load transport rates is then determined. In a previous study, *Turowski* (2010) tested five theoretical probability functions for the Pitzbach, in particular the Birnbaum-Sanders distribution, the Poisson distribution, the gamma distribution, the Hamamori and the Carey-Hubbel distributions. *Turowski's* data set comprises bed load transport rates of the two years 1994 and 1995. In analogy to this study, the data are based on the records of the load membranes but the conversion towards bed load transport rates differs. In this respect, *Turowski* (2010) used the conversion proposed by *Hofer* (1985 and 1987), which is similar to the conversion of this study but does not account for (i) the pressure relocations due to wall friction and (ii) the amount of suspended load (grain sizes smaller than about 1 mm). However, *Turowski* (2010) concludes that the scatter of bed load transport rates ranges of up to four orders of magnitude and it is reproduced best with the gamma probability distribution. In this study, the fluctuations of Q_b are reanalyzed and the parametric log-normal distribution and the gamma distribution are fitted against bed load transport rates of each discharge class separately. The parameters are estimated according to the maximum likelihood method as it is implemented in the package 'fistdistrplus' (*Delignette-Muller et al.*, 2014) in R (*R Core Team*, 2013). The match between the observed (empiric) distribution of binned Q_b data and the fitted distribution is assessed visually and numerically. For the visual comparison, both, the cumulative probability distribution and the density distribution, of the empiric data and the fitted functions are plotted one upon the others. To assess the match numerically, the cumulative probabilities of the empiric data and the fitted functions are compared in terms of probability-probability plots (PP-plots). The root mean squared error (RMSE) of the residuals is then determined as well as the coefficient of agreement of the identity line ($r^2(\text{PP})$) in the PP-plot.

4.3.2 Year-wise and month-wise power functions

The method described in section 4.3.1 is applied the data of the entire observation period (see section 4.4.1). Consequently, the results give information on the overall variability of bed load transport rate but do not account for any temporal differences. Strictly speaking, the bed load transport rate of a given discharge class might be not independently distributed, but depend on time, which contradicts with a basic assumption of several statistical analyses.

In order to investigate the temporal differences of the Q - Q_b relation, the data set is split into annual and monthly intervals. For each of these data subsets, which are either

year-wise or month-wise segregated, bed load transport rate is fitted against water discharge.

For the year-wise segregated data, power functions $Q_b = \alpha_a Q^{\beta_a}$ are fitted by using the linear regression method with log-transformed input variables. The applicability of power functions is first assessed year-wise by visually examining the diagnostic plots (e.g. Quantile-Quantile plots) of the corresponding linear regression of the log-transformed variables Q and Q_b . In case that the diagnostic plots reveal a poor performance of the linear model, the data are rejected. Otherwise, the model's performance is assessed in respect to the coefficient of determination (r^2) and the discrepancy ratio

$$X = \frac{Q_{b,calculated}}{Q_{b,observed}} \quad (\text{B59})$$

Since power functions are fit to each year separately, the question arises whether or not the coefficients significantly differ with respect to the year. In other words, the coefficients derived for the i th year are compared with those of all other years. Therefore, the power functions are fitted to a data set that comprises the data of the i th year and any other year k . In addition, a dummy variable g is introduced which is $g=0$ for all data referring to the i th year, while it is $g=1$ for the k th year. To test if the coefficients differ significantly between the two years, the multivariate linear model

$$\hat{Y} = \alpha + \beta \hat{X} + \gamma(g \hat{X}) + \delta g \quad (\text{B60})$$

is fitted. Herein, $\hat{Y} = \log(Q_b)$, $\hat{X} = \log(Q)$, g is the dummy variable and α , β , γ and δ are the coefficients to be estimated. Now, if the coefficients γ and δ are significant and thus, significantly differ from zero, both coefficients obtained for the i th year differ significantly from those of the k th year (McDowell, 2005). If γ is not significant, any differences of the model coefficients β_i and β_k are probably by chance and not significant. The same is true for α_i and α_k if δ is insignificant, respectively.

For the month-wise segregated data, a multiple step procedure is applied to examine if the Q - Q_b relations reveal major differences in respect to the month. The time span of discrete months is used because of the hydrologic regime. The hydrology of both mountain streams is associated with a snowmelt and glacier melt regime. Thus, the origin of water discharge consistently differs with respect to time, at least when rain-induced discharge fluctuations are neglected. In the late spring, water flow is predominantly attributed snowmelt and the contributing area shifts from lower altitudes to higher altitudes in course of the early summer. In contrast, glacier melt dominates runoff in late summer and thus, the origin of the major runoff are the glaciated parts of the catchment. In October, water discharge at both sites abruptly decreases and reveals a very minute magnitude until May. These inner-annual shifts of the dominant hydrological regime are attributed to a time scale of about months. Since bed load transport occurs predominately during moderate or high flows, it is limited to the summer half-year. Consequently, only the months from May to September are considered.

For each month m within a given year a , a power function is fitted, with the explanatory variable Q and the response variable Q_b . The median exponent $\beta_{a,m50}$ is then determined for each year separately. At the Oberbergbach, $\beta_{a,m50}$ is the median of the power functions obtained from May to September. In contrast, only the months June to August are used at the Pitzbach, since water discharge in May and September is restricted to

low and moderate flows in some years. The month-wise power functions are then refitted by sharing the same exponent $\beta_{a,m50}$. The steps of this procedure are summarized below:

1. Fitting the power function $Q_b = \alpha_{a,m} Q^{\beta_{a,m}}$ to the monthly (m) data of a given year a
2. Determining the median of the month-wise $\beta_{a,m}$ of the year a ($\beta_{a,m50}$)
3. Fitting the power function $Q_b = m\alpha_{a,m} Q^{\beta_{a,m50}}$ to obtain $m\alpha_{a,m}$ of each month m of the year a
4. Dividing $m\alpha_{a,m}$ by its median in order to obtain the relative magnitude

The factor $m\alpha_{a,m}$ corresponds with Q_b at $Q=1$ and thus, defines the vertical position of the $Q-Q_b$ curve in the log scale. Since the power function of each month (of a certain year) shares the same exponent $\beta_{a,m50}$, bed load transport rate at a given discharge is the higher the higher the factor $m\alpha_{a,m}$. This factor is herein termed as transport efficiency.

It is worth to note, that instead of fitting the factor α of the power functions against the monthly data, also both, the factor and the exponent (as for the year-wise segregated data) or only the exponent could be fitted. However, the scope of this analysis is to compare the monthly $Q-Q_b$ relations and thus, a single parameter is much easier to handle than two parameters which nonlinearly depend on each other.

Contrasting with the year-wise analysis, the month-wise factors $m\alpha_{a,m}$ are scaled by their median to obtain the relative magnitude of α (step 4). This enables a comparison between different years in order to investigate if, for instance, α is consistently large in month i than in month j . Otherwise, the comparison is biased, since the exponent $\beta_{a,m50}$ differs in each year, respectively.

B.4.4 Results

4.4.1 Statistics of the $Q-Q_b$ relation

4.4.1.1 Visual interpretation

For the Oberbergbach, the data set comprises about 170,000 reliable measurements of bed load transport rate and water discharge, observed over a period of ten years. In terms of the $Q-Q_b$ relation, the bed load transport rate Q_b reveals a significant breakpoint Q_{bp1} at a low discharge of $Q_{bp1}=1.4 \text{ m}^3/\text{s}$ (Figure B-70a). At discharges lower than $1.4 \text{ m}^3/\text{s}$, Q_b increases with Q^2 ($\beta_1=2$), while it increases with $Q^{4.3}$ ($\beta_2=4.3$) at higher discharges. Consequently, the rating curves for low and high discharges differ significantly, which is well supported by the geometric means of aggregated (binned) data. In addition, the entire data set, as well as the binned means, suggest a second breakpoint at a discharge of about $7 \text{ m}^3/\text{s}$, where the $Q-Q_b$ relation flattens slightly (in the log-log scale). However, this second breakpoint (Q_{bp2}) is not detected by the segmented regression but roughly corresponds with incipient motion of the bed surface D_{50} (Study C, section 5.5.5).

The bed load transport rate scatters over several orders of magnitude at a given discharge, which is illustrated by the 5 % and 95 % quantiles of the binned data. According to the visual judgement, the scatter range is almost constant for $Q \sim 5 \text{ m}^3/\text{s}$, while it tends to decrease at higher discharges (Figure B-70).

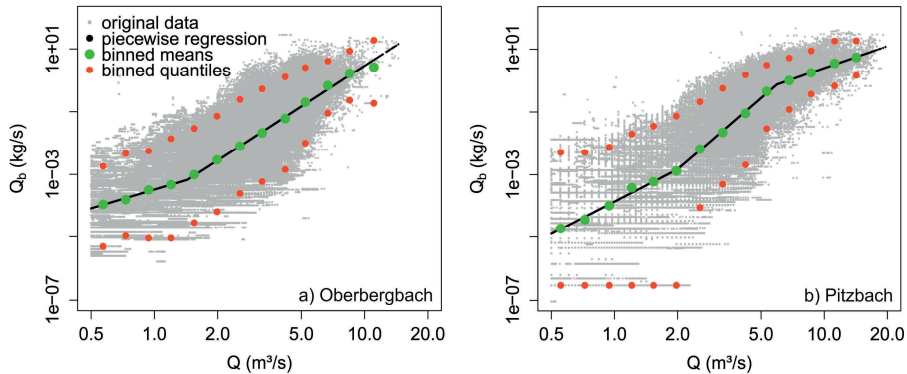


Figure B-70: Bed load transport rate plotted against discharge, with the geometric means (green dots) and 5 % and 95 % quantiles (red dots) of the binned data and the fitted, piecewise regressions

At the water intake of the Pitzbach, the data set comprises bed load transport rates of eight years of observation. The $Q-Q_b$ relation reveals two breakpoints (Figure B-70b). The first breakpoint (Q_{bp1}) is located at a low discharge of about $2 \text{ m}^3/\text{s}$, which is slightly larger than at the Oberbergbach. The second breakpoint appears at a moderate discharge of $Q_{bp2}=5.9 \text{ m}^3/\text{s}$, which is less than the critical discharge of the D_{50} (Study C, section 5.5.5).

The exponent of the lower tail power function is $\beta_1=3.5$, while it increases to $\beta_2=5.7$ for $2 \text{ m}^3/\text{s} < Q < 5.9 \text{ m}^3/\text{s}$. Consequently, the $Q-Q_b$ relation is steeper than at the Oberbergbach ($\beta_2=4.3$). However, at discharges exceeding Q_{bp2} , the log-scaled $Q-Q_b$ relation flattens and reveals an increase of Q_b with $Q^{2.2}$.

The 5 % and 95 % quantiles of the binned data are associated with the scatter of the $Q-Q_b$ relation and the distance between them widens with decreasing discharge. At discharges less than $2.0 \text{ m}^3/\text{s}$, the 5 % quantile is almost constant at a very low rate of $3 \cdot 10^{-7} \text{ kg/s}$. This is attributed to the data inaccuracy that originates from the procedure of determining bed load transport rate at an insignificant increase of the bed load deposition (see section B.1.4).

4.4.1.2 Probability distribution of bed load transport rate

In analogy to section 4.4.1.1, the Q_b data are grouped into logarithmically distributed bins in discharge. For each discharge bin, the empiric probability distribution of bed load transport rates was calculated. As an example, the density distribution and the cumulative probability distribution of the Q_b data within two different discharge bins are plotted in Figure B-71a-b. Furthermore, the lognormal and the gamma distribution are

fitted by using the maximum likelihood estimation. According to Figure B-71, the fluctuations of the Q_b data within the discharge bin $2.2 < Q < 2.9 \text{ m}^3/\text{s}$ are reproduced well with the fitted log-normal distribution, while the deviations are larger for the gamma distribution; regardless of the field site. However, considering the Q_b data of the discharge bin $6.1 < Q < 7.8 \text{ m}^3/\text{s}$, both, the fitted log-normal and the gamma distribution, are close to the empirical distribution.

The observed (empirical) and the fitted cumulative probability distributions are plotted against each other in the PP-plots (Figure B-71c). In the case of a perfect match, the PP-plot coincides with the line of equality, respectively. The deviation between the PP-plot and the line of equality is used as measure of the goodness of fit. It is assessed with the root mean squared error (RMSE) and the coefficient of agreement ($r^2(\text{PP})$). The RMSE and $r^2(\text{PP})$ are calculated for both probability distributions (lognormal and gamma distribution) and each discharge bin separately and they are given in Table B-19. It is evident from Table B-19, that the RMSE of the log-normal distribution is lower than RMSE of the gamma distribution for most discharge bins. Accordingly, the coefficient of agreement between the PP-plot with the lognormal distribution and the line of equality is predominantly larger. The lognormal distribution performs better than the gamma distribution in reproducing the fluctuation of Q_b data of most discharge bins.

Table B-19: Summary of discharge bins used to compare the cumulative probabilities of observed bed load transport rates at the Oberbergbach and the Pitzbach with fitted log-normal, and gamma probability distributions. The abbreviations are as follows: gmQ_b , the geometric mean of bed load transport rates within a certain discharge bin; RMSE, the root mean squared error of observed and fitted the cumulative probabilities and r^2 , the coefficient of variations for the line of equality in the probability-probability plots. Bold numbers indicate the probability function with the better fit.

| Q bins [m ³ /s] | Oberbergbach | | | | | | Pitzbach | | | | | |
|-------------------------------|----------------------------|-------------|----------------|----------------------------|-------------|----------------|----------------------------|-------------|----------------|----------------------------|-------------|----------------|
| | LOG-NORMAL | | | GAMMA | | | LOG-NORMAL | | | GAMMA | | |
| | gmQ _b [kg/s] | RMSE | r ² |
| 0.5 - 0.6 m ³ /s | 1.09E-4 | 0.03 | 0.99 | 0.09 | 0.92 | | 2.10E-5 | 0.05 | 0.97 | 0.11 | 0.87 | |
| 0.6 - 0.8 m ³ /s | 1.55E-4 | 0.03 | 0.99 | 0.11 | 0.88 | | 4.17E-5 | 0.05 | 0.98 | 0.08 | 0.95 | |
| 0.8 - 1.1 m ³ /s | 3.18E-4 | 0.03 | 0.99 | 0.06 | 0.97 | | 1.35E-4 | 0.03 | 0.99 | 0.07 | 0.96 | |
| 1.1 - 1.4 m ³ /s | 4.70E-4 | 0.02 | 1.00 | 0.06 | 0.97 | | 4.75E-4 | 0.04 | 0.99 | 0.05 | 0.98 | |
| 1.4 - 1.7 m ³ /s | 9.85E-4 | 0.02 | 1.00 | 0.10 | 0.89 | | 7.11E-4 | 0.04 | 0.98 | 0.06 | 0.96 | |
| 1.7 - 2.2 m ³ /s | 2.93E-3 | 0.03 | 0.99 | 0.08 | 0.95 | | 1.50E-3 | 0.06 | 0.97 | 0.03 | 0.99 | |
| 2.2 - 2.9 m ³ /s | 8.05E-3 | 0.02 | 1.00 | 0.07 | 0.96 | | 8.16E-3 | 0.02 | 0.99 | 0.06 | 0.98 | |
| 2.9 - 3.7 m ³ /s | 2.13E-2 | 0.03 | 0.99 | 0.07 | 0.97 | | 2.62E-2 | 0.02 | 1.00 | 0.06 | 0.98 | |
| 3.7 - 4.7 m ³ /s | 6.02E-2 | 0.03 | 0.99 | 0.08 | 0.94 | | 1.04E-1 | 0.04 | 0.99 | 0.04 | 0.99 | |
| 4.7 - 6.1 m ³ /s | 2.01E-1 | 0.03 | 0.99 | 0.04 | 0.99 | | 4.60E-2 | 0.05 | 0.98 | 0.01 | 1.00 | |
| 6.1 - 7.8 m ³ /s | 6.70E-1 | 0.02 | 0.99 | 0.05 | 0.98 | | 3.31E-2 | 0.03 | 0.99 | 0.02 | 1.00 | |
| 7.8 - 10 m ³ /s | 1.64E+0 | 0.03 | 0.99 | 0.04 | 0.99 | | 2.79E-2 | 0.02 | 1.00 | 0.05 | 0.98 | |
| 10 - 12.9 m ³ /s | 2.62E+0 | 0.09 | 0.92 | 0.08 | 0.94 | | 4.24E-2 | 0.05 | 0.97 | 0.05 | 0.97 | |
| 12.9 - 16.6 m ³ /s | no data | | | | | | 5.38E-2 | 0.04 | 0.98 | 0.05 | 0.97 | |

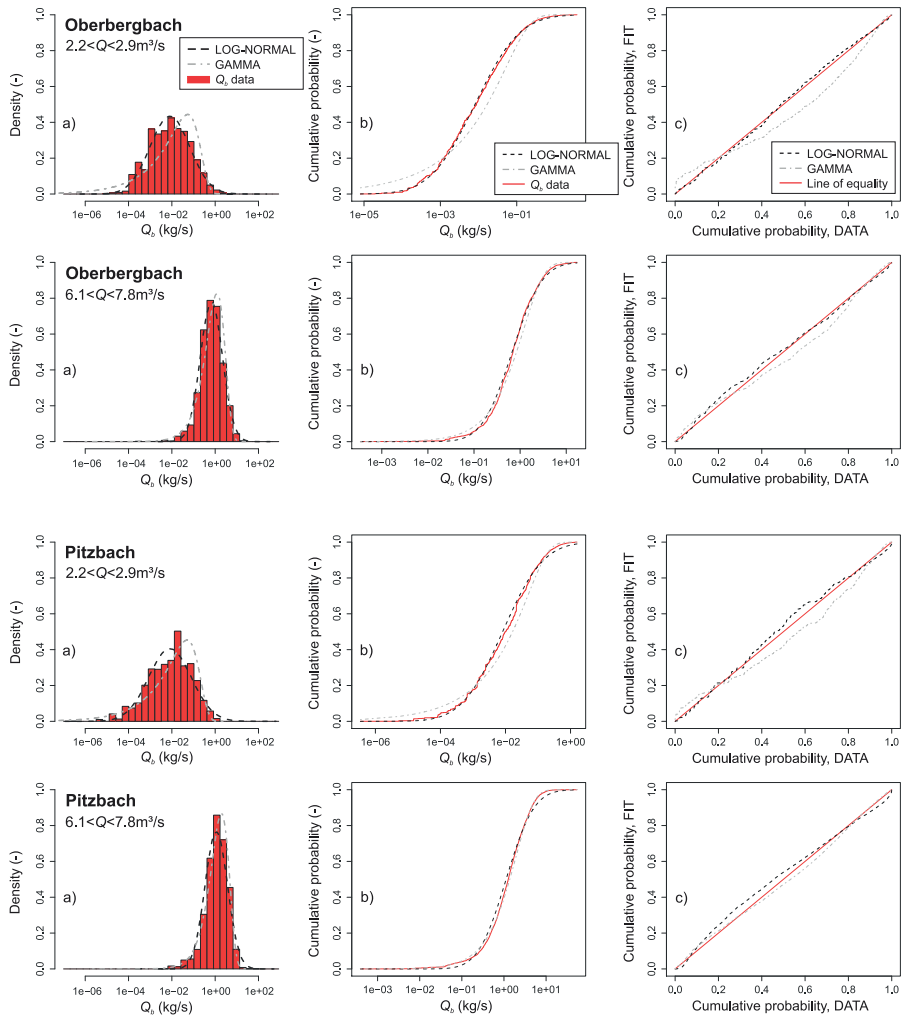


Figure B-71: a) Probability density distribution and b) cumulative probability distribution of the observed of bed load transport rates and the fitted lognormal and gamma distribution for two discharge bins and the two field sites. The cumulative probability distributions of the observed Q_b are plotted those of the fitted lognormal and the fitted gamma distribution in c) (PP-plots).

In a second step, the relationship between the scatter of the Q_b data and the magnitude of water discharge is assessed. Plotting the standard deviation of bed load transport rates $\text{sd}(Q_b)$ of each bin against the corresponding discharge reveals a positive relation (Figure B-72a). It is well described with the power law fits given in Figure B-72a.

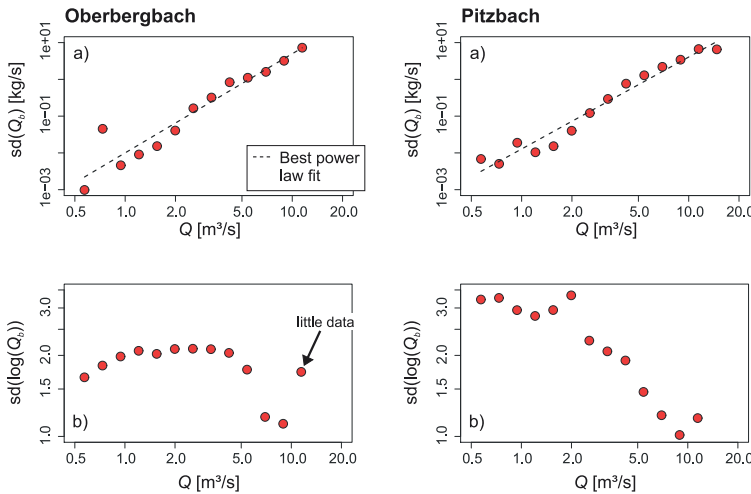


Figure B-72: Variation of the standard deviation of a) bed load transport rate Q_b [kg/s] and b) log-transformed bed load transport rate with discharge for each bin. The left plots refer to the Oberbergbach data and the right plots to the Pitzbach data.

However, the Q_b data of each bin are log-normally distributed and thus, the standard deviation of log-transformed bed load transport rate $sd(\log(Q_b))$ seems more appropriate for comparing the scatter of different bins. Indeed, the relationship between $sd(\log(Q_b))$ and Q differs and somehow reveals a negative relationship. This is strong pronounced for the Pitzbach data (left plot in Figure B-72b), while $sd(\log(Q_b))$ shows a constant level for moderate discharges but decreases at high discharges at the Oberbergbach. In this respect, the large $sd(\log(Q_b))$ at the maximum discharge of the Oberbergbach is attributed to the low number of observations ($n=53$).

4.4.2 Fitted power functions

4.4.2.1 Year-wise power functions

Initially, power functions were fitted to year-wise segregated data. Although the coefficients are highly significant, the diagnostic plots of the regression reveal considerable discrepancies, suggesting the power function not suitable for a rating curve of $Q-Q_b$. For instance, the residuals are occasionally not uniformly distributed over the range of Q , indicating a non-linear relationship of log-transformed variables. This corresponds with the observation of breakpoints in section 4.4.1.1, which are not accounted for by the power functions.

To overcome these problems, only those data are used which exceed the first breakpoint and fall below the second breakpoint of the entire data set (section 4.4.1.1). For those years where the fitted power functions still reveal a poor performance, the data are rejected for subsequent analysis.

The coefficients of the year-wise power functions are given in Table B-20. The large scatter of the $Q-Q_b$ relation preserves even at the annual level. For instance, the discrepancy ratio (equation B59) is on average as low as 30 % for the range [0.5;2], which

means that 70 % of the observed bed load transport rates deviate from the power function more than a factor of 2. However, the discrepancy ratio increases to about 80 % by considering a range of one order of magnitude, which is [0.1,10], respectively.

Table B-20: Fitted power functions of the $Q-Q_b$ relations, with the r^2 and the discrepancy ratio X used to determine their performance

| Year | Oberbergbach | | | | | Pitzbach | | | | |
|------|--|---------|-------|-------------------|----------|--|---------|-------|---------|----------|
| | $Q_b [\text{kg/s}] = \alpha * Q [\text{m}^3/\text{s}]^\beta$ | | | | | $Q_b [\text{kg/s}] = \alpha * Q [\text{m}^3/\text{s}]^\beta$ | | | | |
| | α | β | r^2 | 0.5<X<2 | 0.1<X<10 | α | β | r^2 | 0.5<X<2 | 0.1<X<10 |
| 1994 | | | | | | | | | | |
| 1995 | | | | | | | | | | |
| 1996 | | | | no data available | | | | | | |
| 1997 | | | | | | | | | | |
| 1998 | 4.9E-5 | 4.9 | 0.53 | 26% | 74% | | | | | |
| 1999 | | | | data rejected | | | | | | |
| 2000 | 1.7E-4 | 4.4 | 0.53 | 34% | 85% | | | | | |
| 2001 | 1.4E-4 | 4.7 | 0.61 | 36% | 86% | | | | | |
| 2002 | | | | no data available | | | | | | |
| 2003 | | | | | | | | | | |
| 2004 | | | | data rejected | | | | | | |
| 2005 | 2.4E-4 | 3.8 | 0.37 | 26% | 78% | | | | | |
| 2006 | 2.2E-4 | 4.1 | 0.49 | 28% | 82% | | | | | |
| 2007 | 1.9E-4 | 4.1 | 0.48 | 31% | 85% | | | | | |
| 2008 | 5.6E-5 | 5.2 | 0.47 | 23% | 69% | | | | | |
| 2009 | 1.1E-4 | 5.1 | 0.53 | 26% | 79% | | | | | |
| 2010 | 7.2E-4 | 4.3 | 0.50 | 29% | 82% | | | | | |
| 2011 | | | | no data available | | | | | | |
| 2012 | | | | | | | | | | |
| 2013 | | | | | | | | | | |
| 2014 | | | | data rejected | | | | | | |

The year-wise rating curves reveal significant differences for most of the years regarding both, the factor α_a and the exponent β_a (Table B-21 and Table B-22). For all years either α_a or β_a differs significantly.

Plotting α_a and β_a against each other, suggests for a weak correlation (Figure B-73b), with low factors associated with high exponents and vice versa. In contrast, the correlation diminishes when the coefficients are standardized with their median Figure B-73c, simply because the standardized α_a scatters over a much wider range than the standardized β_a .

Table B-21: Comparison of the factors α_a and the exponents β_a from the year-wise regressions with the Oberbergbach data set in terms of significant differences: 1 refers to non-significant and empty cells to significant difference

| Year | Non-significant difference of α_a | | | | | | | | | | | Year | Non-significant difference of β_a | | | | | | | | | | | | |
|------|--|------|------|------|------|------|------|------|------|------|------|------|---|------|------|------|------|------|------|------|------|------|------|------|--|
| | 1998 | 1999 | 2000 | 2001 | 2004 | 2005 | 2006 | 2007 | 2008 | 2009 | 2010 | | 1998 | 1999 | 2000 | 2001 | 2004 | 2005 | 2006 | 2007 | 2008 | 2009 | 2010 | 2014 | |
| 1998 | 1 | | | | | | | | 1 | | | 1998 | 1 | | | | | | | | | | | | |
| 1999 | | | | | | | | | | | | 1999 | | | | | | | | | | | | | |
| 2000 | | | 1 | 1 | | | | | | | | 2000 | | | 1 | | | | | | | | | | |
| 2001 | | | | 1 | | | | | | | | 2001 | | | | 1 | | | | | | | | | |
| 2004 | | | | | | | | | | | | 2004 | | | | | | | | | | | | | |
| 2005 | | | | | | | | | | | | 2005 | | | | | | | | | | | | | |
| 2006 | | | | | | | | | | | | 2006 | | | | | | | | | | | | | |
| 2007 | | | | | | | | | | | | 2007 | | | | | | | | | | | | | |
| 2008 | 1 | | | | | | | | | | | 2008 | | | | | | | | | | | | | |
| 2009 | | | | | | | | | | | | 2009 | | | | | | | | | | | | | |
| 2010 | | | | | | | | | | | | 2010 | | | | | | | | | | | | | |
| 2014 | | | | | | | | | | | | 2014 | | | | | | | | | | | | | |

Table B-22: Comparison of the factors α_a and the exponents β_a from the year-wise regressions with the Pitzbach data set in terms of significant differences: 1 refers to non-significant and empty cells to significant difference

| Year | Non-significant difference of α_a | | | | | | | | | | | Year | Non-significant difference of β_a | | | | | | | | | | | |
|------|--|------|------|------|------|------|------|------|------|------|------|------|---|--|--|--|--|--|--|--|--|--|--|--|
| | 1994 | 1995 | 1996 | 1997 | 1998 | 2000 | 2001 | 2002 | 2003 | 2004 | 1994 | | 2004 | | | | | | | | | | | |
| 1994 | 1 | | | | | | | | | | 1994 | | | | | | | | | | | | | |
| 1995 | | 1 | | | | | | | | | 1995 | | | | | | | | | | | | | |
| 1996 | | | 1 | | | | | | | | 1996 | | | | | | | | | | | | | |
| 1997 | | | | 1 | | | | | | | 1997 | | | | | | | | | | | | | |
| 1998 | | | | | 1 | 1 | | | | | 1998 | | | | | | | | | | | | | |
| 2000 | | | | | | 1 | 1 | | | | 2000 | | | | | | | | | | | | | |
| 2001 | | | 1 | | | | 1 | | | | 2001 | | | | | | | | | | | | | |
| 2002 | | | | | | | | 1 | | | 2002 | | | | | | | | | | | | | |
| 2003 | | | | | | | | | 1 | | 2003 | | | | | | | | | | | | | |
| 2004 | | | | | | | | | | 1 | 2004 | | | | | | | | | | | | | |

The power law rating curves are plotted in the Q-Q_b plots in Figure B-73a. Some of the rating curves are almost parallel, but shifted along the vertical axes, while the others seem rotated. The year-wise rating curves reveal an overall scatter of about one order of magnitude, independent of the field site. At the Oberbergbach, the rating curves are closer to each other for many years, with some outliers. In contrast, the rating curves are more uniformly distributed over the range of total scatter at the Pitzbach.

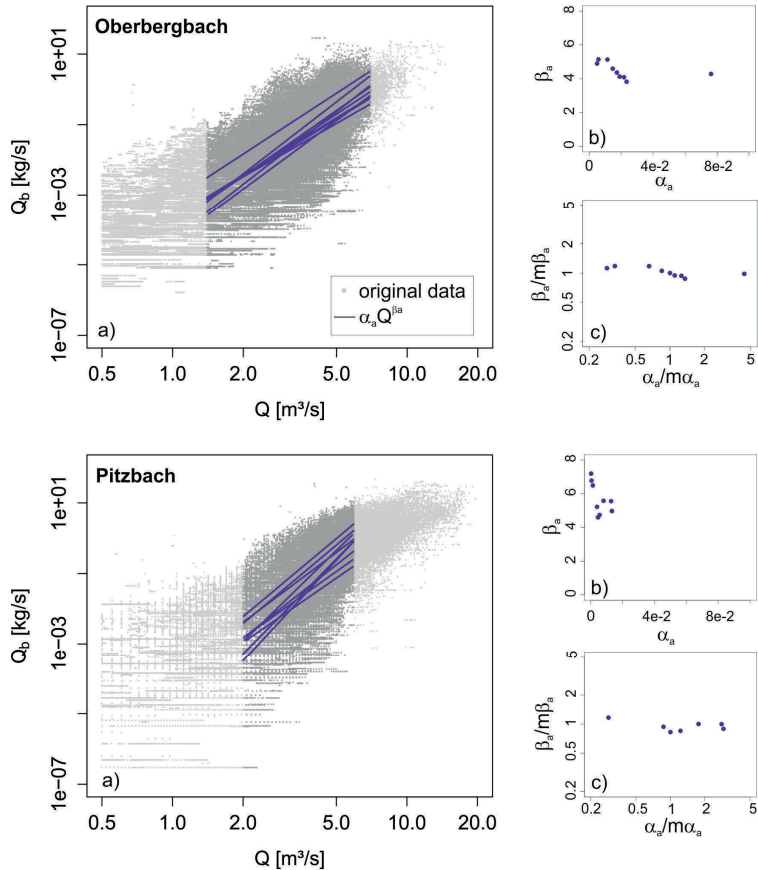


Figure B-73: a) Year-wise, power law rating curves for discharges exceeding breakpoint 1 and falling below breakpoint 2; b-c) the coefficients of the year-wise power functions plotted against each other either in terms of absolute values (b) or standardized by the median (c).

4.4.2.2 Month-wise power functions

Power functions are fitted against month-wise segregated data, in order to investigate if there are any differences in terms of bed load transport efficiency. Transport efficiency is herein defined as the vertical location of the rating curves and thus, associated with the factor α of the power functions. To enable a comparison, the exponent of the power function was kept constant and defined by the month-wise median of each year. Consequently, all rating curves of a certain year reveal the same slope when they are plotted at the log-scale (Figure B-74). In accordance with the year-wise application of power functions, only those Q - Q_b data pairs are used which exceed to first breakpoint and fall below the second breakpoint of the entire data set (section 4.4.1.1), respectively.

At the Oberbergbach, the binned bed load transport rates plot on average lower in the early summer than in the late summer (dots in Figure B-74). Consequently, the mean amount of bed load transported at a given discharge is higher in the late summer. This is well supported by the month-wise rating curves, which are located higher for the months of the late summer. For nine out of twelve years, transport efficiency is largest either in the months of August or September (e.g. Figure B-74). For the remaining three years, bed load transport efficiency is highest for the very early summer month May.

The opposite is the case at the Pitzbach (Figure B-74). The month-wise factor α and thus, bed load transport efficiency is largest in the early summer. In eight out of ten years, the maximum of $ma_{m,a}$ is obtained either for the months May or June.

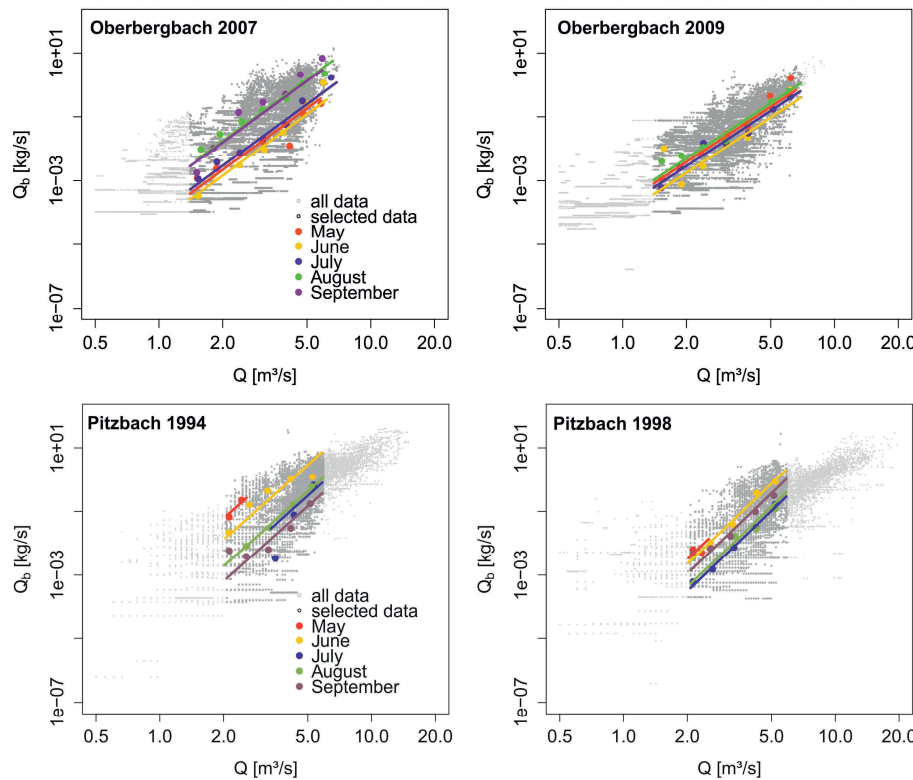


Figure B-74: Q-Q_b plots of year-wise segregated data in combination with the binned means of month-wise data (colored dots) and the corresponding month-wise rating curves (colored lines).

The factors $\alpha_{a,m}$ of the month-wise fitted power functions (with a predefined exponent) are standardized by their year-wise median. Thus, a value larger than unity indicates that the corresponding $\alpha_{j,i}$ (transport efficiency of the i th month and j th year) is larger than the median α of the j th year.

The standardized variables are plotted as boxplots in Figure B-97. Each boxplot includes the standardized, month-wise transport efficiency of all years of observation. As evident from the example plots in Figure B-74, the standardized factors $\alpha_{a,m}$ consistently differ with respect to the month. At the Oberbergbach, they are on average higher in the late summer and occasionally in May, which is associated with a higher transport efficiency in these months. Consequently, transport efficiency is lowest in the mid-summer months June to July.

At the Pitzbach, bed load transport efficiency on average decreases in course of the year. It is highest in the months May and June, while lower in July to September. It is evident from Figure B-75 that the standardized factors of the months May and September reveal a much wider range than for the remaining months. Since the factors are standardized, the scatter does not represent the variability of bed load transport efficiency in terms of absolute values. It only gives information about the variability with respect to the year-wise median transport efficiency. For instance, considering the September at the Pitzbach, the transport efficiency is lower than the year-wise median ($\alpha_{a,m} / m \alpha_{a,m} = 1$) for about 70 % of all years. Within these 70 %, it is sometimes lower but close and sometimes much lower than the year-wise median.

Next to that, the standardized, month-wise $\alpha_{a,m}$ reveals a broader overlapping range at the Pitzbach. For example, the transport efficiency in June is not always but more likely higher than in August. In contrast, the boxplots are less overlapping at the Oberbergbach, particularly in the months June to August (Figure B-79). In this respect, the transport efficiency during August was always higher than in June. Consequently, the month-wise differences of the transport efficiency are more consistent at the Oberbergbach than at the Pitzbach.

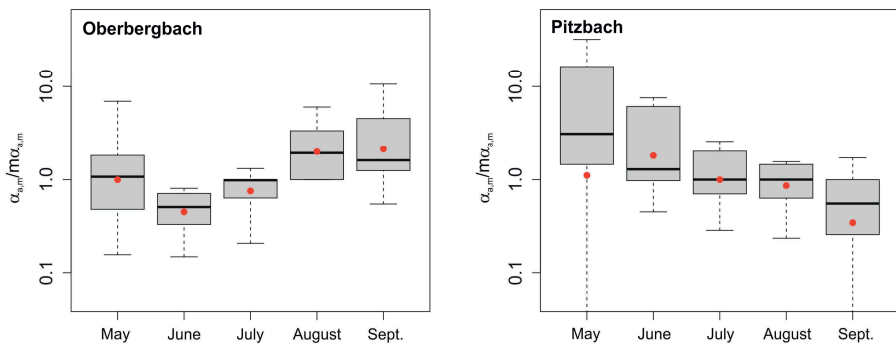


Figure B-75: Boxplot of the month-wise determined $\alpha_{a,m}$ which were standardized by their year-wise median; the red dots represent the arithmetic mean, the bold black line the median, the grey boxes include the 25 % and 75 % percentiles and the whiskers extend to the minimum and maximum.

B.4.5 Discussion

4.5.1 Breakpoints of the Q-Q_b relation

Although the Q-Q_b data pairs scatter over a range of several orders of magnitude, their statistics confirm a nonlinear relationship and the existence of distinct breakpoints. *Bathurst* (2007) as well as *Ryan et al.* (2002) associated the breakpoint of a Q-Q_b relation to the shift from phase 1 to phase 2 transport conditions (the definition of these different phases of bed load transport in steep mountain streams is given in chapter A *Introduction*). According to their data, the breakpoint is close but on average slightly lower than the 1.5 years flow ($Q_{1.5a}$), an often used surrogate for bankful discharge. In both of these studies, the breakpoint was determined by means of linear regressions of Q and Q_b and they found a steeper gradient of the Q-Q_b relation at discharges exceeding the breakpoint.

In this study power functions are fitted, since a linear model is inappropriate because of the residual's statistics. However, there appear two breakpoints: one at a low discharge and another one at a moderate (Pitzbach) or high flow (Oberbergbach). Assuming the shift from phase 1 to phase 2 transport not too far from $Q_{1.5a}$ (which is 8.7 m³/s for the Oberbergbach and 12.9 m³/s for the Pitzbach, respectively), the shift from phase 1 to phase 2 is associated with the second breakpoint.

The question arises how the first breakpoint can be interpreted? The onset of significant bed load transport at the Pitzbach was recently discussed by *Turowski et al.* (2011). Their data are derived from the indirect measurement of bed load transport rate by means of piezo-electric crystals mounted under a steel plate. This measurement device is installed at the weir of the water intake structure of the Pitzbach and it enables to determine the impact of transported bed load coarser than about 20 mm (*Rickenmann and Mc Ardell*, 2007). The critical discharge of grains coarse enough to impact the plate varied from one to another bed load transport event, suggesting a single critical discharge inappropriate to characterize incipient motion (*Turowski et al.*, 2011). However, the overall minimum flow at which significant bed load transport was observed is about 1.5 m³/s. This is close to the first breakpoint Q_{bp1} , which is 2.0 m³/s and corresponds with an average transport rate as low as about 0.001 kg/s or an average specific transport rate of 2e⁻⁴ kg/s/m, respectively. In a consequence, Q_{bp1} is attributed to the shift from the marginal transport of sand-sized sediment to significant bed load transport, revealing a strong increase with discharge and possibly including gravel-sized sediment. In contrast, Q_{bp2} is associated with the transition between phase 1 and phase 2 transport and thus, the significant mobilization of coarse grains ($\sim D_{50}$).

4.5.2 Variability of the Q-Q_b relation

The scatter of the Q-Q_b relation is log-normally distributed, but the results suggest for an interdependence with time. The power functions obtained with year-wise segregated data differ significantly, spanning over 1.5 orders of magnitude in terms of the factor a_a . As *Turowski et al.* (2011) pointed out for the onset of gravel transport, the variability of the Q-Q_b relation may be related to changes in the morphologic patterns at the bed surface, such as the bed surface grain size distribution or the spatial arrangement of the grains. The reason for a change of these morphologic patterns is

either the break-up of the bed surface and the subsequent release of subsurface sediment, or the supply of bed load from upstream reaches (or hillslopes).

The break-up of the bed surface is restricted to high flow events that are large enough to destroy the steps and to mobilize keystones (Turowski *et al.*, 2009; Lenzi *et al.*, 2004). In a consequence, the year-wise differences of the Q - Q_b relation should be somehow correlated with the occurrence of high flow events. According to *Study A* (section B.3), the year-wise differences of bed load transport efficiency are not correlated with the annual peak flow. The consistent difference of month-wise segregated Q - Q_b relations (transport efficiency) additionally contradicts with this hypothesizes: the transport efficiency is highest in May and June at the Pitzbach and in August and September at the Oberbergbach, but high flow events are most likely in July and August at both sites.

In contrast, the supply from upstream reaches or from outer-channel sources results from complex mechanisms, which include the mobilization from the sediment source and its travel through the channel system to the study site. Mao *et al.* (2014) attributed the seasonal increase of the transport efficiency in the Suldar River (Italy) to the alteration of the main sediment sources which are the loosely bedded sediment accumulations and the banks of the lower channel in the early summer and the glacial and periglacial areas in the late summer.

A seasonal increase of the transport efficiency during phase 1 conditions is also evident at the Oberbergbach, at least from June to August. In contrast, the Pitzbach data reveal a seasonal decrease, with the highest transport efficiency in May and the lowest in September. At both streams, the runoff generation is dominated by snowmelt in the early summer, while it predominantly originates from glacier melt in late summer. But, what is the reason for this opposed temporal evolution of transport efficiency?

The basins of both streams are almost equal in size (27 km² at the Pitzbach and 24 km² at the Oberbergbach), while the relative glacier area is larger at the Pitzbach (46 % vs. 28 %), expecting a stronger influence of glacier melt on runoff and sediment supply. However, the longitudinal profile and the morphology of both streams as well as the connectivity with the tributary channels differ.

At the Oberbergbach, the distance from the glacier snout to the water intake structure is about 5 km and the stream reveals a low-gradient water course with braided and single-thread reaches over a total length of about 3 km. Although there are several lateral sub-basins, the sediment connectivity is limited, but the inner-channel bed load accumulations along the low-gradient reaches suggest a high supply of mobile bed load. Both of these patterns (the longitudinal profile and the limited sediment connectivity of the tributaries and the main channel) are quite similar with the study site of Mao *et al.* (2014; the Suldar River); a possible reason for sharing the same temporal evolution of transport efficiency.

In contrast, the distance between the glacier snout and the measuring station is less than 3 km at the Pitzbach and the main channel course is steep and boulder-bedded, with a total length of about 1.7 km. In addition, the tributary channels that enter the main channel are active bed load suppliers. In this respect, Hofer (1985) found a higher transport efficiency during rainfall events at the Pitzbach, which he suggests to result from the additional bed load inflow from the ephemeral tributary channels. However, bed load supply from the tributaries may not be limited to rainfall events but additionally occurs during snowmelt in the early summer. This bed load supply from the tributary

channels might be a reason for the contrary temporal evolution of transport efficiency at both streams.

In accordance with *Mao et al.* (2014), the seasonal increase of transport efficiency at the Oberbergbach is attributed to the increased mobilization of highly abundant and mobile sediment at the glacier forefield during the late summer; simply because the proportion of runoff originating from the glacier increases in course of the summer due to the shift from a snowmelt towards a glacier melt regime. This seasonal increase of bed load supply from the glacier forefield is likely to emerge also at the Pitzbach too, but the bed load supplied from the tributary channels during the snowmelt season might superimpose this trend. Since the magnitude of snowmelt in a certain year differs with respect to the magnitude of snowfall in previous winter, this hypothesizes coincides with the variable nature of transport efficiency in May and June at the Pitzbach (Figure B-75). A proof of this hypothesizes is in need for further research, but little evidence is provided by Figure B-76, where the geometric means of the month-wise binned bed load transport rates of both field sites are plotted against discharge.

Considering the entire data set of both streams (left side of Figure B-76), the average (of log-transformed) bed load transport rates occurring at a certain discharge level in June are higher at the Pitzbach. But, this exceedance is limited to discharges smaller than about $7 \text{ m}^3/\text{s}$. In contrast, the binned means of both sites overlap in July, while the binned means of the Pitzbach are slightly lower in August. This is again limited to moderate discharges, less than $6 \text{ m}^3/\text{s}$.

Since the magnitude of snowmelt and glacier melt depend on the weather, with a warm summer promoting glacier melt and a snowy winter contributing to intense snowmelt, their contribution to total runoff may differ in certain years. Considering the overlapping periods of data availability only (Table B-9), the binned bed load transport rates obtained at the Pitzbach still plot higher in June, while they overlap in August. Two conclusions can be drawn from Figure B-76.

First, the seasonal differences between both streams are limited to phase 1 transport conditions. In this respect, it has to be stated, that the match of the Q - Q_b relation at high discharges is probably by chance, but likely related to the similar characteristics of both reaches at the water intake structures. But the differences of the Q - Q_b relation at lower discharges (with the Pitzbach plotting higher in early summer and almost equal in late summer) must be associated with differences in the temporal evolution of bed load supply conditions. Since these differences are limited to phase 1 conditions, the effect of small-scale changes in bed load supply is probably limited to phase 1 transport conditions as well.

Second, the similar Q - Q_b relations of both sites in July and August suggest a similar contribution of the glacier on bed load transport. Thus, the difference of the seasonal patterns is associated with the difference in the early summer rather than an overall opposite behavior. A possible reason is the bed load entering from the tributaries during snowmelt, but this hypothesizes is in need for additional research.

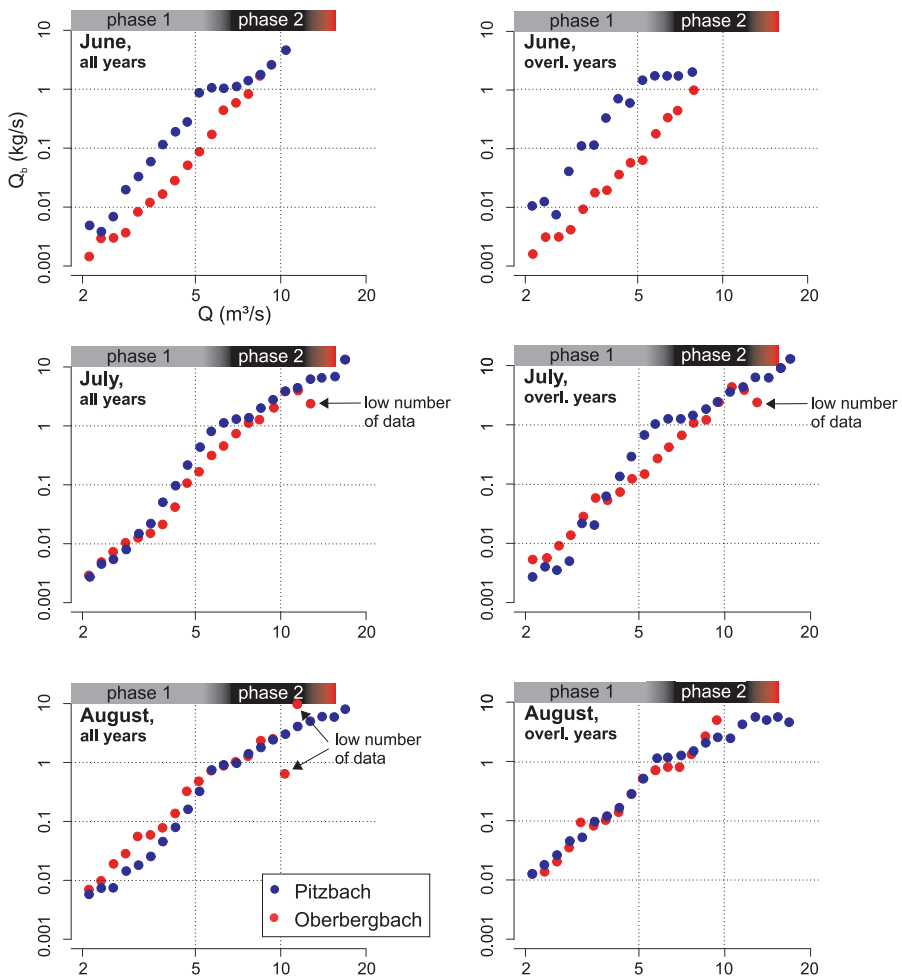


Figure B-76: Binned means of the Q - Q_b relation with month-wise separated data. In the left plots the entire data set, comprising several years of observation, is used, while the Q and Q_b data are restricted to the overlapping years (1998, 1999 and 2001) in the right plots.

B.4.6 References of Study B

- Barry, J. J., J. M. Buffington, and J. G. King (2004), A general power equation for predicting bed load transport rates in gravel bed rivers, *Water Resour. Res.*, 40, W10401, doi: 10.1029/2004WR003190.
- Bathurst, J. C. (2007), Effect of coarse surface layer on bed-load transport, *J. Hydraul. Eng.*, 133(11), 1192-1205.
- Bathurst, J. C. (2013), Critical conditions for particle motion in coarse bed materials of nonuniform size distribution, *Geomorphology*, 197, 170-184.
- Bunte, K., S. R. Abt, K. W., Swingle, D. A. Cenderelli, and J. M. Schneider (2013), Critical Shields values in coarse-bedded steep streams, *Water Resour. Res.*, 49, 7427-7447, doi: 10.1002/2012WR012672.

- Delignette-Muller, M. L., R. Pouillot, J.-B. Denis and C. Dutang (2014), fitdistrplus: help to fit of a parametric distribution to non-censored or censored data, R package version 1.0-2.
- Garcia, C., J. B. Laronne, and M. Sala (2000). Continuous monitoring of bed load flux in a mountain gravelbed river, *Geomorphology*, 34, 23-31.
- Garcia, C., H. Cohen, I. Reid, A. Rovira, X. Ubeda, and J. B. Laronne (2007), Process of initiation of motion leading to bed load transport in gravel-bed rivers, *Geophys. Res. Lett.*, 24, L06403, doi: 10.1029/2006GL028865.
- Habersack, H. M., and J. B. Laronne (2001), Bed load texture in an alpine gravel bed river, *Water Resour. Res.*, 37(12), 3359-3370.
- Hofer, B. (1985), Der Feststofftransport von Hochgebirgsbächen am Beispiel des Pitzbachs (Sediment transport of mountain streams: example of Pitzbach stream), Ph.D. thesis, Univ. Innsbruck, Innsbruck, Austrian, 131 p (in German).
- Lenzi, M. A., L. Mao, and F. Comiti (2004), Magnitude-frequency analysis of bed load data in an Alpine boulder bed stream, *Water Resour. Res.*, 40, W07201, doi: 10.1029/2003WR002961
- Mao, L., A. Dell'Agnese, C. Huincache, D. Penna, M. Engel, G. Niedrist and F. Comiti, (2014), Bedload hysteresis in a glacier-fed mountain river, *Earth Surf. Proc. Land.* 39, 964–976, doi: 10.1002/esp.3563
- McDowell, A. (2005), Testing the equality of coefficients across independent areas, available from Internet: [<http://www.stata.com/support/faqs/statistics/test-equality-of-coefficients/>], received on 13/08/2016.
- R Core Team (2013). R: A language and environment for statistical computing. R Foundation for Statistical Computing, Vienna, Austria. URL <http://www.R-project.org/>.
- Recking, A. (2012), Influence of sediment supply on mountain streams bedload transport, *Geomorphology*, 175-176, 139-150, doi: 10.1016/j.geomorph.2012.07.005.
- Rickenmann, D. (2001), Comparison of bed load transport in torrents and gravel bed streams, *Water Resour. Res.*, 37(12), 3295-3305.
- Rickenmann, D., and B. W. McArdell (2007), continuous measurement of sediment transport in the erlenbach stream using piezoelectric bedload impact sensors, *Earth Surf. Process. Landforms*, 32, 1362-1378, doi: 10.1002/esp.1478.
- Ryan, S. E., L. S. Porth, and C. A. Troendle (2002), Defining phases of bedload transport using piecewise regression, *Earth Surf. Proc. Land.*, 27, 971-990, doi: 10.1002/esp.387.
- Turowski, J. M., E. M. Yager, A. Badoux, D. Rickenmann, and P. Molnar (2009), The impact of exceptional events on erosion, bed load transport and channel stability in a step-pool channel, *Earth Surf. Proc. Land.*, 34, 1661-1673, doi: 10.1002/esp.1855.
- Turowski, J. M. (2010), Probability distributions of bed load transport rates: A new derivation and comparison with field data, *Water Resour. Res.*, 46, W08501, doi: 10.1029/2009WR008488.
- Turowski, J. M., A. Badoux, and D. Rickenmann (2011), Start and end of bed load transport in gravel-bed streams, *Geophys. Res. Lett.*, 38, L04401, doi: 10.1029/2010GL046558.

B.5 Study C: Fractional bed load transport in steep mountain streams

B.5.1 Introduction

5.1.1 Bed load transport relations

In terms of empiric bed load transport relations, two different concepts are commonly used. The first concept refers to threshold-based formulae, where bed load transport is a function of excess flow strength

$$Y_b = k \times (X - X_c)^\alpha, \quad (\text{B61})$$

with Y_b a parameter of bed load transport rate, X a parameter of flow strength (usually dimensionless shear stress τ^* or specific discharge q), X_c the flow strength required to mobilize bed load (incipient motion), and k and α empiric coefficients. There are several threshold-based bed load transport equations available in the literature, where the *Meyer-Peter and Mueller* (1949) equation (MPM) is probably the most famous. According to the MPM equation, bed load transport intensity (ϕ) is in its simplest form a function of dimensionless excess shear stress ($\tau^* - \tau_c^*$)

$$\phi = 8(\tau^* - \tau_c^*)^{1.5}, \text{ with} \\ \phi = \frac{q_b}{\sqrt{(s-1)gD^3}}, \quad \tau^* = \frac{r_h S}{(s-1)D}, \quad \tau_c^* = 0.047 \quad (\text{B62})$$

Herein q_b (m^2/s) is the specific bed load transport rate, s (-) specific solid density, g (m/s^2) gravitational acceleration, D (m) grain size, r_h (m) hydraulic radius and S (m/m) bed gradient. It is worth to note that threshold-based bed load transport formulae are not limited to shear stress as the dependent variable. Especially in studies dealing with steep channels, specific discharge (*Rickenmann*, 1990; *Rickenmann*, 2001) or dimensionless specific discharge (*Ghilardi*, 2013) are often used instead.

However, threshold-based equations often lack in reproducing bed load transport rates derived from field measurements (e.g. *Recking*, 2010; *Gomez and Church*, 1989), which are often associated with low bed load transport intensities. In this respect, the definition of incipient motion is crucial, since the log-log rating curves obtained by threshold-based formulae are usually very steep for flows barely exceeding incipient motion and predict zero transport for $X < X_c$ (Figure B-77).

At discharges close to incipient motion, bed load transport is usually limited to small grain sizes; at least in wide graded mountain streams. In this respect, *Jackson and Beschta* (1982) classified bed load transport into two phases, and *Recking* (2012a) extended this classification to three phases, respectively. Phase 1 refers to moderate flows, where small grains are mobilized from patches of fines or from external sources, but coarse grains are not mobilized at all (size-selective mobility). If the water runoff increases, coarse grains will be partially mobilized but the proportion in total bed load is still much smaller than their abundance at the bed surface (partial mobility; e.g. *Wilkcock and McArdell*, 1997). Finally, the bed material is fully mobile at high flow which is associated with phase 3.

In order to account for size-selective or partial mobility, threshold-based bed load transport equations can be extended to fractional approaches, where bed load

transport rate is calculated for each grain size fraction separately. Therefore, equation B61 is modified to

$$\dots \quad (B63)$$

with the abundance of the i th grain size fraction on the bed surface f_i and its threshold for incipient motion $X_{c,i}$. However, $X_{c,i}$ is not solely dependent of the grain size D_i , due to the interaction of mixed sized sediment (e.g. Einstein, 1950). In general, small grains hide between coarse particles and thus, small grains are more difficult to mobilize than in beds that consist of a uniform material of that size. In contrast, the protrusion of coarse grains is more pronounced in mixed sized beds than in uniformly sized ones. Consequently, coarse grains are easier mobilized. To account for the hiding and exposure effects, hiding functions are applied, which scale the critical conditions of the i th grain size by means of a reference grain size (D_{ref}) according:

$$X_{c,i} = X_{c,ref} \left(\frac{D_i}{D_{ref}} \right)^y \quad (B64)$$

with $X_{c,ref}$ the threshold of that reference grain size and y is the hiding exponent. The hiding exponent differs with respect to the hydraulic parameter used for flow strength X . The reference grain size is commonly defined by the grain size of which 50 % are finer by weight (D_{50}), which is proved as proper surrogate even in mountain streams with wide-graded sediment (Bathurst, 2013). The exponent y in equation B64 regulates the strength of hiding and exposure, and its value depends on the hydraulic parameter used. In terms of dimensionless shear stress (τ^* ; e.g. equation B62), the parameter β is used as the hiding exponent. Equal mobility (incipient motion of all grains corresponds to the same flow; maximum hiding and exposure) is attained with $\beta=1$, while full size-selective conditions (each grain starts to be transported at the same flow as it would start in uniform sized beds of that size; no hiding and exposure) is achieved with $\beta=0$, respectively.

The second concept refers to reference-based equations, where bed load transport is a function of the flow strength X scaled by a reference value X_r :

$$Y_b = k \times \left(\frac{X}{X_r} \right)^\alpha, \quad (B65)$$

Equations associated with this concept do not include a threshold for incipient motion, but transport rate approaches a very minute rate at low flows. In addition, bed load transport rate is often not defined by a single power law equation, but the approaches consist of two (e.g. Recking, 2010; Wilcock and Crowe, 2003) or three formulae (e.g. Parker, 1990) for different ranges of X/X_r . Usually, k is very low and α rather large when X is less or barely exceeds X_{ref} and thus, the rating curve is steep in the log-log scale, but bed load transport rate is of a low magnitude. In contrast, k is large and α approaches similar values as in threshold-based formulae for $X \gg X_{ref}$ (Figure B-77).

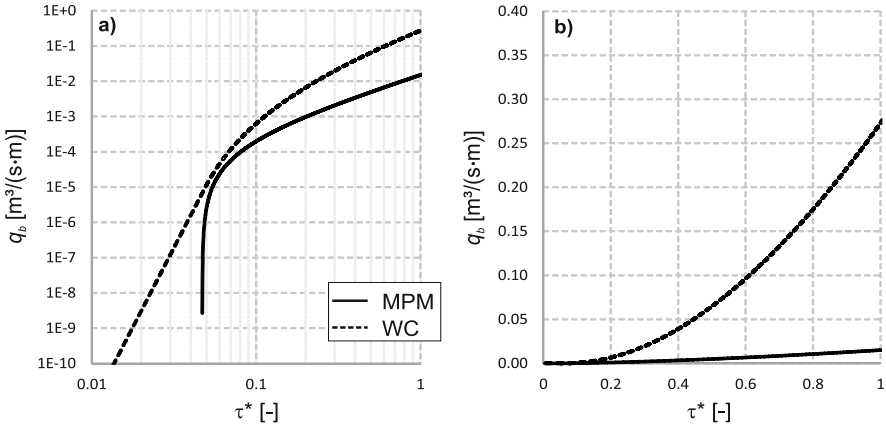


Figure B-77: Rating curves of dimensionless shear stress (τ^*) and specific bed load transport rate (q_b) determined according a simplified version of the threshold-based Meyer-Peter and Müller (1949) equation (MPM; equation B62) and the reference-based Wilcock and Crowe (2003) equation (WC). Both equations were applied to uniform sized sediment with a grain size 0.05 m and an energy slope of 0.02 m/m; the rating curves are plotted in log scale (a) and liner scale (b).

However, many reference-based formulae use the dimensionless bed load transport rate W^* as dependent variable and shear stress (either dimensional (τ) e.g. Wilcock and Crowe (2003) or dimensionless (τ^*) e.g. Parker (1990)) as independent variable:

$$\begin{aligned} W^* &= f\left(\frac{\tau^*}{\tau_r^*}\right) \quad \text{or} \quad W^* = f\left(\frac{\tau}{\tau_r}\right), \quad \text{with} \\ W^* &= \frac{(s-1)gq_b}{u^{*3}} \end{aligned} \quad (\text{B66})$$

Herein, s (-) is the specific solid density, g (m/s^2) the gravitational acceleration, q_b (m^2/s) the specific bed load transport rate and $u^* = \sqrt{gdS}$ the shear velocity. The reference dimensionless shear stress τ_r^* (or τ_r) is commonly defined according to Parker et al. (1982) as the value of τ_r^* (or τ_r) at which dimensionless bed load transport rate is very small with $W^*=0.002$.

In terms of a fractional approach, the reference-based formulae are defined by

$$W_i^* = \frac{(s-1)gq_b}{f_i u^{*3}} = f\left(\frac{\tau_i^*}{\tau_{r,i}^*}\right) \quad (\text{B67})$$

Herein τ_i^* is the dimensionless shear stress with respect to the i th grain size and $\tau_{r,i}^*$ is reference value corresponding with $W_i^*=0.002$, respectively. In analogy with the threshold-based approach, a hiding function is used to account for differences of the mobility of mixed sized sediment.

5.1.2 Incipient motion

Independent of the concept used, the derivation of the critical or reference conditions is a key element in bed load transport equations. Although there exist several methods for describing the conditions of incipient motion (*Buffington and Montgomery*, 1997), most studies either use the flow competence method or the reference transport method (e.g. *Schneider et al.*, 2015; *Green et al.*, 2015).

According to the flow competence method, the coarsest grain that is transported at a given flow ($D_{b,max}$) is related to a hydraulic parameter describing the flow strength. In terms of steep mountain streams this is either the dimensionless shear stress τ^* (equation B62; e.g. *Green et al.*, 2015; *Mao et al.*, 2008) or the dimensionless specific discharge q^* (*Bathurst*, 2013; *Mao et al.*, 2008)

$$q^* = \frac{q}{\sqrt{gD^3}}. \quad (\text{B68})$$

In this respect, *Bathurst* (2013) compiled a large data set of $D_{b,max} - q$ relations for numbers of mountain streams and determined fractional incipient motion conditions by means of a hiding function (equation B64). Within a single site, values of the hiding exponent revealed to be self-consistent, but between-site variability was large. At streams facing snowmelt regimes, equal to moderate size-selective mobility dominated (moderate to strong hiding and exposure effect), while strong size-selective mobility dominated in streams associated with rainfall regimes (small hiding and exposure effect: small grains are mobilized at much smaller flows than coarse ones; *Bathurst*, 2013).

In contrast, when incipient motion is determined by means of the reference transport method, bed load transport is extrapolated either to zero (threshold-based formulae) or a very low reference value (reference-based formulae) by means of a rating curve. Therefore, a suitable relation of measured bed load transport rates and a hydraulic parameter describing the flows strength (e.g. shear stress) first needs to be fitted. In this regard, *Schneider et al.* (2015) used a large field data set of fractional bed load transport rates to determine the reference dimensionless shear stress τ_r^* by means of the methodological framework proposed by *Parker et al.* (1982). Corresponding with former studies (e.g. *Green et al.*, 2015; *Mueller et al.*, 2005), *Schneider et al.* (2015) found that τ_r^* on average increases with bed slope when total boundary shear stress is used. However, in steep mountain streams, only a fraction of total boundary shear stress is available for bed load transport. This is associated with energy losses due to spill and form drag around macro-roughness elements, such as large boulders (e.g. *Rickenmann and Recking*, 2011; *Yager et al.*, 2007). Accounting for these circumstances, the influence of slope on dimensionless reference shear stress vanishes (*Schneider et al.*, 2015).

B.5.2 Field sites

5.2.1 General remarks

In this study, data of a bed load transport measurement campaign at three mountain streams (see section B.1.5) are analyzed regarding incipient motion and fractional bed load transport rate. The three mountain streams and the study reaches are described in more detail in the following subsections.

5.2.2 Oberbergbach

The Oberbergbach is a glacier fed mountain stream, located in the Stubai valley in Austria (Table B-1) and it reveals a moderate sediment supply of mobile bed load. The bed load transport measurements were conducted at two reaches. At the field sites, the Oberbergbach drains a catchment of approximately 24 km² (site 1) and 20 km² (site 2).

Site 1 (Ob #1) refers to the stream reach that encloses upstream of the water intake structure (Figure B-79). This reach has a mean bed gradient of 0.076 m/m and is situated within a gorge, which is 10 m to 20 m wide and confines the flow at high discharges. Upstream of site 1, the bed gradient increases up to 0.30 m/m (Figure B-78).

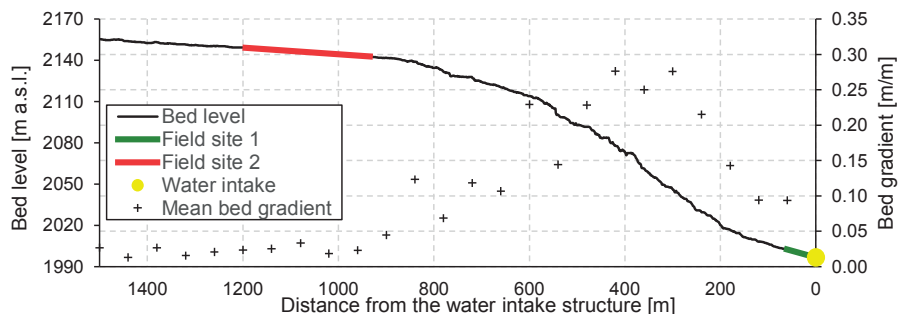


Figure B-78: Longitudinal profile of bed level and bed gradient of the Oberbergbach

Field site 2 (Ob #2) is located upstream of that steep gorge, which ends approx. 800 m upstream of the water intake structure, respectively. At the site 2, the Oberbergbach reveals a low-gradient accumulation reach with a mean bed slope of 0.02 m/m. In contrast to site 1, the channel morphology and geometry is highly dynamic and the water forms its course during ordinary flood events (Figure B-79).

The grain size distributions of the Oberbergbach were measured by means of transect-by-number analyses at seven locations with a range in bed slope from 0.02 m/m to 0.25 m/m, respectively. The transect-by-number frequency distributions were converted to volume-by-weight samples according to a modified approach of Fehr (1987), which proved to be consistent to grid-by-number samples (for further details see '*Verification of the transect-by-number method for assessing the bed surface grain size distribution*' in section A.1.1). The grain size distributions differ along the channel and D_{50} , and D_{84} significantly correlate with bed slope (Figure B-80). The grain size distribution of both field sites is given in Table B-12 in section B.1.5.



Figure B-79: Study reaches at the Oberbergbach with a-b) site 1 ($S=0.076 \text{ m/m}$) at low flow, c-d) site 2 at low-moderate flow before (c) and after a flood event (d) in August 2014

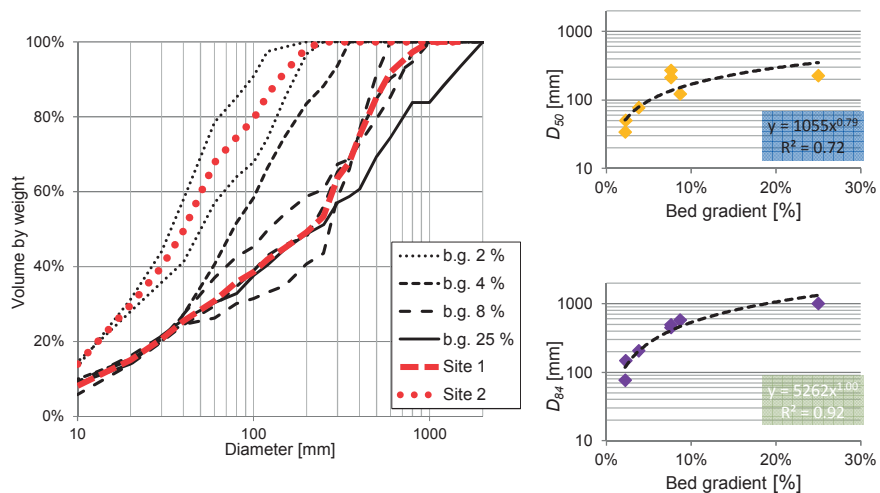


Figure B-80: Grain size distributions upstream of the water intake structure of the Oberbergbach; b.g. is the bed gradient.

5.2.3 Pitzbach

At the field site of the Pitzbach (Pb #1), its watershed is 27 km² in size and 46 % are covered by glaciers (Table B-1). The Pitzbach reveals a moderate (*Recking, 2012b*) to high (*Study A, section B.3*) bed load transport efficiency and bed load transport typically occurs in a diurnal cycle following discharge variations due to glacier melt (*Hofer, 1985; Turowski et al., 2011*).

The channel is located within a “U-shaped” valley that features a homogenous landform. In contrast to the Oberbergbach, the stream flow is not constrained by a gorge but flows along its alluvium. In this respect, the longitudinal profile of the Pitzbach is rather balanced and the bed slope ranges from 0.06 m/m to 0.13 m/m along the first kilometre above the water intake structure (Figure B-81). For more details on catchment characteristics, see Table B-1.

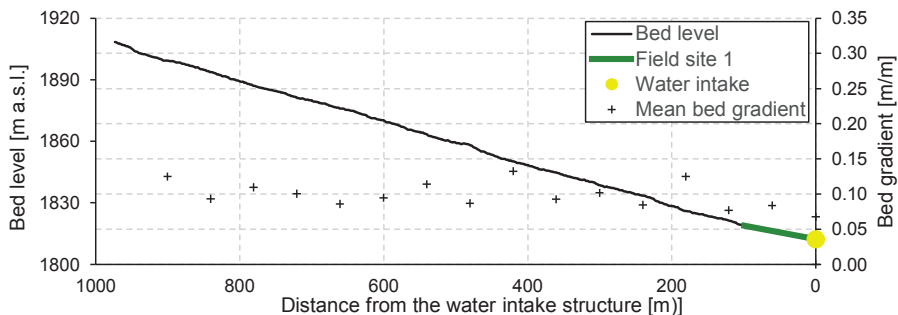


Figure B-81: Longitudinal profile of the Pitzbach upstream of the water intake structure

The field site is located 50 m upstream of the water intake structure (Figure B-82), and the channel reveals a mean flow width of 8 m at moderate flows and a bed gradient of 0.08 m/m, respectively. The grain size distribution is similar with that of the Ob #1 and it is given in Table B6 in section B.1.5.

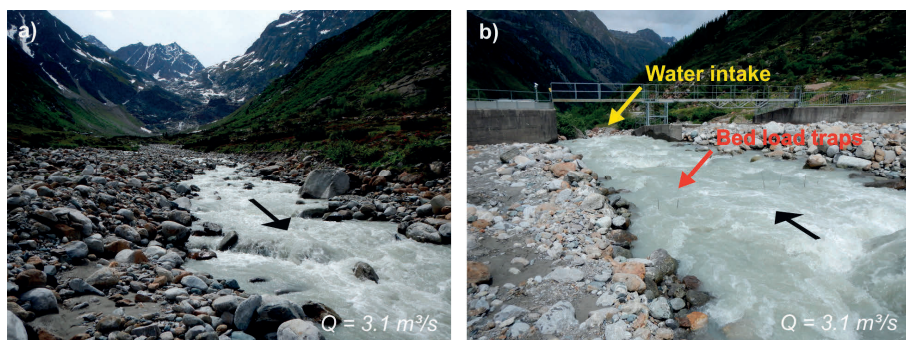


Figure B-82: Field site of the Pitzbach, featuring a homogeneous boulder bed reach (a), and it is located upstream of the water intake structure (b)

5.2.4 Laengentalerbach

The catchment of the Laengentalerbach is minor glaciated (7 %; Table B-1) and the bed load transport efficiency as determined in *Study A* (section B.3) is moderate.

The two study reaches are located next to each other and are situated about 100 m upstream of the water intake structure operated by TIWAG. Site 1 (Lb #1) is a short reach that reveals a plane bed and a low gradient of 0.04 m/m. In contrast, the reach of site 2 (Lb #2) reveals a step-pool morphology and a bed gradient of 0.069 m/m (Figure B-83).

The bed surface grain size distributions were surveyed by means of transect-by-number analyses at several locations with a range in bed slope from 0.03 m/m to 0.23 m/m. In analogy with the Oberbergbach, the D_{50} , and the D_{84} significantly correlate with bed slope (Figure B-84). However, the magnitude of grain size is smaller compared with the Oberbergbach (lower scaling factors), but the increase with bed slope is stronger (larger scaling exponents).



Figure B-83: Study reaches at the Laengentalerbach with a-b) site 1 ($S=0.04 \text{ m/m}$) at low flow and site 2 ($S=0.069 \text{ m/m}$) at low (c) and high flow (d)

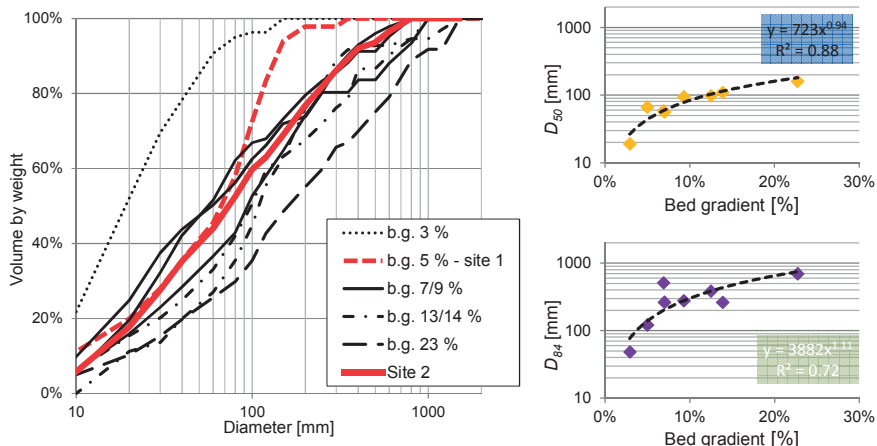


Figure B-84: Grain size distributions upstream of the water intake structure of the Laengentalerbach; b.g. is the bed gradient.

B.5.3 Methods of the field survey

5.3.1 Fractional bed load transport rate

Bed load transport rate was measured with bed load traps according to *Bunte et al.* (2004). The bed load traps consist of a metal frame with an opening of 300 mm (horizontal) x 200 mm (vertical) and a downstream fixed nylon net bag. In contrast to *Bunte's* traps, a mesh opening of 1.4 mm rather than 4.0 mm was used (for further details see *Eichner*, 2015). In this respect, velocity measurements in front of the bed load trap revealed that the flow velocity was not affected by the bed load trap. Therefore, the sampling efficiency is assumed to be unaffected by the tighter net. The effect of the bed load trap on flow hydraulics was investigated in more detail at the hydraulic laboratory of the University of Innsbruck (*Hegenbart*, 2015). According to *Hegenbart's* (2015) measurements, the effect of the bed load trap on flow hydraulics is minor at flow velocities less than 1 m/s. At higher flow velocities, the head loss increased significantly, resulting in high turbulence downstream of the trap. However, the bed load traps are mounted on the stream bed, and they protrude 0.2 m into the flow. The local flow velocity is expected less than 1 m/s at this small depth.

For most of the field measurements, three bed load traps were installed across the stream and the traps occupied at least 13 % of the total bed width. The measuring duration varied between a few minutes and 3 hours, depending on the magnitude of bed load transport rate. However, for 88 % of all measurements, the measuring duration exceeded 30 minutes and thus, short-term fluctuations of bed load transport rate are not expected to influence the results (e.g. *Bunte et al.*, 2004).

The bed load collected in the bed load traps ranged from 0.2 kg during 3 hours of sampling to 78 kg within 7 minutes. The entire samples were dried and sieved in the hydraulic laboratory and the grain size distributions were then converted to full phi-scale.

The measured, fractional bed load transport rate $Q_{b,i}$ (kg/s) refers to the monitored portion of the cross section only and it was extended to the total cross section according

$$Q_{b,i} = \frac{G \times w_a}{t \times n \times 0.3} \times f_i, \quad (B69)$$

with the mass of dried bed load G (kg), the active flow width w_a (m), the sampling duration t (s), the number (n), the width (0.3 m) of the installed bed load traps, and the proportion of the i th grain size fraction in total load f_i , respectively. In order to account for reduced bed load flux in the proximity of the banks, the active channel width refers to the portion of the cross section where flow was unaffected of the banks. The ratio of active and total flow width was in a range of 0.6 and 1.0, with a mean of 0.8. In comparison, *Green et al.* (2015) used a constant factor of 0.8 to reduce extrapolated bed load fluxes.

In total, 54 measurements of bed load transport rate were accomplished during the summer seasons 2014 and 2015. At one study site (Pitzbach), field data are supplemented by 23 measurements, which were derived by *Hofer* (1985), according to a similar procedure.

5.3.2 Water discharge and flow velocity

Water discharge is gauged in 15 min sampling time at the water intake structures which are in the proximity of the field sites. In order to verify these discharge measures or to account for lateral inflows in between, discharge was additionally measured by the salt dilution method (e.g. *Foster*, 2000; *Morgenschweis*, 2010). Therefore, a predefined amount of dissolved salt was poured into the stream and the water conductivity was continuously registered about 100 m downstream. Based on the conductivity curves, the discharge was then determined according

$$Q = \frac{M}{\alpha \times \int_0^t (C(t) - C_0) dt}, \quad (B70)$$

with the mass of injected salt M , the measured (C) and background conductivity (C_0), the duration of the measurement t , the sampling time step dt (1 second) and the calibrated relation of conductivity and salt concentration α , respectively.

Mean flow velocity was assessed sporadically by measuring the distance between salt injection and conductivity measurement and the instant time of both, the injection and the start of measuring the conductivity. The mean duration that the dissolved salt required to pass the measuring location was then determined by the harmonic mean of the concentration curve (e.g. *Nitsche et al.*, 2012; *Waldon*, 2004). This method represents an easy way to measure mean flow velocity, but features several uncertainties. When the dissolved salt is poured into the stream, it takes a while until the salt is homogenously distributed over the cross section. For instance, pouring the dissolved salt into the main flow causes the entire salt to pass the first few meters faster than the mean flow velocity suggests. The opposite is the case when the dissolved salt is injected at a location of calm flow with low velocity. However, due to the highly irregular flow and the frequent alterations of sub- and supercritical flow conditions, the salt is

expected to mix throughout the cross section in course of the first few metres. Nevertheless, the inaccuracy of flow velocity is assumed with +/- 15 %, which must be considered in the subsequent analysis.

5.3.3 Channel geometry

The geometry of the cross sections at which the bed load traps were installed was measured in increments of 0.5 m with a ruler. The longitudinal profile of the reach and additional cross-sectional profiles were derived from high-resolution Lidar data.

B.5.4 Methods of calculations

5.4.1 Flow hydraulics

Bed load transport is assumed to be a function of either shear stress or specific discharge (discharge per unit width). Regarding the shear stress, total and effective shear stress are differentiated. Total boundary shear stress is defined by

$$\tau = \rho g r_h S, \quad (\text{B71})$$

with the water density ρ (kg/m^3), gravitational acceleration g (m/s^2), hydraulic radius r_h (m) and bed gradient S (m/m). In order to account for drag and spill drag due to macro-roughness elements, the effective shear stress (τ') is determined by means of the reduced energy gradient S_{red} (Rickenmann and Recking, 2011) instead of the actual bed gradient S according

$$\tau' = \rho g r_h S_{red}, \quad \text{with}$$

$$S_{red} = S \times \left(\frac{2.5 \left(\frac{r_h}{D_{84}} \right)^{5/6}}{\sqrt{6.5^2 + 2.5^2 \left(\frac{r_h}{D_{84}} \right)^{5/3}}} \right)^{1.5} \quad (\text{B72})$$

Both of these definitions of shear stress are used in this study and those referring to the effective shear stress are marked with an inverted comma ', like τ'^* or W'^* , respectively.

The hydraulic radius which is required for calculating shear stress was not measured in course of the field surveys since there are large measuring uncertainties due to the high spatial variability of flow depth (d) in steep streams. In analogy with the study of Schneider *et al.* (2015), hydraulic parameters were back calculated from measured water discharge by means of a flow resistance equation and the assumption of uniform flow at the reach scale.

Therefore, the variable power law equation (VPE) of Ferguson (2007) was applied, which defines flow velocity U as a function of r_h , D_{84} and S according

$$U = \frac{a_1 a_2 (r_h/D_{84})}{\sqrt{a_1^2 + a_2^2 (r_h/D_{84})^{5/3}}} \sqrt{g r_h S}, \quad (\text{B73})$$

with $a_1=6.5$ and $a_2=2.5$ as suggested by *Rickenmann and Recking* (2011). In its original form, equation B73 is written in terms of flow depth rather than hydraulic radius. But for natural and narrow channels, r_h is preferably used in order to account for bank roughness (e.g. *Nitsche et al.*, 2011; *Schneider et al.*, 2015). In combination with mass continuity

$$Q = U \times A(d), \quad (\text{B74})$$

where A is the flow area, the hydraulic radius can be iteratively computed for a predefined cross section.

The flow depths or hydraulic radii could also be determined by means of mass continuity and measured flow velocity rather than the empiric flow resistance equation B73. But flow velocity data are too sparse for several sites since measurements were conducted sporadically in course of the field work. Thus, measured flow velocities are solely used for the validation of the flow resistance approach.

The hydraulic computations were performed with multiple cross-sections of each study site and for each of them, rating curves of $Q-r_h$, $Q-d$, $Q-q$, $Q-w$ and $Q-S_{red}$ were computed. Hydraulic geometry relations of all these hydraulic parameters were then fitted to the averaged rating curves. It is worth to note, that the hydraulic geometry relations were obtained for the range of water discharge that was present during the field measurements. Thus, the predictive quality of the hydraulic geometry relations is maximized, but its application is limited to low and moderate discharges.

5.4.2 Derivation of fractional reference shear stress by means of the reference transport method

The dimensionless reference shear stress of each grain size fraction was determined in order to collapse fractional dimensionless transport rate (W_i^*) of each study reach separately (Figure B-85c) by means of the methodological framework of *Parker et al.* (1982). In this respect, the fractional bed load transport rate was aggregated into full phi-scale, with the minimum size ranging from 1 mm to 2 mm. W_i^* was first fitted against a reference-based relation and this relation was then used to estimate the corresponding dimensionless reference shear stress at $W_i^*=0.002$, respectively. The sequence of calculation steps corresponds with the recently published study of *Schneider et al.* (2015) and can be summarized as follows:

1. Calculating W_i^* (equation B67) and τ_i^* (equation B62) for each grain size fraction i of a single bed load transport measurement
2. Fitting the power function $W_i^* = \alpha_i \tau_i^{*m_i}$ for each grain size fraction by using all bed load measurements of a single field site
3. Determining the median of the exponent m_i derived in the previous step (m_{i50}) and fitting the functions $W_i^* = \alpha_i \tau_i^{*m_{50}}$ with respect to α_i in order to determine α_{im} (Figure B-85a)
4. Estimating $\tau_{r,i}^*$ by rearranging $W_i^* = \alpha_{im} \tau_{r,i}^{*m_{50}}$ with $W_i^* = 0.002$
5. Fitting the power function $\tau_{r,i}^* = x(D_i/D_{50})^y$, with D_{50} the median diameter of the bed surface (Figure B-85b).

It is worth to note, that the factor x in the power function of step 5 (Figure B-85b) corresponds with the dimensionless reference shear stress of the bed surface D_{50} ($\tau^*_{D_{50}}$ or $\tau^{*D_{50}}$), while y is the hiding exponent (β).

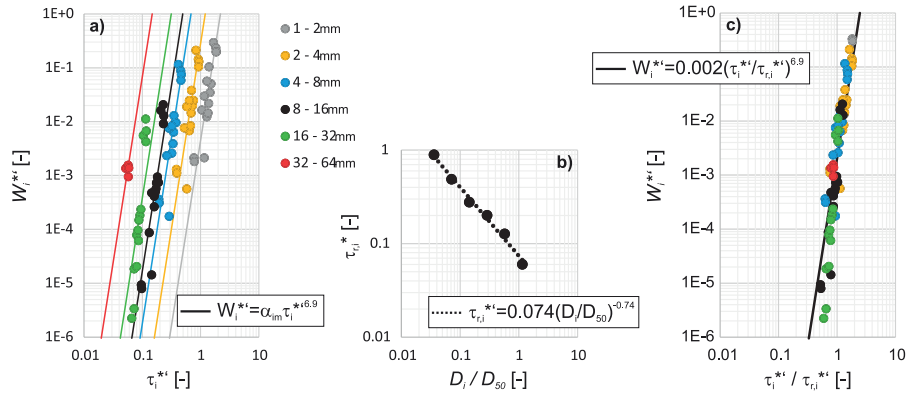


Figure B-85: Reference transport method applied to the study site 2 of the Oberbergbach: a) plot of W_i^* against r_i^{**} with the fitted power function of step 3, b) the hiding function obtained by fitting observed $r_{r,i}^{**}$ against D_i/D_{50} and c) plot of W_i^* against $r_i^{**}/r_{r,i}^{**}$ with the collapse of the fractional bed load transport data.

The same procedure regarding both, measuring bed load transport rate by means of bed load traps and the derivation of the dimensionless reference shear stress (including the computation of flow hydraulics) was applied in the study of Schneider *et al.* (2015; main data set). Due to that, the results obtained from this study are compared against those of Schneider *et al.* (2015) and reported relations with reach characteristics are verified.

5.4.3 Derivation of fractional incipient motion by means of the flow competence method

For each bed load transport measurement, the coarsest grain size fraction that was captured with the bed load trap ($D_{max,b}$) is related to $\tau^*_{D_{max,b}}$, and $q^*_{D_{max,b}}$, which are defined by

$$\tau^*_{D_{max,b}} = \frac{r_h S}{(s-1) D_{max,b}} = \frac{\tau}{\rho g (s-1) D_{max,b}} \quad (B75)$$

$$q^*_{D_{max,b}} = \frac{q}{\sqrt{g D_{max,b}^3}} \quad (B76)$$

The dimensionless shear stress is determined by means of the total boundary shear stress (equation B71) and the effective shear stress (equation B72); the latter is computed by means of S_{red} instead of S , respectively. Contrasting with the derivation of the dimensionless reference shear stress (section 5.4.2), the grain size distribution of the bed load was not aggregated into full phi-scale, but the sieve sizes were used instead, which approximately correspond with the half phi-scale.

Additional data are available for site 1 of the Oberbergbach, where the coarse sediment that deposited on the bottom rack of the water intake structure was surveyed. As described in section 1.1.3, the bottom rack has a clear width of 0.15 cm and thus, grains coarser than that, either deposit on the rack or fall over it. In course of the field surveys, the accumulation of the bed load on the rack and downstream of it was tracked on a weekly to monthly interval. Due to the very limited number of coarse grains, the coarsest particle that came along since the last observation, could be determined. The particle's movement is associated with the peak discharge since the last observation. In the subsequent analysis, these data are termed as flood competence (e.g. *Mao et al.*, 2008).

However, $\tau^*_{D_{max,b}}$ and $q^*_{D_{max,b}}$ are then fitted by means of the power function in order to obtain the hiding functions

$$\tau_{c,i}^* = x(D_i/D_{50})^y \quad (\text{B77})$$

$$q_{c,i}^* = x(D_i/D_{50})^y \quad (\text{B78})$$

Regarding both of these hiding functions, the factor x is associated with the incipient motion of the bed surface D_{50} ($\tau^*_{D_{50}}$ or $q^*_{D_{50}}$), while y is the hiding exponent which is termed as β for the dimensionless shear stress (τ^*) and b for the dimensionless discharge based approach (q^*).

B.5.5 Results

5.5.1 Hydraulic geometry

The computed flow velocities are in a close range with the measurements (Figure B-86) and it is not clear if the differences are attributed to the VPE approach (section 5.4.1) or to the inaccuracy of the measured flow velocities (section 5.3.2). Only at the Laengentalerbach, the computed flow velocity is systematically higher than the observation at high flows, suggesting an overestimation of flow velocity by means of the VPE approach. Nevertheless, the estimation of hydraulic parameters by means of the VPE approach of *Ferguson* (2007) seems justified.

Based on the average rating curve (blue lines in Figure B-86), hydraulic geometry relations were computed by fitting power functions (Table B-23). The correlation coefficients of all hydraulic geometry relations are very close to unity, confirming the applicability of the power functions. Hydraulic parameters required for computing either total or effective shear stress (equation B71 and B72) or specific discharge ($q=Q/w$) are determined from these hydraulic geometry relations throughout this study.

Table B-23: Hydraulic geometry relations for flow velocity U , flow width w , hydraulic radius r_h and reduced energy gradient S_{red} .

| Field site | $U = k * Q^m$ | | | $w = k * Q^m$ | | | $r_{hyd} = k * Q^m$ | | | $S_{red} = k * Q^m$ | | |
|------------|---------------|------|-------|---------------|------|-------|---------------------|------|-------|---------------------|------|-------|
| | k | m | r^2 | k | m | r^2 | k | m | r^2 | k | m | r^2 |
| Ob #1 | 0.70 | 0.45 | 1.0 | 6.35 | 0.29 | 1.0 | 0.22 | 0.26 | 1.0 | 0.010 | 0.36 | 1.0 |
| Ob #2 | 0.83 | 0.45 | 1.0 | 6.38 | 0.15 | 1.0 | 0.19 | 0.40 | 1.0 | 0.008 | 0.29 | 1.0 |
| Lb #1 | 1.35 | 0.43 | 1.0 | 3.65 | 0.22 | 1.0 | 0.20 | 0.32 | 1.0 | 0.018 | 0.30 | 1.0 |
| LB #2 | 0.71 | 0.52 | 1.0 | 7.62 | 0.11 | 1.0 | 0.19 | 0.38 | 1.0 | 0.012 | 0.41 | 1.0 |
| Pb #1 | 0.46 | 0.50 | 1.0 | 11.65 | 0.16 | 1.0 | 0.19 | 0.33 | 1.0 | 0.007 | 0.41 | 1.0 |

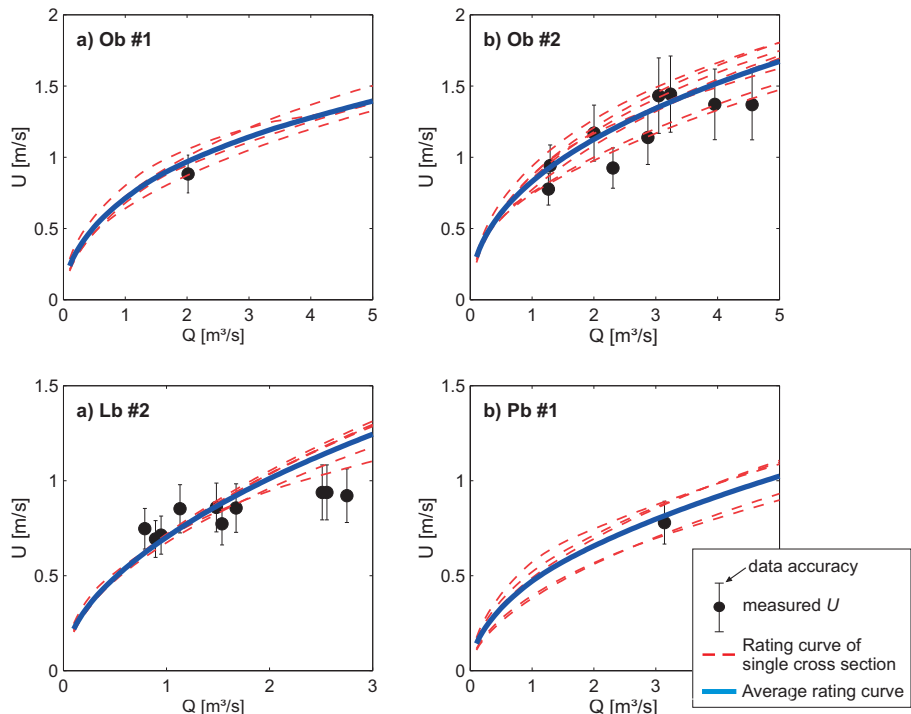


Figure B-86: Comparison of calculated Q - U rating curves with discrete measurements for a) site 1 and b) site 2 of the Oberbergbach, c) site 2 of the Laengentalerbach and d) site 1 of the Pitzbach.

5.5.2 Critical conditions obtained with the reference transport method

The dimensionless reference shear stress obtained by the reference transport method reveals a range from 0.10 to 0.18 if it is based on the total shear stress and 0.01 to 0.08 for the dimensionless effective shear stress (Table B-24).

Table B-24: Dimensionless reference shear stress of the D_{50} and hiding exponent β determined either by means of total boundary shear stress or effective shear stress for each study site

| Field site | Total boundary shear stress | | | | | | Effective shear stress | | | | | |
|--------------------------|---|---------|-------|---|--------------|---------|---|-----------|--------------|--|-------|-----------|
| | $\tau^*_{ri} = \tau^*_{rD50} \times (D_i/D_{50})^\beta$ | | | $Wi^* = 0.002 \times (r^*_{ri} / r^*_{rD50})^{m50}$ | | | $\tau^*_{ri} = \tau^*_{rD50} \times (D_i/D_{50})^\beta$ | | | $Wi^{**} = 0.002 \times (r^*_{ri} / r^*_{rD50})^{m50}$ | | |
| | r^*_{rD50} | β | r^2 | m_{i50} | r^*_{rD50} | β | r^2 | m_{i50} | r^*_{rD50} | β | r^2 | m_{i50} |
| <i>insufficient data</i> | | | | | | | | | | | | |
| Ob #1 | | | | | | | | | | | | |
| Ob #2 | 0.120 | -0.86 | 1.00 | | 12.7 | 0.078 | -0.73 | 0.99 | | 6.7 | | |
| Lb #1 | 0.103 | -0.93 | 1.00 | | 14.2 | 0.056 | -0.85 | 0.99 | | 6.6 | | |
| LB #2 | 0.177 | -0.93 | 1.00 | | 16.8 | 0.041 | -0.84 | 1.00 | | 7.3 | | |
| Pb #1 | 0.099 | -0.96 | 1.00 | | 26.0 | 0.014 | -0.92 | 1.00 | | 10.8 | | |

In Figure B-87 the dimensionless reference shear stresses is plotted against the bed gradient and the results of this study are well within the range of the data from Schneider et al. (2015). Considering τ^*_{rD50} of this study solely, there is no significant correlation with bed gradient (Figure B-87a). However, taking all data into account, the correlation is still significant and the fitted power function is similar but slightly flatter than that of Schneider et al. (2015).

In contrast, τ^*_{rD50} reveals an inverse dependency with bed slope (Figure B-87b). A weak but still significant negative trend of τ^*_{rD50} with bed gradient is supported by the data of Schneider et al. (2015), which is enhanced by taking both data sets into account (red line in Figure B-87b).

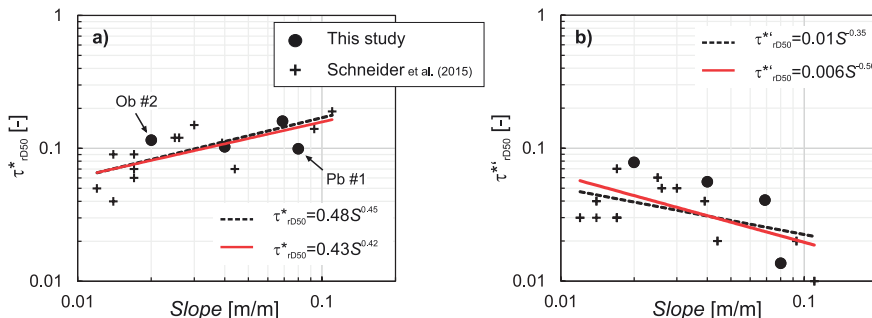


Figure B-87: a) Dimensionless reference shear stress (τ^*_{rD50}) and b) dimensionless effective reference shear stress (τ^*_{ri}) plotted against bed slope. The black, dashed line is the power function given in Schneider et al. (2015) and the red line is a fitted power function with respect to both data sets.

Regarding the relative mobility of the i th grain size (expressed by the hiding exponent β), the bed load transport data reveal hiding exponents that are closer to equal mobility ($\beta=-1$) than full size-selective mobility ($\beta=0$). For comparison, the range of hiding ex-

ponents is aggregated into the four classes ‘almost equal’ ($\beta < -0.95$), ‘weak size-selective’ ($-0.95 < \beta < -0.8$), ‘moderate size-selective’ ($-0.8 < \beta < -0.5$) and ‘strong size-selective’ ($-0.5 < \beta < 0$).

In terms of the dimensionless reference shear stress (τ^*), almost equal mobility is attained only at the Pitzbach, while weak size-selective mobility persists at all other sites (Table B-24). However, values of β are all within a close range, with the minimum at the Pitzbach (steep boulder bed reach with high transport efficiency) and the maximum at the Oberbergbach site 2 (low gradient accumulation reach).

For the dimensionless effective reference shear stress, the values of β are lower and reveal a wider range (Table B-24). The hiding exponents either refer to weak or moderate size-selective mobility.

5.5.3 Fractional bed load transport

The grain size specific dimensionless reference shear stress τ_{ri}^* was derived by means of collapsing fractional bed load transport rates. According to the procedure outlined in section 5.4.2, the power function

$$W_i^* = 0.002 (\tau_i^* / \tau_{r,i}^*)^{mi50} \quad (B79)$$

was fitted for each site. Therein, the exponent $mi50$ represents the median exponent of all grain size fractions of the bed load. However, $mi50$ differs strongly between the field sites (Table B-24) and it is highest for the Pitzbach with $mi50=26$ for total boundary shear stress and $mi50=10.8$ for effective shear stress, respectively.

The scope of this study is neither to derive a new bed load transport equation nor to evaluate existing ones, but Figure B-88 is used to illustrate the collapse of fractional data and the general trend. Therefore, dimensionless fractional bed load transport rates of all study sites are plotted against the corresponding shear stress ratio (Figure B-88), with τ_{ri}^* or $\tau_{r'i}^*$ determined according to the fitted power functions in Table B-24. According to the visual judgement, the measured data are located in the proximity of a power function with the median exponent (Table B-24) of all for field sites used (red lines in Figure B-88). But bed load transport data of this study are limited to low or moderate flows with low $\tau_{ri}^*/\tau_{r'i}^*$. At high shear stress ratios the trend is known to flatten, with W^* approaching a constant value (e.g. Wilcock and Crowe, 2003; Parker, 1990), which is equivalent to an increase of specific bed load transport rate with $\tau^{1.5}$. Since field data of bed load transport rates are sparse for high flows, there is large uncertainty regarding the magnitude of $\tau_{ri}^*/\tau_{r'i}^*$ at which the rating curve starts to flatten. In this respect, Schneider *et al.* (2015) suggested the breakpoints at $\tau_{ri}^*/\tau_{r'i}^*=1.2$ and $\tau_{ri}^*/\tau_{r'i}^*=1.33$ (black dotted line in Figure B-88). This is not supported by the data presented in this study since the trends in Figure B-88 do not change. However, only a few measured bed load transport rates refer to shear stress ratios exceeding these thresholds and thus, no significant conclusion can be drawn on that issue.

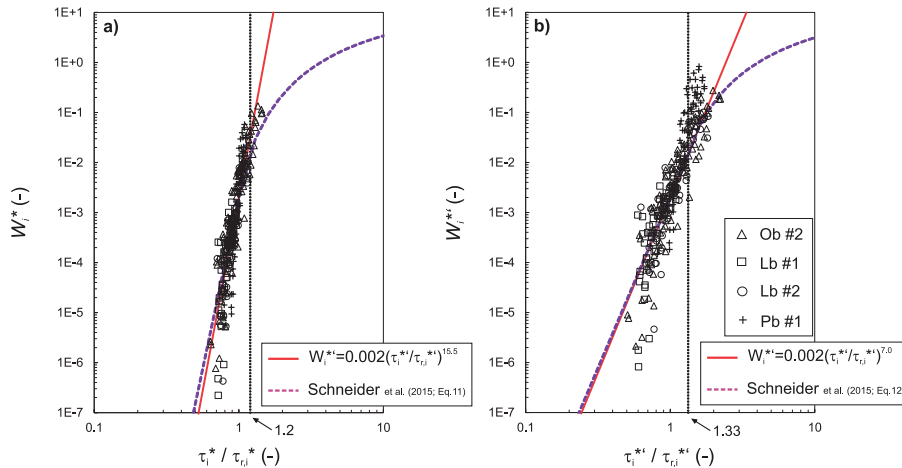


Figure B-88: Collapse of dimensionless fractional bed load transport rates with the shear stress ratio. The red line is a power function with the median of site-specific exponents. The violet dashed line is the bed load transport function of Schneider et al. (2015) in combination with the dimensionless reference shear stress and the hiding exponent derived in this study. The black dotted line represents the breakpoint between the lower and upper bed load transport regime according to Schneider et al. (2015).

5.5.4 Critical conditions obtained with the competence method

The critical conditions (incipient motion) were determined by means of three hydraulic parameters, the dimensionless total boundary shear stress (τ_{ci}^*), the dimensionless effective shear stress (τ_{ci}^{*+}) and the dimensionless specific discharge (q_{ci}^*). For each parameter, power law functions with the relative grain size D_i/D_{50} as the independent variable were fitted.

The factors of these power functions correspond by definition with the critical conditions of the bed surface D_{50} . Regarding τ_{cD50}^* and τ_{cD50}^{*+} , the values obtained with this method (Table B-25) are lower than the corresponding dimensionless reference shear stresses (Table B-24) for all except one site, the Pitzbach.

However, τ_{cD50}^* is still high compared with literature data from low gradient streams (data compilations are given in Lamb et al. (2008) and Recking (2009)), but within the range with previously reported values of τ_{cD50}^* for channels with similar slopes (e.g. Green et al., 2015; Mao et al., 2008). In contrast, τ_{cD50}^{*+} is obviously lower, revealing a similar range as in low gradient gravel rivers.

The dimensionless critical shear stress does not reveal a significant correlation with bed slope when it is determined by means of the total boundary shear stress (τ_{cD50}^* ; Figure B-89a). In contrast, τ_{cD50}^{*+} shows a negative trend with bed slope (Figure B-89b) and thus, the results are consistent with those obtained with the reference transport method.

Table B-25: Incipient motion of D_{50} , the hiding exponent and the coefficients of agreement obtained for each study site determined by either total boundary shear stress, effective shear stress or specific discharge.

| Field site | Total boundary shear stress | | | Effective shear stress | | | Specific discharge | | | | | |
|------------|---|---|---|------------------------|---------|-------|--------------------|---------|-------|--------------|---------|-------|
| | $\tau^*_{ci} = \tau^*_{cD50} \times (D_i/D_{50})^\beta$ | $\tau^{**}_{ci} = \tau^{**}_{cD50} \times (D_i/D_{50})^\beta$ | $q^*_{ci} = q^*_{cD50} \times (D_i/D_{50})^\beta$ | τ^*_{cD50} | β | r^2 | τ^{**}_{cD50} | β | r^2 | q^*_{cD50} | β | r^2 |
| Ob #1 | 0.09 | -0.78 | 0.99 | 0.02 | -0.54 | 0.93 | 2.4 | -0.98 | 0.97 | | | |
| Ob #2 | 0.10 | -0.73 | 0.98 | 0.06 | -0.54 | 0.90 | 19.1 | -0.93 | 0.95 | | | |
| Lb #1 | 0.07 | -0.96 | 1.00 | 0.03 | -0.91 | 0.98 | 5.1 | -1.39 | 0.99 | | | |
| LB #2 | 0.14 | -0.88 | 0.98 | 0.03 | -0.76 | 0.91 | 4.3 | -1.23 | 0.95 | | | |
| Pb #1 | 0.11 | -0.85 | 0.97 | 0.02 | -0.67 | 0.81 | 2.4 | -1.12 | 0.90 | | | |

In terms of q^*_c , Bathurst et al. (1987) and Bathurst (2013) report a dependency of q^*_c with bed gradient for uniform sediment. This relation also exists for q^*_{cD50} presented in this study (Figure B-89) and in addition to the similar trend, both equations of Bathurst (1987 and 2013) match well with the observations (Figure B-89c). Thus, the q^*_{cD50} of mixed sediment is in a close range with q^*_c of uniform sediment, which confirms the D_{50} as reference grain size for fractional entrainment (Bathurst, 2013).

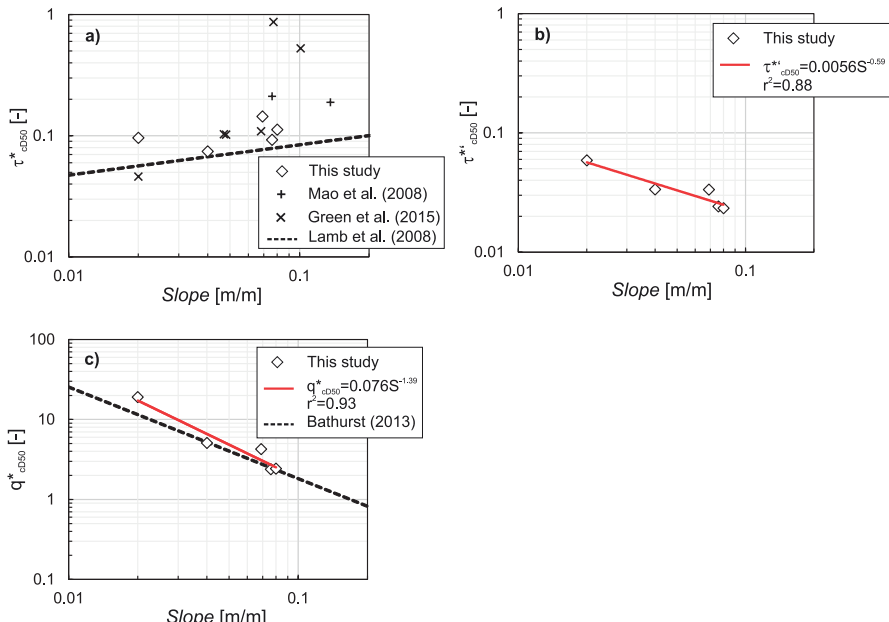


Figure B-89: τ^*_{cD50} (a), τ^{}_{cD50} (b), and q^*_{cD50} (c) plotted against bed slope. The red lines in (b) and (c) are fitted power functions and the black, dashed lines correspond to equations from literature: a) $\tau^*_c=0.15S^{0.25}$ (Lamb et al., 2008; based on flume and field data) and c) $q^*_c=0.13S^{-1.15}$ (Bathurst, 2013; based on flume data with uniform sized sediment)**

The critical conditions of any other grain size than the D_{50} further depends on its relative size D/D_{50} and the hiding exponent. For three sites, this relation is illustrated by plotting r^*_{ci} and $r^{*\epsilon}_{ci}$ against relative grain size (Figure B-90).

In terms of dimensionless total boundary shear stress, almost equal mobility persists at site 1 of the Laengentalerbach, while fractional mobility is shifted towards weak and moderate size-selective conditions for the remaining four sites (Table B-25). Corresponding with the results obtained by the reference transport method, β is obviously lower for dimensionless effective shear stress. All except for one site is associated with moderate size-selective mobility.

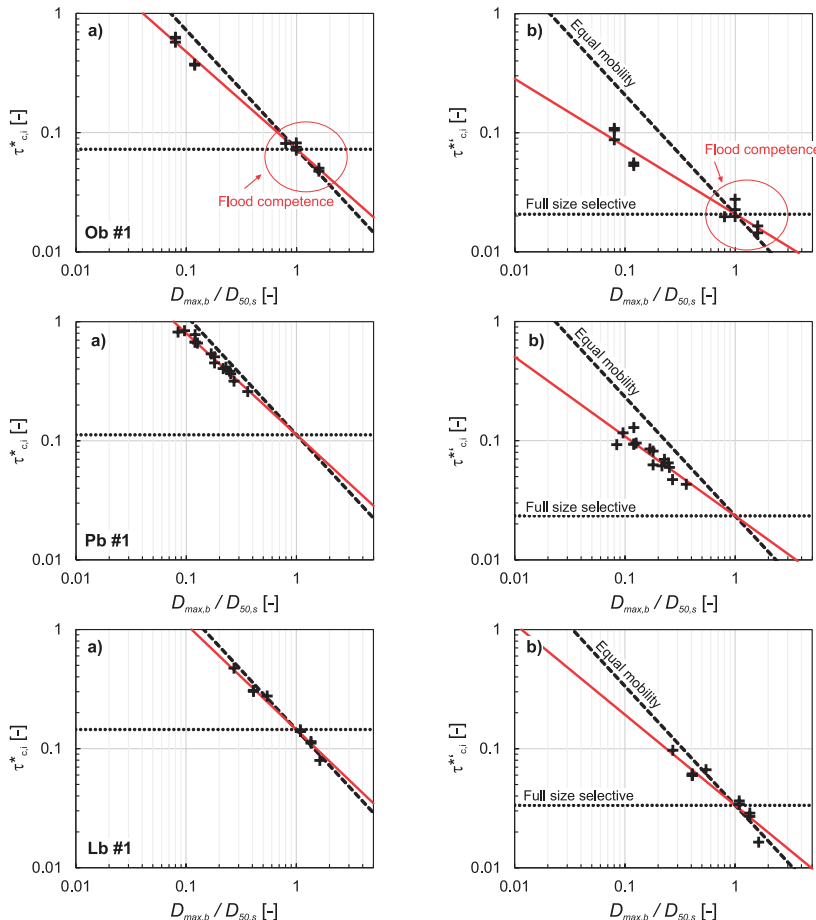


Figure B-90: r^*_{ci} (a) and $r^{*\epsilon}_{ci}$ (b) as a function of D/D_{max} for the three study sites Ob #1, Lb #1 and Pb #1. The red line is the fitted power function, the dashed line refers to equal mobility and the dotted line to full size-selective mobility.

In terms of dimensionless specific discharge, the hiding exponent b is within a range of -0.94 to -1.39 (Table B-25), which is in good agreement with values reported by Mao *et al.* (2008). However, it is not that easy to categorize b into the four classes 'almost equal' to 'strong size-selective' mobility since the specific discharge and the shear stress based approaches are not consistent with each other (see section 5.6.3). Nevertheless, equal mobility is defined by $b=-1.5$, while full size-selective mobility is attained with b in the range of (0;1) and thus, observed hiding exponents are closer to equal than full size-selective mobility.

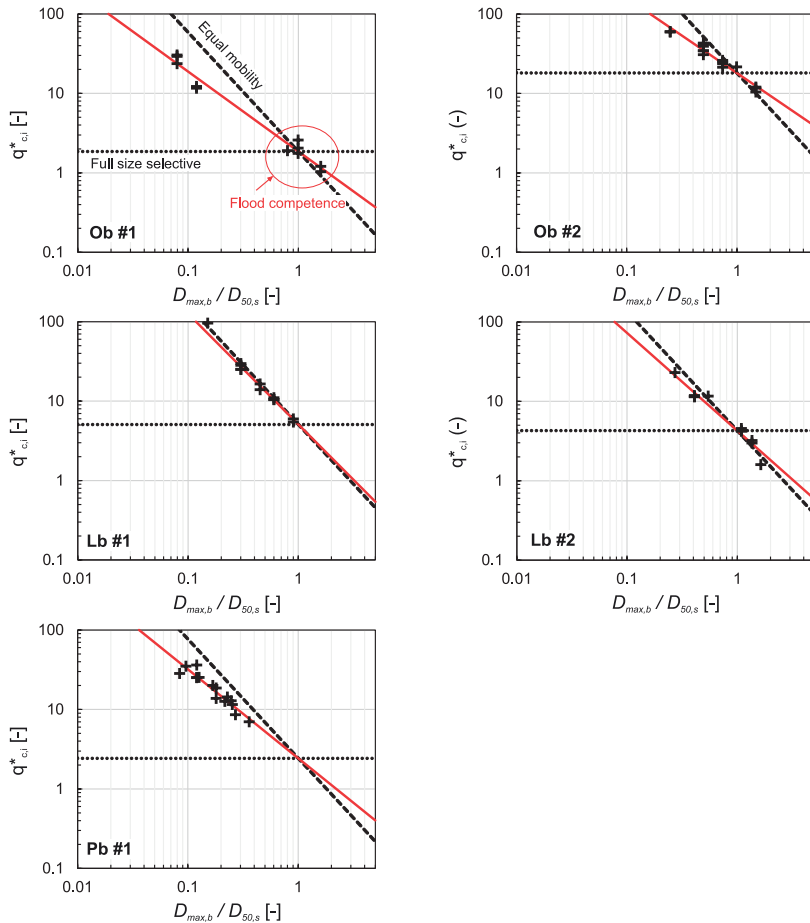


Figure B-91: q^*_{ci} as a function of D_i/D_{max} for all study sites. The red line is the fitted power function, the dashed line refers to equal mobility and the dotted line to full size-selective mobility with $b=0$.

The coarsest ever measured grain size of bed load was larger than the bed surface D_{50} at three out of the five sites (see Figure B-91). According to the visual judgement, the data do not reveal any difference of the hiding exponent with respect to D/D_{50} . This is in agreement with *Mao et al.* (2008) and *Bathurst* (2013) but contradicts with flume experiments facing equilibrium transport at a mobile armor layer (*Wilcock and Crowe*, 2003). However, the number of $D_{max,b} > D_{50}$ is sparse and the diameter of the coarsest grains is less than $1.6D_{50}$, both limiting the significance of assessing the fractional incipient motion for $D_i > D_{50}$.

5.5.5 Incipient motion of the D_{50} and the exceeding duration

All hydraulic parameters associated with the incipient motion (flow competence method) or the reference transport rate (reference transport method) of the bed surface D_{50} (X_{cD50}) differ with respect to the site. This variability is not restricted to independent streams but it is even abundant at the reach-scale.

Considering the streambed of a given reach as a feedback system between the flow conditions and the bed load transport, it is of particular interest, how often incipient motion of the bed surface D_{50} is exceeded.

Therefore, the critical (flow competence method) and the reference parameters (reference method) of the bed surface D_{50} are assigned to the corresponding water discharge in a first step. Water discharge is continuously registered at the water intake structures and high-resolution discharge hydrographs, spanning over several years, are available for each stream (see section B.1.2). However, to account for lateral inflows between the water intake structure at the Oberbergbach and the site 2 (which is about 800 m further upstream), the water discharge was reduced by 15 %, which is the mean deviation of in-situ measured discharge. Based on these discharge hydrographs the duration of exceedance is then determined (Table B-26 and Table B-27).

Table B-26: The discharge associated with the critical shear stress or the critical specific discharge of the bed surface D_{50} and the duration of exceedance

| Field site | Critical discharge of the D_{50} | | | Duration of exceedance | | |
|------------|---|--|--|------------------------------------|-------------------------------------|---------------------------------|
| | $Q(\tau^*_{cD50})$ (m ³ /s) | $Q(\tau'^*_{cD50})$ (m ³ /s) | $Q(q^*_{cD50})$ (m ³ /s) | $Q > Q(\tau^*_{cD50})$ (days/a) | $Q > Q(\tau'^*_{cD50})$ (days/a) | $Q > Q(q^*_{cD50})$ (days/a) |
| Ob #1 | 6.8 | 7.1 | 6.9 | 1.9 | 1.4 | 1.7 |
| Ob #2 | 3.4 | 3.6 | 3.4 | 32.3 | 27.5 | 32.2 |
| Lb #1 | 1.0 | 1.0 | 0.94 | 95.0 | 95.0 | 100.0 |
| LB #2 | 2.4 | 3.0 | 2.2 | 18.8 | 9.5 | 23.8 |
| Pb #1 | 7.0 | 7.9 | 7.7 | 11.6 | 7.1 | 7.9 |

The water discharge exceeds the critical discharge of the bed surface D_{50} over long periods at the low-gradient accumulation reaches (Ob#1 and LB#1), while this duration of exceedance is lower at the sites facing step-pools (Ob#1, Lb#2, Pb#1).

Table B-27: The discharge associated with the reference shear stress of the bed surface D_{50} and the duration of exceedance

| Field site | Reference discharge of the D_{50} | | Duration of exceedance | |
|------------|---|--|------------------------------------|---------------------------------------|
| | $Q(\tau^*_{rD50})$ (m ³ /s) | $Q(\tau^{**}_{rD50})$ (m ³ /s) | $Q > Q(\tau^*_{rD50})$ (days/a) | $Q > Q(\tau^{**}_{rD50})$ (days/a) |
| Ob #1 | <i>insufficient data</i> | | | |
| Ob #2 | 6.8 | 6.2 | 0.5 | 1.2 |
| Lb #1 | 7.8 | 6.8 | 0.02 | 0.06 |
| LB #2 | 4.3 | 2.9 | 1.2 | 10.5 |
| Pb #1 | 5.1 | 3.9 | 30.3 | 51.0 |

The opposite is the case for the water discharge associated with the dimensionless reference shear stress (either based on total boundary shear stress or effective shear stress). It is rarely exceeded in the accumulation reaches, while more often in the step-pool reaches. It is worth to note, that the very large reference discharges at Lb#1 result from the irregular cross section at this site, with a lateral gravel bar which is flooded at flows larger than 2 m³/s. Due to that, the cross-sectional averaged shear stress (as used in this study) reveals a local peak at 2 m³/s, which is exceeded at 6.4 m³/s. However, the reference shear stress is probably attained at a lower discharge in the main channel.

B.5.6 Discussion

5.6.1 Dimensionless references shear stress

Although several compilations of dimensionless critical or reference shear stress from field studies reveal a dependency with channel slope (e.g. Lamb *et al.*, 2008; Recking, 2009), the performance of fitted functions is still poor, suggesting for additional influences.

In this respect, the correlation of several streambed characteristics with either τ^*_{rD50} or τ^{**}_{rD50} were investigated by Schneider *et al.* (2015; supporting information), but the coefficient of correlations of the fitted power functions were very low for all except of two parameters describing the sorting of the bed surface grain size distribution (GSD). High sorting coefficients are attributed to a wide range of different grain sizes and suggest either (i) high supply of mobile sediment (pronounced fine tail of GSD) or (ii) increased flow resistance due to coarse boulders (pronounced coarse tail of GSD). However, the trend of τ^*_{rD50} with the sorting coefficients is positive and thus, the dimensionless shear stress required to transport bed load is the higher the wider the GSD. In addition, the correlation vanishes if momentum losses due to macro-roughness elements are addressed by means of the dimensionless effective shear stress τ^{**}_{rD50} . Due to both of these circumstances, the argument (ii) more likely explains this dependency.

Recking (2012b) accounts for both, bed slope and differences in sediment supply, in his model by adjusting τ^*_r within an upper and lower bound. He argues that τ^*_r at a given bed slope is low in streams with a high supply of mobile sediment and vice versa. According to Study A (section B.3), transport efficiency (a possible proxy for sediment supply) is high at the Pitzbach, high to moderate at the Oberbergbach and moderate

at the Laengentalerbach. In this respect, τ^*_{rD50} of the Pitzbach lies indeed much lower than the regression lines in Figure B-87a, possibly due to the high sediment supply. In contrast, τ^*_{rD50} of the Laengentalerbach sites are both in the proximity of the regression lines. Only τ^*_{rD50} of the Oberbergbach does not support this conclusion, since τ^*_{rD50} plots above the lines in Figure B-87a, although sediment supply conditions are higher than at the Laengentalerbach.

5.6.2 Conformity between dimensionless reference and critical shear stress

The dimensionless critical shear stress obtained with the flow competence method is obviously lower than the dimensionless reference shear stress for all except the Pitzbach site. The differences between τ^*_{cD50} and τ^*_{rD50} seem systematic since the offset is constant for most cases (Figure B-92). This is in good agreement with *Buffington and Montgomery* (1997), who found that competence based τ^*_{cD50} were approx. 15 % to 30 % smaller than reference-based τ^*_{rD50} .

However, the difference of the corresponding water discharge is much larger. In the low-gradient accumulation reaches, the incipient motion of the D_{50} is exceeded over long periods, but the dimensionless reference transport rate ($W^*_{D50}=0.002$) is rarely attained. The difference is less pronounced in the step-pool reaches.

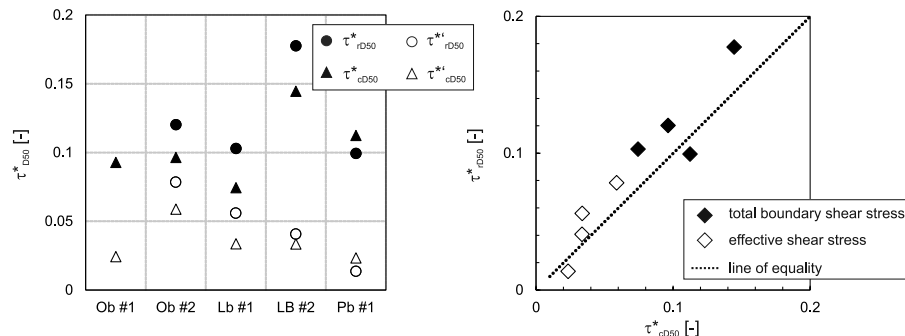


Figure B-92: Differences between τ^*_x whether it is determined with the reference transport method (τ^*_r) or the flow competence method (τ^*_c)

5.6.3 Interpretation of the hiding exponent b

Within this study, the hiding exponents based on either dimensionless total boundary shear stress (β) or dimensionless specific discharge (b) were determined independently. However, it is not clear how to interpret the hiding exponent b , or how to compare it with β . The question arises which of both concepts is more reliable, since they are not consistent:

Equal mobility in entrainment means that all grain sizes are mobilized at the same flow or shear stress. In terms of dimensionless shear stress τ^* (equation B62) this is obtained with $\beta=-1$, while it is $b=-1.5$ for q^* (equation B68), respectively. In contrast, full size-selective entrainment means that each grain size is mobilized independently of the sediment mixture: the flow required to entrain the i th grain size from a mixed sized bed is the same as for a uniform-sized bed. In this respect, *Shields* (1936) found that

incipient motion is attained at $\tau^*=0.06$ for grain related Reynolds numbers larger than 1000 (which is satisfied for steep streams with coarse sediment). Since $\tau^* \propto D^{-1}$ (equation B62) the dimensional shear stress required for entrainment linearly depends on the grain size. For example a shear stress of approx. 50 N/m² is required to entrain a grain size of 0.05 m, while τ needs to be approx. 100 N/m² for a grain size of 0.1 m (assuming a constant specific density of 1.65 and $\tau^*_c=0.06$).

In steep channels, the dimensionless specific discharge is often used for determining flow competence rather than the dimensionless shear stress. Based on flume experiments with uniform grain size, *Bathurst* (2013) reports incipient motion conditions at $q^*=0.13S^{1.14}$. Thus, the critical specific discharge q increases with grain size to the power of 1.5 for equal bed gradients (equation B68). For example assuming a bed gradient of 0.06 m/m, the critical specific discharge of a 0.05 m sized particle is 0.1 m²/s, while it is 0.3 m²/s for $D=0.1$ m, respectively.

Following the qualitative definition of full size-selective entrainment, as it is given above, the corresponding hiding exponents are clearly defined, with $\beta=0$ for dimensionless shear stress τ^* (in order to obtain a critical shear stress τ independent on grain size D ; equation B62) and $b=0$ for dimensionless specific discharge. In a consequence, the range of hiding exponents between equal and full size-selective entrainment are (-1;0) for τ^* and (-1.5,0) for q^* , respectively. Based on this definition, the hiding exponents obtained with $q^*(b)$ are related to β according

$$b = 1.5\beta \quad (\text{B80})$$

which corresponds to the dashed line in Figure B-93.

However, shear stress and specific discharge are not independent of each other, but can be substituted by means of a flow resistance equation. According to *Ferguson* (2007), the dimensionless shear stress based hiding exponent β can be converted to the corresponding dimensionless specific discharge based b by

$$b = (1+\beta)(c + 1.5) - 1.5 \quad (\text{B81})$$

with c ranging between 0.167 and 1, depending on the flow resistance equation applied. For steep mountain streams, c is typically closer to 1 than 0.167 (*Ferguson*, 2007; *Rickenman and Recking*, 2011), which yields $b \sim 1+2.5\beta$.

Summarizing, the empirically derived equations for the incipient motion of uniform sediment which are based on either q or τ are not consistent with each other. Assuming the full size-selective entrainment at $\beta=0$ (acc. *Shields*, 1936), the corresponding b is ~ 1 for steep streams. In contrast, assuming size-selective entrainment at $b=0$ (acc. *Bathurst*, 2013), the corresponding β is ~ -0.6 . This is confirmed by the data presented in this study (Figure B-93a) since the hiding exponents b and β (based on total boundary shear stress) are related to each other according to the conversion of *Ferguson* (2007; equation B81 with $c=1$). However, this inconsistency does not affect the outcomes of this study and it may be a further scientific issue where full size-selective conditions are located exactly.

Anyway, when b is compared with β (based on effective shear stress; Figure B-93b), the hiding exponents are more closely related to equation B80 and thus, full size-selective conditions according to both definitions coincide. The reason for this collapse is the reduced energy gradient used to compute the effective shear stress since this is

the only difference in τ_{rD50}^* and τ_{rD50}' . Thus, both concepts seem to be compatible when shear stress explicitly refers to grain resistance rather than total resistance.

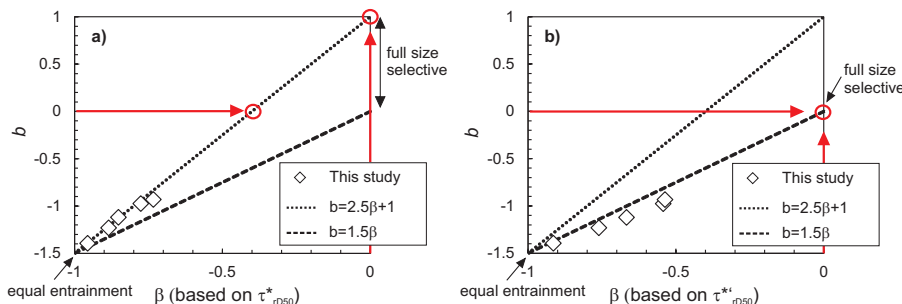


Figure B-93: Comparison between discharge based hiding exponent b and shear stress based β , with a) total and b) effective dimensionless shear stress.

5.6.4 Conclusion

The dimensionless reference shear stresses obtained from the bed load transport data presented in this study correspond well with those reported by Schneider *et al.* (2015). Since the method of both, measuring bed load transport and deriving the dimensionless reference shear stress from it, are identical, their agreement amplifies the empirical relations found by Schneider *et al.* (2015). However, there still remain some uncertainties. For instance, the dependency of bed slope with τ_{rD50}^* is not supported by the data of this study.

Accounting for form resistance by means of the dimensionless effective shear stress, causes τ_{rD50}^* to drop and it reveals a similar range as in low gradient gravel rivers. In addition, the fitted reference bed load transport equation with respect to dimensionless effective shear stress reveals similar exponents as the Wilcock and Crowe (2003) equation, which is based on low gradient flume data. Furthermore, the concepts of specific discharge and shear stress get compatible when effective shear stress is considered. Consequently, using effective shear stress seems a better choice in high-gradient channels.

Finally, field data from different literature sources, which differ in the methods used to determine incipient motion, should be used with caution. According to this study, the dimensionless reference shear stress (τ_{rD50}^* based on the reference transport method; section 5.4.2) is on average 13 % larger than the dimensionless critical shear stress (τ_{cD50}^* based on the flow competence method; section 5.4.3).

B.5.7 References of Study C

- Bathurst, J. C., W. H. Graf and H. H. Cao (1987), Bed load discharge equations for steep mountain rivers, In: *Sediment transport in gravelbed rivers*, C. R. Thorne, J. C. Bathurst, and R. D. Hey, eds., Wiley, Chichester, U.K., p. 453-477.
- Bathurst, J. C. (2013), Critical conditions for particle motion in coarse bed materials of nonuniform size distribution, *Geomorphology*, 197, 170-184.
- Buffington, J. M. and D. R. Montgomery (1997), A systematic analysis of eight decades of incipient motion studies, with special reference to gravel-bedded streams, *Wat. Resour. Res.*, 33(8), 1993-2029.

- Bunte, K., Abt, S., Potyondy, J. P. and Ryan, S. E. (2004), Measurement of coarse gravel and cobble transport using portable bedload traps, *J. Hydraul. Eng.*, 130(9), 879-893, doi: 10.1061/~ASCE!0733-9429-2004!130:9~879
- Eichner, B. (2015), Untersuchungen zum Geschiebetransport in Hochgebirgsbächen, Master thesis, University of Innsbruck, Innsbruck, Austria (in German).
- Einstein, H. A. (1950), The bed load function for sediment transportation in open channel flows, *Technical Bulletin No. 1026*, USDA, Washington, D.C.
- Fehr, R. (1987), Geschiebeanalysen in Gebirgsflüssen - Umrechnung und Vergleich von verschiedenen Analyseverfahren [Bed material analyses in mountain streams - Transformation and comparison of various analyses procedures], *Mitteilungen der Versuchsanstalt für Wasserbau, Hydrologie und Glaziologie an der ETH Zürich*, No. 92, 139 pp., ETH Zurich, Switzerland.
- Ferguson, R. (2007), Flow resistance equations for gravel- and boulder-bed streams, *Water Resour. Res.*, 43, W05427, doi: 10.1029/2006WR005422
- Foster, I. D. L., Ed. (2000), Tracers in Geomorphology, Wiley, Chichester.
- Ghilardi, T. (2013), Sediment transport and flow conditions in steep rivers with large immobile boulders, Ph.D. thesis, Ecole Polytechnique Federal De Lausanne, Lausanna, Switzerland.
- Gomez, B. and M. Church (1989), An assessment of bed load sediment transport formulae for gravel bed rivers, *Wat. Resour. Res.*, 25(6), 1161-1196.
- Green, K., Y. Alila and F. Brardinoni (2015), Patterns of bedload entrainment and transport in forested head water streams of the Columbia Mountains, Canada, *Earth Surf. Proc. Land.*, 40, 427-446, doi: 10.1002/esp.3642
- Hegenbart, N. (2015), Untersuchung zur Auswirkung von Geschiebefallen auf die Hydraulik, Bachelor thesis, Univ. Innsbruck, Innsbruck (in German).
- Hofer, B., 1985, Der Feststofftransport von Hochgebirgsbächen am Beispiel des Pitzbachs (Sediment transport of mountain streams: example of Pitzbach stream), Ph.D. thesis, Univ. Innsbruck, Innsbruck, 131 p (in German).
- Jackson, W. L., and R. L. Beschta (1982), A model of two-phase bed load transport in an Oregon coast range stream, *Earth Surf. Proc. Land.*, 7, 517-527.
- Lamb, M. P., W. E. Dietrich, and J. G. Venditti (2008), Is the critical Shields stress for incipient sediment motion dependent on channel-bed slope?, *J. Geophys. Res.-Earth*, 113(F2), doi: 10.1029/2007jf000831
- Mao, L., G. P. Uyttendaele, A. Iroume, M. A. Lenzi (2008), Field based analysis of sediment entrainment in two high gradient streams located in Alpine and Andine environments, *Geomorphology*, 93, 368-383.
- Meyer-Peter, E., and R. Müller (1948), Formulas for bed-load transport, in *Proceedings of the 2nd Meeting of the International Association for Hydraulic Structures Research*, pp. 39-64, Int. Assoc. Hydraul. Res., Delft, Netherlands
- Morgenschweis, G. (2010), Hydrometrie. Springer Verlag, Berlin Heidelberg.
- Mueller, E. R., J. Pitlick, and J. N. Nelson, (2005), Variation in the reference Shields stress for bed load transport in gravelbed streams and rivers, *Water Resour. Res.*, 41, W04006, doi: 10.1029/2004WR003692
- Nitsche, M., D. Rickenmann, D., J. M. Turowski, A. Badoux, and J. W. Kirchner (2011), Evaluation of bed load transport predictions using flow resistance equations to account for macro roughness in steep streams, *Water Resour. Res.*, 47, W08513, doi: 10.1029/2011WR010645
- Nitsche, M., D. Rickenmann, J. W. Kirchner, J. M. Turowski, and A. Badoux (2012), Macroroughness and variations in reach-averaged flow resistance in steep mountain streams, *Water Resour. Res.*, 48, W12518, doi: 10.1029/2012wr012091
- Parker, G. (1990), Surface-based bedload transport relation for gravel rivers, *J. Hydraul. Res.*, 28(4), 417-436.
- Parker, G., P. C. Klingeman, and D. G. Mclean (1982), Bedload and size distribution in paved gravel-bed streams, *J. Hydraul. Div. Am. Soc. Civ. Eng.*, 108(4), 544-571
- Recking, A. (2009), Theoretical development on the effects of changing flow hydraulics on incipient bed load motion, *Water Resour. Res.*, 45, W04401, doi: 10.1029/2008WR006826
- Recking, A. (2010), A comparison between flume and field bed load transport data and consequences for surface-based bed load transport prediction, *Wat. Resour. Res.*, 46, W03518, doi: 10.1029/2009WR008007
- Recking, A. (2012a), Bedload transport in rivers: from the flume to the field, Habilitation dissertation, Irstea (Cemagref), Grenoble, France. Available from Internet: <http://www.irstea.fr/recking>
- Recking, A. (2012b), Influence of sediment supply on mountain streams bedload transport, *Geomorphology*, 175-176, 139-150, doi: 10.1016/j.geomorph.2012.07.005.

- Rickenmann, D. (1990), Bedload transport capacity of slurry flows at steep slopes, Ph.D. thesis, ETH Zurich, Zurich, Switzerland.
- Rickenmann, D. (2001), Comparison of bed load transport in torrents and gravel bed streams, *Water Resour. Res.*, 37(12), 3295-3305.
- Rickenmann, D. and A. Recking (2011), Evaluation of flow resistance in gravel-bed rivers through a large data set, *Water Resour. Res.*, 47, W07538, doi: 10.1029/2010WR009793
- Schneider, J. M., D. Rickenmann, J. M. Turowski, K. Bunte, and J. W. Kirchner (2015), Applicability of bed load transport models for mixed size sediments in steep streams considering macro-roughness, *Water Resour. Res.*, 51, 5260-5283, doi: 10.1002/2014WR016417
- Shields, A. (1936), Anwendung der Ähnlichkeitsmechanik und der Turbulenzforschung auf die Geschiebebewegung, Vol. 26, 26 pp., Eigenverlag der Preußischen Versuchsanstalt für Wasserbau und Schiffbau Berlin, Berlin, Germany (in German).
- Turowski, J. M., A. Badoux and D. Rickenmann (2011), Start and end of bedload transport in gravel-bed streams, *Geophys. Res. Lett.*, 38, L04401, doi: 10.1029/2010GL046558
- Waldon, M. G. (2004), Estimation of average stream velocity, *J. Hydraul. Eng.*, 130(11), 1119–1122.
- Wilcock, P. R. and B. W. Mc Ardell (1993), Surface-based fractional transport rates: mobilization thresholds and partial transport of a sand-gravel sediment, *Water Resour. Res.*, 29(4), 1297-1312.
- Wilcock, P. R., and J. C. Crowe (2003), Surface based transport model for mixed size sediment, *J. Hydraul. Eng.*, 129(2), doi: 10.1061/(ASCE)0733-9429(2003)129:2(120)
- Yager, E. M., J. W. Kirchner, and W. E. Dietrich (2007), Calculating bed load transport in steep boulder bed channels, *Water Resour. Res.*, 43, W07418, doi: 10.1029/2006WR005432

B.6 Study D: Applicability of bed load transport equations in two glacier fed mountain streams

B.6.1 Introduction

In the field of river engineering, the development of reliable equations for calculating bed load rates has a long history. In the pioneering works of i.e. *Shields* (1936), or *Meyer-Peter and Müller* (1949), the bed load transport was intensively investigated by means of flume experiments and several empiric equations were formulated. However, most of the early works concentrated on large, but low-gradient streams (e.g. gravel bed streams), while steep streams were not addressed separately. But, the sediment transport dynamics in steep mountain streams are quite different from low-gradient channels (*Rickenmann*, 2001). This is accompanied with several topographical and morphological differences between steep natural channels and their lowland counterparts (*Montgomery and Buffington*, 1997), such as (i) overall steep and locally variable channel gradients, (ii) large, immobile boulders or channel spanning bed forms which feature high stability and (iii) low relative flow depths.

The work of *Smart and Jäggi* (1983) represents an early contribution on the topic of bed load transport in steep channels. The authors analyzed a large number of flume experiments with both, steep and low gradient flumes and formulated an empiric bed load transport equation.

Recently, essential research is done by means of measuring bed load transport in the field (e.g. *Schneider et al.*, 2015; *Rickenmann et al.*, 2014; *Bunte et al.*, 2004; *King et al.*, 2004). Amongst others, these data are then used to verify existing empirical approaches. The lesson of these studies is that flume derived bed load transport equations need to be improved when they are applied to natural streams (e.g. *Schneider et al.*, 2015; *Yager et al.*, 2012; *Recking*, 2012; *Recking*, 2010).

One reason for the huge differences between flume and the field data are probably attributed to morphological differences. The flume settings are often simplified and do not account for the bed structures of steep mountain streams (such as step-pools, immobile key stones). But, these bed structures are linked with an increase of bed stability and a decrease of the stream power that acts on the bed. Several studies report an improvement of the (flume derived) empiric bed load transport equations if the energy losses due to form drag are explicitly accounted for (*Yager et al.*, 2012; *Nitsche et al.*, 2011; *Chiari and Rickenmann*, 2010).

Another reason might be differences in the transport stages. Many flume experiments focused on phase 3 bed load transport (full mobility of the particles) with large bed load transport rates, whereas the field data often contain low bed load transport rates that are associated with phase 1 or phase 2 transport conditions (*Recking*, 2010). In this respect, field data with a wide range of bed load transport rates (in particular with large bed load transport rates) are generally sparse; simply because measuring bed load transport at high flows requires a lot of effort.

In this study, a long-term data set of bed load transport rate (Q_b) and water discharge (Q) that was obtained at two steep mountain streams is used to assess the performance of a several empiric bed load transport equations. Therefore, bed load transport equations of different kinds are tested, ranging from strictly flume based approaches (*Smart and Jäggi*, 1983), to flume based approaches which were adjusted by means

of field data (Rickenmann, 1990 in combination with Nitsche et al., 2011; Recking, 2010; Schneider et al., 2015).

B.6.2 Field data

6.2.1 Discharge and bed load transport rates

At the water intake structures situated in the Pitzbach and Oberbergbach, bed load transport rate (Q_b) was determined for a period of several years (see section B.1.4). In addition, the water discharge is gauged at the water intake structures by the hydro-power operator TIWAG and the discharge records are available for the entire period. The Q_b data span over a large discharge range with thousands of individual values, and thus, the data set contains a lot of information about the relationship between Q and Q_b (Study B in section B.4).

Both streams are located in the Central Alps of Northern Tyrol and they drain a partially glaciated catchment of 27 km² (Pitzbach) and 24 km² (Oberbergbach). For a detailed description of the stream morphology the reader is referred to Study B (section B.4.2).

6.2.2 Reach characteristics of the Oberbergbach

The stream reach that encloses upstream of the water intake structure of the Oberbergbach features step-pool morphology with a mean bed gradient of 0.076 m/m. Multiple cross sections were surveyed in course of a field campaign in the years 2014 and 2015. The representative cross section which is used for hydraulic computations is illustrated in Figure B-94a. The bed surface grain size distribution was measured by means of the transect-by-number method and converted into a volume-by-weight distribution according to a validated approach, given in section A.1.1. It is shown in Figure B-94b and it confirms with Ob#1 in

Table B-12 (section B.1.5).

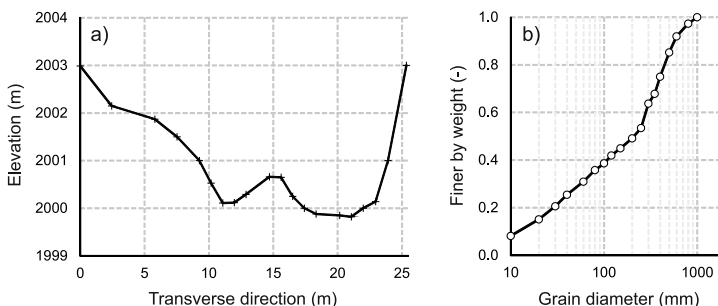


Figure B-94: a) Representative cross section of the stream reach enclosing upstream of the water intake structure at the Oberbergbach and b) the corresponding grain size distribution of the bed surface sediment

6.2.3 Reach characteristics of the Pitzbach

The stream reach that encloses upstream of the water intake structure of the Oberbergbach is boulder bedded and features step-pool morphology. The mean bed gradient is 0.08 m/m and the representative cross section is illustrated in Figure B-95. In analogy with the Oberbergbach, the bed surface grain size distribution was measured according to the transect-by-number method and converted into a volume-by-weight distribution. The grain size distribution is shown in Figure B-95b and it corresponds with Pb#1 in

Table B-12 (section B.1.5).

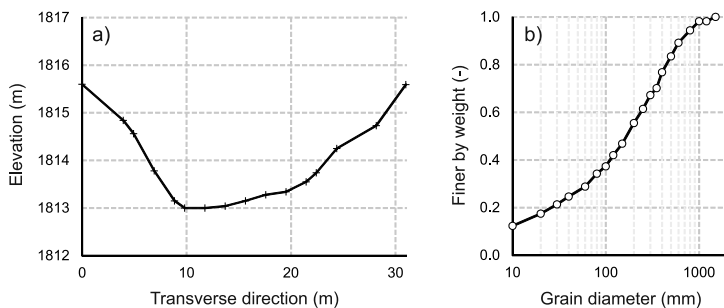


Figure B-95: a) Representative cross section of the stream reach enclosing upstream of the water intake structure at the Pitzbach and b) the corresponding grain size distribution of the bed surface sediment

B.6.3 Methods

6.3.1 Application of bed load transport equations

A variety of empiric bed load transport equations are applied to investigate if the rating curves obtained by these functions display the observed $Q-Q_b$ relationship. However, due to the large scatter of the observed $Q-Q_b$ relationship (see *Study B* in section B.4), any quantitative measure of the goodness of the functions seems not appropriate, but the quality of the bed load transport equations is more efficiently assessed by eye.

In total, six bed load transport equations are tested. Each of them enables to calculate bed load transport rates by means of hydraulic parameters, such as shear stress τ or specific discharge q . Four of these approaches refer to total bed load transport, while the remaining two approaches are based on fractional bed load transport rates.

For all approaches used in this study, the bed load transport rate is either a function of dimensionless shear stress

$$\tau^* = \frac{r_h S}{(s-1)D}, \quad (\text{B82})$$

with hydraulic radius r_h , bed slope S , specific solid density $s=2.65$ and grain size D or specific discharge

$$q = \frac{Q}{w}, \quad (\text{B83})$$

with discharge Q and flow width w , respectively.

6.3.2 Hydraulic computations

The hydraulic parameters required to determine r^* and q are back calculated from the measured water discharge and a representative cross section located immediately upstream of the water intake structure (section B.6.2). Therefore the variable power law equation (VPE) of *Ferguson* (2007)

$$U = \frac{a_1 a_2 (r_h/D_{84})}{\sqrt{a_1^2 + a_2^2 (r_h/D_{84})^{5/3}}} \sqrt{gr_h S}, \quad (\text{B84})$$

and mass continuity

$$Q = U \times A(d), \quad (\text{B85})$$

were iteratively solved. Herein, D_{84} is the grain size of which 84 % are finer by weight, g is the gravity, A is the flow area and a_1 and a_2 are empiric coefficients (*Rickenmann and Recking*, 2011). In its original form, equation B84 is written in terms of flow depth rather than hydraulic radius. But for natural and narrow channels, r_h is preferably used (e.g. *Nitsche et al.*, 2011; *Schneider et al.*, 2015).

In order to account for drag and spill drag due to macro-roughness elements, the effective dimensionless shear stress (r^*) is determined by means of the reduced energy gradient S_{red} (*Rickenmann and Recking*, 2011) instead of the bed gradient S . The reduced energy gradient is defined by

$$S_{\text{red}} = S \times \left(\frac{2.5 \left(\frac{r_h}{D_{84}} \right)^{5/6}}{\sqrt{6.5^2 + 2.5^2 \left(\frac{r_h}{D_{84}} \right)^{5/3}}} \right)^{1.5} \quad (\text{B86})$$

Since the hydraulic parameters are computed by means of a one-dimensional approach, the dimensionless shear stress and specific discharge correspond with the cross-sectional averaged value (fully 1d). However, the cross section of both streams is irregular and thus, r^* and q might differ within the cross section. Since bed load transport is a nonlinear function of hydraulic parameters, the computed bed load transport rates are expected to differ considerably.

To account for the irregularity of the cross section, it is divided into multiple increments (distributed 1d). The flow velocity (equation B84) is computed for each of these cross-sectional increments by means of the local $r_{h,i}$ (Figure B-96) and mass continuity (equation B85). Assuming a horizontal water surface at the cross section, the local $r_{h,i}$ is defined by

$$r_{h,i} = \frac{(h_{ws} - Z_i) w_i}{p_i}, \quad (B87)$$

Herein, h_{ws} is the elevation of the water surface, Z_i the mean bed elevation of the i th increment, its width w_i and wetted perimeter p_i , respectively. In addition, local discharge Q_i was also calculated for each increment and summed up to derive the total discharge Q_{calc} according

$$Q_{calc} = \sum_i^n U_i (h_{ws} - Z_i) W_i. \quad (B88)$$

In order to obtain an iterative solution of this set of equations, h_{ws} was varied until Q_{calc} approximated the measured discharge Q_{meas} with a maximum relative difference of 1e-4, respectively. It is worth to note, that the same method is applied in the simulation tool TomSed (Chiari, 2008).

In this study, the bed load transport equations are applied with respect to both methods, either fully 1d or distributed 1d.

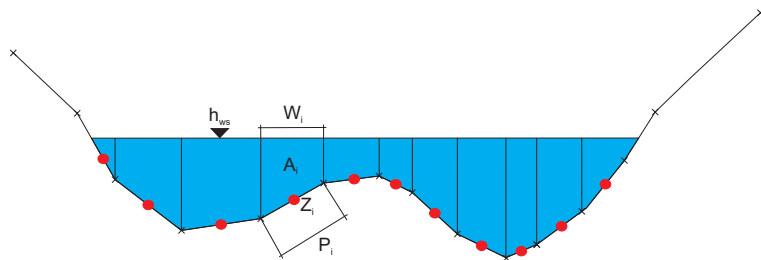


Figure B-96: Schematic illustration of the distributed 1d approach

6.3.3 Bed load transport equations

Smart and Jäggi (1983) derived a bed load transport equation which is based on flume data revealing a wide range of slopes. According to their approach, the specific bed load transport rate q_b (m^2/s) is defined by

$$q_b = \frac{4}{(s-1)} \left(\frac{D_{90}}{D_{30}} \right)^{0.2} q S^{1.6} \left(1 - \frac{\tau_c^*}{\tau^*} \right), \quad (B89)$$

with D_{90} and D_{30} , the grain sizes for which 90 % or 30 % are finer by weight, the critical dimensionless shear stress $\tau_c^* = 0.05$ and the dimensionless shear stress τ^* based on the arithmetic mean grain size.

Rickenmann (1990) expanded the data set of *Smart and Jäggi* (1983) and focused on the effect of the grain-fluid density ratio. The original equation obtained with the entire data set is

$$\phi_b = \frac{3.1}{\sqrt{(s-1)}} \left(\frac{D_{90}}{D_{30}} \right)^{0.2} \sqrt{\tau^*} (\tau^* - \tau_c^*) Fr^{1.1} \quad (B90)$$

with $\phi_b = q_b / [(s-1)gD_{50}^3]^{0.5}$ and the Froude number $Fr = v / \sqrt{gd}$, respectively.

However, equation B90 is often used in terms of a specific discharge based approach (e.g. *Rickenmann*, 2001; *Chiari*, 2008). In addition, the discharge based form of equation B90 was validated against field data by *Nitsche et al.* (2011) and the computations properly matched with the observations when the form drag was accounted for by means of the reduced energy gradient S_{red} (acc. *Rickenmann and Recking*, 2011; equation B86). Finally, the *Rickenmann* equation used in this study is defined by

$$q_b = \frac{3.1}{(s-1)^{1.5}} \left(\frac{D_{90}}{D_{30}} \right)^{0.2} (q - q_c) S_{red}^{1.5} \quad (\text{B91})$$

with the critical specific discharge q_c

$$q_c = 0.065(s-1)^{1.67} S^{1.12} \sqrt{gD_{50}^3}. \quad (\text{B92})$$

Both of these flume based equations reveal a threshold for incipient motion, which is either defined by τ^*_c or q_c . At flows not exceeding the incipient motion criteria, bed load transport rate is by definition zero. In contrast, field data reveal that bed load transport occurs even at low discharges, but at a very minute rate. To account for this phenomenon, non-threshold formulae are nowadays often used to compute bed load transport rate (e.g. *Schneider et al.*, 2015; *Recking*, 2010; *Barry et al.*, 2008; *Wilcock and Crowe*, 2003; *Parker and Klingeman*, 1982).

Recking (2010) proposed an approach which is based on a huge data set, comprising both, field and laboratory measurements. Therein, the bed load transport intensity ϕ is defined by

$$\begin{aligned} \phi_{D84} &= 0.0005 \left(\frac{D_{84}}{D_{50}} \right)^{-18\sqrt{S}} \left(\frac{\tau^*_{D84}}{\tau^*_{c,D84}} \right)^{6.5} && \text{for } \tau^*_{D84} < \tau^*_m \\ \phi_{D84} &= 14(\tau^*_{D84})^{2.5} && \text{for } \tau^*_{D84} > \tau^*_m \end{aligned} \quad (\text{B93})$$

with

$$\begin{aligned} \tau^*_{c,D84} &= (1.32S + 0.037) \left(\frac{D_{84}}{D_{50}} \right)^{-0.93} \\ \tau^*_m &= 12.53 \left(\frac{D_{84}}{D_{50}} \right)^{4.4\sqrt{S}} (\tau^*_{c,D84})^{1.6} \end{aligned} \quad (\text{B94})$$

As denoted by the suffixes, both, ϕ and τ^* , are determined with respect to the D_{84} .

Schneider et al. (2015) fitted the *Wilcock and Crowe* (2003) bed load transport equation to a large, high-quality field data set. In terms of effective shear stress τ^* and total bed load transport rate, the dimensionless reference transport rate W^* is defined by

$$W_{tot}^{*''} = \frac{(s-1)gq_b}{u^{*'^3}} = \begin{cases} 0.002 \times \left(\tau_{D50}^{*'} / \tau_{rD50}^{*'} \right)^{7.8} & \text{for } \tau_{D50}^{*'} / \tau_{rD50}^{*'} < 1.33 \\ 14 \times \left(1 - \frac{0.894}{\left(\tau_{D50}^{*'} / \tau_{rD50}^{*'} \right)^{0.5}} \right)^{4.5} & \text{for } \tau_{D50}^{*'} / \tau_{rD50}^{*'} > 1.33 \end{cases} \quad (B95)$$

Herein $u^{*''}$ is the shear velocity with respect to the effective shear stress $u^{*'} = \sqrt{gdS_{red}}$, $\tau^{*'}_{D50}$ is the dimensionless effective shear stress (equation B82) with respect to the D_{50} and the reduced energy gradient S_{red} (equation B86) and $\tau^{*'}_{rD50}=0.03$ is the dimensionless reference shear stress.

The bed load transport rate obtained with either of these formulae refers to the total bed load. At low to moderate discharges (phase 1 and phase 2 transport conditions), only a fraction of the grain size range is mobile. Typically, the bed load consists of sand and fine gravel for most of the time, while the transport of coarser sediment is restricted to ordinary (*Study C*, section B.5) or even exceptional flood events (e.g. *Turowski et al.*, 2009). To account for the grain size specific mobility, two fractional bed load transport equations are tested. The first approach was again derived by *Schneider et al.* (2015) and fractional bed load transport is defined by

$$W_i^{*''} = \frac{(s-1)gq_{b,i}}{f_i u^{*'^3}} = \begin{cases} 0.002 \times \left(\tau_i^{*'} / \tau_n^{*'} \right)^{6.82} & \text{for } \tau_i^{*'} / \tau_n^{*'} < 1.33 \\ 14 \times \left(1 - \frac{0.894}{\left(\tau_i^{*'} / \tau_n^{*'} \right)^{0.5}} \right)^{4.5} & \text{for } \tau_i^{*'} / \tau_n^{*'} > 1.33 \end{cases} \quad (B96)$$

In contrast to equation B95, $W^{*''}$ is determined for each grain size fraction and scaled by its abundance within the bed surface f_i . Consequently, $q_{b,i}$ is the specific bed load transport rate per unit width of the i th grain size fraction. The dimensionless shear stress $\tau^{*'}_i$ is computed with respect to the mean grain size D_i of the i th grain size fraction and the reference shear stress of the i th grain size fraction is determined by means of the hiding function proposed by *Wilcock and Crowe* (2003)

$$\begin{aligned} \tau_{r,i}^{*'} &= 0.03 \times \left(\frac{D_i}{D_{50}} \right)^\beta, \text{ with} \\ \beta &= \frac{0.67}{1 + \exp \left(1.5 - \frac{D_i}{D_{50}} \right)} - 1. \end{aligned} \quad (B97)$$

The total specific bed load transport rate (all grain size fractions) is obtained by simply summing up $q_{b,i}$ (equation B96).

In addition, the bed load transport rate is computed with the discharge based threshold equation of *Rickenmann* (2001), which is modified for surface based, fractional calculations in the following form:

$$q_{b,i} = f_i \times 1.5 \times (q - q_{c,i}) \times S_{red}^{1.5} \quad (B98)$$

The critical, specific discharge of D_i is determined according to the hiding function

$$q_{c,i} = q_{c,D50} \times \left(\frac{D_i}{D_{50}} \right)^b \quad (B99)$$

with the hiding exponent derived from field measurements (see *Study C*, section B.5), which is $b=0.52$ for the Oberbergbach and $b=0.38$ for the Pitzbach, respectively.

B.6.4 Results

6.4.1 Comparison of bed load transport predictions and observations

The rating curves obtained with the four bed load transport equations that predict the total bed load transport rate are plotted in Figure B-97 (Oberbergbach) and Figure B-98 (Pitzbach). Considering the flume based approach of *Smart and Jäggi* (1983), the rating curve plots considerably above the observed transport rates. This formula overestimates bed load transport of about two orders of magnitude. In contrast, the *Rickenmann* (2001) equation plots lower, which is predominately attributed to the use of S_{red} in order to account energy losses due to the form drag. The rating curves of both threshold-based approaches reveal a very steep lower tail, which is associated with the discharge close to incipient motion. In terms of dimensionless shear stress (*Smart and Jäggi* (1983) equation), incipient motion is attained at lower flows than with specific discharge (*Rickenmann* (1990) equation), respectively. In addition, the steep tailing edge is located at lower flows when hydraulic parameters are derived with the distributed 1d approach. In this respect, the threshold criterion is exceeded in the deeper parts of the cross sections only, which is not accounted for by the fully 1d approach.

The rating curves obtained with the non-threshold equations differ obviously regarding their gradient in the log-log scale. The *Recking* (2010) approach lies within the observed $Q-Q_b$ relation at low flows, while it underestimates the bed load transport rate at higher flows. In contrast, the *Schneider et al.* (2015) equation reproduces the ‘shape’ of the observed $Q-Q_b$ relation for the entire discharges exceeding about $2 \text{ m}^3/\text{s}$ (which is associated with Q_{bp1} in *Study B*) but covers its lower bound. The two different hydraulic methods (fully 1d or distributed 1d) cause the rating curves of the non-threshold equations to shift parallel. At the Oberbergbach, the bed load transport rate obtained with the *Schneider et al.* (2015) equation is about 1.5 orders of magnitude larger when the distributed 1d approach is used, while the difference is about one order of magnitude at the Pitzbach.

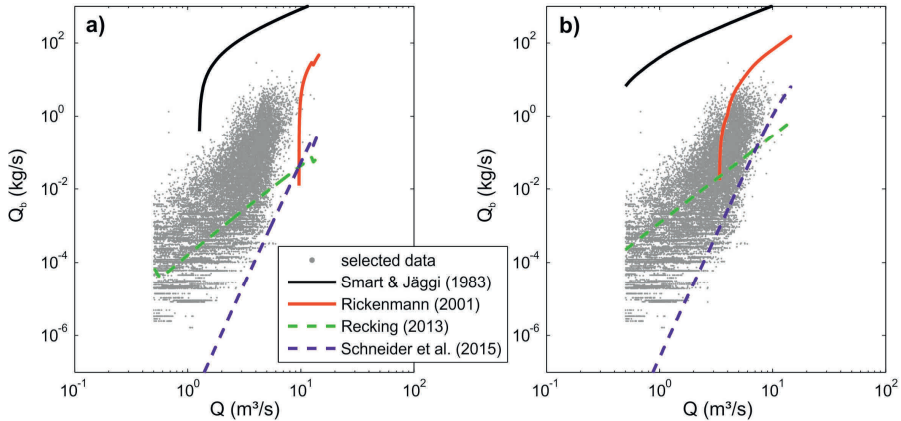


Figure B-97: Rating curves obtained for the Oberbergbach by means of the four formulae associated with total bed load transport rate in combination with the hydraulic approach a) fully 1d and b) distributed 1d.

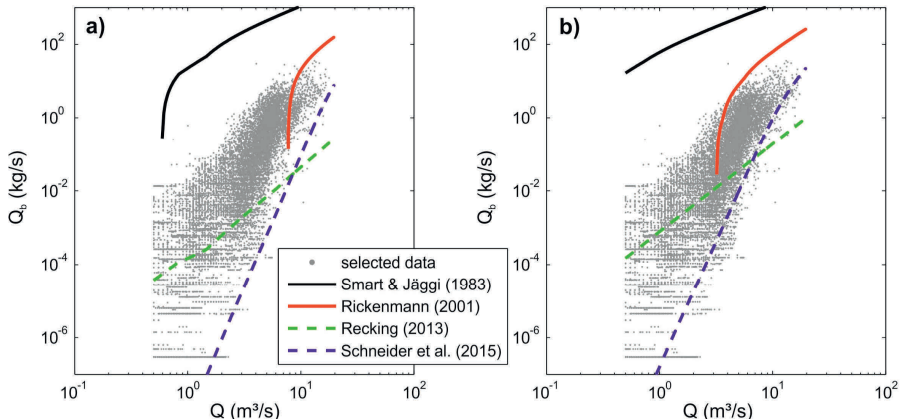


Figure B-98: Rating curves obtained for the Pitzbach by means of the four formulae associated with total bed load transport rate in combination with the hydraulic approach a) fully 1d and b) distributed 1d.

To account for the grain size specific mobility, the bed load transport rate is computed with two fractional bed load transport equations. The bed load transport rate of each grain size fraction is then summed up and the rating curves are plotted in Figure B-99 (Oberbergbach) and Figure B-100 (Pitzbach).

In analogy with the Schneider *et al.* (2015) equation of total bed load transport rate, its fractional variant covers the lower bound of observed Q_b . In contrast, the fractional variant of the Rickenmann (2001) approach covers the upper bound and it somehow reproduces the shape of the observed Q - Q_b relation. In addition, incipient motion is attained within a plausible discharge range. Thus, accounting for grain size specific mobility seems to improve this type of bed load transport formulae.

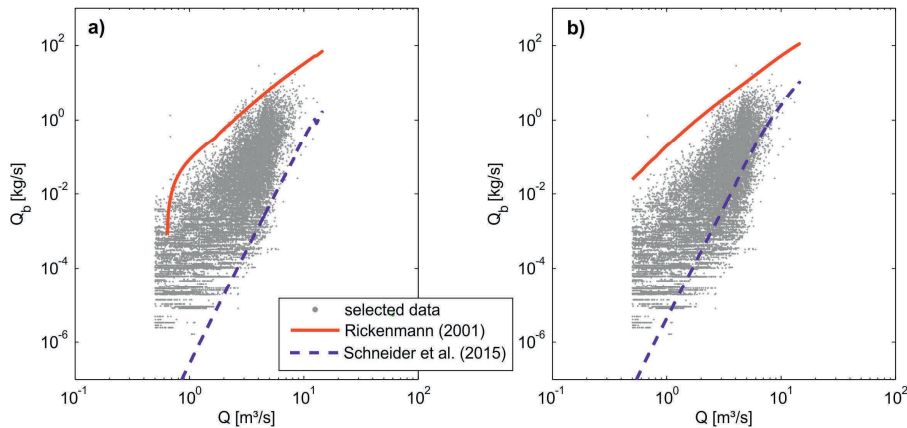


Figure B-99: Rating curves obtained for the Oberbergbach by means of the two formulae associated with fractional bed load transport rate in combination with the hydraulic approach a) fully 1d and b) distributed 1d.

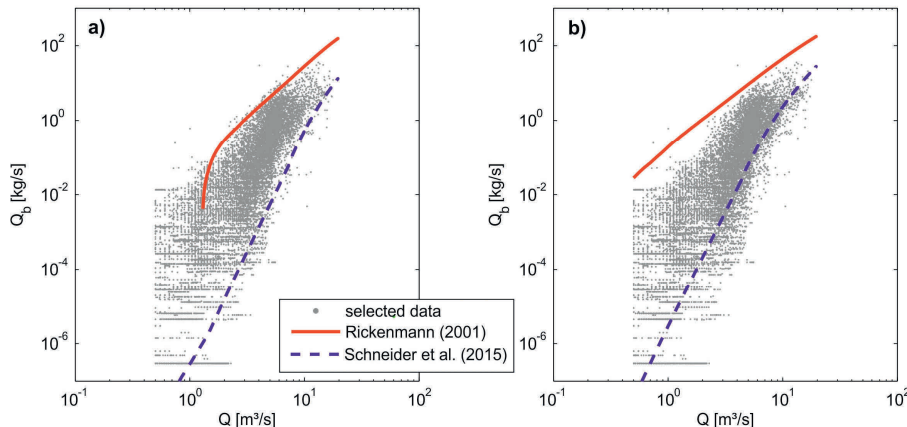


Figure B-100: Rating curves obtained for the Pitzbach by means of the two formulae associated with fractional bed load transport rate in combination with the hydraulic approach a) fully 1d and b) distributed 1d.

6.4.2 Adjusting the Schneider et al. (2015) approach

Summarizing, the shape of the Q - Q_b relation is best reproduced by the approach of Schneider et al. (2015), but it underestimates most of the observed Q_b . To obtain a proper match between calculated and observed Q_b , the rating curve should be located about one or two orders of magnitude higher (along with the y-axis) in Figure B-97 to Figure B-100.

Considering the empiric parameters of the Schneider et al. (2015) approach, the location of the rating curve in the log-log scale depends on the reference shear stress τ_{rD50}^* . However, τ_{rD50}^* is known to vary between sites (e.g. Study C in section B.5; Green et al., 2014; Schneider et al., 2015) and $\tau_{rD50}^* = 0.03$ as suggested by Schneider

et al. (2015) simply represents the mean value of their data set. Taking, for instance, the field data at the Pitzbach the reference shear stress is as low as 0.014 (*Study C*). This leads to the question which constant value of r^{*r}_{D50} causes the bed load transport equations of Schneider *et al.* (2015) to maximize the agreement between observed and computed Q_b . Therefore, Monte Carlo simulations are performed, with each realization differing in r^{*r}_{D50} . The computed bed load transport rates are compared with the observed ones by means of the discrepancy ratio X (equation B80). This procedure is applied to both approaches, the equation associated with total transport rate (equation B95) and its fractional variant (equation B96). Both equations are used in combination with the distributed 1d hydraulics. The best fit is assigned to the realization (or r^{*r}_{D50}) that reveals the largest X by considering the range of $0.1 < X < 10$.

For the total transport variant, the best fit is attained with $r^{*r}_{D50}=0.0162$ at both sites. Considering the fractional approach, the best agreement is obtained with $r^{*r}_{D50}=0.0213$ at the Oberbergbach, while it is $r^{*r}_{D50}=0.0192$ at the Pitzbach. The rating curves are given in Figure B-101 and they are all close to the center of the point cloud of observed $Q-Q_b$ for discharges exceeding Q_{bp1} .

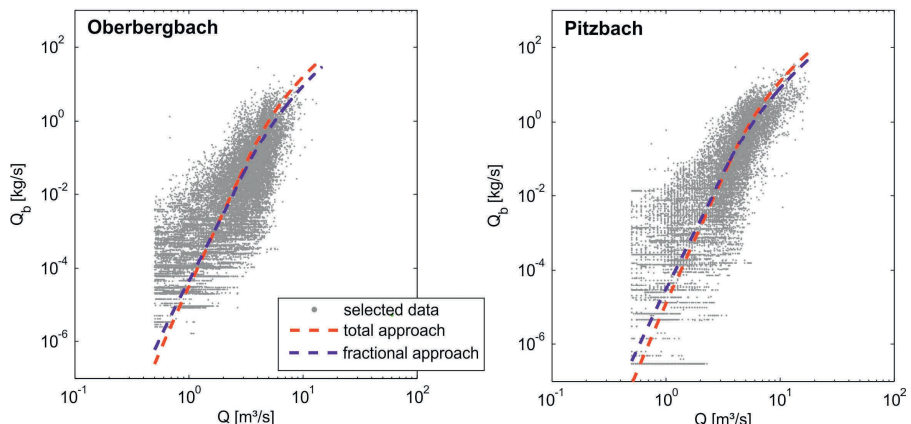


Figure B-101: Rating curves obtained with the Schneider *et al.* (2015) approach by using the fitted r^{*r}_{D50} .

6.4.3 Sensitivity of the parameters

All the approaches are used with constant input parameters. Thus, the corresponding rating curves (e.g. Figure B-101) reveal a constant $Q-Q_b$ relation and do not reproduce the remaining variability. However, one could argue that the variability of Q_b might result from the variability of the input parameters that are not constant over time. These parameters are associated with the geometric (cross section, bed slope) and morphologic (grain size distribution) boundary conditions.

At the Oberbergbach, the channel is constrained by bedrock and thus, the cross-sectional shape is assumed more or less constant over time. At the Pitzbach, the stream course is embedded in a broad alluvium and it changes during flood events, but aerial photographs suggest that the overall form remains constant as well. In a

consequence, there remains the bed surface grain size distribution which indeed alters over time. The grain size distribution depends on the flood history since the armor layer might break up during high flows, accompanied by the release of subsurface sediment. In addition, the sediment input from upstream reaches or from the hillslopes causes a change as well. But what is the range the grain size distribution has to alter that the computed Q_b covers the full range of observed Q_b ? Considering the fractional calculations, this question is hard to answer since both, the abundance of each grain size fraction f_i and the magnitude of the characteristic grain sizes (the reference grain size D_{50} and the proxy for macro-roughness D_{84}) has to be considered. Thus, there are many different grain size distributions that yield the same calculation result of bed load transport rate. Because of that, the total bed load transport equation B95 is used in combination with the fitted $r^{*,D_{50}}$ and only the D_{50} is considered to vary. Several hundred Q - Q_b rating curves are computed, each differing solely with respect to the D_{50} . For each observed data pair of Q - Q_b , the rating curve which is closest is selected. Applying this approach to the entire time series of Q - Q_b data yields a frequency distribution of the D_{50} , respectively.

The range of D_{50} required to cover the full range of observed Q_b is illustrated as boxplot in Figure B-102. It also indicates its frequency distribution. The D_{50} has to vary within a factor of 2 to cover 93 % (Oberbergbach) or 90 % (Pitzbach) of all observed Q_b . Since the D_{50} is about 0.21 m at the Oberbergbach and 0.16 m at the Pitzbach this corresponds to an interval of [0.10 m, 0.42 m] and [0.08 m, 0.33 m] respectively. The range of D_{50} necessary that equation B95 covers the inner quartile range (50 % of all data) of all observed Q_b is much smaller. It is [0.16 m, 0.27 m] at the Oberbergbach and [0.13 m, 0.20 m] at the Pitzbach, respectively.

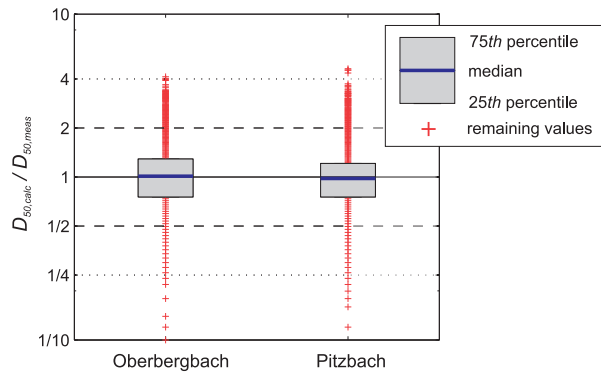


Figure B-102: Range of the bed surface D_{50} to obtain a collapse of observed and predicted bed load transport rates. The prediction is based on the Schneider et al. (2015) approach (equation B95) in combination with the fitted $r^{*,D_{50}}$.

B.6.5 Discussion

In terms of total bed load transport computations, the best performance is attained with the non-threshold equations proposed by Schneider et al. (2015). It reproduces at least

the 'shape' of the observed Q - Q_b relation, but still reveals an offset of about one order of magnitude at the log-log scale.

In terms of fractional bed load transport computations, the *Rickenmann* (2001) equation lies slightly above the upper bound of observed Q_b . This is associated with the maximum bed load transport capacity, which is of particular importance for the design of technical structures. But applying the *Rickenmann* (2001) equation to the annual hydrograph yields a severe overestimation of the annual bed load volume.

The fractional variant of the *Schneider et al.* (2015) approach is again close to the lower bound of observed Q_b . However, the *Schneider et al.* (2015) equations can be easily fitted against the observations by adjusting the reference shear stress r^*_{D50} . In addition, the approach is very sensitive against the bed surface D_{50} . For instance, changing the D_{50} by a factor of less than 1.3 causes the bed load transport predictions to cover 50 % of all observed transport rates. On the one hand, the high sensitivity of the grain size distribution on the bed load transport predictions (acc. to the *Schneider et al.* (2015) bed load transport equations) stresses the accuracy of the grain size data, since the field measurements usually face uncertainties (e.g. *Wohl*, 1996). On the other hand, the question arises if the scatter of the Q - Q_b relation really originates from changes of the bed surface grain size distribution. According to the visual evidence, an alteration of the bed topography at the Oberbergbach was limited to an exceptional flood event in August 2014. Except this event, the bed topography, such as the step-pools and immobile keystones in front of the water intake structure, did not alter since 2014. This suggests for minor alterations of the bed surface grain size distribution even during ordinary flood events. However, significant changes might have occurred at the patch-scale rather than at the reach-scale. *Bathurst* (2013) suggests that the consolidation of the bed sediment or its embedding are additional factors controlling the grain size specific mobility of the bed load. Furthermore, kinetic sorting affects the abundance of fines at the bed surface (*Bacchi et al.*, 2014). These mechanisms are not addressed by the bed load transport equations used in this study. Therefore, a modeling framework is necessary that considers the feedback between the streambed and the fractional bed load transport (e.g. *Heimann et al.*, 2015). The application of such a modeling framework poses severe uncertainties as long as it is not validated by means of simplified experiments, focusing on the effect of sediment supply on bed load transport rate in more detail.

B.6.6 References of Study D

- Bacchi, V., A. Recking, N. Eckert, P. Frey, G. Piton and M. Naaim (2014), The effect of kinetic sorting on sediment mobility on steep slopes, *Earth Surf. Proc. Land.*, doi: 10.1002/esp.3564
- Barry, J. J., J. M. Buffington, P. Goodwin, J. G. King, and W. W. Emmet (2008), Performance of bed-load transport equations relative to significance: predicting effective discharge and its transport rate, *J. Hydraul. Eng.*, 134/5, W10401, doi: 10.1029/2004WR003190.
- Bathurst, J. C. (2013), Critical conditions for particle motion in coarse bed materials of nonuniform size distribution, *Geomorphology*, 197, 170-184.
- Bunte, K., Abt, S., Potyondy, J. P. and Ryan, S. E. (2004), Measurement of coarse gravel and cobble transport using portable bedload traps, *J. Hydraul. Eng.*, 130(9), 879-893, doi: 10.1061/~ASCE!0733-9429~2004!130:9~879
- Chiari, M. (2008), Numerical modelling of bedload transport in torrents and mountain streams, Ph.D. thesis, University of Natural Resources and Applied Life Sciences, Vienna, Austria, 212 p.
- Chiari, M. and D. Rickenmann (2010), Back-calculation of bedload transport in steep channels with a numerical model, *Earth Surf. Process. Landforms*, 36, 805-815, doi: 10.1002/esp.2108

- Ferguson, R. (2007), Flow resistance equations for gravel- and boulder-bed streams, *Water Resour. Res.*, 43, W05427, doi: 10.1029/2006WR005422
- Green, K., Y. Alila and F. Brardinoni (2015), Patterns of bedload entrainment and transport in forested head water streams of the Columbia Mountains, Canada, *Earth Surf. Proc. Land.*, 40, 427–446, doi: 10.1002/esp.3642
- Heimann, F. U. M., D. Rickenmann, J. M. Turowski, and J. W. Kirchner (2015a), sedFlow – a tool for simulating bed load transport and longitudinal profile evolution in mountain streams, *Earth Surf. Dynam.*, 3, p. 15-34, doi: 10.5194/esurf-3-15-2015
- King, J.G., W. W. Emmett, P. J. Whiting, R. P. Kenworthy, and J. J. Barry (2004), Sediment Transport Data and related Information for selected coarse-bed streams and rivers in Idaho, *Gen. Tech. Rep. RMRS-GTR-131*, U.S. Dep. of Agric., For. Serv., Rocky Mt. Res. Stn, Fort Collins, Colo.
- Meyer-Peter, E., and R. Müller (1948), Formulas for bed-load transport, in Proceedings of the 2nd Meeting of the International Association for Hydraulic Structures Research, pp. 39–64, Int. Assoc. Hydraul. Res., Delft, Netherlands.
- Montgomery, D. R., and J. M. Buffington (1997), Channel-reach morphology in mountain drainage basins, *Geol. Soc. Am. Bull.*, 109(5), 596-611.
- Nitsche, M., D. Rickenmann, D., J. M. Turowski, A. Badoux, and J. W. Kirchner (2011), Evaluation of bed load transport predictions using flow resistance equations to account for macro roughness in steep streams, *Water Resour. Res.*, 47, W08513, doi: 10.1029/2011WR010645
- Parker, G., and P. C. Klingeman (1982), On why gravel bed streams are paved, *Water Resour. Res.*, 18(5), 1409-1423.
- Recking, A. (2010), A comparison between flume and field bedload transport data and consequences for surface based bedload transport prediction, *Water Resour. Res.*, 46(3), W03518, doi: 10.1029/2009WR008007
- Recking, A. (2012), Influence of sediment supply on mountain streams bedload transport, *Geomorphology*, 175-176, 139-150, doi: 10.1016/j.geomorph.2012.07.005
- Rickenmann, D. and A. Recking (2011), Evaluation of flow resistance in gravel-bed rivers through a large data set, *Water Resour. Res.*, 47, W07538, doi: 10.1029/2010WR009793
- Rickenmann, D. (1990), Bedload transport capacity of slurry flows at steep slopes, Ph.D. thesis, ETHZ, Zurich, Switzerland, 249 p.
- Rickenmann, D. (2001), Comparison of bed load transport in torrents and gravel bed streams, *Water Resour. Res.*, 37(12), 3295-3305.
- Rickenmann, D., J. M. Turowski, B. Fritsch, C. Wyss, J. Laronne, R. Barzilai, I. Reid, A. Kreisler, J. Aigner, H. Seitz, and H. Habersack (2014), Bed load transport measurements with impact plate geophones: comparison of sensor calibration in different gravel-bed streams, *Earth Surf. Proc. Land.*, 39 (7), 928-942, doi: 10.1002/esp.3499.
- Schneider, J. M., D. Rickenmann, J. M. Turowski, K. Bunte, and J. W. Kirchner (2015), Applicability of bed load transport models for mixedsize sediments in steep streams considering macro-roughness, *Water Resour. Res.*, 51, 5260-5283, doi: 10.1002/2014WR016417.
- Shields, A. (1936), Anwendung der Ähnlichkeitsmechanik und der Turbulenzforschung auf die Geschiebebewegung (Application of similarity mechanics and turbulence research on shear flow), Mitteilungen der Preußischen Versuchsanstalt für Wasserbau (in German), No. 26, Preußische Versuchsanstalt für Wasserbau, Berlin, Germany.
- Smart, G.M. and M.N.R. Jäggi (1983), Sediment transport on steep slopes, *Mitteilungen der Versuchsanstalt für Wasserbau, Hydrologie und Glaziologie an der ETH Zürich*, No. 64, ETH Zurich, Switzerland.
- Turowski, J. M., E. M. Yager, A. Badoux, D. Rickenmann, and P. Molnar (2009), The impact of exceptional events on erosion, bed load transport and channel stability in a step-pool channel, *Earth Surf. Proc. Land.*, 34, 1661-1673, doi: 10.1002/esp.1855.
- Wilcock, P. R., and J. C. Crowe (2003), Surface based transport model for mixed size sediment, *J. Hydraul. Eng.*, 129(2), doi: 10.1061/(ASCE)0733-9429(2003)129:2(120)
- Wohl, E. E., D. J. Anthony, S. W. Madson, and D. M. Thompson (1996), A comparison of surface sampling methods for coarse fluvial sediments, *Wat. Resour. Res.*, 32(10), 3219-3226.
- Yager, E. M., W. E. Dietrich, J. W. Kirchner, and B. W. McArdell (2012), Prediction of sediment transport in step-pool channels, *Water Resour. Res.*, 48, W01541, doi: 10.1029/2011WR010829.

C THE FEEDBACK BETWEEN SUPPLY AND TRANSPORT RATE OF MOBILE BED LOAD IN STEEP STREAMS

C.1 Study E⁴: The effect of sediment supply on bed load transport

C.1.1 Introduction

Mountain streams feature relevant topographical and morphological differences to their lowland counterparts (*Montgomery and Buffington*, 1997), such as (i) overall steep and locally variable channel gradients, (ii) wide grain size distributions, (iii) large, immobile boulders or channel spanning bed forms which feature high stability and (iv) low relative flow depths. Summarizing, the riverbed of mountain streams is often poorly sorted and segregated into a variety of structures. The mobility of single grains is variable and strongly affected by (i) hiding and protrusion (*Bathurst*, 2013; *Bunte et al.*, 2013), (ii) presence of immobile boulders (*Ghilardi et al.*, 2014; *Yager et al.*, 2007), (iii) clustering (*Lamarre and Roy*, 2008; *Hassan and Church*, 2000; *Church et al.*, 1998) and (iv) supply conditions as well (*Yager et al.*, 2012a).

Even though a fully verified theoretical basis on bed load transport in mountain streams is still a topic in need of further research, recently published field data (e.g. *Study C* in chapter B) confirm a weak form of size-selective or partial bed load transport in supply-limited mountain streams, at least up to a certain level of discharge (*Bathurst*, 2013; *Bunte et al.*, 2013; *Mao et al.*, 2008; *Mao and Lenzi*, 2007). While the coarse fractions of the bed surface remain immobile, only material from local patches of fines (gravel and cobble) gets scoured (*Yager et al.*, 2012b; *Mao et al.*, 2008; *Garcia et al.*, 2007; *Laronne et al.*, 2001; *Jackson and Beschta*, 1982). Thus, the availability of fine sediment is a major controlling factor regarding the transport efficiency (*Study A* in chapter B; *Mao et al.*, 2014; *Recking*, 2012; *Barry et al.* 2004; *Habersack and Laronne*, 2001; *Rickenmann*, 2001; *Garcia et al.*, 2000; *Egashira and Ashida*, 1991).

However, the availability of fine bed material changes temporally, due to the sediment inflow from upstream reaches or tributaries. In mountainous environments, sediment is often supplied episodically by debris flows or flood events in steep tributary channels (*Hoffman and Gabet*, 2007; *Gintz et al.*, 1996). But, the bed load availability varies also in a marginal scale, for example, due to differences in runoff origin (*Mao et al.*, 2012), causing an alteration of the $Q-Q_b$ relation at a given site throughout the year (e.g. *Study C* in chapter B). There remains a lack of knowledge regarding bed load transport and morphologic processes facing alterations of the availability of mobile bed load at flow conditions distinctly below the break-up of the bed surface (e.g. *Koll*, 2012). This is even more pronounced when referred to wide-graded mountain streams. Though numerous studies state that fine bed load that originates from upstream reaches is transported over the armored bed surface (*Bunte et al.*, 2013; *Recking*, 2010; *Chin and Wohl*, 2005; *Habersack and Laronne*, 2001; *Lisle*, 1995; *Egashira and Ashida*, 1991; *Jackson and Beschta*, 1982; *Sommer and Lauffer*, 1982), only three studies (*Yu et al.*, 2012; *Yu et al.*, 2009; *Egashira and Ashida*, 1991) could be found in literature, that explicitly dealt with this phenomenon in steep streams.

⁴ A condensed version of this *Study E* is published in the *International Journal of Sediment Research* (doi: 10.1016/j.ijsrc.2017.03.004). The co-authors are Bernhard Gems, Daniel Kößler, and Markus Aufleger.

1.1.1 Propagation of supplied sediment

Egashira and Ashida (1991) tested the hypothesis that fine bed load which is supplied to a steep flume will be transported over the stable bed surface at low flows. Therefore, they performed two experimental tests, where they fed very fine sediment ($D_m=0.63$ mm) to an armored flume ($D_m=26.3$ mm) with a channel gradient of 0.033 m/m and a discharge half of magnitude than the former stabilizing one. The two experiments differed in bed morphology, which was a rough bed and a step-pool bed, respectively. The supplied sediment first filled the interstices of the armor layer or the pools and subsequent arriving grains were transported over it or mobilized the stored sediment, but the bed surface remained unchanged (*Egashira and Ashida*, 1991). The bed load transport rate at the flume outlet showed a temporal evolution which could be separated into five distinct phases: (i) a temporal lag between model input and initial outflow, (ii) an increase of bed load transport rate towards the feeding rate, (iii) an equilibrium condition of input and outflow, (iv) a decrease of transport rate after feeding was stopped until (v) it approached zero again. In this respect, *Egashira and Ashida* (1991) found that the temporal lag (i) was larger for the step-pool bed, suggesting that the magnitude of sediment storage on the bed surface depends on the bed surface roughness.

Feeding experiments in a steep flume are reported in *Koll* (2002). In contrast to *Egashira and Ashida* (1991), the water discharges of the bed surface armoring and the subsequent feeding runs were equal. Similar studies are also available from low-sloped flumes with armored beds and a channel slope of about 0.005 m/m (e.g. *Spiller et al.*, 2012; *Venditti et al.*, 2010a; *Sklar et al.*, 2009). According to these studies, the supplied bed load was immediately transported downstream by featuring a mix of translational and dispersive propagation. The leading edge of the sediment pulse reached the flume outlet after a certain time lag, referring to phase 1 in *Egashira and Ashida* (1991). However, the sediment pulse dispersed (it grew in length) by leaving a fraction of supplied grains behind and thus it spread more on its tailing edge (*Sklar et al.*, 2009). Although the feeding duration exceeded the travelling time (duration of phase 1) only in one out of several experiments, the results of *Sklar et al.* (2009) and *Venditti et al.* (2010a) showed that outflow rate during phase 3 fluctuated but approached on average the feeding rate for all except one experimental run. In contrast, the outflow rate exceeded the feeding rate in most of the experiments of *Koll* (2002). Once feeding was stopped, bed load transport rate firstly decreased rapidly but either remained constant at a low level or slowly approached zero in any of the reported experiments. Hence, the duration of phase 4 (the post-feeding decline of bed load transport rate) was much longer than pre-pulse raising, which partly contradicts with the hypothesis discussed in *Egashira and Ashida* (1991). *Venditti et al.* (2010a) attributed the slow decline to the progressive removal of temporally stored pulse sediment and the mobilization of bed material. Similar patterns could be also found in the course of real-scale experiments in a mountain stream by *Yu et al.* (2009).

Koll (2012) investigated the propagation of a very limited amount of fine bed load which was placed on an armored bed with a channel gradient of 0.0045 m/m beforehand. The propagation velocity of the tracer sediment decreased with time and the leading edge was faster than the center of the tracer bar, but the rate of velocity decline was nearly identical. Thus, the impact of increased availability of fine (more mobile) bed load diminished after a certain distance or time, depending on the magnitude of supply.

In this context, *Koll* (2012) found a linear dependency of non-dimensional tracer velocity u_T^* with non-dimensional tracer mass m_T^* and non-dimensional shear stress of the supplied bed load τ_T^* normalized by non-dimensional time t^* :

$$\dot{u}_T = A \times \frac{m_T^* \times \tau_T^*}{t_T^*} \rightarrow \frac{u_T}{\sqrt{(s-1)gd_T}} = A \times \frac{\frac{m_T}{\rho_s d_T^2} \times \frac{dS}{(s-1)d_T}}{t \sqrt{\frac{g}{d_T}}}, \quad (\text{C1})$$

with the tracer velocity u_T (m/s), gravitational acceleration g (m/s²), mean diameter of the tracer particles d_T (m), an empiric coefficient A (-), the tracer mass per unit bed width m_T (kg/m), solid density ρ_s (kg/m³), flow depth d (m), energy slope S (m/m) and the duration since introducing the tracer sediment t (s), respectively. Thus, the tracer velocity at a certain time and a given flow depends on pulse characteristics according $u_T(t) \propto m_T \times d_T^{-2}$ which means, the larger the supplied mass or the smaller the added grains, the faster the pulse propagates downstream. In contrast to the experiments of *Egashira and Ashida* (1991) as well as those of *Sklar et al.* (2009) and *Venditti et al.* (2010a), tracer sediment were placed onto the bed surface beforehand. By supplying sediment continuously to a flume, the tracer mass per unit width linearly increases with time according

$$m_T(t) = q_{b,in} \times \rho_s \times t, \quad (\text{C2})$$

with the feeding rate per unit width $q_{b,in}$ (m²/s), respectively. Substituting equation C2 into equation C1 yields

$$u_T^* = A \times \frac{q_{b,in}}{\sqrt{gd_T^3}} \times \frac{dS}{(s-1)d_T} = A \times \psi_T \times \tau_T^*. \quad (\text{C3})$$

Hence, the dimensionless propagation velocity (for example of the leading edge) is expected to increase linearly with $\psi_T \times \tau_T^*$ in the case of continuous feeding. While an increase of flow causes the individual grain to move faster (e.g. *Koll et al.*, 2010; *Wong et al.*, 2007; *Ferguson et al.*, 2002), an increase of feeding rate is suggested to fill the interstices of the bed surface more quickly and thus, increases the bed load transport rate of subsequent grains.

In contrast to low-sloped flumes, the bed surface is much coarser in steep streams and a larger amount of bed load is needed to smooth the bed surface (*Egashira and Ashida*, 1991). Additionally, only a fraction of total flow competence is available for bed load transport due to form and spill drag around immobile grains (e.g. *Yager et al.*, 2007; *Ghilardi et al.*, 2014). Hence, the propagation velocity is expected to be much lower in steep, rough channels compared to the experimental results obtained by *Sklar et al.* (2009).

1.1.2 Impact on bed stability

Egashira and Ashida (1991) did not mention that any bed material was eroded during their experiments, letting to suggest that supplied sediment were totally transported

over the bed surface. In contrast, *Koll* (2002) report significant erosion of the bed material when sediment is supplied at a discharge equal the critical discharge of the bed surface. The decrease of bed stability depends on the mobility of the supplied sediment, with small grains promoting bed material erosion. *Venditti et al.* (2010b) found that supplied bed load interacts with the material present on the bed surface and causes a shift from a partial to near equal-mobility regime with respect to the subsurface grain size distribution. In addition, the fraction of supplied sediment in total load typically decreases with time during the post-feeding phase (*Spiller et al.*, 2012; *Venditti et al.*, 2010a). Hence, more bed material is mobilized once the temporary storage of supplied grains is almost empty, which suggests for an overall decrease of bed stability. However, the discharge during the feeding experiments was the flow used to armor the bed surface for all studies except *Egashira and Ashida* (1991).

C.1.2 Flume experiments

1.2.1 Experimental setup

A physical model was constructed at the hydraulic laboratory of the University of Innsbruck in order to investigate bed load transport of relatively fine sediment (smaller than the median diameter of the bed surface) over a stabilized surface layer facing different flow conditions. In contrast to the common experimental setup (e.g. *Egashira and Ashida*, 1991; *Venditti et al.*, 2010a), the flume featured a slightly variable width. As suggested by *Comiti et al.* (2009) and *Zimmermann et al.* (2010), a non-uniform flume favors complex three-dimensional flow patterns which better reproduce conditions typically present in steep mountain streams. Though the vertical rough walls constrain the flow, their irregular course forces the water flow to form its own river bed with respect to both, its cross-sectional shape and its longitudinal thalweg. Therefore, the experimental arrangements were guided by the conditions observed in a reach of the Gurgler Ache River, a mountain stream in the Ötztal Valley in the Tyrolean Alps, Austria. The investigated river reach ($46^{\circ}52'08''$ N, $11^{\circ}01'20''$ E) features a length of 140 m, a slightly irregular water course with a trapezoidal cross section and a mean channel gradient of 0.02 m/m. Bankful channel width spans over roughly 14 m, while flow width is about 8 m at low to moderate discharges. The bed surface dominantly consists of cobbles and boulders, featuring patches of fines (coarse sand and gravel) in their wakes. According to the classification of *Montgomery and Buffington* (1997), the reach exhibits a rough bed with individual, not channel spanning steps (Figure C-1).

The irregular water course of that reach means the prototype reference of the physical model, featuring the scale 1:20 (Froude similarity) and, accordingly, a length of 7 m. Therefore, the lateral extent of the flume was defined by the waterline of the natural reach at moderate flow conditions (Figure C-1). Bed width spanned between 0.27 m and 0.48 m in the scale model and sidewalls were chosen to be vertical.

The flume bed was mobile and the bulk sediment shared a grain size distribution corresponding with that measured in prototype reach, but scaled by 1:20 and truncated at 0.5 mm (model scale). The sediment mixture was generated by mixing sediment of different grain size classes according to the pre-defined proportions. The smallest grain size class featured a diameter range from 0.5 mm to 1.0 mm, while the coarsest class was 16 mm to 32 mm (model scale).

The longitudinal gradient was 2 times the gradient of the prototype reach, in order to allow for rotational erosion in the course of stabilizing the mobile bed. Upstream from this channel section, a 5 m long homogeneous flume acted as a run-up reach.



Figure C-1: Overview of the prototype reach (left) and the physical scale model (right); yellow lines in the leFigure C-2ft picture roughly feature the mobile bed boundaries and the flow section of the flume

1.2.2 Experimental procedure

1.2.2.1 Sequence of the experiments

In total, four experimental series are illustrated, that differed in the grain sizes of the supplied bed load. In order to distinguish the added grains from bed material, the former were colored differently beforehand. In the following, the color of the sediment represents the name of each of the series. In the first three experimental series uniform sediment was used, featuring median grain sizes (D_{50}) of 1.1 mm (range: 0.5 - 2.0 mm; colored green), 2.7 mm (2.0 - 3.2 mm; colored blue) and 3.9 mm (3.2 - 5.6 mm; colored red). Within the fourth series, a mixture of these uniform sediments with $D_{50}=1.3$ mm (0.5 - 5.6 mm; mixture) was tested. Each grain size fraction was colored accordingly.

The initial condition of all four experimental series was a self-stabilized bed surface, which was independently developed according to the procedure which is given in section 1.2.2.2. The D_{50} of the bed surface was in the range of 8.0 mm and 9.4 mm, respectively. Starting from there, several experimental runs were performed successively within one series, each with constant but different water discharge and supply of bed load within the run-up reach of the flume.

1.2.2.2 Channel bed stabilization - initialization

An experimental series started with the generation of a bed surface which featured similar patterns (rough bed surface with non-channel spanning steps and individual keystones) as observed in the prototype reach of the Gurgler Ache River. Therefore, the flow section of the physical model (Figure C-1) was loosely filled with a sediment mixture (Figure C-3b, bulk sediment), which corresponded to the scaled subsurface grain size distribution of the study reach but was truncated at 0.5 mm. Further, the loosely bedded sediment was slowly flooded before it was refilled again, allowing the sediment to consolidate to minimize the settling of fines between larger grains.

Bed surface armoring was then accomplished by means of sediment starving at a constant water discharge of 6.9 l/s. Thereby, the stabilizing discharge (6.9 l/s) represents the model scale of the prototype reach's critical discharge. Once the flume bed was exposed to the water flow, intense bed load transport occurred immediately, accompanied by rotational bed erosion due to the fixed bed level at the lower model boundary. But the initially high transport rates decreased rapidly within the first hour and slowly approached zero after about three hours. A static armor layer developed at the bed surface, with the fines almost completely winnowed, while patches of fines in the wake of boulders could be observed in the prototype reach. In order to better reproduce field conditions, 150 kg of relatively fine sediment (0.5 - 8.0 mm) was supplied at a feeding rate of 2 kg/min, followed by additional 75 min of sediment starving. At its end, the mobile bed surface featured structures similar to those of the prototype reach (clusters of keystones with patches of fines in their wakes) and bed load transport rates were very low, at about 0.1 kg/hr.

The procedure of generating the initial conditions was the same for all four experimental series (green, blue, red and mixture) in order to make them as consistent as possible. Although the initial bed surface, characterized by grain size distribution and morphologic setting, seemed similar in all four series (Figure C-3b), the mean channel gradient differed in a range between 0.026 m/m and 0.032 m/m (Figure C-3a). These differences are attributed to the stochastic and nonlinear nature of morphologic processes, even though marginal fluctuations of the impacting water discharge, controlled by a flap and an inductive flow meter (IDM), were conceivable.

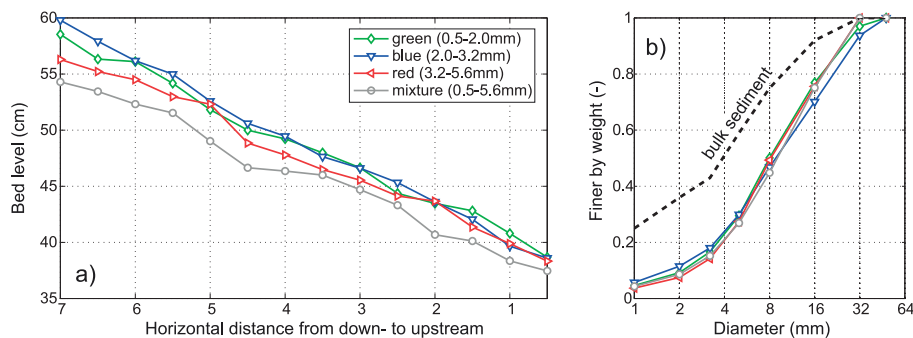


Figure C-3: a) Longitudinal profile (thalweg) at the beginning of each experimental series and b) the corresponding grain size distribution of the bed surface; the procedure of initialization was the same for all four experimental series

1.2.2.3 Experimental runs

Once the armored bed surface had been prepared, several experimental runs were carried out successively (Table C-1), starting with the lowermost discharge at which the supplied sediment was transported.

Within every experimental run, water discharge remained constant while 50 kg of sediment were added approximately 2.5 m upstream of the investigation reach of the flume (in the middle of the run-up section). Sediment feeding was done manually and evenly distributed over the cross section and time. Thereby, the feeding rate was in accordance with the transport capacity at the feeding location by avoiding an aggradation of

sediment near the feeding device and consequently, to avoid a fully dispersive propagation of supplied sediment. Once the 50 kg were completely added, water discharge remained for one-third of the duration of sediment feeding before it was turned off and measurements were carried out. Additionally, for all experimental runs with water discharges smaller than the stabilizing discharge of 6.9 l/s, the run was further continued until transport rates decreased to virtually zero and measurements were carried out again.

Table C-1: Experimental program with all experimental series, which consist of successively performed runs, differing in water discharge. Parameter abbreviations are: discharge Q; flume gradient S; diameters of the bed surface of which 50 % ($D_{50,s}$) and 84 % ($D_{84,s}$) are finer and the median diameter of supplied sediment $D_{50,sup}$.

| Series | Hydraulic conditions at the end of the initialization | | | | Characteristics of the feeding experiments | | | | | |
|---------------------------------|---|---------------------------|----------------------|----------------------|--|------------|--------------|------------------------------|----------------------------|------------------------|
| | Q (l/s) | S (x10 ⁻²) | $D_{50,s}^a$ (mm) | $D_{84,s}^a$ (mm) | Run | Q (l/s) | Mass (kg) | Feeding Duration (min) | Total Duration (min) | $D_{50,sup}^a$ (mm) |
| | | | | | | | | | | |
| Green (0.5 mm - 2.0 mm) | 6.9 | 3.0 | 8.0 | 21.7 | 1 ^b | 2.5 | 50 | 358 | 630 | |
| | | | | | 2 ^b | 4 | 50 | 197 | 494 | |
| | | | | | 3 ^b | 5.5 | 50 | 128 | 400 | |
| | | | | | 4 | 6.9 | 50 | 85 | 111 | 1.1 |
| | | | | | 5 | 10 | 50 | 30 | 40 | |
| | | | | | 6 | 15 | 50 | 20 | 27 | |
| Blue (2.0 mm - 3.2 mm) | 6.9 | 3.3 | 9.1 | 25.4 | 1 ^b | 4 | 50 | 300 | 632 | |
| | | | | | 2 ^b | 5.5 | 50 | 141 | 450 | |
| | | | | | 3 | 6.9 | 50 | 66 | 87 | 2.7 |
| | | | | | 4 | 10 | 50 | 22 | 31 | |
| | | | | | 5 | 15 | 50 | 15.5 | 20 | |
| | | | | | | | | | | |
| Red (3.2 mm - 5.6 mm) | 6.9 | 2.8 | 8.2 | 21.5 | 1 ^b | 5.5 | 50 | 164 | 476 | |
| | | | | | 2 | 6.9 | 50 | 133 | 178 | |
| | | | | | 3 | 10 | 50 | 66 | 88 | 3.9 |
| | | | | | 4 | 15 | 50 | 24 | 33 | |
| Mixture (0.5 mm - 5.6 mm) | 6.9 | 2.8 | 9.4 | 21.7 | 1 ^b | 3.8 | 50 | 235 | 345 | |
| | | | | | 2 ^b | 5.5 | 50 | 160 | 442 | |
| | | | | | 3 | 6.9 | 50 | 44 | 58 | |
| | | | | | 4 | 10 | 50 | 15 | 20 | |
| | | | | | 5 | 15 | 50 | 19 | 25 | |
| | | | | | | | | | | |

^a Volume-by-weight distribution

^b Experimental runs were stopped after a duration of 1.33 times the feeding duration and continued until bedload transport decreased to virtually zero

Since the grain sizes of the added sediment differed for each experimental series and the discharge of the first experimental run was set in proximity to incipient motion conditions of the supplied sediment, the discharge of the first run differed as well (Table C-1). While the lowermost discharge was 2.5 l/s for the experimental series with the smallest grains (0.5 - 2.0 mm, green), it amounted to 5.5 l/s for the coarsest ones (3.2 - 5.6 mm, red). Due to the structured and mixed sized bed surface, the incipient motion of the added sediment grains was not very easy to assess, since individual grains were transported over a small distance until they were deposited in the wake of coarser ones. The incipient motion was therefore determined by eye, as water discharge was continuously increased until the majority of added grains started to move. For all following runs, the discharge was increased to predefined levels, thereby focusing on the comparability of the series (Table C-1). Every experimental series ended as intense erosion was observed at the end of a run. Since initial conditions were the same (to the best possible extent) for all series, this criterion was reached at the same level, at a discharge of 15 l/s.

1.2.3 Measurement devices

1.2.3.1 Boundary conditions – water and sediment

Water discharge was recirculated by a pumping system, regulated by a computer-operated flap and measured by a magnetic flow meter. In order to minimize and damp any discharge fluctuations originated by the pumps, a water inlet tank was positioned at the upstream boundary of the flume. The bed level at the lower end of the flume was fixed by a small plank at its front side. The hydraulic boundary condition was critical and the water (and the sediment) overflowed into a detached tailwater box. Water further passed over this tailwater box and returned to the water reservoir of the pumping system.

1.2.3.2 Bed load transport rates

Sediment was caught within the tailwater box placed at the downstream end of the flume. A baffle and a fine-screened grid provided complete sedimentation of the incoming sediment, even of the smallest grains. The tailwater box was mounted on four electronic load cells (SOEMER 3510-C325T-2000, <http://www.soemer.de>), continuously registering total weight at a measuring frequency of 10 Hz and an accuracy of 0.02 %. Additionally, two ultrasonic levels recorded the water level within the box. Together, the measurement devices enabled the quantification of bed load accumulation within the box; divided by a certain time interval, bed load transport rates could be delivered. Due to unsteady momentum transfers originated by the impinging jet into the tailwater box, the raw data (ten values per second) showed considerable fluctuations. In addition, the weight of the bed load accumulation (about 50 kg) was far less than the entire weight of the water filled tailwater box (about 1,800 kg), both negatively effecting accurate measuring. Therefore, the data were post processed by applying a filtering scheme which accounts for the different feeding intensities of each of the experimental runs.

1.2.3.3 Source and grain size distribution of bed load

At the end of each experimental run, a sample of about 15 kg was taken from the sediment collected in the tailwater box. For the case that the deposited sediment was

less than that, the entire volume was analyzed, respectively. The wet sample was then evenly distributed on a tray of 0.75 m length and 0.4 m width and dried. Plan view photographs of the sample were taken at constant lighting conditions and the areal proportion of colored sediment in the total sample was then calculated with a color filter. Therefore, the free image processing and analysis software ImageJ (Image Processing and Analysis in Java; <http://rsb.info.nih.gov/ij>) was used (e.g. Piedra et al., 2012). This tool allows for the identification of a specific color from an image by setting thresholds to the value ranges of hue, saturation, and brightness. These thresholds were calibrated manually by means of analyzing an artificially compounded sample of known proportions beforehand.

Further, the samples were sieved in order to assess the grain size distribution of the total bed load transport. Sieving analyses of the experimental series with uniform tracer sediment (green, blue and red) needed to be post-corrected due to a mistakable handling of the sieving device. Thus, they differ from the results presented in Kößler (2014). However, the uncertainties introduced by the post-correction do not influence the outcomes of this study but need to be considered in more detailed analyses.

1.2.3.4 Bed level, grain size distribution of bed surface and bed stability

At the end of each run, a longitudinal section was measured with a point gauge in intervals of 0.5 m and with five points evenly distributed over every corresponding cross section. Additionally, the entire investigation reach of the flume was photographed in longitudinal intervals of 0.5 m. Two of these photographs, which were located in the middle of the investigation reach, were further used to determine the grain size distribution of the bed surface. The commercial software BASEGRAIN (© ETH Zürich; Detert and Weitbrecht, 2013) was applied to derive an area-by-number distribution from the photographs, which was further transformed to a volume-by-weight distribution according to the modified cube model of Diplas and Sutherland (1988).

The impact of feeding fine bed load on the bed stability was assessed by measuring the displacement of coarse stones via plan view photographs. Coarse stones are defined by diameters larger than the bed surface D_{70} , which is associated with the minimum size of isolated keystones. Within a segment of approximately one meter in length all coarse grains (about 100 stones) were marked and their displacement within two sequent runs was classified manually into the categories "unchanged", "smaller than one diameter", "larger than one diameter" and "out of picture". This procedure was done for all runs with discharges smaller or equal to the critical discharge of the bed surface (6.9 l/s). For the experimental runs with discharges exceeding this level (independent of the experimental series), the displacement of larger calibers was too intense to be assessed, giving evidence that the bed surface was unstable and highly mobile.

1.2.4 Flow hydraulics

Due to the rough bed and the very small relative flow depths, with $1 < d/D_{84,s} < 2$, flow conditions varied at a small scale and the effort to measure the mean flow depth d exceeded the capabilities of the measuring setup. In a consequence, flow hydraulics were determined by means of a numerical approach suitable for steep mountain streams. Therefore, the flume was subdivided into 14 reaches each featuring a length of 0.5 m and represented by the cross-section measured at its upper end. Steady state

hydraulics were applied reach-wise by iteratively solving the governing equations of mass continuity ($Q=uA$, with discharge Q , mean flow velocity u and wetted flow area A) and energy conservation (Bernoulli equation). Therein, the flow resistance was calculated according to the equation of *Ferguson (2007)* with the coefficients used and tested by *Rickenmann and Recking (2011)*:

$$\sqrt{\frac{8}{f}} = \frac{u}{\sqrt{gdS_e}} = \frac{6.5 \times 2.5 \times \left(\frac{d}{D_{84,s}} \right)}{\sqrt{6.5^2 + 2.5^2 \times \left(\frac{d}{D_{84,s}} \right)^{5/3}}} \quad (C4)$$

The total shear stress is defined by $\tau = \rho gdS_e$, while shear stress acting on the mobile bed is computed with the reduced energy slope as recommended by *Nitsche et al. (2011)* and *Rickenmann and Recking (2011)* according

$$S_{e,red} = S_e \times \left(\sqrt{\frac{f_{tot}}{f_0}} \right)^{1.5}, \text{ with} \\ \sqrt{\frac{8}{f_0}} = 6.5 \times \left(\frac{d}{D_{84,s}} \right)^{1/6}. \quad (C5)$$

Herein, f_{tot} and f_0 are the total and base level flow resistance (*Rickenmann and Recking, 2011*) and S_e the energy gradient. This calculation scheme was applied to all experimental runs, with the corresponding discharge and surveyed cross sections of the start of each run. In contrast, the $D_{84,s}$ of the initial bed surface was used for all calculations, since it hardly changed in course of the experimental runs of a series (see later in section 1.3.5). In the following, the hydraulic parameters of every experimental run are determined by the arithmetic mean of reach-wise calculations and a detailed overview is given in Table C-2.

Table C-2: Flow hydraulics of every experimental run. Parameter abbreviations are: discharge Q ; mean bed slope S ; energy gradient S_e ; reduced energy gradient S_{red} ; flow width w ; flow depth d ; mean flow velocity u ; Froude number $Fr=u/(gd)^{0.5}$.

| Flow conditions at the start of each feeding experiment | | | | | | | | | |
|---|-----|--------|------------------------|------------------------|------------------------|-------|-------|-------|--------|
| Series | Run | Q | S | S_e^a | S_{red}^a | w^a | d^a | u^a | Fr^a |
| | | (l /s) | (10 ⁻² m/m) | (10 ⁻² m/m) | (10 ⁻² m/m) | (mm) | (mm) | (m/s) | (-) |
| Green (0.5 mm - 2.0 mm) | 1 | 2.5 | 3.0 | 3.0 | 0.89 | 0.38 | 25 | 0.26 | 0.52 |
| | 2 | 4.0 | 2.8 | 2.9 | 1.01 | 0.38 | 32 | 0.33 | 0.59 |
| | 3 | 5.5 | 3.0 | 3.1 | 1.21 | 0.38 | 36 | 0.39 | 0.66 |
| | 4 | 6.9 | 3.0 | 3.1 | 1.32 | 0.38 | 40 | 0.45 | 0.73 |
| | 5 | 10 | 2.9 | 3.2 | 1.52 | 0.38 | 48 | 0.54 | 0.79 |
| | 6 | 15 | 2.8 | 3.1 | 1.7 | 0.38 | 58 | 0.68 | 0.90 |
| Blue (2.0 mm - 3.2 mm) | 1 | 4.0 | 3.3 | 3.3 | 1.0 | 0.38 | 33 | 0.32 | 0.57 |
| | 2 | 5.5 | 3.4 | 3.4 | 1.2 | 0.38 | 38 | 0.38 | 0.63 |
| | 3 | 6.9 | 3.4 | 3.4 | 1.3 | 0.38 | 41 | 0.44 | 0.69 |
| | 4 | 10 | 3.4 | 3.3 | 1.5 | 0.39 | 49 | 0.52 | 0.75 |
| | 5 | 15 | 3.1 | 3.4 | 1.7 | 0.39 | 60 | 0.64 | 0.84 |
| Red (3.2 mm - 5.6 mm) | 1 | 5.5 | 2.8 | 2.8 | 1.12 | 0.38 | 37 | 0.39 | 0.65 |
| | 2 | 6.9 | 2.9 | 3.0 | 1.27 | 0.38 | 41 | 0.45 | 0.71 |
| | 3 | 10 | 2.7 | 2.9 | 1.4 | 0.38 | 48 | 0.54 | 0.78 |
| | 4 | 15 | 2.7 | 3.2 | 1.71 | 0.39 | 59 | 0.66 | 0.87 |
| Mixture (0.5 mm - 5.6 mm) | 1 | 3.8 | 2.8 | 2.7 | 0.97 | 0.36 | 30 | 0.34 | 0.63 |
| | 2 | 5.5 | 2.8 | 2.8 | 1.14 | 0.37 | 36 | 0.41 | 0.68 |
| | 3 | 6.9 | 2.8 | 2.8 | 1.23 | 0.38 | 41 | 0.45 | 0.71 |
| | 4 | 10 | 2.9 | 2.8 | 1.41 | 0.38 | 48 | 0.55 | 0.80 |
| | 5 | 15 | 2.7 | 3.0 | 1.62 | 0.39 | 59 | 0.65 | 0.86 |

^a Hydraulic parameters are calculated as described in section C 1.2.4

C.1.3 Results

1.3.1 Incipient motion of supplied bed load

As described in section 1.2.2.3, the lowermost discharge (first experimental run of each series) approximately corresponded with incipient motion conditions of the supplied sediment. While it was 2.5 l/s for the smallest grains (0.5 mm - 2.0 mm, green), critical discharge increased to 5.5 l/s for the red colored grains (3.2 mm - 5.6 mm), demonstrating size-selective incipient motion conditions in the case of feeding relatively fine bed load to an armored bed. In this respect, the incipient motion was assessed by eye, following the criterion that the added sediment did not accumulate in an extent that downstream propagation of grains was only dispersive.

1.3.2 Bed load transport rate and its temporal progression

1.3.2.1 Discharges smaller or equal the stabilizing discharge

Once supplied to the flume, the added grains propagated downstream by partly filling the pockets on the bed surface or the interstices between coarse particles. The protrusion of coarse grains decreased and the exposure of supplied sediment towards the water flow increased. But it is worth to note that the coarse grains still protruded into the flow and the bed surface was not totally covered with the supplied sediment.

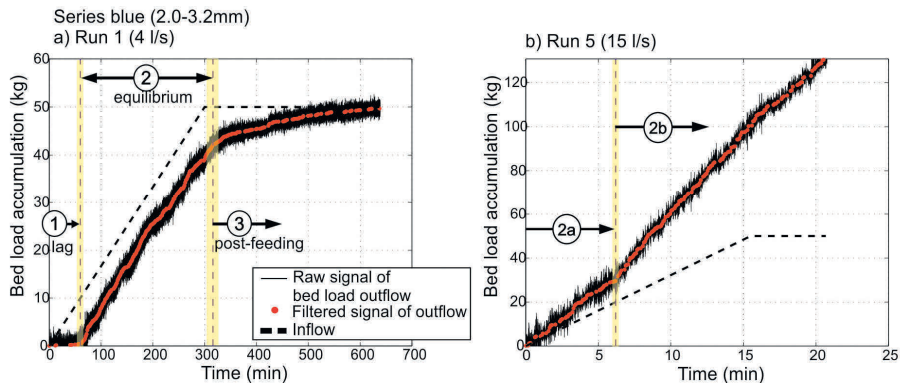


Figure C-4: Sediment feeding at the upper end (dashed line) and measured bed load transport at the lower end of the flume (red circles) for two selected experimental runs of the series ‘blue’ (2.0 - 3.2 mm); circled numbers indicate different phases of response to sediment feeding

For all experimental runs with discharges smaller or equal than the stabilizing discharge of 6.9 l/s, the temporal evolution of bed load accumulation showed a similar pattern, which roughly corresponds with the observations made by Egashira and Ashida (1991). In the following, three different phases are distinguished (Figure C-4a): (1) the lag phase (the temporal lag between feeding start and initial outflow of added sediment), (2) the equilibrium phase (outflux equals feeding rate) and (3) the post-feeding phase (decrease of bed load transport after feeding).

The lag phase represents the temporal lag (t_{lag}) between model input and initial outflow of sediments. It further represents a surrogate for the propagation velocity of the leading edge of added sediment. It is defined by $u_T = L/t_{lag}$, with the longitudinal distance between sediment feeding and outflow ($L=9.5$ m), respectively. It is worth to note, that the propagation velocity does not represent the travel speed of a single particle, but the time needed to adjust morphologic boundary conditions (smoothing the bed surface) along the traveling distance in order to approach the feeding rate. The experimental data reveal a positive dependency with the grain size and the magnitude of flow (Figure C-5a). However, Figure C-5a does not account for the differences in feeding rate which was the larger the higher the water discharge or the smaller the grain size of added sediment (Table C-1).

In this respect, a certain similarity collapse is achieved when non-dimensional tracer velocity is plotted against $\psi_T \times \tau_T^*$ (Figure C-5b), with both parameters significantly correlated with $u^* \tau$. These quantities properly explain the differences of the propagation velocity which were observed over a wide range of boundary conditions (Table C-2). Since feeding rate oriented on the transport capacity, the dimensionless feeding rate and the dimensionless shear stress are intercorrelated and thus, the influence of either of these parameters is unknown.

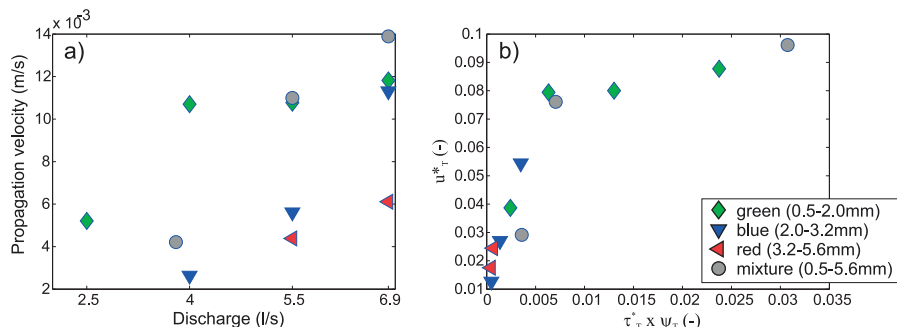


Figure C-5: a) Tracer velocity of the leading edge (which is defined by the flume length between input and outflow location divided by the duration of the lag phase) plotted against discharge and b) the non-dimensional propagation velocity ($u^* \tau$) plotted against Shields stress times feeding intensity ($\tau_T^* \times \psi_T$), both with respect to the grain size supplied.

Once the supplied sediment reached the lower end of the flume, the transport rate increased rapidly and the lag phase changed over to the equilibrium phase (Figure C-4a). Regardless of the grain size, the mean transport rate of this phase approximately approached the rate of sediment feeding (Figure C-6a).

Instantaneous bed load transport rates varied during the equilibrium phase (e.g. Figure C-7). In Figure C-6b the bounds of instantaneous transport rates are assessed by their 90th and 10th percentiles, both standardized by the median of instantaneous transport rate. Results reveal an asymmetric scatter, with the 90th percentile of about 2.3 times the median, while the 10th percentile is on average one-tenth of the median. Hence, high instantaneous transport intensities are less pronounced than low ones with the skewness being independent of the grain size and the discharge.

In contrast to experiments in which sediment was supplied continuously to a steep flume that was not stabilized beforehand (e.g. Ghilardi *et al.*, 2014; Recking *et al.*, 2009), the time series of the instantaneous transport rate do not reveal distinct cyclic patterns. At least the moving average of transport rates insignificantly indicates that periods of high transport rate generally alternate with periods of low transport rate (Figure C-7). However, the fluctuations are not consistent and a detailed analysis is beyond the scope of this study.

After sediment feeding was stopped (Table C-1), equilibrium transport conditions remained for a certain time and then, bed load transport declined, approaching a very minute transport rate (post-feeding phase; Figure C-4a). In contrast to the transition

towards the equilibrium phase, the transition towards the post-feeding phase was more continuous (e.g. Figure C-4a).

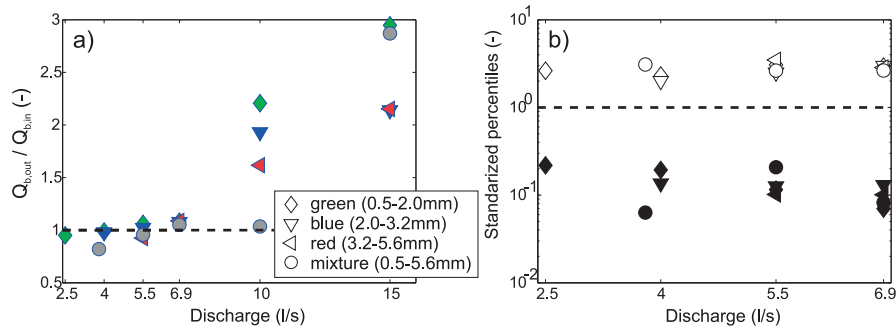


Figure C-6: a) Ratio of mean bed load outflow during the equilibrium phase and feeding rate; b) 10th (black symbols and 90th percentiles (white symbols) of instantaneous bed load transport rates scaled by the corresponding medians (b)

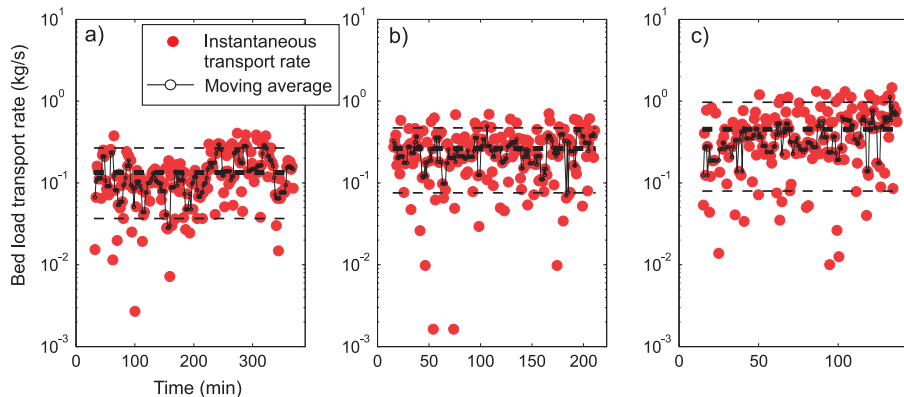


Figure C-7: Instantaneous bed load transport rates observed during the equilibrium phase of the experimental run a) 1 ($Q=2.5$ l/s), b) 2 ($Q=4.0$ l/s) and c) 3 ($Q=5.5$ l/s) of the series 'green'. Horizontal dashed lines indicate the 10th, median (bold) and 90th percentile of the instantaneous bed load transport rate

1.3.2.2 Discharges exceeding the stabilizing discharge

In the experimental runs exceeding the critical discharge of 6.9 l/s, the bed load was transported out of the flume as soon as the experimental run started (phase 2a, Figure C-4b). This indicates that the bed stability was exceeded, at least to some extent. After a certain period, the bed load transport rate further increased (transition of 2a and 2b in Figure C-4b). The occurrence of this breakpoint is attributed to the arrival of added grains at the lower end of the flume (Figure C-4b). In addition, the bed load transport rate exceeded the feeding rate by far, except for the run 4 of the experimental series

'mixture' (Figure C-6a). This inconsistency is attributed to the high feeding rate during this run.

1.3.3 Partitioning of total bed load

The collected bed load was split according to its source into "bed material load", originating from the initial mobile bed, and colored "added material" by their areal proportions (section 1.2.3.3). The latter dominated the overall bed load in all runs with discharges smaller or equal to the critical discharge by far, while there appears to be a breaking point at any higher discharges (Figure C-8).

Considering only the experimental series with the uniform material (green, blue and red), the highest proportions were delivered with the smallest grains (green), ranging up to almost 100 %. Thereby, the smallest size of added material corresponds to the smallest size fraction of the bulk sediment mixture of the bed material. Proportions were lower for the intermediate (blue) and the coarse material (red) but still dominated total bed load in case of discharges smaller or equal 6.9 l/s. Only in the last runs with the highest discharge (15 l/s) the proportions were nearly identical (Figure C-8a). In contrast, the proportions evolve in a slightly more continuous arrangement in case that mixed sized sediment was added to the flume. Although the mixture's mean diameter was rather small, proportions were comparatively small at low discharges and high at larger discharges.

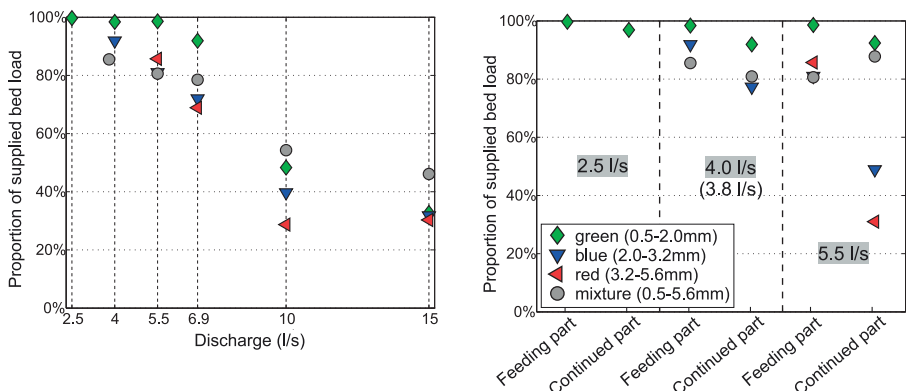


Figure C-8: a) Proportion of added sediment in the total bed load outflow; b) same as a) but separated into the feeding part (duration of sediment feeding plus one-third of feeding time) and the continued part of each experimental run with discharges smaller than 6.9 l/s.

Further, the total mass of bed load is split to its source by multiplying it by the areal proportions. This procedure assumes that the areal proportions equal the volumetric ones, which might not be the case for non-uniform grain size distributions (e.g. *Bunte and Abt, 2001*). Typically, areal proportions assessed by plan view photographs overestimate the presence of large grains because they protrude above the surface (*Diplas and Sutherland, 1988*) and underestimate fines. However, the bias is minor, since the wet sample was flattened on a 0.3 m² tray before being dried and photographed. As

illustrated in section 1.3.2, the total mass of bed load accumulation is similar to the feeding mass (50 kg) for all runs with discharges smaller or equal 6.9 l/s (Figure C-9). Summarizing, the supplied sediment dominated the overall bed load outflow at discharges below incipient motion of the bed surface, regardless of the experimental series. Although there were fine grains abundant at the bed surface, supplied grains were more likely transported, even when these were coarser. Consequently, the increased supply of certain grain fractions dominated over the theoretically higher mobility of finer grains. This seems to be confirmed by comparing proportions at the end of the feeding parts (duration of feeding plus one-third of time sediment starving) with those assessed at the end of the continued parts (Figure C-8b), the latter facing sediment starving conditions until transport rates decreased to a very minute rate. In general, the proportions of supplied sediment were lower for the continued parts, except for the 5.5 l/s run of the series ‘mixture’.

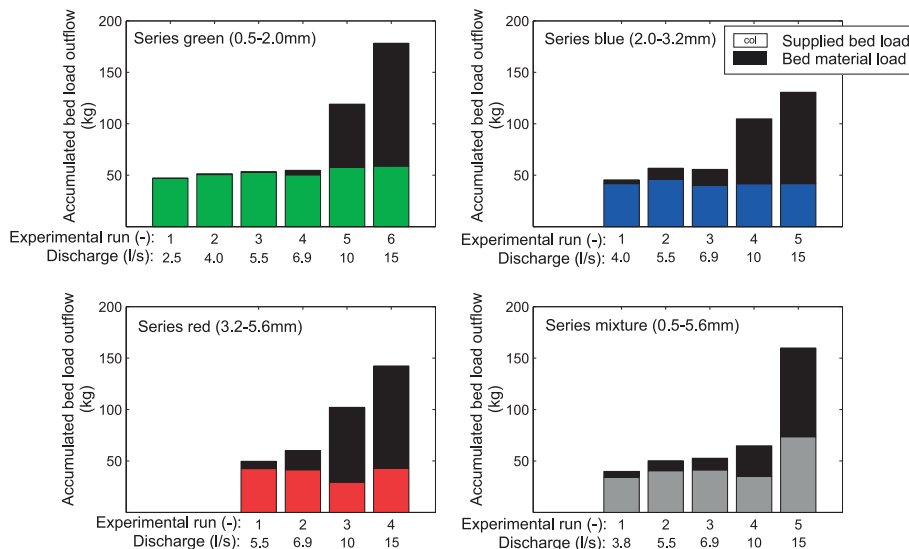


Figure C-9: Total mass of bed load accumulation is split into its origin, the supplied material (lower, colored bar) and the bed material (upper, black bar). Each plot comprises the results of one entire experimental series with the experimental runs being ordered with increasing discharge (Table C-1).

1.3.4 Grain size distribution of total bed load

The coarser the supplied sediment, the higher was the fraction of bed material in the total load (Figure C-8; Figure C-9). Surprisingly, the grain size distribution of the bed material load (non-colored sediment) was not predominately made up of the fine fractions, as the theory of size-selective bed load transport would suggest for (Figure C-10).

The proportions of grains smaller and coarser than supplied sediment were similar, independent of the grain size of supplied sediment. It seems that the grain size distri-

butions were shifted relative to the supplied grain size (Figure C-10 lower row). In contrast, more fine bed sediment was mobilized during the continued part, which is associated to the post-feeding phase. Although the added grain size still dominated in the total bed load, the fine tail approached the size distribution of the bulk sediment in the experimental series 'blue' and 'red' (Figure C-11). It seems that bed load transport progressively became size-selective again by mobilizing fine sediment from the bed surface during the post-feeding phase since formerly buried patches of fines might have been exposed again.

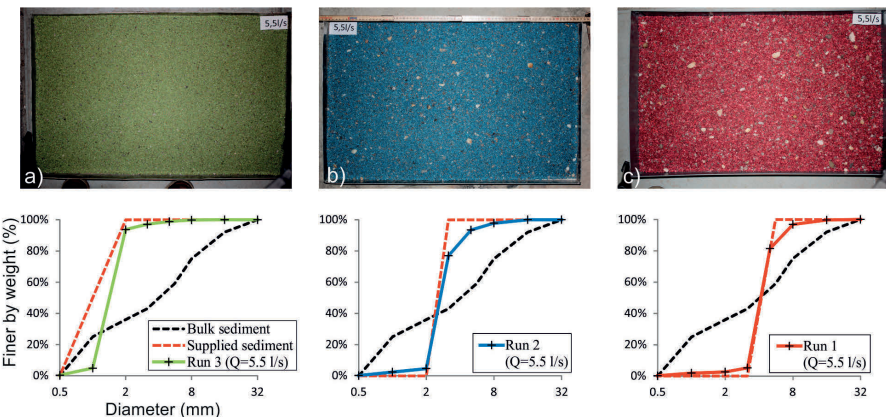


Figure C-10: Upper row: samples of total bed load taken at the end of the feeding part of the 5.5 l/s runs of a) the series 'green' (1.0 – 2.0 mm), b) series 'blue' (2.0 – 3.2 mm) and c) series 'red' (3.2 – 5.6 mm); lower row: grain size distribution obtained by sieving and post-correction (see section 1.2.3.3)

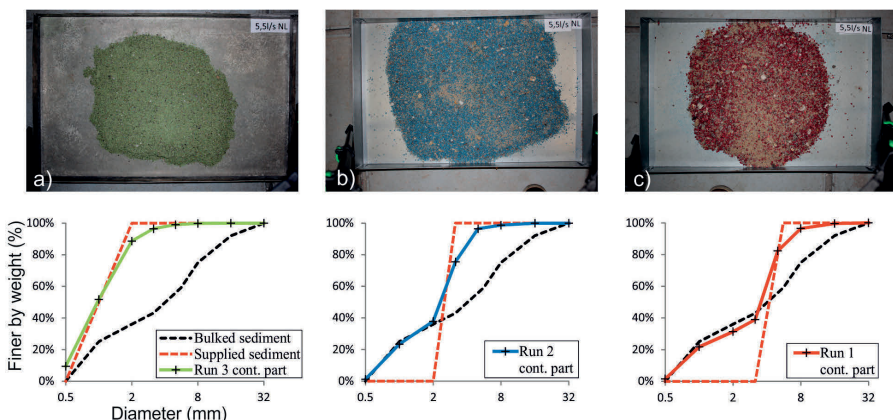


Figure C-11: Upper row: samples of total bed load taken at the end of the continued part of the 5.5 l/s runs of a) series 'green' (1.0 – 2.0 mm), b) series 'blue' (2.0 – 3.2 mm) and c) series 'red' (3.2 – 5.6 mm); lower row: grain size distribution obtained by sieving (see section 1.2.3.3)

The D_{84} of the total bed load means a proxy for its coarseness. For the experimental series 'green', the D_{84} of the total bed load is identical to the D_{84} of the supplied sediment for all runs smaller or equal the stabilizing discharge (Figure C-12a). This is not surprising since total bed load almost totally consisted of added grains (see section 1.3.3). In contrast, the D_{84} exceeds the bounds of supplied grain sizes for most of the other runs with uniform material and consistently increases with discharge (Figure C-12a).

For the experimental runs with discharges exceeding the critical discharge, the D_{84} of the bed load is coarsest for the fine and intermediate material and attains the D_{84} of the bulk sediment, while it is smaller for the coarsest material supplied (red) and the mixture. However, the increase of D_{84} is continuous for all except the 'green' experimental series, where there is a severe break point between the 6.9 l/s and the 10 l/s run (Figure C-12a). Furthermore, the grain size distributions of the transported bed load develop towards the bulk sediment at discharges larger than 6.9 l/s (Figure C-12b).

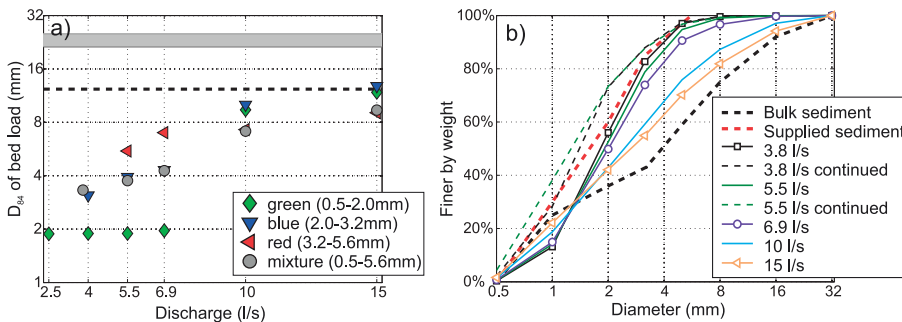


Figure C-12: a) Diameter for which 84 % of total bed load transport is finer; with the D_{84} of the bulk sediment (dotted line) and the bed surface (grey bar) and b) grain size distributions of total bed load transport obtained within the experimental series 'mixture' (0.5 - 5.6 mm)

1.3.5 Grain size distribution of the bed surface

Feeding of relatively fine sediment to an armored bed resulted in a partial fill-up of irregularities of the coarse bed surface (Figure C-13). Consequently, the supplied bed load partly covered the former bed surface and following grains overpassed, which is in accordance with previous studies (Koll, 2012; Spiller et al., 2012; Venditti et al., 2010a). Although the evolution of the bed surface grain size distribution was not assessed during the experimental runs, visual observations revealed that the increased embedding of macro-roughness elements smoothed the bed surface. But the supplied sediment did not cover the entire bed surface and coarse grains still protruded into the flow.

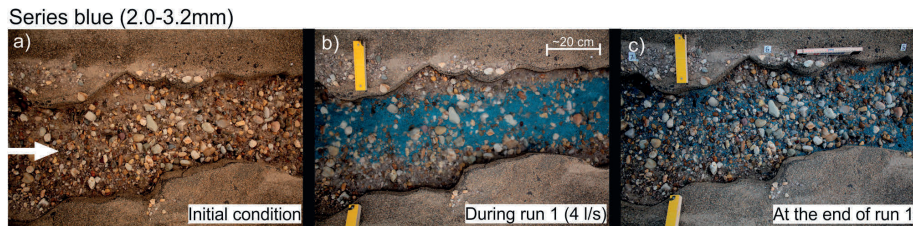


Figure C-13: Evolution of the bed surface during the experimental run 1 with 4 l/s water discharge and the blue colored sediment (2.0 - 3.2 mm); a) initial condition (self-stabilized bed surface); b) during the equilibrium phase; c) at the end of the continued part

The bed surface grain size distributions at the end of the experimental runs of the series ‘mixture’ hardly differed from the initial bed, as long as the discharges were smaller than the stabilizing discharge; results reveal a minor fining for the 6.9 l/s run (Figure C-14). Complementary to Venditti *et al.* (2010a), the bed surface approached the pre-feeding conditions during the post-feeding phase even at discharges below the stabilizing discharge, though a certain amount of added grains remained on it (see Figure C-13). For the subsequent runs (10 l/s and 15 l/s) an obvious fining of the bed surface was observed, which is associated with the break-up of the armored bed surface and the subsequent release of fine sediment from the subsurface. However, only the lower part of the grain size distributions changed, while the coarser part, controlling flow resistance, remained almost entirely constant (Figure C-14b).

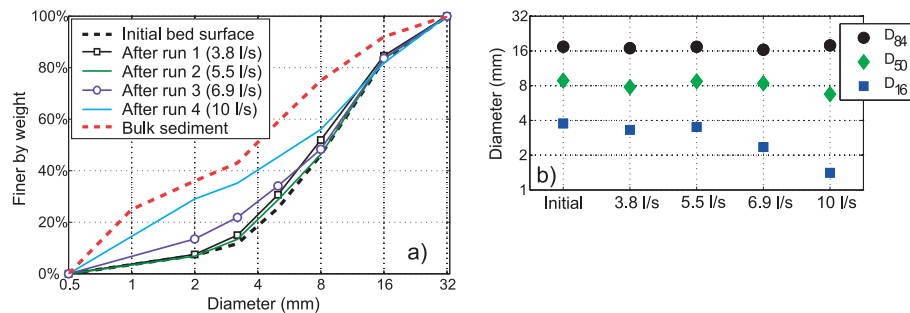


Figure C-14: a) Grain size distribution of the bed surface at the end of four runs of the experimental series ‘mixture’ (0.5 - 5.6 mm) and b) characteristic diameters of the bed surface (chronology is left to right); grain size distributions were assessed in a rather small area compared to those illustrated in Figure C-3

1.3.6 Bed stability

In addition to the mobilization of bed material and the evolution of the bed surface grain size distribution, the stability of the bed surface is assessed separately. The analysis focusses on both, the displacement of coarse grains and changes of the bed level.

Displacement was categorized into four classes (section 1.2.3.4). In contrast, only three out of four categories are given in Figure C-15, since only one out of 1,878 cases belonged to the fourth category “out of picture”. At a discharge of 6.9 l/s, 17 % to 40 %

of the coarse grains were moved, with on average 20 % further than one diameter in length (Figure C-15). Considering that the bed surface was initially stabilized with a water discharge of 6.9 l/s, this represents an obvious decrease of bed stability, which is in accordance with several other studies (Koll, 2012; Venditti *et al.*, 2010b; Koll, 2002; Hassan and Church, 2000). The impact on the bed stability was at a similar magnitude in the series 'green' (smallest grains) and 'red' (coarsest grains), while it was less for the remaining series 'blue' and 'mixture'.

Particle displacement was observed also at discharges smaller than the stabilizing discharge (Figure C-15), exhibiting a positive dependency with discharge. Additionally, the proportions are slightly higher for the feeding part, revealing the effect of sediment feeding on bed stability.

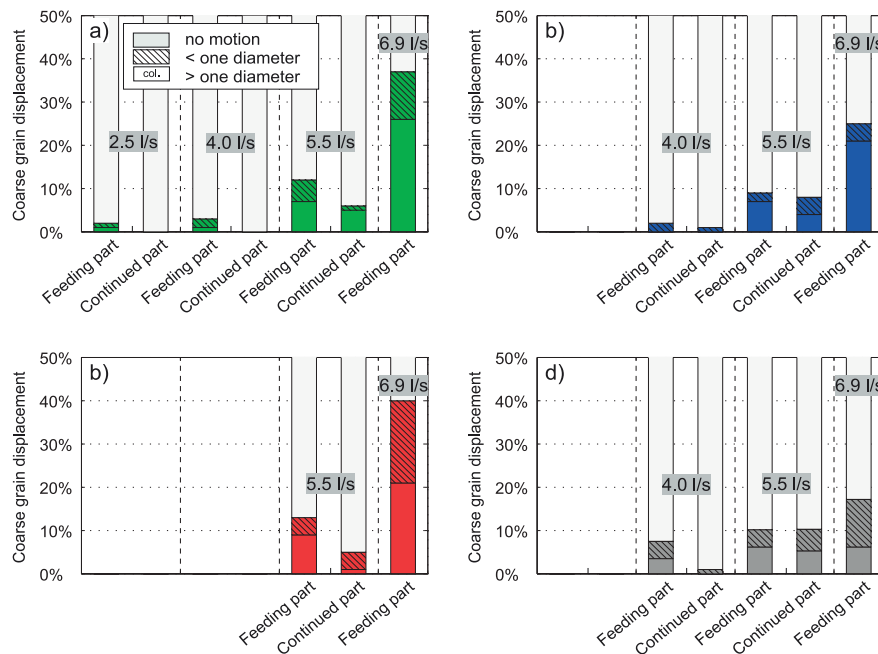


Figure C-15: Displacement of coarse surface grains which were relocated (displaced) further or less than one diameter in length during the experimental runs with discharge smaller or equal 6.9 l/s of a) the series 'green' (1.0 - 2.0 mm), b) series 'blue' (2.0 - 3.2 mm), c) series 'red' (3.2 - 5.6 mm) and d) the series 'mixture' (0.5 - 5.6 mm)

Despite individual coarse grains moved, hardly any erosion of the flume bed was observed after all experimental runs with discharges smaller or equal to 6.9 l/s. Total bed load outflow was approximately equal in mass to the feeding. Consequently, the bed level did not change to a measurable extent. During subsequent runs with discharges larger than 6.9 l/s, a substantial shift of bed load transport and erosion processes could be observed. The flow strength exceeded the bed stability and the armor layer broke

up, followed by a subsequent fining of the bed surface (section 1.3.5). Bed load accumulation at the tailwater box surpassed feeding by 30 % to 140 % at a discharge of 10 l/s and by 164 % to 240 % at 15 l/s, resulting in an incision of the flume bed and a final bed slope up to 15 % lower than the initial one (Table C-2).

C.1.4 Discussion

1.4.1 Propagation of supplied bed load over an armored bed surface

Results reveal that the propagation velocity non-linearly depends on the shear stress and the feeding rate in case bed load is fed at a constant rate. Further, the propagation of supplied bed load is size-selective since non-dimensional velocity (u^*_T) of different grain sizes collapses with Shields stress (τ^*_T) and non-dimensional feeding intensity (ψ_T) when referred to the supplied grain size.

The initial hypothesis was that the propagation velocity is lower in mountain streams than in their low-sloped counterparts. Comparisons with literature data do not confirm that. Although the non-dimensional propagation velocity measured in course of this study plots in a close range with those of *Egashira and Ashida* (1991) and *Yu et al.* (2009), results obtained in a low-sloped flume (*Sklar et al.*, 2009) plot slightly lower (Figure C-16). Hence, the dimensionless propagation velocity is higher in steep streams when boundary conditions regarding flow competence (Shields stress) and feeding intensity are identical. In this respect, it is worth to note that Shields stress used in Figure C-16 is based on the effective shear stress and thus already accounts for momentum losses due to macro-roughness.

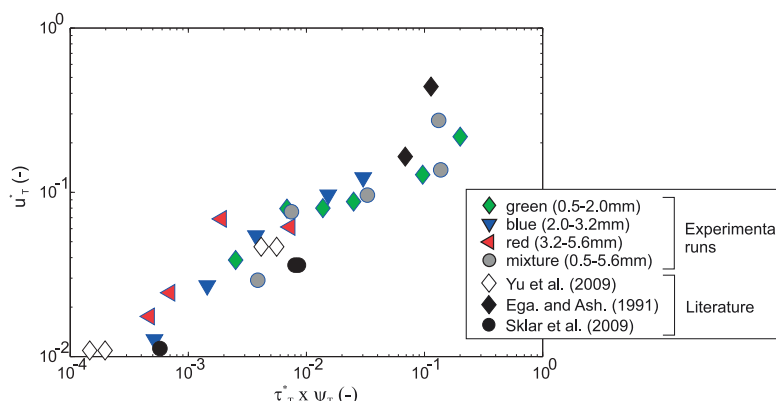


Figure C-16: Dimensionless propagation velocity (u^*_T) plotted against macro-roughness corrected Shields stress (τ^*_T) times the dimensionless feeding rate (ψ_T); literature data on propagation velocity were obtained by graph reading, while τ^*_T and ψ_T were determined by the scheme given in section 1.2.4, assuming uniform flow.

1.4.2 Effect of sediment supply on bed load transport

In the experimental runs with discharges smaller or equal than the stabilizing discharge, the bed load transport rate was marginal during the lag phase but rapidly approached the feeding rate once the pulse reached the flume outlet (transition towards the equilibrium phase). This increase of bed load transport was accompanied with the filling of the main pockets on the bed surface during the lag phase. It caused the protrusion of coarse grains to decrease (bed surface smoothing) and the exposure of supplied sediment towards the water flow to increase.

Possible reasons for this increase of bed load transport rate are either the decrease of the form resistance and thus, a reduction of the momentum loss due to macro-roughness, or the increase of the shear stress acting on the mobile bed load due to an increase of the particles' exposure (Yager, 2007).

The amount of bed load supplied during the lag phase is a surrogate for the magnitude of bed surface smoothing which is associated with the magnitude of form resistance, respectively. The mass of bed load supplied in the course of the lag phase ranges between 4 kg and 13 kg. Assuming that the bed surface layer within the flume, which is 9.5 m long (from the feeding station to the lower end of the flume) and on average 0.38 m wide, was covered with supplied sediment by two third of its area, this corresponds with a deposit height of 1 mm to 3 mm when a pore content of 30 % is considered. Hence, the virtual deposit height of the temporally stored sediment is rather small when compared, i.e. with the D_{84} of the bed surface (21.5 - 25.4 mm), an often used parameter for macro-roughness. Furthermore, the picture in Figure C-17 also reveals that flow was still affected by the macro-roughness elements during the equilibrium phase, due to impinging or surface jets.

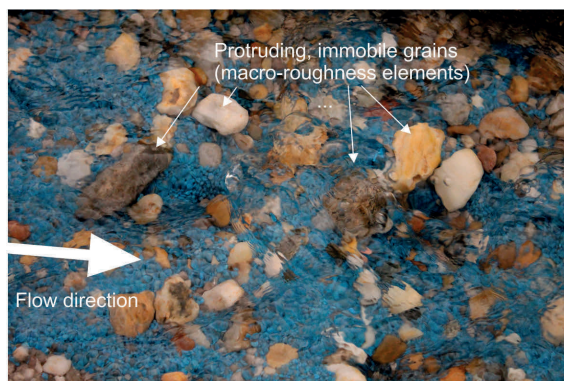


Figure C-17: Photograph of the bed surface taken during the equilibrium phase of the experimental run 1 of the series 'blue' (2.0 - 3.2 mm)

In a consequence, the increase of the bed load mobility is not solely attributed to a decrease of the form resistance. The reduction of form resistance was probably accompanied by an increase of the grain resistance, causing an increase of the shear stress that acts on the mobile bed load. However, the flow hydraulics were not meas-

ured in course of the experiments, but little evidence is provided by Yager (2007). Similar to the observations, the protrusion of immobile spheres declined with sediment supply, but the total flow resistance did not change. In contrast, an increase of flow velocity with sediment supply is reported in Koll (2002). But, considering only those experiments of Koll (2002) where the supplied sediment did probably not cover the total bed surface, the increase of flow velocity during feeding is not consistent.

The experiments reveal that minor changes of morphologic patterns (e.g. flow roughness, bed surface structures) cause major alterations of the bed load transport rate. Since non-dimensional propagation velocity in steep flumes plots higher than results obtained in low-sloped flumes (Figure C-16), bed load transport rate in steep mountain streams is suggested to be more sensitive to alterations of the bed surface than in their lowland counterparts.

Furthermore, the results of this study confirm that changes in the supply of mobile bed load are one possible explanation of the variable nature of bed load transport at moderate flows (Mao *et al.*, 2014; Turowski *et al.* 2011). In this respect, Turowski *et al.* (2011) suggest that the temporal variability of incipient motion in a single stream reach results from small-scale changes of the bed surface grain size distribution and the grain's arrangement. Mao *et al.* (2014) attribute seasonal alterations of the transport efficiency in a glacier fed mountain stream with differences of the runoff origin. Both of these patterns are probably associated with changes in the supply of mobile bed load from upstream reaches.

But unlike prototype mountain streams, the feeding rates of the experiments oriented on the transport capacity. Transferred to real-scale conditions (scale of 1:20), feeding rates ranged between 0.5 kg/s/m and 13.3 kg/s/m, which is very high compared with recent field data (*Study C* in chapter B, Schneider *et al.*, 2015; Recking, 2013; Turowski, 2010). Feeding experiments with rates distinctly below transport capacity were addressed by Koll (2002). Considering only the supplied sediment (and neglecting bed material erosion), the lag phase lasts the longer the lower the feeding rate is, but the temporal patterns remain unchanged (experimental runs V1 to V3 in Koll, 2002). Consequently, the mobile bed load propagates downstream even at low feeding rates, but it is slower.

1.4.3 Effects of bed load supply on bed stability

In contrast to the hypothesis of Egashira and Ashida (1991), the supplied sediment did not fully overpass the armored bed surface, but interacted with the bed sediment. Although the bed load transport rate approached the feeding rate, results reveal a certain exchange of supplied bed load and bed material. In a consequence and in accordance with previous studies in low-sloped flumes (Venditti *et al.*, 2010b; Koll, 2002; Hassan and Church, 2000), a certain decrease of bed stability is observed as fine bed load is supplied, even at discharges distinctly below the stabilizing discharge. Despite a certain amount of bed material was mobilized in course of sediment feeding, the overall structure of the armored bed surface was only minimally affected as long as water discharge was below the stabilizing discharge. Only a few, coarse grains were dislocated which means that the release of subsurface sediment was at least restricted to small areas, probably associated with the patches of fines. Hence, the exchange of bed load and bed material predominantly took place on the bed surface. This contradicts with the processes observed in gravel bed streams that reveal equal mobility with respect to the subsurface sediment (Parker and Klingeman, 1982). Supplied bed load

might have simply deposited on the bed surface and impacted the mobility of their neighboring grains as suggested by Koll (2002). This would explain why the coarseness of the bed material load revealed a positive dependency on the grain size of supplied bed load: coarse supply covered the patches of fines and thus, prevented them from being mobilized, while they increased the mobility of neighboring grains which still protruded into the flow.

In contrast, feeding sediment to a mobile bed at the same discharge with which the bed surface was formerly armored causes a severe decrease of bed stability. On average 30 % of the coarse tail of bed surface sediment was mobilized and subsurface material was released. But the results do not reveal a consistent dependency between the grain size of supplied material and the impact on the bed stability, as it is reported in Koll (2002). Despite the relocation of coarse stones, the grain size distribution of the bed surface shifted for small grain sizes only, while the D_{50} and D_{84} remained almost unchanged (Figure C9). This corresponds with experiments in lower gradient flumes (Venditti et al., 2010b; Hassan and Church, 2000).

C.1.5 Conclusion

The availability of mobile bed load strongly controls the occurrence and the magnitude of bed load transport in armored mountain streams featuring a wide grain size distribution of bed surface sediment and small relative flow depths. The flume experiments demonstrate that supplied bed load is even transported below incipient motion of the bed surface. The adjustment of the bed surface necessary to attain an equilibrium between feeding rate and outflow rate is small. Thus, the increase of bed load transport rate is not solely attributed to a decrease of momentum losses due to form drag but might be accompanied by an increase of exposure of mobile sediment towards the flow.

C.1.6 References of Study E

- Barry, J. J., J. M. Buffington, and J. G. King (2004), A general power equation for predicting bed load transport rates in gravel bed rivers, *Water Resour. Res.*, 40, W10401, doi: 10.1029/2004WR003190
- Bathurst, J. C. (2013), Critical conditions for particle motion in coarse bed materials of nonuniform size distribution, *Geomorphology*, 197, 170-184.
- Bunte, K., and S. R. Abt (2001), Sampling surface and subsurface particle-size distributions in wadable gravel- and cobble-bed streams for analyses in sediment transport, hydraulics, and streambed monitoring, *Gen. Techn. Rep. RMRS-GTR-74*, 428 pp, U.S. Department of Agriculture, Forest Service, Fort Collins, CO.
- Bunte, K., S. R. Abt, K. W. Swingle, D. A. Cenderelli, and J. M. Schneider (2013), Critical Shields values in coarse-bedded steep streams, *Water Resour. Res.*, 49, 7427-7447, doi: 10.1002/2012WR012672
- Chin, A., and E. Wohl (2005), Towards a theory for step pools in stream channels, *Prog. Phys. Geog.*, 29(3), 275-296.
- Church, M., M. A. Hassan, and J. F. Wolcott (1998), Stabilizing self-organized structures in gravel-bed stream channels: Field and experimental observations, *Water Resour. Res.*, 34(11), 3169-3179.
- Church, M., and A. Zimmermann (2007), Form and stability of step-pool channels: Research progress, *Water Resour. Res.*, 43, W03415, doi: 10.1029/2006WR005037
- Comiti, F., D. Cadol, and E. Wohl (2009), Flow regimes, bed morphology, and flow resistance in self-formed step-pool channels, *Water Resour. Res.*, 45, W04424, doi: 10.1029/2008WR007259
- Detert, M., and V. Weitbrecht (2013), User guide to gravelometric image analysis by BASEGRAIN, in S. Fukukawa, H. Nakagawa, T. Sumi, and H. Zhang (Eds.), *Advances in Science and Research* (pp. 1789-1795), London, UK: Taylor and Francis Group, ISBN 978-1-138-00062-9

- Diplas, P., and A. J. Sutherland (1988), Sampling Techniques for Gravel Sized Sediments, *J. Hydraul. Eng.*, 114(5), 484-501.
- Egashira, S., and K. Ashida (1991), Flow resistance and sediment transport in streams with step-pool bed morphology, *Lecture Notes in Earth Sciences*, Vol. 37, 45-58.
- Ferguson, R. I., D. J. Bloomer, T. B. Hoey, and A. Werrity (2002), Mobility of river tracer pebbles over different timescales, *Water Resour. Res.*, 38(5), 1045-1052, doi: 10.1029/2001WR000254
- Ferguson, R. I. (2007), Flow resistance equations for gravel- and boulder-bed streams, *Water Resour. Res.*, 43, W05427, doi: 10.1029/2006WR005422
- Garcia, C., J. B. Laronne, and M. Sala (2000), Continuous monitoring of bed load flux in a mountain gravel-bed river, *Geomorphology*, 34, 23-31.
- Garcia, C., H. Cohen, I. Reid, A. Rovira, X. Ubeda, and J. B. Laronne (2007), Process of initiation of motion leading to bed load transport in gravel-bed rivers, *Geophysical Research Letters*, 24, L06403, doi: 10.1029/2006GL028865
- Ghilardi, T., M. J. Franca, and A. J. Schleiss (2014), Bed load fluctuations in a steep channel, *Water Resour. Res.*, 50, 6557-6576, doi: 10.1002/2013WR01444
- Gintz, D., M. A. Hassan, and K.-H. Schmidt (1996), Frequency and magnitude of bedload transport in a mountain river, *Earth Surf. Proc. Land.*, 21, 443-445.
- Habersack, H. M., and J. B. Laronne (2001), Bed load texture in an alpine gravel bed river, *Water Resour. Res.*, 37(12), 3359-3370.
- Hassan, M. A., and M. Church (2000), Experiments on surface structure and partial sediment transport on a gravel bed, *Water Resour. Res.*, 36(7), 1885-1895.
- Hoffman, D. F., and E. J. Gabet (2007), Effects of sediment pulses on channel morphology in a gravel-bed river, *Geol. Soc. Am. Bull.*, 119, no. 1-2, 116-125, doi: 10.1130/B25982.1
- Jackson, W. L., and R. L. Beschta (1982), A model of two-phase bed load transport in an Oregon coast range stream, *Earth Surf. Proc. Land.*, 7, 517-527.
- Koll, K. (2002), Feststofftransport und Geschwindigkeitsverteilung in Raugerinnen, Ph.D. thesis, Univ. Fridericiana zu Karlsruhe, Karlsruhe, Germany, (in German).
- Koll, K., K. Koll, and A. Dittrich (2010), Sediment transport over static armour layers and its impact on bed stability, in A. Dittrich (Ed.), *River Flow 2010: Proceedings of the International Conference on Fluvial Hydraulics* (pp. 929-936), Braunschweig, Germany, ISBN 978-3-939230-00-7
- Koll, K. (2012), Untersuchungen des Geschiebetransports auf statischen Deckschichten, Ph.D. thesis, Univ. Carolo-Wilhelmina zu Braunschweig, Braunschweig, Germany, (in German).
- Kößler, D. (2014), Physikalische Untersuchungen zum Geschiebetransport über die Deckschicht eines alpinen Gebirgsflusses, Master thesis, Univ. of Innsbruck, Innsbruck, Austria, (in German).
- Lamarre, H., and A. G. Roy (2008), A field study on the development of sedimentary structures in a gravel-bed river, *Earth Surf. Proc. Land.*, 33, 1064-1081, doi: 10.1002/esp.1602
- Laronne, J. B., C. Garcia, and I. Reid (2001), Mobility of patch sediment in gravel bed streams: patch character and its implications for bed load, in P. Mosley (Ed.), *Gravel-Bed Rivers V* (pp. 249-289), Wellington, New-Zealand: Hydrological Society Inc., ISBN 0-473-07486-9
- Lisle, T. E. (1995), Particle size variation between bed load and bed material in natural gravel bed channels, *Water Resour. Res.*, 31(4), 1107-1118.
- Mao, L., and M. A. Lenzi (2007), Sediment mobility and bed load transport conditions in an alpine stream, *Hydrolog. Process.*, 21, 1882-1891.
- Mao, L., G. P. Uyttendaele, A. Iroume, and M. A. Lenzi (2008), Field based analysis of sediment entrainment in two high gradient streams located in Alpine and Andine environments, *Geomorphology*, 93, 368-383.
- Mao, L., A. Dell'Agnese, C. Huincache, D. Penna, M. Engel, G. Niedrist, and F. Comiti (2014), Bedload hysteresis in a glacier-fed mountain river, *Earth Surf. Process. Landforms*, 39, 964-976, doi:10.1002/esp.3563
- Montgomery, D. R., and J. M. Buffington (1997), Channel-reach morphology in mountain drainage basins, *Geol. Soc. Am. Bull.*, 109(5), 596-611.
- Nitsche, M., D. Rickenmann, J. M. Turowski, A. Badoux, and J. W. Kirchner (2011), Evaluation of bed load transport predictions using flow resistance equations to account for macro roughness in steep streams, *Water Resour. Res.*, 47, W08513, doi: 10.1029/2011WR010645
- Piedra, M. M., H. Haynes, and T. B. Hoey (2012), The spatial distribution of coarse surface grains and the stability of gravel river beds, *Sedimentology*, 59, 1014-1029, doi: 10.1111/j.1365-3091.2011.01290

- Recking, A., P. Frey, A. Paquier, and P. Belleudy (2009), An experimental investigation of mechanisms involved in bed load sheet production and migration. *J. Geophys. Res.*, 114, F03010, doi: 10.1029/2008JF000990
- Recking, A. (2010), A comparison between flume and field bed load transport data and consequences for surface-based bed load transport prediction, *Water Resour. Res.*, 46, W03518, doi: 10.1029/2009WR008007
- Recking, A. (2012), Influence of sediment supply on mountain streams bedload transport, *Geomorphology*, 175-176, 139-150, doi: 10.1016/j.geomorph.2012.07.005
- Recking, A. (2013), An analysis of nonlinearity effects on bed load transport prediction, *J. Geophys. Res.: Earth Surface*, 118, 1264-1281, doi: 10.1002/jgrf.2009
- Rickenmann, D. (2001), Comparison of bed load transport in torrents and gravel bed streams, *Water Resour. Res.*, 37(12), 3295-3305.
- Rickenmann, D., and Recking, A. (2011), Evaluation of flow resistance in gravel-bed rivers through a large data set, *Water Resour. Res.*, 47, W07538, doi: 10.1029/2010WR009793
- Schneider, J. M., D. Rickenmann, J. M. Turowski, K. Bunte, and J. W. Kirchner (2015), Applicability of bed load transport models for mixed size sediments in steep streams considering macro-roughness, *Water Resour. Res.*, 51, 5260-5283, doi: 10.1002/2014WR016417
- Sklar, L. S., J. Fadde, J. G. Venditti, P. Nelson, M. A. Wydzga, Y. Cui, and W. E. Dietrich (2009), Translation and dispersion of sediment pulses in flume experiments simulating gravel augmentation below dams, *Water Resour. Res.*, 45, W08439, doi: 10.1029/2008WR007346
- Sommer, N., and H. Lauffer (1982), Untersuchungen über den Feststofftransport in Gebirgsbächen der Ostalpen. *Proceedings of the 14th International Dam Conference* (pp. 119-138), Rio de Janeiro, Brazil, (in German).
- Spiller, S., N. Rüther, K. Koll, and K. Koll (2012), Bed load movement over a fully developed armor layer - A tracer experiment, in R. E. Murillo Muñoz, *River Flow 2012* (pp. 465-471), London, UK: Taylor and Francis Group, ISBN 978-0-415-62129-8
- Turowski, J. M., E. M. Yager, A. Badoux, D. Rickenmann, and P. Molnar (2009), The impact of exceptional events on erosion, bed load transport and channel stability in a step-pool channel, *Earth Surf. Proc. Land.*, 34, 1661-1673, doi: 10.1002/esp.1855
- Venditti, J. G., W. E. Dietrich, P. A. Nelson, M. A. Wydzga, J. Fadde, and L. Sklar (2010a), Effect of sediment pulse grain size on sediment transport rates and bed mobility in gravel bed rivers, *J. Geophys. Res.*, 115, F03039, doi: 10.1029/2009JF001418
- Venditti, J. G., W. E. Dietrich, P. A. Nelson, M. A. Wydzga, J. Fadde, and L. Sklar (2010b), Mobilization of coarse surface layers in gravel-bedded rivers by finer gravel bed load, *Water Resour. Res.*, 46, W07506, doi: 10.1029/2009WR008329
- Wilcock, P. R., and J. C. Crowe (2003), Surface based transport model for mixed size sediment, *Journal of Hydraulic Engineering*, 129(2), 120-128. doi: 10.1061/(ASCE)0733-9429(2003)129:2(120)
- Wong M., G. Parker, P. DeVries, T. M. Brown, and S. J. Burges (2007), Experiments on dispersion of tracer stones under lower-regime plane-bed equilibrium bed load transport, *Water Resour. Res.*, 43, W03440, doi: 10.1029/2006WR005172
- Yager, E. M., J. W. Kirchner, and W. E. Dietrich (2007), Calculating bed load transport in steep boulder bed channels, *Water Resour. Res.*, 43, W07418, doi: 10.1029/2006WR005432
- Yager, E. M., J. M. Turowski, D. Rickenmann, and B. W. McArdell, (2012a), Sediment supply, grain protrusion, and bed load transport in mountain streams, *Geophysical Research Letters*, 39, L10402, doi: 10.1029/2012GL051654
- Yager, E. M., W. E. Dietrich, J. W. Kirchner, and B. W. McArdell (2012b), Prediction of sediment transport in step-pool channels, *Water Resour. Res.*, 48, W01541, doi: 10.1029/2011WR010829
- Yu, G., Z. Wang, K. Zhang, T. Chang, and H. Liu (2009), Effect if incoming sediment on the transport rate of bed load in mountain streams, *International Journal of Sediment Research*, 29, 260-273.
- Yu, G., Z. Wang, H. Q. Huang, H. Liu, B. Blue, and K. Zhang (2012). Bed load transport under different streambed conditions – a field experimental study in a mountain stream, *International Journal of Sediment Research*, 27, 426-438.
- Zimmermann, A., M. Church, and M. A. Hassan (2010), Step-pool stability: Testing the jammed state hypothesis. *J. Geophys. Res.*, 115, F02008, doi: 10.1029/2009JF001365

C.2 Study F: Numerical approach for simulation of phase 1 bed load transport in steep streams

C.2.1 Introduction

The effect of sediment supply on bed load transport is addressed by means of experimental modeling in *Study E* (section C.1). In these experiments, relatively fine bed load was fed to a steep, armored bed at discharges ranging from one-third to twice the critical discharge of the bed surface. Confirming with earlier studies (e.g. *Egashira and Ashida*, 1991), the supplied bed load propagated downstream by partially filling the irregularities of the bed surface at low discharges. After a certain time lag, the bed load transport at the downstream flume end was in equilibrium with the feeding rate and the total bed load was predominately made up of the supplied sediment (*Study E*, section C.1). *Study E* reveals that minor changes in channel morphology (due to increased supply of fine bed load) cause major alteration of bed load transport rate. This suggests that the mobility of supplied grains was larger than that of the bed surface sediment: although fine sediment was abundant at the bed surface before sediment was supplied, the bed load predominately consisted of supplied sediment. It is worth to note, that supplied grain sizes exceeded the finest grains size of the bed surface up to a factor of 5.

Yager et al. (2007) attribute the increase of mobility with increasing bed load supply to a reduction of the form resistance due to the burial of coarse grains. Though the temporal alteration of the flow resistance was not addressed in *Study E*, visual observations revealed minor changes of the coarse grain's protrusion. Even in the experimental data of *Yager et al.* (2007), the flow velocity hardly changed as protrusion of macro-roughness elements decreased. In addition, a decrease of form drag might cause an increase in bed load transport rate, but it does not explain why supplied grains were preferentially transported.

In the present study, it is hypothesized that the mobility of fine bed load is controlled by its exposure to the flow rather than overall form drag. Since the supplied bed load partially deposits on the bed surface, it is more exposed to the flow than the bed material. This hypothesis is tested by means of a numerical model and two approaches are developed which address the exposure of sediment. A large number of flume experiments dealing with that phenomenon are back-calculated with this numerical model and computed results are compared with the observations. The numerical simulations are performed by modeling flow hydraulics and fractional bed load transport including mass balancing of the fractional bed load and bed material. Therefore, a set of equations, which on their bases are already tested and evaluated for steep mountain streams, were programmed in MATLAB (© The Mathworks, Inc.; <http://de.mathworks.com/products/matlab/>). To address the effect of bed load supply on bed load transport rate, the focus is put on two distinct model elements, the hiding function and the mixing of the bed load and bed material.

C.2.2 Theory development

2.2.1 Bed state dependence of the hiding function

The mobility of non-uniform sediment is affected by hiding and exposure (*Parker and Klingeman, 1982*) which is usually accounted with a hiding function. Though there exist several types of hiding functions (e.g. *Einstein, 1950; Parker and Klingeman, 1982; Hunziker and Jaeggi, 2002; Wilcock and Crowe, 2003*), the overall principle remains similar: scaling incipient motion conditions (threshold based formulas) or mobility (reference based formulas) of a reference grain size. In terms of the critical specific discharge, the incipient motion of the *i*th grain size is determined by

$$q_{c,i}/q_{c,ref} = (D_i/D_{ref})^b, \quad (C6)$$

with the grain size of the *i*th grain size fraction D_i , the reference grain size D_{ref} , the critical specific discharge of the *i*th, and the reference grain size $q_{c,i}$ and $q_{c,ref}$, and the hiding exponent b . Commonly, the reference grain size is the median diameter (D_{50}), which proved to be proper surrogate even in mountain streams with wide-graded sediment (*Bathurst, 2013*).

In a comprehensive study, *Bathurst (2013)* found the hiding exponent b to vary between different mountain streams and reported values are in the range of 0.2 to 1.3. A hiding exponent of 0.2 is close to equal mobility, which means that small and coarse grains are mobilized at similar flows. Equal mobility is typically observed in paved gravel bed streams (e.g. *Parker and Klingeman, 1982*). In contrast, a hiding exponent of 1.2 indicates strong size-selective mobility and thus, small grains are mobilized at considerable lower flows than coarse grains.

The hiding function accounts for the differences in the particle's exposure. In the case of equal mobility, fine grains hide between coarse grains, while the coarse ones are more abundant to the flow. In the present study, the hiding and exposure effect is assumed to vary according to the supply of fine bed load. As fine bed load enters from upstream reaches, it temporally deposits on the bed surface and thus, it might be more exposed to the flow than small grains of the former bed surface (see *Study E*, section C.1). The exposure of individual sediment grains is hard to assess within numerical simulations since the stratigraphy of the bed material is simplified to multiple layers, each sharing a homogeneous grain size distribution (e.g. *Hirano, 1971, Parker, 1991*). A suitable proxy for the overall exposure of fine bed load is the embedding of the bed surface since it shares information regarding the extent in which irregularities of a coarse bed surface are filled up. Embedding is already proven to be one component of the bed structure that controls particle entrainment of wide-graded bed sediment (*Bathurst, 2013; Yager et al., 2007*). In the case of low embedding (Figure C-18), hiding and exposure is expected to be large, favoring equal rather than size-selective mobility. Contrary to this, fine sediment ($D_i < D_{50}$) is assumed to be more exposed at bed states featuring large embedding and thus, these grains can be easier mobilized.

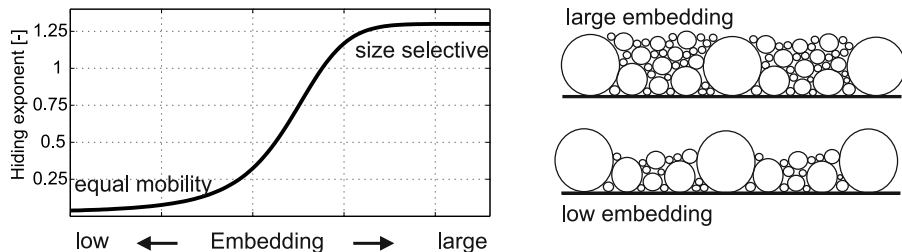


Figure C-18: Arbitrary dependence of the hiding exponent b on the embedding of the bed surface

In the present study, an approach is developed that enables to determine the hiding exponent b (equation C6) amongst others on the current state of embedding. This new hiding function is then tested against four common hiding functions which encompass the full range of observed exponents in *Bathurst* (2013).

2.2.2 Active layer thickness – flow strength dependence

In terms of modeling bed load transport, the stratigraphy of the bed material is usually simplified to multiple layers, each sharing a homogeneous grain size distribution. The uppermost layer that interacts with the transported bed load is called active layer (e.g. *Hirano*, 1971, *Parker*, 1991). According to the fractional active layer concept (*Parker*, 1991), the probability of erosion is the same for all grains of equal size within the active layer.

The thickness of the active layer (H_{al}) controls the speed of grain sorting. In the case of size-selective erosion (small grains are more mobile than coarse ones) the grain size distribution of the active layer coarsens the faster the thinner it is. In analogy, a thin active layer fines faster than a thick one in case that fine sediment accumulates. The speed of grain sorting has a severe impact on bed load transport rate since the latter is determined on the basis of the grain size distribution of the active layer.

Parker (1991) suggests a constant active layer thickness referring to the grain size which is 90 % finer by weight (D_{90}). It proved to accurately reproduce the downstream fining in alluvial rivers. In common modeling tools, there exist more sophisticated approaches for determining the active layer thickness. *Heimann et al.* (2015a) implemented the approach of *van de Wiel* (2007) in their model *sedFlow*, with the active layer thickness varying within an upper and lower bound depending on the history of channel bed aggradation and erosion. In the simulation program *BASEMENT*, the approach of *Borah et al.* (1982) is used, which differentiates the two cases of net erosion and net deposition; for further details see *Vetsch et al.* (2015).

According to field tracer experiments in mountain streams, the active layer thickness further depends on the stream power (*Schneider et al.*, 2014; *Haschenburger and Church*, 1998). The active layer is rather thin at low flows and approaches a thickness equal with the D_{90} at high flows (*Schneider et al.*, 2014). In this respect, *van Niekerk et al.* (1992) proposed an approach that determines the active layer thickness (H_{al}) at each simulation time step according

$$H_{al} = 2D_{50} \left(\tau / \tau_{c,D50} \right), \quad (C7)$$

with the bed shear stress τ and the critical shear stress $\tau_{c,D50}$ with respect to the D_{50} . Equation C7 yields a thin active layer at low shear stresses. Since any surplus of sediment in the active layer is balanced by the bed layer below, a thin active layer fines faster than a thick one when fine bed load deposits. Consequently, the reference grain size (D_{ref} in equation C6) or any other characteristic grain sizes (e.g. D_{84}) decreases fast as well, which increases the bed load mobility. In steep, wide-graded mountain streams, the coarse tail of the bed surface grain size distribution strongly affects the flow resistance (Ghilardi *et al.* 2014), which is commonly expressed by the D_{84} (e.g. Rickenmann and Recking, 2011). According to the example case stated above, the approach of Niekerk *et al.* (1992) causes a faster decrease of the roughness scale at low shear stresses, which is counterintuitive.

In this study, it is supposed that bed load is mobilized from the immediate bed surface at low flows, regardless of the active layer thickness. In contrast, the erosion of individual grains extends further into the active layer as flow intensity increases. To test this hypothesis, a mixing approach is developed that accounts for the entrainment probability of certain grain sizes depending on their origin (incoming bed load or bed material) and on flow intensity. Results obtained by this new mixing concept are compared with two common approaches.

C.2.3 Experimental data

2.3.1 General remarks

A variety of experimental tests dealing with bed load transport in steep channels were accomplished at the hydraulic laboratory of the University of Innsbruck. The first data set comprises feeding experiments where relatively fine bed load was supplied to an armored bed at constant but run-wise different discharge. The second data set refers to armoring experiments facing sediment starving except for few runs where fine bed load was supplied at a very minute rate.

2.3.2 Feeding experiments

2.3.2.1 Experimental procedure

The first data set comprises experimental tests, focusing on the effect of sediment supply on bed load transport rate in an armored flume. Twenty experiments were conducted in a 12 m long and on average 0.38 m wide scale model at the hydraulic laboratory of the University of Innsbruck. The experimental design is briefly summarized in the section below; for further details, the reader is referred to *Study E* (section C.1) or to the Master thesis of Daniel Kößler (2014).



Figure C-19: Illustration of the chronology and boundary conditions of the experimental runs that are accomplished within one experimental series of the feeding experiments

Table C-3: Experimental program with all experimental series which consist of successively performed runs, differing in water discharge. Parameter abbreviations are: discharge Q; flume gradient S; diameters of the bed surface of which 50 % ($D_{50,s}$) and 84 % ($D_{84,s}$) are finer, the median diameter $D_{50,sup}$ and the sorting coefficient $\sigma = \sqrt{D_{84}/D_{16}}$ of the surface (σ_s) and the supplied sediment (σ_{sup}).

| Series | Hydraulic conditions at the end of the initialization | | | | | Run | Characteristics of the feeding experiments | | | | | |
|--------|---|---------------------------|---------------------------------|---------------------------------|-------------------|----------------|--|--------------|---------------------------|-------------------------|----------------------|-----------------------|
| | Q (l s ⁻¹) | S (x10 ⁻²) | $D_{50,s}$ ^a (mm) | $D_{84,s}$ ^a (mm) | σ_s (-) | | Q (l/s) | Mass (kg) | Feeding Duration (min) | Total Duration (min) | $D_{50,sup}$ (mm) | σ_{sup} (-) |
| #1 | 6.9 | 3.0 | 8.0 | 20.4 | 2.6 | 1 ^b | 2.5 | 50 | 358 | 630 | 1.1 | 1.2 |
| | | | | | | 2 ^b | 4 | 50 | 197 | 494 | | |
| | | | | | | 3 ^b | 5.5 | 50 | 128 | 400 | | |
| | | | | | | 4 | 6.9 | 50 | 85 | 111 | | |
| | | | | | | 5 | 10 | 50 | 30 | 40 | | |
| | | | | | | 6 | 15 | 50 | 20 | 27 | | |
| #2 | 6.9 | 3.3 | 8.8 | 24.1 | 2.9 | 1 ^b | 4 | 50 | 300 | 632 | 2.7 | 1.2 |
| | | | | | | 2 ^b | 5.5 | 50 | 141 | 450 | | |
| | | | | | | 3 | 6.9 | 50 | 66 | 87 | | |
| | | | | | | 4 | 10 | 50 | 22 | 31 | | |
| | | | | | | 5 | 15 | 50 | 15.5 | 20 | | |
| #3 | 6.9 | 2.8 | 8.2 | 20.3 | 2.4 | 1 ^b | 5.5 | 50 | 164 | 476 | 3.9 | 1.6 |
| | | | | | | 2 | 6.9 | 50 | 133 | 178 | | |
| | | | | | | 3 | 10 | 50 | 66 | 88 | | |
| | | | | | | 4 | 15 | 50 | 24 | 33 | | |
| #4 | 6.9 | 2.8 | 9.0 | 20.5 | 2.5 | 1 ^b | 3.8 | 50 | 235 | 345 | 1.3 | 1.9 |
| | | | | | | 2 ^b | 5.5 | 50 | 160 | 442 | | |
| | | | | | | 3 | 6.9 | 50 | 44 | 58 | | |
| | | | | | | 4 | 10 | 50 | 15 | 20 | | |
| | | | | | | 5 | 15 | 50 | 19 | 25 | | |

^a Volume-by-weight distributions of the bed surface

^b Experimental runs were stopped after a duration of 1.33 times the feeding duration and continued until bedload transport decreased to virtually zero

In total four experimental series were conducted, each differing in the grain size of the supplied bed load. The initial condition of each of these four series was a self-stabilized bed surface, generated by sediment starving at a flow of 6.9 l/s. During channel bed stabilization, the bed slope decreased from initially 0.04 m/m to about 0.03 m/m and the bed surface grain size distribution coarsened. The bed surface featured similar bed structures as observed in the prototype mountain streams, the Gurgler Ache (i.e. immobile keystones, submerged steps). Starting from there, several experimental runs were performed successively within a series, each with constant but run-wise increasing water flow (Figure C-19 and Table C-3). Thus, every experimental run either differed in discharge, the grain size of supplied bed load or both.

During each run, 50 kg of colored bed load was supplied at a rate corresponding with the transport capacity within the uppermost section of the flume. After feeding was accomplished, water flow remained at least for one-third of the feeding duration. For all runs with discharges smaller than the stabilizing discharge (6.9 l/s), the runs were continued until bed load transport approached a very minute rate. Summarizing, discharges ranged between one-third and twice the critical flow of the bed surface (6.9 l/s) and the median grain size of supplied sediment was between 1/7 and half of the bed surface's D_{50} (Table C-3).

2.3.2.2 Measurements

The bed surface grain size distribution of the initially armored bed was determined by photosieving and converted to a volume-by-weight distribution according to the method proposed by *Diplas and Sutherland* (1988). During each experimental run, the bed load transport was assessed by registering the bed load accumulation in a tailwater box situated at the downstream end of the flume. After each run, the grain size distribution of the total bed load outflow was obtained by sieving a representative sample which was also split according to its source (bed material and supplied colored bed load). The longitudinal profile of the flume was measured manually with a point gauge and the bed surface grain size distribution was determined again by photosieving, but for the experimental series 4 only.

2.3.2.3 Main results

During the experimental runs with discharges not exceeding the critical discharge of 6.9 l/s (see Table C-3), the time series of bed load transport rate featured consistent patterns which were attributed to three distinct phases: (1) a temporal lag, (2) an equilibrium and (3) a post-feeding phase (Figure C-20). The temporal lag represents the duration between feeding start and initial outflow of supplied bed load. During this phase, supplied bed load propagated downstream by partially filling the pockets of the bed surface. The magnitude of bed load deposition was small and the coarse grains still protruded into the flow, affecting flow hydraulics. Once the supplied bed load reached the downstream end of the flume, the transport rate increased rapidly and the bed load outflow was in equilibrium with the rate of feeding (equilibrium phase). As the feeding was stopped, equilibrium transport conditions remained for a certain time, which is attributed to the erosion of temporally deposited bed load. Afterwards, the bed load transport rate declined (post-feeding phase), approaching a very minute transport rate. Accumulated bed load transport was majorly made up by the supplied bed load, suggesting for an overpassing rather than an exchange with the bed material. The

results also revealed a decrease of bed stability, but the bed surface grain size distribution and the bed structures hardly changed.

At higher flows, the processes differed. Total bed load outflow exceeded the mass of feeding and the break-up of the armor layer caused the bed surface to fine. Thus, the temporal lag and the post-feeding decline were hardly or not all existent (Figure C-20).

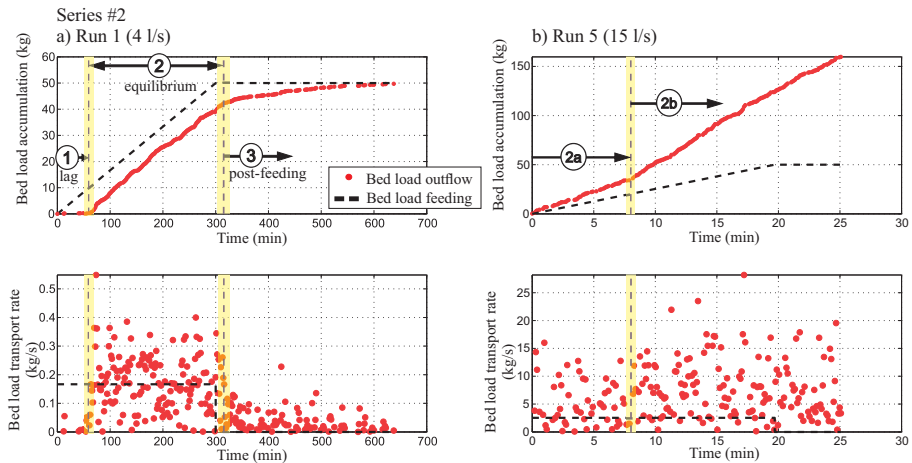


Figure C-20: Bed load feeding at the upper flume end (dashed line) and measured bed load transport at the lower end of the flume (red circles) for two selected experimental runs of the series #2; circled numbers indicate different phases of response to feeding.

2.3.3 Armoring experiments

2.3.3.1 Experimental procedure

The second data set comprises experimental tests, focusing on an alteration of bed load supply and its feedback on bed surface armoring and bed load transport rate. Therefore, two experimental series were conducted in a 7 m long and 0.5 m wide flume at the hydraulic laboratory of the University of Innsbruck. The two series differed in the initial flume gradient which was either 0.05 m/m or 0.10 m/m. The flume bed was mobile and the bulk sediment shared a grain size distribution similar to those measured in prototype mountain streams, but scaled by 1:15 and truncated at 0.5 mm (model scale). The smallest grain size class featured a diameter range from 0.5 mm to 1.0 mm, while the coarsest class was 16 mm to 32 mm for the series 1 ($S=0.05$ m/m; Table C-4) and 60 mm to 100 mm for the series 2 ($S=0.1$ m/m; Table C-4).

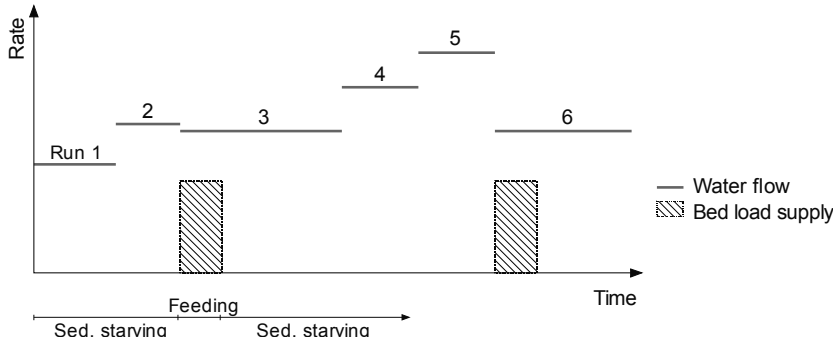


Figure C-21: Illustration of the chronology and the boundary conditions of the experimental runs that are accomplished within one experimental series of the armoring experiments

Table C-4: Experimental program of the armoring experiments, which consist of two experimental series (differing in bed slope and grain size distribution) with successively performed runs (differing in water discharge). Parameter abbreviations are: discharge Q ; flume gradient S ; diameters of the bed surface of which 50 % ($D_{50,s}$) and 84 % ($D_{84,s}$) are finer by weight; the median diameter $D_{50,sup}$ of the supplied bed load and the sorting coefficient $\sigma = \sqrt{D_{84}/D_{16}}$ of the surface (σ_s) or the supplied sediment (σ_{sup}).

| Series | Run | Q (l s ⁻¹) | Initial conditions | | | | Characteristics of the experimental run | | | | |
|--------|-----|-----------------------------|-----------------------------|--------------------|--------------------|-------------------|---|--------------------|---------------------------|----------------------|-----------------------|
| | | | S (x10 ⁻²) | $D_{50,s}$ (mm) | $D_{84,s}$ (mm) | σ_s (-) | Total Duration (min) | Feed. Mass (kg) | Feeding Duration (min) | $D_{50,sup}$ (mm) | σ_{sup} (-) |
| #1 | a1 | 4.6 | 5.0 | 7.0 | 21.5 | 3.3 | 232 | 0 | - | - | - |
| | a2 | 6.8 | 5.1 | 9.1 | 22.4 | 3.0 | 138 | 0 | - | - | - |
| | f3 | 6.4 | 5.0 | 10.0 | 23.0 | 2.7 | 1599 | 40 | 600 | 1.3 | 1.9 |
| | a4 | 9.0 | 5.1 | 10.4 | 23.2 | 3.0 | 346 | 0 | - | - | - |
| | a5 | 11.0 | 4.9 | 11.7 | 24.2 | 2.7 | 512 | 0 | - | - | - |
| | f6 | 6.4 | 4.5 | 12.7 | 24.7 | 2.8 | 318 | 16 | 240 | 1.3 | 1.9 |
| | a7 | 6.4 | 5.4 | 10.0 | 24.0 | 3.5 | 1079 | 0 | - | - | - |
| #2 | a1 | 4.6 | 10.0 | 11.2 | 29.8 | 4.0 | 239 | 0 | - | - | - |
| | a2 | 5.7 | 9.9 | 13.1 | 32.5 | 3.5 | 338 | 0 | - | - | - |
| | a3 | 6.5 | 9.9 | 14.7 | 41.5 | 3.2 | 284 | 0 | - | - | - |
| | f4 | 6.5 | 9.9 | 17.8 | 45.4 | 2.9 | 287 | 16 | 240 | 1.3 | 1.9 |
| | a5 | 6.5 | 9.9 | 19.0 | 47.0 | 3.7 | 977 | 0 | - | - | - |
| | a6 | 9.2 | 9.9 | 18.2 | 49.6 | 3.2 | 400 | 0 | - | - | - |
| | a7 | 10.3 | 9.9 | 19.4 | 50.1 | 2.8 | 356 | 0 | - | - | - |
| | a8 | 11.2 | 9.8 | 20.4 | 51.2 | 2.9 | 269 | 0 | - | - | - |
| | f9 | 6.5 | 9.7 | 21.7 | 54.1 | 2.7 | 432 | 24 | 360 | 1.3 | 1.9 |
| | a10 | 6.5 | 9.6 | 19.4 | 51.7 | 4.6 | 457 | 0 | - | - | - |
| | a11 | 12.4 | 9.5 | 20.7 | 52.4 | 3.3 | 245 | 0 | - | - | - |
| | a12 | 15.0 | 9.8 | 20.8 | 51.7 | 2.8 | 436 | 0 | - | - | - |

Several experimental runs were performed successively within a series, each with constant water discharge (Figure C-21). Most of the runs faced sediment starving (zero supply at the flume inlet), provoking either channel bed incision or bed surface armoring. Between these runs, single feeding experiments were accomplished, each with a minute feeding rate of 1.11×10^{-3} kg/s. The sequence of experimental runs is given in Table C-4 and the runs indicated with “a” (armorizing) refer to the runs featuring sediment starving, while “f” (feeding) refers to the runs where bed load was supplied at a very minute rate.

For the armorizing runs, the discharge was increased according to a constant ratio of $q/q_{c,D50} = 1.14$, with the specific discharge q and the critical discharge $q_{c,D50}$ determined according to *Rickenmann* (1991; equation C13). In contrast, the discharge of the feeding runs was always 6.4 l/s in series 1 and 6.5 l/s in series 2. For further details, the reader is referred to the Master thesis of *Bernd Steidl* (2015).

2.3.3.2 Measurements

In analogy with the feeding experiments (section 2.3.2.2), the bed load transport was assessed by registering the bed load accumulation in a tailwater box situated at the downstream end of the flume. The grain size distribution of the bed load was measured by sieving at the end of each run. The bed surface grain size distribution was determined by the grid-by-number method, which is assumed to correspond with the volume-by-weight distribution (*Bunte and Abt*, 2001). It is worth to note, that the small and the coarse tail of the grain size distribution, and the supplied sediment were colored differently beforehand. This enabled to split total bed load according to its source and was helpful for the grid-by-number pebble counts.

2.3.3.3 Main results

In course of the armorizing runs, the bed surface grain size distribution coarsened and step-pool structures evolved (Table C-5). By that, the thalweg slope hardly declined (at maximum -11 % during series 1 and -5 % during series 2), suggesting for a self-stabilization of the bed surface. In contrast, the standard deviation of the detrended longitudinal profile, as well as the D_{50} and the D_{84} of the bed surface, revealed an increase with discharge. However, the coarsening of the D_{84} was weak during the series 1, which featured a moderate gradient of 0.05 m/m (Table C-5). The D_{84} at end of the run with the maximum discharge (run a5 in series 1) was only 15 % larger than the D_{84} of the initial bed surface. In contrast, the D_{84} exceeded its initial value by 87 % at the end of the last run of the series 2 (Table C-5).

Summarizing, the self-stabilization of the flume is attributed to both, bed material coarsening and bed surface structuring. The coarsening results from the partial winnowing of the fine tail of the bed material grain size distribution and the bed surface structuring is associated with the clustering of keystones in order to maximize bed stability (jammed state; e.g. *Church and Zimmermann*, 2007).

Table C-5: Results of the armoring experiments with the total bed load transport that accumulated in the tailwater box during an experimental run BL , the total bed load transport normalized by the mass of supplied sediment $relBL$ (only for feeding experiments), the 50th and 84th percentile of the bed load's grain size distribution $D_{50,out}$ and $D_{84,out}$, the relative change of the bed surface D_{50} (RCD₅₀) and D_{84} (RCD₈₄) with respect to the initial condition of the experimental series (Table C-4), the standard deviation of the de-trended longitudinal profile $\sigma_{l,p}$ at the end of the run and the relative change of $\sigma_{l,p}$ ($RC\sigma_{l,p}$) and channel slope S (RCS) with respect to their initial values.

| Series | Run | Q (l s ⁻¹) | Bed load transport | | | | Bed surface | | | | |
|--------|-----|---------------------------|--------------------|---------------|----------------------|----------------------|--------------------------|--------------------------|------------------------|--------------------------|------------|
| | | | BL (kg) | rel BL (%) | $D_{50,out}$ (mm) | $D_{84,out}$ (mm) | RCD ₅₀ (-) | RCD ₈₄ (-) | $\sigma_{l,p}$ (mm) | RC $\sigma_{l,p}$ (-) | RCS (-) |
| #1 | a1 | 4.6 | 17.7 | | 1.7 | 5.2 | 29% | 4% | 0.31 | 27% | 0% |
| | a2 | 6.8 | 16.8 | | 2.1 | 7.3 | 42% | 7% | 0.36 | 49% | 0% |
| | f3 | 6.4 | 44.4 | 111% | 2.1 | 4.3 | 47% | 8% | 0.34 | 42% | 1% |
| | a4 | 9.0 | 26.8 | | 3.0 | 11.4 | 67% | 13% | 0.33 | 36% | -4% |
| | a5 | 11.0 | 183.2 | | 11.1 | 23.7 | 80% | 15% | 0.42 | 77% | -11% |
| | f6 | 6.4 | 6.8 | 69% | - | - | 41% | 12% | 0.39 | 61% | 7% |
| | a7 | 6.4 | 4.3 | | 2.0 | 3.7 | 72% | 13% | 0.40 | 68% | 6% |
| #2 | a1 | 4.6 | 19.1 | | 5.2 | 16.8 | 18% | 9% | 0.40 | 8% | -1% |
| | a2 | 5.7 | 27.5 | | 5.0 | 19.7 | 31% | 39% | 0.58 | 57% | -1% |
| | a3 | 6.5 | 10.9 | | 3.6 | 18.5 | 59% | 52% | 0.57 | 53% | -1% |
| | f4 | 6.5 | 18.8 | | 3.8 | 6.6 | 70% | 58% | 0.61 | 63% | -1% |
| | a5 | 6.5 | 10.2 | 181% | 2.1 | 6.0 | 63% | 66% | 0.62 | 68% | -1% |
| | a6 | 9.2 | 41.5 | | 5.0 | 19.5 | 73% | 68% | 0.67 | 81% | -1% |
| | a7 | 10.3 | 23.7 | | 4.6 | 19.4 | 82% | 72% | 0.75 | 101% | -2% |
| | a8 | 11.2 | 9.9 | | 5.7 | 21.7 | 94% | 81% | 0.73 | 96% | -3% |
| | f9 | 6.5 | 14.5 | 71% | 2.7 | 4.6 | 73% | 73% | 0.75 | 102% | -4% |
| | a10 | 6.5 | 2.4 | | 1.5 | 3.4 | 85% | 76% | 0.77 | 108% | -5% |
| | a11 | 12.4 | 27.4 | | 4.8 | 20.3 | 86% | 73% | 0.88 | 137% | -2% |
| | a12 | 15.0 | 86.4 | | 14.2 | 27.6 | 118% | 87% | 0.75 | 103% | -5% |

The time series of bed load accumulations featured a severe increase at the very beginning of each run at which the discharge was increased. Afterwards, the bed load accumulation hardly increased during all armoring runs of the series 1 ($S=0.05$ m/m). In contrast, several runs of series 2 ($S=0.1$ m/m) revealed further peaks of bed load transport, which occurred sporadically in course of the experimental runs. These peaks are attributed to the mobilization of individual keystones, causing the bed surface locally to break up. This corresponds very well with the observations made by Zimmermann *et al.* (2010). In addition, the magnitude of total bed load outflow differed, regardless of the series. For example, 26.8 kg of bed material was eroded during run a4 of the series 1 ($Q=9.0$ l/s), while it was seven times larger during the subsequent run a5 ($Q=11.0$ l/s). This variable response to increased flow as well as the occurrence of transport peaks during one run facing constant flow are attributed to the stochastic nature of bed load transport (e.g. Zimmermann *et al.*, 2010).

The next issue is the response to an addition of fine bed load at a low rate. Corresponding with the feeding experiments (section 0 or *Study E*), the time series of bed load outflow could be separated into three phases: (i) a temporal lag with no transport,

followed by (ii) an equilibrium phase with the bed load outflow approaching the feeding rate and (iii) a post-feeding phase during which bed load transport rate declined towards zero. It is worth to note, that the subsequent runs a7 of series 1, as well as a5 and a10 of series 2, are attributed to the post-feeding phase.

The total bed load transport of the feeding runs f3 (series 1) and f4 (series 2; including the subsequent post feeding run a5) exceeded the amount of supplied sediment. The discharge of these runs corresponds with the stabilizing discharge of the previous armoring run. Thus, the increase of bed load transport is attributed to the decrease of bed stability due to increased sediment supply (see *Study E*, section C.1). In contrast total bed load transport was smaller than the supply for the runs f6+a7 (series 1) and f9+a10 (series 2). The supplied sediment that was not transported out of the flume, remained on the bed surface.

C.2.4 Modeling framework

2.4.1 Model discretization and flow hydraulics

The numerical modeling is accomplished in scale model dimensions, but the applied equations enable an application to natural (prototype) conditions.

The flume is discretised into a sequence of numerical segments, each 0.5 m long and represented by a rectangular cross section at the beginning of each section. For the feeding experiments (section 0), the width of the cross sections differs according to the flume geometry, ranging between 0.27 m and 0.48 m. In contrast, the width of the cross sections of the armoring experiments (section 2.3.3) is constant ($w=0.5$ m).

Flow hydraulics are modeled in a one-dimensional way by assuming uniform flow. Furthermore, the wave propagation is neglected, which is justified since both experimental tests featured steady state conditions of water flow. Based on flume geometrics and the step-wise discharge hydrograph, flow hydraulics can be modeled by a set of two equations, the mass continuity, and a flow resistance equation. Due to the simplifications made, mass continuity is defined by:

$$Q = U \times A, \quad (C8)$$

with the mean flow velocity U and wetted area A , which is a function of flume width w and flow depth d . The variable power law approach of *Ferguson* (2007) is used to determine the flow resistance. According to this approach, the flow resistance is a function of relative flow depth with respect to the D_{84} :

$$\sqrt{\frac{8}{f}} = \frac{a_1 a_2 (d/D_{84})}{\sqrt{a_1^2 + a_2^2 (d/D_{84})^{5/3}}}. \quad (C9)$$

Equation C9 is applied with $a_1=6.5$ and $a_2=2.5$ as suggested by *Rickenmann and Recking* (2011) and the mean flow velocity is defined by

$$U = \sqrt{\frac{8}{f} \sqrt{gdS}}, \quad (C10)$$

with the acceleration of gravity g and bed slope S . The equations C8 and C10 are solved iteratively for d until the ratio of the predefined and calculated discharge is within the tolerance criterion of $1 \pm 1e^{-4}$.

2.4.2 Flow resistance partitioning

The flow patterns in mountain streams are strongly affected by macro-roughness elements, such as immobile boulders (Ghilardi et al., 2014; Yager et al., 2007) or bed structures (Church and Zimmerman, 2007; Montgomery and Buffington, 1997). To account for the loss of momentum due to form and spill drag around these macro-roughness elements, the approach of Rickenmann and Recking (2011), which has been successfully tested in terms of bed load transport modeling by Nitsche et al. (2011) and Heimann et al. (2015b), is applied. Therein, the energy gradient S is reduced to S_{red} according to the proportion of base level resistance (skin friction) in total flow resistance:

$$S_{red} = S \times \left(\frac{2.5 \left(\frac{d}{D_{84}} \right)^{\frac{5}{6}}}{\sqrt{6.5^2 + 2.5^2 \left(\frac{d}{D_{84}} \right)^{\frac{5}{3}}}} \right)^{1.5} \quad (C11)$$

2.4.3 Bed load transport rate

2.4.3.1 General remarks

Two different bed load transport equations are incorporated in the numerical model and the simulations are performed with both equations separately.

The first bed load transport equation is a discharge based approach that was initially developed by means of flume data (Rickenmann, 2001; Rickenmann, 1991) but verified against field data of several flood events in Switzerland (Nitsche et al., 2011).

The second bed load transport equation is a reference-based approach corresponding with the surface based bed load transport equation of Wilcock and Crowe (2003) but modified for steep mountain streams by means of field data (Schneider et al., 2015).

2.4.3.2 Rickenmann (2001) bed load transport equation

The bed load transport rate is computed with the discharge based threshold equation of Rickenmann (2001), which is an empiric equation that is based on flume data but modified and validated by means of field data (Nitsche et al., 2011). The original formulation is modified in terms of surface-based, fractional calculations in the following form:

$$q_b = \sum_{i=1}^n f_i \times 1.5 \times (q - q_{c,i}) \times S_{red}^{1.5} \quad (C12)$$

where q_b is the bed load transport rate per unit width (m^2/s), f_i the proportion of the i th grain fraction of the bed surface grain size distribution, q the specific discharge (m^2/s) and $q_{c,i}$ the critical specific discharge (m^2/s) of the i th grain size fraction, respectively.

Incipient motion of the D_{50} of the bed surface is expressed as critical specific discharge ($q_{c,D_{50}}$) and determined with the equation of *Rickenmann* (1991), which is an empirical function of the median diameter D_{50} , bed slope S , gravity g and specific solid density $\varsigma = \rho_s / \rho_w = 2.65$:

$$q_{c,D_{50}} = 0.065 \times (s - 1)^{1.67} \times \sqrt{gD_{50}^3} \times S^{-1.12} \quad (\text{C13})$$

The critical specific discharge of each grain size fraction, $q_{c,i}$, is then derived in combination with a hiding function, according:

$$q_{c,i} = q_{c,D_{50}} \times \left(\frac{D_i}{D_{50}} \right)^b \quad (\text{C14})$$

where D_i is the geometric mean of each grain size fraction and the hiding exponent b controls the relative mobility of each grain size fraction. In this respect, the term 'mobility' is attributed to both, the incipient motion of a particle and its mobility in terms of transport rate.

In accordance to the results of *Study C* (section 5.6.3 in chapter B), *Bathurst* (2013) suggests an exponent of 1.5 for full size-selective mobility, while equal mobility is by definition attained with $b=0$. Equal mobility means that incipient motion of all grain sizes occurs at the same flow and thus, fractional bed load transport rate is independent of the individual grain size but depends solely on the D_{50} (equations C12-C14). In contrast, full size-selective mobility assumes that each particle size is as mobile as it would be in a bed composed of uniform material of that size and thus, a non-uniform grain size distribution has no influence on the particle's mobility. On the basis of a comprehensive study of field data, *Bathurst* (2013) concludes that b (referring to discharge based approach) typically varies between 0.2 and 1.3. The hiding exponents derived in *Study C* (Table B25 in *Study C* in chapter B) reveal a smaller range with $0.11 < b < 0.52$.

A new approach is presented in which the hiding exponent b depends on the embedding of the bed surface and covers the full range of observed values (b_5 , section 2.5.1). It is tested against four commonly applied functions or constants of the hiding exponent b , each suitable for mountain streams (b_1 to b_4):

b_1 to b_3 are defined by the constant values of 0.3, 0.8 and 1.3, which are all within the range of typically observed exponents (e.g. *Bathurst*, 2013). In contrast, b_4 is defined by the equation of *Wilcock and Crowe* (2003) but multiplied with 1.5 in order to account for the discharge based transport formula:

$$b_4 = \frac{0.67}{1 + \exp\left(1.5 - \frac{D_i}{D_{50}}\right)} \times 1.5 \quad (\text{C15})$$

Thus, b_4 depends on the relative grain size with respect to the bed surface D_{50} . Equation C15 is a sigmoid function and approaches 0.18 for very small values of D_i/D_{50} (small hiding effect) and 1 for very large ratios (small protrusion effect).

2.4.3.3 Schneider et al. (2015) bed load transport equation

Schneider et al. (2015) fitted a reference shear stress based bed load transport equation to a large field data set. In terms of effective shear stress, the dimensionless reference transport rate W^{*r} of a certain grain size fraction i is defined by

$$W_i^{*r} = \frac{(s-1)gq_{b,i}}{f_i u^{*r^3}} = \begin{cases} 0.002 \times \left(\tau_i^{*r} / \tau_{ri}^{*r} \right)^{6.82} & \text{for } \tau_i^{*r} / \tau_{ri}^{*r} < 1.33 \\ 14 \times \left(1 - \frac{0.894}{\left(\tau_i^{*r} / \tau_{ri}^{*r} \right)^{0.5}} \right)^{4.5} & \text{for } \tau_i^{*r} / \tau_{ri}^{*r} > 1.33 \end{cases} \quad (\text{C16})$$

Herein $q_{b,i}$ (m^2/s) is the specific bed load transport rate of the i th grain size fraction, u^{*r} is the shear velocity with respect to the effective shear stress $u^{*r} = \sqrt{gdS_{red}}$, τ_i^{*r} is the dimensionless effective shear stress with respect to the i th grain size fraction

$$\tau_i^{*r} = \frac{dS_{red}}{(s-1)D_i}, \quad (\text{C17})$$

and τ_{ri}^{*r} is the dimensionless reference shear stress

$$\tau_{ri}^{*r} = 0.03 \times \left(\frac{D_i}{D_{50}} \right)^\beta. \quad (\text{C18})$$

In this respect, the mobility of each grain size fraction depends on the hiding exponent β . In the case of equal mobility, the ratio $\tau_i^{*r} / \tau_{ri}^{*r}$ at a given flow has to be equal for all grain size fractions considered. Since $\tau_i^{*r} \propto D_i^{-1}$ (equation C17), equal mobility is defined by $\beta = -1$, while full size-selective mobility is achieved with $\beta = 0$, respectively. In this regard, equal mobility assumes that all grain sizes are equally mobile at a certain flow and thus, the fractional bed load transport rate is independent of the individual grain size but solely depends on the D_{50} . In contrast, full size-selective mobility assumes that each particle size is as mobile as it would be in a bed composed of uniform material of that size and thus, a non-uniform grain size distribution has no influence on the particle's mobility.

The equation C16 is based on a huge field data set of fractional bed load transport rate, where the hiding exponent was determined for each field site separately (Schneider et al., 2015). According to their data, the hiding exponent was predominately within a close range of approx. $-0.7 < D_i / D_{50} < 1$ for grain sizes smaller than the D_{50} ; only at very few sites this exponent was either greater than -0.7 or less than -1 and thus, referring to moderate size-selective ($\beta > -0.7$) or even inverse size-selective conditions ($\beta < -1$; coarse grains are mobilized easier than fine ones). In a consequence, individual particles are almost equally mobile with respect to their grain size for most of the field sites, with a median of $\beta = -0.88$. This is confirmed by the hiding exponents reported in Study C (Table C24 in Study C in chapter B). However, the field data of Schneider et al. (2015), and those of Study C hardly contain fractional bed load of grains coarser than the D_{50} of the bed surface. This is attributed to the fact that coarse grains are only

mobile during high flows which are insufficiently represented in many field data sets (e.g. Schneider *et al.*, 2015).

Despite this relatively close range of hiding exponents observed in steep mountain streams, a much wider range is considered within the modeling framework. The hiding exponents used with the dimensionless shear stress approach are convertible with those of the discharge based bed load transport equation according

$$\beta = \frac{b}{1.5} - 1 \quad (\text{C19})$$

In this respect, equation C19 assumes a linear relation between equal and size-selective mobility of both, the discharge based and shear stress based approaches. It has to be noted, that this transformation is based on empirics (see *Study C* in chapter B) rather than on a mathematical conversion of these approaches. The latter is done by means of a flow resistance equation and yields a numerator in the range from 1.67 to 2.5 (depending on the flow resistance equation), rather than 1.5 (Bathurst, 2013).

However, β_1 , β_2 , and β_3 are defined by constants values of -0.87 (almost equal or weak size-selective mobility), -0.47 (moderate size-selective mobility) and -0.13 (strong size-selective mobility). Furthermore, β_4 is defined by substituting equation C19 into equation C15 which yields

$$\beta_4 = \frac{0.67}{1 + \exp\left(1.5 - \frac{D_i}{D_{50}}\right)} - 1 \quad (\text{C20})$$

and the new, bed state dependent hiding function with the hiding exponent β_5 is given in section 2.5.1.

2.4.4 Mixing – mass balancing

2.4.4.1 General remarks

The substrate is idealized into three horizontal layers, each with a homogeneous grain size distribution. The topmost layer represents the active layer in which the interactions of the bed material and the bed load (erosion and deposition) are balanced with respect to each grain size fraction. Below the active layer, the bed layer regulates any fluxes from or to the active layer and the lowermost substrate layer acts as an additional source of bed material.

The mixing of bed load and bed material within these layers (the mass balancing) is accomplished in a way that the active layer thickness is either (i) of constant thickness (e.g. Parker and Klingeman, 1982) or (ii) confined by an upper and lower threshold (e.g. van de Wiel *et al.*, 2007; Heimann *et al.*, 2015a).

2.4.4.2 Mixing concept 1 – constant active layer thickness

2.4.4.2.1 Concept

The active layer thickness (H_a) is always constant and it is defined by the D_{84} of the initial grain size distribution of the active layer ($x [m]$ in Figure C-22). The input and output of bed load within a numeric segment is balanced during each hydraulic time

step and any surplus or deficit of sediment within the active layer is immediately balanced by the bed layer below (Figure C-22). In contrast, the bed layer thickness is confined by a lower and upper threshold with respect to the D_{84} of the bed layer grain size distribution ($D_{84,bl}$). These thresholds are defined by $1D_{84,bl}$ and $3D_{84,bl}$, respectively. In order to preserve mass continuity, a substrate layer of infinite thickness balances vertical bed load fluxes in case that one of these thresholds are reached. This is justified since the mobile bed of the experimental model was by far thicker than observed bed incision.

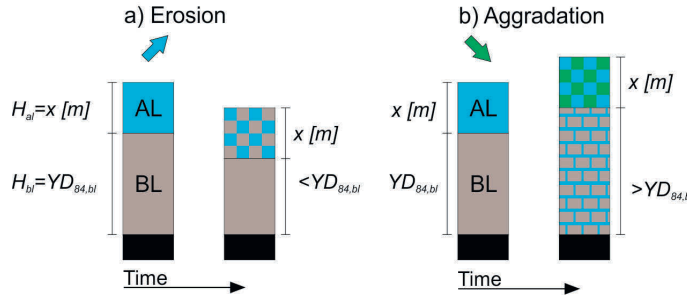


Figure C-22: a) Bed material erosion: sediment is eroded from the active layer which is immediately filled up to the constant thickness x [m] by the sediment of the bed layer; b) bed load aggradation: bed load is added to the active layer and bed material of the active layer is released to the bed layer in order to maintain the constant thickness of x [m].

2.4.4.2.2 Application

In the numerical model the volume of the layers is used instead of their thickness for simplicity, with

$$\begin{aligned} aV &= H_{al} \times w_j \times l_j \\ bV &= H_{bl} \times w_j \times l_j. \end{aligned} \tag{C21}$$

Herein, aV , bV is the volume of the active layer and bed layer, H_{al} , H_{bl} the thickness of the active layer and bed layer and w_j , l_j the mobile width and length of the model section. It is worth to note, that aV and bV refer to solid volumes with no pores and H_{al} and H_{bl} represent a virtual length scale. Since the mobile width w_j and section length l_j are geometric boundary conditions, the active layer thickness H_{al} has to be increased by the pore content of the bed material in order to obtain a physical length scale of depth.

The mixing approach is performed during each hydraulic calculation time step and thus, the volume, the grain size distribution of each layer and the bed level is updated corresponding to this time step.

First, the fractional bed load input and output of the numerical section is balanced within the active layer according:

$$aV_{i,t} = aV_{i,t-1} - outV_{i,t} + inV_{i,t-1}, \tag{C22}$$

with i the grain size fraction, $outV_{i,t}$, the volume of the i th grain size fraction that was transported out of the section during time step t , and $inV_{i,t+1}$, the volume of the i th grain

size fraction that entered from the upstream section during the time step $t-1$. The total solid volume of the active layer (a/V) is defined by the sum of all fractional volumes

$$a/V_t = \sum_{i=1}^n a/V_{i,t}, \quad (\text{C23})$$

where n is the number of grain size fractions.

In the case of net erosion, bed material of the bed layer is incorporated into a/V_t in order to preserve the constant active layer thickness. In analogy, bed material of the active layer is released to the bed layer in the case of net deposition.

The bed layer varies in its thickness, depending on the history of the sediment flux. In the case that the bed layer reaches its lower bound ($H_{bl} = D_{84,bl}$), any further erosion is directly compensated by the substrate layer. The opposite is the case when the bed layer thickness reaches its maximum ($H_{bl} = 3D_{84,bl}$). In addition, the bed layer is filled up at very high flows (for further details see section 2.4.4.3.2).

After the mixing of the bed load and the bed material, the grain size distribution of each layer is updated. The proportion of each grain size class at time t within a layer is simply obtained by the volume of this grain size fraction (e.g. $a/V_{i,t}$) divided by the total volume a/V_t , with

$$f_{i,t} = \frac{a/V_{i,t}}{a/V_t}, \quad g_{i,t} = \frac{b/V_{i,t}}{b/V_t}. \quad (\text{C24})$$

Herein $f_{i,t}$ and $g_{i,t}$ are the proportions by volume of the i th grain size in the active and bed layer. The grain size distribution (F_t and G_t) is defined by the vector of the cumulative sum of the grain size densities

$$\bar{F}_t = \sum_{i=1}^n \frac{a/V_{i,t}}{a/V_t}, \quad \bar{G}_t = \sum_{i=1}^n \frac{b/V_{i,t}}{b/V_t}. \quad (\text{C25})$$

2.4.4.3 Mixing concept 2 – variable active layer thickness

2.4.4.3.1 Concept

According to this concept, the active layer thickness (H_{al}) is variable but restricted to a lower and upper threshold with respect to the actual D_{84} of the bed surface grain size distribution. In mountain streams, a very thin active layer is counterintuitive since the grain diameters of the coarse sediment would exceed the active thickness by far. In addition, a very thick active layer is implausible as well, since the entrainment probability of a single grain size is the same for the entire active layer, regardless if the grain is on the active layer bottom or on the bed surface. Thus, a very thick active layer suggests that sediment from far below the bed surface is as likely entrained as sediment on the bed surface.

However, the upper and lower thresholds of the active layer thickness are defined dynamically by increments of the D_{84} of the bed surface: $0.5D_{84}$ for the lower bound and $1.1D_{84}$ for the upper bound. In the case that one of these thresholds is reached, bed load is either incorporated into the active layer by sharing the grain size distribution of the bed layer (in case of erosion) or released from the active layer into the bed layer

below (in case of aggradation). In addition, the sediment of the bed layer is incorporated into the active layer if the discharge exceeds incipient motion of the active layer's D_{84} , regardless of the current active layer thickness but as long as it is below $1.1D_{84}$. Thus, the active layer is filled up at high flows, accounting for the release of subsurface material due to the partial destruction of the armored bed surface.

The bed layer is of constant relative thickness, defined by $3D_{84}$ and represents the subsurface. In analogy to the mixing concept 1 (section 2.4.4.2), a substrate layer of infinite thickness balances additional vertical bed load fluxes. It is worth to note again, that this mixing concept is again applied during each hydraulic time step which was set to a constant value of two seconds. The concept of mixing the bed material and the bed load is schematically illustrated in Figure C-23 and the model application is given in the section below.

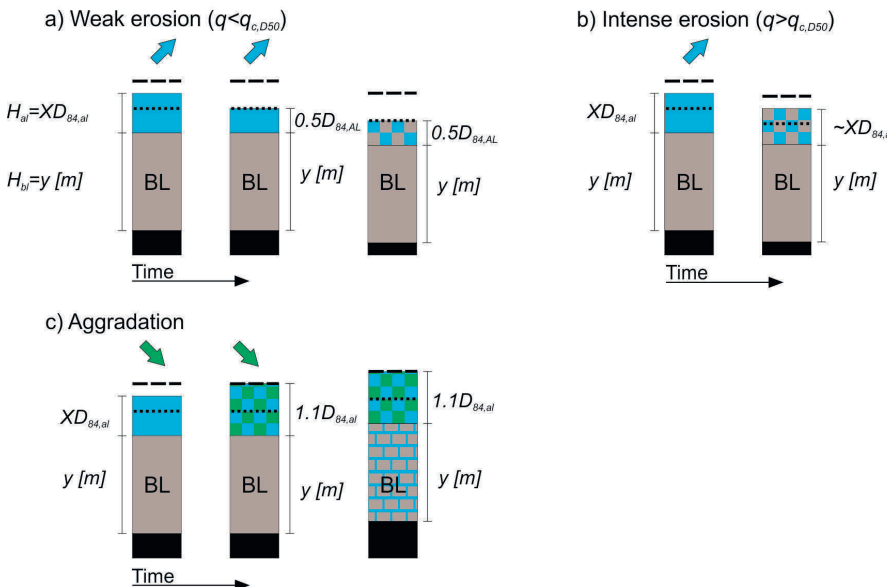


Figure C-23: a) Bed material erosion at $q < q_{c,D50}$: sediment is removed from the active layer without any interactions with the bed layer as long as H_{al} is larger than $0.5D_{84}$ (dotted lines); otherwise the active layer is refilled to $0.5D_{84}$ by the sediment of the bed layer; b) bed material erosion at $q > q_{c,D50}$: sediment is removed from the active layer and the active layer is partly filled up by the bed material of the bed layer; c) bed load aggradation: sediment is added to the active layer and once the active layer thickness is larger than $1.1D_{84}$ (dashed lines), the surplus is transferred to the bed layer.

2.4.4.3.2 Application

In analogy with the first mixing concept (section 2.4.4.2), the fractional bed load inflow and outflow are balanced within the active layer according to equation C22 in a first step.

The active layer thickness at the time t is determined by rearranging equation C21 to

$$H_{al,t} = \frac{a/V_t}{w_i l_i} \quad (C26)$$

and the grain size densities of the active layer and bed layer are updated according to equation C24, respectively. Based on these grain size distributions, the characteristic grain diameters (i.e. D_{50} and D_{84}) are determined by logarithmic interpolation according to *Bunte and Abt* (2001).

In the case of high flows ($q \geq q_{c,D50}$ or $\tau^* \geq \tau_c^*$), the sediment of the bed layer is incorporated into the active layer. The amount of subsurface release is set to the volume that was transported out of the section during the current time step ($outV_t$) without considering the magnitude of bed load inflow. The magnitude of subsurface release is additionally restricted by the upper bound of a/V_t , which is defined by

$$a/V_{MAX} = 1.1 \times D_{84,al} \times w_i \times l_i \quad (C27)$$

and must not be exceeded. In addition, the sediment of the active layer is shifted to the bed layer in case [$a/V_t > a/V_{MAX}$] or material of the bed layer is incorporated into the active layer in case [$a/V_t < a/V_{MIN}$].

In contrast, the bed layer is of constant relative size with respect to the D_{84} of the bed layer grain size distribution ($D_{84,bl}$):

$$b/V_t = 3 \times D_{84,bl} \times w_i \times l_i \quad (C28)$$

Thus, any vertical fluxes between the active layer and bed layer are immediately compensated by the substrate layer, which is of infinitive thickness.

2.4.5 Progress of simulation

Each experimental series of the feeding (Table C-3) and armoring experiments (Table C-4) was modeled numerically. The hydraulic boundary condition is the time series of discharge and bed load supply of the entire experimental series. Consequently, the sequence of experimental runs is simulated in one pass. This corresponds with the progress of the laboratory experiments, in which the final conditions of an experimental run were the initial conditions of the next run.

The initial condition of the active layer corresponds with the measured (volume-by-weight) grain size distribution of the initial bed surface. In contrast, the bed layer and substrate layer share the grain size distribution of bulked sediment.

C.2.5 Theory Application

2.5.1 Bed state dependence of the hiding function (b_5 and β_5)

2.5.1.1 Concept

The hypothesis of this concept is a relationship between the embedding of the bed surface and the hiding effect of small grains. Incorporating this dependency into the hiding function is suggested to enhance the performance of the modelling framework in reproducing the experimental observations.

Considering the mixing concept 2 (section 2.4.4.3), the ratio of the active layer thickness (H_{al}) and its D_{84} is a suitable measure for embedding. Its ratio varies within a lower and upper bound depending on previous supply conditions. This ratio is used to determine the hiding exponent (b in equation C14 and β in equation C18).

2.5.1.2 Application

The proposed approach is a linear function. In terms of the discharge based bed load transport equation, the hiding exponent b is defined by

$$b_5 = 1.67 \times \frac{H_{al}}{D_{84}} - 0.63 \quad \text{for (i) } q \leq q_{c,D50} \text{ and (ii)} \left(\frac{D_i}{D_{50}} \right) \leq 1 \quad (\text{C29})$$

Since the active layer thickness (H_{al}) is confined by $0.5D_{84}$ and $1.1D_{84}$ (see mixing concept 2 in section 2.4.4.3), b_5 varies between almost 0.2 and 1.2. This range somewhat corresponds with the range of hiding exponents compiled by Bathurst (2013) in the course of a field data review. However, equation C29 is only applied to grain sizes finer than the D_{50} of the bed surface. For grain sizes larger than the D_{50} , the hiding exponent is determined according to the equation C15. In addition, the equation C15 is used for all grain sizes at flows exceeding the $q_{c,D50}$.

To obtain the corresponding hiding exponent β_5 (for the dimensionless shear stress based approach), the equation C29 is used in combination with equation C19, respectively. In analogy to the discharge based approach, the equation C29 (in combination with equation C19) is only used for the grain sizes smaller than the D_{50} and at flows exceeding $T_{r,D50}^*$. Otherwise, the hiding exponent β_5 is determined according to equation C20.

According to this new hiding function, almost equal mobility conditions (critical discharge is almost the same for all grain sizes) are assumed for the finer fractions if the active layer approaches its lower bound (Figure C-24). Typically, this is the case for supply limitation and static armor conditions, resulting in a maximum level of hiding.

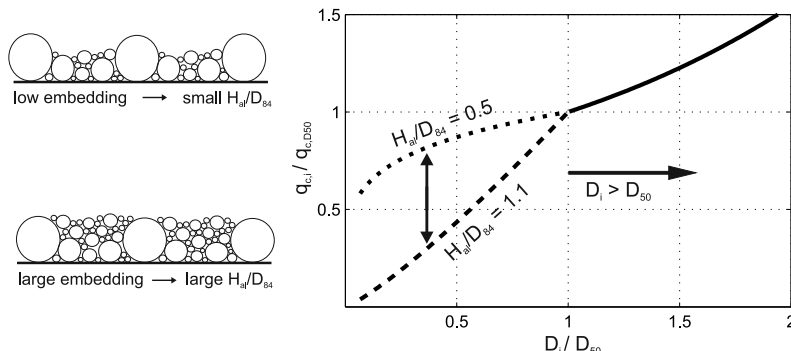


Figure C-24: The critical specific discharge of the i th grain size depending on the embedding

On the other hand, if fine sediment is supplied, the irregularities of the bed surface will be partly filled up. Thus, the active layer thickness increases and with it the ratio of H_{al} and D_{84} increases as well. Consequently, the hiding/exposure effect is expected to decrease, approaching almost full size-selective mobility at least for the sediment finer than the D_{50} (Figure C-24).

2.5.2 Active layer thickness – flow strength dependence (mixing concept 3)

2.5.2.1 Concept

The new mixing concept accounts for the relationship between the current flow strength and the penetrating depth into the stream bed. It is hypothesized that the bed load is mobilized from the immediate bed surface at low flows, while the erosion of individual grains extends further into the active layer at high flows.

Therefore, the mixing concept 2 is extended by introducing a new layer at the bed surface, which is called the active surface layer. The mixing of the bed load and the bed surface sediment is accomplished within both, the active layer and the active surface layer. Corresponding to the mixing concept 2, the active layer thickness varies within an upper and lower bound and thus, it enables for an efficient bed armoring in the case of erosion (see section 2.4.4.3). Furthermore, the D_{50} of the active layer represents the reference grain size for determining the incipient motion (section 2.4.3) and the D_{84} is used as roughness scale for determining flow hydraulics (section 2.4.1).

However, the bed load transport capacity of a certain grain size is also scaled by its abundance at the bed surface. Commonly and corresponding with the mixing concepts 1 and 2, the abundance is defined by the volume proportion of a grain size fraction in the entire active layer (f_i in equation C24). In contrast, this new mixing concept determines the abundance of a certain grain size fraction by means of the active surface layer. It represents the uppermost part of the active layer. The thickness of this new layer depends on the flow strength and it is smaller or equal than the thickness of the entire active layer (Figure C-25).

The flow strength (fs) is either defined by the specific discharge ratio or by the dimensionless shear stress ratio, depending on the bed load transport equation used (section 2.4.3)

$$fs = \frac{q}{q_{c,D84}} \quad \text{or} \quad fs = \frac{\tau_{D84}^*/0.03}{0.03}. \quad (\text{C30})$$

Herein, where $q_{c,D84}$ is the critical discharge and τ_{D84}^* is the dimensionless shear stress, both with respect to the D_{84} of the active layer grain size distribution (equation C13 or equation C17). The thickness of the active surface layer (H_{asl}) is then determined according:

$$H_{asl} = \min \left(D_{16} + \max \left(\left(\frac{q}{q_{c,D84}} \right)^2, 1 \right) \times (D_{84} - D_{16}), H_{al} \right) \quad (\text{C31})$$

$$H_{asl} = \min \left(D_{16} + \max \left(\left(\frac{\tau_{D84}^*/0.03}{0.03} \right)^2, 1 \right) \times (D_{84} - D_{16}), H_{al} \right).$$

At low flow intensities, the thickness of the active surface layer is small, but at minimum equal the D_{16} of the active layer. A thin active surface layer (referring to low flow intensities) provokes a fast alteration of the grain size distribution in the case of size-selective bed load inflow or outflow. By that, the probability of erosion increases for those grain sizes that either remained (in the case of size-selective erosion) or deposited (in the case of size-selective influx) on the bed surface. In contrast, the active surface layer thickness approaches the D_{84} at very high flows.

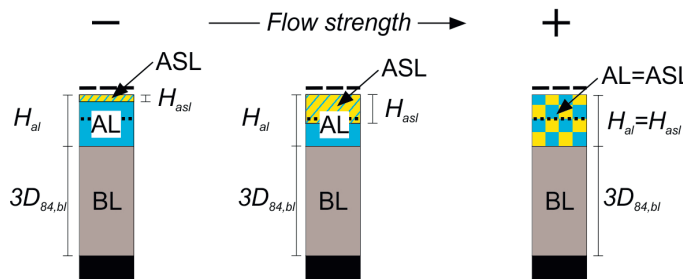


Figure C-25: Illustrative scheme of the different layers of the new mixing concept 3. The active surface layer (ASL) is the uppermost part of the active layer (AL). The inflowing and outflowing bed load is balanced in both of these layers separately. The balancing of the active layer is accomplished according to the mixing concept 2 (with a minimum (dotted line) and maximum thickness (dashed line) of H_{al}). The grain size distribution of the active layer is then used to determine the characteristic grain sizes of the bed surface (e.g. D_{50} , D_{84}). The thickness of the active surface layer (H_{asl}) depends on the flow strength. In the case of a surplus of sediment, the sediment is released into the active layer; otherwise it is taken from it. The grain size distribution of the active surface layer is then used to determine the availability (abundance) of each grain size fraction for bed load transport. The bed layer (BL) is of constant relative thickness and it balances the vertical exchange if the active layer reaches its lower or upper bound.

2.5.2.2 Application

Any influx or outflux of sediment is balanced in both, the active surface layer and the active layer separately. The grain size distribution of the active layer is used to calculate the characteristic grain sizes, but the grain size distribution of the active surface layer is used to determine the abundance of each grain size fraction.

In analogy to the mixing concepts 1 and 2, the volume of each layer is used instead of its thickness for simplicity, with

$$\begin{aligned} \text{asl/V} &= H_{asl} \times w_j \times I_j \\ \text{al/V} &= H_{al} \times w_j \times I_j \\ \text{bl/V} &= H_{bl} \times w_j \times I_j. \end{aligned} \quad (\text{C32})$$

First, the volume of the active surface layer is updated after each hydraulic time step and for each grain size fraction according:

$$\text{asl/V}_{i,t} = \text{asl/V}_{i,t-1} - \max(\text{asl/V}_{i,t-1} - \text{outV}_{i,t}, 0) + \text{inV}_{i,t-1}. \quad (\text{C33})$$

Herein, the term $\max(aslV_{i,t-1} - outV_{i,t}, 0)$ limits the erosion of a certain grain size fraction to its supply within the active surface layer. It is worth to note that this limitation only regulates the mixing of the active surface layer and does not reduce the bed load transport.

Afterwards, the volume of the active surface layer is resized to the volume that corresponds with H_{asl} (equation C32). In case that there is a surplus of sediment within the active surface layer, sediment is released by sharing the grain size distribution of the active surface layer itself. In contrast, bed material sharing the grain size distribution of the active layer is incorporated into the active surface layer in the case of a deficit of sediment. If equation C30 yields $fs > 1$ the grain size distribution of the active surface layer is set to the grain size distribution of the active layer.

The final grain size distribution of the active surface layer is then used to determine the probability that the i^{th} grain size fraction is transported at time t . Therefore, f_i in equation C12 or C16 is replaced by

$$e_{i,t} = \frac{aslV_{i,t}}{aslV_i}. \quad (\text{C34})$$

In addition, the mixing concept 2 is applied to balance sediment inflow and outflow of the active layer and the bed layer (section 2.4.4.3).

C.2.6 Results

2.6.1 Feeding experiments

2.6.1.1 Total bed load volumes

2.6.1.1.1 General remarks

Based on the numerically modeled time series of bed load transport at the lowermost numerical section, the total bed load volume of each experimental run was determined and compared with the observed bed load accumulation in the tailwater box. Therefore, the ratio of numerically modeled and observed bed load volumes is used to assess the performance of all model realizations. The latter differ regarding the bed load transport equation (section 2.4.3), the hiding function (section 2.4.3) and the mixing concept (section 2.4.4).

2.6.1.1.2 Rickenmann (2001) bed load transport equation

2.6.1.1.2.1 Mixing concept 1

The ratios of modeled and observed bed load volumes are illustrated by means of box plots in Figure C-26. The modeling results refer to the 'Rickenmann (2001) bed load transport equation' (equation C12) and the constant active layer thickness (mixing concept 1). Figure C-26a shows the scatter of these ratios for each hiding function, by considering all (twenty) experimental runs (regardless of the series; Table C-3). In each box, the central mark (blue line) is the median, the black circle is the arithmetic mean, the edges of the box are the 25th and 75th percentiles (inner quartile range) and the red crosses indicate the remaining outliers.

Most of the modeled bed load volumes deviate from the observations within the bounds of a factor of 2. In this respect, the ratio of modeled and observed bed load volumes predominately ranges between 0.5 and 2 and the boxes do not consistently reveal a systematic over- or underestimation; the same is true for the arithmetic mean, which is in the proximity of unity. In contrast, the median is distinctly lower than unity for the hiding functions b_2 and b_3 , which means that the model more often underestimated the observations.

Considering only the experimental runs with discharges lower or equal than the stabilizing discharge (6.9 l/s), the overall scatter is slightly larger (Figure C-26b) and thus, the model performance is worse for these low flow runs. In addition, the effect of different hiding functions on total bed load is more consistent since the median and the mean of the ratios differ with respect to the strength of hiding. The hiding function b_1 is associated with almost equal mobility of different grain sizes (maximum of hiding) and the results reveal an underestimation of most of the observed total bed loads. In contrast, b_3 is attributed to strong size-selective transport that, on average, yields an overestimation, while the hiding functions b_2 and b_4 are somewhere in between.

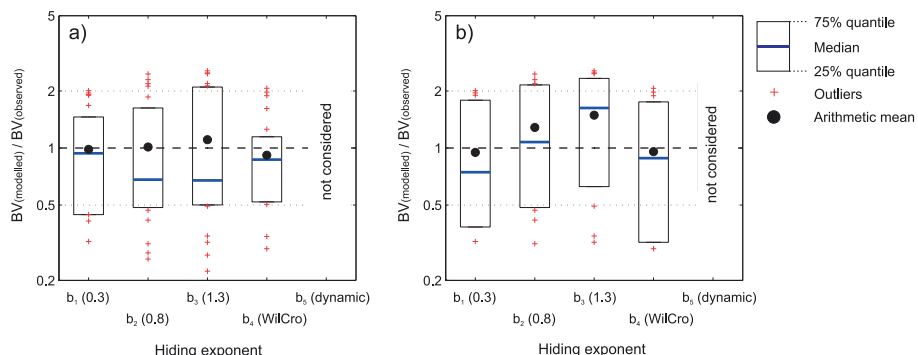


Figure C-26: Ratios of numerically modeled total bed load outflux and observed bed load volumes for the model realization ‘Rickenmann (2001) bed load transport equation and mixing concept 1’; a) boxplots include all experimental runs (differing in discharge) of all four series (differing in grain size added) and b) only those experimental runs with discharges smaller or equal to the stabilizing discharge of 6.9 l/s are considered.

2.6.1.1.2.2 Mixing concept 2

The ratio of simulated and observed total bed load volumes is on average closer to unity when the mixing concept 2 is applied. But in analogy to the mixing concept 1, the total bed load volumes are more often underestimated (median lower than unity in Figure C-27a). The inner quartile range is largest for the hiding function b_1 , while it is smallest for the hiding function of Wilcock and Crowe (2003; b_4) and the bed state dependent hiding function b_5 . It is worth to note, that the relative mobility of small grain sizes is similarly low for both of the functions b_1 and b_4 since b_4 is small for low D_i/D_{50} (equation C16). In contrast, b_4 yields a lower mobility than b_1 for the coarse grain fractions ($D_i > D_{50}$). Thus, the better performance of b_4 is attributed to the low mobility of coarse fractions.

The model performance features different trends when the experimental runs with discharges lower or equal the stabilizing discharge are considered solely (Figure C-27b). The hiding functions b_1 and b_4 reveal the largest scatter, while it is smallest for the dynamic hiding function b_5 . In contrast, the model performance is somewhat different when the mean or the median is used for evaluation rather than the inner quartile range.

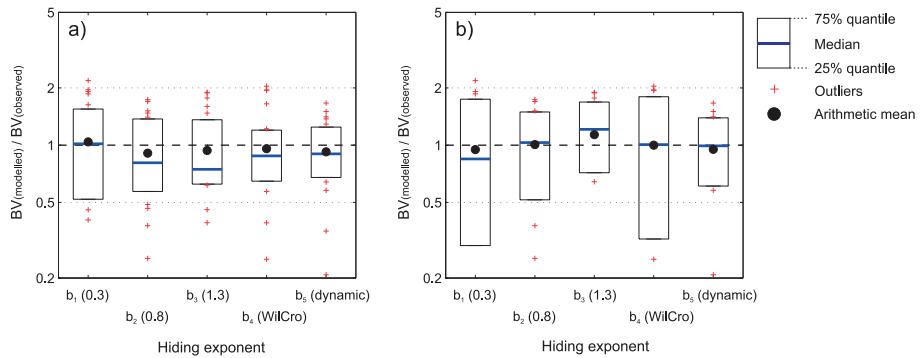


Figure C-27: Ratios of numerically modeled total bed load outflux and observed bed load volumes for the model realization ‘Rickenmann (2001) bed load transport equation and mixing concept 2’. The boxplots include either a) all experimental runs of all four series or b) only those experimental runs with discharges smaller or equal the stabilizing discharge of 6.9 l/s.

2.6.1.1.2.3 Mixing concept 3

The total bed load volumes obtained with the mixing concept 3 are close to the observations for most of the experimental runs. The inner quartile range is rather small, regardless of the hiding function used (Figure C-28).

The model performance is even better by considering only those experimental runs with discharges lower or equal the stabilizing discharge. In this respect, the modeled total bed load volumes hardly differ from the observations when the hiding functions b_2 , b_3 or b_5 are applied.

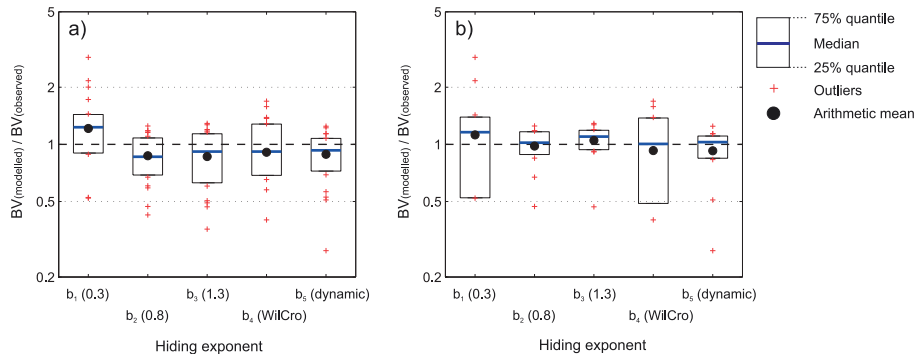


Figure C-28: Ratios of numerically modeled total bed load outflux and observed bed load volumes for the model realization ‘Rickenmann (2001) bed load transport equation and mixing concept 3’. The boxplots include either a) all experimental runs of all four series or b) only those experimental runs with discharges smaller or equal to the stabilizing discharge of 6.9 l/s.

2.6.1.1.3 Schneider et al. (2015) bed load transport equation

The numerical model realization with the ‘Schneider et al. (2015) bed load transport equation’ does not sufficiently reproduce the magnitude observed bed load volumes (Figure C-29a-c). In addition, the results do not differ with respect to the mixing concept.

Most of the data plot below unity which means that calculated bed load volumes are underestimated. If only those runs with discharges smaller or equal the stabilizing discharge are considered, the magnitude of underestimation is even more pronounced.

In contrast to the observations, the supplied bed load supply accumulates on the bed at low flows, which causes severe bed level aggradation. In a consequence, the active layer grain size distribution is dominated by the supplied grain sizes at the end of the first run. Thus, the boundary conditions of the subsequent experimental tests deviate by far from those of the numerical model. Because of that, the numerical model realization with the ‘Schneider et al. (2015) bed load transport equation’ is not considered and no further results are presented.

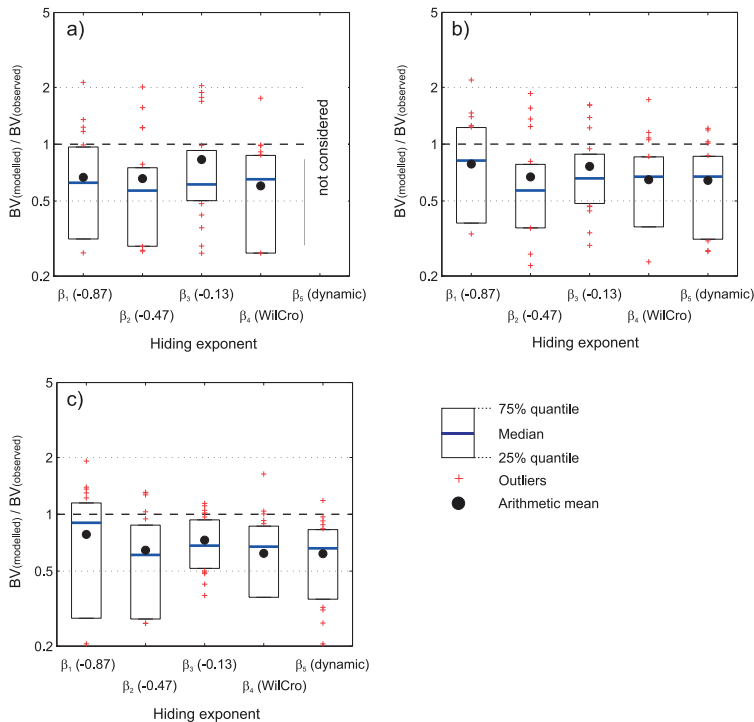


Figure C-29: Ratios of numerically modeled total bed load outflux and observed bed load volumes for the model realization ‘Schneider et al. (2015) bed load transport equation’ with the mixing concept a) 1, b) 2 and c) 3.

2.6.1.2 Time series of bed load transport at low discharges

2.6.1.2.1 General remarks

The temporal evolution of bed load transport in case of sediment feeding at low discharges could be consistently separated into three subsequent phases (Figure C-20): a lag phase, an equilibrium phase and a post-feeding phase (section 2.3.2.3; for a more detailed description see *Study E* in section C.1).

In order to evaluate the performance of the numerical model, the time series of accumulated bed load outflow at the lowermost numerical section is compared against measured bed load accumulation within the tailwater box. Therefore, only the results obtained with the ‘Rickenmann (2001) bed load transport equation’ are considered.

2.6.1.2.2 Mixing concept 1

The time series of bed load accumulation is given in Figure C-30, which comprises the experimental and numerical results of all four experimental series. It is worth to note that the x-axis refers to the cumulative time in minutes but with nonlinear scaling. Since the experimental runs with low flows lasted much longer than those with high flows (Table C-3), a linear scaling is inappropriate to assess the temporal evolution of the

bed load accumulation. Therefore, the scaling of the x-axis differs for each run, with the feeding duration (Table C-3) being equal in length.

With respect to the experimental results, the bed load accumulation increased step-wise for all runs with discharges smaller or equal the stabilizing discharge (6.9 l/s); for a detailed summary of experimental results the reader is referred to *Study E* (section C.1). In contrast, the results of the numerical model do not reproduce these temporal features. The bed load accumulation evolves much more continuous.

The bed load accumulation obtained with the five hiding functions differ considerably during run 1 of each series. The onset of bed load transport (a surrogate of bed load accumulation) is much later for b_1 and b_4 . Both of these hiding exponents refer to almost equal mobility, either for the entire grain size distribution (b_1) or its fine tail (b_4 ; equation C15). Thus, the finer grain fractions are less mobile compared to the hiding functions b_2 and b_3 .

In contrast, the bed load accumulation obtained with hiding function b_1 is largest at high flows (discharges larger than 6.9 l/s). This is attributed to the higher mobility of coarse grains due to the low hiding exponent ($b_1=0.3$), favoring equal mobility.

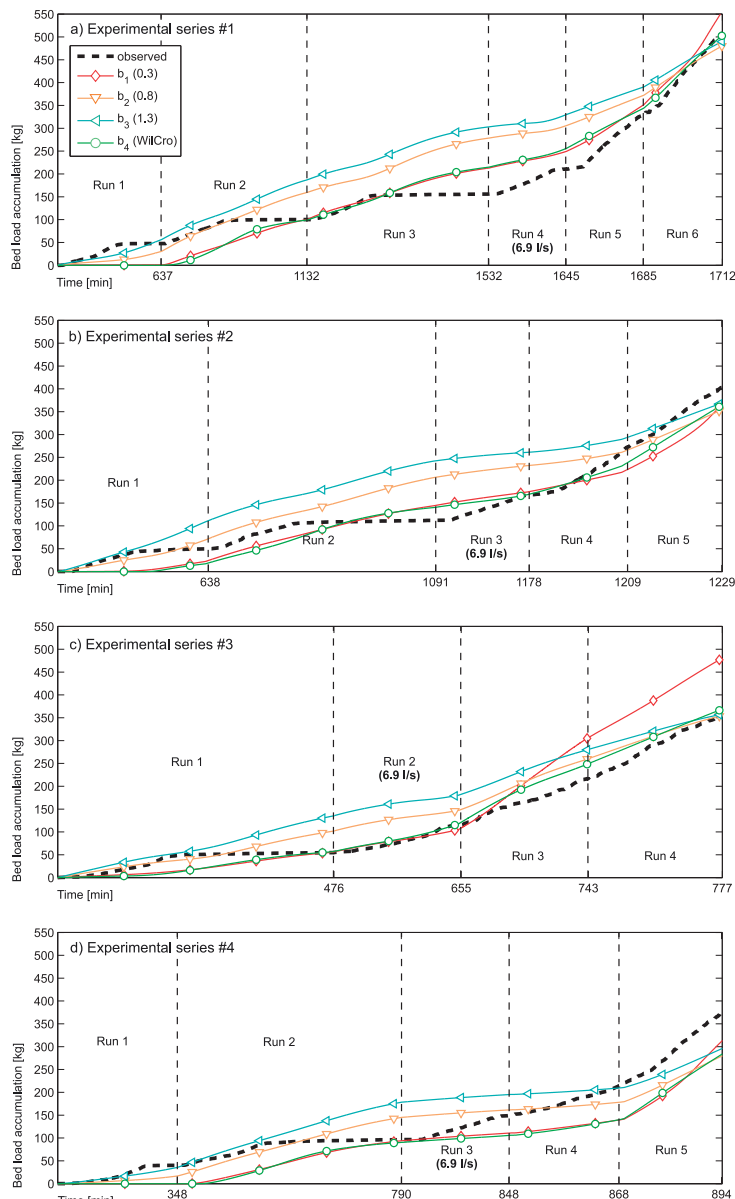


Figure C-30: Time series of bed load accumulation obtained at the lower end of the model. The numerical results (b_1 to b_4) are obtained with the Rickenmann (2001) bed load transport equation and the mixing concept 1. They refer to a) the experimental series #1 with supplied grain sizes 0.5 – 2.0 mm, b) the experimental series #2 (2.0 – 3.2 mm), c) the experimental series #3 (3.2 – 5.6 mm), and d) the experimental series #4 (0.5 – 5.6 mm). The time scale is nonlinear and orients on the feeding duration of each experimental run.

2.6.1.2.3 Mixing concept 2

The application of the mixing concept 2 yields a far better match towards the observations (Figure C-31); especially if the experimental runs with low flows are considered.

The onset of the bed load accumulation is still much too late for the model realizations with the hiding functions b_1 and b_4 and features rather small differences compared to the mixing concept 1. But, the step-wise increase of bed load accumulation at low flows (discharges smaller or equal 6.9 l/s) is much better reproduced, regardless of the hiding function (Figure C-31).

At high flows, the differences of all hiding functions except b_1 are less pronounced than with the mixing concept 1. The rate of increase matches with the observation of most runs, but for few runs (run 3 of series #2 and runs 3-4 of series #4) it is far too low. This is rather surprising since the increase of bed load transport rate due to sediment feeding is sufficiently reproduced for the runs featuring low flows but not for the subsequent high flow runs. A possible reason is that the feeding rate during the high flow runs was very high and the duration of the lag phase rather low. Thus, the modeled downstream propagation (of supplied bed load) might be too slow. This becomes evident by comparing the time series of the active layer's D_{50} ($D_{50,al}$) of the uppermost section (feeding location) and the lowermost section (flume outlet). The $D_{50,al}$ is a sensitive parameter for the bed load transport rate at a given discharge. The $D_{50,al}$ is expected to decrease due to the feeding of fine bed load. The fining starts at the feeding location, causing an increase of bed load transport rate. The bed load of this uppermost (first) section is then transferred to the (second) section below. Depending on the bed load's grain size distribution, the active layer of this second section fines as well. Due to that, the effect of feeding fine sediment propagates downstream and the propagation velocity depends on both, the hiding function that affects the bed load's grain size distribution and the mixing approach. For those high flow runs which are not sufficiently reproduced by the numerical model (run 3 of series #2 and runs 3-4 of series #4), the $D_{50,al}$ at the outlet started to decrease at the very end of the runs and thus, the propagation velocity is too low compared with the observations.

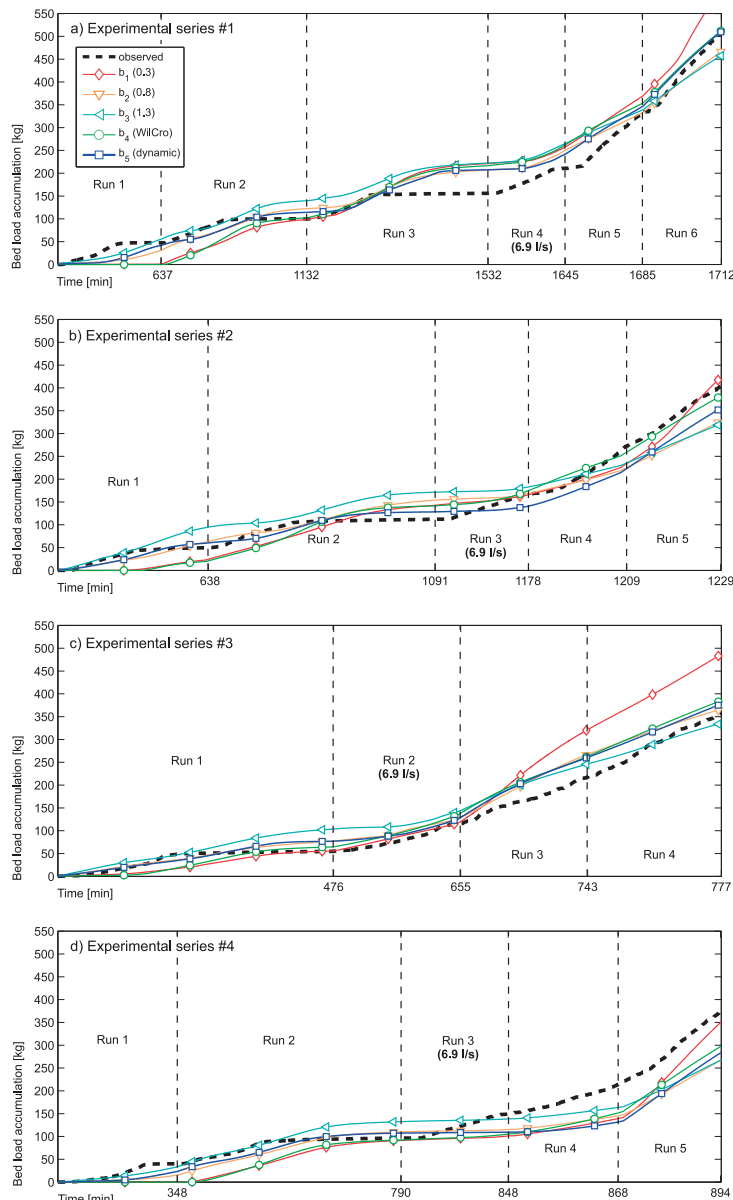


Figure C-31: Time series of bed load accumulation obtained at the lower end of the model. The numerical results (b_1 to b_4) are obtained with the Rickenmann (2001) bed load transport equation and the mixing concept 2. They refer to a) the experimental series #1 with supplied grain sizes 0.5 – 2.0 mm, b) the experimental series #2 (2.0 – 3.2 mm), c) the experimental series #3 (3.2 – 5.6 mm), and d) the experimental series #4 (0.5 – 5.6 mm). The time scale is nonlinear and orients on the feeding duration of each experimental run.

The bed load accumulation of the experimental runs 2 and 3 of the series #1 (Figure C-31a) is given in more detail in Figure C-32. The observed time series of bed load accumulation features distinct break points. In contrast, the simulation results reveal a much more continuous course, but out of all hiding functions, b_5 yields the most sudden increase or decrease of bed load accumulation. But the occurrence of these breakpoints are way too late and thus, the modeled time series are shifted to the right (Figure C-32). Anyway, accounting for a bed state dependence of the hiding exponent (like b_5) seems to improve the temporal progression of modeled bed load accumulation. In the case of channel aggradation (large H_a/D_{84}), b_5 features size-selective mobility, with the small grain sizes being much more mobile than the D_{50} . In a consequence, the bed load transport rate, a surrogate of bed load accumulation, increases faster. Conversely, b_5 features equal mobility of small grain sizes in case of channel erosion (small H_a/D_{84}), resulting in a decrease of transport rate, at least at low discharges.

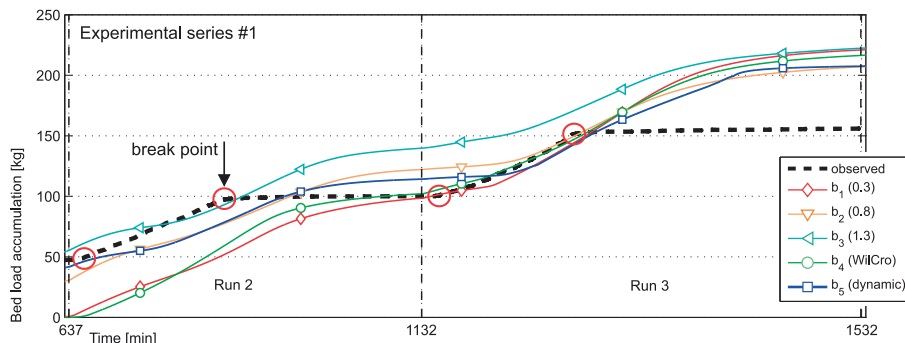


Figure C-32: Detailed view of the time series of bed load accumulation during the experimental runs 2, and 3 of series #1. The distinct breakpoints of observed bed load accumulation are highlighted by the red circles.

2.6.1.2.4 Mixing concept 3

At low flows, the temporal evolution of bed load accumulation obtained by the numerical simulations with the mixing concept 3 matches very well with the observations (Figure C-33); at least when the hiding functions b_2 , b_3 , and b_5 are considered. The onset of bed load accumulation is still much too late for the hiding functions featuring equal mobility (b_1 and b_4), but the shape of increase seems similar compared to the observations. Thus, the time series of bed load accumulation obtained with b_1 and b_4 plot lower but almost parallel.

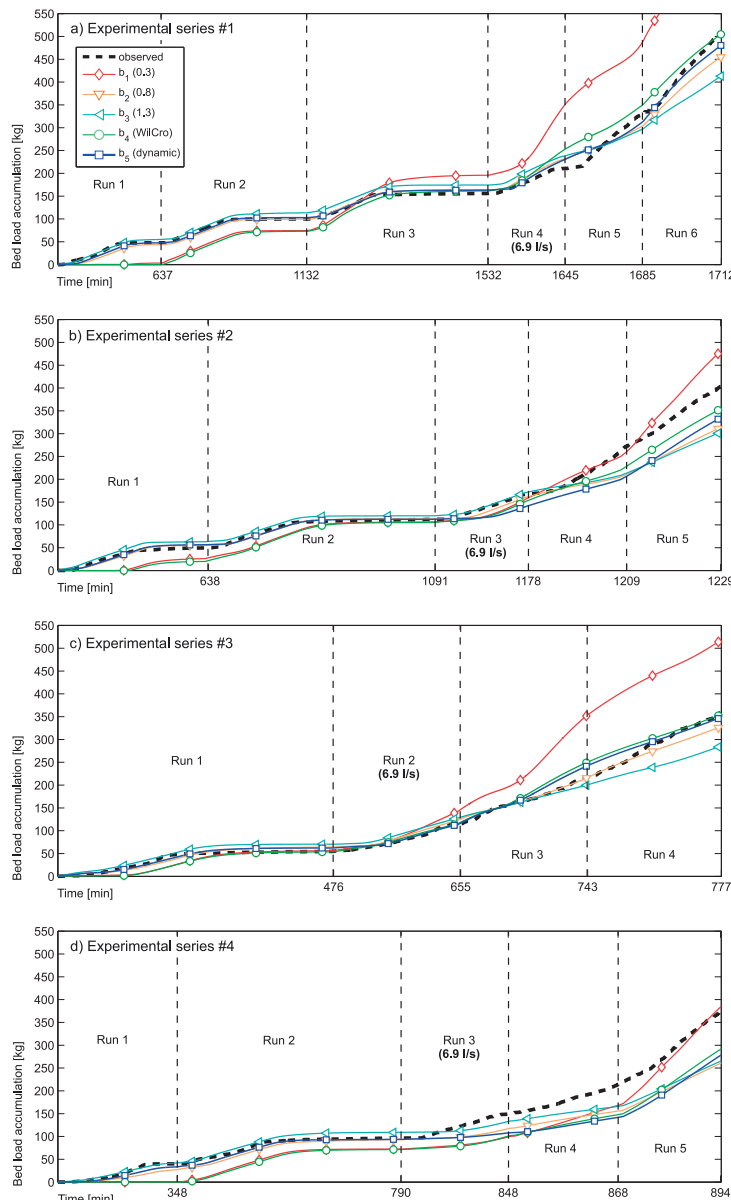


Figure C-33: Time series of bed load accumulation obtained at the lower end of the model. The numerical results (b_1 to b_4) are obtained with the Rickenmann (2001) bed load transport equation and the mixing concept 3. They refer to a) the experimental series #1 with supplied grain sizes 0.5 – 2.0 mm, b) the experimental series #2 (2.0 – 3.2 mm), c) the experimental series #3 (3.2 – 5.6 mm), and d) the experimental series #4 (0.5 – 5.6 mm). The time scale is nonlinear and orients on the feeding duration of each experimental run.

The response of sediment feeding on bed load transport is sufficiently reproduced with the mixing concept 3. The active surface layer is rather thin at low flows. Thus, even small amounts of supplied sediment cause a shift of the active surface layer's grain size distribution, making them more available for bed load transport. This is in good agreement with the observations made in course of the experiments: initially, the supplied bed load deposited on the bed surface by filling the gaps between coarse grains, while subsequently added grains passed over it. It is worth to explicitly mention, that the characteristic grain sizes used to determine incipient motion (D_{50} ; section 2.4.3) or flow resistance (D_{84} ; section 2.4.2) are determined according to the grain size distribution of the entire active layer. Since the active layer is much thicker (at least at low flows), its grain size distribution is much more inert, causing the characteristic grain sizes to change slowly.

At flows exceeding the bed stability, the modeled bed load accumulation fits either well or it is too little for all hiding functions except b_1 . This corresponds with the results obtained by the two other mixing concepts 1 and 2.

2.6.1.3 High-frequency fluctuations of bed load transport rate

2.6.1.3.1 *Rickenmann (2001) bed load transport equation*

Next to the different phases of bed load transport, the measured bed load transport rates fluctuated even during the equilibrium phase. These high-frequency fluctuations are hardly or not at all visible by plotting the accumulated bed load transport against time.

The time series of bed load transport rates that was observed during the experimental series #2 is compared with the model results obtained with each mixing concept and hiding function in Figure C-34. These high-frequency fluctuations are not reproduced by any of the numerical approaches used.

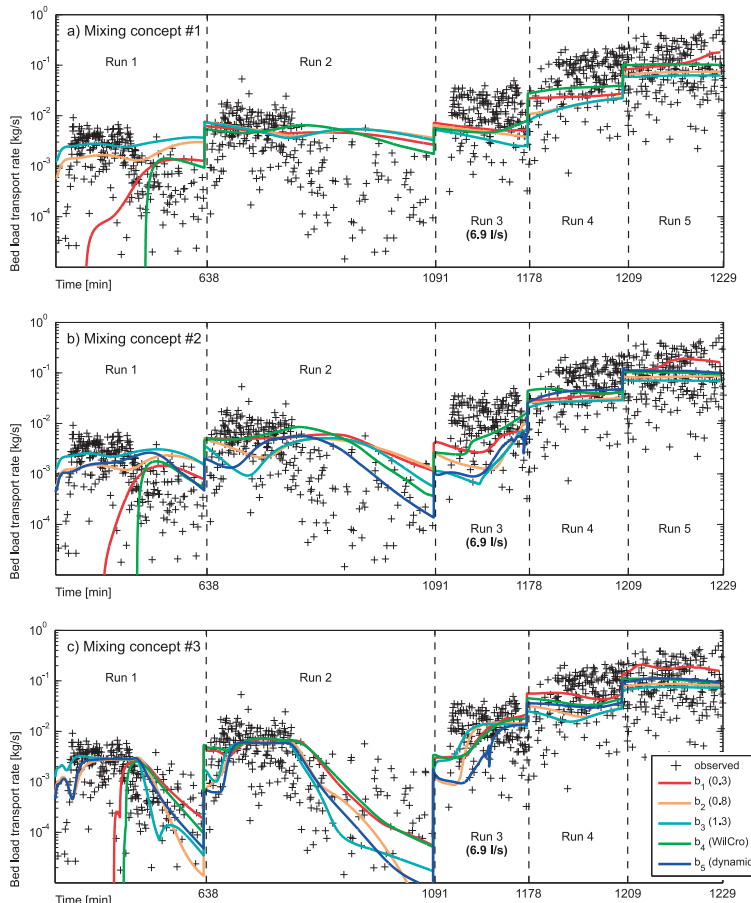


Figure C-34: Time series of bed load rate during series# 2 (2.0 – 3.2 mm) obtained with the Rickenmann (2001) bed load transport equation and a) the mixing concept 1, b) mixing concept 2, and c) mixing concept 3. The time scale is nonlinear and orients on the feeding duration of each experimental run.

2.6.1.4 Grain size distribution of accumulated bed load transport

2.6.1.4.1 General remarks

At the end of each experimental run (and sometimes even in between; Table C-3), samples of the accumulated bed load were taken and sieved. The characteristic grain sizes D_{50} and D_{84} of the measured grain size distributions are compared against those obtained by the numerical model with the ‘Rickenmann (2001) bed load transport equation’. In this respect, the grain size distributions refer to the bed load that accumulated during each feeding part of an experimental run (duration of sediment feeding plus one-third of that time with sediment starving).

2.6.1.4.2 Mixing concept 1

In Figure C-35 the ratios of the D_{50} (a) and the D_{84} (b) of the numerically modeled and observed bed load are illustrated by boxplots. Each boxplot comprises the ratios of all experimental runs, regardless of the experimental series.

The characteristic grain sizes obtained by the numerical model are on average smaller than the observed ones; for all except one boxplot, the median and the arithmetic mean plot lower than unity. In most cases, even the 75th percentile is smaller than unity, which means that grain sizes are underestimated for almost every experimental run. In addition, the results hardly differ with respect to the hiding function. Since the relative mobility of different grain sizes is regulated by the hiding function, this outcome is rather surprising.

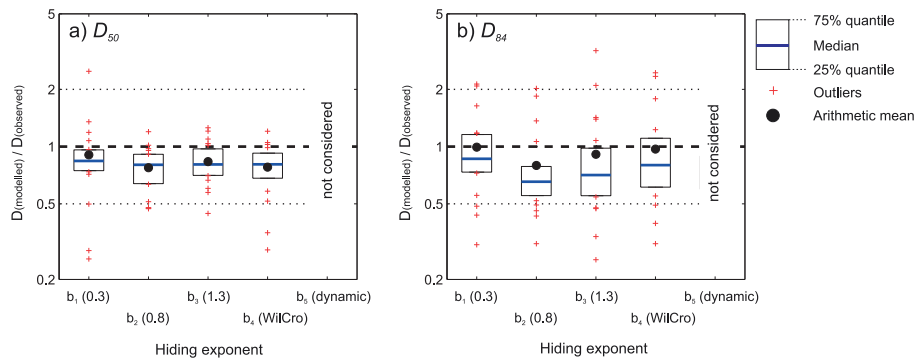


Figure C-35: Ratio of numerically modeled and observed characteristic grain sizes of accumulated bed load, with a) the D_{50} and b) D_{84} . The numerical model results refer to the mixing concept 1 in combination with the Rickenmann (2001) bed load transport equation.

2.6.1.4.3 Mixing concept 2

The ratios of numerically modeled and observed characteristic grain sizes feature similar statistics as for the mixing concept 1 (Figure C-36). The D_{50} of bed load are underestimated by the numerical model for most of the experimental runs (Figure C-36a). The inner quartile range is smallest and the median is closest to unity with the hiding functions b_3 and b_4 . These two hiding functions were initially expected to differ. According to the theory, b_3 is associated with strong size-selective mobility favoring small grain sizes, while b_4 refers to almost equal mobility for the grains smaller than the D_{50} . The effect of hiding is suggested to be compensated by the differences of the active layer's grain size distribution or their D_{50} . The hiding function b_3 in combination with a very coarse D_{50} yields similar size-selective mobility as b_4 with a rather fine D_{50} . Thus, the influence of different hiding functions is not straight forward, but the model framework reveals complex internal dynamics by adjusting the grain size distribution of both, the active layer and the bed load.

Considering the bed load's D_{84} ratios (Figure C-36b), the scatter is more pronounced with the medians close to unity. Corresponding with the bed load's D_{50} , the median of the D_{84} ratios is largest for the hiding functions b_3 and b_4 .

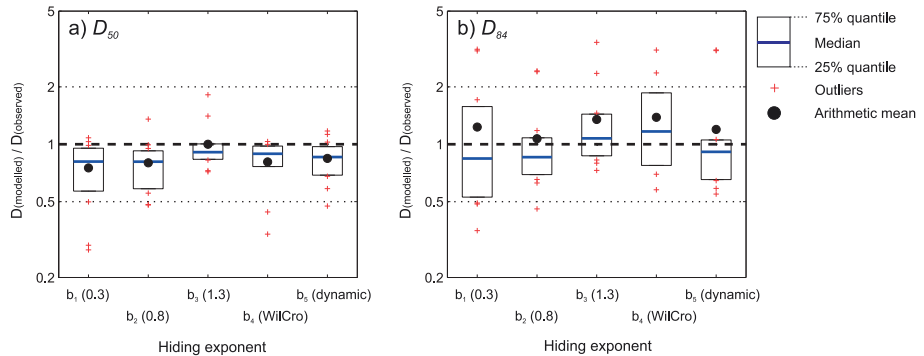


Figure C-36: Ratio of numerically modeled and observed characteristic grain sizes of accumulated bed load, with a) the D_{50} and b) D_{84} . The numerical model results refer to the mixing concept 2 in combination with the Rickenmann (2001) bed load transport equation.

2.6.1.4.4 Mixing concept 3

The bed load grain size distributions obtained by numerical simulations with the mixing concept 3 reveal characteristic grain sizes which match well with the observations (Figure C-37). The scatter of the D_{50} ratios is very small with all hiding functions, although the results reveal a small but consistent underestimation. The results are similar when the D_{84} ratios are considered: medians close but consistently lower than unity.

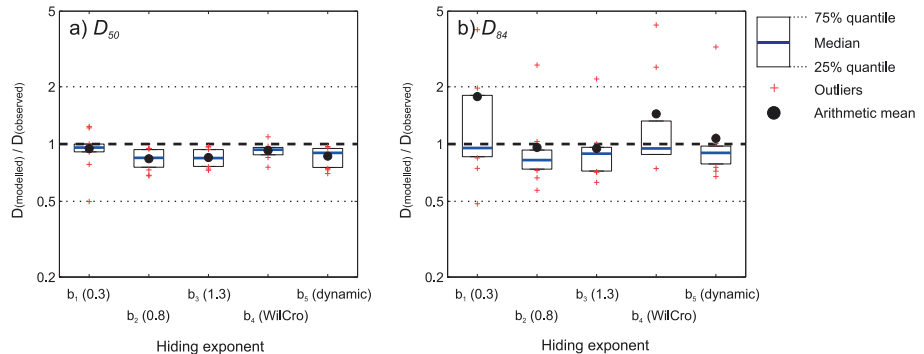


Figure C-37: Ratio of numerically modeled and observed characteristic grain sizes of accumulated bed load, with a) the D_{50} and b) D_{84} . The numerical model results refer to the mixing concept 3 in combination with the Rickenmann (2001) bed load transport equation.

In Figure C-38, some bed load grain size distributions are shown, with each subplot referring to a certain experimental run of the series #4 (Table C-3). The measured grain size distribution reveals a consistent coarsening with each run, which is reproduced well by the numerical model.

At very low flows (run 1), the modeled bed load outflow is much finer, with no grains coarser than 3.2 mm. In contrast, the measured bed load was even made up by grains

of the size 5.6 mm to 8.0 mm. The application with the hiding functions b_1 and b_4 did not yield any bed load outflow during run 1 and thus, there are no grain size distributions available.

For the subsequent runs, the modeled grain size distributions of bed load outflow are closer to the measured ones, but none of the hiding functions performing consistently better than the others. In this respect, the largest differences remain for the coarse tail of the grain size distributions, which corresponds with the slightly weaker performance in reproducing the D_{84} of bed load rather than the D_{50} (Figure C-37).

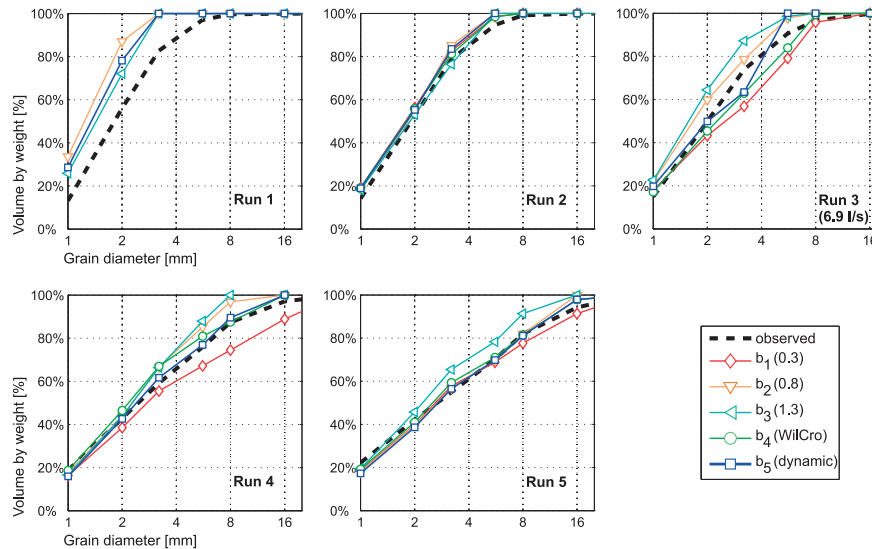


Figure C-38: Numerically modeled and observed grain size distributions of accumulated bed load that are obtained during each experimental run of the series #4 (0.5 – 5.6 mm). The numerical model results (b_1 to b_5) refer to the mixing concept 3 in combination with the Rickenmann (2001) bed load transport equation.

2.6.1.5 Grain size distribution of the bed surface

2.6.1.5.1 General remarks

At the end of the experimental runs 1 to 4 of the series #4, the grain size distribution of the bed surface was measured by means of photosieving (section 2.3.2.2). The measured distributions are compared against the grain size distributions of the active layer, representing the bed surface of the numerical model. The grain size distribution was measured in the middle of the investigation reach of the flume and the calculated grain size distributions refer to the corresponding numerical section. However, only the results obtained with the 'Rickenmann (2001) bed load transport equation' are considered.

2.6.1.5.2 Mixing concept 1

The coarse tail of the bed surface grain size distribution is accurately predicted by all hiding functions (Figure C-39). This is not surprising since hardly any coarse grains were transported and thus, remained on the bed surface.

But the bed surface grain size distributions differ regarding their fine tail. At the end of run 1, the proportion of sediment finer than 3.2 mm is overestimated: it is 25 % to 35 %, depending on the hiding function, while it was 15 % in the experiments (Figure C-39). The fining of the bed surface is most pronounced for the hiding functions b_1 and b_4 . Both of them are associated with almost equal mobility of either all grain sizes or only the finer fractions. In this respect, small grains are only a little bit more mobile than the D_{50} of the bed surface. It is likely, that the feeding rate exceeded the bed load transport capacity and the supplied sediment was incorporated in the active layer and thus, caused the active layer's grain size distribution to fine. In contrast, the magnitude of fining is smaller for the hiding functions b_2 and b_3 , both referring either to a weak (b_2) or strong (b_3) size-selective mobility. This differentiation is consistent for all experimental runs with discharge smaller or equal the stabilizing discharge (6.9 l/s), since the grain size distributions obtained by b_1 and b_4 always plot above those of b_2 and b_3 .

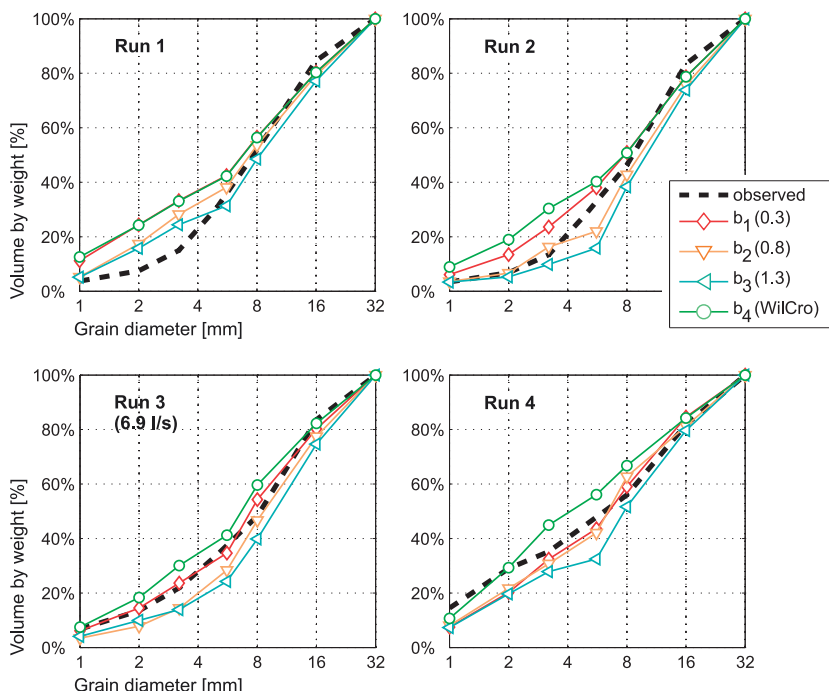


Figure C-39: Numerically modeled and observed grain size distributions of the bed surface at to the end of the experimental runs 1 to 4 of the series #4 (0.5 – 5.6 mm). The numerical model results are obtained with the mixing concept 1 and the Rickenmann (2001) bed load transport equation.

2.6.1.5.3 Mixing concept 2

The bed surface grain size distributions obtained with the mixing concept 2 reveal similar patterns as those of the mixing concept 1. The hiding functions referring to size-selective mobility (b_2 and b_3) yield an intense bed surface coarsening during run 2, with most of the fine sediment eroded from the active layer. A possible reason for this strong bed surface armoring is that the active layer thickness varies within an upper and lower bound. In a consequence, the active layer is not refilled by (fine) subsurface sediment after each time step (as it is with the mixing concept 1). The magnitude of bed surface armoring is less pronounced for b_5 , which features size-selective mobility in case of channel aggradation and almost equal mobility otherwise, while it is totally absent for b_2 , b_3 , and the observations.

During the runs 3 and 4, the bed surface grain size distributions obtained by any hiding function except b_4 approximate towards the observed distribution.

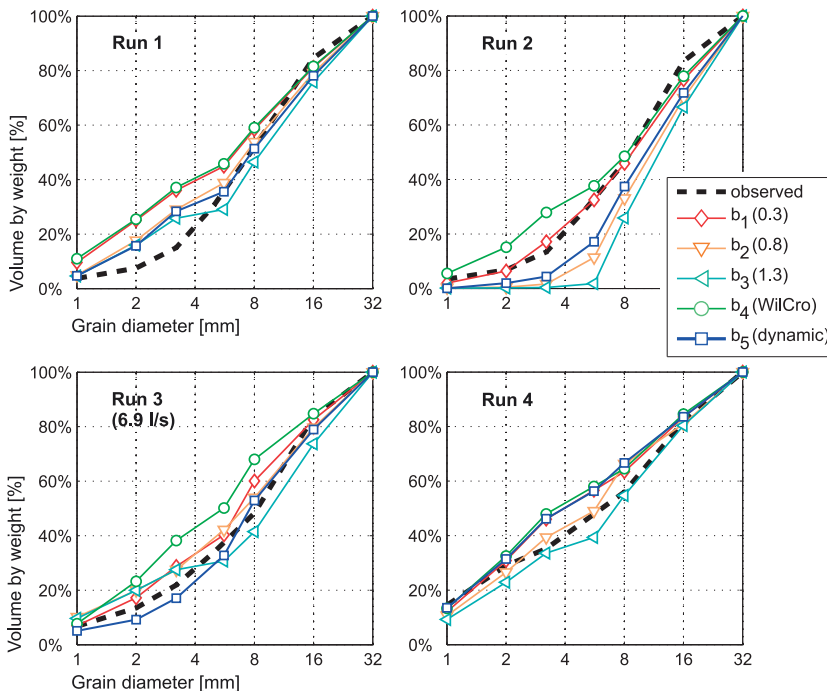


Figure C-40: Numerically modeled and observed grain size distributions of the bed surface at the end of the experimental runs 1 to 4 of the series #4 (0.5 – 5.6 mm). The numerical model results are obtained with the mixing concept 2 and the Rickenmann (2001) bed load transport equation.

2.6.1.5.4 Mixing concept 3

The numerical model application of the mixing concept 3 in combination with the hiding functions b_2 , b_3 and b_5 yield bed surface grain size distributions that are in good agreement with the observations (Figure C-41). In accordance with the observations, the bed surface grain size distribution of these model applications hardly changed in course of the experimental runs facing low flows, while there was a bed surface fining at high flows. In contrast, the fine tail of the bed surface grain size distributions is overestimated with the hiding functions b_1 and b_4 , both associated with almost equal mobility.

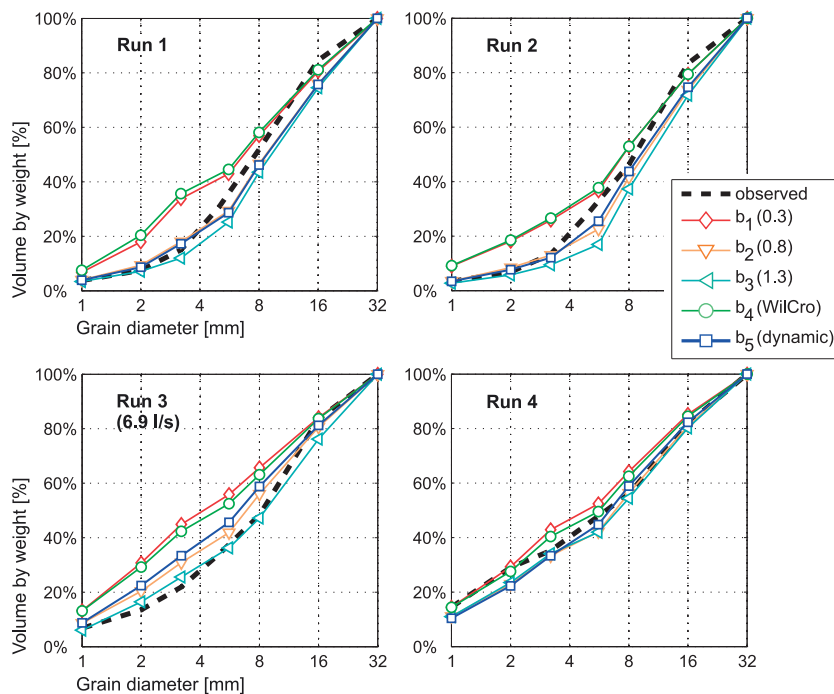


Figure C-41: Numerically modeled and observed grain size distributions of the bed surface referring to the end of the experimental runs 1 to 4 of the series #4 (0.5 – 5.6 mm). The numerical model results are obtained with the mixing concept 3 and the Rickenmann (2001) bed load transport equation.

2.6.2 Armoring experiments

2.6.2.1 Total bed load volumes

2.6.2.1.1 General remarks

In analogy to the feeding experiments, total bed load volumes of all runs of the armoring experiments are compared with the corresponding accumulated bed load transport at the lowermost section of the numerical model, with both in terms of solid bed load volume.

2.6.2.1.2 Rickenmann (2001) bed load transport equation

2.6.2.1.2.1 Mixing concept 1

The ratios of numerically modeled and observed bed load volumes are illustrated as boxplot in Figure C-42, with the majority plotting above unity. Thus, the numerical model with the mixing concept 1 on average overestimates total bed load transport of the armoring experiments.

In addition, the results reveal a larger scatter as those of the feeding experiments (section 2.6.1.1.2.1) and individual outliers differ from the observations up to a factor of 10. However, the observed total bed load volumes of the experimental runs were best reproduced with the hiding functions b_1 and b_4 , which are associated with almost equal mobility. While the inner quartile range is smallest for b_1 , the median is closest to unity for b_4 . The hiding functions referring to size-selective mobility (b_2 and b_3) performed worse than b_1 regarding both, the overall scatter and the median.

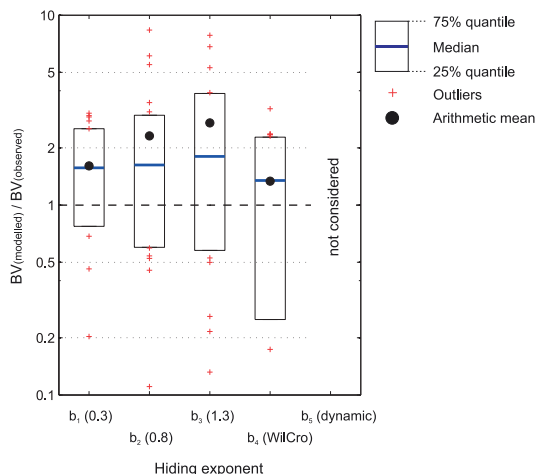


Figure C-42: Ratios of numerically modeled and observed bed load volumes with respect to the model realization ‘Rickenmann (2001) bed load transport equation and mixing concept 1’

2.6.2.1.2.2 Mixing concept 2

In contrast to the results obtained with the mixing concept 1, the medians of the ratios of numerically modeled and observed bed load volumes are close to unity, except the hiding function b_3 (Figure C-43). The numerical model as likely over- and underestimated the observations and the scatter is smallest for b_2 (moderate size-selective mobility).

The arithmetic mean plots consistently above unity, which means that the absolute magnitude of overestimation is on average larger than the absolute magnitude of underestimation.

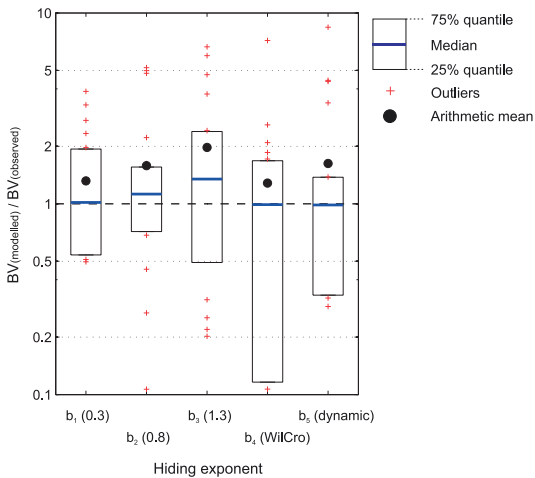


Figure C-43: Ratios of numerically modeled and observed bed load volumes with respect to the model realization ‘Rickenmann (2001) bed load transport equation and mixing concept 2’

2.6.2.1.2.3 Mixing concept 3

The inner quartile range of the ratios of numerically modeled and observed bed load volumes hardly differs with respect to the hiding function, when the mixing concept 3 is applied (Figure C-44). This contradicts with the results obtained with the mixing concepts 1 and 2.

The inner quartile range of all hiding functions is within 0.5 and 2.3 and the median is closest to unity for the hiding functions b_2 . In addition, the median consistently decreases from equal (b_1) to size-selective mobility (b_2, b_3). This means that calculated bed load volumes are larger when hiding and exposure are considered to be strong, which contradicts again with the results obtained with the mixing concepts 1 and 2.

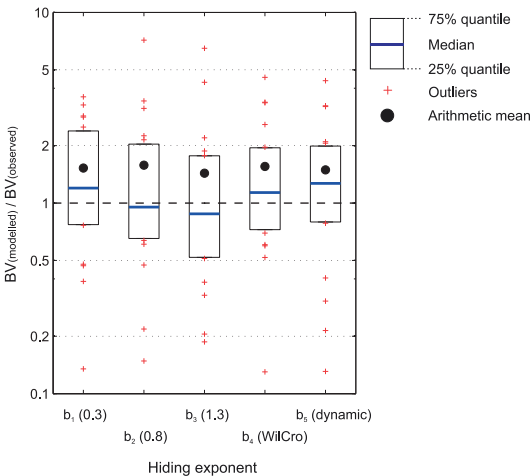


Figure C-44: Ratios of numerically modeled and observed bed load volumes with respect to the model realization ‘Rickenmann (2001) bed load transport equation and mixing concept 3’

2.6.2.1.3 Schneider et al. (2015) bed load transport equation

The bed load volume ratios obtained with the ‘Schneider et al. (2015) bed load transport equation’ are given in Figure C-45. Considering the mixing concepts 1 and 2 (Figure C-45a-b), the ratios differ dramatically with respect to the hiding function. In a consequence, the hiding function has a severe effect on the model’s outcome. This contradicts with the results obtained with the ‘Rickenmann (2001) bed load transport equation’, which is attributed to the strong nonlinearity of the reference based approach (equation C16). In contrast, the mixing concept 3 compensates the effect of the hiding function on bed load transport, since the medians are in a closer range.

Despite the overall discrepancy of numerically modeled and observed bed load volumes, the hiding functions β_2 and β_3 reproduce the observations best, regardless of the mixing concept.

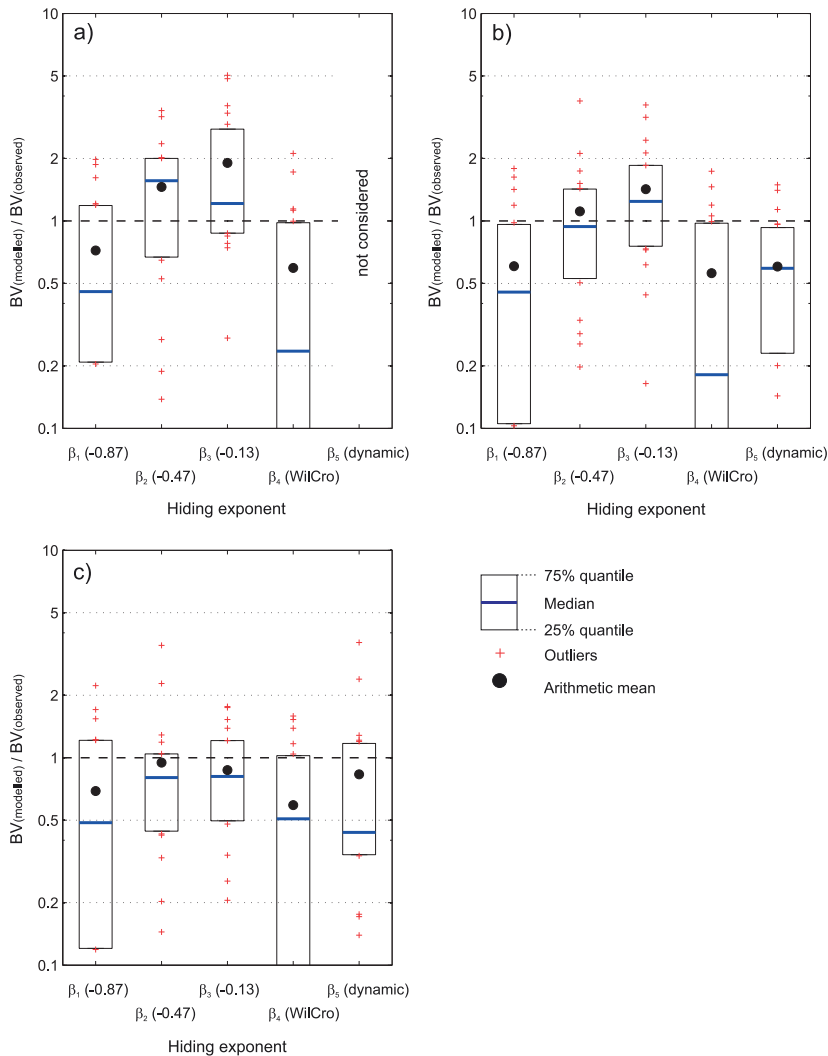


Figure C-45: Ratios of numerically modeled total bed load outflux and observed bed load volumes for the model realization ‘Schneider et al. (2015) bed load transport equation’ with the mixing concept a) 1, b) 2 and c) 3.

2.6.2.2 Time series of bed load transport at low discharges

2.6.2.2.1 General remarks

The temporal evolution of bed load transport is assessed by the time series of bed load accumulation at the lower end of the flume. In analogy with the feeding experiments,

the measured time series is compared with the numerically modeled ones. The latter refer to the accumulated bed load outflow at the lowermost numerical section.

2.6.2.2.2 Rickenmann (2001) bed load transport equation

2.6.2.2.2.1 Mixing concept 1

The time series of bed load accumulation is given in Figure C-46 and it comprises the experimental and numerical results of the two series of the armoring experiments. An experimental series consists of several experimental runs, each differing in discharge or bed load supply. In this respect, the runs indicated with 'a' (armoring) refer to the runs featuring sediment starving, while 'f' (feeding) refers to the runs where bed load was supplied at a very minute rate of 1.11×10^{-3} kg/s. Furthermore, the individual runs are separated by the dashed lines and the total bed load outflow during a single run is defined by the difference of the bed load accumulation at the beginning (left line) and end (right line) of the run.

The observed time series of bed load accumulation features similar patterns, depending on whether or not sediment was supplied.

In the case of sediment starving, the time series of most runs reveals a logarithmic function, with a strong increase at the beginning of each run and hardly any changes afterwards (e.g. a5 in Figure C-46a). But the magnitude of total bed load outflow differs considerably for individual runs (e.g. a5 in series #1 and a12 in series #2). Although the bed surface grain size distribution did not change abnormally in course of these experimental runs (Table C-5), a partial break-up of the bed surface at the very beginning might occurred and thus, an intense transport of subsurface sediment. In addition, individual keystones were eroded occasionally in course of few runs of the series #2 ($S=0.1$ m/m), causing a temporally limited increase of bed load transport at any time (e.g. a7).

In contrast, the bed load transport was more continuous when sediment was fed at flows lower than the critical discharge of the bed surface (e.g. f3 in Figure C-46a). After a temporal lag (response time), bed load transport rate approached the feeding rate and declined to the pre-feeding rate after feeding.

The numerical results obtained with the mixing concept 1 do not match with the observed time series of bed load accumulation. Bed load accumulation is far too high for the first few runs (a1-a2 in series #1 and a1-a3 in series #2) and there is hardly any decrease in course of each armoring run. This is attributed to an insufficient modeling of bed surface armoring, which is way too slow compared to the experimental results. First, the active layer is of constant thickness and any erosion in the active layer is immediately compensated by a release of subsurface sediment. Thus, the grain size distribution of the active layer only coarsens in case that eroded bed load is finer than the subsurface sediment. In addition, the active layer is rather thick, which slows the coarsening once more.

Next to that, the overestimation of bed load transport is largest with the hiding functions b_2 and b_3 . Both of these functions refer to size-selective transport, which means that fine sediment is much more mobile and can be eroded at smaller discharges or at a higher rate as for equal mobility conditions.

At higher flows (a4-a5 in series #1 and a7-a8, a11-a12 in series #2), the total bed load volumes correspond well with the measurements, except the run a5 in series #1. But

the temporal evolution of bed load transport rate is still too continuous for most of the runs. The bed surface coarsening is either too slow, indicating an insufficient mixing of bed load and bed material or the bed load transport is overestimated by the bed load transport equation. Since a variety of hiding functions (differing in the hiding exponents) are tested, the slow decline of bed load transport rate is attributed to the mixing approach.

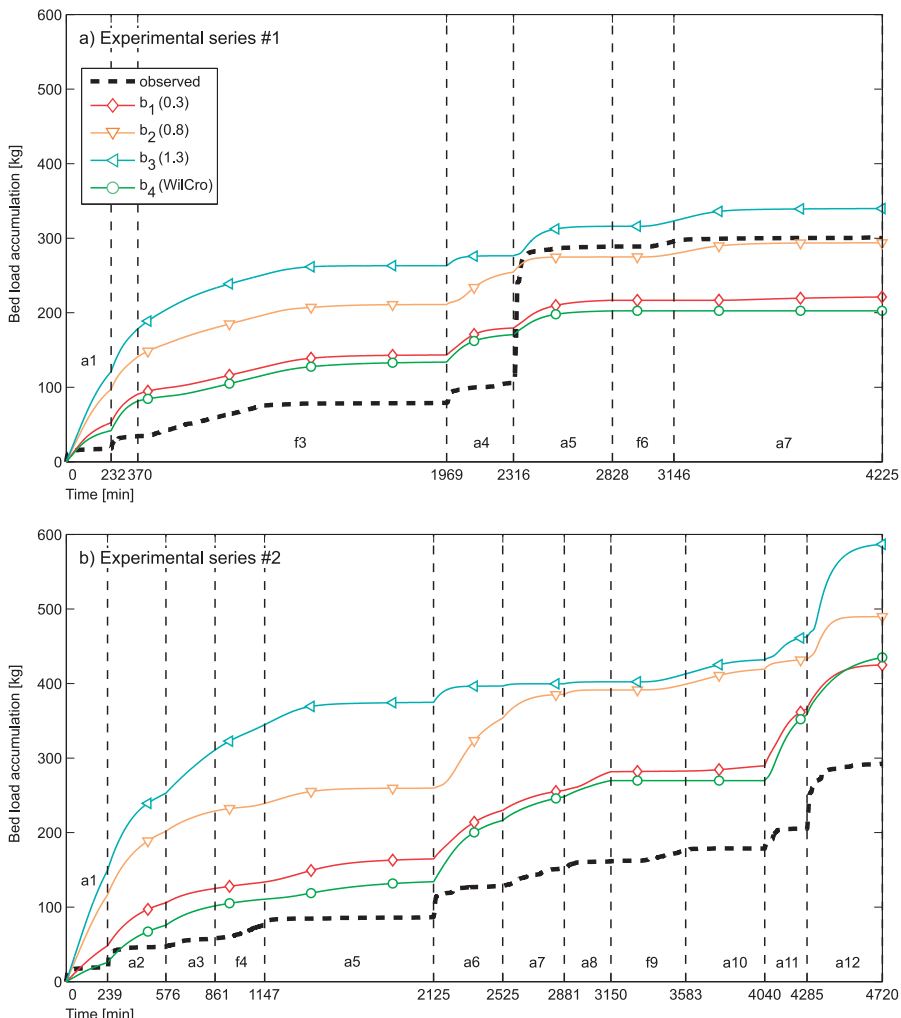


Figure C-46: Time series of bed load accumulation obtained by numerical simulation with model realization ‘Rickenmann (2001) bed load transport equation and the mixing concept 1’. The results refer to the at the lower end of the flume of a) the experimental series #1 with a flume gradient of 0.05 m/m and b) the experimental series #2 with a flume gradient of 0.1 m/m.

2.6.2.2.2.2 Mixing concept 2

By applying the mixing concept 2, the active layer thickness is variable but restricted to an upper and lower bound; whereas it is of constant thickness if the mixing concept 1 is used. Thus, the bed surface coarsening is initially faster, since the eroded (fine) sediment is not immediately replaced by subsurface sediment. However, this is only valid as long as the active layer does not approach its minimum thickness.

The temporal evolution of bed load accumulation obtained by numerical simulation with the mixing concept 2 is given in Figure C-47. Corresponding to the mixing concept 1, the curves do not follow the measurements at low flows and the bed load transport is overestimated strongest with the hiding functions b_2 and b_3 , but the magnitude of overestimation is less than with the mixing concept 1. This is attributed to the variable active layer thickness, which enables the bed surface sediment to coarsen faster. It is worth to note, that the active layer approached its minimum thickness in course of the first (series #2) or second run (series #1) for the hiding functions b_2 and b_3 , while it was later for the remaining functions.

At high flows, the time series of bed load accumulation obtained with b_1 , b_4 and b_5 are close to the measured ones, when a_5 of series #1 is neglected. But, the step-wise increase is still less pronounced than observed. Surprisingly, the numerical model reproduces the magnitude of bed load transport during the last run a_{12} of series #2 well. The observed bed load volume is significantly larger than during all other runs, which is attributed to a partial break-up of the bed surface. In terms of modeling, the specific discharge (q) exceeded $q_{c,D50}$, which caused a limited release of subsurface sediment and thus, a fining of the active layer's grain size distribution. Regarding the new hiding function b_5 , this subsurface release occurred already during a_{11} of series #2 and its effect on bed load transport is overestimated. In contrast, the severe increase of bed load accumulation during run a_5 of series #1 is not reproduced by any hiding function.

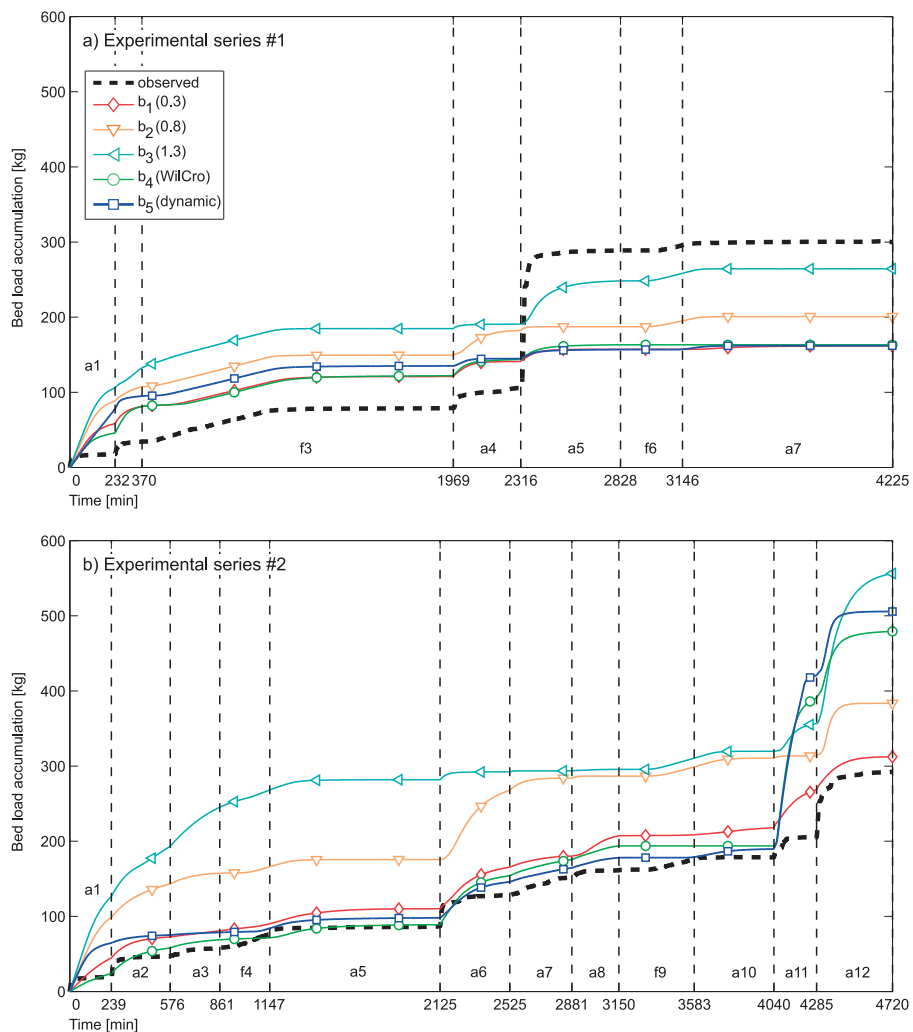


Figure C-47: Time series of bed load accumulation obtained by numerical simulation with model realization ‘Rickenmann (2001) bed load transport equation and the mixing concept 2’. The results refer to the at the lower end of the flume of a) the experimental series #1 with a flume gradient of 0.05 m/m and b) the experimental series #2 with a flume gradient of 0.1 m/m.

2.6.2.2.3 *Mixing concept 3*

The temporal evolution of bed load accumulation obtained by numerical simulation with the mixing concept 3 is given in Figure C-47. In contrast to the mixing concepts 1 and 2, the curves are close to the observations at low flows, suggesting for an accurate representation of the speed of bed surface armoring. Since the active surface layer is very thin at low flows, the mobile (fine) sediment is eroded fast and thus, not available for bed load transport anymore. This contradicts with the observations that were made during the experiments, where fine sediment was abundant at the bed surface throughout the series, but hidden in the wake of coarse grains. Anyway, the mixing concept 3 is capable in reproducing the response of sediment starving on bed load transport rate at low flows but simplifies the processes involved.

In addition, the response of bed load transport due to marginal feeding (f3, f6 in series #1 and f5, f9 in series #2) is reproduced well, regardless of the hiding function: after a certain temporal lag, bed load transport rate increases and reveals constant for the duration of feeding, followed by a sudden decrease afterwards.

Although the curve's shape is in good agreement even for several runs with high flows, the magnitude of bed load transport is occasionally overestimated. This is attributed to the dynamics of the active surface layer's thickness which depends on the flow strength. Since the flow is run-wise increasing (at least for the armoring experiments), the active surface layer's thickness increases as well by filling it with sediment from the active layer. In a consequence, fine sediment that was formerly exhausted is again available for bed load transport.

In general, these internal dynamics of the mixing concept 3 compensate the effect of the hiding functions, since the different hiding functions yield similar time series of bed load accumulation.

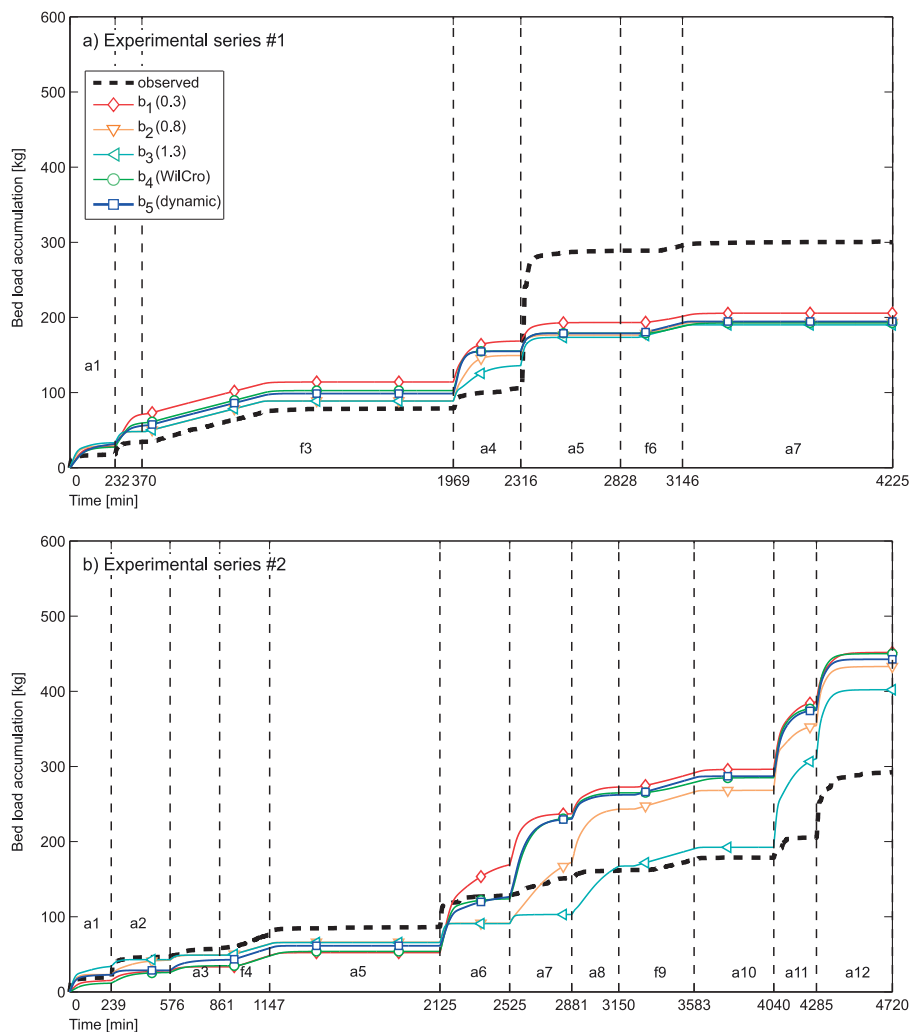


Figure C-48: Time series of bed load accumulation obtained by numerical simulation with model realization ‘Rickenmann (2001) bed load transport equation and the mixing concept 3’. The results refer to the at the lower end of the flume of a) the experimental series #1 with a flume gradient of 0.05 m/m and b) the experimental series #2 with a flume gradient of 0.1 m/m.

2.6.2.2.3 Schneider et al. (2015) bed load transport equation

In Figure C-49 the temporal progression of bed load accumulation is illustrated for all three mixing concepts and all five hiding functions, but the results are limited to series #2.

Corresponding with the 'Rickenmann (2001) bed load transport equation', the mixing concepts 1 and 2 totally lack in reproducing the temporal progression of bed load transport. The increase of bed load accumulation is too continuous and the model does not reproduce the temporal patterns observed. This is independent whether the armouring runs or the two feeding runs are considered.

In contrast, these temporal patterns are at least slightly reproduced with the mixing concept 3, although the magnitude of bed load accumulation is by a factor of two smaller than observed.

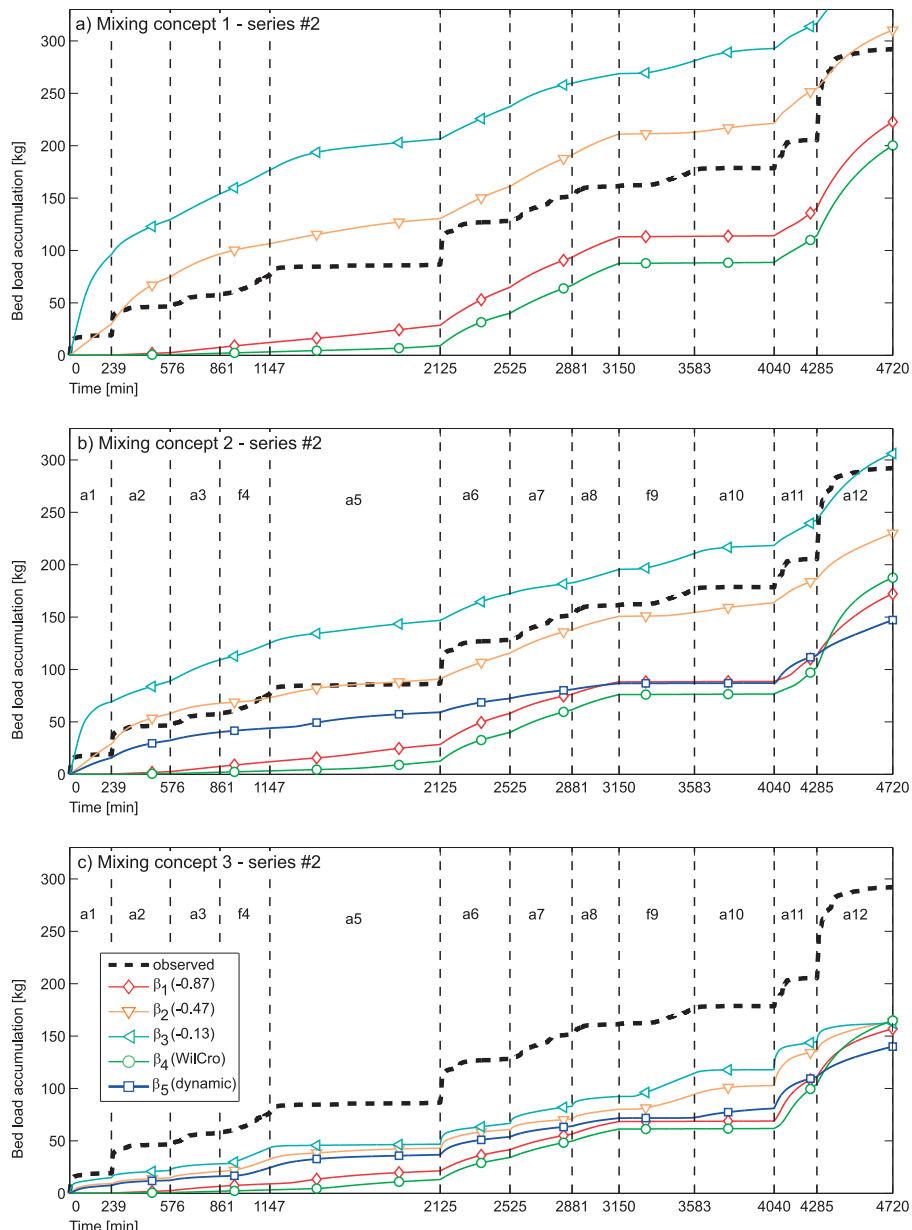


Figure C-49: Time series of bed load accumulation of the experimental series #2 that is obtained by numerical simulations with the Schneider et al. (2015) bed load transport equation and the mixing concept a) 1, b) 2 and c) 3.

2.6.2.3 Grain size distribution of the accumulated bed load

2.6.2.3.1 General remarks

At the end of each experimental run, samples of the accumulated bed load were taken and sieved. The characteristic grain sizes D_{50} and D_{84} of the measured grain size distributions are compared with those obtained by the numerical model. In this respect, the grain size distributions refer to the total bed load of each run.

2.6.2.3.2 Rickenmann (2001) bed load transport equation

2.6.2.3.2.1 Mixing concept 1

In Figure C-50 the ratios of the D_{50} (a) and the D_{84} (b) of the modeled and observed bed load are illustrated by boxplots. Each boxplot comprises the ratios of all experimental runs of the armoring experiments, regardless of the experimental series.

The bed load's characteristic grain sizes obtained with the numerical model are much too fine for the hiding functions associated with almost equal mobility (b_1 and b_4), while the ratios are closer to unity for the remaining functions b_2 and b_3 . This is very surprising since coarse sediment should be more mobile at almost equal mobility conditions and thus, the bed load's D_{84} is expected to be coarser as well. In contrast, the modeling results reveal the opposite. However, the critical discharge of the bed surface's D_{50} was rarely exceeded in course of the numerical modeling, since the bed surface D_{50} coarsened dramatically (see section 2.6.2.4.2.1). Under these circumstances, the bed load solely consists of sediment smaller than the D_{50} and the maximum grain size is coarser at size-selective conditions; simply because the critical discharge of sediment finer than the D_{50} is the smaller the larger the hiding exponent.

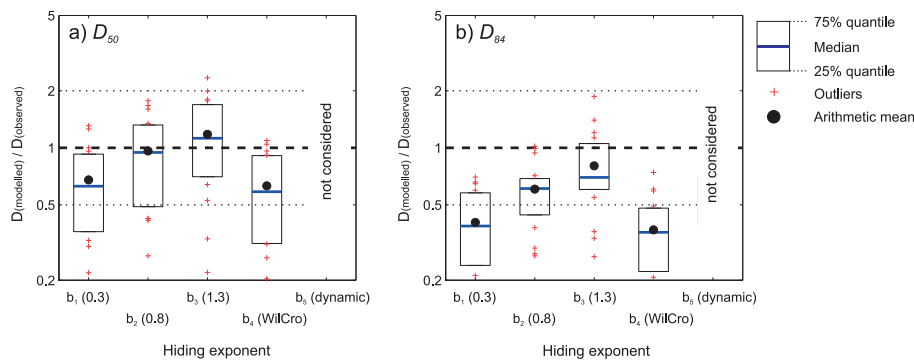


Figure C-50: Ratio of numerically modeled and observed characteristic grain sizes of accumulated bed load, with a) the D_{50} and b) D_{84} . The model results refer to the Rickenmann (2001) bed load transport equation and the mixing concept 1.

2.6.2.3.2.2 Mixing concept 2

The ratios of the bed load's characteristic grain sizes obtained with the mixing concept 2 reveal a similar scatter as with the mixing concept 1 (Figure C-51). In a consequence, the active layer thickness, either constant or variable, does not cause severe

differences in the bed load's grain size distribution in the case of long-lasting sediment starving.

Like b_1 and b_4 also the new hiding function b_5 severely underestimates the bed load's grain size. Since sediment starving dominated in course of the experiments, the active layer was close to its lower bound and thus, b_5 approached a very small value which is associated with equal mobility (like b_1 and b_4).

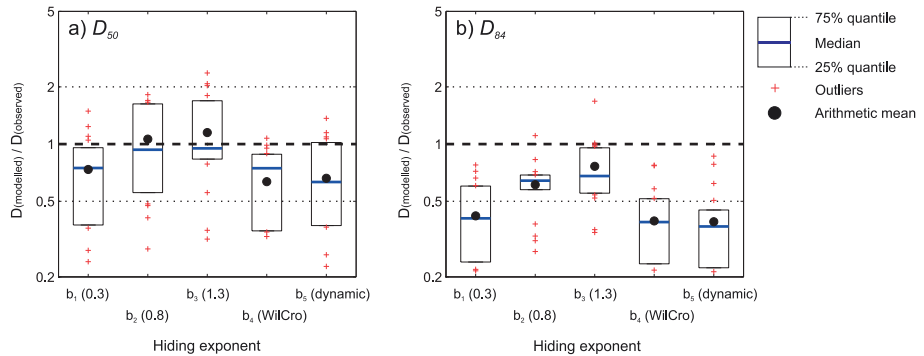


Figure C-51: Ratio of numerically modeled and observed characteristic grain sizes of accumulated bed load, with a) the D_{50} and b) D_{84} . The model results refer to the Rickenmann (2001) bed load transport equation and the mixing concept 2.

2.6.2.3.2.3 Mixing concept 3

The modeled bed load grain size distribution corresponds fairly better with the observations when the mixing concept 3 is applied (Figure C-52). The results are more or less independent of the hiding function with a median close to unity for the D_{50} and a weak underestimation for the D_{84} .

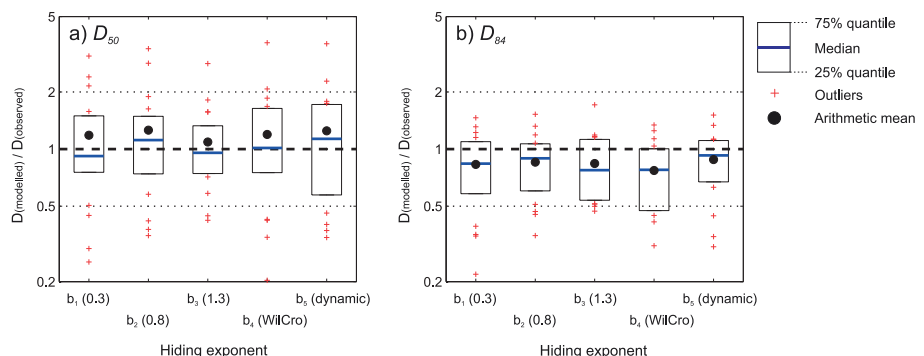


Figure C-52: Ratio of numerically modeled and observed characteristic grain sizes of accumulated bed load, with a) the D_{50} and b) D_{84} . The model results refer to the Rickenmann (2001) bed load transport equation and the mixing concept 3.

2.6.2.3.3 Schneider et al. (2015) bed load transport equation

The results obtained with the 'Schneider et al. (2015) bed load transport equation' confirm with those obtained with the 'Rickenmann (2001) bed load transport equation'. According to the D_{50} ratios the hiding functions associated with almost equal mobility underestimate the observations, while the match is best with β_3 (Figure C-53).

The mixing concept 3 does not improve the modeling results, but the discrepancy among the hiding functions is reduced (Figure C-53c).

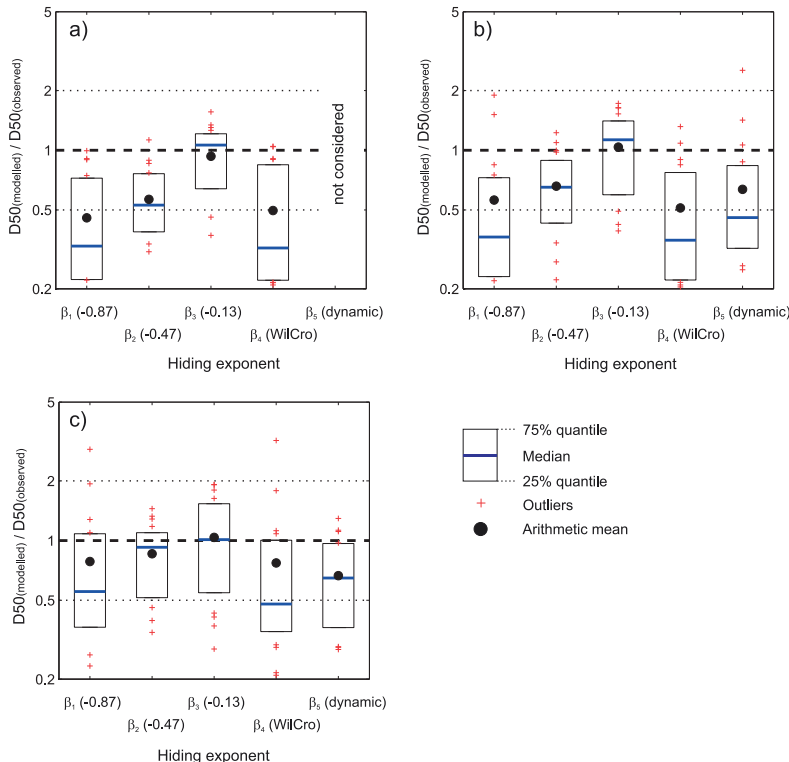


Figure C-53: D_{50} ratio of the accumulated bed load obtained by numerical simulations with the mixing concept a) 1, b) 2 and c) 3 in combination with the Schneider et al. (2015) bed load transport equation.

2.6.2.4 Grain size distribution of the bed surface

2.6.2.4.1 General remarks

At the end of each experimental run, the grain size distribution of the bed surface was measured by means of grid-by-number pebble counts (section 2.3.3.2). The frequency distributions obtained by this method corresponds to the volume-by-weight distribution (Bunte and Abt, 2001). In a consequence, the experimental measurements

can be compared with the grain size distributions of the active layer (obtained by numerical simulations) without any transformations.

2.6.2.4.2.2 Rickenmann (2001) bed load transport equation

2.6.2.4.2.1 Mixing concept 1

In Figure C-54 the ratios of the D_{50} (a) and the D_{84} (b) of the modeled and observed bed surface are illustrated by means of boxplots. Each boxplot comprises the ratios of all experimental runs of the armoring experiments, regardless of the experimental series.

The boxplots feature a very little scatter, but the ratios referring to the bed surface D_{50} are all above unity. Thus, the modeled D_{50} is coarser than the observed one, which means that the magnitude of bed surface armoring is overestimated by the numerical model. In contrast, the ratios referring to the D_{84} are closer but still above unity.

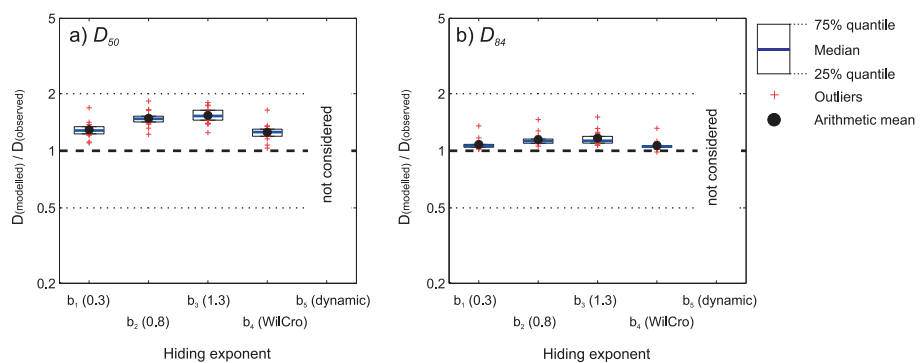


Figure C-54: Ratio of modeled and observed characteristic grain sizes of the bed surface (active layer), with a) the D_{50} and b) D_{84} . The model results refer to the Rickenmann (2001) bed load transport equation and the mixing concept 1.

In Figure C-55 the grain size distributions are illustrated that refer to the end of the experimental runs with the highest discharge. It is evident that the numerical model predicted a grain size distribution that is too coarse, with the fine tail totally winnowed. In addition, the bed surface grain size distribution is very steep at its coarse tail, especially for the run a5 of series #1 (Figure C-55a). This explains why the modeled and observed D_{84} are in a closer range than the D_{50} .

The hiding functions associated with almost equal mobility reproduce the observations best. In contrast, the fine sediment of the active layer is totally eroded within the first few runs if the hiding functions that are associated with size-selective transport are used.

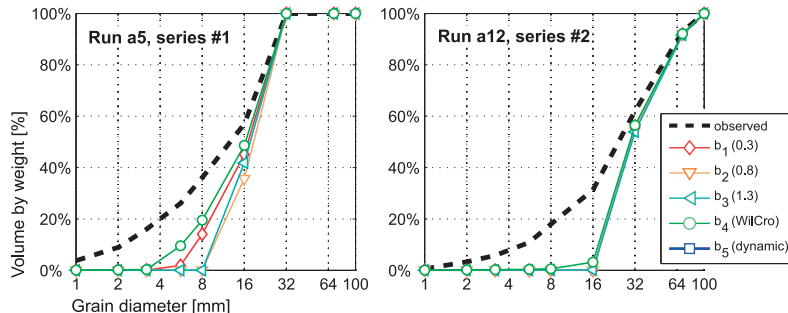


Figure C-55: Bed surface grain size distributions (active layer) at the end of the runs with the largest discharge applied in a) series #1 and b) series #2. The model results are based on the Rickenmann (2001) bed load transport equation and the mixing concept 1.

2.6.2.4.2.2 Mixing concept 2

The bed surface grain size distributions obtained with the mixing concept 2 (Figure C-56) are very similar compared to the mixing concept 1 (Figure C-54). This similarity is not surprising, since the mixing concepts 1 and 2 do not affect the bed load mobility, but differ in the speed of bed surface armoring. The fine sediment within the active layer was eroded until either the D_{50} coarsened to an extent that the critical discharge of the i th grain size fraction (equation C13 and C14) exceeded the current discharge or the fine sediment was totally winnowed, with its abundance in the active layer approaching zero.

The bed surface grain size distribution at the end of the runs with the largest flow is given in Figure C-57. The new hiding function b_5 reveals a grain size distribution that is close to b_1 and b_4 . This is in good agreement with the model theory, which suggests equal mobility in case of sediment starving.

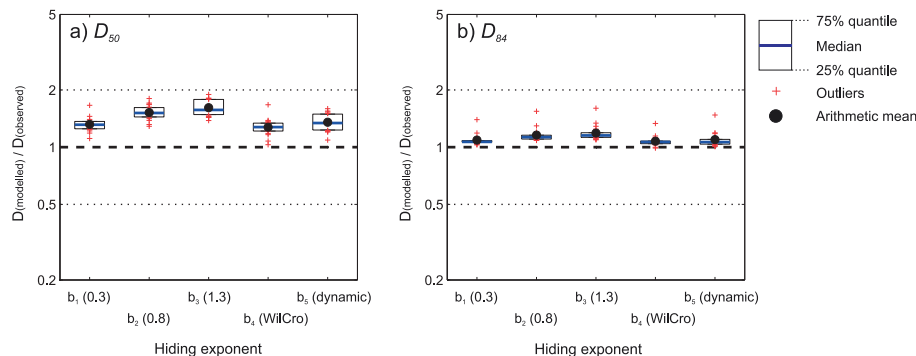


Figure C-56: Ratio of modeled and observed characteristic grain sizes of bed surface (active layer), with a) the D_{50} and b) D_{84} . The numerical model results refer to the Rickenmann (2001) bed load transport equation and the mixing concept 2.

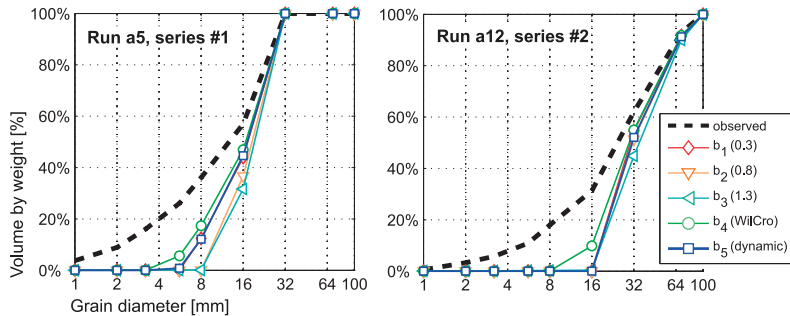


Figure C-57: Bed surface grain size distributions (active layer) at the end of the runs with the largest discharge applied in a) series #1 and b) series #2. The model results are based on the Rickenmann (2001) bed load transport equation and the mixing concept 2.

2.6.2.4.2.3 Mixing concept 3

In contrast to the mixing concepts 1 and 2, the bed surface D_{50} and the D_{84} are much better reproduced by applying the mixing concept 3. Independent of the hiding function, the ratios are close to unity (Figure C-58). But, the abundance of fine sediment is overestimated. The fine tail of the modeled bed surface grain size distributions is located above the observations (e.g. Figure C-59).

The overestimation of fines is attributed to the refilling of the active layer in case the discharge exceeds the critical discharge of the bed surface D_{50} . In this respect, the question arises whether the grain size distribution of the bed surface is equivalent to the grain size distribution of the active layer. While the pebble counts solely consider the bed surface sediment, the active layer reveals a thickness in the range of 0.7 or 1.6 times the D_{84} when a pore content of 30 % is assumed. Visual observations suggest a vertical sorting even within the topmost centimetres (Figure C-60). However, it is not the scope of the study to discuss this issue, but it is possible that fine sediment is slightly underrepresented by the measured bed surface grain size distributions.

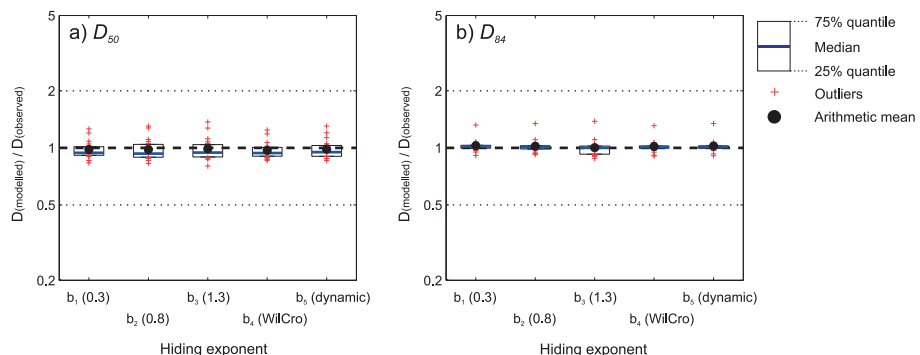


Figure C-58: Ratio of modeled and observed characteristic grain sizes of bed surface (active layer), with a) the D_{50} and b) D_{84} . The numerical model results refer to the Rickenmann (2001) bed load transport equation and the mixing concept 3.

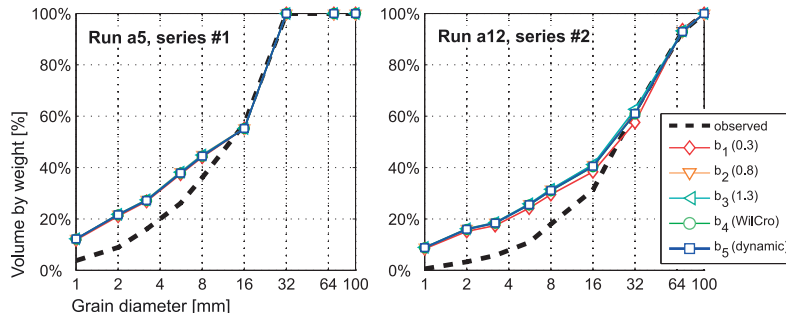


Figure C-59: Bed surface grain size distributions (active layer) at the end of the runs with the largest discharge applied in a) series #1 and b) series #2. The model results are based on the Rickenmann (2001) bed load transport equation and the mixing concept 3.

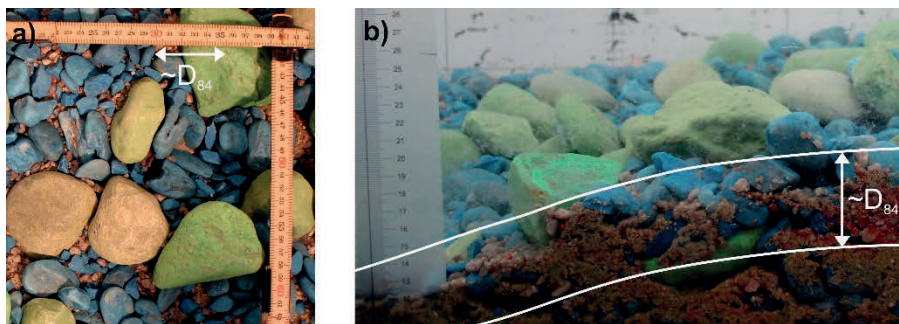


Figure C-60: Bed surface at the end of run a12 of series #2: a) top down view and b) side view. The white line indicates the active layer thickness according to the numerical model

2.6.2.4.3 Schneider et al. (2015) bed load transport equation

In analogy with the bed load's grain size distribution, the results obtained with the 'Schneider et al. (2015) bed load transport equation' confirm those obtained with the 'Rickenmann (2001) bed load transport equation'. Considering the mixing concepts 1 and 2, the hiding functions associated with almost equal mobility (β_1 , β_4 , and β_5) perform best, while those referring to size-selective mobility yield a bed surface D_{50} which is too coarse (Figure C-61).

This result is rather attributed to the internal dynamics of the numerical model and the strong feedback between fractional bed load and bed surface, than to the model performance. In this respect, the bed load volumes, as well as the bed load's D_{50} , are underestimated by applying the hiding functions β_1 , β_4 , and β_5 , while they match better with β_2 and β_3 (Figure C-53).

The differences among the hiding functions are less pronounced with the mixing concept 3 (Figure C-61c), which also corresponds with the results obtained with the 'Rickenmann (2001) bed load transport equation'.

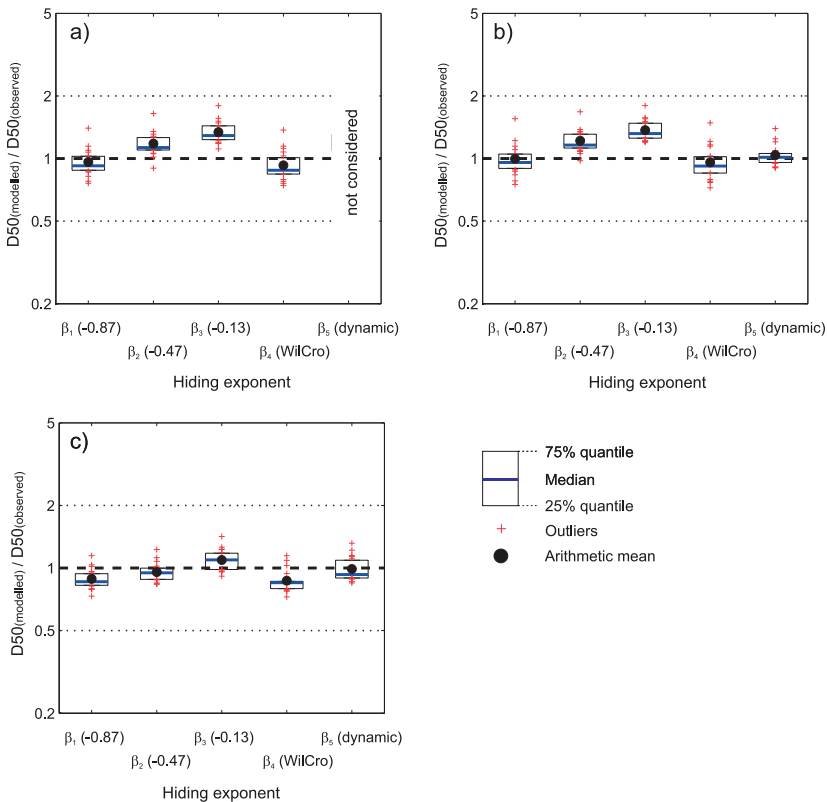


Figure C-61: D_{50} ratio of the bed surface obtained by numerical simulations with the mixing concept a) 1, b) 2 and c) 3 in combination with the Schneider et al. (2015) bed load transport equation

2.6.3 Summary of model results

2.6.3.1 Method of model evaluation

According to the results presented in sections 2.6.1 and 2.6.2, several model applications reveal both, pros and cons in reproducing any of the observed parameters. In order to overcome the complexity of the model results, the overall performance of each model application is evaluated by means of a ranking that enables for a conclusion which model application is best or worst.

The ranking is based on the results presented in the sections above and includes the parameters (i) total bed load volumes of individual runs, the characteristic grain sizes D_{16} , D_{50} and D_{84} of (ii) the bed load and (iii) the bed surface (only for the armoring experiments) as well as (iv) the temporal progression of bed load transport.

The parameters (i) to (iii) are evaluated by means of the statistics of the ratios of numerically modeled and observed results. The statistical descriptors used are the 25th, 50th and 75th percentile of the cumulative density distribution of each ratio. Depending

on the magnitude of these descriptors, the model's performance in reproducing this parameter is classified into one out of five classes. In this respect, class 1 refers to a very good agreement with the observation, while class 5 is associated with a very poor performance. The thresholds for each class are given in Table C-6 and the classification orients on the limiting descriptor: starting with class 1, the criterions of all three descriptors (median, 25 % and 75 % percentiles) are checked and any model application is assigned to the best class of which all descriptors are within the given thresholds (Table C-6).

Table C-6: Matrix of the thresholds for ranking each statistical descriptor of any parameter ratio (X), with the median P50 and the 25th (P25) and 75th percentile (P75).

| Class 1 | Class 2 | Class 3 | Class 4 | Class 5 |
|----------------------|----------------------|--------------------|--------------------|--------------------|
| $0.8 < P50(X) < 1.2$ | $0.7 < P50(X) < 1.5$ | $0.5 < P50(X) < 2$ | $0.3 < P50(X) < 3$ | $0.2 < P50(X) < 5$ |
| $0.7 < P25(X)$ | $0.5 < P25(X)$ | $0.3 < P25(X)$ | $0.2 < P25(X)$ | $0.1 < P25(X)$ |
| $P75(X) < 1.5$ | $P75(X) < 2$ | $P75(X) < 3$ | $P75(X) < 5$ | $P75(X) < 10$ |

In contrast, the performance of each model application in reproducing (iv) the temporal evolution of observed bed load accumulation is judged by eye. This is done due to the lack of a suitable methodological framework for assessing its match numerically.

2.6.3.2 Results of model evaluation

2.6.3.2.1 Rickenmann (2001) bed load transport equation

In Figure C-62 and Figure C-63 the classification of all parameters considered is illustrated, with the green color associated with a very good agreement between numerically modeled and observed results. According to these figures, the mixing concept 3 reproduces the observations of both experimental data sets best.

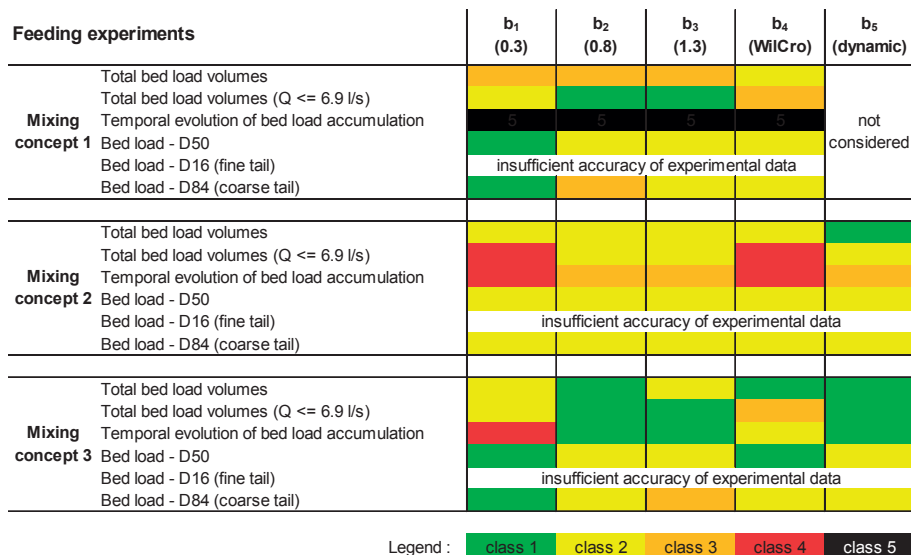


Figure C-62: Classification of the numerical model performance in reproducing the feeding experiments. The 14 numerical model applications differ regarding the hiding exponent b and/or the mixing concept; the definitions of the classes are given in Table C-6.

In order to summarize these classifications to a single goodness-of-fit measure, each class is assigned with a metric value, which is simply 1 for class 1, up to 5 for class 5. For each model application (differing in the mixing concept and/or the hiding function) and each experimental data set (feeding or armoring experiments), the scores are summed up and standardized by the counts of parameters considered. In this respect, the model application with the lowest score is associated with the best performance and vice versa.

The score matrices of both experimental data sets are then combined and ranked ascendingly. According to this evaluation procedure, the model application with the new formulated mixing concept 3 and the new approach of the hiding function b_5 performs best (Table C-7). It is marginally better than b_2 and b_3 , both in combination with the mixing concept 3, placing second.

Table C-7: Ranking matrix of the 14 numerical model applications with the Rickenmann (2001) bed load transport equation; '1' is associated with the best performance.

| Model performance | b_1 (0.3) | b_2 (0.8) | b_3 (1.3) | b_4 (WilCro) | b_5 (dynamic) |
|-------------------------|----------------|----------------|----------------|-------------------|--------------------|
| Mixing concept 1 | 10 | 11 | 12 | 14 | not cons. |
| Mixing concept 2 | 9 | 6 | 7 | 12 | 8 |
| Mixing concept 3 | 5 | 2 | 2 | 4 | 1 |

| Armoring experiments | b_1 (0.3) | b_2 (0.8) | b_3 (1.3) | b_4 (WilCro) | b_5 (dynamic) |
|---|----------------------------|----------------|----------------|-------------------|--------------------|
| Total bed load volumes | | | | | |
| Temporal evolution of bed load accumulation | | | | | |
| Mixing | | | | | |
| Bed load - D50 | | | | | |
| concept 1 | Bed load - D16 (fine tail) | | | | |
| Bed load - D84 (coarse tail) | | | | | not considered |
| Bed surface - D50 | | | | | |
| Bed surface - D16 (fine tail) | | | 5 | | |
| Bed surface - D84 (coarse tail) | | | | | |
| | | | | | |
| Total bed load volumes | | | | 5 | |
| Temporal evolution of bed load accumulation | | | | | |
| Mixing | Bed load - D50 | | | | |
| concept 2 | Bed load - D16 (fine tail) | | | | |
| Bed load - D84 (coarse tail) | | | | | |
| Bed surface - D50 | | | | | |
| Bed surface - D16 (fine tail) | | 5 | 5 | | |
| Bed surface - D84 (coarse tail) | | | | | |
| | | | | | |
| Total bed load volumes | | | | | |
| Temporal evolution of bed load accumulation | | | | | |
| Mixing | Bed load - D50 | | | | |
| concept 3 | Bed load - D16 (fine tail) | | | | |
| Bed load - D84 (coarse tail) | | | | | |
| Bed surface - D50 | | | | | |
| Bed surface - D16 (fine tail) | | | | | |
| Bed surface - D84 (coarse tail) | | | | | |

Legend : class 1 class 2 class 3 class 4 class 5

Figure C-63: Classification of the numerical model performance in reproducing the armoring experiments with the Rickenmann (2001) bed load transport equation. The 14 numerical model applications differ regarding the hiding exponent b and/or the mixing concept; the definitions of the classes are given in Table C-6.

2.6.3.2.2 Schneider et al. (2015) bed load transport equation

Since none of the numerical model realizations with the 'Schneider et al. (2015) bed load transport equation' reproduce the feeding experiments sufficiently, the model evaluation is restricted to the armoring experiments (Figure C-64).

However, the ranking is hardly affected by that and it reveals that the model realizations 'mixing concept 3' with the hiding exponent β_2 or β_3 performs best (Table C-8). Furthermore, the score matrix in Table C-8 shows the strong influence of the hiding function on the overall performance. Six out of the best seven realizations refer either to β_2 or β_3 . This contradicts with the model performance obtained with the 'Rickenmann (2001) bed load transport equation', where the best performance is limited to the mixing concept 3 (regardless of the hiding function used; Table C-7). It is worth to note that the hiding functions referring to almost equal mobility yield the worst results. This contradicts with many field observations in mountain streams, which is discussed in more detail in section 2.7.1.



Figure C-64: Classification of the numerical model performance in reproducing the armoring experiments with the Schneider et al. (2015) bed load transport equation. The 14 numerical model applications differ regarding the hiding exponent β and/or the mixing concept; the definitions of the classes are given in Table C-6.

Table C-8: Ranking matrix of the 14 numerical model applications with the Schneider et al. (2015) bed load transport equation; '1' is associated with the best performance.

| Model performance (armoring experiments) | β_1 (-0.87) | β_2 (-0.47) | β_3 (-0.13) | β_4 (WilCro) | β_5 (dynamic) |
|---|----------------------|----------------------|----------------------|-----------------------|------------------------|
| Mixing concept 1 | 13 | 6 | 7 | 14 | not cons. |
| Mixing concept 2 | 11 | 3 | 4 | 11 | 8 |
| Mixing concept 3 | 9 | 1 | 1 | 9 | 5 |

C.2.7 Discussion and conclusion

2.7.1 Bed load transport equation

2.7.1.1 The Rickenmann (2001) bed load transport equation

The 'Rickenmann (2001) bed load transport equation' proved to be suitable for the back-calculation of the experimental tests. Depending on the hiding function and the mixing concept, total bed load volumes either match well, or they are over- or underestimated, but model results do not reveal a systematic bias. In this respect, the hiding

functions referring to size-selective mobility overestimate bed load volumes more likely at low flows but underestimate them at high flows.

This good agreement of modeled and observed bed load volumes comes along with the interaction of the fractional bed load transport and the bed material sorting. According to the armoring experiments, the modeled bed surface is way too coarse when a simple mixing approach (like the mixing concepts 1 and 2) is applied. The fine tail of the bed surface grain size distribution is totally eroded which contradicts with the observations. Thus, the bed load volumes might have been severely overestimated if the observed bed surface grain size distribution would have been used throughout the simulation instead. Surprisingly, this is not only the case for the hiding functions referring to moderate or strong size-selective transport (b_2 or b_3), but even for those associated with almost equal mobility (section 2.6.2.4). In this respect ‘almost’ means a hiding exponent of 0.2, which is the lower bound of observed values in mountain streams (Bathurst, 2013). However, assuming a sediment particle which is six times smaller than the median diameter (for example $D_i = 0.025$ m and $D_{50} = 0.15$ m), the critical discharge of this particle is still 30 % less than the critical discharge of the D_{50} when a hiding exponent of 0.2 is considered (while it is 90 % at strong size-selective conditions). According to the model results, this rather small difference is enough that fine bed load is eroded completely from the active layer.

In contrast, the new mixing concept 3 prevents the fine sediment to be winnowed totally from the active layer, since the fractional availability of bed material is regulated by means of the active surface layer. Anyway, the mixing concept 3 does not improve the performance of the bed load transport equation, since the fine sediment is still winnowed, but from the thin active surface layer instead of the entire active layer. Thus, the mixing concept 3 simply limits the effect but does not eliminate the cause of the overestimation of the fine grain’s mobility by the ‘Rickenmann (2001) bed load transport equation’.

2.7.1.2 The Schneider et al. (2015) bed load transport equation

Regarding the ‘Schneider et al. (2015) bed load transport equation’, the numerical model underestimates bed load transport of the feeding experiments by far. Thus, the effect of feeding fine sediment is not sufficiently reproduced by the model. This is surprising since the ‘Schneider et al. (2015) bed load transport equation’ was used in combination with five different hiding functions, which revealed a very wide range of fractional mobility conditions (from almost equal mobility to strong size-selective mobility).

The performance of the ‘Schneider et al. (2015) bed load transport equation’ is better for the armoring experiments, where model results somehow match with the observations, at least for two hiding functions. These two hiding functions are associated either with a moderate or strong size-selective mobility, while those referring to equal mobility again underestimate bed load transport. This severely contradicts with field observations in mountain streams, where fractional bed load transport predominately reveals equal or at least weak size-selective (e.g. Study C in chapter B; Schneider et al., 2015; Mao et al., 2008; Mao and Lenzi, 2007; Marion and Weirich, 2003). Additionally, it is worth to note that the ‘Schneider et al. (2015) bed load transport equation’ is originally derived with the hiding function of b_4 , which assumes almost equal mobility of the fine grains.

At low flows, the bed load transport rate is usually the larger the more pronounced the size-selective mobility is; simply because the large mobility of small grains overcompensates equal mobility. The numerical model confirms with this since bed load volumes of (i) the armoring experiments (Figure C-29) and (ii) the low flow runs of the feeding experiments (not illustrated) are larger for β_2 and β_3 . Because of that, the 'Schneider et al. (2015) bed load transport equation' (in its original form) might underestimate the bed load transport rate of the flume experiments and this overall underestimation is partly compensated by the hiding functions referring to size-selective mobility. In a consequence, the better performance of β_2 and β_3 is not attributed to a better representation of fractional mobility, but to the overall increase of total bed load transport rate. This is in an inverse agreement with several studies that found flume based bed load transport equations to generally overestimate bed load transport rate within in natural streams (*Recking, 2010; Rickenmann, 2001; Gomez and Church, 1989*).

2.7.2 Modeling the effect of bed load supply on transport rate

According to the feeding experiments, the supply of fine bed load causes the bed load transport rate to increase. This is even the case for flows distinctly lower than the critical discharge of the bed surface. Possible reasons for this increase of bed load transport rate are (i) the fining of the bed surface which is expected to decrease bed stability, (ii) the decrease of the form drag (*Yager et al., 2012*) or (iii) the increase of the fine sediment's exposure (*Study E* in section C.1), both due to the partial filling of the pockets between immobile grains. Each of these components is addressed within the model framework:

- (i) The balancing of fractional bed load and bed material causes the grain size distribution of the active layer to fine when fine sediment is supplied. In a consequence, the D_{50} decreases, causing the critical discharge of the D_{50} (a proxy for bed stability) to decrease and thus, the bed load transport capacity to increase. Since $q_{c,D_{50}} \propto D_{50}^{1.5}$ (equation C13), the temporal evolution of the bed stability is illustrated by means of $D_{50}^{1.5}$ in Figure C-65b. According to the model results obtained with the mixing concepts 1 and 2, there is a long-lasting decline with $D_{50}^{1.5}$ decreasing to half of its initial value. Thus, bed stability is reduced by 50 % in course of this run due to the fining of the active layer (minor changes in channel slope are neglected).
- (ii) In addition, the model accounts for momentum losses due to form drag. Therefore, the flow resistance partitioning of *Rickenmann and Recking (2011)* is applied and any decrease of the D_{84} is accompanied with an increase of S_{red} (equation C11). Since bed load transport rate depends on S_{red} to the power of 1.5 (acc. to the *Rickenmann (2001)* equation), Figure C-65c shows the time series of $S_{red}^{1.5}$. For the mixing concepts 1 and 2, $S_{red}^{1.5}$ increases to almost twice of its initial value, which is associated with a doubling of transport rate, respectively.
- (iii) In accordance with *Bathurst's (2013)* suggestion that the embedding of the bed surface influences the mobility of finer fractions, a new hiding function was developed. The ratio of active layer thickness H_{al} and D_{84} is used as a proxy for the embedding. The hiding/exposure effect is assumed to be maximized (almost equal mobility) at very low ratios and

vice versa. Due to the variation of sediment feeding and sediment starving, H_{al}/D_{84} altered in course of the runs and the time series of the hiding exponent for $D < D_{50}$ is given in Figure C-66b. In this respect, the new hiding function slightly improved the model performance in reproducing the temporal progression of bed load accumulation (Figure C-66a). However, in respect to the overall performance (Figure C-62) the improvement remains marginal. The model realization 'mixing concept 2 with hiding function b_5 ' ranks eighth out of 14 realizations and thus, it is close behind the constant hiding exponents referring to moderate (b_2) and strong size-selective mobility (b_3).

Summarizing, all three mechanisms have a severe influence on calculated bed load transport rate. In terms of total bed load volumes, the effect of bed load supply is not that bad reproduced by the numerical model, which is primarily attributed to the first two mechanisms. In contrast, the time series of bed load transport rate does not match at all with the mixing concept 1, while it is slightly better reproduced with the mixing concept 2 and especially in combination with the hiding function that accounts for differences in bed state (b_5). Anyway, the feedback between bed load supply and transport rate and thus, the propagation velocity of supplied sediment is still too slow compared with the observations (Figure C-65a). While the observations revealed certain break points at which bed load transport rate either increased (while feeding) or decreased (after feeding), the numerically modeled progression is very continuous.

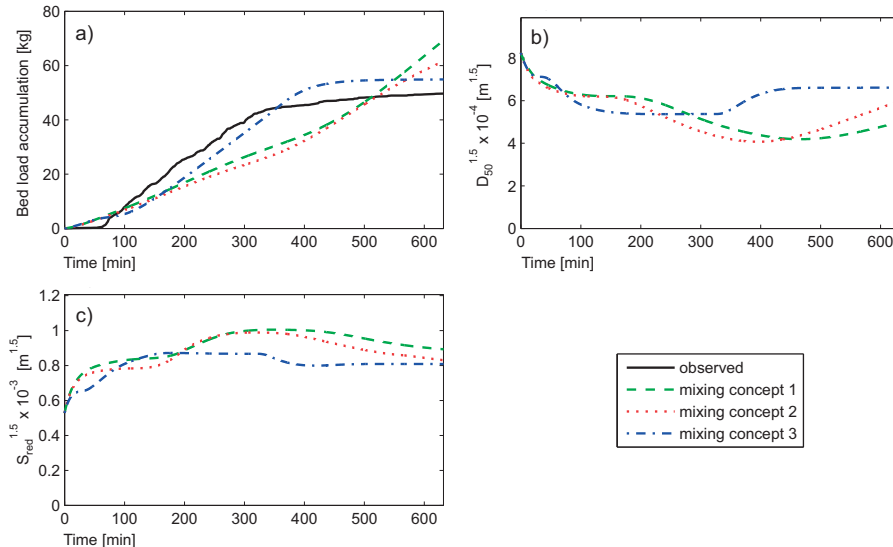


Figure C-65: Times series of a) bed load accumulation, b) active layer $D_{50}^{1.5}$ and c) $S_{red}^{1.5}$ during run 1 of series #2 of the feeding experiments. The model results refer to the Rickenmann (2001) bed load transport equation with the hiding function b_2 .

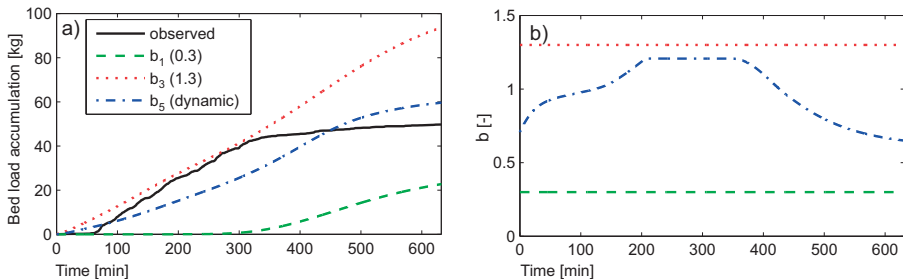


Figure C-66: Times series of a) bed load accumulation and b) the hiding exponent for $D_l < D_{50}$ during run 1 of series #2 of the feeding experiments. The model results refer to the Rickenmann (2001) bed load transport equation with the mixing concept 2.

Since two out of three mechanisms, the reduction of bed stability and the reduction of form drag, depend on the D_{50} and D_{84} of the active layer, it was initially hypothesized that this weakness of the numerical model is attributable to the mixing concept. According to the visual observations in course of the experiments, the interaction of bed load and bed material was limited to the bed surface during the low flow runs (*Study E*, section C.1). In contrast, the mixing concepts 1 and 2 assume that bed load and bed material is mixed throughout the entire active layer.

Therefore, the new formulated mixing concept 3 accounts for the dependence between mixing depth and flow strength: bed load is eroded or deposited on the bed surface at low flows (thin active surface layer) while mixing depth extends over the entire active layer at very high flows (e.g. Schneider *et al.*, 2014; Haschenburger and Church, 1998). But the characteristic grain sizes used to determined bed stability (D_{50}) or flow resistance (D_{84}) are unaffected by that and they are determined with respect to the grain size distribution of the entire active layer.

According to the model evaluation, the application of this new mixing concept improved the model, regardless of the hiding function used. The magnitude and the time series of bed load accumulation as well as the grain size distribution of both, the bed load and the bed surface, are in a good agreement with the observations.

2.7.3 Modeling the bed surface coarsening in response to sediment starving

The effect of sediment starving on both, the bed load transport rate and the channel morphology, was addressed by the armoring experiments (Steidl, 2015). Corresponding with many previous studies (e.g. Zimmermann *et al.*, 2010; Hassan and Church, 2000; Rosport, 1997; Günter, 1971), the bed stabilized by means of bed surface coarsening and structuring of immobile keystones. In a consequence, the bed load transport rate declined in course of the armoring runs. This decline occurred soon after the beginning of each run and thus, the bed surface armoring must have been fast. In this respect, the accumulated bed load transport was rather small for most runs which is confirmed by the low magnitude of bed erosion.

All model realizations reproduce the bed surface coarsening due to sediment starving. Regarding the mixing concepts 1 and 2, the modeled bed surface D_{50} and D_{84} are too coarse and the fines are eroded way too intense. But next to the coarsening, the increase of bed stability is additionally affected by the structuring keystones. According

to the experiments, the initially plane bed evolved towards a rough bed with individual step (experimental series #1 with a bed slope of 0.05 m/m) or a step-pool channel (experimental series #2 with a bed slope of 0.1 m/m). In contrast, the bed surface structuring and its impact on bed stability are not addressed by the numerical model, since the model is based on a Eulerian approach with the control volumes extending the scale of bed structures. In terms of modeling, the bed stability is solely determined by means of the bed surface grain size distribution. This might be one reason, why the modeled grain size distributions are way too coarse, at least in the case of the mixing concepts 1 and 2.

In addition, the bed surface coarsening is assumed to be modeled too slowly, since the decline of bed load transport rate lasts too long. To some extent, this is attributed to the fact, that the modeled bed surface coarsening was more intense than the observed one. But the magnitude of the temporal delay suggests that this is not the only reason. This deficiency of the numerical model also corresponds with the findings in section 2.7.2 and is eliminated by the mixing concept 3, which enables a much faster alteration of the bed surface grain size distribution. Thus, accounting for a dependence of the mixing depth and flow strength also improves the back-calculation of the armoring experiments.

However, there remains one issue which is not captured by any model realization: in accordance with Zimmermann *et al.* (2010), the observed bed load transport rate did not always decline monotonically in course of sediment starving, but was intermittent by sporadic peaks of bed load transport. These peaks are associated with the local destruction of individual keystones or entire steps, causing a limited release of finer subsurface material and thus, a temporal increase of bed load transport. The stability of a particular keystone or step is affected by the stochastic nature of incipient motion (e.g. Papanicolaou *et al.*, 2002) and it is not predictable by means of purely deterministic approaches.

Instead, the release of subsurface material is regulated by the mixing concept (at least within the model framework of this study). Regarding the mixing concepts 2 and 3, subsurface material (sediment from the bed layer) is released into the active layer as discharge or shear stress exceed a certain threshold. In the current version of the numerical model, this threshold is defined by $q_{c,D50}$, (or $T^*_{c,D50}$) but could be replaced by a stochastic variable, reflecting the probability of a local bed surface break-up (e.g. Zimmermann *et al.*, 2010). In this respect, a criterion for the release of the subsurface sediment by means of a probabilistic approach might represent a novel way to account for the stochastic nature of bed load transport. However, this was not tested in course of this study but is in need for future research.

C.2.8 References of Study F

- Bathurst, J. C. (2013), Critical conditions for particle motion in coarse bed materials of nonuniform size distribution, *Geomorphology*, 197, 170-184.
- Bunte, K., and S. R. Abt (2001a), Sampling surface and subsurface particle-size distributions in wadable gravel- and cobble-bed streams for analyses in sediment transport, hydraulics, and streambed monitoring. *Gen. Techn. Rep. RMRS-GTR-74*, 428 pp, U.S. Department of Agriculture, Forest Service, Fort Collins, CO.
- Borah D. K., C. V. Alonso, S. N. Prasad (1982), Routing graded sediments in streams: formulations. *J. Hydraul. Div.*, ASCE, 108(12), 1486-1503.
- Church, M. and A. Zimmermann (2007), Form and stability of step-pool channels: Research progress, *Water Resour. Res.*, 43, W03415, doi: 10.1029/2006WR005037

- Diplas, P., and A. J. Sutherland (1988), Sampling Techniques for Gravel Sized Sediments, *J. Hydraul. Eng.*, 114(5), 484-501.
- Egashira, S., and K. Ashida (1991), Flow resistance and sediment transport in streams with step-pool bed morphology, *Lecture Notes in Earth Sciences*, Vol. 37, 45-58.
- Einstein, H. A. (1950), The Bed-Load Function for Sediment Transportation in Open Channel Flows, *Technical Bulletin No. 1026*, USDA, Washington, D.C.
- Ferguson, R. (2007), Flow resistance equations for gravel- and boulder-bed streams, *Water Resour. Res.*, 43, W05427, doi: 10.1029/2006WR005422
- Ghilardi, T., M. J. Franca, and A. J. Schleiss (2014), Bed load fluctuations in a steep channel, *Water Resour. Res.*, 50, 6557-6576, doi: 10.1002/2013WR01444
- Gomez, B. and M. Church (1989), An assessment of bed load sediment transport formulae for gravel bed rivers, *Wat. Resour. Res.*, 25/6, 1161-1186.
- Günter, A. (1971), Die kritische mittlere Sohlenschubspannung bei Geschiebemischungen unter Berücksichtigung der Deckschichtbildung und der turbulentenbedingten Sohlenschubspannungsschwankungen, *Mitteilungen der Versuchsanstalt für Wasserbau, Hydrologie und Glaziologie*, Nr. 3, ETH Zurich, Switzerland (in German).
- Haschenburger, J. K., and M. Church (1998), Bed material transport estimated from the virtual velocity of sediment, *Earth Surf. Proc. Land.*, 23(9), 791-808.
- Hassan, M. A. and M. Church (2000), Experiments on surface and partial sediment transport on a gravel bed, *Wat. Resour. Res.*, 36/7, 1885-1895.
- Heimann, F. U. M., D. Rickenmann, J. M. Turowski, and J. W. Kirchner (2015a), sedFlow – a tool for simulating bed load transport and longitudinal profile evolution in mountain streams, *Earth Surf. Dynam.*, 3, 15-34, doi: 10.5194/esurf-3-15-2015
- Heimann, F. U. M., D. Rickenmann, M. Böckli, A. Badoux, J. M. Turowski, and J. W. Kirchner (2015b), Recalculation of bed load transport observations in Swiss mountain rivers using the model sedFlow, *Earth Surf. Dynam.*, 3, 35-54, doi: 10.5194/esurf-3-35-2015
- Hirano, M. (1971), River bed degradation with armoring, *Proc.*, Japan Society of Civil Engineers, Tokyo, Japan, 195, 55-65.
- Hunziker, R. P., and M. N. R. Jaeggi (2002), Grain Sorting Processes, *J. Hydraul. Eng.*, 128(12), 1060-1068, doi: 10.1061/(ASCE)0733-9429(2002)128:12(1060)
- Kößler, D. (2014), Physikalische Untersuchungen zum Geschiebetransport über die Deckschicht eines alpinen Gebirgsflusses, Master thesis at the University of Innsbruck, Innsbruck, Austria (in German).
- Mao, L., and M. A. Lenzi, (2007), Sediment mobility and bed load transport conditions in an alpine stream, *Hydrol. Process.*, 21, 1882-1891.
- Mao, L., G. P. Uyttendaele, A. Iroume, and M. A. Lenzi (2008), Field based analysis of sediment entrainment in two high gradient streams located in Alpine and Andine environments, *Geomorphology*, 93, 368-383.
- Marion, D. A. and F. Weirich (2003), Equal-mobility bed load transport in a small, step-pool channel in the Outachita Mountains, *Geomorphology*, 55, 139-154, doi: 10.1016/S0169-555X(03)00137-5
- Montgomery, D. R., and J. M. Buffington (1997), Channel-reach morphology in mountain drainage basins, *Geol. Soc. Am. Bull.*, 109(5), 596-611.
- Nitsche, M., D. Rickenmann, D., J. M. Turowski, A. Badoux, and J. W. Kirchner (2011), Evaluation of bed load transport predictions using flow resistance equations to account for macro roughness in steep streams, *Water Resour. Res.*, 47, W08513, doi: 10.1029/2011WR010645
- Papanicolaou, A. N., P. Diplas, N. Evangelopoulos and S. Fotopoulos (2002), Stochastic incipient motion criterion for spheres under various bed packing conditions, *J. Hydraul. Eng.*, 128(4), 369-380, doi: 10.1061/(ASCE)0733-9429(2002)128:4(369)
- Parker, G., and P. C. Klingeman (1982), On why gravel bed streams are paved, *Water Resour. Res.*, 18(5), 1409-1423.
- Parker, G. (1991), Selective sorting and abrasion of river gravel I: theory, *J. Hydraul. Eng.*, 117(2), 131-149.
- Recking, A. (2010), A comparison between flume and field bed load transport data and consequences for surface-based bed load transport prediction, *Water Resour. Res.*, 46, W03518, doi: 10.1029/2009WR008007
- Rickenmann, D. (1991), Hyperconcentrated flow and sediment transport at steep flow, *J. Hydraul. Eng.*, 117(11), 1419-1439, doi: 10.1061/(ASCE)0733-9429(1991)117:11(1419)
- Rickenmann, D. (2001), Comparison of bed load transport in torrents and gravel bed streams, *Water Resour. Res.*, 37(12), 3295-3305.

- Rickenmann, D. and A. Recking (2011), Evaluation of flow resistance in gravel-bed rivers through a large data set, *Water Resour. Res.*, 47, W07538, doi: 10.1029/2010WR009793
- Rosport M. (1997), Fließwiderstand und Sohlstabilität steiler Fließgewässer unter Berücksichtigung gebirgsbachtypischer Sohlstrukturen, Mitteilungen des Instituts für Wasserwirtschaft und Kulturtechnik, Universität Karlsruhe, Heft 196, Karlsruhe Institute of Technology, Germany (in German).
- Schneider, J. M., J. M. Turowski, D. Rickenmann, R. Hegglin, S. Arrigo, L. Mao and J. W. Kirchner (2014), Scaling relationships between bed load volumes, transport distances, and stream power in steep mountain channels, *J. Geophys. Res.-Earth*, 119, doi: 10.1002/2013JF002874
- Schneider, J. M., D. Rickenmann, J. M. Turowski, K. Bunte, and J. W. Kirchner (2015), Applicability of bed load transport models for mixedsize sediments in steep streams considering macro-roughness, *Water Resour. Res.*, 51, 5260–5283, doi: 10.1002/2014WR016417
- Steidl, B. (2015). Deckenschichtentwicklung und Auswirkung externer Geschiebezugabe auf die Sohlmorphologie und die Fließgeschwindigkeit bei Wildbächen, Master thesis at the University of Innsbruck, Innsbruck, Austria (In German).
- van de Wiel, M. J., Coulthard, T. J., Macklin, M. G., and Lewin, J. (2007), Embedding reach-scale fluvial dynamics within the CAESAR cellular automaton landscape evolution model, *Geomorphology*, 90, 283–301, doi: 10.1016/j.geomorph.2006.10.024
- van Niekerk, A., K. R. Vogl, R. L. Slingerland and J. S. Bridge (1992), Routing of heterogeneous sediment over moveable bed: model development, *J. Hydraul. Eng.*, 118(2), 246–262.
- Vetsch D., A. Siviglia, D. Ehrbar, M. Facchini, M. Gerber, S. Kammerer, S. Peter, L. Vonwiller, C. Volz, D. Farshi, R. Mueller, P. Rousselot, R. Veprek, R. Faeh (2015), System Manuals of BASEMENT, Version 2.5, Laboratory of Hydraulics, Glaciology and Hydrology (VAW), ETH Zurich.
- Wilcock, P. R., J. C. and Crowe (2003), Surface based transport model for mixed size sediment, *J. Hydraul. Eng.*, 129(2), doi: 10.1061/(ASCE)0733-9429(2003)129:2(120)
- Yager, E. M., J. W. Kirchner, and W. E. Dietrich (2007), Calculating bed load transport in steep boulder bed channels, *Water Resour. Res.*, 43, W07418, doi: 10.1029/2006WR005432
- Yager, E. M., W. E. Dietrich, J. W. Kirchner and B. W. McArdell (2012), Prediction of sediment transport in step-pool channels, *Water Resour. Res.*, 48, W01541, doi: 10.1029/2011WR010829
- Zimmermann, A., M. Church, and M. A. Hassan (2010), Step-pool stability: Testing the jammed state hypothesis, *J. Geophys. Res.*, 115, F02008, doi: 10.1029/2009JF001365

D CONCLUSION

D.1 Overview of the thesis' research issues

The first part of this thesis is dedicated to the long-term dynamics of bed load transport in steep mountain streams. Large field data sets are analyzed in the *Studies A* and *B*. On the one hand, the results give evidence about the variable nature of bed load transport in small mountain catchments and during hydrological ordinary years without extreme flood events or debris flows. The variability persists at multiple time scales and it is attributed to temporal differences in sediment supply conditions. On the other hand, the annual amount of bed load transport is linked to topographic parameters and the relationship is quantified in terms of a multiple regression equation.

However, in engineering practice, bed load transport equations are widely used to compute bed load transport rate by means of parameters describing the flow's strength and the retaining forces of the sediment. Therefore, the empiric parameters of such formulae are derived from field data in *Study C* and the performance of several bed load transport equations is evaluated in *Study D*.

The second part of this thesis focuses on the feedback between sediment supply and bed load transport in more detail. Flume experiments give insights into the transport processes under variable supply conditions. Finally, a new computational approach is developed that improves the performance of a numerical model in reproducing the feedback between sediment supply and bed load transport.

D.2 Part 1 - Long-term dynamics of bed load transport in steep mountain streams

D.2.1 Study A: Variability of annual bed load volumes in small, high-altitude mountain streams

2.1.1 Contribution to research⁵

Study A addresses the magnitude and variability of annual bed load volumes in high-altitude mountain streams. Therefore, the records of operational flushings at water intake structures are used to determine annual bed load volumes of twenty mountain catchments with a time span of up to 49 years. Error analyses reveal an overall uncertainty of the annual bed load volumes of a factor of 2 and hence, they represent a unique data set on the long-term bed load budget of small mountain creeks. But it is worthwhile to note, that the annual bed load volumes used in this *Study A* are only reliable for hydrological normal years without exceptional flood events or debris flow events. According to operational records of TIWAG, the occurrence interval of such extreme events is site-specific and spans between five and >30 years.

The correlation analysis of the mean annual bed load volumes with site-specific parameters yields an almost linear dependence with the catchment size and an exponential increase with the relative glacier area. In contrast, any topographic parameters such the mean slope of either the basin or the stream, the relief ratio (Schumm, 1954), and the Melton ratio (Melton, 1657) are not correlated with the mean annual bed load volumes. In this respect, the catchment size is associated with the annual channel flow, while glaciation affects both, water discharge due to glacier melt and transport efficiency due to an increased sediment supply. Of course, the magnitude of sediment supply might be affected by other geomorphologic patterns than the relative glacier area as well, i.e. the erodibility of the hillslopes (scree slopes) and their connectivity to the main channel (Cavalli *et al.*, 2013). However, all field sites of this study feature similar geologic boundary conditions, suggesting a similar sediment production by means of weathering. In addition, the deviation of observed and predicted (equation B46 in *Study A*) mean annual bed load volumes is not consistently associated with the occurrence of open scree slopes in the proximity of the main channel. Possibly, an extended data set, comprising field sites with different geology, yields an empiric relation between mean annual bed load volumes and additional morphologic parameters, attributing these kinds of sediment sources.

For most of the field sites, the frequency distribution of annual bed load volumes is log-normal distributed and the data reveal a large variability even within a given site. This variability is attributed to the two main drivers of bed load transport: the water runoff and the availability of mobile bed load. To separate their contribution to the annual bed load volume, rating curves are derived for those streams where high-resolution discharge data (15 min interval) are available. These rating curves account for the non-linear relation of bed load transport rate and discharge and are somehow based on the bed load transport equation of Schneider *et al.* (2015). However, the results reveal that the variability of the annual bed load volumes is not solely explained by the variability

⁵ The first paragraph of this chapter was slightly extended and it differs from the original version of the dissertation.

of the annual discharge hydrograph. Considering a single site, the annual bed load volume is indeed on average larger in wet years, but the transport efficiency is lower. In other words, the amount of bed load transported at a certain discharge is on average higher in dry and lower in wet years. This negative correlation of transport efficiency and cumulative flow competence is attributed to the influence of the sediment availability on the bed load transport. However, at one field site, a substantial increase of both, sediment supply and transport efficiency, was observed after an exceptional flood event. This is in agreement with former studies (Turowski *et al.*, 2009; Lenzi *et al.*, 2004) and suggests a differentiation between micro-scale sediment sources which are abundant almost every year and macro-scale disturbances which are limited to exceptional events such as major floods, debris flows or hillslope failures.

Practical application

2.1.2 Practical application: Estimation of annual bed load volumes

In *Study A*, an empiric equation is presented that enables for an estimation of the mean (*mABV*) and the frequency distribution of annual bed load volumes of steep mountain catchments (in terms of solid bed load volumes). The equations are based on a field data set of small, high-altitude mountain catchments that are all located in the Central Alps of Northern Tyrol (Austria). The site characteristics are given in section 1.1.2 in chapter B.

However, the mean annual bed load volume is related to the catchment size and the relative glacier area and it is estimated according

$$mABV = 6.63 \times A^{0.986} \times \exp(5.65 \times G) \quad (D1)$$

with the *mABV* in m³ referring to the solid volume without pores, catchment size *A* in km² and relative glacier area *G* in km²/km². Furthermore, the frequency distribution of annual bed load volumes is sufficiently approximated by a lognormal probability distribution which is defined by

$$f(ABV) = \frac{1}{ABV\sigma\sqrt{2\pi}} \exp\left[-\frac{(\ln(ABV) - \mu)^2}{2\sigma^2}\right] \quad \text{for } ABV > 0 \quad (D2)$$

with the two parameters μ and σ . Both of these parameters are correlated with topographic parameters and are estimated according

$$\hat{\mu} = 1.27 + 0.96 \ln(A) + 6.22G \quad (D3)$$

$$\hat{\sigma} = -0.046 + 0.031 \text{meanCS} \quad (D4)$$

with the catchment size *A* in km², the relative glacier area *G* in km²/km² and the mean catchment slope *meanCS* in degree (°).

As an example, the approach is applied to the Taschachbach, a steep mountain stream that is close to one of the field sites (Pitzbach) and features similar geologic conditions. At the Taschachbach, the hydropower operator TIWAG operates a water intake structure (constructed as a small arch dam). However, Sommer and Lauffer (1982) used the records on reservoir flushings to determine the annual bed load volumes (*ABV*) of the Taschachbach for the period 1965 to 1978 (Table DD-1). These values refer to the deposit volumes of bed load. To account for the porosity of the sediment deposition,

the values reported in Sommer and Lauffer (1982) are reduced by 30 %, respectively. Hence, the mean annual bed load volume without pores of this period is about 1051 m³.

Table DD-1: Annual bed load volumes at the water intake structure of the Taschachbach (Pitztal, Austria) as reported by Sommer and Lauffer (1982)

| Year | ABV (acc. Sommer and Lauffer, 1982) | |
|-------------|-------------------------------------|-----------------------------------|
| | deposit volume [m ³] | solid volume [m ³] |
| 1965 | 667 | 467 |
| 1966 | 848 | 594 |
| 1967 | 970 | 679 |
| 1968 | 970 | 679 |
| 1969 | 848 | 594 |
| 1970 | 1879 | 1315 |
| 1971 | 848 | 594 |
| 1972 | 970 | 679 |
| 1973 | 848 | 594 |
| 1974 | 970 | 679 |
| 1975 | 4181 | 2927 |
| 1976 | 2788 | 1951 |
| 1977 | 1757 | 1230 |
| 1978 | 2485 | 1739 |
| Mean | 1502 | 1051 |

At the water intake structure, the Taschachbach drains an area of 60.6 km², with a relative glacier area of 0.22 km²/km² (according to the glacier survey of 2006 published in Fischer et al., 2015) and a mean catchment slope of 32 degrees. Estimating *mABV* by means of equation D1 yields 1285 m³ which is close to the observed *mABV* (1051 m³). The parameters of the lognormal frequency distribution are estimated by means of the equations D3 and D4 to $\mu=6.55$ and $\sigma=1.04$. Finally, the probability density function of annual bed load volumes is estimated with equation D2. Based on the density distribution, the probability of exceedance of each quantity of *ABV* can be derived. It is compared with the probability distribution of the observed *ABV* in Figure D-1a, and it reveals a proper match. However, there remain some discrepancies which are visually more pronounced by plotting a histogram of observed and estimated *ABV* (Figure D-1b). But nevertheless, the approach represents a novel way to acquire some information on the variability of *ABV*.

Of course, the application of this approach is restricted to field sites with similar boundary conditions as those of the field sites (Table B1 and B2 in chapter B) and the results should always be checked for plausibility. Furthermore, the approach is developed with respect to hydrological ordinary years without extreme flood events. Thus, the tails of the frequency distribution must be treated with caution and the approach is explicitly not suitable for estimations of years in which very large *ABV* are attributed to single extreme flood events.

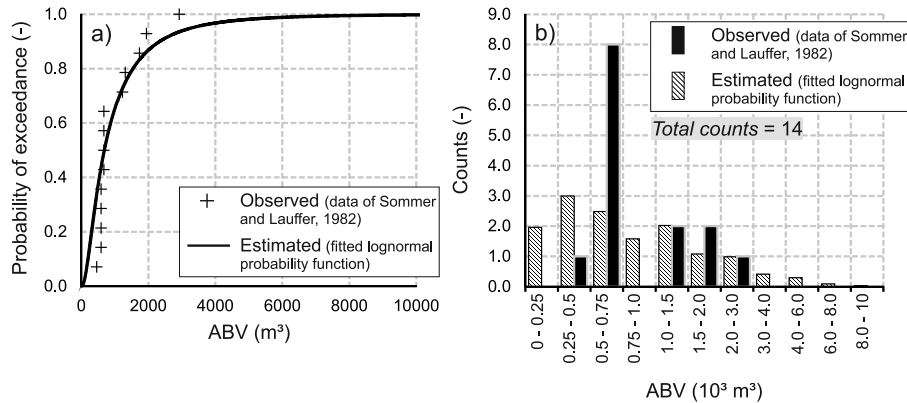


Figure D-1: a) Cumulative probability and b) histogram of observed (acc. Sommer and Lauffer (1982), but in terms of solid volume) and estimated ABV at the Taschachbach.

D.2.2 Study B: Temporal variability of bed load transport rate in two glacier-fed mountain streams

The variable nature of bed load transport in steep mountain streams is investigated by means of annual bed load volumes in *Study A*. However, the variability is likely to occur at multiple time scales (e.g. *Heimann et al.*, submitted) and is not restricted to years. Therefore, large time series of simultaneously measured bed load transport rate (Q_b) and water discharge (Q) from two steep mountain streams, the Oberbergbach and the Pitzbach, are analyzed, by means of the Q - Q_b relation and its seasonal patterns.

For both streams, the Q - Q_b relation of the total time series scatters within a range of up to four orders of magnitude. The bed load transport rates observed at a certain discharge level are log-normal distributed and their standard deviation is constant for low to moderate flows but decreases at high flows. In addition, the Q - Q_b reveals two distinct breakpoints. The first breakpoint is associated with the shift from the marginal transport of sand to significant (but still low) transport of sand and gravel, which is accompanied by an increase of the exponent of the power relation. Beyond the second breakpoint, the gradient of the log-scaled Q - Q_b relation decreases, which corresponds to a decrease of the rating curve's exponent. The second breakpoint is associated with the shift from phase 1 to phase 2 transport conditions, which means a shift from over-passing bed load and the initial mobilization of coarse sediment from the bed surface (*Recking, 2012*).

Considering the discharge range of phase 1 transport conditions, the year-wise fitted power functions reveal significant differences regarding both, the exponent and the factor of the equation. To detect any seasonal patterns, power functions were also fitted with month-wise segregated data. In accordance with the study site of *Mao et al.* (2014), a seasonal increase of transport efficiency is evident at the Oberbergbach, with the lowest transport efficiency in May and the highest in September. This seasonal increase is attributed to the shift from snowmelt-dominated runoff in early summer towards glacier melt in late summer, which is accompanied with the increased mobiliza-

tion of highly abundant and mobile sediment at the glacier forefield. In contrast, a seasonal decrease of transport efficiency is present at the Pitzbach, although both streams feature similar characteristics regarding catchment size and glaciation. A possible reason for this opposite behavior is the significance of bed load supply from the ephemeral tributaries during the snow-melt season. While the connectivity of the tributary channels and the main channel is limited at the Oberbergbach, it is significant at the Pitzbach (e.g. Hofer, 1985). A proof of this hypothesis is in need for further research, but some evidence is provided by comparing the Q-Q_b relations of both streams. However, the month-wise differences of the transport efficiency are attributed to the contribution of different sediment sources and thus, they reflect the influence of the sediment supply on bed load transport rate. It is worth to note that these seasonal differences are strongly pronounced for phase 1 transport conditions only, while the Q-Q_b relation does not reveal consistent differences at phase 2 transport conditions.

D.2.3 Study C: Fractional bed load transport in steep mountain streams

In *Study A* and *Study B*, the availability of mobile bed load was found to confine the bed load transport efficiency. But, what is mobile bed load? Or, what is the grain size distribution of bed load at discharges below the break-up of the bed surface armor layer? Based on field measurements, the incipient motion and the mobility of the bed sediment are derived in *Study C*.

Incipient motion is defined by the dimensionless specific discharge (q^*) or the shear stress (τ^*) required to mobilize the bed sediment. It is determined with the flow competence approach (Buffington and Montgomery, 1997) and thus, the water discharge during the bed load transport measurement is associated with the incipient motion of the coarsest particle of the bed load. Since the bed sediment reveals a wide range of different grain sizes, hiding functions are derived, which scale the incipient motion of any grain size (τ_{ci}^* or q_{ci}^*) by the incipient motion of the bed surface D_{50} (τ_{cD50}^*).

In addition, the mobility of bed load is determined by means of the reference transport approach as proposed by Parker *et al.* (1982) and recently applied to steep mountain streams by Schneider *et al.* (2015). Therefore, power functions, with the dimensionless shear stress as the explanatory variable and dimensionless bed load transport rate as the response variable, are fitted to each grain size fraction (full phi-scale) and the functions are collapsed by means of a hiding function.

In comparison with low-gradient streams, the derived reference (τ_{rD50} ; reference approach) or critical shear stresses (τ_{cD50}^* , flow competence approach) are high, but they correspond well with earlier studies dealing with steep mountain streams. However, accounting for the energy losses due to form resistance by means of the effective shear stress, causes τ_{rD50} and τ_{cD50}^* to drop and they reveal a similar range as in low-gradient gravel bed rivers.

The hiding exponents suggest a weak or moderate form of size-selective mobility (reference approach) or incipient motion (flow competence approach). Consequently, the mobilization of small grains from the mixed-sized bed surface requires higher discharges as in a riverbed with uniform sediment. Nevertheless, the incipient motion of small particles is exceeded even by moderate discharges. In contrast, the incipient motion of medium calibers (e.g. D_{50}) is attained at moderate flood events, while no transport of keystones (e.g. D_{84}) was observed during the field surveys.

Furthermore, the hiding exponents derived either with the critical specific discharge and critical shear stress are inconsistent when total shear stress is used. This inconsistency disappears with the effective shear stress.

D.2.4 Study D: Applicability of bed load transport equations in two glacier-fed mountain streams

2.4.1 Contribution to research

In *Study D*, several bed load transport equations are applied and plotted together with the measured $Q-Q_b$ data. The *Schneider et al.* (2015) equation reproduces at least the gradient of the $Q-Q_b$ relation (in log dimensions, corresponding with the relative increase of bed load transport rate with discharge) for both, total and fractional bed load transport calculations, but generally underestimates its magnitude. Furthermore, this type of equation can be easily fitted to the data by adjusting the references shear stress ($\tau_{r,D50}^*$) to any goodness of fit criteria.

2.4.2 Practical application

An engineer often faces the task to define a rating curve between discharge and bed load transport rates for unmonitored steep mountain streams. For example, numerical simulations of the long-term evolution of the river morphology are more and more evolving. In a mountainous environment, the (cobble-bedded) mountain streams at the valley floors are of particular interest. But the bed load budget of these high-order streams is linked to the supply from the steep headwaters or the tributary catchments. Thus, an engineer has to define a time series of bed load transport rates for each tributary that enters the receiving stream in the model area. A common way is to compute bed load transport rate by means of a discharge hydrograph and a bed load transport equation (*Klar*, 2016).

According to *Study D*, the bed load transport equations of *Schneider et al.* (2015) sufficiently reproduced the observed relation once the reference shear stress ($\tau_{r,D50}^*$) was adjusted. Recent field data (e.g. *Study C*) show that $\tau_{r,D50}^*$ varies between different reaches, but its estimation by means of any empiric relation still poses severe uncertainties. Concurrently, this parameter is very sensitive and a small deviation has a huge impact on the computed bed load transport rates.

Usually, a data set of simultaneously measured bed load transport rate and water discharge is necessary to directly derive a suitable estimate of $\tau_{r,D50}^*$. In many engineering applications, the effort of in-situ measurements is too large, especially if several tributary streams need to be considered. Another possibility to adjust $\tau_{r,D50}^*$ is a calibration with respect to a cumulative quantity of bed load transport and a discharge hydrograph. It means that $\tau_{r,D50}^*$ should be chosen in a way that the cumulative sum of computed bed load transport rate for a predefined period is equal to an observed (or simply estimated) volume.

As an example, the *Schneider et al.* (2015) equation with respect to effective dimensionless shear stress and total bed load transport (see *Study D*) is applied to a particular reach of the Laengentalerbach. The example location is about 100 m upstream of the water intake structure of TIWAG and it corresponds with the field site 2 in *Study C*. The cross section is almost rectangular with a flow width of approx. 7 m and the bed gradient is about 0.07 m/m. The mean annual bed load volume at the water intake

structure is reported in *Study A* and it is 238 m³ in terms of the solid volume without pores. This quantity is a reasonable estimate for the example location as well. Additionally, the discharge is gauged at the water intake structure and a mean annual flow duration curve is derived from the 28-year records.

For each discharge value of this ‘mean annual runoff hydrograph’, the bed load transport rate is computed according to the Schneider et al. (2015) bed load transport equation; the procedure of calculation is described in detail in *Study D*. The computed bed load transport rates (in terms of m³/s) are then summed up and multiplied with the temporal interval of the hydrograph (which is 900 s). This quantity represents the cumulative volume of computed bed load transport and it should match the observed mean annual bed load volume.

In order to calibrate the parameter $T_{r,D50}^{**}$ these computation steps are performed several times, each with a different value of $T_{r,D50}^{**}$. The best fit corresponds to the value of $T_{r,D50}^{**}$ that ‘produces’ the smallest absolute difference between computed and observed cumulative bed load volume. In the example case of the Laengentalerbach, the minimum difference is attained with $T_{r,D50}^{**}=0.04$. This value is very close to $T_{r,D50}^{**}$ derived from the field measurements in *Study C*. Furthermore, the computed rating curve between discharge and bed load transport rate reproduces the trend of in-situ measured bed load transport rates (Figure D-2).

To conclude, this procedure enables a reasonable assessment of a straightforward relation between discharge and bed load transport rate. However, the long-term field data presented in *Study A* and *B* show that this relation rather varies with time. This is explicitly not accounted for in the approach illustrated above.

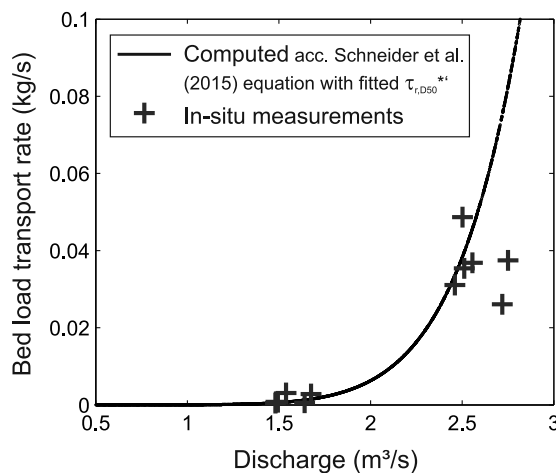


Figure D-2: Computed and observed bed load transport rates at the field site 2 of the Laengentalerbach are plotted against the water discharge. The computation is based on the Schneider et al. (2015) equation but with a fitted value of $T_{r,D50}^{**}$ that reproduces the mean annual bed load volume if the equation is applied to the mean annual discharge hydrograph. The fitting procedure is independent of the in-measurements.

D.3 Part 2 - The feedback between supply and transport rate of mobile bed load in steep streams

D.3.1 Study E: Effect of sediment supply on bed load transport

The availability of mobile bed load reveals a strong influence on the bed load transport rate (*Study B*) and the corresponding bed load volumes (*Study A*). In this respect, *Study E* addresses the feedback between the sediment supply and the bed load transport by means of experimental investigations. Thereby, the primary focus is put on low discharges which are associated with phase 1 transport conditions, i.e. at flows below the critical discharge of the bed surface.

In course of the initialization of the flume settings, a stable armor layer was achieved by a cycle of sediment starving and sediment feeding. The bed surface of the flume showed similar morphologic patterns as typically observed in natural mountain channels. The coarse grains protruded into the flow, while fine sediment cumulated in patches, preferably in the wakes of the very large grains.

Supplying fine sediment to the flume caused the introduced grains to travel downstream, revealing an increased mobility compared with the fine sediment of the bed material. The downstream propagation occurred even at flows much lower than the critical flow of the bed surface. This increased mobility is accompanied with an increased exposure towards the flow since parts of the bed surface were covered by the supplied sediment. However, the magnitude of burying macro-roughness elements was small and thus, a decrease of the form resistance (e.g. Yager *et al.*, 2007) is not likely to explain the severe increase of mobility. Furthermore, the supplied sediment dominated in the total bed load except for discharges that exceeded the critical discharge of the bed surface. Both, the low incipient motion of the supplied sediment and the dominance in total load, indicate that supplied sediment passes over the bed surface.

Of course, if a single grain or a very limited amount (e.g. Koll, 2012) is supplied, it will not travel downstream but deposit at some location with low shear stress. In addition, the propagation velocity of supplied sediment depends, amongst others, on the feeding rate. But, additional experiments which are not presented in detail reveal a significant downstream travel even at low feeding rates (Steidl, 2015).

In respect to the seasonal variations of bed load transport in mountain streams at phase 1 transport conditions (*Study B*), this study reinforces the hypothesis that small-scale changes of sediment supply, possibly due to an increased mobilization of bed load at the glacier forefield or from tributary channels, affect the magnitude of bed load transport rate. Simply speaking, the transport efficiency adjusts towards the magnitude of bed load input, without major changes in the morphologic patterns. Instead, the mechanism involved is attributed to a minor adjustment of the streambed, i.e. of the arrangement and exposure of mobile sediment.

Considering the example of the experiences made at water diversions (*Introduction*), far less water flow transports the same amount of bed load as upstream. In comparison with the residual flow, the magnitude of bed load supply is large, boosting the transport efficiency and thus, achieving a new equilibrium. Clearly, this resilience is constraint by an upper bound: once the magnitude of arriving sediment exceeds this range, bed load accumulates, which is accompanied with the burying of the immobile boulders

and subsequent changes of the flow hydraulics and the bed load transport processes (e.g. *Ghilardi et al.*, 2014). But the adaptability of the streambed seems quite large.

This conclusion contradicts with the observations from gravel bed rivers, where the dominant bed load source is attributed to the subsurface material and its exchange with the transported bed load is regulated by armor layer (*Parker and Klingeman*, 1982). In steep mountain streams, this mechanism might occur at high flows, possibly associated with phase 2 transport conditions, but not at moderate flows.

D.3.2 Study F: Numerical approach for the simulation of phase 1 bed load transport in steep stream

3.2.1 Contribution to research

Study F deals with the question how the effect of bed load supply on transport rate can be assessed by means of computational calculations. Therefore, a simulation framework was developed that accounts for differences in the sediment mobility (at least for the fine fractions) in respect to their availability. Basically, existing approaches for fractional bed load transport computations (e.g. *Heimann et al.*, 2015b) are extended by two model elements, a bed-state dependent hiding function, and a flow-strength dependent mixing approach. This simulation framework is then used to back-calculate a set of flume experiments, all focusing on the effect of sediment supply on bed load transport rate and the streambed adjustment. The simulated results are finally compared with the observed experimental results and the model performance is evaluated.

Using the embedding of the bed surface as a parameter for grain size specific mobility (almost equal mobility at low embedding and strong size-selective mobility at large embedding; e.g. *Bathurst*, 2013) yields a proper match with the observations, but it does not really improve the numerical model. Simply speaking, the model shows an equal performance when common (less sophisticated) approaches are used. In contrast, accounting for a dependence between the active layer thickness and the flow strength (field evidence is provided by *Schneider et al.*, 2014 or *Haschenburger and Church*, 1998) improves the model in reproducing the experimental results.

3.2.2 Outlook for practical application

The question arises if this simulation model is also applicable to the field conditions, i.e. the Oberbergbach. In contrast to the flume experiments, the boundary conditions are much more complex in natural mountain streams. For instance, the water discharge, as well as the feeding rate and its grain size distribution, were constant throughout an experimental run, which is of course not the case in natural mountain streams. However, an application of the simulation model proposed in this thesis is in need for further research. But what are possible benchmarks a suitable simulation model should achieve?

Let us consider the stream section upstream of the water intake structures of the Oberbergbach, which consists of multiple reaches with different channel gradient (from 0.02 m/m to 0.3 m/m) and bed surface grain size distribution. Although the morphologic patterns differ in a large extent within short spatial scales, it is likely that a similar Q-Q_b relation is attained in any of these upstream reaches, at least in periods with phase 1 transport conditions. In contrast, the magnitude of bed load transport rate will differ in times of high flows (i.e. exceptional flood events), probably with the more transport the

steeper the reach is. A numerical model should be capable of preserving both of these features: transport capacity during high flows and a balance between bed load inflow and outflow at moderate flows. As stated above, a test of the proposed numerical simulation framework to natural conditions is not part of this thesis, but it seems worth a try for future research.

D.4 References of chapter D Conclusion

- Bathurst, J. C. (2013), Critical conditions for particle motion in coarse bed materials of nonuniform size distribution, *Geomorphology*, 197, 170-184.
- Buffington, J. M. and D. R. Montgomery (1997), A systematic analysis of eight decades of incipient motion studies, with special reference to gravel-bedded streams, *Wat. Resour. Res.*, 33(8), 1993-2029.
- Cavalli, M., S. Trevisani, F. Comiti, and L. Marchi (2014), Geomorphometric assessment of spatial sediment connectivity in small Alpine catchments, *Geomorphology*, 188, 31-41, doi: 10.1016/j.geomorph.2012.05.007
- Ghilardi, T., M. J. Franca, and A. J. Schleiss (2014), Bed load fluctuations in a steep channel, *Water Resour. Res.*, 50, 6557-6576, doi: 10.1002/2013WR01444
- Haschenburger, J. K., and M. Church (1998), Bed material transport estimated from the virtual velocity of sediment, *Earth Surf. Proc. Land.*, 23(9), 791–808.
- Heimann, F. U. M., D. Rickenmann, M. Böckli, A. Badoux, J. M. Turowski, and J. W. Kirchner (2015a), Recalculation of bed load transport observations in Swiss mountain rivers using the model sedFlow, *Earth Surf. Dynam.*, 3, 35-54, doi: 10.5194/esurf-3-35-2015
- Heimann, F. U. M., D. Rickenmann, J. M. Turowski, and J. W. Kirchner (2015b), sedFlow – a tool for simulating bed load transport and longitudinal profile evolution in mountain streams, *Earth Surf. Dynam.*, 3, 15-34, doi: 10.5194/esurf-3-15-2015
- Heimann, F. U. M. et al. (submitted), Spectral characteristics of bedload transport, in Heimann, F. U. M. (2015), Bedload transport in mountain streams: model development, numerical simulation and time series analysis, Ph.D. thesis, ETHZ, Zurich, Switzerland.
- Hofer, B., 1985, Der Feststofftransport von Hochgebirgsbächen am Beispiel des Pitzbachs (Sediment transport of mountain streams: example of Pitzbach stream), Ph.D. thesis, Univ. of Innsbruck, Innsbruck, 131 p (in German).
- Klar, R. (2016), Langzeitsimulation des Geschiebetransports in alpinen Tälern - Weiterentwicklung von Methoden zur Modellierung der langfristigen Sohlagenentwicklung und zur Ermittlung von Hochwassergefahren in inneralpinen Tälern, Ph.D. thesis, Univ. of Innsbruck, Innsbruck, Austria, 331 p, (in German).
- Koll, K. (2012), Untersuchungen des Geschiebetransports auf statischen Deckschichten, Ph.D. thesis, Univ. Carolo-Wilhelmina zu Braunschweig, Braunschweig, Germany, 146 p., (in German).
- Lamb, M. P., W. E. Dietrich, and J. G. Venditti (2008), Is the critical Shields stress for incipient sediment motion dependent on channel-bed slope?, *J. Geophys. Res.*, 113, F02008, doi: 10.1029/2007JF000831
- Lenzi, M. A., L. Mao, and F. Comiti (2004), Magnitude-frequency analysis of bed load data in an Alpine boulder bed stream, *Water Resour. Res.*, 40, W07201, doi: 10.1029/2003WR002961
- Mao, L., A. Dell'Agnese, C. Huincache, D. Penna, M. Engel, G. Niedrist and F. Comiti, (2014), Bedload hysteresis in a glacier-fed mountain river, *Earth Surf. Proc. Land.*, 39, 964–976, doi: 10.1002/esp.3563
- Melton, M.A., (1957) An analysis of the relations among elements of climate, surface properties, and geomorphology. *Technical Report 11 389-042*. Office of Naval Research, Dep. Of Geology, Columbia University, New York.
- Parker, G., and P. C. Klingeman (1982), On why gravel bed streams are paved, *Water Resour. Res.*, 18(5), 1409-1423.
- Parker, G., P. C. Klingeman, and D. G. Mclean (1982), Bedload and size distribution in paved gravel-bed streams, *J. Hydraul. Div. Am. Soc. Civ. Eng.*, 108(4), 544–571
- Recking, A. (2010), A comparison between flume and field bed load transport data and consequences for surface-based bed load transport prediction, *Water Resour. Res.*, 46, W03518, doi: 10.1029/2009WR008007
- Recking, A. (2012), Bedload transport in rivers: from the flume to the field, Habilitation dissertation, Univ. of Grenoble, Grenoble, France, 88 p. Available from the Internet: <http://www.irstea.fr/recking>
- Schneider, J. M., J. M. Turowski, D. Rickenmann, R. Hegglin, S. Arrigo, L. Mao and J. W. Kirchner (2014), Scaling relationships between bed load volumes, transport distances, and stream power in steep mountain channels, *J. Geophys. Res.-Earth*, 119, doi: 10.1002/2013JF002874
- Schneider, J. M., D. Rickenmann, J. M. Turowski, K. Bunte, and J. W. Kirchner (2015), Applicability of bed load transport models for mixed size sediments in steep streams considering macro-roughness, *Water Resour. Res.*, 51, 5260-5283, doi: 10.1002/2014WR016417
- Sommer, N., and H. Lauffer (1982), Untersuchungen über den Feststofftransport in Gebirgsbächen der Ostalpen (Sediment transport in mountain streams of the Eastern Alps), in *Proceedings of the 14th International Dam Conference*, Rio de Janeiro, Brazil.

- Steidl, B. (2015). Deckschichtentwicklung und Auswirkung externer Geschiebezugabe auf die Sohlmorphologie und die Fließgeschwindigkeit bei Wildbächen, Master thesis. Univ. of Innsbruck, Innsbruck, Austria, (in German).
- Schumm, S.A., (1954), The relation of drainage basin relief to sediment loss, *Int. Assoc. Hydrol. Sci.* 36, 216-219.
- Turowski, J. M., E. M. Yager, A. Badoux, D. Rickenmann, and P. Molnar (2009), The impact of exceptional events on erosion, bed load transport and channel stability in a step-pool channel, *Earth Surf. Proc. Land.*, 34, 1661-1673, doi: 10.1002/esp.1855.
- Yager, E. M., J. W. Kirchner, and W. E. Dietrich (2007), Calculating bed load transport in steep boulder bed channels, *Water Resour. Res.*, 43, W07418, doi: 10.1029/2006WR005432

E LIST OF FIGURES AND TABLES

E.1 List of Figures

Chapter B Long-term dynamics of bed load transport in steep mountain streams

| | |
|---|----|
| Figure B-1: Examples of the water intake structures analyzed in this thesis with a) the Oberbergbach, b) the Pitzbach, c) the Laengentalerbach, and d) the Schoentalbach water intake structure of TIWAG | 15 |
| Figure B-2: Location of the field sites - western part. The water intake structures belong to the Kaunertal hydropower station of TIWAG. | 17 |
| Figure B-3: Location of the field sites - eastern part. The water intake structures belong to the hydropower station Sellrain-Silz of TIWAG | 18 |
| Figure B-4: Schematic ground plan of a water intake structure operated by TIWAG..... | 20 |
| Figure B-5: Schematic longitudinal view of the settling basin of a water intake structure operated by TIWAG21 | |
| Figure B-6: Example of the continuous discharge data with a temporal resolution of 15min..... | 22 |
| Figure B-7: Differences of annual counts of hydraulic flushings either determined from the logbook or the discharge hydrograph | 22 |
| Figure B-8: Absolute difference of mean annual count of hydraulic flushings, determined either manually from the discharge hydrographs (N_{hyd}) or from the logbook (N_b), plotted against the mean of the logbook data | 30 |
| Figure B-9: Longitudinal profiles of the sediment deposition in the settling basin of the Pitzbach according to Hofer (1985). The data are separated into three groups, depending on the mean discharge since the previous hydraulic flushing. | 31 |
| Figure B-10: The deposit volume in the settling basin (a) and the scaling factors (b) plotted against the mean water discharge (Qmean) since the last hydraulic flushing (reanalyzed from Hofer, 1985). | 32 |
| Figure B-11: Uncertainty of annual bed load volumes of all study sites | 33 |
| Figure B-12: a) Submerged specific weight plotted against deposit height and b) boxplot of $\gamma'_{z,sed}$, separated according to the four load membranes (mem 1 to mem 4); the data are based on the measurements conducted in the years 1979 to 1983 by Hofer (1985). | 38 |
| Figure B-13: a) Submerged specific weight plotted against deposit height and b) boxplot of $\gamma'_{z,sed}$, separated according to the four load membranes (mem 1 to mem 4); data are based on the measurements conducted in the years 1994 and 1995 (TIWAG, unpublished) | 39 |
| Figure B-14: a) Time series of the maximum deposit height at the time a hydraulic flushing was initiated (red dots) and the theoretical triggering height (180 cm) at the Pitzbach settling basin. The maximum deposit heights were back-calculated from the vertical stress measured by the four membranes and by solving equation B12 iteratively; b) year wise boxplots of maximum deposit heights..... | 40 |
| Figure B-15: Longitudinal profile of back-calculated deposit heights along the settling basin of the Oberbergbach: a) using the original attribution of load membranes and b) changing membrane #2 and #3. The latter is much more plausible since a bimodal deposition was never observed in course of the field surveys. | 41 |
| Figure B-16: a) The calibration factor $\gamma'_{z,sed}$ (which is determined by the ratio of vertical stress and deposit height) is plotted against deposit height and b) boxplot of derived values separated according to the four load membranes (mem 1 to mem 4); data of deposit heights are based on the field measurements conducted in summer 2015, while vertical stress was recorded automatically by TIWAG | 42 |
| Figure B-17: Geometry of the water intake structures | 43 |
| Figure B-18: Longitudinal profile of the accumulated sediment in the settling basin of the Pitzbach water intake structure | 44 |
| Figure B-19: Comparison of calculated volumes obtained by using all data of deposit heights (x-axis) or only those which are located at the load membranes (y-axis)..... | 45 |
| Figure B-20: Location (left) and characteristic grain sizes (right) of the sediment samples of Strobl (1980)...46 | |
| Figure B-21: Mean longitudinal profile of deposit height and characteristic grain sizes in the settling basin of the Pitzbach on 5 th August 2015 | 46 |

| | |
|---|----|
| Figure BB-22: Comparison of calculated bed load volumes obtained by using all data of deposit height (x-axis) or only those four which are located at the weighing membranes (y-axis); in contrast to Figure B19 volumes refer to bed load only, neglecting any sediment accumulation in the lower half of the settling basin..... | 47 |
| Figure B-23: Mean longitudinal profile of deposit height and characteristic grain sizes in the settling basin of the Oberbergbach on 24 th July 2015 | 47 |
| Figure B-24: a) The calibration factor $\gamma_{z, \text{sed}}$ plotted against deposit height and b) the histogram of the residuals; all data refer to the Pitzbach only..... | 50 |
| Figure B-25: Longitudinal profiles of deposit height based on 10,000 realisations in which the calibration factor $\gamma_{z, \text{sed}}$ varies according to a normal distribution with a standard deviation of 0.29; a) total sediment deposition and b) sediment accumulation that is attributed to bed load only..... | 52 |
| Figure B-26: Uncertainty range of the bed load volume determined by four weighing membranes; the scenario comprises the sediment deposition on 25 th July 2015 in the settling basin of the Oberbergbach water intake structure | 52 |
| Figure B-27: Time series of bed load accumulation within the settling basin and total water discharge at the water intake structure of the Oberbergbach..... | 53 |
| Figure B-28: The time series of bed load volumes at the Oberbergbach is split into the group (i) which already features a monotonic increase (blue rectangles) and (ii) which needs to be smoothed acc. equation B25 and B26 (red dots) to get non-negative transport rates | 55 |
| Figure B-29: Scheme of the algorithm that determines if the time series of bed load accumulation is monotonically increasing at a certain time (equation B23) | 55 |
| Figure B-30: Scheme of the algorithm that smooths the time series to get a monotonic increasing graph (equation B25 and B26)..... | 56 |
| Figure B-31: Water intake structure at the Oberbergbach with the water discharge slightly exceeding the design discharge of 5.5 m ³ /s | 57 |
| Figure B-32: Bed load transport rates at given times at the Oberbergbach determined by either the field measurements (with bed load traps acc. <i>Bunte et al., 2004</i>) or the bed load accumulation in the settling basin. The transport rates are plotted against the discharge measured at the study site, respectively. | 60 |
| Figure B-33: Conformity of bed load transport rates at the Oberbergbach either determined by field measurements (with bed load traps acc. <i>Bunte et al. (2004)</i>) or by bed load accumulation in the settling basin | 60 |
| Figure B-34: Physical scale model of a bottom rack intake at which the efficiency in trapping bed load is investigated..... | 68 |
| Figure B-35: Scheme of the experimental setup..... | 68 |
| Figure B-36: Proportion of total bed load that overpassed the bottom rack intake | 69 |
| Figure B-37: Size-specific proportion of overpassing grains determined by using either sediment of uniform size or a sediment mixture | 70 |
| Figure B-38: Flow structures in the intake channel at a) flows barely exceeding the design discharge and b) sufficiently larger than the design discharge | 70 |
| Figure B-39: Grain size distribution (left) and characteristic grain sizes (right) at the sample site 1 of the Oberbergbach | 77 |
| Figure B-40: Characteristic grain sizes of the converted transect-by-number grain size distributions divided by the reference size from the Wolman count: dots represent the mean of all four (2x2) field sites and the error bars represent the standard deviations | 77 |
| Figure B-41: Grain size distribution (left) and characteristic grain sizes (right) in the flume ($S=0.1$ m/m) that was exposed to 15 l/s while sediment starving..... | 78 |
| Figure B-42: Characteristic grain sizes of the converted transect-by-number grain size distributions divided by the reference size of the Wolman count: dots represent the mean of all flume samples and the error bars represent the standard deviations | 78 |
| Figure B-43: Illustration of two possibilities to fit a bed load transport equation to measured data: adjusting the pre-factor k (left) or the reference parameter (right) | 82 |
| Figure B-44: a) Bed load transport rates plotted in terms of non-dimensional bed load transport intensity and relative shear stress (acc. <i>Schneider et al., 2015a</i>) with the rating curve according to equation B37 and b) bed load transport rate plotted against relative discharge with equation B42 fitted by eye to both, the | |

| | |
|---|-----|
| Pitzbach (historic data) and the Laengentalerbach (Lb #2) data. The data are given in Table B13 in section B.1.5 | 85 |
| Figure B-45: Bed load transport rate plotted against water discharge. Dots refer to the Laengentalerbach, where Lb #1 (a short low-gradient reach with $S=0.04 \text{ m/m}$) was about 50 m downstream of Lb #2 ($S=0.069 \text{ m/m}$); triangles represent the data of the Oberbergbach, where Ob #1 ($S=0.076 \text{ m/m}$) is immediately upstream of the water intake structure and Ob #2 ($S=0.02 \text{ m/m}$) is a long, low-gradient reach approx. 800 m upstream of Ob #1. The data are given in Table B13 in section B.1.5 | 87 |
| Figure B-46: Box and whiskers plot of the specific mean annual bed load volume ($\text{spec.mABV} = \text{mABV} / \text{CS}$). The data are separated according a) the catchment size and b) the relative glacier area, with n the number of data each class are. The unit of spec.mABV is m^3/km^3 with m^3 referring to solid density without pores..... | 89 |
| Figure B-47: Comparison between calculated and observed mean annual bed load volumes (ABV)..... | 90 |
| Figure B-48: a) Probability distribution and b) kernel density estimation (smoothed histogram) of ABV of all 20 sites..... | 91 |
| Figure B-49: Certain percentiles generated from the fitted probability distributions and divided by the same percentiles of the empiric distribution (measured data) | 92 |
| Figure B-50: Correlation and regression analysis of the parameter estimates μ (a) and σ (b) of the log-normal probability distribution with topographic parameters of the field sites..... | 93 |
| Figure B-51: Certain percentiles generated from the a) fitted log-normal probability distribution (identical to Figure B49) and b) estimated log-normal probability distribution (equation B48 and B49) divided by the observed percentiles..... | 94 |
| Figure B-52: a) Box plot of the annual transport efficiency for each site. The sites (x-axis) are ordered according to the mean specific annual bed load volume (m^3/km^2), and b) the standard deviation of log-transformed K (sd of $\log(K)$) plotted against mean annual transport efficiency (mK); the black line represents a linear regression, with the four outliers (blue triangles) neglected..... | 95 |
| Figure B-53: Geometric mean transport efficiency K plotted against a) catchment size (data reveal no correlation) and b) relative glacier area with a significant exponential regression fitted to the data | 96 |
| Figure B-54: Geometric mean transport efficiency K plotted against a) mean gradient of the reach immediately upstream of the water intake structure ($meanRG$), b) mean gradient of the stream draining two third of the total catchment ($meanSG$), c) standard deviation of stream gradient ($sdsG$) and d) the 10 th percentile of stream gradient. Dashed lines represent non-significant trends including all data, while solid lines refer to significant trend lines excluding outliers (blue diamonds with site names) with the p -value of the coefficient of the explanatory variable smaller than 0.05, respectively. Regression equations are only given for significant trends | 97 |
| Figure B-55: Annual flow competence is standardized by the site-specific median and plotted against time. The data are separated according to the relative glacier area of the field sites (G) with a) no glacier in the catchment upstream of the water intake structure, b) $0 < G < 0.2$ and c) $G > 0.2$ | 98 |
| Figure B-56: Annual transport efficiency is standardized by the site-specific median and plotted against time. The data are separated according to the relative glacier area of the field sites (G) with a) no glacier in the catchment upstream of the water intake structure, b) $0 < G < 0.2$ and c) $G > 0.2$ | 98 |
| Figure B-57: Annual transport efficiency plotted against the corresponding annual flow competence, with both parameters standardized by their site-specific medians | 99 |
| Figure B-58: Bed load transport rates of three different sites (a, b, c) plotted against relative discharge. The rate of change is similar as assumed by equation B43a with an exponent of 6.44 (dashed line is fitted by eye)..... | 100 |
| Figure B-59: Annual transport efficiency plotted against the corresponding annual flow competence, with both parameters standardized by their site-specific medians for a) the field sites with low and moderate mK and a relative glacier area $G < 0.2 \text{ km}^2/\text{km}^2$ and b) the field sites with large mK and a relative glacier area $G > 0.2 \text{ km}^2/\text{km}^2$ | 101 |
| Figure B-60: Time series of annual transport efficiency (black) with the whiskers representing the error acc. equation B7 in section 1.1.5.5 and standardized annual peak discharge (red line) for three different sites with increasing mean transport efficiency from a) to f) (see Figure B52): a-b) the Mittertalbach and the Schoentalbach represent supply limited mountain streams without obvious morphologic changes during the last decades; but nevertheless, the yearwise transport efficiency fluctuates strongly; c) the transport efficiency of the Langentalerbach reveals cyclic patterns which are attributed to sporadic sediment pulses from a small tributary channel immediately upstream of the water intake structure; d) the temporal evolution of the transport efficiency at the Tscheybach is very homogeneous which indicates a yearwise | |

| | |
|--|-----|
| consistent relation between discharge and transport rate; e-f) the intensively glaciated Pitzbach and Oberbergbach feature overall large transport efficiencies with low scatter..... | 102 |
| Figure B-61: Temporal evolution of the transport efficiency at the Kraspesbach. The strong increase of K in the year 2002 is attributed to an exceptional event which caused large relocations of sediment from the hillslopes in the river..... | 103 |
| Figure B-62: Ratio of the log-transformed standard deviations of calculated annual bed load volumes (multiplying mean transport efficiency (mK) and annual cumulative flow competence) and the standard deviation of observed annual bed load volumes. A ratio larger than unity means that the calculated bed load volumes are more variable than the observed ones..... | 105 |
| Figure B-63: Relationship between dimensionless discharge and dimensional velocity scaled by the D_{84} of the bed surface grain size distribution..... | 109 |
| Figure B-64: Overview of the Oberbergbach and the basin that contributes to the runoff at the water intake structure..... | 113 |
| Figure B-65: Longitudinal profile of the bed level and the bed gradient of the Oberbergbach..... | 113 |
| Figure B-66: Overview of Pitzbach and the basin that contributes to the runoff at the water intake structure | 114 |
| Figure B-67: Longitudinal profile of the bed level and the bed gradient of the Pitzbach..... | 115 |
| Figure B-68: Bed load transport rate determined by means of the time series of bed load accumulation within the settling basin of a) the Oberbergbach and b) the Pitzbach water intake structure (see section B.1.4). The data of these plots refer to the period a) 2008 to 2010 and b) 2002 to 2004. For comparison, bed load transport rate measured with the bed load traps in the summer seasons 2014 and 2015 (see section B.1.5) and those of Hofer (1985) are additionally included..... | 116 |
| Figure B-69: Selected bed load transport rate data for subsequent analysis (magenta crosses) of a) the Oberbergbach (period 2008 to 2010) and b) the Pitzbach (period 2002 to 2004). For comparison, the total data set is plotted in the background and thus, the visible black crosses correspond with the rejected data..... | 117 |
| Figure B-70: Bed load transport rate plotted against discharge, with the geometric means (green dots) and 5 % and 95 % quantiles (red dots) of the binned data and the fitted, piecewise regressions | 121 |
| Figure B-71: a) Probability density distribution and b) cumulative probability distribution of the observed of bed load transport rates and the fitted lognormal and gamma distribution for two discharge bins and the two field sites. The cumulative probability distributions of the observed Q_b are plotted those of the fitted lognormal and the fitted gamma distribution in c) (PP-plots)..... | 123 |
| Figure B-72: Variation of the standard deviation of a) bed load transport rate Q_b [kg/s] and b) log-transformed bed load transport rate with discharge for each bin. The left plots refer to the Oberbergbach data and the right plots to the Pitzbach data..... | 124 |
| Figure B-73: a) Year-wise, power law rating curves for discharges exceeding breakpoint 1 and falling below breakpoint 2; b-c) the coefficients of the year-wise power functions plotted against each other either in terms of absolute values (b) or standardized by the median (c)..... | 127 |
| Figure B-74: Q - Q_b plots of year-wise segregated data in combination with the binned means of month-wise data (colored dots) and the corresponding month-wise rating curves (colored lines) | 128 |
| Figure B-75: Boxplot of the month-wise determined $a_{a,m}$ which were standardized by their year-wise median; the red dots represent the arithmetic mean, the bold black line the median, the grey boxes include the 25 % and 75 % percentiles and the whiskers extend to the minimum and maximum..... | 129 |
| Figure B-76: Binned means of the Q - Q_b relation with month-wise separated data. In the left plots the entire data set, comprising several years of observation, is used, while the Q and Q_b data are restricted to the overlapping years (1998, 1999 and 2001) in the right plots..... | 133 |
| Figure B-77: Rating curves of dimensionless shear stress (τ^*) and specific bed load transport rate (q_b) determined according a simplified version of the threshold-based Meyer-Peter and Müller (1949) equation (MPM; equation B62) and the reference-based Wilcock and Crowe (2003) equation (WC). Both equations were applied to uniform sized sediment with a grain size 0.05 m and an energy slope of 0.02 m/m; the rating curves are plotted in log scale (a) and liner scale (b)..... | 137 |
| Figure B-78: Longitudinal profile of bed level and bed gradient of the Oberbergbach..... | 139 |
| Figure B-79: Study reaches at the Oberbergbach with a-b) site 1 ($S=0.076$ m/m) at low flow, c-d) site 2 at low-moderate flow before (c) and after a flood event (d) in August 2014 | 140 |
| Figure B-80: Grain size distributions upstream of the water intake structure of the Oberbergbach; $b.g.$ is the bed gradient..... | 140 |
| Figure B-81: Longitudinal profile of the Pitzbach upstream of the water intake structure | 141 |

| | |
|---|-----|
| Figure B-82: Field site of the Pitzbach, featuring a homogeneous boulder bed reach (a), and it is located upstream of the water intake structure (b)..... | 141 |
| Figure B-83: Study reaches at the Laengentalerbach with a-b) site 1 ($S=0.04 \text{ m/m}$) at low flow and site 2 ($S=0.069 \text{ m/m}$) at low (c) and high flow (d) | 142 |
| Figure B-84: Grain size distributions upstream of the water intake structure of the Laengentalerbach; b.g. is the bed gradient..... | 143 |
| Figure B-85: Reference transport method applied to the study site 2 of the Oberbergbach: a) plot of W_i^{**} against τ_i^{**} with the fitted power function of step 3, b) the hiding function obtained by fitting observed $\tau_{r,i}^{**}$ against D/D_{50} and c) plot of W_i^{**} against $\tau_i^{**}/\tau_{r,i}^{**}$ with the collapse of the fractional bed load transport data..... | 147 |
| Figure B-86: Comparison of calculated Q-U rating curves with discrete measurements for a) site 1 and b) site 2 of the Oberbergbach, c) site 2 of the Laengentalerbach and d) site 1 of the Pitzbach. | 149 |
| Figure B-87: a) Dimensionless reference shear stress ($\tau_{r,D50}^*$) and b) dimensionless effective reference shear stress ($\tau_{e,D50}^*$) plotted against bed slope. The black, dashed line is the power function given in Schneider et al. (2015) and the red line is a fitted power function with respect to both data sets..... | 150 |
| Figure B-88: Collapse of dimensionless fractional bed load transport rates with the shear stress ratio. The red line is a power function with the median of site-specific exponents. The violet dashed line is the bed load transport function of Schneider et al. (2015) in combination with the dimensionless reference shear stress and the hiding exponent derived in this study. The black dotted line represents the breakpoint between the lower and upper bed load transport regime according to Schneider et al. (2015)..... | 152 |
| Figure B-89: $\tau_{r,D50}^*$ (a), $\tau_{e,D50}^*$ (b), and $q^*_{c,D50}$ (c) plotted against bed slope. The red lines in (b) and (c) are fitted power functions and the black, dashed lines correspond to equations from literature: a) $r_c^*=0.15S^{0.25}$ (Lamb et al., 2008; based on flume and field data) and c) $q^*c=0.13S^{-1.15}$ (Bathurst, 2013; based on flume data with uniform sized sediment)..... | 153 |
| Figure B-90: $\tau_{r,ci}^*$ (a) and $\tau_{e,ci}^*$ (b) as a function of D/D_{max} for the three study sites Ob #1, Lb #1 and Pb #1. The red line is the fitted power function, the dashed line refers to equal mobility and the dotted line to full size-selective mobility..... | 154 |
| Figure B-91: q^*_{ci} as a function of D/D_{max} for all study sites. The red line is the fitted power function, the dashed line refers to equal mobility and the dotted line to full size-selective mobility with $b=0$ | 155 |
| Figure B-92: Differences between τ_x^* whether it is determined with the reference transport method (τ_r^*) or the flow competence method (τ_c^*) | 158 |
| Figure B-93: Comparison between discharge based hiding exponent b and shear stress based β , with a) total and b) effective dimensionless shear stress. | 160 |
| Figure B-94: a) Representative cross section of the stream reach enclosing upstream of the water intake structure at the Oberbergbach and b) the corresponding grain size distribution of the bed surface sediment | 164 |
| Figure B-95: a) Representative cross section of the stream reach enclosing upstream of the water intake structure at the Pitzbach and b) the corresponding grain size distribution of the bed surface sediment | 165 |
| Figure B-96: Schematic illustration of the distributed 1d approach | 167 |
| Figure B-97: Rating curves obtained for the Oberbergbach by means of the four formulae associated with total bed load transport rate in combination with the hydraulic approach a) fully 1d and b) distributed 1d..... | 171 |
| Figure B-98: Rating curves obtained for the Pitzbach by means of the four formulae associated with total bed load transport rate in combination with the hydraulic approach a) fully 1d and b) distributed 1d..... | 171 |
| Figure B-99: Rating curves obtained for the Oberbergbach by means of the two formulae associated with fractional bed load transport rate in combination with the hydraulic approach a) fully 1d and b) distributed 1d | 172 |
| Figure B-100: Rating curves obtained for the Pitzbach by means of the two formulae associated with fractional bed load transport rate in combination with the hydraulic approach a) fully 1d and b) distributed 1d..... | 172 |
| Figure B-101: Rating curves obtained with the Schneider et al. (2015) approach by using the fitted $\tau_{r,D50}^*$ | 173 |
| Figure B-102: Range of the bed surface D_{50} to obtain a collapse of observed and predicted bed load transport rates. The prediction is based on the Schneider et al. (2015) approach (equation B95) in combination with the fitted $\tau_{r,D50}^*$ | 174 |

Chapter C The feedback between supply and transport rate of mobile bed load in steep streams

- Figure C-1: Overview of the prototype reach (left) and the physical scale model (right); yellow lines in the leFigure C-2ft picture roughly feature the mobile bed boundaries and the flow section of the flume ..181
- Figure C-3: a) Longitudinal profile (thalweg) at the beginning of each experimental series and b) the corresponding grain size distribution of the bed surface; the procedure of initialization was the same for all four experimental series.....182
- Figure C-4: Sediment feeding at the upper end (dashed line) and measured bed load transport at the lower end of the flume (red circles) for two selected experimental runs of the series 'blue' (2.0 - 3.2 mm); circled numbers indicate different phases of response to sediment feeding188
- Figure C-5: a) Tracer velocity of the leading edge (which is defined by the flume length between input and outflow location divided by the duration of the lag phase) plotted against discharge and b) the non-dimensional propagation velocity ($u^*\tau$) plotted against Shields stress times feeding intensity ($\tau^*\tau \times \psi_T$), both with respect to the grain size supplied189
- Figure C-8: a) Ratio of mean bed load outflow during the equilibrium phase and feeding rate; b) 10th (black symbols and 90th percentiles (white symbols) of instantaneous bed load transport rates scaled by the corresponding medians (b).....190
- Figure C-9: Instantaneous bed load transport rates observed during the equilibrium phase of the experimental run a) 1 ($Q=2.5$ l/s), b) 2 ($Q=4.0$ l/s) and c) 3 ($Q=5.5$ l/s) of the series 'green'. Horizontal dashed lines indicate the 10th, median (bold) and 90th percentile of the instantaneous bed load transport rate190
- Figure C-10: a) Proportion of added sediment in the total bed load outflow; b) same as a) but separated into the feeding part (duration of sediment feeding plus one-third of feeding time) and the continued part of each experimental run with discharges smaller than 6.9 l/s.191
- Figure C-11: Total mass of bed load accumulation is split into its origin, the supplied material (lower, colored bar) and the bed material (upper, black bar). Each plot comprises the results of one entire experimental series with the experimental runs being ordered with increasing discharge (Table C28).192
- Figure C-12: Upper row: samples of total bed load taken at the end of the feeding part of the 5.5 l/s runs of a) the series 'green' (1.0 – 2.0 mm), b) series 'blue' (2.0 – 3.2 mm) and c) series 'red' (3.2 – 5.6 mm); lower row: grain size distribution obtained by sieving and post-correction (see section 1.2.3.3).....193
- Figure C-13: Upper row: samples of total bed load taken at the end of the continued part of the 5.5 l/s runs of a) series 'green' (1.0 – 2.0 mm), b) series 'blue' (2.0 – 3.2 mm) and c) series 'red' (3.2 – 5.6 mm); lower row: grain size distribution obtained by sieving (see section 1.2.3.3).....193
- Figure C-14: a) Diameter for which 84 % of total bed load transport is finer; with the D_{84} of the bulk sediment (dotted line) and the bed surface (grey bar) and b) grain size distributions of total bed load transport obtained within the experimental series 'mixture' (0.5 - 5.6 mm).....194
- Figure C-15: Evolution of the bed surface during the experimental run 1 with 4 l/s water discharge and the blue colored sediment (2.0 - 3.2 mm); a) initial condition (self-stabilized bed surface); b) during the equilibrium phase; c) at the end of the continued part.....195
- Figure C-16: a) Grain size distribution of the bed surface at the end of four runs of the experimental series 'mixture' (0.5 - 5.6 mm) and b) characteristic diameters of the bed surface (chronology is left to right); grain size distributions were assessed in a rather small area compared to those illustrated in Figure C104195
- Figure C-17: Displacement of coarse surface grains which were relocated (displaced) further or less than one diameter in length during the experimental runs with discharge smaller or equal 6.9 l/s of a) the series 'green' (1.0 - 2.0 mm), b) series 'blue' (2.0 - 3.2 mm), c) series 'red' (3.2 - 5.6 mm) and d) the series 'mixture' (0.5 - 5.6 mm).....196
- Figure C-18: Dimensionless propagation velocity ($u^*\tau$) plotted against macro-roughness corrected Shields stress ($\tau^*\tau$) times the dimensionless feeding rate (ψ_T); literature data on propagation velocity were obtained by graph reading, while $\tau^*\tau$ and ψ_T were determined by the scheme given in section 1.2.4, assuming uniform flow.....197
- Figure C-19: Photograph of the bed surface taken during the equilibrium phase of the experimental run 1 of the series 'blue' (2.0 - 3.2 mm)198
- Figure C-20: Arbitrary dependence of the hiding exponent b on the embedding of the bed surface205
- Figure C-21: Illustration of the chronology and boundary conditions of the experimental runs that are accomplished within one experimental series of the feeding experiments.....207

- Figure C-22: Bed load feeding at the upper flume end (dashed line) and measured bed load transport at the lower end of the flume (red circles) for two selected experimental runs of the series #2; circled numbers indicate different phases of response to feeding.....209
- Figure C-23: Illustration of the chronology and the boundary conditions of the experimental runs that are accomplished within one experimental series of the armoring experiments.....210
- Figure C-24: a) Bed material erosion: sediment is eroded from the active layer which is immediately filled up to the constant thickness $x [m]$ by the sediment of the bed layer; b) bed load aggradation: bed load is added to the active layer and bed material of the active layer is released to the bed layer in order to maintain the constant thickness of $x [m]$ 218
- Figure C-25: a) Bed material erosion at $q < q_{c,D50}$: sediment is removed from the active layer without any interactions with the bed layer as long as H_a is larger than $0.5D_{84}$ (dotted lines); otherwise the active layer is refilled to $0.5D_{84}$ by the sediment of the bed layer; b) bed material erosion at $q > q_{c,D50}$: sediment is removed from the active layer and the active layer is partly filled up by the bed material of the bed layer; c) bed load aggradation: sediment is added to the active layer and once the active layer thickness is larger than $1.1D_{84}$ (dashed lines), the surplus is transferred to the bed layer.....220
- Figure C-26: The critical specific discharge of the i th grain size depending on the embedding222
- Figure C-27: Illustrative scheme of the different layers of the new mixing concept 3. The active surface layer (ASL) is the uppermost part of the active layer (AL). The inflowing and outflowing bed load is balanced in both of these layers separately. The balancing of the active layer is accomplished according to the mixing concept 2 (with a minimum (dotted line) and maximum thickness (dashed line) of H_a). The grain size distribution of the active layer is then used to determine the characteristic grain sizes of the bed surface (e.g. D_{50} , D_{84}). The thickness of the active surface layer (H_{asl}) depends on the flow strength. In the case of a surplus of sediment, the sediment is released into the active layer; otherwise it is taken from it. The grain size distribution of the active surface layer is then used to determine the availability (abundance) of each grain size fraction for bed load transport. The bed layer (BL) is of constant relative thickness and it balances the vertical exchange if the active layer reaches its lower or upper bound.224
- Figure C-28: Ratios of numerically modeled total bed load outflux and observed bed load volumes for the model realization 'Rickenmann (2001) bed load transport equation and mixing concept 1'; a) boxplots include all experimental runs (differing in discharge) of all four series (differing in grain size added) and b) only those experimental runs with discharges smaller or equal to the stabilizing discharge of 6.9 l/s are considered.226
- Figure C-29: Ratios of numerically modeled total bed load outflux and observed bed load volumes for the model realization 'Rickenmann (2001) bed load transport equation and mixing concept 2'. The boxplots include either a) all experimental runs of all four series or b) only those experimental runs with discharges smaller or equal to the stabilizing discharge of 6.9 l/s.227
- Figure C-30: Ratios of numerically modeled total bed load outflux and observed bed load volumes for the model realization 'Rickenmann (2001) bed load transport equation and mixing concept 3'. The boxplots include either a) all experimental runs of all four series or b) only those experimental runs with discharges smaller or equal to the stabilizing discharge of 6.9 l/s.228
- Figure C-31: Ratios of numerically modeled total bed load outflux and observed bed load volumes for the model realization 'Schneider et al. (2015) bed load transport equation' with the mixing concept a) 1, b) 2 and c) 3.229
- Figure C-32: Time series of bed load accumulation obtained at the lower end of the model. The numerical results (b₁ to b₄) are obtained with the Rickenmann (2001) bed load transport equation and the mixing concept 1. They refer to a) the experimental series #1 with supplied grain sizes 0.5 – 2.0 mm, b) the experimental series #2 (2.0 – 3.2 mm), c) the experimental series #3 (3.2 – 5.6 mm), and d) the experimental series #4 (0.5 – 5.6 mm). The time scale is nonlinear and orients on the feeding duration of each experimental run.231
- Figure C-33: Time series of bed load accumulation obtained at the lower end of the model. The numerical results (b₁ to b₄) are obtained with the Rickenmann (2001) bed load transport equation and the mixing concept 2. They refer to a) the experimental series #1 with supplied grain sizes 0.5 – 2.0 mm, b) the experimental series #2 (2.0 – 3.2 mm), c) the experimental series #3 (3.2 – 5.6 mm), and d) the experimental series #4 (0.5 – 5.6 mm). The time scale is nonlinear and orients on the feeding duration of each experimental run.233
- Figure C-34: Detailed view of the time series of bed load accumulation during the experimental runs 2, and 3 of series #1. The distinct breakpoints of observed bed load accumulation are highlighted by the red circles.234
- Figure C-35: Time series of bed load accumulation obtained at the lower end of the model. The numerical results (b₁ to b₄) are obtained with the Rickenmann (2001) bed load transport equation and the mixing

| | |
|--|-----|
| concept 3. They refer to a) the experimental series #1 with supplied grain sizes 0.5 – 2.0 mm, b) the experimental series #2 (2.0 – 3.2 mm), c) the experimental series #3 (3.2 – 5.6 mm), and d) the experimental series #4 (0.5 – 5.6 mm). The time scale is nonlinear and orients on the feeding duration of each experimental run..... | 235 |
| Figure C-36: Time series of bed load rate during series# 2 (2.0 – 3.2 mm) obtained with the Rickenmann (2001) bed load transport equation and a) the mixing concept 1, b) mixing concept 2, and c) mixing concept 3. The time scale is nonlinear and orients on the feeding duration of each experimental run. | 237 |
| Figure C-37: Ratio of numerically modeled and observed characteristic grain sizes of accumulated bed load, with a) the D_{50} and b) D_{84} . The numerical model results refer to the mixing concept 1 in combination with the Rickenmann (2001) bed load transport equation..... | 238 |
| Figure C-38: Ratio of numerically modeled and observed characteristic grain sizes of accumulated bed load, with a) the D_{50} and b) D_{84} . The numerical model results refer to the mixing concept 2 in combination with the Rickenmann (2001) bed load transport equation..... | 239 |
| Figure C-39: Ratio of numerically modeled and observed characteristic grain sizes of accumulated bed load, with a) the D_{50} and b) D_{84} . The numerical model results refer to the mixing concept 3 in combination with the Rickenmann (2001) bed load transport equation..... | 239 |
| Figure C-40: Numerically modeled and observed grain size distributions of accumulated bed load that are obtained during each experimental run of the series #4 (0.5 – 5.6 mm). The numerical model results (b ₁ to b ₅) refer to the mixing concept 3 in combination with the Rickenmann (2001) bed load transport equation. | 240 |
| Figure C-41: Numerically modeled and observed grain size distributions of the bed surface at to the end of the experimental runs 1 to 4 of the series #4 (0.5 – 5.6 mm). The numerical model results are obtained with the mixing concept 1 and the Rickenmann (2001) bed load transport equation. | 241 |
| Figure C-42: Numerically modeled and observed grain size distributions of the bed surface at to the end of the experimental runs 1 to 4 of the series #4 (0.5 – 5.6 mm). The numerical model results are obtained with the mixing concept 2 and the Rickenmann (2001) bed load transport equation. | 242 |
| Figure C-43: Numerically modeled and observed grain size distributions of the bed surface referring to the end of the experimental runs 1 to 4 of the series #4 (0.5 – 5.6 mm). The numerical model results are obtained with the mixing concept 3 and the Rickenmann (2001) bed load transport equation..... | 243 |
| Figure C-44: Ratios of numerically modeled and observed bed load volumes with respect to the model realization 'Rickenmann (2001) bed load transport equation and mixing concept 1' | 244 |
| Figure C-45: Ratios of numerically modeled and observed bed load volumes with respect to the model realization 'Rickenmann (2001) bed load transport equation and mixing concept 2' | 245 |
| Figure C-46: Ratios of numerically modeled and observed bed load volumes with respect to the model realization 'Rickenmann (2001) bed load transport equation and mixing concept 3' | 246 |
| Figure C-47: Ratios of numerically modeled total bed load outflux and observed bed load volumes for the model realization 'Schneider et al. (2015) bed load transport equation' with the mixing concept a) 1, b) 2 and c) 3. | 247 |
| Figure C-48: Time series of bed load accumulation obtained by numerical simulation with model realization 'Rickenmann (2001) bed load transport equation and the mixing concept 1'. The results refer to the at the lower end of the flume of a) the experimental series #1 with a flume gradient of 0.05 m/m and b) the experimental series #2 with a flume gradient of 0.1 m/m. | 249 |
| Figure C-49: Time series of bed load accumulation obtained by numerical simulation with model realization 'Rickenmann (2001) bed load transport equation and the mixing concept 2'. The results refer to the at the lower end of the flume of a) the experimental series #1 with a flume gradient of 0.05 m/m and b) the experimental series #2 with a flume gradient of 0.1 m/m. | 251 |
| Figure C-50: Time series of bed load accumulation obtained by numerical simulation with model realization 'Rickenmann (2001) bed load transport equation and the mixing concept 3'. The results refer to the at the lower end of the flume of a) the experimental series #1 with a flume gradient of 0.05 m/m and b) the experimental series #2 with a flume gradient of 0.1 m/m.... | 253 |
| Figure C-51: Time series of bed load accumulation of the experimental series #2 that is obtained by numerical simulations with the Schneider et al. (2015) bed load transport equation and the mixing concept a) 1, b) 2 and c) 3 | 255 |
| Figure C-52: Ratio of numerically modeled and observed characteristic grain sizes of accumulated bed load, with a) the D_{50} and b) D_{84} . The model results refer to the Rickenmann (2001) bed load transport equation and the mixing concept 1..... | 256 |

| | |
|--|-----|
| Figure C-53: Ratio of numerically modeled and observed characteristic grain sizes of accumulated bed load, with a) the D_{50} and b) D_{84} . The model results refer to the Rickenmann (2001) bed load transport equation and the mixing concept 2..... | 257 |
| Figure C-54: Ratio of numerically modeled and observed characteristic grain sizes of accumulated bed load, with a) the D_{50} and b) D_{84} . The model results refer to the Rickenmann (2001) bed load transport equation and the mixing concept 3..... | 257 |
| Figure C-55: D_{50} ratio of the accumulated bed load obtained by numerical simulations with the mixing concept a) 1, b) 2 and c) 3 in combination with the Schneider et al. (2015) bed load transport equation. | 258 |
| Figure C-56: Ratio of modeled and observed characteristic grain sizes of the bed surface (active layer), with a) the D_{50} and b) D_{84} . The model results refer to the Rickenmann (2001) bed load transport equation and the mixing concept 1 | 259 |
| Figure C-57: Bed surface grain size distributions (active layer) at the end of the runs with the largest discharge applied in a) series #1 and b) series #2. The model results are based on the Rickenmann (2001) bed load transport equation and the mixing concept 1. | 260 |
| Figure C-58: Ratio of modeled and observed characteristic grain sizes of bed surface (active layer), with a) the D_{50} and b) D_{84} . The numerical model results refer to the Rickenmann (2001) bed load transport equation and the mixing concept 2..... | 260 |
| Figure C-59: Bed surface grain size distributions (active layer) at the end of the runs with the largest discharge applied in a) series #1 and b) series #2. The model results are based on the Rickenmann (2001) bed load transport equation and the mixing concept 2. | 261 |
| Figure C-60: Ratio of modeled and observed characteristic grain sizes of bed surface (active layer), with a) the D_{50} and b) D_{84} . The numerical model results refer to the Rickenmann (2001) bed load transport equation and the mixing concept 3..... | 261 |
| Figure C-61: Bed surface grain size distributions (active layer) at the end of the runs with the largest discharge applied in a) series #1 and b) series #2. The model results are based on the Rickenmann (2001) bed load transport equation and the mixing concept 3. | 262 |
| Figure C-62: Bed surface at the end of run 12 of series #2: a) top down view and b) side view. The white line indicates the active layer thickness according to the numerical model | 262 |
| Figure C-63: D_{50} ratio of the bed surface obtained by numerical simulations with the mixing concept a) 1, b) 2 and c) 3 in combination with the Schneider et al. (2015) bed load transport equation..... | 263 |
| Figure C-64: Classification of the numerical model performance in reproducing the feeding experiments. The 14 numerical model applications differ regarding the hiding exponent b and/or the mixing concept; the definitions of the classes are given in Table C33. | 265 |
| Figure C-65: Classification of the numerical model performance in reproducing the armoring experiments with the Rickenmann (2001) bed load transport equation. The 14 numerical model applications differ regarding the hiding exponent b and/or the mixing concept; the definitions of the classes are given in Table C33. | 266 |
| Figure C-66: Classification of the numerical model performance in reproducing the armoring experiments with the Schneider et al. (2015) bed load transport equation. The 14 numerical model applications differ regarding the hiding exponent β and/or the mixing concept; the definitions of the classes are given in Table C33. | 267 |
| Figure C-67: Times series of a) bed load accumulation, b) active layer $D_{50}^{1.5}$ and c) $S_{red}^{1.5}$ during run 1 of series #2 of the feeding experiments. The model results refer to the Rickenmann (2001) bed load transport equation with the hiding function b_2 | 270 |
| Figure C-68: Times series of a) bed load accumulation and b) the hiding exponent for $D < D_{50}$ during run 1 of series #2 of the feeding experiments. The model results refer to the Rickenmann (2001) bed load transport equation with the mixing concept 2..... | 271 |

Chapter D Conclusion

| | |
|--|-----|
| Figure D-1: a) Cumulative probability and b) histogram of observed (acc. Sommer and Lauffer (1982), but in terms of solid volume) and estimated ABV at the Taschachbach..... | 280 |
| Figure D-2: Computed and observed bed load transport rates at the field site 2 of the Laengentalerbach are plotted against the water discharge. The computation is based on the Schneider et al. (2015) equation but with a fitted value of $r_{r,D50}^{**}$ that reproduces the mean annual bed load volume if the equation is applied to the mean annual discharge hydrograph. The fitting procedure is independent of the in-measurements. | 283 |

E.2 List of Tables

Chapter B Long-term dynamics of bed load transport in steep mountain streams

| | |
|---|----|
| Table B-1: List of main characteristics of the study sites – part 1..... | 19 |
| Table B-2: List of main characteristics of the study sites – part 2..... | 19 |
| Table B-3: Annual counts of hydraulic flushings at the water intake structures of the hydropower station Sellrain-Silz. The left (first) number refers to the annual count of hydraulic flushings which were triggered automatically by exceeding a predefined deposit height and the right (second) number represents the manually triggered flushings. In case the second number is replaced by ‘–’, the count data were derived from the discharge hydrograph rather than the logbook. In years with no data, the annual counts of hydraulic flushings were either not available or they were rejected due to bad quality..... | 23 |
| Table B-4: Annual counts of hydraulic flushings at the water intake structures of the Kaunertal hydropower station. The left (first) number refers to the annual count of hydraulic flushings which were triggered automatically by exceeding a predefined deposit height and the right (second) number represents the $\sigma = \sqrt{D_{84}/D_{16}}$ manually triggered flushings..... | 24 |
| Table B-5: Summary of the large data set of the annual count of hydraulic flushings and the parameters necessary to determine the mean bed load volume per flushing. Definitions are as follows: Q_A , design discharge of the water intake structure; dh , deposit height at which the hydraulic flushing is initiated; tV , volume in case the settling basin is evenly filled up to dh ; sf , scaling factor; dV , volume of the sediment deposition; bV , bed load volume without pores. | 27 |
| Table B-6: Annual bed load volumes at the water intake structures of the Kaunertal hydropower station. In years with no data, the annual counts of hydraulic flushings were either not available or they were rejected due to bad quality. The data refer to the solid volume without pores. To obtain the deposit volume, the solid volume has to be divided by 0.7 (see Table B5). | 28 |
| Table B-7: Annual bed load volumes at the water intake structures of the hydropower station Sellrain-Silz. In years with no data, the annual counts of hydraulic flushings were either not available or they were rejected due to bad quality. The values refer to the solid volume without pores. To obtain the deposit volume, the solid volume has to be divided by 0.7 (see Table B5). | 29 |
| Table B-8: Period in which reliable discharge data are available for subsequent analysis. The temporal resolution of discharge records is 15 minutes..... | 35 |
| Table B-9: Data of sediment weight (vertical stress) used for subsequent analysis | 36 |
| Table B-10: Summary of all parameters used to determine the deposit volume of either the total sediment or only the bed load, based on the deposit height at six integration points and the corresponding five subsections (Figure B-17) | 49 |
| Table B-11: Overview of reach characteristics of the study sites at the Ob: Oberbergbach, Lb: Laengentalerbach and Pb: Pitzbach, with the bed surface grains sizes of which 50 % ($D_{50,S}$) and 84 % ($D_{84,S}$) are finer by weight..... | 62 |
| Table B-12: Bed surface grain size distribution of the five field sites, with the upper bound D_{ub} and the representative diameter D_r of the grain size class..... | 62 |
| Table B-13: Measurements of bed load transport rate, with the total flow width w_t at the measuring cross section, the active width associated with bed load transport w_a , the mean discharge during the measurement Q , the duration of the measurement md and the bed load transport rate extrapolated to the cross-section Q_b | 63 |
| Table B-14: Volume-by-weight proportion of fractional bed load transport, with the sieving range given in the headline. The ld enables for an attribution to the data presented in Table B-13..... | 64 |
| Table B-15: Characteristic measures of the bottom rack intakes considered in this study | 67 |
| Table B-16: Overview of the boundary conditions (grain size and discharge) and the bed load transport rate [kg/min; in model scale] of each experimental run | 69 |
| Table B-17: Methods used to convert the transect-by-number sample into a volume-by-weight distribution of the bed surface | 75 |
| Table B-18: List of main characteristics of the empiric population of annual bed load volumes of each site; the variables refer to the solid volume. To obtain the deposit volume (m^3) requires, the values need to be divided by 0.7 and to obtain the mass requires a multiplication with 2650 kg/m 3 , respectively. | 91 |
| Table B-19: Summary of discharge bins used to compare the cumulative probabilities of observed bed load transport rates at the Oberbergbach and the Pitzbach with fitted log-normal, and gamma probability | |

| | |
|---|-----|
| distributions. The abbreviations are as follows: gmQ_b , the geometric mean of bed load transport rates within a certain discharge bin; RMSE, the root mean squared error of observed and fitted the cumulative probabilities and r^2 , the coefficient of variations for the line of equality in the probability-probability plots. Bold numbers indicate the probability function with the better fit | 122 |
| Table B-20: Fitted power functions of the $Q-Q_b$ relations, with the r^2 and the discrepancy ratio X used to determine their performance | 125 |
| Table B-21: Comparison of the factors α_a and the exponents β_a from the year-wise regressions with the Oberbergbach data set in terms of significant differences: 1 refers to non-significant and empty cells to significant difference | 126 |
| Table B-22: Comparison of the factors α_a and the exponents β_a from the year-wise regressions with the Pitzbach data set in terms of significant differences: 1 refers to non-significant and empty cells to significant difference | 126 |
| Table B-23: Hydraulic geometry relations for flow velocity U , flow width w , hydraulic radius r_h and reduced energy gradient S_{red} | 149 |
| Table B-24: Dimensionless reference shear stress of the D_{50} and hiding exponent β determined either by means of total boundary shear stress or effective shear stress for each study site | 150 |
| Table B-25: Incipient motion of D_{50} , the hiding exponent and the coefficients of agreement obtained for each study site determined by either total boundary shear stress, effective shear stress or specific discharge. | 153 |
| Table B-26: The discharge associated with the critical shear stress or the critical specific discharge of the bed surface D_{50} and the duration of exceedance | 156 |
| Table B-27: The discharge associated with the reference shear stress of the bed surface D_{50} and the duration of exceedance..... | 157 |

Chapter C The feedback between supply and transport rate of mobile bed load in steep streams

| | |
|---|-----|
| Table C-1: Experimental program with all experimental series, which consist of successively performed runs, differing in water discharge. Parameter abbreviations are: discharge Q ; flume gradient S ; diameters of the bed surface of which 50 % ($D_{50,s}$) and 84 % ($D_{84,s}$) are finer and the median diameter of supplied sediment $D_{50,sup}$ | 183 |
| Table C-2: Flow hydraulics of every experimental run. Parameter abbreviations are: discharge Q ; mean bed slope S ; energy gradient S_e ; reduced energy gradient S_{red} ; flow width w ; flow depth d ; mean flow velocity u ; Froude number $Fr=u/(gd)^{0.5}$ | 187 |
| Table C-3: Experimental program with all experimental series which consist of successively performed runs, differing in water discharge. Parameter abbreviations are: discharge Q ; flume gradient S ; diameters of the bed surface of which 50 % ($D_{50,s}$) and 84 % ($D_{84,s}$) are finer, the median diameter $D_{50,sup}$ and the sorting coefficient of the surface (σ_s) and the supplied sediment (σ_{sup}) | 207 |
| Table C-4: Experimental program of the armoring experiments, which consist of two experimental series (differing in bed slope and grain size distribution) with successively performed runs (differing in water discharge). Parameter abbreviations are: discharge Q ; flume gradient S ; diameters of the bed surface of which 50 % ($D_{50,s}$) and 84 % ($D_{84,s}$) are finer by weight; the median diameter $D_{50,sup}$ of the supplied bed load and the sorting coefficient $\sigma = \sqrt{D_{84}/D_{16}}$ of the surface (σ_s) or the supplied sediment (σ_{sup})..... | 210 |
| Table C-5: Results of the armoring experiments with the total bed load transport that accumulated in the tailwater box during an experimental run BL , the total bed load transport normalized by the mass of supplied sediment re/BL (only for feeding experiments), the 50th and 84th percentile of the bed load's grain size distribution $D_{50,out}$ and $D_{84,out}$, the relative change of the bed surface D_{50} (RCD50) and D_{84} (RCD84) with respect to the initial condition of the experimental series (Table C-4), the standard deviation of the de-trended longitudinal profile σ_{lp} at the end of the run and the relative change of σ_{lp} ($RC_{\sigma_{lp}}$) and channel slope S (RCS) with respect to their initial values..... | 212 |
| Table C-6: Matrix of the thresholds for ranking each statistical descriptor of any parameter ratio (X), with the median P50 and the 25th (P25) and 75th percentile (P75)..... | 264 |
| Table C-7: Ranking matrix of the 14 numerical model applications with the Rickenmann (2001) bed load transport equation; '1' is associated with the best performance | 265 |
| Table C-8: Ranking matrix of the 14 numerical model applications with the Schneider et al. (2015) bed load transport equation; '1' is associated with the best performance | 267 |

Chapter D Conclusion

Table DD-1: Annual bed load volumes at the water intake structure of the Taschachbach (Pitztal, Austria) as reported by Sommer and Lauffer (1982).....279